

1D Nanomaterials 2011

Guest Editors: Yanqiu Zhu, Raymond L. D. Whitby, Renzhi Ma,
and Steve F. A. Acquah





1D Nanomaterials 2011

Journal of Nanomaterials

1D Nanomaterials 2011

Guest Editors: Yanqiu Zhu, Raymond L. D. Whitby,
Renzhi Ma, and Steve F. A. Acquah



Copyright © 2012 Hindawi Publishing Corporation. All rights reserved.

This is a special issue published in "Journal of Nanomaterials." All articles are open access articles distributed under the Creative Commons Attribution License, which permits unrestricted use, distribution, and reproduction in any medium, provided the original work is properly cited.

Editorial Board

Katerina Aifantis, Greece
Nageh K. Allam, USA
Margarida Amaral, Portugal
Xuedong Bai, China
L. Balan, France
Enrico Bergamaschi, Italy
Theodorian Borca-Tasciuc, USA
C. Jeffrey Brinker, USA
Christian Brosseau, France
Xuebo Cao, China
Shafiul Chowdhury, USA
Kwang-Leong Choy, UK
Cui ChunXiang, China
Miguel A. Correa-Duarte, Spain
Shadi A. Dayeh, USA
Ali Eftekhari, USA
Claude Estournes, France
Alan Fuchs, USA
Lian Gao, China
Russell E. Gorga, USA
Hongchen Chen Gu, China
Mustafa O. Guler, Turkey
John Zhanhu Guo, USA
Smrati Gupta, Germany
Michael Harris, USA
Zhongkui Hong, USA
Michael Z. Hu, USA
David Hui, USA
Y.-K. Jeong, Republic of Korea
Sheng-Rui Jian, Taiwan
Wanqin Jin, China
Rakesh K. Joshi, India
Zhenhui Kang, China

Fathallah Karimzadeh, Iran
Do Kyung Kim, Republic of Korea
Kin Tak Lau, Australia
Burtrand Lee, USA
Benxia Li, China
Jun Li, Singapore
Shijun Liao, China
Gong Ru Lin, Taiwan
J.-Y. Liu, USA
Jun Liu, USA
Tianxi Liu, China
Songwei Lu, USA
Daniel Lu, China
Jue Lu, USA
Ed Ma, USA
Gaurav Mago, USA
Santanu K. Maiti, Israel
Sanjay R. Mathur, Germany
A. McCormick, USA
Vikas Mittal, UAE
Weihai Ni, Germany
Sherine Obare, USA
Edward Andrew Payzant, USA
Kui-Qing Peng, China
Anukorn Phuruangrat, Thailand
Ugur Serincan, Turkey
Huaiyu Shao, Japan
Donglu Shi, USA
Suprakas Sinha Ray, South Africa
Vladimir Sivakov, Germany
Marinella Striccoli, Italy
Bohua Sun, South Africa
Saikat Talapatra, USA

Nairong Tao, China
Titipun Thongtem, Thailand
Somchai Thongtem, Thailand
Valeri P. Tolstoy, Russia
Tsung-Yen Tsai, Taiwan
Takuya Tsuzuki, Australia
Raquel Verdejo, Spain
Mat U. Wahit, Malaysia
Shiren Wang, USA
Yong Wang, USA
Ruibing Wang, Canada
Cheng Wang, China
Zhenbo Wang, China
Jinquan Wei, China
Ching Ping Wong, USA
Xingcai Wu, China
Guodong Xia, Hong Kong
Zhi Li Xiao, USA
Ping Xiao, UK
Shuangxi Xing, China
Yangchuan Xing, USA
N. Xu, China
Doron Yadlovker, Israel
Ying-Kui Yang, China
Khaled Youssef, USA
Kui Yu, Canada
William W. Yu, USA
Haibo Zeng, China
Tianyou Zhai, Japan
Renyun Zhang, Sweden
Yanbao Zhao, China
Lianxi Zheng, Singapore
Chunyi Zhi, Japan

Contents

ID Nanomaterials 2011, Yanqiu Zhu, Raymond L. D. Whitby, Renzhi Ma, and Steve F. A. Acquah
Volume 2012, Article ID 535697, 2 pages

Impact of Specifically Adsorbing Anions on the Electroless Growth of Gold Nanotubes, Falk Muench, Cornelia Neetzel, Stefan Lauterbach, Hans-Joachim Kleebe, and Wolfgang Ensinger
Volume 2012, Article ID 104748, 10 pages

Design and Construction of a One-Dimensional DNA Track for an Artificial Molecular Motor, Suzana Kovacic, Laleh Samii, Derek N. Woolfson, Paul M. G. Curmi, Heiner Linke, Nancy R. Forde, and Gerhard A. Blab
Volume 2012, Article ID 109238, 10 pages

Thermal Stability and Rheological Behaviors of High-Density Polyethylene/Fullerene Nanocomposites, Liping Zhao, Ping'an Song, Zhenhu Cao, Zhengping Fang, and Zhenghong Guo
Volume 2012, Article ID 340962, 6 pages

Effect of the on/off Cycling Modulation Time Ratio of C₂H₂/SF₆ Flows on the Formation of Geometrically Controlled Carbon Coils, Young-Chul Jeon, Jun-Ho Eum, Sung-Hoon Kim, Jung-Chul Park, and Sung Il Ahn
Volume 2012, Article ID 908961, 6 pages

Electrochemical Degradation Characteristics of Refractory Organic Pollutants in Coking Wastewater on Multiwall Carbon Nanotube-Modified Electrode, Yan Wang, Shujing Sun, Guifu Ding, and Hong Wang
Volume 2012, Article ID 614032, 5 pages

WPG-Controlled Quantum BDD Circuits with BDD Architecture on GaAs-Based Hexagonal Nanowire Network Structure, Hong-Quan ZHao and Seiya Kasai
Volume 2012, Article ID 726860, 6 pages

Plasmonic Properties of Vertically Aligned Nanowire Arrays, Hua Qi, O. J. Glembocki, and S. M. Prokes
Volume 2012, Article ID 843402, 7 pages

Carbon Nanotubes/Gold Nanoparticles Composite Film for the Construction of a Novel Amperometric Choline Biosensor, Baoyan Wu, Zhongmin Ou, Xiaojuan Ju, and Shihua Hou
Volume 2011, Article ID 464919, 6 pages

Electromagnetic Wave Interactions with 2D Arrays of Single-Wall Carbon Nanotubes, Taha A. Elwi and Hussain M. Al-Rizzo
Volume 2011, Article ID 709263, 7 pages

Carbide Nanoparticles Encapsulated in the Caves of Carbon Nanotubes by an In Situ Reduction-Carbonization Route, Chunli Guo, Yitai Qian, and Pengju Han
Volume 2011, Article ID 987530, 5 pages

Fabrication and Optical Property of Periodic Sn_{1-x}Ti_xO₂ Nanostructures Patterned by the Polystyrene Microsphere Templates, Shutian Chen, Zhengcao Li, and Zhengjun Zhang
Volume 2011, Article ID 510237, 7 pages

Electrocatalytic Activity for CO, MeOH, and EtOH Oxidation on the Surface of Pt-Ru Nanoparticles Supported by Metal Oxide, Kwang-Sik Sim, Sin-Mook Lim, Hai-Doo Kwen, and Seong-Ho Choi
Volume 2011, Article ID 614983, 8 pages

ZnO Nanowire Formation by Two-Step Deposition Method Using Energy-Controlled Hollow-Type Magnetron RF Plasma, Hideki Ono and Satoru Iizuka
Volume 2011, Article ID 850930, 7 pages

Direct Deposition of Micron-Thick Aligned Ceramic TiO₂ Nanofibrous Film on FTOs by Double-Needle Electrospinning Using Air-Turbulence Shielded Disc Collector, T. Krishnamoorthy, V. Thavasi, V. Akshara, A. Senthil Kumar, D. Pliszka, S. G. Mhaisalkar, and S. Ramakrishna
Volume 2011, Article ID 739241, 7 pages

Design Modifications in Electrospinning Setup for Advanced Applications, Rahul Sahay, Velmurugan Thavasi, and Seeram Ramakrishna
Volume 2011, Article ID 317673, 17 pages

Room Temperature Ferromagnetism of (Mn,Fe) Codoped ZnO Nanowires Synthesized by Chemical Vapor Deposition, Yongqin Chang, Pengwei Wang, Qingling Sun, Yongwei Wang, and Yi Long
Volume 2011, Article ID 367156, 6 pages

The Synthesis of Highly Aligned Cupric Oxide Nanowires by Heating Copper Foil, Jianbo Liang, Naoki Kishi, Tetsuo Soga, and Takashi Jimbo
Volume 2011, Article ID 268508, 8 pages

Carbon Nanostructures Production by AC Arc Discharge Plasma Process at Atmospheric Pressure, Shenqiang Zhao, Ruoyu Hong, Zhi Luo, Haifeng Lu, and Biao Yan
Volume 2011, Article ID 346206, 6 pages

Toward 3D Integration of 1D Conductors: Junctions of InAs Nanowires, Phillip M. Wu, Lars Samuelson, and Heiner Linke
Volume 2011, Article ID 268149, 5 pages

Surface Effects on the Vibration and Buckling of Double-Nanobeam-Systems, Dong-Hui Wang and Gang-Feng Wang
Volume 2011, Article ID 518706, 7 pages

Effect of Applied Potential on the Formation of Self-Organized TiO₂ Nanotube Arrays and Its Photoelectrochemical Response, Chin Wei Lai and Srimala Sreekantan
Volume 2011, Article ID 142463, 7 pages

Acoustic Phonons in Nanowires with Embedded Heterostructures, Hussein M. Ayedh and Andreas Wacker
Volume 2011, Article ID 743846, 7 pages

Synthesis and Characterization of 1D Ceria Nanomaterials for CO Oxidation and Steam Reforming of Methanol, Sujan Chowdhury and Kuen-Song Lin
Volume 2011, Article ID 157690, 16 pages

Use of the Thermal Chemical Vapor Deposition to Fabricate Light-Emitting Diodes Based on ZnO Nanowire/p-GaN Heterojunction, Sheng-Po Chang and Ting-Hao Chang
Volume 2011, Article ID 903176, 4 pages

Structural and Optical Characteristics of γ -In₂Se₃ Nanorods Grown on Si Substrates, M. D. Yang, C. H. Hu, S. C. Tong, J. L. Shen, S. M. Lan, C. H. Wu, and T. Y. Lin
Volume 2011, Article ID 976262, 5 pages

Contents

Study on the Electrospun CNTs/Polyacrylonitrile-Based Nanofiber Composites, Bo Qiao, Xuejia Ding, Xiaoxiao Hou, and Sizhu Wu
Volume 2011, Article ID 839462, 7 pages

Influence of pH, Precursor Concentration, Growth Time, and Temperature on the Morphology of ZnO Nanostructures Grown by the Hydrothermal Method, G. Amin, M. H. Asif, A. Zainelabdin, S. Zaman, O. Nur, and M. Willander
Volume 2011, Article ID 269692, 9 pages

Characteristics of Progressive Damage of ZnO Nanowires during Contact Sliding under Relatively Low Loads, Kyeong Hee Kang, Hae Jin Kim, and Dae-Eun Kim
Volume 2011, Article ID 624195, 7 pages

Fabrication of VO₂ (B) Nanobelts and Their Application in Lithium Ion Batteries, Shibing Ni, Haibo Zeng, and Xuelin Yang
Volume 2011, Article ID 961389, 4 pages

Growth Behaviors of ZnO Nanorods Grown with the Sn-Based Bilayer Catalyst-Covered Substrates, Dong-Hau Kuo and Bo-Jie Chang
Volume 2011, Article ID 603098, 9 pages

A Facile Method for Preparing Transparent, Conductive, and Paper-Like Silver Nanowire Films, Yajie Wang, Tao Feng, Kai Wang, Min Qian, Yiwei Chen, and Zhuo Sun
Volume 2011, Article ID 935218, 5 pages

Editorial

1D Nanomaterials 2011

Yanqiu Zhu,¹ Raymond L. D. Whitby,² Renzhi Ma,³ and Steve F. A. Acquah⁴

¹ College of Engineering, Mathematics and Physical Sciences, University of Exeter, Exeter EX4 4Qf, UK

² Nanoscience & Nanotechnology Group, University of Brighton, Faculty of Science & Engineering, Huxley Building, Brighton, BN2 4GJ, UK

³ International Center for Materials Nanoarchitectonics (MANA), National Institute for Materials Science, Tsukuba, Ibaraki 305-0044, Japan

⁴ Department of Chemistry & Biochemistry, Florida State University, Tallahassee, Florida 32306-4390, USA

Correspondence should be addressed to Yanqiu Zhu, y.zhu@exeter.ac.uk

Received 24 November 2011; Accepted 24 November 2011

Copyright © 2012 Yanqiu Zhu et al. This is an open access article distributed under the Creative Commons Attribution License, which permits unrestricted use, distribution, and reproduction in any medium, provided the original work is properly cited.

Following the first report on the concentric nature of carbon nanotube (CNTs) in 1991, an era of global nanomaterials research quickly emerged. Over decades of effort, significant progresses have been made by scientists of diverse disciplines from different prospects, which contribute to and become the foundation of the current Nanoscience and Nanotechnology revolution, alongside other three ground breaking inventions of steam engine, electricity, and possibly the internet in our history. It is fair to say that new nanomaterials with unique and fundamentally superior properties, against their conventional bulk forms, naturally become the core element for this revolution. Amongst the seemingly countless nanomaterials that have been documented today, 1-dimensional nanotubes and nanowires (also called nanorods, nanofibres or nanowhiskers) stand out as a class of important structures alongside CNTs, primarily owing to their high aspect ratios against the 0-dimensional nanoparticles, and their lattice stacking features (close to bulk crystal) as opposed to CNTs that formed by wrapping concentric layers of atoms. As a result of the bulk-like stacking within nanowires, elements and compounds of almost any known combinations could be candidates for the construction of new nanowires with specialty, thus offering huge potentials for applications. In fact, successes to date have been achieved in the generation of tens and hundreds of 1D nanowires with the broadest compositional combinations across the periodic table, in contrast to only a handful of nanotubes reported, and more successes are expected in the near future. It is believed that the flourish of new 1D nanomaterial research will continue for some time, and many newly proposed

promising applications based on their unique structural characteristics and versatile properties are waiting to be explored.

Over the last decade, the development in this most rapidly increasing research field has been periodically summarised and reviewed by many colleagues, focusing on one topic or the other regarding specific technical aspects. Given the significant amounts of work involved globally and the unique elongated feature of the 1D nanomaterials, it is important to have a platform that allows active researchers to present their new development in a timely and efficient manner. With this intention in mind, the first special issue "1D Nanomaterials", containing 16 carefully selected papers, was published in 2010 in the Journal of Nanomaterials and was obviously a moderate success.

Time flies rapidly, and research develops almost at the same pace. Two years on, we feel it is the high time to summarise the hard works focusing on the 1D nanomaterials again, thus leading to the second special issue by the same group of Guest Editors.

Comparing with the first special issue, we have noticed a clear focus shift in the current issue. In the 16 articles presented in the 2010 issue, 12 of which studied the synthesis related subjects, and 6 are property-oriented, with 2 articles covering both the synthesis and property investigation. In terms of research material, CNTs (3), ZnO (3), and TiO₂ (3) shared the most attention, with several other inorganic nanowires. In the present issue in which 31 articles are included (out of 57 manuscript submissions, i.e., ~57% acceptance rate), the research focus and research materials

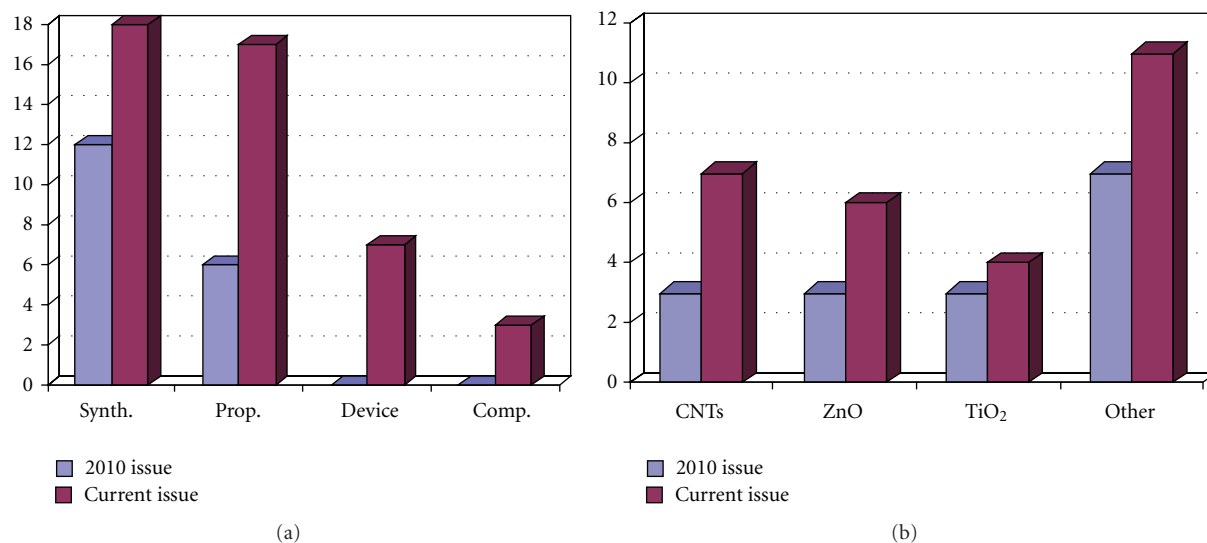


FIGURE 1: Comparison of research category and subjects included in 2010 and 2011 “1D nanomaterials.”

are clearly diversified. Figure 1 shows the classification of the articles based on broad research category (Synthesis, Property/Application, Device Construction, and Nanocomposites Fabrication), and research materials. 31 articles are not enough for offering a convincing statistic representation, particularly quite a few papers with overlaps across two or more categories; however they nevertheless exhibit the diversity and possibly the direction of current and future research associated with 1D nanomaterials.

Whilst studies on Synthesis (18) and Property (17) remain dominant in numbers, it is encouraging to see a total of 10 papers reporting progresses in Device Construction (7) and Nanocomposite Fabrication (3). This extension offers a solid evidence for importance of such 1D nanomaterials as a key element for the continuous development of nanoscience and nanotechnology.

On the research object materials front, CNT and ZnO nanowires maintain the leading status, followed by TiO₂ nanorods (4 papers), accompanied with a variety of new comers such as InAs, In₂Se₃, VO₂, CeO₂, CuO, GaAs, GaN and and so forth, and several of which appear in complex compositions. We believe this is a fair representation of current activities, and property and application-oriented research emerge strongly.

Overall, as Guest Editors for this second issue, we are pleased with the flourish and diverse research activities in this area. Given the specific 1D and huge aspect ratio characteristics that making nanotubes and nanowires so special, we feel three major research areas are understudied or under-represented in this issue, notably the toxicity, processing, and recycling issues concerning 1D nanomaterials. Whilst a handful reports concentrate on the toxicity behaviour of CNTs, even less research has been carried out to address the recycling issue which not only impacts the economic concerns over 1D nanomaterials in future engineering applications but also directly associates with the end of life disposal of such materials/devices in long term, thus

an environmental issue. The structural characteristics and properties of 1D nanomaterials may change under certain processing conditions such as under Joule effect, or pressure or electric and magnetic field, such processing underpins the stability of 1D nanomaterials. These areas certainly deserve more attention in order for 1D nanomaterials to be safely and economically utilised in practical engineering applications.

Finally, we hope this special issue will be well-received by the reader and we hope to present a further developed and a more balanced research activity in the near future in the next issue.

Yanqiu Zhu
Raymond L. D. Whitby
Renzhi Ma
Steve F. A. Acquah

Research Article

Impact of Specifically Adsorbing Anions on the Electroless Growth of Gold Nanotubes

Falk Muench, Cornelia Neetzel, Stefan Lauterbach, Hans-Joachim Kleebe, and Wolfgang Ensinger

Department of Materials and Geoscience, Technische Universität Darmstadt, Petersenstraße 23, 64287 Darmstadt, Germany

Correspondence should be addressed to Falk Muench, muench@ca.tu-darmstadt.de

Received 14 July 2011; Accepted 28 October 2011

Academic Editor: Renzhi Ma

Copyright © 2012 Falk Muench et al. This is an open access article distributed under the Creative Commons Attribution License, which permits unrestricted use, distribution, and reproduction in any medium, provided the original work is properly cited.

Electroless metal deposition on nanochannel-containing templates is a versatile route towards metal nanotubes and nanowires if the plating reaction can be sufficiently controlled. In this study, disulfiteaurate-formaldehyde-based gold plating baths were modified by the addition of halides, pseudohalides, and EDTA. The introduction of specifically adsorbing anions strongly affected the heterogeneously autocatalyzed plating reaction and allowed the regulation of the reaction rate and the product morphology. The new plating baths showed enhanced stability and allowed the synthesis of homogeneous nanotubes of high aspect ratios (>150) in $30\ \mu\text{m}$ thick ion track-etched polymer templates. Depending on the reaction conditions, solid and porous structures consisting of gold nanoparticles of differing size and shape were accessible. The presented strategy offers adapted gold thin films, nanotubes, and nanowires for applications in catalysis or sensing.

1. Introduction

Nanotubes (NTs) are an important class of virtually one-dimensional nanomaterials [1], which are deployed in various applications of high academical and practical interest. The versatility of NTs is supported by the broad range of materials from which they can be created. Besides carbon [2], NTs can be prepared from polymers [3, 4], metals [1, 4–8], and compounds such as oxides, sulfides, or nitrides [1] next to composites [1, 3]. Among the presented materials, metal NTs exhibit a combination of unique physical and chemical properties such as electrical conductivity, plasmon resonance [5], catalytic activity [6, 7], and a rich surface chemistry involving adsorbates such as thiols [7, 8]. Their superior properties lead to the implementation of Au NTs in a wide range of applications. For instance, they were effectively applied as biosensors [5], nanoreactors [6], supportless CO oxidation catalysts [7], and molecular sieves [8].

Usually, Au NTs are prepared according to a versatile template-based method introduced by Martin et al. [4, 7–10]. In this protocol, Au is electrolessly plated on ion track-etched polymer membranes. Electroless depositions are solution-based reactions in which metal cations are selectively reduced

on a substrate surface by a chemical agent [11]. Electroless Au plating leads to the development of polycrystalline films consisting of interconnected Au nanoparticles (NPs) [9, 10]. If the metal film covers the nanochannel walls inside the template, Au NTs are formed.

While template preparation by ion track etching is well understood and ensures a high degree of control over the NT diameter, length, and shape [12], less effort has been devoted to the development of new electroless Au baths allowing to adjust the morphology of the plated Au thin films and NTs [6]. Preceding synthetic studies elucidated the effect of different parameters like the Au precursor concentration [9], the temperature [9], the pH value [9, 10], and the delayed introduction of the reducing agent [10] without changing the general bath composition. The results of these studies show relatively large Au NP sizes (typical average diameters lie between 30 and more than 100 nm) and a limitation of the NP shape to globular morphologies [9, 10]. However, control over the size and shape of metal NPs is of major nanotechnological importance since these parameters considerably affect properties such as catalytic selectivity and activity, optical absorption, and local field enhancement [13–15].

As the presence of adsorbates strongly influences the growth of metal NPs [15], the introduction of adsorbing species is a straightforward measure to control both the deposition kinetics of electroless plating reactions and the morphology of the obtained products [6]. Halides are common reagents that readily adsorb specifically on noble metal surfaces [16] and show pronounced shape-directing effects in metal NP syntheses [15, 17, 18]. Thus, they are promising additives in the electroless fabrication of Au nanomaterials. In this study, we therefore examine the influence of halides and pseudohalides on the electroless synthesis of Au thin films and NTs and show how they can be used to optimize the obtained nanostructures towards a desired product.

2. Experimental Procedure

2.1. General, Chemicals. All glassware was cleaned with aqua regia prior to use, and all procedures were performed with purified water (Milli Q 18-M Ω water). The sensitization and plating solutions were prepared freshly, and the activation solution was stored dark and cold. The following chemicals were used without further purification: AgNO₃ (Grüssing, p.a.), EDTA disodium salt dihydrate (Fluka, puriss. p.a.), ethanol (Brenntag, 99.5%), formaldehyde solution 37% in water, methanol stabilized (Grüssing, p.a.), KBr (Merck, suprapur), KI (Grüssing, 99.5%), KSCN (Merck, cryst. pure), methanol (Sigma-Aldrich, laboratory reagent), NaCl (Merck, suprapur), NaCN (Merck, p.a.), Na₂SO₃ (Merck, p.a.), NH₃ 33% in water (Merck, puriss.), SnCl₂ dihydrate (Sigma-Aldrich, ACS reagent), sodium hydroxide solution 32% in water (Fluka, puriss. p.a.), and trifluoroacetic acid (Riedel-de Haën, >99%). A commercial electroplating solution (El-Form Galvano Goldbad, Schütz Dental GmbH) was used as the Au source (15 g 99.9% Au per liter, present as (NH₄)₃[Au(SO₃)₂]).

2.2. Synthesis. Polycarbonate foils (Makrofol, Bayer MaterialScience AG, nominal thickness 30 μ m) were irradiated with Au ions (energy: 11 MeV per nucleon, fluence: 1 · 10⁸ ions cm⁻²) at the Helmholtz centre for heavy ion research (GSI). Subsequently, they were irradiated with UV light in the presence of air (1 h per side, UV source provides 1.5 and 4 Wm⁻² in the ranges of 280 nm–320 nm and 320 nm–400 nm, resp.) and etched in stirred sodium hydroxide solution (6 M, 50 °C, time depending on desired diameter, ranging from 100 to 200 nm). The as-prepared templates were thoroughly washed with water and dried. Prior to electroless plating, the polycarbonate substrates were activated with Ag NPs according to a previously reported procedure [6] (for a description of the process, see Section 3.1 and Figure 1). After washing with ethanol and water, the freshly activated substrates were immersed in the electroless plating solutions. The pH of all plating solutions was adjusted to 9.3–9.4 with NaOH since moderately basic pH values favor dense nucleation, low reaction rates and small crystallite sizes, and hence tube formation [10]. Temperature was held constant at 8 °C to ensure slow deposition necessary for formation of tubes of homogeneous wall thickness [9]. The

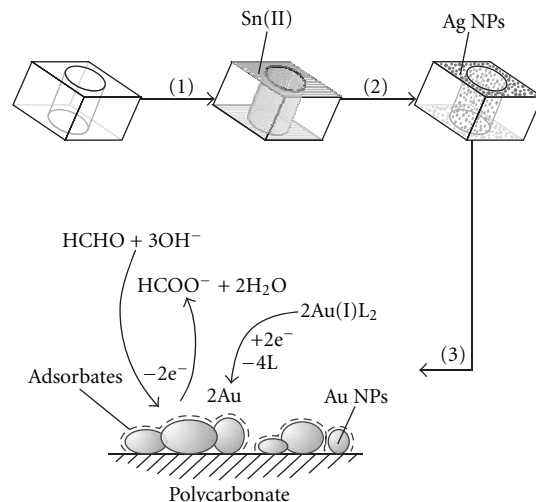


FIGURE 1: Scheme of the Au NT fabrication in ion-track-etched polymer templates. (1) Sensitization by anchoring Sn(II) ions on the template. (2) Activation by immersion in a Ag(I) solution, leading to the formation of Ag NPs on the inner and outer template surface. (3) Electroless Au plating using a Au(I) complex (L = ligand) as the oxidizing and formaldehyde as the reducing agent. The deposition reaction is altered by specifically adsorbing additives.

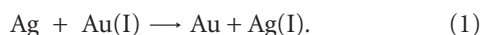
Au plating baths contained 7.0 mM Au(I), 125 mM Na₂SO₃, and 625 mM formaldehyde. All additives have been initially applied in a concentration of 100 mM. In case of strong interference with the plating reaction, the concentrations have been reduced to the values stated in the text. In the cases of mixed addition of EDTA and salts containing specifically adsorbing anions, the concentration of EDTA was held constant at 100 mM while the salt concentrations were varied. After the desired reaction time, the membranes were washed with water and dried.

2.3. Characterization. TEM (FEI CM20 microscope (Netherlands), 200 kV acceleration voltage, LaB₆-cathode): the NT-containing templates were embedded in Araldit 502 (polymerization at 60 °C for 16 h) and examined as ultrathin sections (70 nm thickness, Reichert-Jung Ultracut E ultramicrotome, DKK diamond knife). EDS (Oxford Model 6767 EDS-system (England)): in combination with TEM, EDS measurements were performed to confirm the composition of the obtained nanostructures. A representative EDS spectrum is shown in Figure 6. SEM (JEOL JSM-7401F, 5–10 kV acceleration voltage): prior to the measurement, the template was removed with dichloromethane. The freed metal structures were collected on silicon wafer pieces sputter-coated with Au.

3. Results and Discussion

3.1. Synthetic Strategy. Generally, electroless plating reactions are not catalyzed by pristine polymer surfaces [11]. Therefore, polymer substrates have to be modified to initiate

metal deposition. In case of ion-track-etched polymer templates, catalytic activity is usually established by covering the substrate with Ag NPs [4, 6, 9, 10]. This process involves two steps. First, the template is immersed in an SnCl_2 solution, leading to the formation of surface complexes between Sn(II) and polar groups of the polymer (sensitization, see step (1) in Figure 1). After washing off the excess of unbound SnCl_2 , the template is dipped in an $[\text{Ag}(\text{NH}_3)_2]\text{NO}_3$ solution. The Ag(I) oxidizes Sn(II) forming Sn(IV), while Ag(I) is reduced to elemental Ag. This leads to the precipitation of Ag NPs on the template surface (activation, see step (2) in Figure 1) [9, 10]. After activation, the template membranes are washed and finally immersed in the plating solution (step (3) in Figure 1). Electroless plating baths applied in the synthesis of Au NTs contain $[\text{Au}(\text{SO}_3)_2]^{3-}$ as the stabilized Au(I) source and formaldehyde as the reducing agent [7–10]. During the heterogeneously autocatalyzed plating reaction, formaldehyde is oxidized to formate, while Au(I) is reduced to elemental Au [9]. A side reaction is the cementation of Au on the less noble Ag introduced during activation (1) [9]:



Heterogeneous reactions severely respond to interfacial changes. For instance, Pt catalysts are poisoned by strongly bonding species such as CO [19], whereas the adsorption of chiral molecules such as cinchona alkaloids can lead to enhanced reaction rates and asymmetric induction on them [20]. Adsorbing species such as cationic surfactants, halides, and silver salts play a major role in the wet-chemical synthesis of anisotropic Au NPs [21]. Analogous to colloidal approaches, electroless plating is based on metal NP formation by the reduction of dissolved cationic precursors. Correspondingly, the presence of adsorbates strongly affects the reaction kinetics and the shape of the evolving nanostructures [6, 21]. Furthermore, adsorbate-forming additives can improve the stability of plating baths towards homogeneous nucleation [6]. This issue is an important quality criterion in electroless plating. If the metal reduction is not limited to the substrate surface, homogeneous nucleation leads to the formation of metal nuclei in the bulk solution. Continued nucleation and the growth of existing particles quickens the depletion of the plating solution and gives rise to undesired metal precipitation. In addition, homogeneous nucleation negatively affects plating rates and often leads to deteriorated metal films [22]. Applying the outlined concept, we investigated the influence of different halides and pseudohalides (chloride, bromide, iodide, cyanide, and thiocyanate) on the electroless growth of Au NTs. Next to adsorbing anions, the universal ligand EDTA was tested as a complementary complexing agent. In contrast to the reactive components Au(I) and formaldehyde, the applied additives are not consumed during the plating reaction (step (3) in Figure 1).

3.2. Isolated Effect of Additives

3.2.1. EDTA. Due to its relatively low-binding strength towards low-valent metal cations and its competition with sulfite as a soft sulfur-containing ligand well suited for the

coordination of the soft Lewis acid Au(I), the presence of EDTA should not lead to a pronounced additional stabilization of the oxidizing component Au(I). Accordingly, the addition of EDTA does not alter the electroless deposition reaction to a relevant degree.

Similar product morphologies and reaction speeds were obtained for the plating baths containing sulfite and sulfite next to EDTA (Figures 2(a)-2(b)). In both cases, the Au NTs were found to be composed of granular NPs of approximately 15–20 nm size. Also, the Au NTs showed fragmentation when the polycarbonate template was removed. With increasing distance to their openings, the tubes become crumbly and finally break after some micrometers (Figure 2(b), see arrow). Longer fragments were found in the presence of EDTA, revealing slightly improved NT formation. The inhomogeneous deposition of Au alongside the template nanochannels is caused by the relatively high-deposition rate [9]. While the reactive species of the plating bath are consumed on the whole inner template surface, mass transport from the bulk solution is limited by the narrow tube openings. This leads to reagent depletion and reduced plating rates inside the NTs.

3.2.2. Halides. The addition of 100 mM chloride or bromide lead to similar changes in Au plating concerning the product morphology and the deposition rate. At the beginning of the plating reaction, a relatively quick color-shift of the activated templates from brownish to pink occurred, which was attributed to Au cementation (1). The electroless deposition of larger amounts of Au, which was indicated by the development of a dark purple or bluish color was decelerated in the presence of chloride and bromide. While chloride leads to a moderate reduction of the deposition rate, bromide caused a drastic deceleration. In both cases, the development of continuous Au films and well-defined Au NTs was hampered. Instead, the growth of separated NPs was observed (Figures 3(a)-3(b), arrow indicates an isolated particle). Compared to chloride, bromide had a more pronounced effect on the product morphology. While in case of chloride tube fragments were found after a reaction of one day (Figure 3(a)), no NTs were observed in the case of the addition of 100 mM bromide even after a deposition time of 10 days (Figure 3(b)). However, the formation of fine NTs of approximately 100 nm diameter was confirmed by TEM (Figure 3(c)). The NTs consist of particles of 7.7 ± 1.5 nm size. As no continuous Au film growth was observed in this experiment, the tubular structures are probably composed of Au NPs stemming from the Ag conversion (1).

The deceleration of electroless plating in the presence of halides can be explained by partial poisoning of the Au surface due to adsorbate formation. Compared to chloride, the heavier halide bromide has a higher polarizability and interacts stronger with Au surfaces [16]. As a result, bromide leads to a higher surface coverage at identical solution concentration [16]. With increasing blockage of the reactive sites on the Au surface, the plating reaction should be increasingly constrained. In accordance with this expectation, bromide has a stronger effect on the electroless Au deposition.

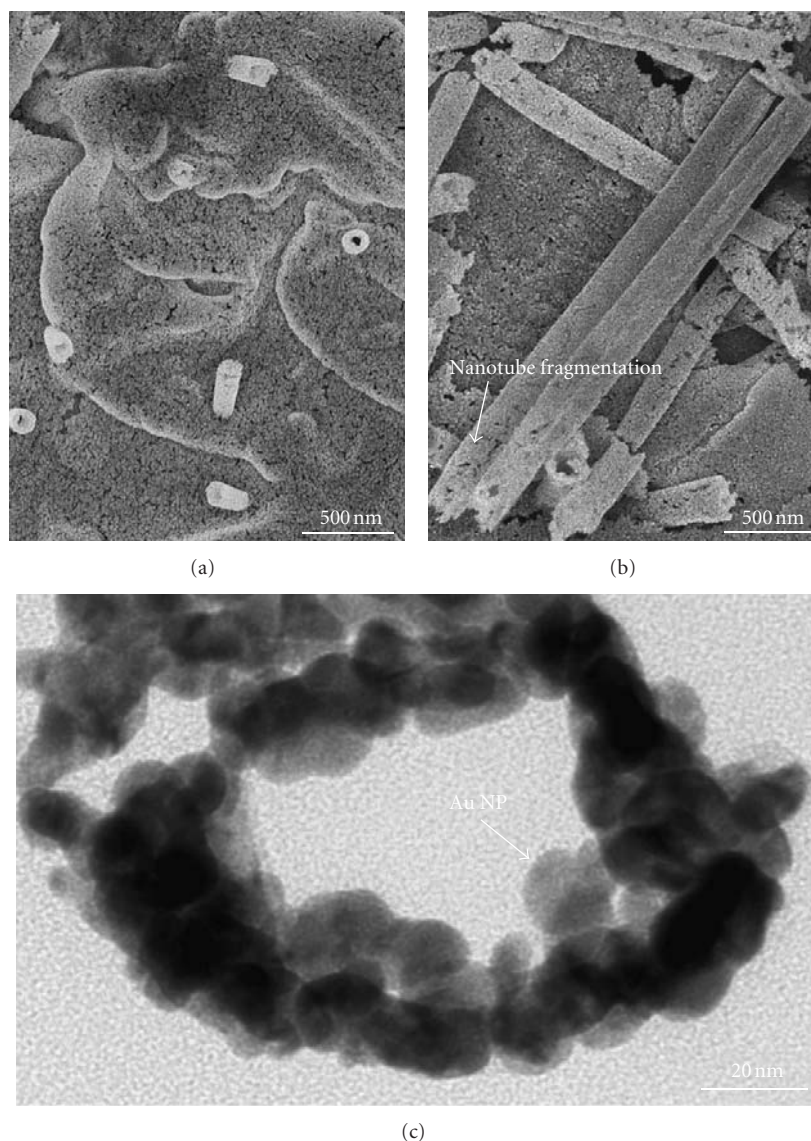
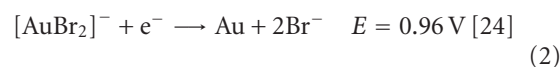


FIGURE 2: Electron microscopy images of Au NTs grown without (a) and with (b-c) addition of EDTA. (a) and (b) comprise SEM images of template freed Au NTs, (c) a TEM image of a microtomed Au NT (c). Both depositions took place for 21 h in templates with nanochannels of approximately 200 nm entrance diameter.

Interestingly, the trend did not extend to the heaviest homologue iodide. In contrast to the expectation of an efficient reduction of surface activity, electroless plating baths containing 100 mM iodide quickly decomposed to form Au suspensions. Even extremely reduced iodide concentrations below 1 mM accelerated both the homogeneous and heterogeneous gold reduction and were thus detrimental to NT formation. The opposing behavior of iodide compared to its lighter homologues is surprising, but highly reproducible. An increase of the speed of electrochemical reactions on metal surfaces with anion adlayers is a known phenomenon. It can be explained by the lowering of the activation energy of intermediate species by the adsorbed anions [16]. In the case of accelerated Au plating, either formaldehyde oxidation or the integration of Au atoms in the evolving Au film may be supported by iodide. The responsible mechanism

is evidently ineffective in the case of chloride or bromide addition. Another example for an unexpected change of surface reactivity in the presence of iodide is the anodic dissolution of Pd [23]. In contrast to the corrosion-enhancing behavior of chloride, which depends on the bulk chloride concentration, even a monolayer of iodide was sufficient to increase the Pd dissolution rate by a factor of nearly 200 [23].

The formation of halide complexes as an explanation for the altered deposition kinetics is improbable due to the strong tendency of Au(I) to form sulfite complexes. This is indicated by the significantly more negative standard potential of the disulfitoaurate complex compared to the analogous bromo- and iodoaurate complexes:



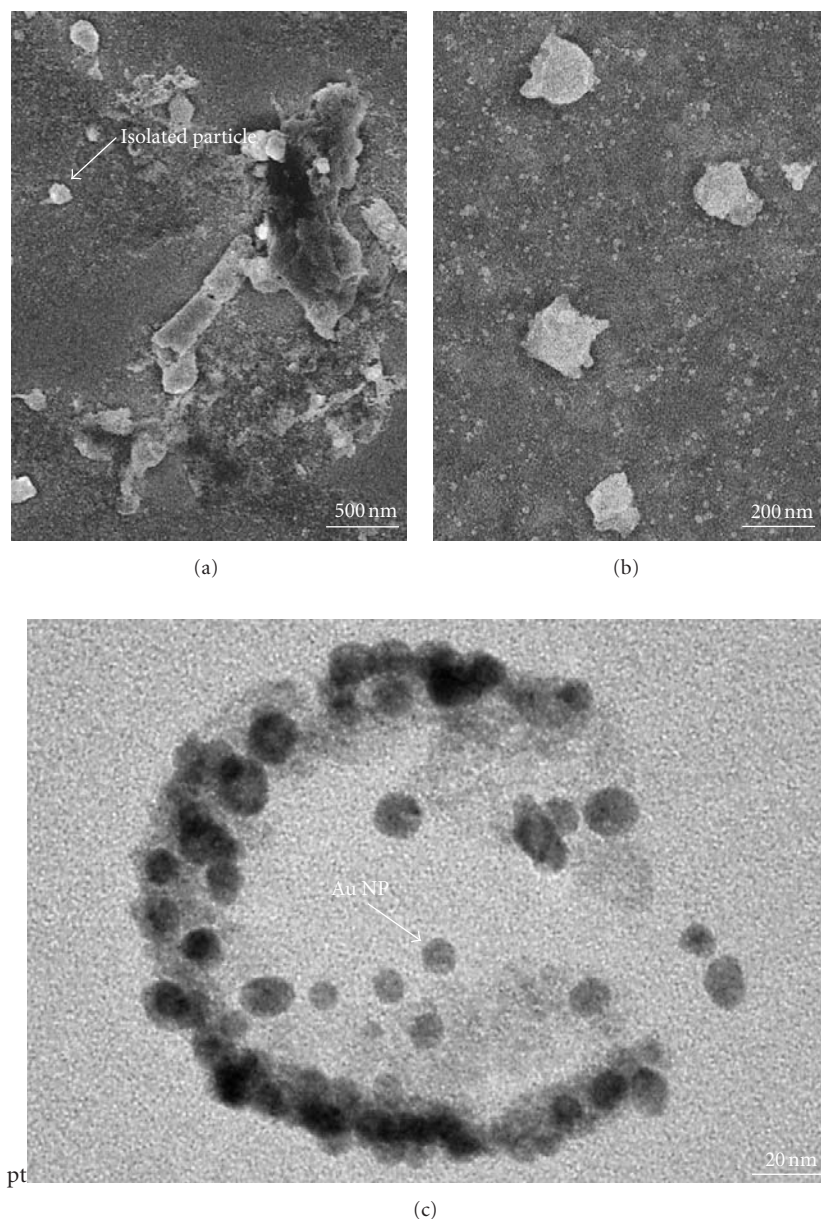
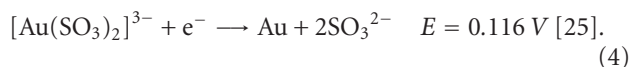
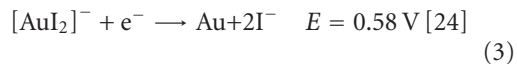


FIGURE 3: Electron microscopy images of Au nanostructures grown with the addition of 100 mM chloride (a) or 100 mM bromide (b-c). (a) and (b) comprise SEM images of template-free Au nanostructures and (c) a TEM image of a microtomed Au NT. The reaction time was 21 h for the samples shown in (a) and (c) and 10 days for the sample shown in (b).



If the lowered standard potential of a metal complex is ascribed to the reduced concentration of free metal ions (in this case solvated Au(I)), its complex formation constant can be calculated on basis of the Nernst equation. The difference between the standard potentials E_n of two complexes is related to the ratio of their complex formation constants

K_n in the following way (z : charge, F : Faraday constant, R : universal gas constant, T : temperature):

$$\frac{K_1}{K_2} = e^{(E_2 - E_1)zF/RT}. \quad (5)$$

With Au(I) as a monovalent cation ($z = 1$) and $T = 298 \text{ K}$, a potential difference of 59 mV corresponds to K values deviated by one order of magnitude. The application of (5) to (2)–(4) leads to K ratios between the sulfite complex and the bromo- and iodo complexes of $1.9 \cdot 10^{14}$ and $7.0 \cdot 10^7$, respectively. Due to the markedly stronger complexation of Au(I) by sulfite, it can be stated clearly that even the heavy

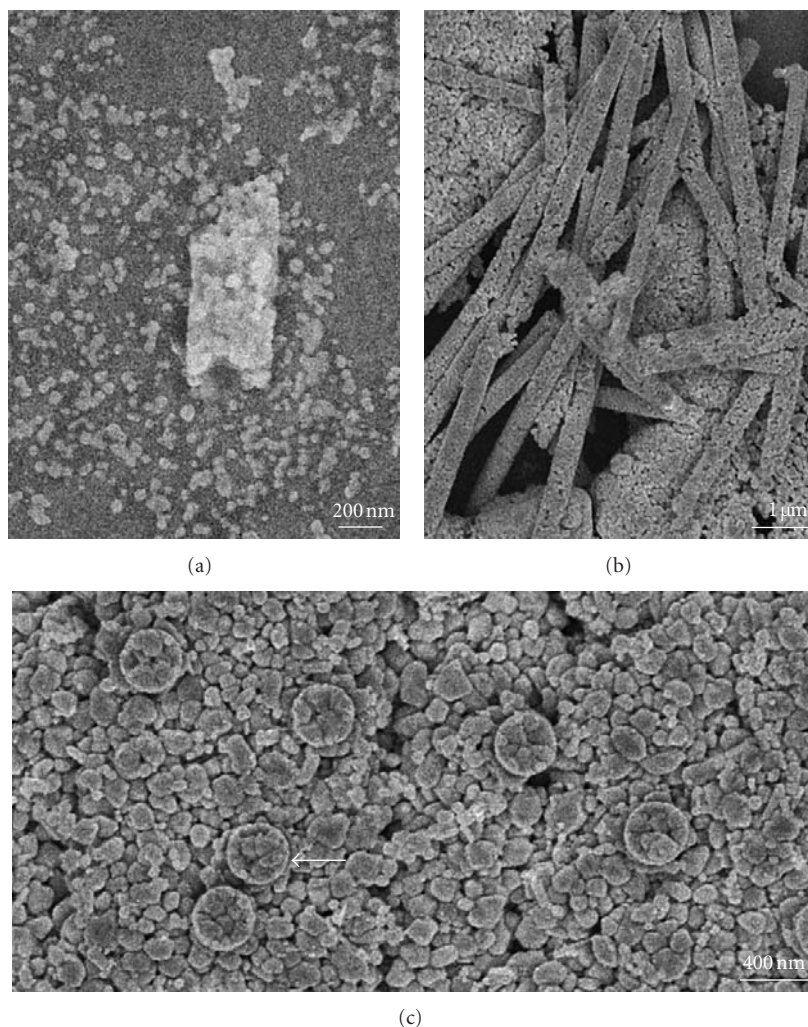


FIGURE 4: SEM images of template-free Au nanostructures grown in the presence of 100 mM thiocyanate. (a) Au structures yielded after a reaction time of 21 h. (b) Au NTs obtained after a deposition time of 4 days. (c) Magnified image of the Au surface film of the sample shown in (b), the arrow marks a nanowire stump.

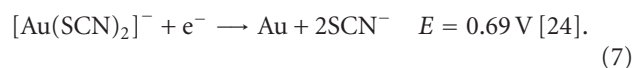
halides bromide and iodide do not significantly contribute as ligands under the given experimental conditions (similar concentrations of sulfite and halides, no excess of Au(I)).

3.2.3. Pseudohalides. The presence of 100 mM cyanide completely stopped the electroless deposition reaction. One reason for this behaviour is the formation of the strongly stabilized dicyanoaurate complex. Its standard potential (6) is significantly negative-shifted compared to the disulfitoaurate complex (3):



The high thermodynamic driving force towards dicyanoaurate even allows etching of Au by molecular oxygen [24], a technique which is used in gold extraction as [25] well as in the shape modification of Au nanomaterials [26]. In our plating bath, formaldehyde with a standard potential of -0.927 V [27] could still reduce $[\text{Au}(\text{CN})_2]^-$. But in addition

to the thermodynamic stabilization of Au(I), cyanide is known to poison Au surfaces in electroless plating [28].



In contrast to cyanide, thiocyanate cannot compete with sulfite as a ligand (7). Application of (5) results in a sulfite complex formation constant, which is $5.1 \cdot 10^9$ times higher than the corresponding value for thiocyanate. Therefore, the change of the Au deposition induced by thiocyanate can be related to its adsorption behaviour. Its presence has a considerable effect on the Au film growth, leading to a reduced plating rate, improved suppression of homogeneous Au precipitation, and enlarged Au crystallites (Figure 4). During 21 h of deposition, a granular Au film and fragile NTs develop (Figure 4(a)). After extended reaction times, a coarsening of the Au NPs occurs and Au nanowires are formed due to the complete filling of the template nanochannels (Figures 4(b)-4(c)). The rough Au films consist of

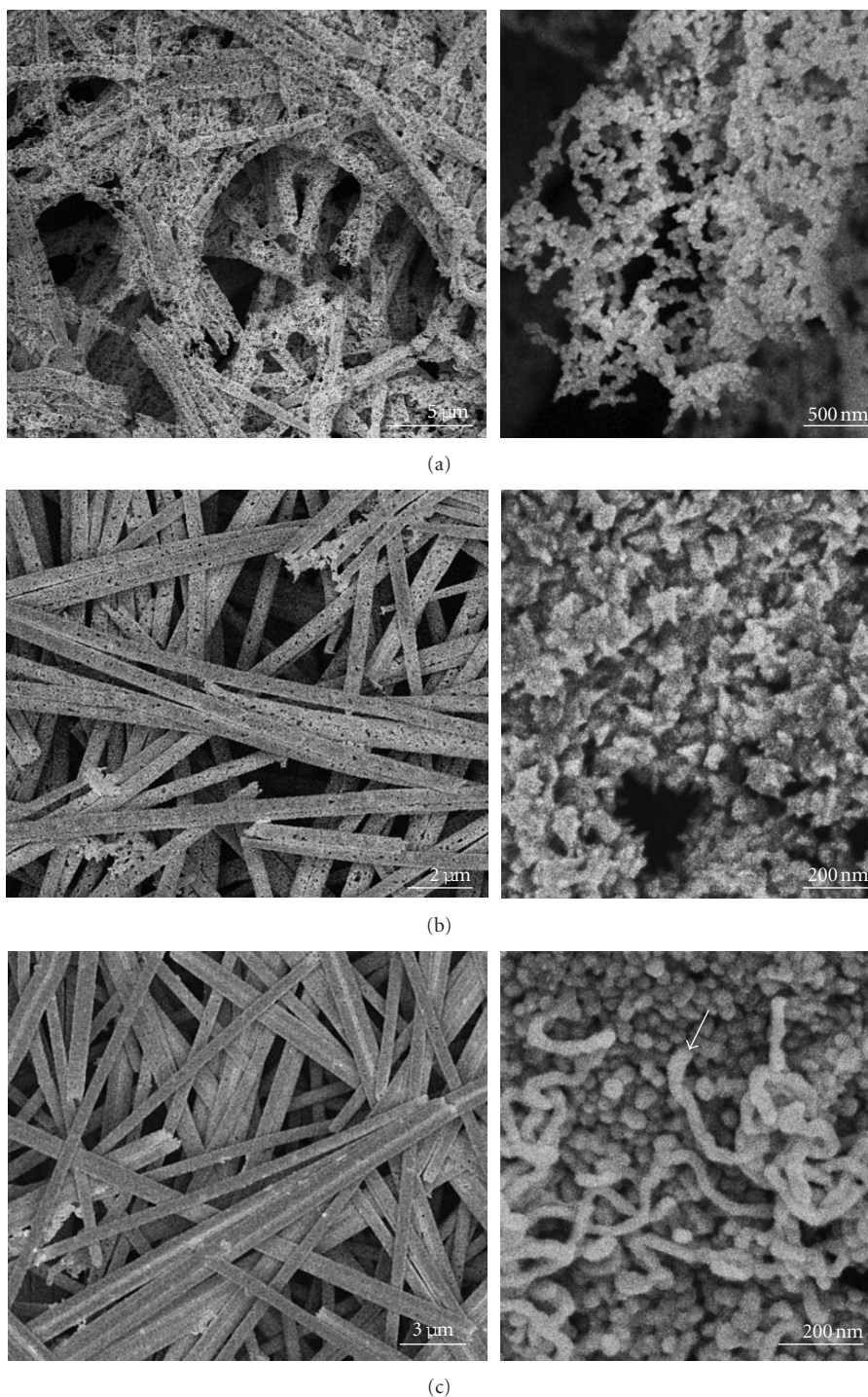


FIGURE 5: SEM images of template-free Au nanostructures obtained with combined addition of EDTA and (a) 20 mM chloride, (b) 0.25 mM bromide, and (c) 0.25 mM iodide. The images on the right show magnified features of the obtained structures (porous Au NTs in (a), Au surface film in (b), and nanowires emerging from the surface film in (c)).

interconnected, edge grains, and many small gaps remain between the particles (Figure 4(c)). Therefore, thiocyanate is a suitable additive for the electroless synthesis of roughened Au nanostructures. Surface roughness is an important factor considering implementation in catalysis, superhydrophobicity, and sensing. For instance, rough Au films can be applied

as surface enhanced Raman spectroscopy (SERS) substrates [29] or in adsorbate sensing [30].

3.3. *Combined Effect of EDTA and (Pseudo)halides.* The effects of halides on the plating reaction are strongly altered

by the addition of EDTA. In all depositions, significantly reduced plating rates and morphology changes were observed. According to the halide adsorption tendency, bromide and iodide have the most intense effect on the electroless plating. All halides allow the synthesis of high aspect ratio Au NTs with homogeneous wall structure (Figure 5). Also the reduced reaction rates correlate with increased bath stabilities. In all mixed EDTA-halide experiments, homogeneous nucleation could be successfully suppressed. The Au NTs obtained with EDTA and thiocyanate were not coherent and completely disintegrated to form NP suspensions during washing of the NT-containing polycarbonate membranes. Some NP loss also occurred in the case of Au films grown in the presence of chloride and bromide.

In case of chloride, the initially formed Au NPs are only partly connected, leading to porous Au films and NTs in the early stages of the plating reaction. In Figure 5(a), the product obtained after a reaction time of one day is shown, revealing a particle size of approximately 30 nm. In later stages, closed Au films and NTs are obtained. Removing the template from a porous sample leads to the formation of a spongy Au NT network (Figure 5(a)). This structure is interesting because of its hierarchical porosity with macropores defined by the tube interiors and mesoporous tube walls. Similar Ag structures have been implemented as effective substrates for surface-enhanced Raman scattering (SERS) [31]. Also, porous metal NTs are a promising class of unsupported heterogeneous catalysts [32].

In the EDTA-bromide system, grain size is tunable by adjusting the bromide concentration. A bromide concentration of 2.0 mM leads to the formation of small globular particles of less than 10 nm size, approaching the product morphology obtained in the case of EDTA-free bromide baths (see Figures 3(b)-3(c)). At a concentration of 0.25 mM and a reaction time of 8 days, the Au nanostructures are composed of sharp and interconnected grains with a size of few tens of nm (see right image in Figure 5(b)). Under these conditions, robust Au NTs are formed. Since metal NPs with high curvatures produce high field enhancements [21, 33], the obtained spiky Au films and NTs are interesting for SERS applications. In a seed-mediated approach, similar Au NP morphologies (branched and star-like) were yielded by the reduction of HAuCl_4 in the presence of cetyltrimethylammonium bromide (CTAB) and optionally traces of AgNO_3 [34]. Another solution-based route towards multibranching Au NPs is the reduction of HAuCl_4 with hydrazine in the presence of polyvinylpyrrolidone. These structures have been implemented as effective SERS substrates [33].

Like in the experiments performed without EDTA, high iodide concentrations increase the deposition rate and the susceptibility to homogeneous nucleation. However, low iodide contents in combination with EDTA delay the plating reaction and suppress bath decomposition. Figure 5(c) shows the product obtained by the addition of 0.25 mM iodide next to 100 mM EDTA after a reaction time of two days. Next to nonfragmenting Au NTs, fibrous deposits are found on top of the solution-sided face of the Au surface film. The nanowires originate from single NPs of the surface films (see arrow in Figure 5(c)) and are even found at a

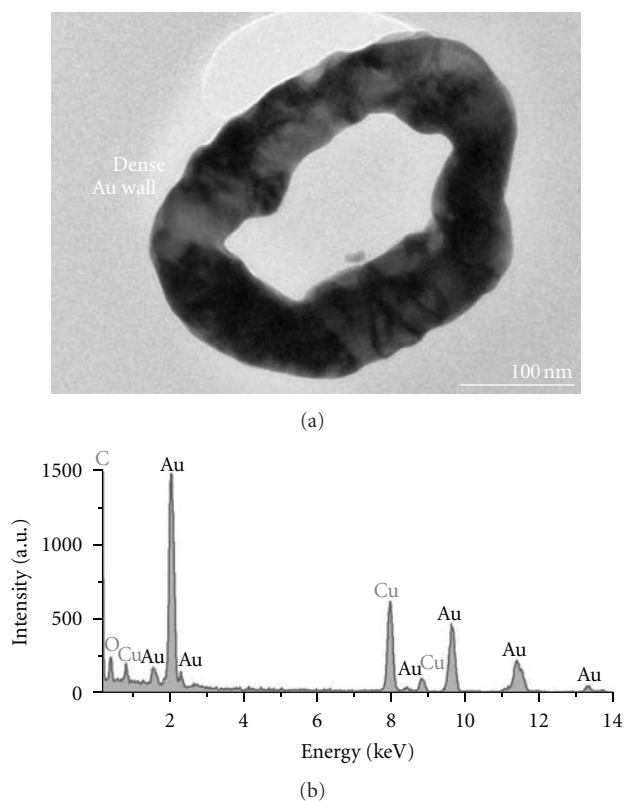


FIGURE 6: (a) TEM image of a microtomed sample of the Au NTs grown in the presence of 0.25 mM iodide and 100 mM EDTA. (b) Representative EDS spectrum of the Au nanostructures. The C and O signals are due to the polymer matrix and the Cu signals due to the TEM grid, respectively.

drastically reduced iodide concentration of $25 \mu\text{M}$. The EDTA-iodide system yields NT walls composed of densely interconnected Au NPs (Figure 6(a)). By EDS, no significant Ag residues can be detected (Figure 6(b)). The obtained Au NTs are very robust and endure the template removing process without major deformation or fragmentation. A high mechanical strength of metal NTs allows the fabrication of free-standing NT arrays and increases the resistance of the nanostructures under stress. For instance, a quick loss of NPs would decrease the lifetime of metal NT catalysts. In addition, the nanotube structure affects its electrical conductivity. These factors are important for applications in catalysis [35, 36], nanocircuitry [37], plasmonic biosensing, or the nanoprobing of living cells [5].

4. Conclusion

Specifically adsorbing anions strongly affect the deposition kinetics and the product morphology in the disulfiteaurate-formaldehyde plating system. Especially the heavy halides bromide and iodide with their high affinity towards Au surfaces show pronounced effects even in catalytic concentrations. This observation is in accordance with the high sensitivity of colloidal Au crystal growth towards the presence of specifically adsorbing anions [17, 18, 21]. Because of

the increased bath stabilities and the improved plating behaviour, the addition of (pseudo)halides and optionally EDTA to disulfiteaurate-formaldehyde-based electroless plating baths is a facile route towards Au thin films and derived nanomaterials of variable morphology. Significantly reduced plating rates allow to cover substrates with complex and badly accessible surfaces with homogeneous Au NP films. In contrast to the standard plating procedure, sophisticated structures such as homogeneous and stable Au NTs of high aspect ratio could be synthesized using the refined plating procedures. With maximum tube entrance diameters between 150 and 200 nm, the presented NTs approach aspect ratios of more than 150. The stable Au NTs could be freed from the template without fragmentation, allowing straightforward processing and application of the nanostructures for example, in heterogeneous catalysis or sensing.

Acknowledgments

The authors thank Professor Reinhard Neumann and Dr. Christina Trautmann (GSI Helmholtz Centre for Heavy Ion Research) for support with the template preparation and for the possibility to use the SEM of the materials research group. Thanks are given to Ulrike Kunz for sample preparation and TEM imaging. The supply of gold solution by Schütz Dental GmbH is gratefully acknowledged.

References

- [1] C. N. R. Rao and A. Govindaraj, "Synthesis of inorganic nanotubes," *Advanced Materials*, vol. 21, no. 42, pp. 4208–4233, 2009.
- [2] D. Vairavapandian, P. Vichchulada, and M. D. Lay, "Preparation and modification of carbon nanotubes: review of recent advances and applications in catalysis and sensing," *Analytica Chimica Acta*, vol. 626, no. 2, pp. 119–129, 2008.
- [3] J. Martín and C. Mijangos, "Tailored polymer-based nanofibers and nanotubes by means of different infiltration methods into alumina nanopores," *Langmuir*, vol. 25, no. 2, pp. 1181–1187, 2009.
- [4] C. R. Martin, "Nanomaterials: a membrane-based synthetic approach," *Science*, vol. 266, no. 5193, pp. 1961–1966, 1994.
- [5] J. McPhillips, A. Murphy, M. P. Jonsson et al., "High-performance biosensing using arrays of plasmonic nanotubes," *ACS Nano*, vol. 4, no. 4, pp. 2210–2216, 2010.
- [6] F. Muench, U. Kunz, C. Neetzal, S. Lauterbach, H. J. Kleebe, and W. Ensinger, "4-(dimethylamino)pyridine as a powerful auxiliary reagent in the electroless synthesis of gold nanotubes," *Langmuir*, vol. 27, no. 1, pp. 430–435, 2011.
- [7] M. A. Sanchez-Castillo, C. Couto, W. B. Kim, and J. A. Dumescic, "Gold-nanotube membranes for the oxidation of CO at gas-water interfaces," *Angewandte Chemie—International Edition*, vol. 43, no. 9, pp. 1140–1142, 2004.
- [8] S. Yu, S. B. Lee, M. Kang, and C. R. Martin, "Size-based protein separations in poly(ethylene glycol)-derivatized gold nanotubule membranes," *Nano Letters*, vol. 1, no. 9, pp. 495–498, 2001.
- [9] R. J. Gilliam, S. J. Thorpe, and D. W. Kirk, "A nucleation and growth study of gold nanowires and nanotubes in polymeric membranes," *Journal of Applied Electrochemistry*, vol. 37, no. 2, pp. 233–239, 2007.
- [10] M. De Leo, F. C. Pereira, L. M. Moretto, P. Scopece, S. Polizzi, and P. Ugo, "Towards a better understanding of gold electroless deposition in track-etched templates," *Chemistry of Materials*, vol. 19, no. 24, pp. 5955–5964, 2007.
- [11] I. A. Abu-Isa, "Metal plating of polymeric surfaces," *Polymer-Plast Technol Eng*, vol. 2, no. 1, pp. 29–65, 1973.
- [12] P. Apel, "Track etching technique in membrane technology," *Radiation Measurements*, vol. 34, no. 1–6, pp. 559–566, 2001.
- [13] I. Lee, F. Delbecq, R. Morales, M. A. Albiter, and F. Zaera, "Tuning selectivity in catalysis by controlling particle shape," *Nature Materials*, vol. 8, no. 2, pp. 132–138, 2009.
- [14] T. K. Sau, A. L. Rogach, F. Jäkel, T. A. Klar, and J. Feldmann, "Properties and applications of colloidal nonspherical noble metal nanoparticles," *Advanced Materials*, vol. 22, no. 16, pp. 1805–1825, 2010.
- [15] Y. Xia, Y. Xiong, B. Lim, and S. E. Skrabalak, "Shape-controlled synthesis of metal nanocrystals: simple chemistry meets complex physics?" *Angewandte Chemie—International Edition*, vol. 48, no. 1, pp. 60–103, 2009.
- [16] O. M. Magnussen, "Ordered anion adlayers on metal electrode surfaces," *Chemical Reviews*, vol. 102, no. 3, pp. 679–725, 2002.
- [17] T. H. Ha, H. J. Koo, and B. H. Chung, "Shape-controlled syntheses of gold nanoprisms and nanorods influenced by specific adsorption of halide ions," *Journal of Physical Chemistry C*, vol. 111, no. 3, pp. 1123–1130, 2007.
- [18] D. K. Smith, N. R. Miller, and B. A. Korgel, "Iodide in CTAB prevents gold nanorod formation," *Langmuir*, vol. 25, no. 16, pp. 9518–9524, 2009.
- [19] H. Siwek, M. Łukaszewski, and A. Czerwiński, "Electrochemical study on the adsorption of carbon oxides and oxidation of their adsorption products on platinum group metals and alloys," *Physical Chemistry Chemical Physics*, vol. 10, no. 25, pp. 3752–3765, 2008.
- [20] T. Bürgi and A. Baiker, "Heterogeneous enantioselective hydrogenation over cinchona alkaloid modified platinum: mechanistic insights into a complex reaction," *Accounts of Chemical Research*, vol. 37, no. 11, pp. 909–917, 2004.
- [21] C. J. Murphy, T. K. Sau, A. M. Gole et al., "Anisotropic metal nanoparticles: synthesis, assembly, and optical applications," *Journal of Physical Chemistry B*, vol. 109, no. 29, pp. 13857–13870, 2005.
- [22] C. R. K. Rao and D. C. Trivedi, "Chemical and electrochemical depositions of platinum group metals and their applications," *Coordination Chemistry Reviews*, vol. 249, no. 5–6, pp. 613–631, 2005.
- [23] J. R. McBride and M. P. Soriaga, "Adsorbate-catalyzed corrosion. Anodic dissolution of palladium catalyzed by chemisorbed iodine in halide-free acid solutions," *Journal of Electroanalytical Chemistry*, vol. 303, no. 1–2, pp. 255–259, 1991.
- [24] Z. Hu and T. Ritzdorf, "Cyanide- and thiourea-free electrochemical etching of gold for microelectronics applications," *Journal of the Electrochemical Society*, vol. 154, no. 10, pp. D543–D549, 2007.
- [25] G. Baltrūnas, A. Valiūnienė, J. Vienožinskis, E. Gaidamauskas, T. Jankauskas, and Ž. Margarian, "Electrochemical gold deposition from sulfite solution: application for subsequent polyaniline layer formation," *Journal of Applied Electrochemistry*, vol. 38, no. 11, pp. 1519–1526, 2008.
- [26] N. R. Jana, L. Gearheart, S. O. Obare, and C. J. Murphy, "Anisotropic chemical reactivity of gold spheroids and nanorods," *Langmuir*, vol. 18, no. 3, pp. 922–927, 2002.
- [27] H. P. Fong, Y. Wu, Y. Y. Wang, and C. C. Wan, "Electroless Cu deposition process on TiN for ULSI interconnect fabrication

- via Pd/Sn colloid activation,” *Journal of Electronic Materials*, vol. 32, no. 1, pp. 9–17, 2003.
- [28] C. D. Iacovangelo and K. P. Zarnoch, “Substrate-catalyzed electroless gold plating,” *Journal of the Electrochemical Society*, vol. 138, no. 4, pp. 983–988, 1991.
- [29] S. Hrapovic, Y. Liu, G. Enright, F. Bensebaa, and J. H. T. Luong, “New strategy for preparing thin gold films on modified glass surfaces by electroless deposition,” *Langmuir*, vol. 19, no. 9, pp. 3958–3965, 2003.
- [30] G. A. Fried, Y. Zhang, and P. W. Bohn, “Effect of molecular adsorption at the liquid-metal interface on electronic conductivity: the role of surface morphology,” *Thin Solid Films*, vol. 401, no. 1-2, pp. 171–178, 2001.
- [31] H. He, W. Cai, Y. Lin, and Z. Dai, “Silver porous nanotube built three-dimensional films with structural tunability based on the nanofiber template-plasma etching strategy,” *Langmuir*, vol. 27, no. 5, pp. 1551–1555, 2011.
- [32] S. M. Alia, G. Zhang, D. Kisailus et al., “Porous platinum nanotubes for oxygen reduction and methanol oxidation reactions,” *Advanced Functional Materials*, vol. 20, no. 21, pp. 3742–3746, 2010.
- [33] G. H. Jeong, Y. W. Lee, M. Kim, and S. W. Han, “High-yield synthesis of multi-branched gold nanoparticles and their surface-enhanced Raman scattering properties,” *Journal of Colloid and Interface Science*, vol. 329, no. 1, pp. 97–102, 2009.
- [34] T. K. Sau and C. J. Murphy, “Room temperature, high-yield synthesis of multiple shapes of gold nanoparticles in aqueous solution,” *Journal of the American Chemical Society*, vol. 126, no. 28, pp. 8648–8649, 2004.
- [35] C. H. Cui, H. H. Li, and S. H. Yu, “A general approach to electrochemical deposition of high quality free-standing noble metal (Pd, Pt, Au, Ag) sub-micron tubes composed of nanoparticles in polar aprotic solvent,” *Chemical Communications*, vol. 46, no. 6, pp. 940–942, 2010.
- [36] E. Antolini and J. Perez, “The renaissance of unsupported nanostructured catalysts for low-temperature fuel cells: from the size to the shape of metal nanostructures,” *Journal of Materials Science*, vol. 46, no. 13, pp. 4435–4457, 2011.
- [37] J. J. Boote and S. D. Evans, “Dielectrophoretic manipulation and electrical characterization of gold nanowires,” *Nanotechnology*, vol. 16, no. 9, pp. 1500–1505, 2005.

Research Article

Design and Construction of a One-Dimensional DNA Track for an Artificial Molecular Motor

Suzana Kovacic,¹ Laleh Samii,¹ Derek N. Woolfson,^{2,3} Paul M. G. Curmi,^{4,5} Heiner Linke,⁶ Nancy R. Forde,¹ and Gerhard A. Blab⁷

¹Department of Physics, Simon Fraser University, 8888 University Drive, Burnaby, BC, Canada V5A 1S6

²School of Chemistry, University of Bristol, Bristol BS8 1TS, UK

³School of Biochemistry, University of Bristol, Bristol BS8 1TD, UK

⁴School of Physics, University of New South Wales, Sydney, NSW 2052, Australia

⁵Centre for Applied Medical Research, St. Vincent's Hospital, Darlinghurst, Sydney, NSW 2010, Australia

⁶The Nanometer Structure Consortium (nmC@LU) and Division of Solid State Physics, Lund University, Box 118, 22100 Lund, Sweden

⁷Molecular Biophysics, Utrecht University, Postbus 80'000, 3508 TA Utrecht, The Netherlands

Correspondence should be addressed to Gerhard A. Blab, g.a.blab@uu.nl

Received 16 July 2011; Accepted 18 October 2011

Academic Editor: Raymond Whitby

Copyright © 2012 Suzana Kovacic et al. This is an open access article distributed under the Creative Commons Attribution License, which permits unrestricted use, distribution, and reproduction in any medium, provided the original work is properly cited.

DNA is a versatile heteropolymer that shows great potential as a building block for a diverse array of nanostructures. We present here a solution to the problem of designing and synthesizing a DNA-based nanostructure that will serve as the track along which an artificial molecular motor processes. This one-dimensional DNA track exhibits periodically repeating elements that provide specific binding sites for the molecular motor. Besides these binding elements, additional sequences are necessary to label specific regions within the DNA track and to facilitate track construction. Designing an ideal DNA track sequence presents a particular challenge because of the many variable elements that greatly expand the number of potential sequences from which the ideal sequence must be chosen. In order to find a suitable DNA sequence, we have adapted a genetic algorithm which is well suited for a large but sparse search space. This algorithm readily identifies long DNA sequences that include all the necessary elements to both facilitate DNA track construction and to present appropriate binding sites for the molecular motor. We have successfully experimentally incorporated the sequence identified by the algorithm into a long DNA track meeting the criteria for observation of the molecular motor's activity.

1. Introduction

DNA presents significant advantages as a building block for nanostructured materials, as specific sequences of DNA can be easily manipulated using a large set of biochemical tools and protocols. These can both modify its existing biological functions and design and construct completely novel functionality [1]. In addition to its standard role of encoding genetic information, DNA also possesses unique physical properties that make it amenable for use as a template or material for nanostructures. These include its mechanical stiffness [2] and its ability to self-assemble driven by the specific recognition of complementary bases. Exciting

new applications have been designed which exploit the ease of use of DNA. "Nonstandard" DNAs include such examples as DNA origami, in which the directed folding into arbitrary 2- and 3-dimensional shapes is achieved by DNA crosslinks or "staples" [3]. This technique promises immense potential to use DNA as a building block for self-assembled nanopatterning [4] or for presenting an array of substrates for addressable chemical reactions on the single molecule level [5]. Other examples include "DNA spiders," which have been designed to exhibit molecular motor properties [6–9], active folds of DNA called aptamers [10], which can be used as highly sensitive biosensors, and catalytic nucleic acid structures, ribozymes [11]. Another type of structures

is based on the self-recognition of the DNA base guanine that can generate linear aggregates, termed “G-wires,” which have shown promise as the basis of future molecular-scaled electronic devices [12]. Despite the many different designs and applications of these nonstandard DNAs, one common challenge for these uses of DNA is the task of identifying and linking biologically relevant motifs into functional units [13]. This challenge becomes increasingly more complex the further away one moves from an existing biological system to a man-made structure.

In this paper, we report on the design and construction of a periodic one-dimensional DNA track for a novel artificial molecular motor, the tumbleweed (TW) [14, 15]. The tumbleweed is designed to consist of a central hub connecting three different DNA repressor proteins: R_A (methionine repressor MetJ (Q44K) [16, 17]), R_B (tryptophan repressor TrpR [18, 19]), and R_C (purine repressor PurR [20, 21]). Each repressor acts as a foot of the motor that can be made to bind and unbind from its well-defined recognition sequence on the DNA track, depending on the concentration of its specific ligand present in solution [22–24]. The directionality of stepping is determined both by the order of ligand exchanges and by the spatial order of the recognition sequences A, B, and C on the periodic track. We propose to implement a DNA curtain technique [25] to allow simultaneous measurements of the movement of many TW motors along parallel DNA tracks (Figure 1).

On the length scale of the TW step, DNA is not a featureless molecule but presents two distinct sides (grooves) that twist helically around the length of the molecule with an 11 base-pair (bp) pitch. Therefore, one needs to ensure that all three recognition sites present on the same side of the DNA molecule to avoid steric hindrance caused by the motor “corkscrewing” around the DNA track instead of stepping along it. This is especially a concern if the track is on or close to a surface as is typically the case for single-molecule tracking experiments [26].

The proper sequence, spacing, and spatial orientation of the recognition sites on the track are thus important requirements for the design of the DNA track. In addition, in order to demonstrate motor motion over significant distances, the track needs to be highly repetitive. Furthermore, we need to be able to modify an end of the DNA construct so that it can be anchored and stretched on a surface and form a linear track along which we can observe the movements of the TW motor. A further challenge is presented by the unavoidable drift of the sample on the microscope during the single-molecule visualization of tumbleweed dynamics. As such, the DNA track needs to incorporate fluorescent fiducial markers at specified intervals that provide a readout of this drift, allowing us to measure the position of the TW relative to the track, thus removing any effect of the movement of the whole sample during the experiment. Lastly, the track has to be designed in a way so that it can be constructed and modified easily and quickly.

Here we present a method for constructing a long DNA track containing a periodic sequence of repressor binding sites. The problem of design is both theoretical—how to find

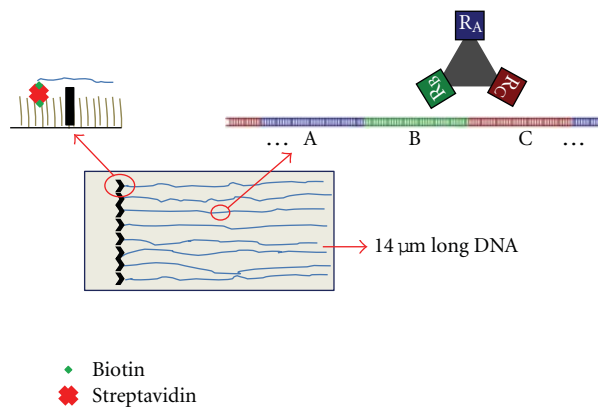


FIGURE 1: Schematic of the DNA track and the TW motor running along it. The track is anchored to a surface, which has been made inert by means of a lipid bilayer, using a biotin/streptavidin interaction (left top). Several DNA tracks of about $14\ \mu\text{m}$ length can be stretched into a DNA curtain and allow observation of the movement of many TW motors at the same time. The DNA track consists of several repeats of the ABC motif of recognition sequences along which the tripedal TW motor steps (top right: R_A , R_B , and R_C indicate the three repressor “feet,” step size $\sim 11\ \text{nm}$).

a sequence with the desired properties—and experimental—how to quickly and economically construct a long, periodic sequence of DNA. This design problem has relevance not only to molecular motor experiments but also to many of the aforementioned applications. Our experimental approach takes advantage of modular “cassette” sequences of the form $L(ABC)_N R$. Each cassette contains N -repeating units of the ordered recognition sequences A, B, and C. We show how cassettes with large N can be generated from a primary cassette with $N = 1$, by designing well-defined handles on both ends (L, R) of the cassette. The handles also allow us to specifically bind one or both ends of the track to a surface, or to attach the fiducial markers that will be necessary to follow the progress of the TW motor along the track. We, furthermore, describe the development and application of a genetic algorithm used to select an appropriate sequence for this primary cassette, which satisfies the imposed constraints. Finally, we illustrate the incorporation of the sequence selected by the algorithm into a long ($>10\ \mu\text{m}$) DNA track as required for DNA curtains, suitable for visualization experiments of motor dynamics.

2. Results and Discussion

2.1. Approach. The tumbleweed (TW) motor is designed to be a self-assembled biomolecular complex that can move by rectified diffusion along a DNA track. It consists of a triangular, peptide-based hub connecting three protein-“feet.” The hub can be labelled with a fluorophore, a quantum dot, or a small colloidal bead to facilitate detection. Each foot of the TW motor is a DNA-repressor protein, approximately 5 nm in size, that can attach tightly to its DNA recognition sequence in the presence of a specific ligand molecule, and which will release quickly once the ligand

is removed. The feet are attached to the hub by means of flexible linkers or “legs,” such that the motor can reach the next recognition site on the track and take steps of approximately 11 nm in size (Figure 1).

The DNA track provides a one-dimensional substrate along which the TW motor processes by presenting multiple repeats of the A, B, and C recognition sites in the appropriate sequence to allow binding and unbinding of the repressor feet in the presence of the appropriate ligands. The track takes into consideration such factors as appropriate spacing and orientation such that the TW motor steps along one face of the DNA molecule rather than twisting around it. To establish the necessary spacing between the repressor sequences in this ABC unit, models of all three repressors (from crystal structures of the repressors complexed with DNA, namely, PDB structures 1TRO, 1MJM, and 1F5T) were docked to a model of ideal B-form DNA (nucleic acid builder NAB), by performing least squares fits involving all atoms in the DNA portion of the crystal structure. Starting from equal spacing between the binding sites, the repressor models were moved until all resided on the same side of the DNA track. Additional sites are necessary to allow the incorporation of fiducial markers and to provide attachment points by which the DNA molecule can be bound and stretched into a linear track.

2.2. DNA Track Design by Genetic Algorithm. Our first challenge in this project was to develop the necessary tools to find a suitable DNA sequence that incorporates the appropriate repressor binding sequences with the correct spacing and orientation as well as additional sequences necessary for construction of the DNA track. For reasons of flexibility and economy, we decided to follow a bottom-up process in which we built the primary cassette *de novo* from oligonucleotides. The 11 nm stepsize of the TW motor translates into a repeating ABC unit which is 103 bp long. Together with the flanking sequences, which are required for the anchoring, doubling, and amplification of the track, the primary cassette has a total length of 169 bp (Figure 2). 101 bp of the cassette are fully defined by being in a recognition, restriction, or connection site, and 58 are variable, that is, only partly defined or arbitrary. However, only a small subpopulation ($p \ll 10^{-4}$) of the resulting 2.60×10^{33} distinct sequences is actually usable for our purpose. Besides the obvious requirement that no additional recognition or restriction sites may be formed by the variable bases, the different parts of the resulting cassette also need to present amenable thermodynamic properties (in our case the melting temperature), be easily constructible from oligonucleotides, and need to be sufficiently dissimilar to each other to minimize deletion and recombination artifacts in later molecular biological steps. An attempt to find a suitable primary cassette by brute force—testing several thousand sequences by randomly selecting the variable bases—did not yield satisfactory results. Unsurprisingly, such a brute force search is feasible only for very short cassettes, as some of the required tests (such as hybridization tests and calculation of the melting temperature) scale super-linearly with sequence length. In consequence, we describe

here our implementation of a genetic algorithm [27, 28] to find an acceptable cassette within the search space that meets all the requirements to synthesize the desired DNA track.

Our approach is centered on the design of a primary cassette $L(ABC)_1R$, also called K_1 , as shown in Figure 2 where A, B, and C correspond to the repressor binding site sequences and L and R correspond to the left and right handles which facilitate ligation and cassette doubling. An extra sequence, marked as “internal primer,” was designed to fit between C and A and contains additional recognition sites, for example, for a fiducial marker. This sequence was not used in the initial experiments.

In order to successfully identify a DNA sequence, a search algorithm is needed that can be employed practically on a large, sparse search space. Appropriately, genetic algorithms are exceedingly well suited for this type of problem [27–29]. We implemented the algorithm in Octave [30]. The scripts, which are compatible with the commercial MATLAB platform, are available from the authors. The thermodynamic properties of DNA are calculated using the freely available UNAFold suite of programs by Markham and Zuker [31, 32]. In a genetic algorithm, initially random sequences are repeatedly evaluated (scored) according to predetermined properties and restrictions and allowed to recombine according to their score. In our example, the score was the sum of penalties incurred by a sequence. A “high” penalty of 0.05/base was assessed for bases that resided in user-defined sequences exhibiting unsatisfactory thermodynamic properties—that is a melting temperature that deviated 10°C or more from the target melting temperature (56°C)—or formed an unwanted restricted or recognition site. If the melting temperature of a subsequence deviated from the target by between 5°C and 10°C , or if the same base occurred more than three times in a row, a lower penalty of 0.01/base was used. Additionally, each sequence had a small chance to incur random changes (mutations) in every round. As only the best scored sequences “survive” between rounds, the sequences quickly converge on a solution.

The parameters of the algorithm, that is, the scoring function (see Section 4), the number of sequences in the gene pool (100), the rate of random sequence changes (“mutations,” $p_m = 10^{-3}/\text{base}$), and the magnitude of the penalties, were initially optimized and are now robust. The goal was to set the penalties and mutation rate low enough to ensure, on average, one or less random change per 169 bp sequence, but to make the gene pool large enough to obtain at least one random change per generation in the population. Small populations, or populations with too small penalties, tend to get stuck with nonoptimal results, while too large mutation rate p_m or penalties that are too high will not allow the population to retain good sequences. Figure 3 shows a screen shot of the genetic algorithm during its run. Each line in the graph represents one candidate sequence, and the colour indicates the penalty, that is, the deviation from a practical cassette, on a base-pair by base-pair level. Beneficial properties quickly spread in the population (the leftmost handle has a low or no penalty for all candidates). The algorithm usually terminates within 30 cycles and will find a slightly different cassette every time it is run.

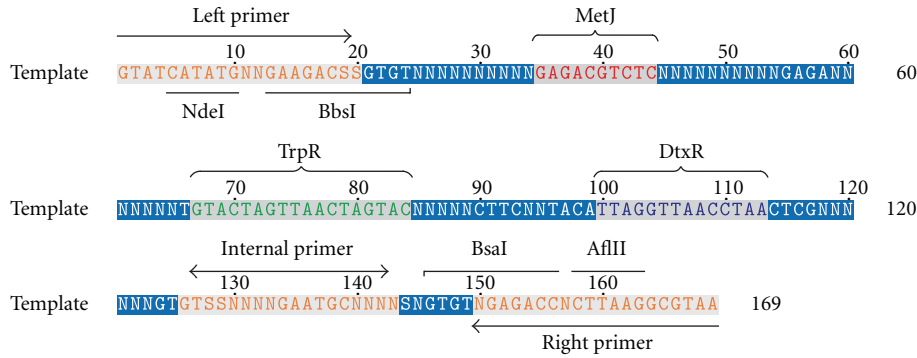


FIGURE 2: The 169 base-pair design template for a cassette $L(ABC)_1R \equiv K_1$ for building a motor track. The template contains an additional sequence, marked “internal primer,” which would allow for modification, for example, to attach a fiducial marker. Necessary design elements are noted: brackets mark repressor recognition sequences; arrows represent potential primer sites (also referred to as “handles” in the text); bars show where the template can be cut using restriction enzymes. In addition to the fully determinate bases (ATCG), the template also contains ambiguous bases (N for “any” base, S for a strong base, i.e., C or G). This template describes a total of 2.60×10^{33} distinct sequences.

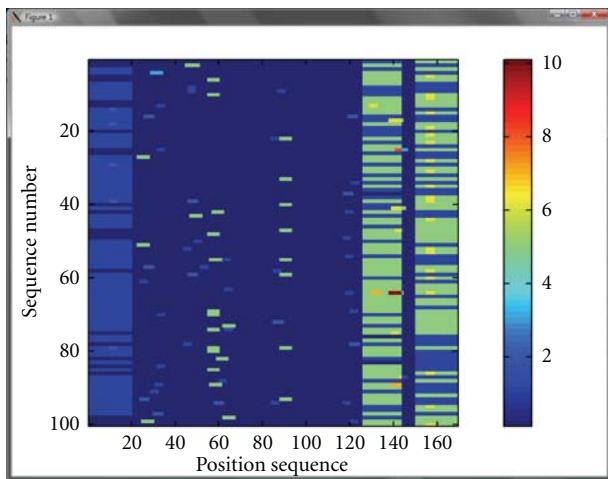


FIGURE 3: Screen shot of the genetic algorithm during its search for a suitable sequence for the primary cassette K_1 . Each line represents one candidate sequence of 169 bp, and colour denotes penalty scores assessed.

2.3. DNA Track Construction. The algorithm yielded a number of suitable sequences that could be employed to construct the desired DNA track. Table 1 shows the 10 oligonucleotide sequences chosen for the actual construction of the DNA track. Every pair of complementary oligonucleotides forms nonpalindromic single-stranded overhangs that allow it to be ligated to its neighbours. The primary cassette $L(ABC)R$, which is also referred to as K_1 , was generated by annealing and sequential ligation as described in Section 4 (“Assembly and Amplification of the Primary Cassette,” below) and K_1 is 142 bp long and contains a single ABC unit where A, B, and C correspond to the repressor binding sites for MetJ, TrpR, and DtxR, respectively. The primary cassette K_1 was subsequently subcloned into a high copy-number bacterial plasmid (pYIC), thus, creating a primary plasmid pK_1 . Working with a plasmid permits the production of

sufficient quantities of DNA, and thus the track itself, by growing it in bacteria. The sequences of the handles L and R were taken from the plasmid itself, to permit easy insertion and subsequent handling.

To observe the movement of the TW motor, the track must be sufficiently long such that it contains multiple copies of the ABC repeat along which the TW motor can move. In order to construct the long track, we made use of the L and R handles flanking the ABC repeat which each carry important restriction sites. A digest of the plasmid pK_N (where N stands for the number of ABC repeats in the plasmid) using the restriction enzymes NdeI and BbsI linearizes the plasmid and excises a short, unneeded 14 base-pair region in the left handle. Digesting a pK_N plasmid instead with NdeI and BsaI excises the K_N cassette. This can then be ligated into the linearized plasmid to form a new, circular plasmid DNA containing a doubling of the ABC unit (Figure 4). The localization of the enzyme recognition and restriction sites are shown in Figure 2. After each doubling, the new plasmid was directly subcloned into the chemically competent *E. coli* strain DH5⁺ for amplification (see Section 4). We have taken care to design the template such that the restriction sites are maintained exclusively at the ends of the cassette in this doubling process so that this step can be repeated. Thus, starting from pK_1 , after only 5 doubling steps, we can go from a 30 nm $(ABC)_1$ track to a plasmid pK_{32} which contains 32 copies of the ABC repeat and measures over 1 μ m.

One difficulty raised by this doubling scheme is the repetitiveness of the track itself. Bacteria do not usually tolerate repetitive sequences and tend to remove them from plasmids rather efficiently [33]. The decision to choose DH5⁺ was based on its tolerance for DNA repeats due to its lack of the recA protein that is responsible for recombination of homologous (repeating) sequences of DNA. Figure 5 shows plasmids ranging from pK_1 to pK_{32} double-digested with BbsI and BsaI. These restriction enzymes have their recognition sites in the left and right handle regions and thus excise the $(ABC)_N$ cassette as a whole from the plasmid (and also generate two fragments of constant length 1221

TABLE 1: Sequence of the individual oligonucleotides used to construct the repetitive TW track; the top oligo of each pair is shown 5' → 3', while the complementary strand is shown in reverse 3' → 5' direction. Bold bases indicate the recognition sites for the TW protein feet. This primary cassette K_1 is shorter than 169 bp because it does not contain the sequence for the fiducial marker shown in Figure 2.

Handle L	GTATCATATGCTGAAGACGG CATAGTATACGACTTCTGCCACA
A	GTGTCATATAGCCA GAGACGTCTCGGCACGCGTC GTATATCGGT CCTCTGCAGAGCCGTGCGCAGCTCT
B	GAGAATTTAAAT GTACTAGTTAACTAGTACGGTGA TAAATTTA CATGATCAATTGATCATGCCACTGAAG
C	CTTCAGCTCCT TAGGTTAACCTAACTCGAGCATA TCGAGGAAT CCAATTGGATTGAGCTCGTATCACA
Handle R	GTGTAGAGACCACTTAAGGCGTAA TCTCTGGTGAATTCCGCATT

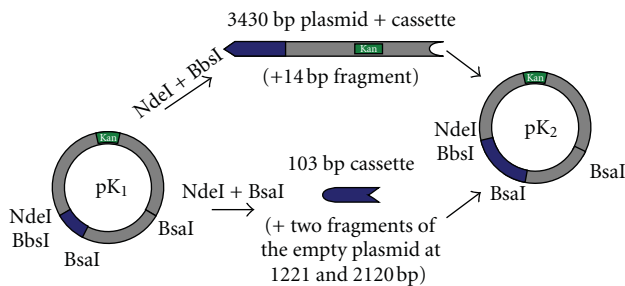


FIGURE 4: To double the length of the (ABC) unit, the pK_1 plasmid (left, with relevant restriction sites noted) was double-digested with either BbsI and NdeI (donor, including the kanamycin resistance gene “Kan,” center top) or NdeI and BsaI (recipient, center bottom). Digestion with BbsI or BsaI produces compatible overhangs between donor and recipient. Donor and recipient fragments, obtained from gel purification of each double digest, were ligated together to form a pK_2 plasmid. The two repeats of the ABC sequence in the plasmid pK_2 are joined without forming additional restriction sites.

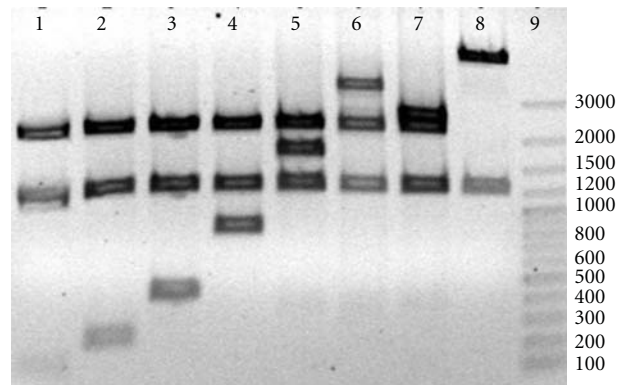


FIGURE 5: Agarose gel electrophoresis of BbsI/BsaI double-digested plasmids containing repeat sequences $(ABC)_N$. Lanes 1 to 6 correspond to $N = 1, 2, 4, 8, 16,$ and 32 . Lane 7 shows an unexpected $N = 24$ clone generated from a doubling of pK_{16} . Lanes 8 and 9 are controls (digest of the parent $pYIC$ plasmid and 1 kbp ladder, resp.). Numbers on the right indicate fragment lengths in base pairs.

and 2120 bp). The cassettes show up as bands of increasing molecular weight in lane 1 to 6 of Figure 5. The cassette in lane 7, which was expected to be pK_{32} , appears shortened and demonstrates that highly repetitive constructs can become unstable even in DH5 α , highlighting the need for vigilant monitoring of the constructs at each doubling step.

After obtaining a sufficiently long $(ABC)_N$ cassette in a plasmid, two steps remain to obtain a proper DNA track for our TW motor: modification of the handles to allow us to anchor the track to a surface and the attachment of fiducial markers.

For our initial experiments, we utilized the pK_8 plasmid, as it was determined to be stable in our chosen bacterial system and at the same time contained enough repeats of the ABC unit to provide a sufficient number of binding and unbinding steps by the TW motor. We propose to use DNA curtains [25] to stretch many DNA molecules in parallel and observe movement of TW motors along the tracks (Figure 1). The K_8 motif, however, is too short to be stretched as a DNA curtain, as this typically requires DNA which is more than $10\ \mu\text{m}$ long. We, therefore, lengthened the K_8 track from 250 nm to $14\ \mu\text{m}$ by attaching long DNA handles derived

from lambda DNA to the ends of the track. Lambda DNA is approximately $16\ \mu\text{m}$ long, contains a number of restriction sites which facilitate the insertion of the TW DNA track, and, importantly, does not contain repressor binding sites which could compete for binding with the TW motor. DNA curtains technology additionally requires a biotin tag at one end of the DNA molecule. Biotin is used to attach the DNA to a lipid bilayer via streptavidin (Figure 1; see Section 4.3 for details). The success of the ligation and end modification by biotinylation using a labelled primer was confirmed by agarose gel electrophoresis and blotting (Figure 6).

The TW motor itself will be labelled to visualize the motor dynamics. However, unless the track is also fluorescently labelled, it would be difficult to establish that the TW motor is stepping along the track rather than simply appearing to move because of drift of the sample. Fluorescent markers are thus incorporated into the DNA track to flank the $L(ABC)_N R$ motif. These act as fiducial markers to provide fixed reference points against which the movement of the TW motor is monitored. Here, we design a fiducial marker consisting of a highly fluorescent 300 bp region of DNA. Fiducial markers flanking a 32-repeat



FIGURE 6: (a) EcoRV digestion of the K_8 -lambda fragment ligation product shows that the ligation was successful, as evidenced by the extra high-molecular weight band in lane 3 compared with the digest of lambda DNA alone (lane 2). Lane 1 contains a 1 kb ladder with numbers on the left indicating fragment lengths in base pairs. (b) Biotinylation of the K_8 -lambda DNA construct, using short biotinylated duplex DNA, was successful. (A) EtBr-stained gel showing the expected molecular weight of the construct (open arrow). (B) Construct transferred to a nitrocellulose membrane, probed with streptavidin horseradish peroxidase, and visualized by chemiluminescence (ECL Plus, Pierce). Streptavidin binding coincides with the predicted size of the construct (filled arrow), indicating the presence of a biotin label on this high-molecular-weight DNA.

region of ABC sequences would be separated by 3296 base pairs (approximately $1.1 \mu\text{m}$). The use of a shorter ABC repeat sequence would result in fiducial marker sites that are closer together and are therefore difficult to resolve by fluorescence microscopy. The preliminary track built on the $(ABC)_8$ repeat sequence has the fiducial markers incorporated within the Lambda DNA handles to ensure resolution of the markers.

The fiducial marker is generated by PCR and subsequent click chemistry to incorporate fluorophores. The natural deoxythymidine triphosphate is fully replaced with an alkyne-modified deoxyuridine triphosphate during PCR amplification to generate a 300 bp DNA product incorporating 151 alkyne groups. The primers used to generate the 300-base pair DNA products were designed such that alkyne-modified deoxynucleotides are not incorporated into the restriction sequences which flank the two ends of the DNA. It is possible that alkyne modification at the restriction site could affect digestion and/or ligation. As such, EagI and PspOMI (recognition sequences—EagI CGGCCG; PspOMI GGGCCC) were chosen since these restriction sequences lack alkyne-modified bases following PCR amplification. Furthermore, these two restriction enzymes produce compatible sticky ends allowing end-to-end ligation of the 300-base pair pieces should a longer fiducial marker sequence be necessary. They also permit ligation into existing restriction sites flanking the $(ABC)_N$ cassette. Fluorescent DNA is generated by click chemistry between the alkyne-labelled DNA and azide-labelled carboxyrhodamine-110. When the fluorophore was added in 10-fold excess relative to alkyne (1500 equivalents per DNA molecule), the resulting highly fluorescent DNA exhibited unusual physicochemical properties as previously observed [31]. The DNA did not stain with ethidium bromide nor migrate as expected by agarose gel electrophoresis. When the amount of fluorophore was reduced to 10 mole equivalents per mole equivalent

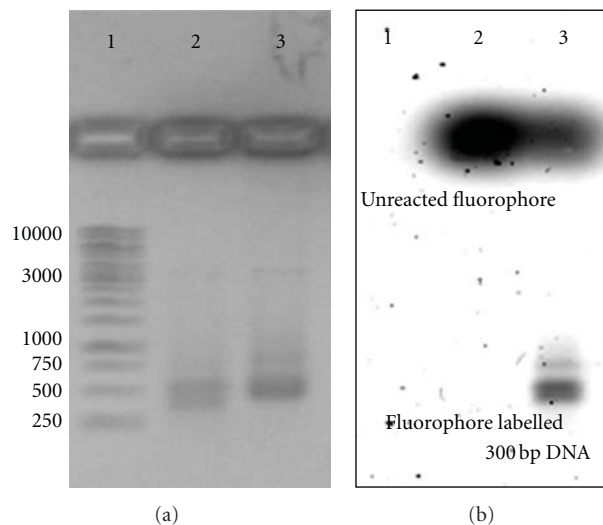


FIGURE 7: Labelling of 1 mole equivalent 300 bp alkyne DNA with 10 mole equivalents of carboxyrhodamine 110. A 1% agarose gel was stained with ethidium bromide (a) and scanned at 532 nm excitation and 555/20 nm emission (b) showing the reaction product between carboxyrhodamine 110-PEG3-azide and 300 bp alkyne-labelled DNA (lane 3) or 300 bp DNA (no alkyne incorporation) (lane 2). Lane 1: 1 kbp DNA ladder, numbers on the left indicating selected fragment lengths in base pairs.

DNA, the fluorophore-modified DNA migrated as expected on an agarose gel and could be detected by both ethidium bromide staining and fluorescence. Alkyne-labelled DNA ran slightly slower on a 1% agarose gel relative to control samples (Figure 7).

It is possible that fluorophore-modified DNA will be more difficult to incorporate at fiducial marker sites than alkyne-modified DNA due to the greater steric bulk of the fluorophore which may hinder digestion and/or ligation. Should this prove the case, alkyne-modified DNA will be ligated into the fiducial marker sites followed by click chemistry to introduce the fluorophore label. Alkyne-modified DNA has been successfully ligated in tandem demonstrating that the restriction enzymes EagI and PspOMI and T4 DNA ligase retain the ability to digest and ligate alkyne-modified DNA (Figure 8).

3. Conclusions

We have presented the *de novo* design and implementation of an extended one-dimensional DNA track for use in single-molecule experiments. For this goal, we have adapted molecular biology protocols which have allowed us to modularly construct, amplify, and extend a functional repetitive DNA track to a length of several micrometres. This track is amenable for modification and contains an anchoring point to the surface and fluorescent fiducial markers. Even though we introduce a specific application, the methods described in this paper are widely applicable to the construction of custom-made one-dimensional nanostructures based on DNA.

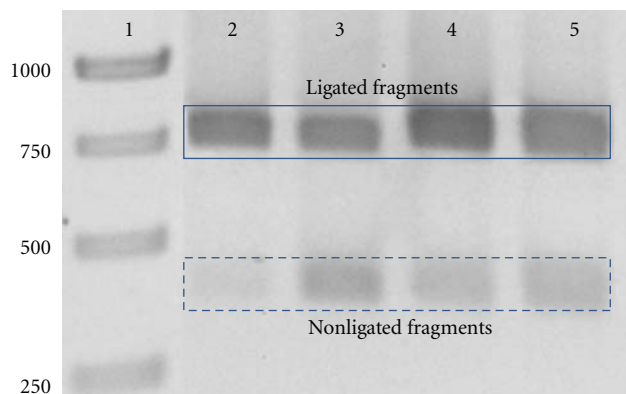


FIGURE 8: Alkyne modification does not interfere with digestion and ligation reactions. Lanes 4 and 5 show the successful self-ligation of 371 bp alkyne DNA after an *EagI* digest and a *PspOMI* digest, respectively, which each generate 738 bp fragments. Self-ligations of *EagI*- and *PspOMI*-digested control DNA (no alkyne modification) are shown in lanes 2 and 3, respectively. Lane 1 contains a 1 kb ladder, with numbers on the left indicating selected fragment lengths in base pairs. Alkyne DNA runs slightly slower than unmodified DNA.

At the heart of the paper is a computational toolbox that uses a heuristic search program, based on a genetic algorithm, to quickly and reliably identify suitable long DNA sequences with a set of specific structural, molecular biological, and thermodynamic properties from within the exceedingly vast, sparse space of possible DNA sequences. Our results show that by artful combination of established molecular biology techniques and targeted design using appropriate algorithms, completely new nanostructures with novel, not necessarily biological functions can be constructed from this versatile polymer.

4. Methods

4.1. Design of the Primary DNA Cassette. The genetic algorithm was implemented as a set of scripts in the freely available mathematical environment Octave [34] that is compatible with MATLAB (Mathwork, Natick, MA, USA). Thermodynamic properties of the DNA sequences of interest were established using an external application, UNAFold [31, 32].

At the heart of the genetic algorithm lies a template string that describes the general layout of the required DNA sequence using the upper-case one-letter codes. The allowed alphabet contains the standard bases “A,” “T,” “G,” and “C”; the IUBMB definitions for incompletely specified nucleobases [35], and the additional character “Q” indicating a nonbinding base. The template is divided into immutable “sequence features,” which include defined base sequences such as recognition or restriction sites, and “subsequences,” for which thermodynamic properties (entropic and enthalpic contributions to the binding energy, formation of secondary structures, or melting temperature T_M) can be defined. Subsequences can also be required to be unique, in which

case the subsequence is tested for “substantial similarity” by calculating the relative difference in melting temperatures between the subsequence with its complement and with the rest of the template. A set of “restricted sites” (recognition and restriction sites) can be defined that must not occur anywhere but in predefined positions on either strand of the template. Restricted sites are again defined using the same upper-case one-letter codes for nucleobases as in the case of the template. The use of regular expressions [36, 37] is permissible.

The genetic algorithm starts with a set of n candidate sequences (user defined; typically $n \sim 100$) that conform to the sequence features specified for the template (see Figure 2 for the requirements of our template). Each candidate sequence is scored by applying penalties to bases that reside in subsequences exhibiting unsatisfactory thermodynamic properties (a melting temperature T_M outside a set range, or which are too similar to other parts of the track), form additional restriction or recognition sites, or are repetitive (Figure 3). The penalties are user defined and are typically graduated (high penalty, low penalty), to generate gradual convergence towards a satisfying sequence. Sequences in the lowest quartile survive and all sequences with higher penalty scores are deleted. The surviving sequences have then a small probability of mutation, proportional to the penalty assessed, typically at most 1 mutation per template, and are used to generate a new set of n candidates by random crossover. The algorithm terminates if a sequence without penalties is found, or if a set number of iterations (typically 50) is exceeded. The sequence chosen by the genetic algorithm and used in our experiments is shown in Table 1.

The collection of scripts is freely available from the authors.

4.2. Construction of the Primary Cassette

4.2.1. Assembly and Amplification of the Primary Cassette.

The TW track was constructed modularly from a set of 10 oligonucleotides (Table 1: integrated DNA technologies). Each oligonucleotide was phosphorylated using T4 polynucleotide kinase (New England Biotech, NEB, Ipswich, MA, USA), following the manufacturer’s protocol. Complementary oligonucleotides were annealed by heating to 85°C, followed by slow cooling ($\Delta T = 0.6^\circ\text{C}/\text{min}$) to room temperature to generate five double-stranded DNA components. Three of these components correspond to the binding sites of the MetJ, TrpR, and PurR repressor proteins used in the TW motor and are denoted A, B, and C. The remaining two DNA components consist of sequences which permit subcloning and cassette doubling and are labelled L and R. The five components were ligated in the appropriate order using T4 DNA ligase (NEB). Products of each sequential ligation were separated by agarose gel electrophoresis, and bands of appropriate length were recovered using a commercial extraction kit (QIAGEN).

The primary cassette $L(ABC)_1R \equiv K_1$ was then ligated into a high copy-number plasmid (pYIC, Addgene plasmid 18673) using unique *AflII* and *NdeI* (NEB) restriction sites.

This generated the primary plasmid, pK₁, containing the cassette K₁ (one repeat of the ABC sequence).

Plasmids pK₁ were transformed into the DH5 strain of *E. coli* (Invitrogen) according to the manufacturer's protocol and were selected at 37°C on LB-agar plates supplemented with 25 µg/mL kanamycin. Following cell growth in liquid LB-kanamycin medium, plasmids were purified using a miniprep kit (QIAGEN). Correct incorporation of cassettes was confirmed by restriction assays (Figure 4) and sequencing (MWG Operon, Huntsville, AL, USA).

4.2.2. Doubling of Cassettes. The doubling of the cassette is illustrated schematically in Figure 4. To double the length of the (ABC) repeating unit, the pK₁ plasmid was double-digested with either BbsI and NdeI (donor) or NdeI and BsaI (recipient) (all enzymes: NEB). Appropriately sized fragments were gel purified (QIAGEN). Donor and recipient were ligated together, and the new construct (pK₂ plasmid) was transformed into DH5 cells as described above. This process was repeated to generate pK₄, pK₈, pK₁₆, and pK₃₂ plasmids.

4.3. Track Elongation and Biotinylation. pK₈ plasmid (4179 bp) was digested with EagI and RsrII (NEB) to generate two fragments, of which the 3573 bp was gel purified. Lambda DNA (NEB) was digested with PspOMI to generate a 38416 bp fragment which was isolated by agarose gel electrophoresis and extraction (agarose gel-digesting preparation, GELase). This was subsequently ligated to the purified 3573 bp fragment of the pK₈ plasmid using the compatible cohesive ends from the PspOMI and EagI digest.

A biotin tag was introduced into the construct by using the 5'-GAC overhang, produced by initial digestion of the pK₈ plasmid with RsrII, and ligation to a short sticky-ended duplex DNA made from oligonucleotide 5'-biotin-CGGCATCAGAGCAGATGAC-3' and its complement 5'-ATCTGCTCTGATGCCG-3'. To probe for the presence of the biotin tag on the construct, the sample was run on a 0.7% TBE agarose gel to separate the construct from any unligated short oligonucleotides, then transferred to a nitrocellulose membrane (Trans-Blot, Bio-Rad). The membrane was washed and blocked (with 2% BSA in 1X DPBST + 0.1% Tween) and probed according to the manufacturer's protocol with horseradish peroxidase-conjugated streptavidin (Figure 6).

4.4. Labelling of a DNA Track with Fiducial Markers

4.4.1. Preparation of 300 Base-Pair Alkyne DNA. A 300 bp DNA product which incorporates alkyne-modified deoxynucleotides was prepared following a literature protocol [38]. Briefly, PCR amplification of pUC19 plasmid DNA was performed using the following primer pairs: 5'-ATGCTTCGGCCGTATGCGGTGTGAAA-3' and 5'-TCTTATGGGCCCTGTGGAATTGTGAG-3'. These primers generate EagI and PspOMI restriction sites at the two ends of the PCR product. In the PCR reaction mixture, the natural dTTP was replaced with the alkyne-modified

deoxynucleotide analog, C8-alkyne-dUTP (Jena Bioscience). DNA was amplified using Pwo polymerase (Roche). Products of PCR reactions were purified using the QiaQuick PCR purification kit (QIAGEN), and their size was confirmed by agarose gel electrophoresis. Alkyne-labelled DNA ran slightly slower on a 1% agarose gel relative to control samples (Figure 8).

4.4.2. Preparation of Carboxyrhodamine 110-Labelled DNA. To 1 pmol of alkyne-labelled, 300-base pair DNA was added 10 pmol of azide-fluor 488 (carboxyrhodamine 110-PEG3-azide, Jena Bioscience). Quantitative incorporation of the fluorophore would result in one fluorophore per 30 bp of sequence. The reaction was catalyzed by the addition of copper (II) sulphate (0.5 mM) and ascorbic acid (0.5 mM) in the presence of 0.5 mM tris[(1-benzyl-1H-1,2,3-triazol-4-yl)methyl] amine (TBTA) in 50% DMSO according to a manufacturer's protocol (Lumiprobe). TBTA was added to protect the DNA from Cu(I)-mediated DNA strand breaks [39]. The reaction was incubated at room temperature for 1 hour with rotary mixing. A control reaction, in which the DNA contained all natural bases and no alkynes, was similarly treated. The reaction mixture was purified by ethanol precipitation using glycogen to aid precipitation. Appropriate labelling of the alkyne DNA was confirmed by running the sample on a 1% agarose gel and scanning the gel at 532 nm and monitoring emission at 555 nm (555/20 nm band-pass filter, Figure 7).

4.4.3. Ligation of Alkyne-Labelled DNA. Alkyne-labelled 371 bp DNA was generated by PCR using the following primers which are modified from those described above in order to further exclude alkyne-labelled nucleotides from the vicinity of the EagI and PspOMI recognition sites: 5'-TTGCTTCGGCCGTGTACTGAGAGTGCACC-3' and 5'-TCTTGTGGGCCCTGTGGAATTGTGAGCG-3'. Alkyne-labelled DNA was digested using either EagI or PspOMI. After product clean-up (PCR purification kit, QIAGEN), a self-ligation reaction of each batch was run using T4 DNA ligase. Ligation products were run on a 1% agarose gel to confirm ligation and were compared with the self-ligations of EagI- and PspOMI-digested DNA from control 371 bp fragments lacking the alkyne modification (Figure 8).

Authors' Contribution

S. Kovacic and L. Samii contributed equally to this paper and they shared the first authorship.

Acknowledgments

The authors would like to thank their collaborators in the HFSP motors team, and especially Andrew Wieczorek for fruitful discussions and his assistance in the construction of the DNA track. This work has been funded by the Human Frontier Science Program (RGP31/2007) and the Natural Sciences and Engineering Research Council of Canada (NSERC; NRF).

References

- [1] A. S. Khalil and J. J. Collins, "Synthetic biology: applications come of age," *Nature Reviews Genetics*, vol. 11, no. 5, pp. 367–379, 2010.
- [2] C. Bustamante, J. F. Marko, E. D. Siggia, and S. Smith, "Entropic elasticity of λ -phage DNA," *Science*, vol. 265, no. 5178, pp. 1599–1600, 1994.
- [3] P. W. K. Rothmund, "Folding DNA to create nanoscale shapes and patterns," *Nature*, vol. 440, no. 7082, pp. 297–302, 2006.
- [4] A. M. Hung, C. M. Micheel, L. D. Bozano, L. W. Osterbur, G. M. Wallraff, and J. N. Cha, "Large-area spatially ordered arrays of gold nanoparticles directed by lithographically confined DNA origami," *Nature Nanotechnology*, vol. 5, no. 2, pp. 121–126, 2010.
- [5] N. V. Voigt, T. Tørring, A. Rotaru et al., "Single-molecule chemical reactions on DNA origami," *Nature Nanotechnology*, vol. 5, no. 3, pp. 200–203, 2010.
- [6] R. Pei, S. K. Taylor, D. Stefanovic, S. Rudchenko, T. E. Mitchell, and M. N. Stojanovic, "Behavior of polycatalytic assemblies in a substrate-displaying matrix," *Journal of the American Chemical Society*, vol. 128, no. 39, pp. 12693–12699, 2006.
- [7] K. Lund, A. J. Manzo, N. Dabby et al., "Molecular robots guided by prescriptive landscapes," *Nature*, vol. 465, no. 7295, pp. 206–210, 2010.
- [8] L. Samii, H. Linke, M. J. Zuckermann, and N. R. Forde, "Biased motion and molecular motor properties of bipedal spiders," *Physical Review E*, vol. 81, no. 2, Article ID 021106, 2010.
- [9] L. Samii, G. A. Blab, E. H. C. Bromley et al., "Time-dependent motor properties of multipedal molecular spiders," *Physical Review E*, vol. 84, no. 3, Article ID 031111, 2011.
- [10] A. K. H. Cheng, D. Sen, and H. Z. Yu, "Design and testing of aptamer-based electrochemical biosensors for proteins and small molecules," *Bioelectrochemistry*, vol. 77, no. 1, pp. 1–12, 2009.
- [11] D. Rueda and N. G. Walter, "Fluorescent energy transfer read-out of an aptazyme-based biosensor," *Methods in Molecular Biology*, vol. 335, pp. 289–310, 2006.
- [12] T. C. Marsh and E. Henderson, "G-wires: self-assembly of a telomeric oligonucleotide, d(GGGGTTGGGG), into large superstructures," *Biochemistry*, vol. 33, no. 35, pp. 10718–10724, 1994.
- [13] C. Lin, Y. Liu, S. Rinker, and H. Yan, "DNA tile based self-assembly: building complex nanoarchitectures," *ChemPhysChem*, vol. 7, no. 8, pp. 1641–1647, 2006.
- [14] E. H. C. Bromley, N. J. Kuwada, M. J. Zuckermann et al., "The tumbleweed: towards a synthetic protein motor," *HFSP Journal*, vol. 3, no. 3, pp. 204–212, 2009.
- [15] N. J. Kuwada, G. A. Blab, and H. Linke, "A classical Master equation approach to modeling an artificial protein motor," *Chemical Physics*, vol. 375, no. 2–3, pp. 479–485, 2010.
- [16] A. Cooper, A. McAlpine, and P. G. Stockley, "Calorimetric studies of the energetics of protein-DNA interactions in the E. coli methionine repressor (MetJ) system," *FEBS Letters*, vol. 348, no. 1, pp. 41–45, 1994.
- [17] I. D. Parsons, B. Persson, A. Mekhalfia, G. M. Blackburn, and P. G. Stockley, "Probing the molecular mechanism of action of co-repressor in the E.coli methionine repressor-operator complex using surface plasmon resonance (SPR)," *Nucleic Acids Research*, vol. 23, no. 2, pp. 211–216, 1995.
- [18] R. W. Schevitz, Z. Otwinowski, A. Joachimiak, C. L. Lawson, and P. B. Sigler, "The three-dimensional structure of trp repressor," *Nature*, vol. 317, no. 6040, pp. 782–786, 1985.
- [19] R. G. Zhang, A. Joachimiak, C. L. Lawson, R. W. Schevitz, Z. Otwinowski, and P. B. Sigler, "The crystal structure of trp aporepressor at 1.8 Å shows how binding tryptophan enhances DNA affinity," *Nature*, vol. 327, no. 6123, pp. 591–597, 1987.
- [20] A. Nagadoi, S. Morikawa, H. Nakamura et al., "Structural comparison of the free and DNA-bound forms of the purine repressor DNA-binding domain," *Structure*, vol. 3, no. 11, pp. 1217–1224, 1995.
- [21] M. A. Schumacher, K. Y. Choi, H. Zalkin, and R. G. Brennan, "Crystal structure of LacI member, PurR, bound to DNA: minor groove binding by helices," *Science*, vol. 266, no. 5186, pp. 763–770, 1994.
- [22] J. Carey, "Gel retardation at low pH resolves trp repressor-DNA complexes for quantitative study," *Proceedings of the National Academy of Sciences of the United States of America*, vol. 85, no. 4, pp. 975–979, 1988.
- [23] K. L. B. Borden, P. Beckmann, and A. N. Lane, "Determination of the orientations of tryptophan analogues bound to the trp repressor and the relationship to activation," *European Journal of Biochemistry*, vol. 202, no. 2, pp. 459–470, 1991.
- [24] K. Phillips and S. E. V. Phillips, "Electrostatic activation of Escherichia coli methionine repressor," *Structure*, vol. 2, no. 4, pp. 309–316, 1994.
- [25] T. Fazio, M. L. Visnapuu, S. Wind, and E. C. Greene, "DNA curtains and nanoscale curtain rods: high-throughput tools for single molecule imaging," *Langmuir*, vol. 24, no. 18, pp. 10524–10531, 2008.
- [26] J. Gorman, T. Fazio, F. Wang, S. Wind, and E. C. Greene, "Nanofabricated racks of aligned and anchored DNA substrates for single-molecule imaging," *Langmuir*, vol. 26, no. 2, pp. 1372–1379, 2010.
- [27] S. Forrest, "Genetic algorithms: principles of natural selection applied to computation," *Science*, vol. 261, no. 5123, pp. 872–878, 1993.
- [28] P. Willett, "Genetic algorithms in molecular recognition and design," *Trends in Biotechnology*, vol. 13, no. 12, pp. 516–521, 1995.
- [29] M. Affenzeller, S. Winkler, S. Wagner, and A. Beham, *Genetic Algorithms and Genetic Programming: Modern Concepts and Practical Applications*, Chapman & Hall/CRC, New York, NY, USA, 2009.
- [30] J. W. Eaton, *GNU Octave Manual*, Network Theory Limited, 2002.
- [31] N. R. Markham and M. Zuker, "DINAMelt web server for nucleic acid melting prediction," *Nucleic Acids Research*, vol. 33, no. 2, pp. W577–W581, 2005.
- [32] N. R. Markham and M. Zuker, "UNAFold: software for nucleic acid folding and hybridization," *Methods in Molecular Biology*, vol. 453, pp. 3–31, 2008.
- [33] A. M. Albertini, M. Hofer, M. P. Calos, and J. H. Miller, "On the formation of spontaneous deletions: the importance of short sequence homologies in the generation of large deletions," *Cell*, vol. 29, no. 2, pp. 319–328, 1982.
- [34] J. W. Eaton, D. Bateman, and S. Hauberg, *GNU Octave Manual Version 3*, Network Theory Limited, 2008.
- [35] C. Liébecq, *Compendium of Biochemical Nomenclature and Related Documents*, Portland Press, 1992.
- [36] D. Kozen, "A completeness theorem for Kleene algebras and the algebra of regular events," in *Proceedings of the 6th Annual IEEE Symposium on Logic in Computer Science (LICS '91)*, pp. 214–225, July 1991.
- [37] T. Stubblebine, *Regular Expression Pocket Reference*, O'Reilly Media, Inc., 2003.

- [38] J. Gierlich, K. Gutsmedl, P. M. E. Gramlich, A. Schmidt, G. A. Burley, and T. Carell, "Synthesis of highly modified DNA by a combination of PCR with alkyne-bearing triphosphates and click chemistry," *Chemistry*, vol. 13, no. 34, pp. 9486–9494, 2007.
- [39] T. R. Chan, R. Hilgraf, K. B. Sharpless, and V. V. Fokin, "Polytriazoles as copper(I)-stabilizing ligands in catalysis," *Organic Letters*, vol. 6, no. 17, pp. 2853–2855, 2004.

Research Article

Thermal Stability and Rheological Behaviors of High-Density Polyethylene/Fullerene Nanocomposites

Liping Zhao,^{1,2} Ping'an Song,³ Zhenhu Cao,^{1,2} Zhengping Fang,^{1,2}
and Zhenghong Guo¹

¹Laboratory of Polymer Materials and Engineering, Ningbo Institute of Technology, Zhejiang University, Ningbo 315100, China

²MOE Key Laboratory of Macromolecular Synthesis and Functionalization, Zhejiang University, Hangzhou 310027, China

³Department of Materials, College of Engineering, Zhejiang Agriculture & Forest University, Hangzhou 300311, China

Correspondence should be addressed to Zhenghong Guo, guozhenghong@nit.zju.edu.cn

Received 3 June 2011; Accepted 20 October 2011

Academic Editor: Steve Acquah

Copyright © 2012 Liping Zhao et al. This is an open access article distributed under the Creative Commons Attribution License, which permits unrestricted use, distribution, and reproduction in any medium, provided the original work is properly cited.

High-density polyethylene/fullerene (HDPE/C₆₀) nanocomposites with the C₆₀ loading that varied from 0.5 to 5.0% by weight were prepared via melt compounding. Thermogravimetric analysis (TGA) and differential scanning calorimetry (DSC) results showed that the presence of C₆₀ could remarkably enhance the thermal properties of HDPE. A very low C₆₀ loading (0.5 wt%) increased the onset degradation temperature from 389°C to 459°C and decreased the heat release from 3176 J/g to 1490 J/g. The larger the loading level of C₆₀, the better the thermal stability of HDPE/C₆₀ nanocomposites. Rheological investigation results showed that the free radical trapping effect of C₆₀ was responsible for the improved thermal stability of HDPE.

1. Introduction

Soon after the discovery of buckminsterfullerene, C₆₀, it was able to be produced in bulk quantities, which inspired scientists worldwide to explore its fascinating chemistry, and it has now become the most intensely researched single molecule in modern science [1–3]. A significant aspect of the C₆₀ chemistry is its high reactivity towards free radicals, and C₆₀ has 30 carbon-carbon double bonds which can trap more than 34 free radicals; thus it is known as a radical sponge [4]. The free radical reaction of C₆₀ with various compounds has been extensively studied [4–7].

Since the thermal degradation of polymers is a free radical chain reaction, the presence of C₆₀ in polymer may trap the free radicals produced during the degradation process. These suggest the possible use of fullerene as an effective radical scavenger in chain reactions during thermal degradation. It has been reported that 2 wt% fullerene (C₆₀) could increase the onset degradation temperature (T_{onset}) and the maximum degradation temperature (T_{max}) of PP by 20 and 62°C, respectively [8, 9]. The presence of C₆₀ could delay the thermal oxidation and improve the thermal

stability of PP, which could be attributed to the high reactivity of C₆₀ towards free radicals.

The present paper mainly focused on studying the influence of C₆₀ on the thermal degradation behavior and rheological properties of high-density polyethylene. Concerning that the thermal degradation of polyethylene is done also via a free radical chain scission process as PP, C₆₀ is expected to have positive effect on improving the thermal stability of PE.

2. Materials and Methods

2.1. Materials. High-density Polyethylene (HDPE, 5000 S, MFR = 0.9 g/10 min) was purchased from Yangzi Petrochemical Co., Ltd, and C₆₀ (purity: >99%) was bought from Henan Puyang Co., Ltd.

2.2. Preparation of HDPE/C₆₀ Nanocomposites. HDPE/C₆₀ nanocomposites were prepared via melt compounding at 180°C in a ThermoHaake rheomixer with a rotor speed of 60 rpm for 8 min. Nanocomposites containing 0.5 wt%, 1.0 wt%, 2.5 wt%, and 5.0 wt% C₆₀ were designated as C₆₀-0.5%, C₆₀-1.0%, C₆₀-2.5%, and C₆₀-5.0%.

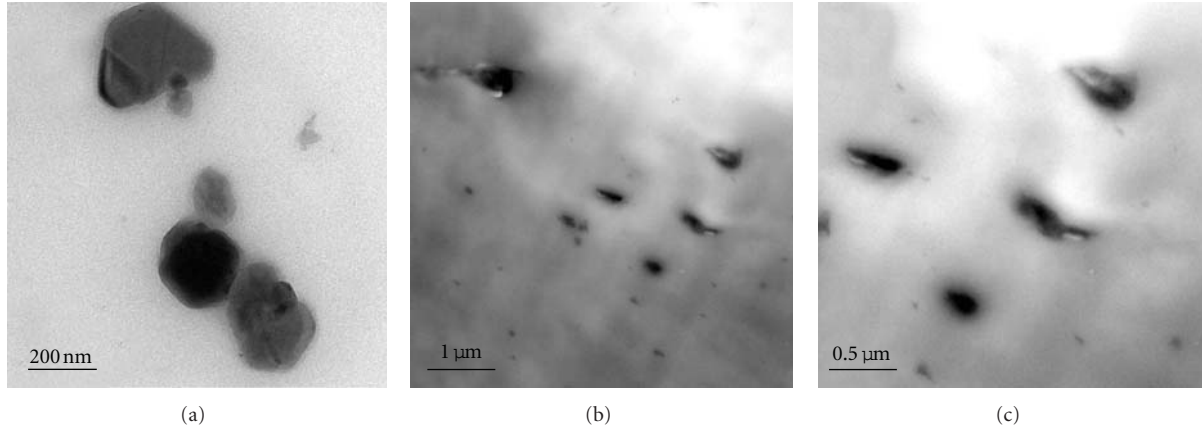


FIGURE 1: TEM microphotographs for pristine C_{60} (a) and C_{60} -5.0% (b) and (c).

2.3. Measurements and Characterization. Thermogravimetric analysis (TGA) was performed on a STA 409 PC thermal analyzer at a heating rate of $20^{\circ}\text{C}/\text{min}$ in air atmosphere and N_2 atmosphere, with a scanning range from 30 to 700°C , and each specimen was examined in triplicate.

The rheological properties of HDPE and its nanocomposites were conducted on a controlled strain rheometer (Haake MARS) in air environment. The samples were pressed at 180°C under 15 MPa to get the disklike specimens with 25 mm in diameter and 1.2 mm in thickness. The isothermal dynamic frequency sweeps were performed under the condition of the frequency range, strain amplitude, and temperature being $100\text{--}0.01\text{ rads}^{-1}$ with the strain of 1% at 180°C and 300°C , respectively. Temperature scanning test was performed in the range from 180 to 300°C with the 1% strain and a fixed frequency at 1 rads^{-1} .

The dispersion of C_{60} in the HDPE matrix was observed by transmission electron microscopy (TEM, JEM-1200EX).

3. Results and Discussion

3.1. Dispersion of C_{60} in HDPE Matrix. The diameter of the spherical C_{60} molecule is 0.71 nm, and its crystal size differs with different methods of fabrication [9]. Figure 1 shows the TEM images for pure C_{60} and C_{60} -5%. The size of C_{60} crystals used in this work from Figure 1(a) is from 70 to 200 nm. From Figure 1(c), it is shown that many of C_{60} crystallites in the HDPE matrix were shaped in ellipsoidal, rodlike. This phenomenon may be caused by the strong shear force during blending. The shear force could destroy the primary stack of C_{60} crystallites and these crystallites rearrange to different type. In the HDPE matrix, C_{60} crystallites aggregates and does not disperse well through melt blending, as observed from Figure 1(b). The size of some C_{60} domains in nanocomposites is about 500 nm or even large.

3.2. Thermal Properties of HDPE/ C_{60} Nanocomposites. The thermal stability of HDPE and HDPE/ C_{60} nanocomposites was tested by TGA, and their TG and DTG curves in nitrogen

TABLE 1: Detailed data obtained from TGA tests for HDPE and HDPE/ C_{60} nanocomposites in nitrogen.

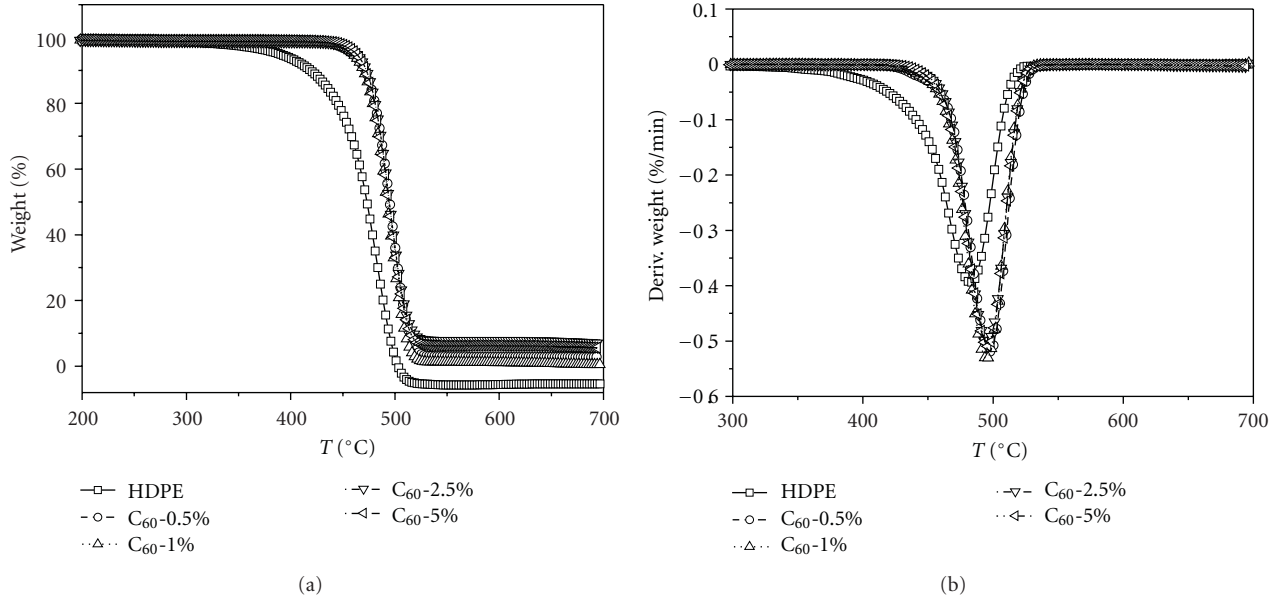
Sample	T_{onset} ($^{\circ}\text{C}$)	T_{max} ($^{\circ}\text{C}$)
HDPE	389	483
C_{60} -0.5%	459	497
C_{60} -1.0%	460	496
C_{60} -2.5%	462	496
C_{60} -5.0%	463	495

atmosphere are shown in Figure 2, with detailed data listed in Table 1. At the initial stage of degradation (before 400°C), C_{60} reacts easily with low-molecular-weight alkyl radicals with formation of remarkable persistent products $\text{Rn}C_{60}$ (where $n = 1, 2, 3, \dots$) [10, 11], which caused that the decomposition of HDPE/ C_{60} nanocomposites is slower than pure HDPE. The onset thermal decomposition temperature (T_{onset}) of HDPE is noticeably increased with the addition of C_{60} . For example, the T_{onset} of C_{60} -0.5% is 459°C , about 70°C higher than pure HDPE. With increasing C_{60} content, the onset temperature of HDPE/ C_{60} nanocomposites changes slightly. From DTG curves, the maximum decomposition temperature (T_{max}) is obtained, with T_{max} 497°C for C_{60} -0.5%, about 14°C higher than pure HDPE.

Figures 3 and 4 present the TG and DSC curves for HDPE and its composites in air atmosphere, with detailed data given in Table 2. In air atmosphere, the presence of oxygen could enhance the thermal oxidation decomposition of HDPE nanocomposites remarkably. HDPE experiences a rapid thermal oxidation decomposition accompanied by hydrogen abstraction [12]. The (T_{onset}) of HDPE is about 323°C , and two-step decomposition processes are observed at around 398°C and 456°C (see Table 2). The first step decomposition is the oxidation of HDPE [13]. The second step may be the decomposition of oxidation products formed by the oxidation of HDPE. C_{60} , as the radical sponge, could capture the free radicals produced during the degradation process. Obviously, the presence of C_{60} delays the oxidation degradation of parent polymer and the first-step T_{max} disappears, and the T_{onset} of the nanocomposites noticeably

TABLE 2: Detailed data obtained from TGA and DSC tests for HDPE and HDPE/C₆₀ nanocomposites in air.

Sample	T_{onset} (°C)	Data from TGA		T_{max}	Data from DSC ΔH_d (J/g)
		Stage 1	Stage 2		
HDPE	323	398	456		3176
C ₆₀ -0.5%	361	—	451		1490
C ₆₀ -1.0%	387	—	444		1521
C ₆₀ -2.5%	431	—	461		842
C ₆₀ -5.0%	416	—	448		1892

FIGURE 2: TG (a) and DTG (b) curves for pristine HDPE and HDPE/C₆₀ nanocomposites in nitrogen.

increase with the increase of C₆₀ content. As for C₆₀-2.5%, its T_{onset} is around 431°C, 108°C higher than pure HDPE, which indicates that the presence of C₆₀ slows down the thermal oxidation decomposition of HDPE remarkably. However, when the contents of C₆₀ in the matrix exceed 2.5 wt%, the T_{onset} of the nanocomposites decreases with the content of C₆₀. At high loading (as for C₆₀-5.0%), C₆₀ may tend to attract each other, which causes the agglomeration (as shown in Figure 1) instead of trapping the alkyl fragments radicals bringing down the thermal stability of HDPE/C₆₀ nanocomposites.

The difference in thermal behavior between air and nitrogen atmospheres indicates that the presence of oxygen could speed up the thermal oxidation decomposition of HDPE nanocomposites remarkably. The oxygen and alkyl fragment radicals trapped by C₆₀ in nanocomposites during the thermal decomposition are competitive.

DSC measurements could provide the heat enthalpy of thermal degradation during the decomposition process of materials. Figure 4 presents the DSC curves of HDPE/C₆₀ nanocomposites in air atmosphere. In air atmosphere, HDPE/C₆₀ nanocomposites experiences rapid exothermal oxidation decomposition at high temperature. The enthalpy

(ΔH_d) is an important parameter since it could quantify the heat evolution produce in the process of oxidation decomposition. The enthalpies of the nanocomposites are greatly reduced from 3176 J/g for HDPE to 1490 J/g for C₆₀-0.5%, indicating that the nanocomposites release much less heat in the process of oxidation dehydrogenation and this phenomenon is favorable to flame retarded polymer materials.

3.3. Mechanism for the Thermal Stability of HDPE/C₆₀ Nanocomposites. In order to clarify the mechanism for C₆₀ improving the thermal stability of HDPE, the rheological measurements were introduced to investigate the viscoelastic behaviors of the nanocomposites. For investigating the viscoelastic behavior of the nanocomposites in the heating process, temperature scanning measurements were performed. Figure 5 presents the curves of temperature dependence of complex viscosity (η^*) for HDPE and its nanocomposites. Clearly, with the increase of temperature, the complex viscosity (η^*) of nanocomposites decreases, and then increases sharply. The critical temperature is defined as T_c , at which η^* starts to increase or crosslink reaction occurs. The easier movement of polymer chains during heating, or

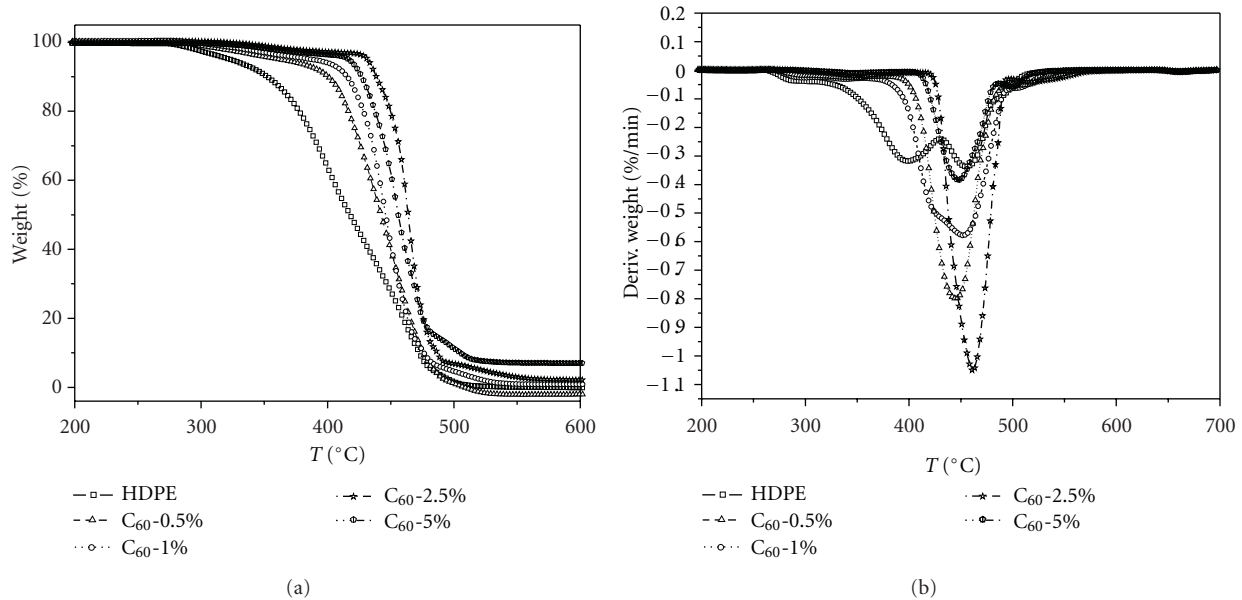


FIGURE 3: TG (a) and DTG (b) curves for pristine HDPE and nanocomposites in air.

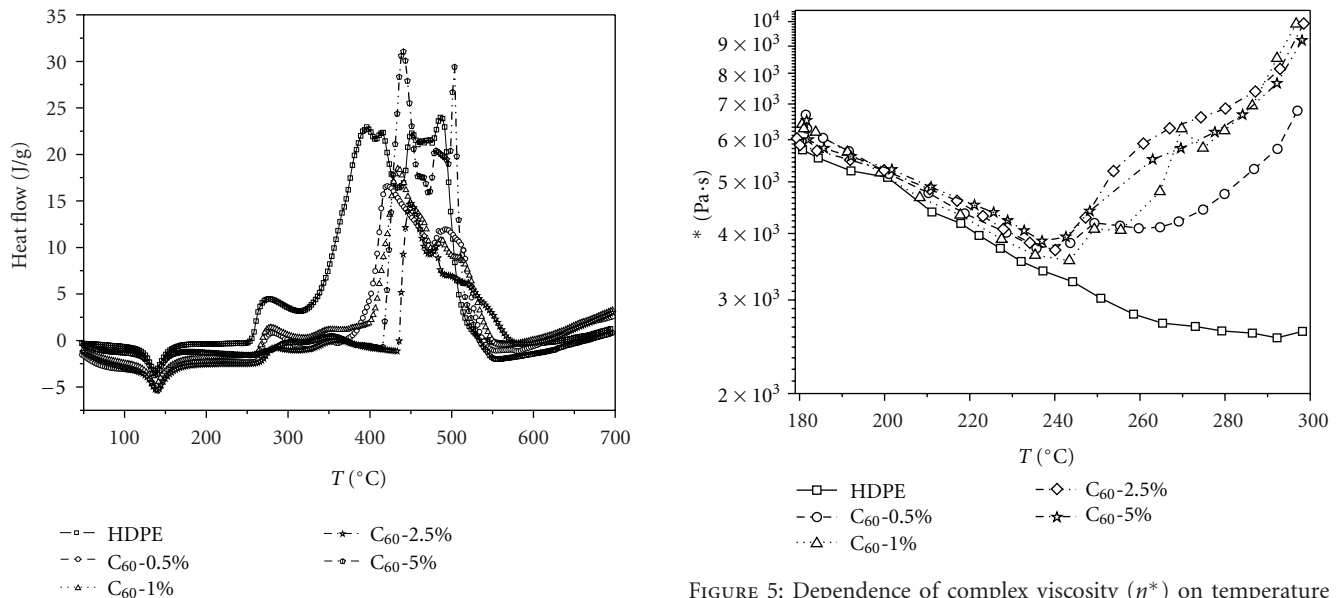


FIGURE 4: DSC curves for HDPE and HDPE/C₆₀ nanocomposites.

the occurrence of degradation of polymer can cause the decrease of η^* . The increase of η^* is due to the occurrence of an oxidation crosslink or the oxidation crosslink reaction overwhelming the polymer decomposition. In the case of pure HDPE, it gives a T_c of 285°C. For HDPE/C₆₀ nanocomposites, their T_c is about 45°C lower than that of HDPE, implying that another kind of crosslink reaction occurred in the process of heating for HDPE/C₆₀ systems, which speeds up the crosslink reaction whether before or after oxidation crosslinking takes place.

FIGURE 5: Dependence of complex viscosity (η^*) on temperature for HDPE and HDPE/C₆₀ nanocomposites.

The viscoelastic behaviors of the nanocomposites at 180°C were studied and those of parent polymer, HDPE, were also used as a comparison. Figures 6 and 7 show the storage moduli (G') and complex viscosity (η^*) as a function of frequency (ω) of HDPE and its nanocomposites. Some researchers have found that both G' and η^* have much larger values than those of parent polymers in the low ω regime for the nanocomposites containing CNTs [14–17] or clay [18, 19], suggesting that the presence of CNTs or clay affects the relaxation and motion of polymer chains due to their spatial geometry. Most authors attribute these viscoelastic behaviors to the formation of CNT or clay networks in the

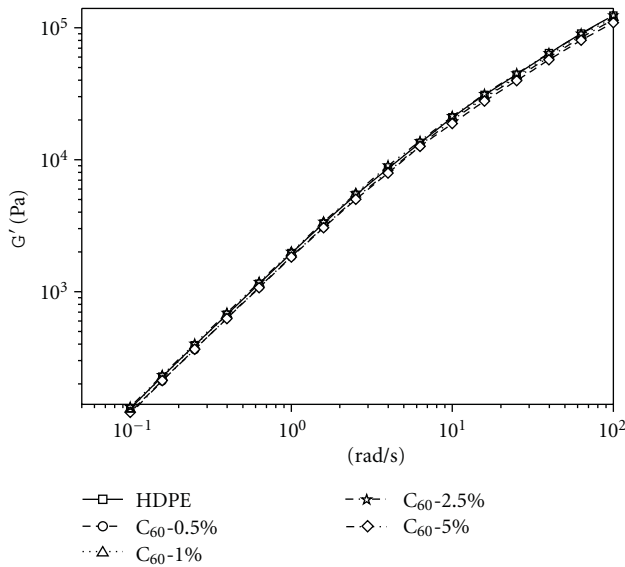


FIGURE 6: Plots of storage moduli (G') versus shifted frequency for consecutive small amplitude oscillatory shear sweeps performed at 180°C .

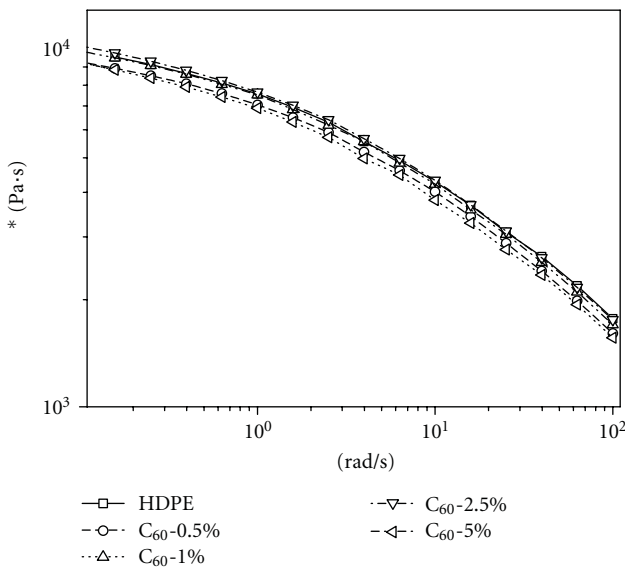


FIGURE 7: Plots of complex viscosity versus shifted frequency for consecutive small amplitude oscillatory shear sweeps performed at 180°C .

polymer matrix. However, in the high ω region, the addition of CNTs and clay does not significantly affect the G' or η^* of polymers. Unlike CNTs and clay, whether in the low ω region or high ω region, not much obvious difference in G' and η^* is observed for the HDPE/ C_{60} nanocomposites with various C_{60} contents. The oxidation degradation of HDPE does not occur at 180°C (as shown in Figure 3 and Table 2). And not enough free radicals react with C_{60} . Therefore, the incorporation of C_{60} does not affect the movement and relaxation of polymer chain segments remarkably.

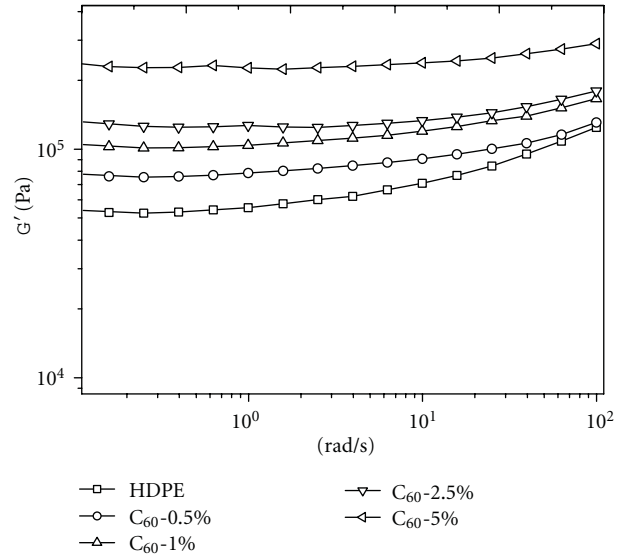


FIGURE 8: Plots of storage modulus versus shifted frequency for consecutive small amplitude oscillatory shear sweeps performed at 300°C .

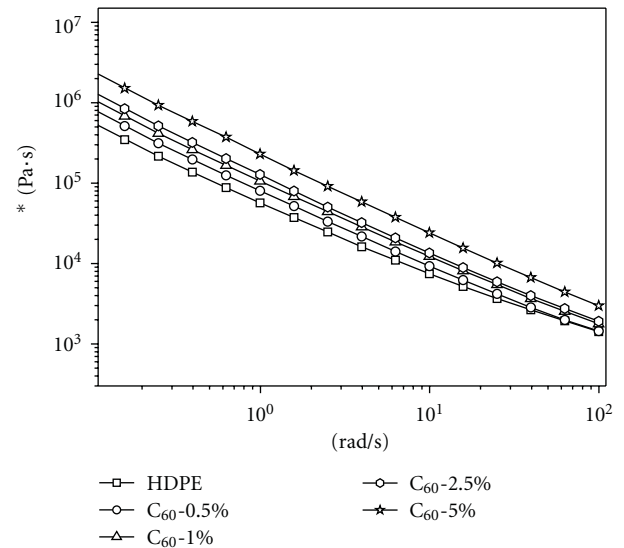


FIGURE 9: Plots of complex viscosity versus shifted frequency for consecutive small amplitude oscillatory shear sweeps performed at 300°C .

The viscoelastic behaviors of the nanocomposites at 300°C after dynamic temperature scanning measurements were also studied. Figures 8 and 9 show the storage moduli (G') and complex viscosity (η^*) as a function of frequency (ω) of HDPE and its nanocomposites at 300°C . The increase of complex viscosity with C_{60} content is concomitant with the increase of the storage moduli. The storage moduli for the nanocomposites show a monotonic increase at all frequencies with increasing C_{60} content. The G' versus frequency curve for the nanocomposites appears to be approaching a plateau at low frequencies. It has been proposed that this “plateau” effect is derived from interconnected structures of

isometric fillers that result in an apparent yield stress which is manifest by a plateau in either G' or η^* versus frequency plots [20, 21]. Exposed at 300°C for a long time, many alkyl radicals appear, coupled with the interfacial interactions between free radicals and C₆₀. The restraint for the move and relaxation of polymer chains increased G' and η^* , which is the evidence for the presence of a chemical reaction between the HDPE matrix and C₆₀.

4. Conclusion

The presence of C₆₀ could enhance the thermal stability of HDPE. A very low C₆₀ loading (0.5 wt%) increases the T_{onset} from 389°C to 459°C and decreases the heat release from 3176 J/g to 1490 J/g. The free radical trapping effect of C₆₀ is responsible for the improved thermal stability of HDPE. Thus, C₆₀ is expected to be an efficient thermal stabilizer to the polymer materials that degraded with a free radical chain scission process.

Acknowledgment

This work was financially supported by the National Natural Science Foundation of China (no. 51073140).

References

- [1] D. E. H. Jones, "The academic sphere," *Nature*, vol. 381, no. 6581, pp. 381–384, 1996.
- [2] R. Taylor and D. R. M. Walton, "The chemistry of fullerenes," *Nature*, vol. 363, no. 24, pp. 685–693, 1993.
- [3] F. Diederich and C. Thilgen, "Covalent fullerene chemistry," *Science*, vol. 271, no. 5247, pp. 317–323, 1996.
- [4] P. J. Krusic, E. Wasserman, P. N. Keizer, J. R. Morton, and K. F. Preston, "Radical reactions of C₆₀," *Science*, vol. 254, no. 5035, pp. 1183–1185, 1991.
- [5] L. B. Gan, S. H. Huang, X. Zhang et al., "Fullerenes as a tert-butylperoxy radical trap, metal catalyzed reaction of tert-butyl hydroperoxide with fullerenes, and formation of the first fullerene mixed peroxides C₆₀(O)(OO^tBU)₄ and C₇₀(OO^tBU)₁₀," *Journal of the American Chemical Society*, vol. 124, no. 45, pp. 13384–13385, 2002.
- [6] B. Z. Tang, S. M. Leung, H. Peng, N. T. Yu, and K. C. Su, "Direct fullerenation of polycarbonate via simple polymer reactions," *Macromolecules*, vol. 30, no. 10, pp. 2848–2852, 1997.
- [7] T. Cao and S. E. Webber, "Free radical copolymerization of styrene and C₆₀," *Macromolecules*, vol. 29, no. 11, pp. 3826–3830, 1996.
- [8] Z. P. Fang, P. A. Song, L. F. Tong, and Z. H. Guo, "Thermal degradation and flame retardancy of polypropylene/C₆₀ nanocomposites," *Thermochimica Acta*, vol. 473, no. 1-2, pp. 106–108, 2008.
- [9] P. A. Song, Z. P. Fang, Y. Zhu, and L. Tong, "C₆₀ reduces the flammability of polypropylene nanocomposites by *in situ* forming a gelled-ball network," *Nanotechnology*, vol. 19, no. 22, Article ID 225707, 2008.
- [10] P. J. Krusic, E. Wasserman, B. A. Parkinson et al., "Electron spin resonance study of the radical reactivity of C₆₀," *Journal of the American Chemical Society*, vol. 113, no. 16, pp. 6274–6275, 1991.
- [11] J. R. Morton, K. F. Preston, P. J. Krusic, S. A. Hill, and E. Wasserman, "The dimerization of RC₆₀ radicals," *Journal of the American Chemical Society*, vol. 114, no. 13, pp. 5454–5455, 1992.
- [12] M. Zanetti, G. Camino, P. Reichert, and R. Mulhaupt, "Thermal behaviour of poly(propylene) layered silicate nanocomposites," *Macromolecular Rapid Communications*, vol. 22, no. 3, pp. 176–180, 2001.
- [13] G. Wu, Y. Song, Q. Zheng, M. Du, and P. Zhang, "Dynamic rheological properties for HDPE/CB composite melts," *Journal of Applied Polymer Science*, vol. 88, no. 9, pp. 2160–2167, 2003.
- [14] T. Kashiwagi, E. Grulke, J. Hilding, R. Harris, W. Awad, and J. Douglas, "Thermal degradation and flammability properties of poly(propylene)/carbon nanotube composites," *Macromolecular Rapid Communications*, vol. 23, no. 13, pp. 761–765, 2002.
- [15] T. Kashiwagi, F. Du, K. I. Winey et al., "Flammability properties of polymer nanocomposites with single-walled carbon nanotubes: effects of nanotube dispersion and concentration," *Polymer*, vol. 46, no. 2, pp. 471–481, 2005.
- [16] T. Kashiwagi, F. Du, J. F. Douglas, K. I. Winey, R. H. Harris, and J. R. Shields, "Nanoparticle networks reduce the flammability of polymer nanocomposites," *Nature Materials*, vol. 4, no. 12, pp. 928–933, 2005.
- [17] S. B. Kharchenko, J. F. Douglas, J. Obrzut, E. A. Grulke, and K. B. Migler, "Flow-induced properties of nanotube-filled polymer materials," *Nature Materials*, vol. 3, no. 8, pp. 564–568, 2004.
- [18] M. A. Trece and J. P. Oberhauser, "Soft glassy dynamics in polypropylene-clay nanocomposites," *Macromolecules*, vol. 40, no. 3, pp. 571–582, 2007.
- [19] C. O. Rohlmann, M. D. Failla, and L. M. Quinzani, "Linear viscoelasticity and structure of polypropylene-montmorillonite nanocomposites," *Polymer*, vol. 47, no. 22, pp. 7795–7804, 2006.
- [20] P. Potschke, M. Abdel-Goad, I. Alig, S. Dudkin, and D. Lellinger, "Rheological and dielectrical characterization of melt mixed polycarbonate-multiwalled carbon nanotube composites," *Polymer*, vol. 45, no. 26, pp. 8863–8870, 2004.
- [21] L. A. Utracki, "Flow and flow orientation of composites containing anisometric particles," *Polymer Composites*, vol. 7, no. 5, pp. 274–282, 1986.

Research Article

Effect of the on/off Cycling Modulation Time Ratio of C_2H_2/SF_6 Flows on the Formation of Geometrically Controlled Carbon Coils

Young-Chul Jeon, Jun-Ho Eum, Sung-Hoon Kim, Jung-Chul Park, and Sung Il Ahn

Department of Engineering in Energy and Applied Chemistry, Silla University, Busan 617-736, Republic of Korea

Correspondence should be addressed to Sung-Hoon Kim, shkim@silla.ac.kr

Received 16 July 2011; Accepted 30 October 2011

Academic Editor: Steve Acquah

Copyright © 2012 Young-Chul Jeon et al. This is an open access article distributed under the Creative Commons Attribution License, which permits unrestricted use, distribution, and reproduction in any medium, provided the original work is properly cited.

Carbon coils could be synthesized using C_2H_2/H_2 as source gases and SF_6 as an incorporated additive gas under thermal chemical vapor deposition system. Nickel catalyst layer deposition and then hydrogen plasma pretreatment were performed prior to the carbon coils deposition reaction. To obtain the geometrically controlled carbon coils, the cycling on/off modulation process for C_2H_2/SF_6 flows was introduced during the initial reaction. According to the different reaction processes, the different cycling on/off ratio and the different cycling numbers for C_2H_2/SF_6 flows were carried out. The characteristics (formation density, morphology, and geometry) of the deposited carbon coils on the substrate were investigated. Microsized coils as well as nanosized coils could be existed under the higher growing/etching time ratio (180/30 s) condition. On the other hand, the formation of nanosized coils could be mainly observed under the lower growing/etching time ratio (30/180 s) condition. With increasing the numbers of cycles, the diameters of carbon nanofilaments composed the coils decreased. The enhanced etching ability by the fluorine species was considered the main cause to control the geometry of carbon coils according to the growing/etching time ratio of the cycling on/off modulation process for C_2H_2/SF_6 flows.

1. Introduction

Although the unique springlike geometry of carbon coils have been noticed as the promising material candidate for the micro/nanoelectronic devices, some problems should be solved for their practical applications [1–4]. The most urgent problems to solve would be the achievement of the geometrically controlled carbon coils as well as the mass production of carbon coils [5]. In general, the carbon coils at as-grown state had a randomly shaped geometry. Carbon coils having a randomly shaped geometry could give rise to unpredictable electrical characteristics, because the electrical properties of carbon coils were supposed to be varied according to their geometries including diameter [6]. Therefore, the controlled characteristics of carbon coils, resulting from the controlled coil morphology and geometry (diameter, pitch, length, and turning direction), are indispensable for their practical application in micro/nanoelectronic devices.

Thermal chemical vapor deposition (TCVD) technique using the metal catalyst has been noticed for the practical synthesis techniques of carbon coils because of its relative inexpensive and applicable features [7–9]. However, due to the low yield of carbon coils, normal TCVD process is not suitable for the scaled-up production of carbon coils. Therefore, it is desired to explore a more efficient and reliable TCVD method for the growth of carbon coils.

Recently, an *in situ* cycling on/off modulation process of C_2H_2/H_2 flow has been introduced to enhance the formation density of carbon nanofilaments (CNFs) [10]. It can be simply achieved by turning a source gas flow rate in a reaction system on or off during an initial deposition stage. It seems that the *in situ* process is more advantageous than *ex situ* process because one can combine an *in situ* process and an *ex situ* process without altering the detailed reaction condition. In this work, an *in situ* cycling on/off modulation process of C_2H_2/SF_6 flow has been adopted.

Meanwhile, a trace of sulfur species [11–14] was usually incorporated as an additive to readily form carbon coils. In this paper, a trace of sulfur species was incorporated as an SF₆ form. Fluorine species, as an SF₆ form, was intentionally introduced in this work in order to take the advantage for fluorine species characteristics regarding the enhancement of the nucleation sites of carbon coils. For the diamond, as an allotrope of carbon coils, it was known that the addition of fluorine would enhance the rate of hydrogen abstraction, thereby opening more nucleation sites for possible interaction with growth species even in the low-temperature case [15–17]. Like the diamond film deposition case, fluorine species in this work was expected to play a role for enhancing nucleation sites of carbon coils by hydrogen abstraction.

Therefore, in this work, the injection of fluorine species, as an SF₆ form, was combined with an *in situ* cyclic on/off modulation process of C₂H₂/SF₆ flow. The investigation on the influence of C₂H₂/SF₆ flow on/off ratio on the characteristics of carbon coils was focused. According to the different reaction processes, the different cycling on/off ratio and the different cycling numbers for C₂H₂/SF₆ flows were carried out. In this process, the relative concentrations of hydrogen and fluorine species during the reaction could be varied by the cycling on and off control of C₂H₂ and SF₆ flows. Finally, we could achieve the large-scale production of the geometrically controlled carbon coils merely by adjusting the cycling on/off ratio for C₂H₂/SF₆ flows. Characteristics of as-grown carbon coils, namely, the formation density and the geometry were examined and discussed.

2. Experimental Details

The SiO₂ substrates in this work were prepared by the thermal oxidation of 2.0 × 2.0 cm² p-type Si (100) substrates. The thickness of silicon oxide (SiO₂) layer on Si substrate was estimated about 300 nm. A 0.1 mg Ni powder (99.7%) was evaporated for 1 min to form Ni catalyst layer on the substrate using thermal evaporator. The estimated Ni catalyst layer on the substrate was estimated about 100 nm.

Prior to carbon coils deposition, Ni-coated substrate was placed in plasma-enhanced chemical vapor deposition (PECVD) system. H₂ gas was introduced into PECVD chamber, and then the substrate was precleaned for 5 minutes using H₂ plasma.

For carbon coils deposition, thermal chemical vapor deposition (TCVD) system was employed. C₂H₂ and H₂ were used as source gases. SF₆, as an incorporated additive gas, was injected into the reactor during the reaction. The flow rate for C₂H₂, H₂, and SF₆ were fixed at 15, 35, and 35 standard cm³ per minute (sccm), respectively.

The *in situ* cyclic modulation process of the source gas flow in this work was merely carried out by the on/off control of C₂H₂ flow and simultaneously off/on control of SF₆ flow. According to the reaction processes, the sequence of source gas flow was the iterative order of procedures, C₂H₂ + H₂ flow (C₂H₂ flow on and SF₆ flow off) and then SF₆ + H₂ flow (C₂H₂ flow off and SF₆ flow on). The cyclic modulation period was defined as the time the source gas was composed

of H₂ and C₂H₂ plus the time the source gas was H₂ and SF₆. In this manner, carbon species to form carbon coils are generated from the C₂H₂ + H₂ flow (C₂H₂ flow on and SF₆ flow off). This is termed as the growing time. On the other hand, the SF₆ + H₂ flow (C₂H₂ flow off and SF₆ flow on) may etch carbon components. Therefore, the SF₆ + H₂ flow time is termed as the etching time. We defined the time ratio of C₂H₂ flow on/off (SF₆ flow off/on) as the growing/etching time ratio.

For objectively examining the effect of the growing/etching time ratio on the characteristics of carbon coils, we first fixed H₂ flow rate as 35 sccm. C₂H₂ flow on and off times (SF₆ flow off and on times) were varied as two kinds of C₂H₂ flow on/off time ratio, namely, 180/30 s and 30/180 s. So the time for one cyclic was 7.0 min. The numbers of cycles for these experiments were 2 and 16 times. For the steady process, we deposited carbon coils for 90 min without incorporating the cyclic modulation process. Namely, continuous C₂H₂ + H₂ flow or C₂H₂ + SF₆ + H₂ flow was introduced for 90 min.

To elucidate the effect of the growing/etching time ratio on the characteristics of carbon coils, six samples having the different reaction processes were prepared. Sample A is the steady process of C₂H₂ + H₂ flow. For sample B, the cyclic modulation process was applied during the initial deposition stage at the number of cycles = 2. The growing/etching time ratio of this sample was 180/30 s (higher growing/etching time ratio). For sample C, the cyclic modulation process was also applied during the initial deposition stage at the number of cycles = 2. However, the growing/etching time ratio of this sample was 30/180 s (lower growing/etching time ratio). For sample D, the cyclic modulation process having the higher growing/etching time ratio (180/30 s) was applied during the initial deposition stage at the number of cycles = 16. For sample E, the cyclic modulation process having the lower growing/etching time ratio (30/180 s) was applied during the initial deposition stage at the number of cycles = 16. Sample F is the steady process of C₂H₂ + SF₆ + H₂ flow. Figure 1 shows the detailed manipulation processes for these gases flows. The reaction conditions according to different processes were shown in Table 1. Detailed morphologies of carbon coils-deposited substrates were investigated using field emission scanning electron microscopy (FESEM).

3. Results and Discussion

Figure 2 shows FESEM images showing the surface morphologies of the samples A~C. These images indicate the formation of carbon coils for the cyclic process having the higher growing/etching time ratio (180/30 s) (see Figure 2(b)) and for the cyclic process having the lower growing/etching time ratio (30/180 s) (see Figure 2(c)). Without SF₆ gas flow injection, we could merely observe the embryos for carbon nanofilaments (CNFs) as shown in Figure 2(a). Any geometry related with carbon coils-type could not be observed. Therefore, it is clear that the incorporation of SF₆ even for a few minutes would play a significant role for the formation of the carbon coils-related geometry.

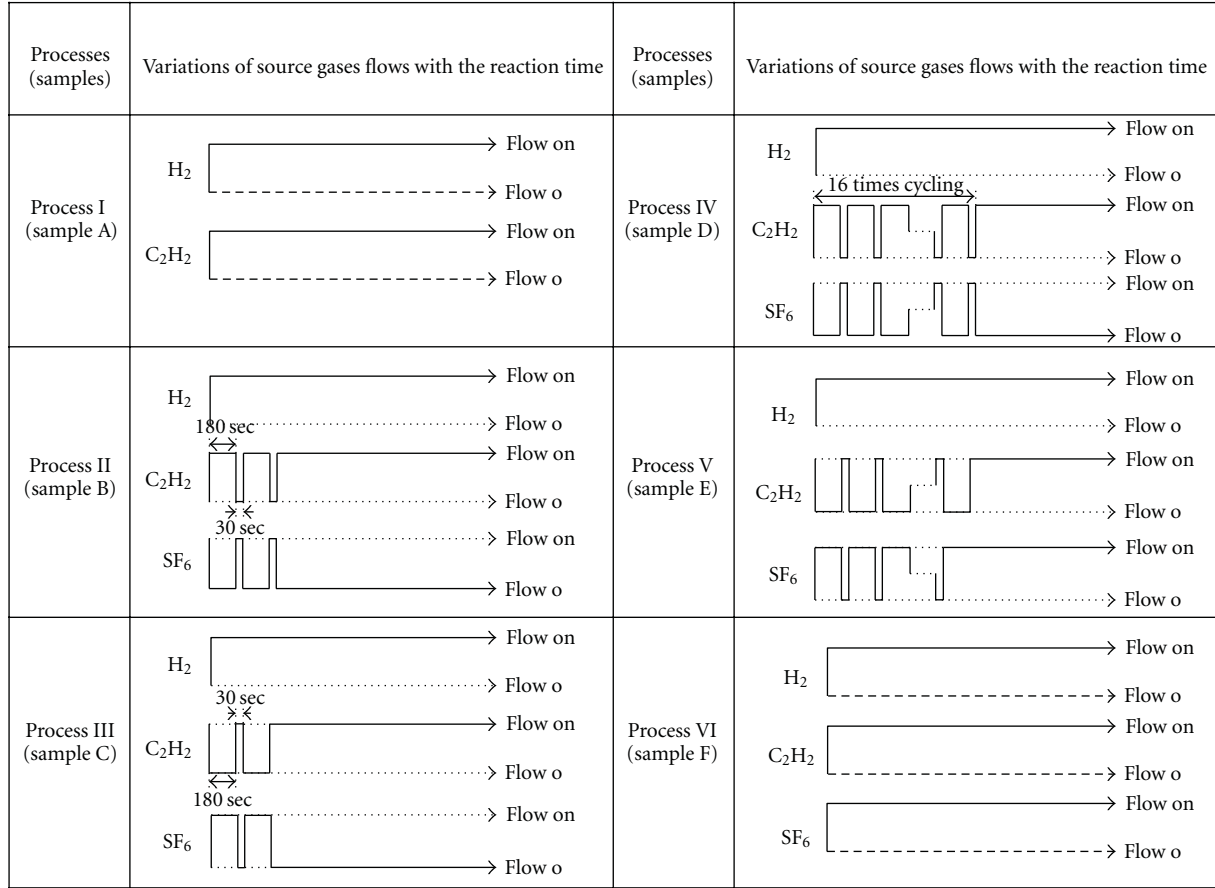


FIGURE 1: Different reaction processes: the steady injection process without incorporating the cycling modulation process for $C_2H_2 + H_2$ flows (process I, sample A) and $C_2H_2 + H_2 + SF_6$ flows (process VI, sample F), the cycling on/off modulation of C_2H_2/SF_6 flows having the higher growing/etching time ratio (180/30 s) for two cycles (process II, sample B) and for sixteen cycles (process IV, sample D), the cycling on/off modulation of C_2H_2/SF_6 flows having the lower growing/etching time ratio (30/180 s) for two cycles (process III, sample C) and for sixteen cycles (process V, sample E).

TABLE 1: Experimental conditions for the deposition of carbon coils on the substrates for samples A, B, C, D, E, and F.

Processes	Samples	C_2H_2 flow rate (sccm)	H_2 flow rate (sccm)	SF_6 flow rate (sccm)	Total pressure (Torr)	Total deposition time (min)	Source gases flow time (min)			Substrate temp. ($^{\circ}C$)
							C_2H_2	H_2	SF_6	
I	A	15	35	—	100	90	90	—	750	
II	B	15	35	35	100	90	89	1	750	
III	C	15	35	35	100	90	84	6	750	
IV	D	15	35	35	100	90	82	8	750	
V	E	15	35	35	100	90	42	48	750	
VI	F	15	35	35	100	90	90	90	750	

Figure 3(a), the magnified image of sample A, clearly shows merely the embryos formation for the carbon nanofilaments under the $C_2H_2 + H_2$ flow steady process condition. Figure 3(b), the magnified image of sample B, shows the existence of microsized coils as well as nanosized coils under the higher growing/etching time ratio (180/30 s) condition. On the other hand, the dominant formation of the nanosized coils could be observed under the lower growing/etching time ratio (30/180 s) condition as shown in the magnified image of sample C (see Figure 3(c)). The highest magnified

($\times 50,000$) image of the nanosized coils area of samples B (Figure 4(a)) and the highest magnified image of sample C (Figure 4(b)) show the existence of the tangled geometries in some parts of the coils. The diameters sizes of the individual carbon nanofilaments composed the coils seemed to be invariant even by the change of growing/etching time ratio in the cyclic modulation process.

Figure 5 shows FESEM images showing the surface morphologies of the samples D and E. At number of cycles = 16, a few number of the carbon coils having the microsized

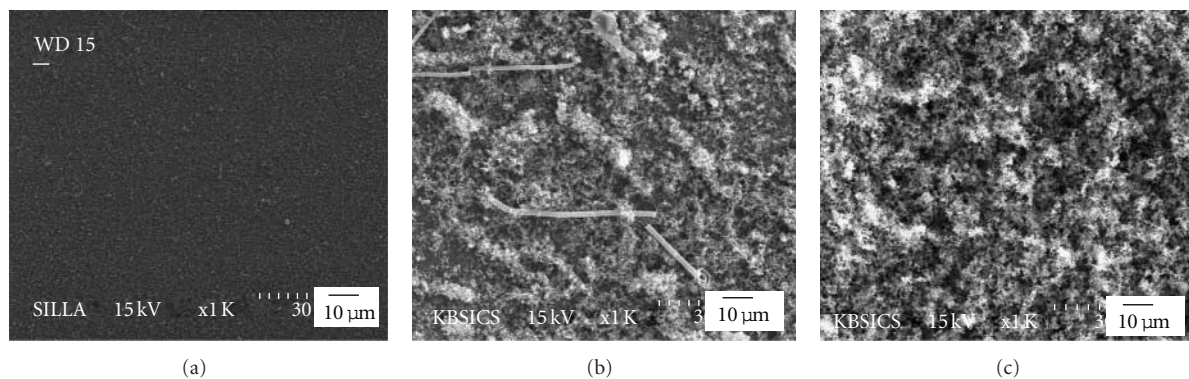


FIGURE 2: FESEM images showing the surface morphologies for (a) sample A, (b) sample B, and (c) sample C.

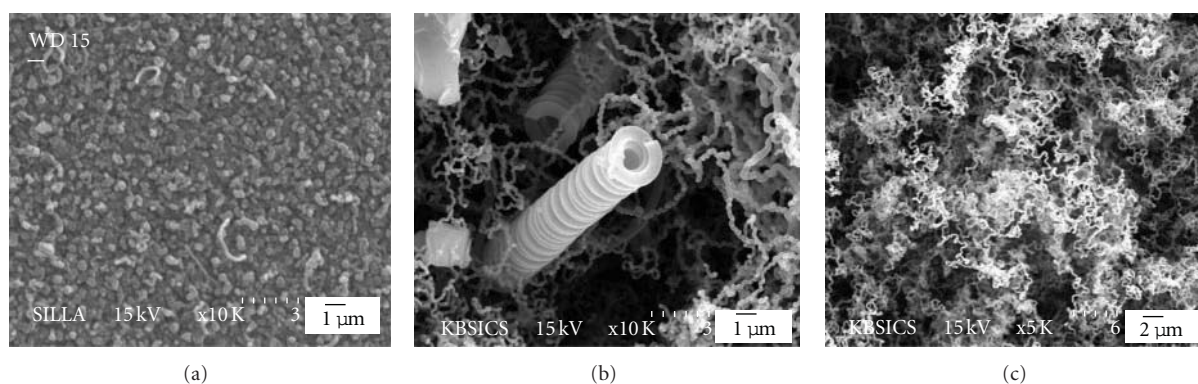


FIGURE 3: The magnified FESEM images showing the surface morphologies for (a) sample A, (b) sample B, and (c) sample C.

diameter of carbon nanofilaments composed the coils could be still observed under the higher growing/etching time ratio (180/30 s) condition (see the arrow position in Figure 5(a)). However, any geometry related with microsized carbon nanofilaments composed the coils could not be observed under the lower growing/etching time ratio (30/180 s) condition as shown in Figure 5(c). At 50,000-high magnified FESEM images, the existence of the tangled geometries seemed to be prevalent under the lower growing/etching time ratio (30/180 s) condition as shown in Figure 5(d). The diameter sizes of the carbon nanofilaments composed the coils seemed to be about 100 nm under the higher growing/etching time ratio (180/30 s). However, their sizes seemed to be less than 100 nm under the lower growing/etching time ratio (30/180 s) condition (compare the diameter sizes of carbon nanofilaments of Figure 5(b) with those of Figure 5(d)). Furthermore, the comparing results of the images for Figures 4 and 5 give rise to the information for the decrease in the diameter sizes with increasing the number of cycles under the lower growing/etching time ratio (30/180 s) condition.

Carbon coils deposition reaction in a steady flow process with SF_6 incorporation was also carried out. Dominant formation of the coil geometries having the microsized diameters of carbon nanofilaments composed the coils

could be observed on as-grown sample surface as shown in Figure 6. For the nanosized ones, indeed, a relatively a small amount of the coil geometries could be observed.

Considering fluorine's characteristics for etching other materials or enhancing nucleation sites, we propose that the increased SF_6 incorporation in the reaction with decreasing the cycling on/off modulation time ratio of $\text{C}_2\text{H}_2/\text{SF}_6$ flows could etch away the relatively soft microsized carbon coils-related materials due to fluorine species' etching capability. In addition, the increase in the etching amount of fluorine + hydrogen species under the lower growing/etching time ratio (30/180 s) may facilitate the decrease in the diameter sizes with increasing the number of cycles. Meanwhile, the existence of the tangled geometries, instead of spring-like-coiled geometries, seemed to be more prevalent under the lower growing/etching time ratio (30/180 s) condition with increasing the number of cycles. Therefore, the increase in the etching gases amount of fluorine + hydrogen species seemed to deteriorate the formation of the coiled geometry. However, the continuous supply of fluorine species with carbon source gas, as $\text{C}_2\text{H}_2 + \text{SF}_6 + \text{H}_2$ flow in this work, may develop the microsized geometry formation of carbon coils. In this case, the fluorine species with carbon source gas seems to work as a promoter for the formation of the microsized carbon coils. Finally, we could obtain the

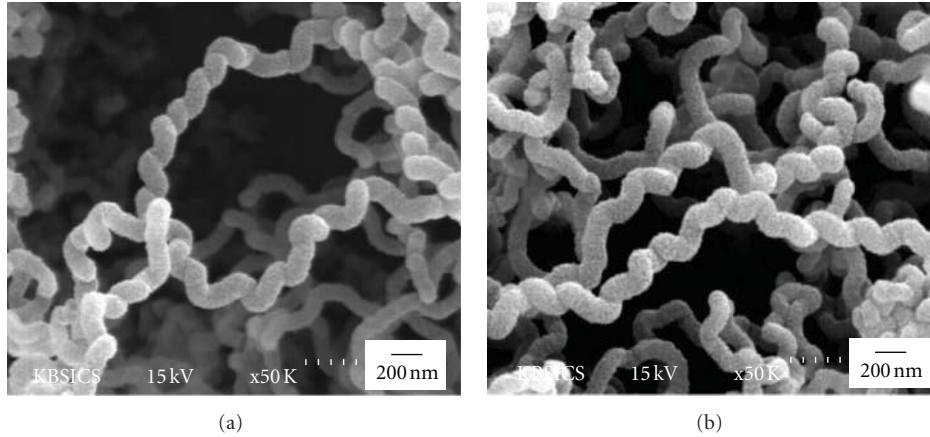


FIGURE 4: The high-magnified images for (a) the nanosized coils area of sample B and (b) the randomly chosen area of sample C.

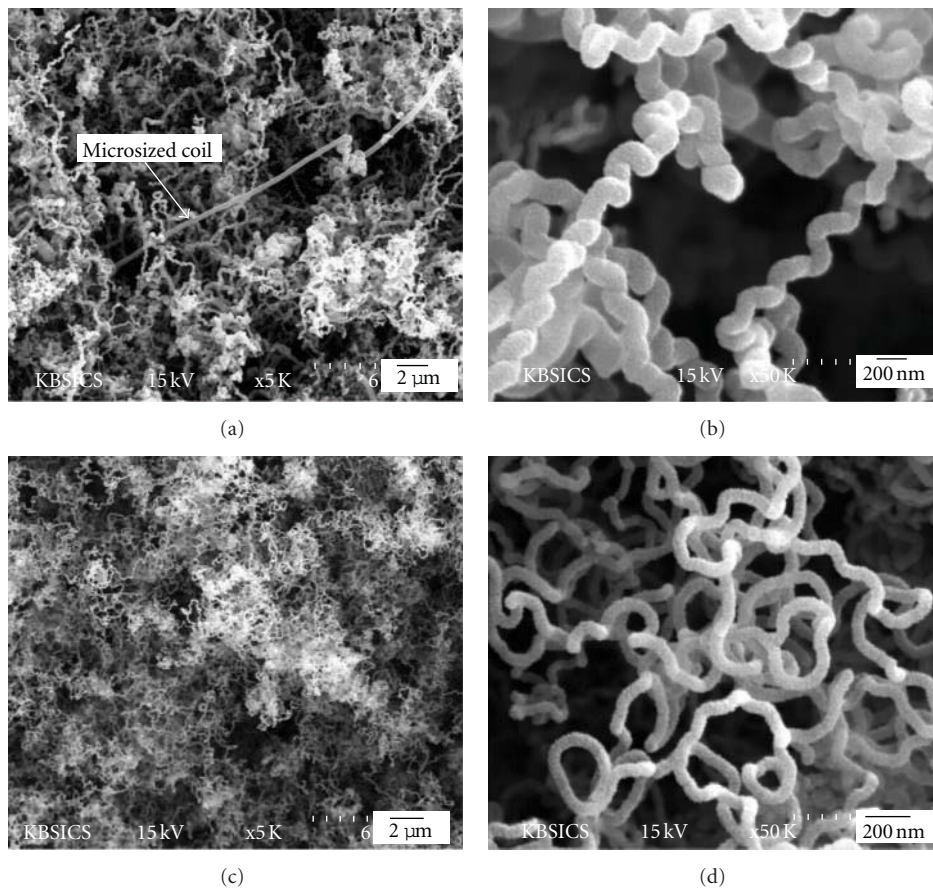


FIGURE 5: FESEM images showing the surface morphologies for (a) sample D and (c) sample E and the high-magnified FESEM images for (b) the nanosized coils area of sample D and (d) the randomly chosen area of sample E.

dominant geometry, namely, nanostructured geometry, by simply decreasing the cycling on/off modulation time ratio of C_2H_2/SF_6 flows in the reaction. However, the increase in the number of cycles at this condition may deteriorate the formation of the coiled geometry.

4. Conclusion

By SF_6 gas flow injection during the reaction, micro- and/or nanosized carbon coils could be formed on the samples surfaces. The microsized carbon coils were suppressed with

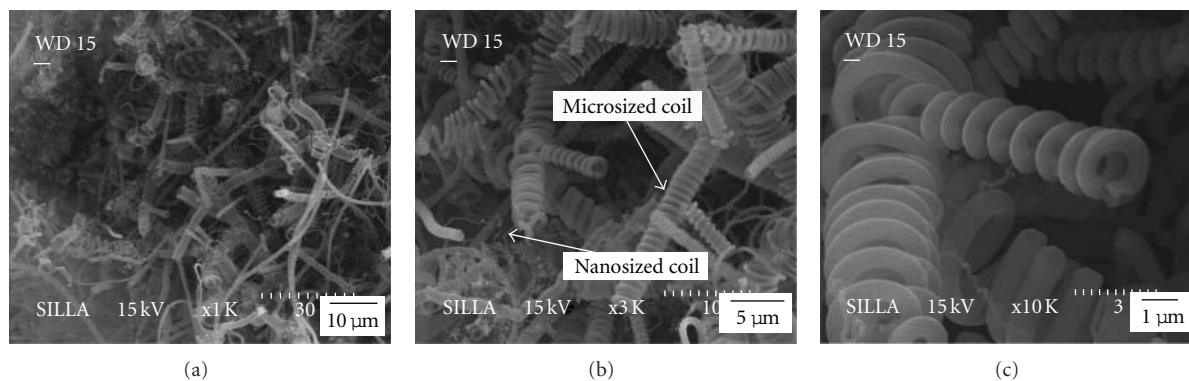


FIGURE 6: (a) FESEM images showing the surface morphology of sample F, (b) the magnified FESEM image for (a), and (c) the high-magnified FESEM image for (b).

decreasing the cycling on/off modulation time ratio for the C_2H_2/SF_6 flows in the reaction. With further increasing the SF_6 incorporation in the reaction via increasing the numbers of cycles, even the diameters of carbon nanofilaments composed the coils decreased and the entangled geometries, instead of coiled geometries, could be developed. Finally, the dominant formation of the controlled geometry of carbon coils could be achieved by manipulating the cycling on/off modulation time ratio for C_2H_2/SF_6 flows in the reaction.

References

- [1] S. Ihara and S. Itoh, "Helically coiled and toroidal cage forms of graphitic carbon," *Carbon*, vol. 33, no. 7, pp. 931–939, 1995.
- [2] L. Pan, T. Hayashida, M. Zhang, and Y. Nakayama, "Field emission properties of carbon tubule nanocoils," *Japanese Journal of Applied Physics*, vol. 40, no. 3, pp. L235–L237, 2001.
- [3] R. T. K. Baker, "Catalytic growth of carbon filaments," *Carbon*, vol. 27, no. 3, pp. 315–323, 1989.
- [4] S. Amelinckx, X. B. Zhang, D. Bernaerts, X. F. Zhang, V. Ivanov, and J. B. Nagy, "A formation mechanism for catalytically grown helix-shaped graphite nanotubes," *Science*, vol. 265, no. 5172, pp. 635–639, 1994.
- [5] J.-H. Eum, S.-H. Kim, S. S. Yi, and K. Jang, "Large-scale synthesis of the controlled-geometry carbon coils by the manipulation of the SF_6 gas flow injection time," *Journal of Nanoscience and Nanotechnology*. In press.
- [6] K. Akagi, R. Tamura, M. Tsukada, S. Itoh, and S. Ihara, "Electronic structure of helically coiled cage of graphitic carbon," *Physical Review Letters*, vol. 74, no. 12, pp. 2307–2310, 1995.
- [7] M. Lu, H. L. Li, and K. T. Lau, "Formation and growth mechanism of dissimilar coiled carbon nanotubes by reduced-pressure catalytic chemical vapor deposition," *Journal of Physical Chemistry B*, vol. 108, no. 20, pp. 6186–6192, 2004.
- [8] C. J. Su, D. W. Hwang, S. H. Lin, B. Y. Jin, and L. P. Hwang, "Self-organization of triple-stranded carbon nanoropes," *PhysChemComm*, vol. 5, pp. 34–36, 2002.
- [9] V. Ivanov, J. B. Nagy, P. Lambin et al., "The study of carbon nanotubes produced by catalytic method," *Chemical Physics Letters*, vol. 223, no. 4, pp. 329–335, 1994.
- [10] K. D. Kim, S. H. Kim, N. S. Kim, and D. U. Kim, "Effect of the on/off cyclic modulation time ratio of C_2H_2/H_2 flow on the low temperature deposition of carbon nanofilaments," *Journal of Nanoscience and Nanotechnology*, vol. 7, no. 11, pp. 3969–3973, 2007.
- [11] S. Motojima, Y. Itoh, S. Asakura, and H. Iwanaga, "Preparation of micro-coiled carbon fibres by metal powder-activated pyrolysis of acetylene containing a small amount of sulphur compounds," *Journal of Materials Science*, vol. 30, no. 20, pp. 5049–5055, 1995.
- [12] X. Chen and S. Motojima, "Morphologies of carbon micro-coils grown by chemical vapor deposition," *Journal of Materials Science*, vol. 34, no. 22, pp. 5519–5524, 1999.
- [13] S. Motojima, S. Asakura, T. Kasemura, S. Takeuchi, and H. Iwanaga, "Catalytic effects of metal carbides, oxides and Ni single crystal on the vapor growth of micro-coiled carbon fibers," *Carbon*, vol. 34, no. 3, pp. 289–296, 1996.
- [14] S. Yang, X. Chen, and S. Motojima, "Tactile sensing properties of protein-like single-helix carbon microcoils," *Carbon*, vol. 44, no. 15, pp. 3352–3355, 2006.
- [15] M. Asmann, J. Heberlein, and E. Pfender, "A review of diamond CVD utilizing halogenated precursors," *Diamond and Related Materials*, vol. 8, no. 1, pp. 1–16, 1999.
- [16] M. S. Wong and C. H. Wu, "Complications of halogen-assisted chemical vapor deposition of diamond," *Diamond and Related Materials*, vol. 1, no. 2–4, pp. 369–372, 1992.
- [17] E. J. Corat, V. J. Trava-Airoldi, N. F. Leite, M. C. A. Nono, and V. Baranauskas, "Diamond growth with CF_4 addition in hot-filament chemical vapour deposition," *Journal of Materials Science*, vol. 32, no. 4, pp. 941–947, 1997.

Research Article

Electrochemical Degradation Characteristics of Refractory Organic Pollutants in Coking Wastewater on Multiwall Carbon Nanotube-Modified Electrode

Yan Wang, Shujing Sun, Guifu Ding, and Hong Wang

National Key Laboratory of Nano/Micro Fabrication Technology, Key Laboratory for Thin Film and Microfabrication, Ministry of Education, Shanghai Jiaotong University, Shanghai 200240, China

Correspondence should be addressed to Yan Wang, wyyw@sjtu.edu.cn

Received 19 May 2011; Accepted 7 August 2011

Academic Editor: Steve Acquah

Copyright © 2012 Yan Wang et al. This is an open access article distributed under the Creative Commons Attribution License, which permits unrestricted use, distribution, and reproduction in any medium, provided the original work is properly cited.

The multiwall carbon nanotube-mollified electrode (MWCNT-ME) was fabricated and its electrocatalytic activity of refractory organic pollutants of coking wastewater was investigated. The surface morphology, absorption properties, and the electrochemical behavior of phenol and aniline at the MWCNT-ME were analyzed. Using ultraviolet-visible adsorption spectroscopy (UV-vis), Gas chromatography mass spectrometry (GC/MS), and chemical oxygen demand (COD) test, the electrochemical oxidation properties of refractory organic pollutants of coking wastewater using the MWCNT-ME and the IrSnSb/Ti electrode were analyzed. Compared with the powder adsorption media, the MWCNT-ME was proved to have weaker adsorption activity, which means electrochemical degradation is the decisive factor of the removal of organic pollutants. The MWCNT-ME shows high electrochemical reactivity with oxidation peaks of 0.18 A and 0.12 A for phenol and aniline, respectively. Under the same working conditions, the MWCNT-ME COD removal rate 51% is higher than IrSnSb/Ti electrode's rate 35%. The MWCNT-ME has application potential of electrochemical oxidation of refractory organic pollutants of coking wastewater.

1. Introduction

The increasing emission of refractory organic pollutants has challenged the conventional biological treatment. These contaminants such as polynuclear aromatic hydrocarbons PAHs, nitrogen-, oxygen-, and sulfur-containing heterocyclic compounds possess high resistance to microbial degradation or utilization. As one of the advanced treatment systems, electrochemical oxidation has drawn significant attention in water treatment research [1], because of its environmental compatibility, small space requirement, and powerful oxidation ability [2]. The electrode material must have high electrocatalytic activity towards the electrochemical oxidation of organics to CO₂ and H₂O [3]. In addition, this process depends on the activity of coating materials on the electrodes. Recent research has focused on surface modification of the conventional anodes by nanotube (NT) arrays [4]. The nanoarchitecture of NT arrays features a high surface-to-volume ratio due to the additional area enclosed inside the

hollow structure. As a result of the larger surface area, higher catalytic activity is readily accessible.

With the combination of high aspect ratio, nanometer-sized dimensions, good electrical conductivity [5], and low capacitance in the pristine state, carbon nanotube film electrodes were used extensively for the electrochemical detection of organic compounds [6] and have potential activity for degradation of organic pollutants [7].

This paper is focused on the electrochemical degradation characteristics of refractory organic pollutants in coking wastewater on a multiwall carbon nanotube-modified electrode (MWCNT-ME). To the best of our knowledge, few studies on electrocatalytic properties of CNT-modified electrodes for degradation of refractory organic pollutants in actual wastewater have been reported. Coking wastewater after biologically purification was chosen as model reactant, in which constituents are low concentration, refractory, toxic, and carcinogenic. The basic electrode configuration of the MWCNT-ME is randomly dispersed multiwall carbon

nanotubes (MWCNTs) in polytetrafluoroethylene (PTFE) dropped on the surface of a Ti conducting support macro-electrode. Firstly, phenol and aniline were chosen as the model reactants to exam the electrocatalytic characteristics of the MWCNT-ME. As priority pollutants, phenol and aniline are ubiquitous in the environment and have been chosen frequently as typical pollutants because many data are available on their removal and destruction, in particular, with respect to wastewater treatments [8]. Adsorption experiments of organic pollutants were carried out with activated carbon, CNT powder, and MWCNT-ME. The results dedicate that electrochemical oxidation plays the main role for removal of organic compounds. Ultraviolet-visible adsorption spectroscopy (UV-vis), gas chromatography mass spectrometry (GC/MS), and chemical oxygen demand (COD) measurement were carried out to investigate the change of organic compositions in the electrochemical oxidation process. The degrading efficiency of the MWCNT-ME was compared with that of the IrSnSb/Ti electrode which is the widely and typically used dimension-stable anode (DSA).

2. Experimental Details

MWCNTs were purchased from Shenzhen Nanotech Port Co., Ltd. (Shenzhen, China), a commercial supplier of carbon nanotubes. MWCNTs have tube diameters of 60–100 nm, lengths of 5–15 μm , and a purity of more than 95%. PTFE solution with concentration of 30% (mass percent) was purchased from QINAIRUN Co., Ltd. (Shanghai, China). IrSnSb/Ti electrode was supplied by Suzhou FengGang Co., Ltd. The biologically pretreated coking wastewater was collected from Shanghai Baoshan Iron and Steel Company. Activated carbon, NaSO_4 , phenol, and aniline were obtained from China National Pharmaceutical Group Corporation (Beijin, China). All the chemicals reagents were of analytical grade and used without further purification. All solutions for voltammeter study were prepared, using doubly distilled water.

2.1. Electrode Preparation. PTFE is a chemically stable material. The fluoropolymer composite film prepared with PTFE and MWCNTs had a high resistance to solvents, acids, and bases [9]. Titanium electrode will be used as the support macroelectrode because it is widely used in the industry of electrochemistry. Titanium meshes (10 cm \times 6 cm \times 0.1 cm, 99.5% purity) whose oxide removed with alkali were rinsed in two 10 min steps in ultrasonicated acetone and deionized distilled water (DDW) before drying in flowing N_2 stream. PTFE solution with concentration of 30% (mass percent) was used as dispersion fluid. The PTFE solution and MWCNTs were mixed in ethanol with ultrasonic dispersion. The composite dip coated on the prepared titanium mesh and then dried in oven with temperature-programmed mode to 150°C for forming the MWCNT-ME (2 mm thickness, 60 cm^2 area).

2.2. Adsorption Experiment. The MWCNTs and activated carbon with same quantity of 1 g were fed into the two beak-

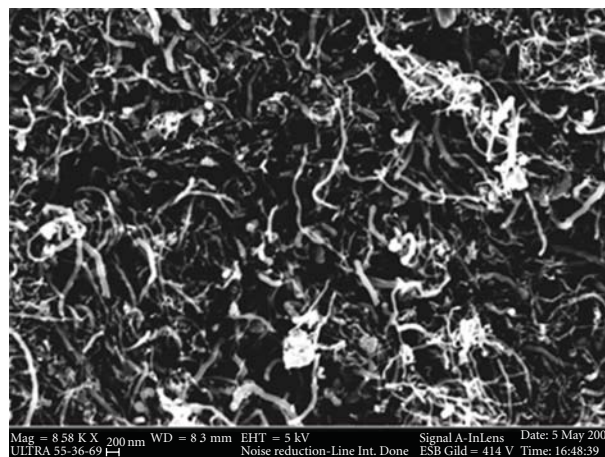


FIGURE 1: The Field-emission SEM (FESEM) top-view image of the MWCNT-ME.

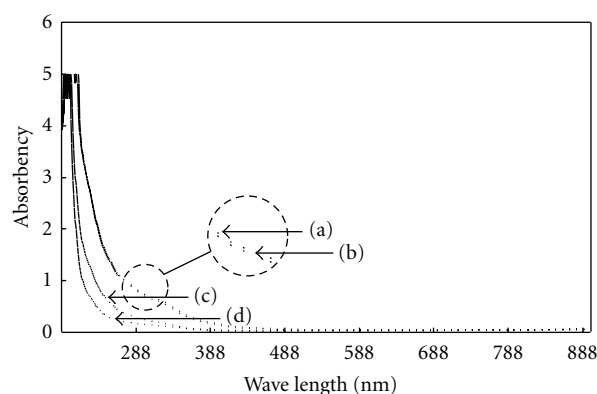


FIGURE 2: UV-Vis spectrum of coking wastewater (a) untreated, (b) treated by the MWCNT-ME, (c) treated by active carbon, and (d) treated by MWCNTs powder.

ers filled with the wastewater with volume of 1 L, respectively. The adsorption experiment lasted for 1 h and proceeded with magnetic stirring. 5 mL each of treated wastewater before and after adsorption experiment were taken for UV-vis spectrum test. The same experiment was carried out for the MWCNT-ME which contains 1 g MWCNTs.

2.3. Electrochemical Measurement. All the electrochemical experiments were performed at $25 \pm 1^\circ\text{C}$. The working anodes were tested for their cyclic voltammetry (CV) by CHI-660 electrochemical workstation (Shanghai Chenhua Instrument Company, China), using the CHI version 10.08 software package. The reference electrode is a saturated calomel electrode (SCE). A standard three-electrode configuration was employed along with a cell whose volume was fixed for 250 mL. The area of working-electrode-contacting solution was 1 cm^2 . Distance between working electrode and counter electrode was fixed to be 2 cm. A 200 mL Na_2SO_4 (20 g/L) solution containing phenol (0.6 g/L) and a 200 mL Na_2SO_4 (20 g/L) solution containing aniline (0.6 g/L) were

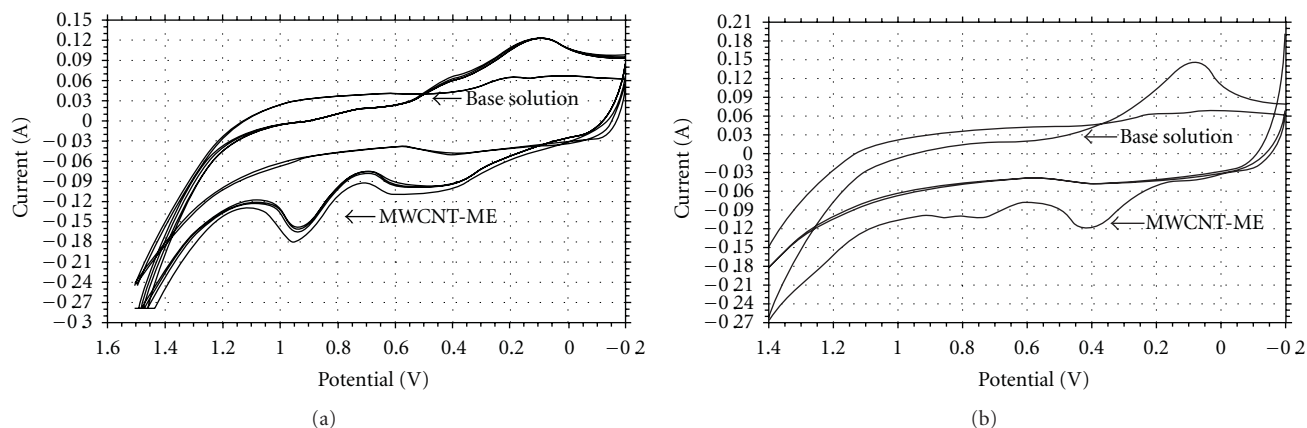


FIGURE 3: Performance of MWCNT-ME in oxidation of phenol and aniline, scan rate: 0.01 V/s (a) 0.06 g/L phenol in 20 g/L NaSO₄ and (b) 0.06 g/L aniline in 20 g/L NaSO₄.

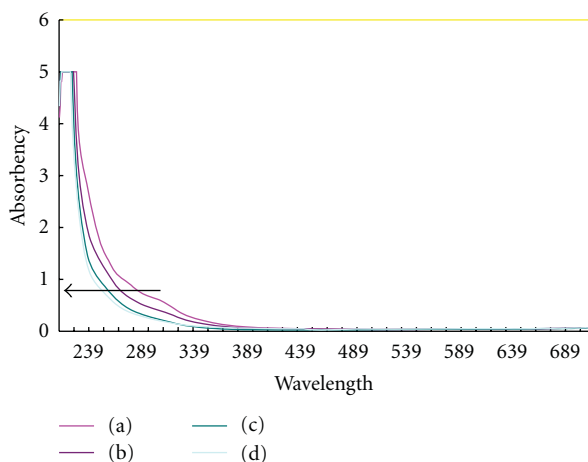


FIGURE 4: UV-Vis spectra of coking wastewater oxidized by MWCNT-ME for (a) 0 min, (b) 30 min, (c) 60 min, (d) 120 min.

used for test. The electrode was scanned between -0.2 V and 1.4 V, the scan rate was 0.01 V/S.

2.4. Electrochemical Degradation. The degradation experiment of coking wastewater was carried out in an electrochemical cell under magnetic stirring with a volume of 1 L. The performing temperature was at $25 \pm 1^\circ\text{C}$. Prior to degradation experiment, coking wastewater was purified biologically and filtered by filter paper to remove solid. The supporting electrolyte was 10 g/L Na₂SO₄. The MWCNT-ME with wet surface area of 60 cm² was used as the anode and the platinum sheet with the same wet surface area was used as the cathode. The distance between electrodes was fixed at 5 mm. The applied current density was set at 15 mA/cm². The experiment proceeded until total passed charge reached 7200 coulombs. The samples of the wastewater were collected with time interval of 30 min for UV-vis analysis. The organic constituents of the initial wastewater were analyzed with GC/MS-QP2010 (Shimadzu). The same GC/MS tests were carried out for treated wastewater with the MWCNT-ME

and the IrSnSb/Ti electrode. The chemical oxygen demand (COD) of wastewater was measured by a titrimetric method using dichromate as the oxidant in acidic solution at 150°C for 2 h (CHEMetrics, USA).

3. Results and Discussion

3.1. Morphology of MWCNT-ME. Figure 1 shows a top-down view of representative field-emission SEM image of the MWCNT-ME. As illustrated in Figure 1, MWCNTs with ends and edges exposed on the surface are dispersed homogeneously in PTFE. MWCNTs with mesh-like structure are effectively interwoven around each other and make up an electric mesh with electrochemical sensitive sites on the interface. The dispersed MWCNTs possess high specific volume and large surface area. On the other hand, there exists so many pores forming transition adsorption sites among interwoven MWCNTs, and capillarity provides fast penetration channels in electrochemical degradation process, which enhances the infiltration force of three-phase boundary.

3.2. Adsorption Experiment. As quantum wires made up of curled graphite layers, MWCNTs have obvious adsorption ability for fluid and gas. UV-vis spectrums of samples before and after degradation experiment were shown in Figure 2. It is clear that no distinct adsorption occurring on the MWCNT-ME compared with active carbon and MWCNTs powder.

For single-ring aromatic organic pollutants whose absorbency of UV-vis lies in the range from 200 nm to 250 nm, active carbon has better adsorption ability than MWCNTs powder. Basic structure cell of the active carbon is graphite-like microcrystalline with hybrid of sp^2 , graphite-like microcrystalline cells form the ultrafine particles with nanoscale, and pore structures with different scales can be found in this system in which adsorption can be easy going. For MWCNTs, the adsorption sites lie on inner walls of tubes with open ports and accumulation pores formed among MWCNTs. However, lack of open ports of MWCNTs affects adsorption

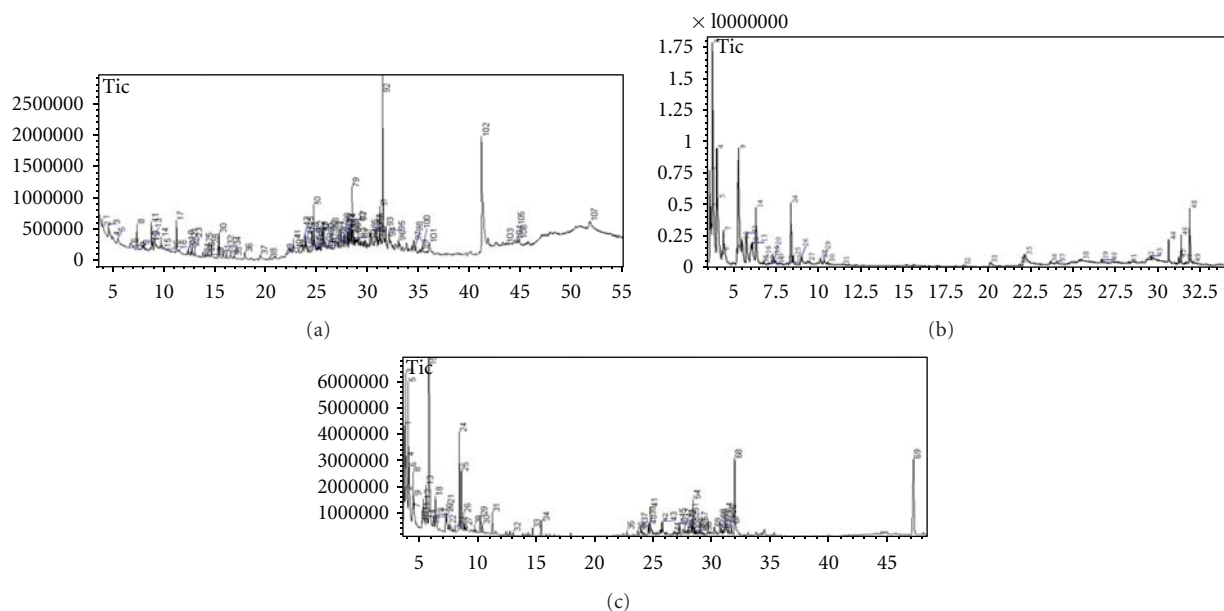


FIGURE 5: GC/MS spectra of the coking wastewater samples of (a) untreated, (b) treated by the MWCNT-ME for 120 min, (c) treated by the IrSnSb/Ti electrode for 120 min.

efficiency of single-ring aromatic organic pollutants with small molecular diameter in coking wastewater, which is consistent with the result in UV-vis spectrum. As the binder of the MWCNT-ME, infiltration of PTFE over the MWCNTs will decrease adsorption sites. In addition, only MWCNTs on the surface of MWCNT-ME can react with pollutants in the solution. Compared with the powder adsorption, media active adsorption sites on the MWCNT-ME were reduced. Adsorption ability is weakened, which makes electrochemical degradation be the determinant of concentration reduction of the pollutants.

3.3. Electrochemical Measurement. Electrochemical oxidation is a common way to abate phenol and Aniline. MWCNT-ME is expected to have good performance when used for electrochemical oxidation of phenol and aniline. Figure 3(a) shows the cyclic voltammeter of the MWCNT-ME in base solution and solution with trace phenol in the potential range from -0.2 V to 1.4 V. Compared with base solution, the CV curve of phenol solution has an obvious oxidation peak on the potential of about 0.95 V. This oxidation peak is corresponding to electrocatalytic oxidation of phenol and the current at oxidation peak reaches 0.18 A. The same trend was observed in electrochemical oxidation of aniline (Figure 3(b)). Compared with base solution, the oxidation peak with current of 0.12 A on the potential of about 0.45 V occurred on the CV curve in the potential range from -0.2 V to 1.4 V. Above trend indicates that oxidation of phenol and aniline are carried on obviously, which means that MWCNT-ME can improve the sensitivity and electrocatalytic activity to oxidation of phenol and aniline in coking wastewater.

3.4. Electrochemical Degradation. The UV-vis spectrum during electrochemical oxidation of coking wastewater by

MWCNT-ME was showed in Figure 4. An absorption band from 200 nm to 400 nm was observed. An absorption peak occurred in the range of $190\sim 250$ nm. There exist B absorption band and E absorption band of unsaturated structures of organic pollutants in the UV-vis region. Maximum wavelength of E absorption band of single-ring aromatic compounds (such as phenol and aniline) is in the range of 200 nm ~ 250 nm. The maximum wavelength of B absorption band of single-ring aromatic compounds is about 275 nm. The maximum wavelength of the E absorption band and B absorption band of polycyclic aromatic hydrocarbons and heterocyclic compounds (such as naphthalene, acridine, quinoline, and indole) is about 275 nm and in the range of $300\sim 375$ nm, respectively. According to the above policies, the adsorption peak in the range of $200\sim 250$ nm is formed by E adsorption band of single-ring aromatic compounds in the coking wastewater. Weak adsorption peak in the range of $250\sim 300$ nm is formed by B adsorption band of single-ring aromatic compounds and E adsorption band of polycyclic aromatic hydrocarbons and heterocyclic organic compounds in the coking wastewater. The adsorption band in the range of $300\sim 370$ nm is formed by B adsorption band of polycyclic aromatic hydrocarbons and heterocyclic organic compounds. With the degradation, the adsorption band became weaker and weaker. The concentration of the organic pollutants decreased. In the first 30 mins, adsorption bands ($200\sim 250$ nm and $250\sim 300$ nm) decreased significantly, which was consistent with the electrochemical degradation of the phenol and aniline. At 60 mins, the adsorption band in $250\sim 300$ nm fall with flat trend. When the time reached 120 min, the significant downward trend of the entire absorption band cannot be found. From the overall trend, different types of organic pollutants in the coking wastewater have been degraded to varying degrees.

TABLE 1: COD of coking wastewater treated by IrSnSb/Ti electrode and MWCNT-ME.

	IrSnSb/Ti	MWCNT-ME
COD (after two-hour electrochemical degradation)	93	71
Degradation efficiency (%)	35.9	51

Figure 5 gives the GC/MS spectra of coking wastewater samples untreated and treated by IrSnSb/Ti electrode and MWCNT-ME. One hundred and seven kinds of organic compounds were detected in the untreated coking wastewater. Forty kinds of organic compounds were removed by electrochemical degradation with IrSnSb/Ti electrode. Fifty-eight kinds of organic compounds were removed by electrochemical degradation with MWCNT-ME. In addition, preliminary quantitative analysis of COD test was carried out for two electrodes after two-hour electrochemical degradation. Degradation efficiencies were shown in Table 1. The result shows that the MWCNT-ME has better degradation reactivity than IrSnSb/Ti electrode.

4. Conclusion

An MWCNT-ME was made. Basic electrode configuration of the MWCNT-ME is randomly dispersed MWCNTs in PTFE dropped on the surface of a Ti conducting support macroelectrode. Adsorption activity of MWCNT-ME was proved to be weaker than powder adsorption media. The removal of refractory organic pollutants in coking wastewater mainly depends on electrochemical degradation occurred on MWCNT-ME. The CV curves for phenol and aniline have obvious oxidation and reduction peaks which reflect electrochemical reactivity of MWCNT-ME for some refractory organic pollutants. Such reactivity is furthermore reflected in the concentration decrease of the organic pollutants expressed in the UV-vis spectrum. The COD removal and change of organic pollutant species showed that MWCNT-ME has better performance than IrSnSb/Ti electrode on degradation efficiency. MWCNT-ME could be applied to process degradation of refractory organic pollutant in coking wastewater.

Acknowledgment

The financial support of Shanghai Science and Technology Cooperation Foundation (08230707200 and 0952nm06300) and Natural Science Foundation of China (91023029) is gratefully acknowledged.

References

- [1] Y. H. Cui, X. Y. Li, and G. Chen, "Electrochemical degradation of bisphenol A on different anodes," *Water Research*, vol. 43, no. 7, pp. 1968–1976, 2009.
- [2] C. A. Martínez-Huitle, A. De Battisti, S. Ferro, S. Reyna, M. Cerro-López, and M. A. Quiro, "Removal of the pesticide methamidophos from aqueous solutions by electrooxidation using Pb/PbO₂, Ti/SnO₂, and Si/BDD electrodes," *Environmental Science and Technology*, vol. 42, no. 18, pp. 6929–6935, 2008.
- [3] F. Montilla, E. Morallón, and J. L. Vázquez, "Evaluation of the electrocatalytic activity of antimony-doped tin dioxide anodes toward the oxidation of phenol in aqueous solutions," *Journal of the Electrochemical Society*, vol. 152, no. 10, pp. B421–B427, 2005.
- [4] C. Tan, B. Xiang, Y. Li, J. Fang, and M. Huang, "Preparation and characteristics of a nano-PbO₂ anode for organic wastewater treatment," *Chemical Engineering Journal*, vol. 166, no. 1, pp. 15–21, 2011.
- [5] R. Saito, M. Fujita, G. Dresselhaus, and M. S. Dresselhaus, "Electronic structure of chiral graphene tubules," *Applied Physics Letters*, vol. 60, no. 18, pp. 2204–2206, 1992.
- [6] F. Wu, G. Zhao, and X. Wei, "Electrocatalytic activity of multi-walled carbon nanotubes modified electrode for p-benzenediol," *Fenxi Huaxue*, vol. 32, no. 8, pp. 1057–1060, 2004.
- [7] L. C. Chen, Y. C. Ho, W. S. Guo, C. M. Huang, and T. C. Pan, "Enhanced visible light-induced photoelectrocatalytic degradation of phenol by carbon nanotube-doped TiO₂ electrodes," *Electrochimica Acta*, vol. 54, no. 15, pp. 3884–3891, 2009.
- [8] G. Busca, S. Berardinelli, C. Resini, and L. Arrighi, "Technologies for the removal of phenol from fluid streams: a short review of recent developments," *Journal of Hazardous Materials*, vol. 160, no. 2-3, pp. 265–288, 2008.
- [9] Y. Show and H. Itabashi, "Electrically conductive material made from CNT and PTFE," *Diamond and Related Materials*, vol. 17, no. 4-5, pp. 602–605, 2008.

Research Article

WPG-Controlled Quantum BDD Circuits with BDD Architecture on GaAs-Based Hexagonal Nanowire Network Structure

Hong-Quan ZHao¹ and Seiya Kasai^{1,2,3}

¹ Research Center for Integrated Quantum Electronics, Hokkaido University, N13, W8, Sapporo 060-8628, Japan

² Graduate School of Information Science and Technology, Hokkaido University, N14, W9, Sapporo 060-0814, Japan

³ PRESTO, Japan Science and Technology Agency, 4-1-8, Honcho, Kawaguchi-shi, Saitama 332-0012, Japan

Correspondence should be addressed to Hong-Quan ZHao, zhao@es.hokudai.ac.jp

Received 15 July 2011; Accepted 20 October 2011

Academic Editor: Steve Acquah

Copyright © 2012 H.-Q. ZHao and S. Kasai. This is an open access article distributed under the Creative Commons Attribution License, which permits unrestricted use, distribution, and reproduction in any medium, provided the original work is properly cited.

One-dimensional nanowire quantum devices and basic quantum logic AND and OR unit on hexagonal nanowire units controlled by wrap gate (WPG) were designed and fabricated on GaAs-based one-dimensional electron gas (1-DEG) regular nanowire network with hexagonal topology. These basic quantum logic units worked correctly at 35 K, and clear quantum conductance was achieved on the node device, logic AND circuit unit, and logic OR circuit unit. Binary-decision-diagram- (BDD-) based arithmetic logic unit (ALU) is realized on GaAs-based regular nanowire network with hexagonal topology by the same fabrication method as that of the quantum devices and basic circuits. This BDD-based ALU circuit worked correctly at room temperature. Since these quantum devices and circuits are basic units of the BDD ALU combinational circuit, the possibility of integrating these quantum devices and basic quantum circuits into the BDD-based quantum circuit with more complicated structures was discussed. We are prospecting the realization of quantum BDD combinational circuitries with very small of energy consumption and very high density of integration.

1. Introduction

One of the interesting issues for the next-generation LSI technology is how to utilize a variety of quantum devices, for their manipulation of individual electrons, dissipation of little power, and fabrication in sizes ranging to molecular scale. However, on the other hand, it is quite difficult to introduce quantum devices to the current mainstream Si CMOS technology, since extremely precise and very complicated architecture as well as fabrication process is required. A simple circuit technology is necessary. Tucker and Yoshikawa et al. suggested the use of single-electron tunneling transistors in an architecture very similar to CMOS [1, 2]. Likharev and Korotkov proposed reversible logic elements with small energy dissipation per switching event much less than $K_B T$ [3]. At present, there are lots of reports about individual single-electron devices (SET) that work at room temperatures. Those fabrication processes do not allow wires to cross, and no voltage gain existed. These two conditions

are necessary for making complex logic circuits. Another problem that SET circuitries are confronting is the parasitic components; the operation of many circuits is completely disrupted by the presence of the parasitic capacitance [4].

Binary decision diagram (BDD) technique provides a possible way to utilize quantum devices due to its simple and graphical logic architecture and passive operation characters with no gain [5, 6]. It is similar to pass gate logic. It has also been applied to non-Si circuits such as rapid single flux quantum (RSFQ) circuits [7, 8]. Recently, a hexagonal BDD logic circuit was proposed and has been developed. A logic function is represented by a directed graph with hexagonal topology [9–11], and the logical structure is directly implemented on a semiconductor nanowire network also having the same topology [10, 11]. This technique makes it possible to simplify design, circuit layout, device structure, and fabrication process. Redundancy available in nanostructures is also useful. Redundant network gives simplicity and flexibility in design and layout. It can give an opportunity to

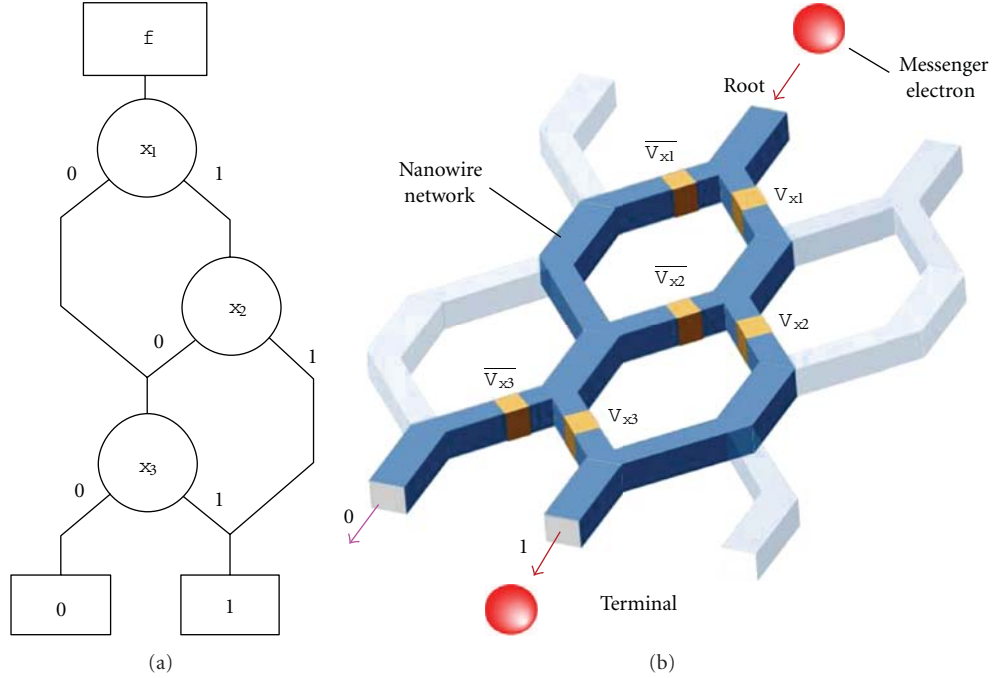


FIGURE 1: (a) Example of circuit with BDD-based logical architecture and (b) method of the physical implementation directly transferred from the graphical logic architecture.

add reconfigurable capability to the circuitry [12]. Successful demonstration of 2-bit full adder [13] and implementation of small signal processor utilizing the hexagonal BDD by circuit simulation [14] has confirmed its feasibility. It is noted that the BDD allows us to use quantum nanodevices such as quantum wire or single-electron transistors in small circuits [11, 15] although these devices have been understood quite difficult to implement conventional logic gate architecture due to small gain, small current drivability, and fluctuation. From the features described above, the hexagonal BDD circuit is found to have better possibility to apply nanowires, their networks, and nanodevices produced by various nanotechnologies to electronic circuits as compared with the Si CMOS logic circuit technology.

In this study, we demonstrate the correct operation of quantum device fabricated on the GaAs-based 1-DEG nanowire and characterized the quantum logic AND and OR units. The capability of the hexagonal BDD circuit to implement a highly functional circuit, ALU, was also characterized. The ALU integrating a set of subsystems is designed with a simple and regular structure and is implemented using GaAs-based hexagonal nanowire network together with Schottky wrap gates (WPGs). From elemental device characteristics and the measured ALU operations, the possibility to operate it in low voltage or in the quantum transport regime is discussed for the future option.

2. Experimental

2.1. Physical Implementation. Physical implementation method is schematically shown in Figure 1(a). In this study,

hexagonal nanowire network formed of AlGaAs/GaAs heterostructure is used as the host network structure. The logical structure in Figure 1(a) is directly transferred to the physical network structure in Figure 1(b). Logic can be directly verified by checking the physical network structure on the chip even in ALU-level functional circuits. Node devices are implemented by attaching a nanometer-scale Schottky wrap gate (WPG) on each exit branch in the suitable network node, as shown in Figure 2(a) [16]. The WPG controls the carrier density in the channel by the field effect. As the logic input, complementary WPG voltages are given to the two exit branches. The path switching is carried out by on/off the conduction of exit branches by WPGs in complementary fashion. The overall network can be formed with unipolar channel nanowires. Each node device needs neither Ohmic contact nor pn junction. Physical architectures of the device and the circuit and their operations are very simple.

The WPG can squeeze the nanowire electrostatically, and thus, a one-dimensional channel is formed [15, 17]. Therefore, the BDD node device in Figure 2(a) can operate as a quantum wire device which precisely switches the path of a small number of electrons at suitable temperature. Although the quantum wire device with conductance quantization has voltage gain less than unity, the BDD circuit is expected to operate correctly with a passive operation style.

2.2. Fabrication Processes. The hexagonal nanowire network was fabricated by electron beam (EB) lithography and wet chemical etching on a conventional AlGaAs/GaAs modulation-doped heterostructure wafer. The mobility and carrier density of the 2-dimensional electron gas (2DEG)

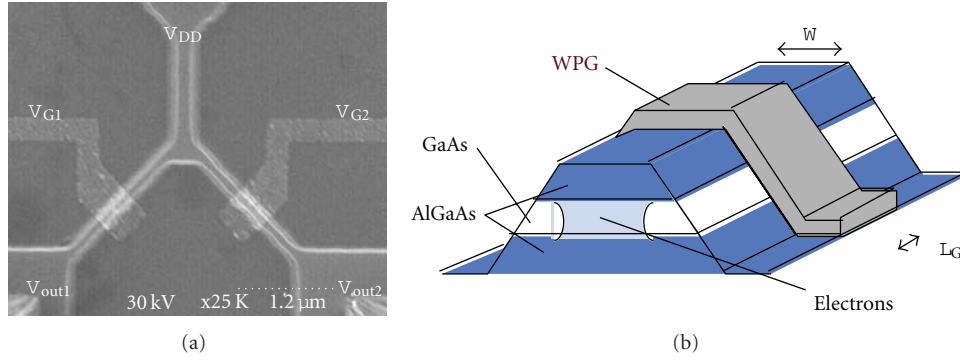


FIGURE 2: (a) BDD node device controlled by WPG and (b) WPG-controlled device structure.

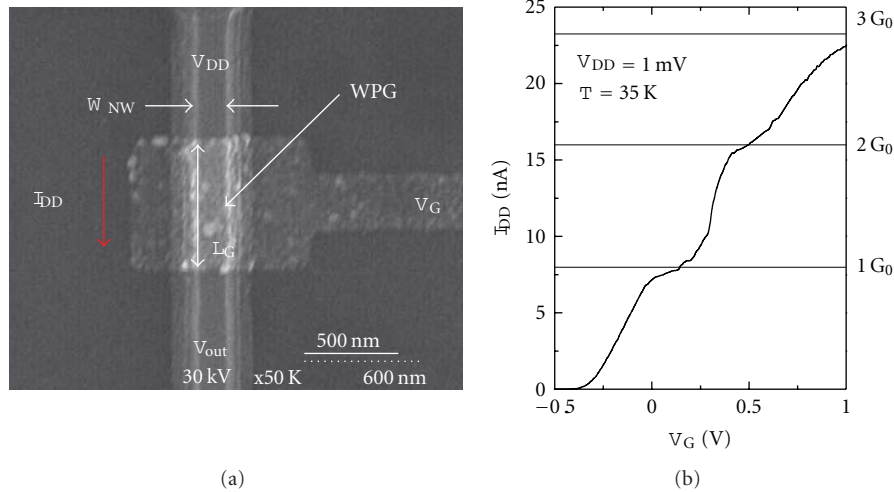
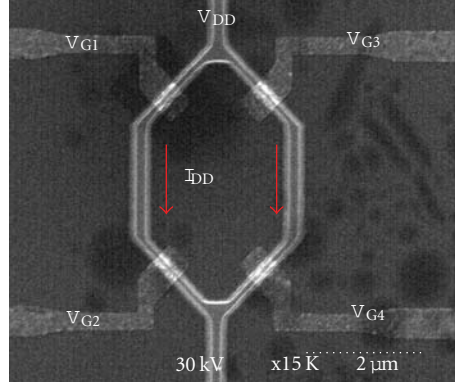


FIGURE 3: (a) SEM image of a quantum device controlled by a WPG on the hexagonal nanowire network (b) quantized conductance of the device measured at 35 K ($G_0=2e^2/h$), where V_{DD} is the driving voltage for the device, I_{DD} is the driving current in the 1-DEG channel, V_G is the applied voltage on the wrap gate (WPG), and V_{out} is the output voltage from the device.

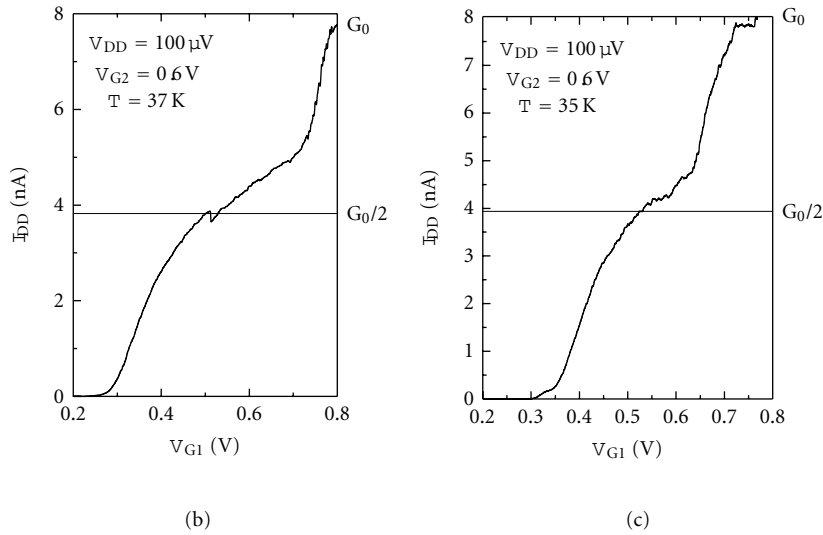
were $5.0 \times 10^3 \text{ cm}^2 \text{ V}^{-1} \text{ s}^{-1}$ and $1 \times 10^{12} \text{ cm}^{-2}$ at 297 K and $1.1 \times 10^5 \text{ cm}^2 \text{ V}^{-1} \text{ s}^{-1}$ and $1 \times 10^{12} \text{ cm}^{-2}$ at 77 K, respectively. Mean free path was 90 nm at 297 K and 1,800 nm at 77 K. The etching depth was 150 nm, reaching the GaAs buffer. Using an isotropic chemical etching and choosing low index $\langle -110 \rangle$ and $\langle 111 \rangle$ directions, uniform nanowires with faceted smooth sidewalls could be formed. Fabricated nanowire width W_{NW} was typically 100 nm for the quantum conductance devices and 500 nm for ALU circuit. The node density was 2×10^6 nodes/cm². Next, Ohmic contacts for the roots and terminals were made by Ge/Au/Ni/Au deposition and subsequent alloying. Then, Schottky wrap gates were formed by EB lithography, Pd/Pt or Cr/Au deposition, and lift-off with a typical length of 600 nm. Interconnect metal lines with 100 nm width were formed at the same level to WPGs. Although they were directly formed on the nanowires without insulators, they did not work as gate, since the threshold voltage was kept in negative by the short channel effect.

3. Experimental Results and Discussion

3.1. Quantum Devices on the 1-DEG Hexagonal Nanowire Network. The 1-dimensional electron gas (1-DEG) device structure is schematically shown in Figure 2(b). Clear quantized conductance was measured at 35 K on a WPG-controlled quantum device, confirming one-dimensional quantum transport controlling a small number of electrons, as shown in Figure 3(b). The typical nanowire width W_{NW} is about 100 nm, with the WPG length L_G 600 nm. Reducing the nanowire width, temperature where the quantum transport took place was found to increase, and the probability of appearance of conductance quantization also increased, and 80% of devices showed the conductance quantization at 30 K when $W_{NW} = 200$ nm [18]. From viewpoint of circuit application, the abrupt current switch at the edge of the quantized conductance is expected to give ultrasmall input voltage swing [19]. Measured slope of the quantized conductance edge also depended on the temperature as expected



(a)



(b)

(c)

FIGURE 4: (a) SEM image of the quantum logic AND and OR units on the hexagonal nanowire unit, (b) left side (when right sides of input voltages were zero), and (c) right side (when left sides of input voltages were zero) of quantized conductance dependence on one input voltage. The parameters in this figure stand for the same meaning as in Figure 3.

theoretically [20]. Very steep edge with large V_G -to- E_F scaling factor of $\alpha = 0.7$ could be obtained by reducing the nanowire width in the present device structure [18] although conventional quantum wire (point contact) devices with split gate structures showed $\alpha < 0.1$ [21]. WPG-controlled nanowire showed small input voltage swing for path switching in wide temperature range.

Logic AND and OR quantum units were fabricated on the GaAs-based hexagonal nanowire unit controlled by four WPGs as shown in Figure 4(a), with about 100 nm of nanowire width and 600 nm of gate length. Experiments were performed at 35 K cooled by a liquid Helium system. When the left or right side of the wrap gate input voltages were set to zero, the other side of the hexagon worked as a quantum logic AND. For example, when $V_{G1} = V_{G2} = 0$ V, the V_{G3} and V_{G4} worked as a quantum logic AND circuit. When the upside or downside of the input voltages is set to a high voltage

level, for example, $V_{G2} = V_{G4} = 0.6$ V, V_{G1} and V_{G3} worked as a quantum logic OR circuit. The quantized conductance characterization was shown in Figures 4(b) and 4(c) for the left side (when right side inputs were zero) and right side (when left side inputs were zero), respectively. Both sides of the circuit can be operated in the quantized conductance region correctly. This provided the possibility for the circuit unit to be applied in the quantum integration circuitries.

3.2. 4-Instruction 2-Bit ALU Circuit on the Hexagonal Nanowire Network. Figure 5(a) shows an SEM image of the fabricated 4-instruction 2-bit ALU. This unit integrated 32 node devices with 47 WPGs. It was realized by using 3 M nodes/cm² fabrication process, in which size of each hexagon was $6 \times 6 \mu\text{m}^2$. Total circuit area was $70 \times 45 \mu\text{m}^2$. L_G and W_{NW} were 550 nm and 570 nm, respectively. The fabrication process was completely the same as that for

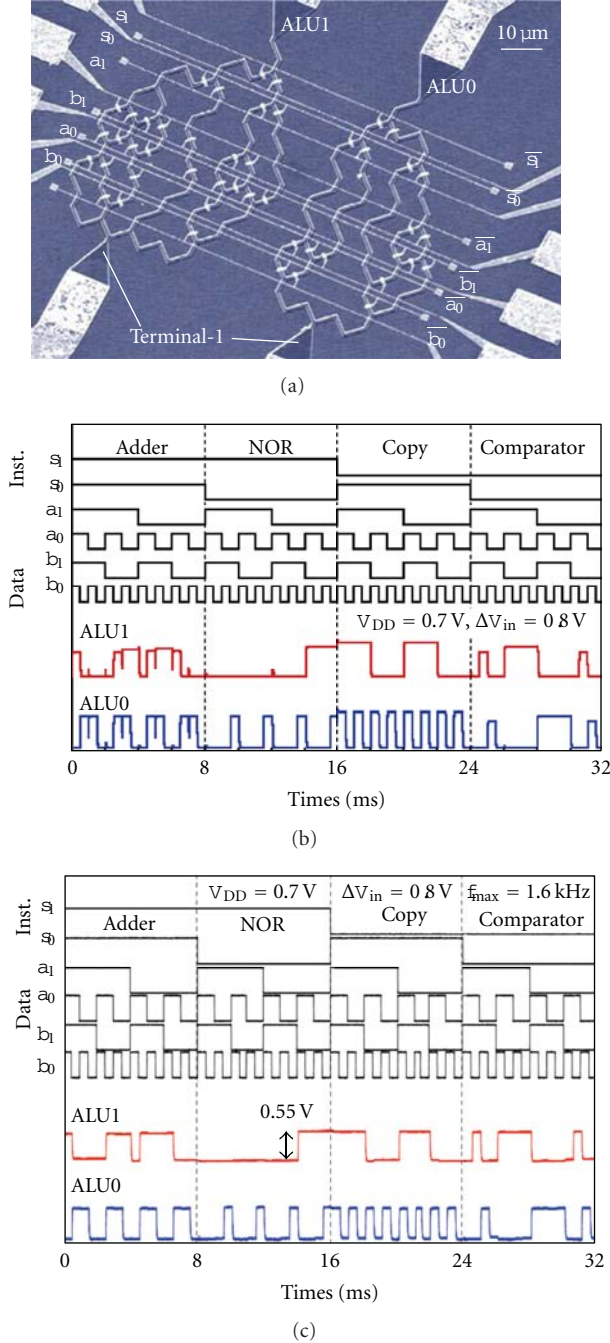


FIGURE 5: (a) SEM image of the fabricated 4-instruction 2-bit ALU on hexagonal nanowire network, (b) measured input-output waveforms, and (c) input-output waveforms obtained from circuit simulation of the ALU circuit.

discrete node devices. Higher-density fabrication process for 45 M nodes/cm² was already developed [22], which would result in 93% smaller area of the circuit in Figure 5(a).

Measured input-output waveforms are shown in Figure 5(b). In this measurement, supply voltage was applied to the terminals. Output voltages were measured in the roots through 1 MΩ resistance. The same DC offset voltage of 0.2 V was applied to all the WPGs except S₁ to obtain

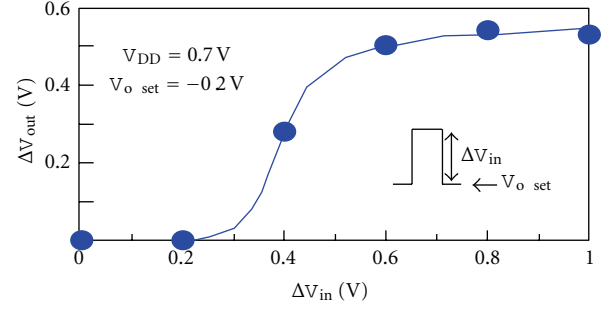


FIGURE 6: Input voltage swing dependence of the output of the fabricated 4-instruction 2-bit ALU circuit.

uniform high value of outputs. Supply voltage, V_{DD} , of -0.8 V was applied to the roots for sending electron from the root to terminals. Relatively large input voltage swing, ΔV_{in} , of 0.7 V was applied to overcome the threshold variation. The fabricated ALU operated correctly. Obtained output logic values reproduced the result from the circuit simulation in Figure 5(c).

To find possible voltage condition for the ALU operation in detail, input voltage swing dependence of the output was characterized. The obtained result is shown in Figure 6. The fabricated ALU showed output signals when $\Delta V_{in} > 0.2$ V, and V_{out} increased with increasing ΔV_{in} . V_{out} was saturated when $\Delta V_{in} > 0.8$ V, since the WPGs operated in the saturated region of the FET. The threshold of ΔV_{in} is roughly evaluated by the next formula:

$$\Delta V_{in} = \frac{4kT}{\alpha e} + \Delta V_{th}, \quad (1)$$

where α is V_G -to- E_F scaling factor. The former term in the right side of the equation is switching voltage to overcome the thermal energy, kT . The latter term expresses the excess voltage for compensating the V_{th} variation, ΔV_{th} . α can be estimated by $1/\alpha = S_{exp}/\{kT/e \ln(10)\}$. S_{exp} is the measured subthreshold swing. This equation is also applicable to the switching in the quantum transport regime [18]. Evaluated ΔV_{in} by (1) with measured α and ΔV_{th} was 0.21 V. This value is reasonably in agreement with the measured value of 0.2 from Figure 6. WPG-controlled nanowire can operate as a quantum wire transistor, and the BDD circuit is also expected to operate in the quantum transport regime, even though the scale of the circuit is increased. It is noted that the quantum wire device has voltage transfer gain less than 1 [23, 24]. According to (1) and measured α in the quantum transport regime, ΔV_{in} was determined by ΔV_{th} rather than input voltage swing, since small ΔV_{in} was obtained in low temperatures. On the other hand, giving enough large ΔV_{in} , the circuit is expected to operate even in the quantum transport regime. Due to the operation principle of the present circuit, V_{DD} can be independently set and can be kept small so as not to smear out the conductance quantization, which is not possible in conventional CMOS logic gate architecture.

4. Conclusion

One-dimensional nanowire quantum devices and basic quantum logic AND and OR unit on hexagonal nanowire units controlled by wrap gate (WPG) were designed and fabricated on GaAs-based regular 1-DEG nanowire network with hexagonal topology and worked correctly at 35 K. BDD-based arithmetic logic unit (ALU) is realized on GaAs-based regular nanowire network with hexagonal topology with the same fabrication process. It exhibits correct output waveforms at room temperature, allowing V_{th} variation of 0.2 V. Applicability for quantum nanodevice is also discussed. These circuits can be fabricated using completely the same process without any special technique.

Acknowledgments

This work was supported in part by Grant-in-Aid for Young Scientists (A) (no. 17686028) from Ministry of Education, Culture, Sports, Science and Technology, Japan. The authors thank Professor T. Fukui for his continuous support.

References

- [1] J. R. Tucker, "Complementary digital logic based on the "Coulomb blockade";" *Journal of Applied Physics*, vol. 72, no. 9, pp. 4399–4413, 1992.
- [2] N. Yoshikawa, Y. Jinguu, H. Ishibashi, and M. Sugahara, "Complementary digital logic using resistively coupled single-electron transistor," *Japanese Journal of Applied Physics*, vol. 35, no. 2, pp. 1140–1145, 1996.
- [3] K. K. Likharev and A. N. Korotkov, "Single-electron parametron: reversible computation in a discrete-state system," *Science*, vol. 273, no. 5276, pp. 763–765, 1996.
- [4] A. B. Zorin, F. J. Ahlers, J. Niemeyer et al., "Background charge noise in metallic single-electron tunneling devices," *Physical Review B*, vol. 53, no. 20, pp. 13682–13687, 1996.
- [5] S. B. Akers, "Binary decision diagram," *IEEE Transactions on Computers*, vol. 27, no. 6, pp. 509–516, 1978.
- [6] N. Asahi, M. Akazawa, and Y. Amemiya, "Binary-decision-diagram device," *IEEE Transactions on Electron Devices*, vol. 42, no. 11, pp. 1999–2003, 1995.
- [7] N. Yoshikawa, H. Tago, and K. Yoneyama, "A new design approach for RSFQ logic circuits based on the binary decision diagram," *IEEE Transactions on Applied Superconductivity*, vol. 9, no. 2, pp. 3161–3164, 1999.
- [8] N. Yoshikawa, F. Matsuzaki, N. Nakajima, K. Fujiwara, K. Yoda, and K. Kawasaki, "Design and component test of a tiny processor based on the SFQ technology," *IEEE Transactions on Applied Superconductivity*, vol. 13, no. 2, pp. 441–445, 2003.
- [9] S. N. Yanushkevich, D. M. Miller, V. P. Shmerko, and R. S. Stankovic, *Decision Diagram Techniques for Micro- and Nanoelectronic Design Handbook*, CRC Press, Boca Raton, Fla, USA, 2006.
- [10] H. Hasegawa and S. Kasai, "Hexagonal binary decision diagram quantum logic circuits using Schottky in-plane and wrap-gate control of GaAs and InGaAs nanowires," *Physica E*, vol. 11, no. 2-3, pp. 149–154, 2001.
- [11] S. Kasai and H. Hasegawa, "A single electron binary-decision-diagram quantum logic circuit based on Schottky wrap gate control of a GaAs nanowire hexagon," *IEEE Electron Device Letters*, vol. 23, no. 8, pp. 446–448, 2002.
- [12] S. Eachempati, V. Saripalli, N. Vijaykrishnan, and S. Datta, "Reconfigurable BDD based quantum circuits," in *Proceedings of the IEEE/ACM International Symposium on Nanoscale Architectures (NANOARCH '08)*, pp. 61–67, June 2008.
- [13] S. Kasai, M. Yumoto, T. Sato, and H. Hasegawa, "Design and implementation of ultra-small and ultra-low-power digital systems on GaAs-based hexagonal nanowire networks utilizing an hexagonal BDD quantum circuit approach," *ECS Proceeding*, vol. 2004-13, pp. 125–146, 2004.
- [14] S. Kasai, T. Nakamura, Y. Shiratori, and T. Tamura, "Schottky wrap gate control of semiconductor nanowire networks for novel quantum nanodevice-integrated logic circuits utilizing BDD architecture," *Journal of Computational and Theoretical Nanoscience*, vol. 4, no. 6, pp. 1120–1132, 2007.
- [15] M. Yumoto, S. Kasai, and H. Hasegawa, "Graph-based quantum logic circuits and their realization by novel GaAs multiple quantum wire branch switches utilizing Schottky wrap gates," *Microelectronic Engineering*, vol. 63, no. 1–3, pp. 287–291, 2002.
- [16] M. Yumoto, S. Kasai, and H. Hasegawa, "Novel quantum wire branch-switches for binary decision diagram logic architecture utilizing schottky wrap-gate control of GaAs/AlGaAs nanowires," *Japanese Journal of Applied Physics*, vol. 41, no. 4, pp. 2671–2674, 2002.
- [17] M. Yumoto, S. Kasai, and H. Hasegawa, "Gate control characteristics in GaAs nanometer-scale Schottky wrap gate structures," *Applied Surface Science*, vol. 190, no. 1–4, pp. 242–246, 2002.
- [18] Y. Shiratori and S. Kasai, "Effect of size reduction on switching characteristics in GaAs-based Schottky-wrap-gate quantum wire transistors," *Japanese Journal of Applied Physics*, vol. 47, no. 4, pp. 3086–3090, 2008.
- [19] H. Q. Zhao, S. Kasai, Y. Shiratori, and T. Hashizume, "A binary-decision-diagram-based two-bit arithmetic logic unit on a GaAs-based regular nanowire network with hexagonal topology," *Nanotechnology*, vol. 20, no. 24, Article ID 245203, 2009.
- [20] P. F. Bagwell and T. P. Orlando, "Landauers conductance formula and its generalization to finite voltages," *Physical Review B*, vol. 40, no. 3, pp. 1456–1464, 1989.
- [21] J. M. Elzerman, R. Hanson, L. H. Willems Van Beveren, L. M. K. Vandersypen, and L. P. Kouwenhoven, "Excited-state spectroscopy on a nearly closed quantum dot via charge detection," *Applied Physics Letters*, vol. 84, no. 23, pp. 4617–4619, 2004.
- [22] S. Kasai and H. Hasegawa, "Binary-decision-diagram quantum circuits based on Schottky wrap gate control of GaAs honeycomb nanowires," in *Proceedings of the 59th Annual Device Research Conference (DRC '01)*, pp. 131–132, Notre Dame, Ind, USA, June 2001.
- [23] G. Timp, R. E. Howard, and P. Mankiewich, "Nanoelectronics for advanced computation and communications," in *Nanotechnology*, G. Timp, Ed., pp. 7–89, Springer, 1999.
- [24] H. Q. Zhao, S. Kasai, T. Hashizume, and N. J. Wu, "Fabrication and characterization of active and sequential circuits utilizing schottky-wrap-gate-controlled GaAs hexagonal nanowire network structures," *IEICE Transactions on Electronics*, vol. E91-C, no. 7, pp. 1063–1069, 2008.

Research Article

Plasmonic Properties of Vertically Aligned Nanowire Arrays

Hua Qi, O. J. Glembocki, and S. M. Prokes

Electronics Science and Technology Division, US Naval Research Laboratory, Washington, DC 20375, USA

Correspondence should be addressed to Hua Qi, qhqi@nrl.navy.mil

Received 13 July 2011; Revised 20 September 2011; Accepted 4 October 2011

Academic Editor: Steve Acquah

Copyright © 2012 Hua Qi et al. This is an open access article distributed under the Creative Commons Attribution License, which permits unrestricted use, distribution, and reproduction in any medium, provided the original work is properly cited.

Nanowires (NWs)/Ag sheath composites were produced to investigate plasmonic coupling between vertically aligned NWs for surface-enhanced Raman scattering (SERS) applications. In this investigation, two types of vertical NW arrays were studied; those of ZnO NWs grown on nanosphere lithography patterned sapphire substrate via vapor-liquid-solid (VLS) mechanism and Si NW arrays produced by wet chemical etching. Both types of vertical NW arrays were coated with a thin layer of silver by electroless silver plating for SERS enhancement studies. The experimental results show extremely strong SERS signals due to plasmonic coupling between the NWs, which was verified by COMSOL electric field simulations. We also compared the SERS enhancement intensity of aligned and random ZnO NWs, indicating that the aligned NWs show much stronger and repeatable SERS signal than those grown in nonaligned geometries.

1. Introduction

Nanostructures, especially nanowires (NWs), have inspired much interest due to their potential applications in electronics, photonics, and life science [1–5]. In particular, NWs used for surface-enhanced Raman scattering (SERS) are of significant interest since SERS spectra can provide trace level detection and a chemical fingerprint by which a molecule can be identified. Several NWs types have been used to investigate the SERS effect, including silver NWs [6, 7], gold NWs [8], semiconductor NWs [9], and dielectric NWs [10–12]. It has been demonstrated that the geometry of the nanowires and the orientation of the molecules play an important role in the SERS process [10–14]. However, most of the reported NW structures were randomly distributed on a surface, where the largest SERS enhancements noted were in the NW crossing [10] and between the NW and the substrate [14]. Since it has been shown experimentally that the largest enhancements were between two closely aligned parallel NWs [13], an obvious extension of this result is to investigate the SERS enhancements of a large number of aligned parallel NW arrays. Thus, in this work, we have investigated the effect of close parallel NW alignment on the SERS response and on the reproducibility of the SERS signal. In addition, we have also investigated the plasmonic properties of periodic and nonperiodic NW arrays.

Since the “hot spots” or regions of plasmon coupling are the region from which SERS would have the largest enhancement and closely aligned NW should experience coupling along the whole lengths of the wires, we have produced arrays of plasmonic nanowires to investigate this SERS effect. Here we used two types of vertical NWs, ZnO NWs, and Si NWs, respectively, to investigate SERS enhancement due to the plasmonic coupling between closely packed NWs. Many lithographic techniques have been used to fabricate ordered patterns on a surface, including photolithography, e-beam lithography [15, 16], ion beam lithography [17], X-ray lithography [18, 19], nanoimprint lithography [20, 21], and scanning probe lithography [22, 23]. However, all of these techniques are time consuming and costly. Here we employed the nanosphere lithography (NSL) approach [24–26], which has the advantages of low cost and simplicity, to produce the hexagonal gold dot patterns on c-sapphire and to successfully grow vertically aligned ZnO nanowires by the well-known VLS process. In this way, the ZnO NWs can be arranged in a repeatable hexagonal pattern creating ordered and aligned NW arrays for surface-enhanced Raman scattering (SERS) applications. The closely packed vertical Si NWs were fabricated by wet chemical etching [27]. The Si NWs and ZnO NWs arrays were coated with a thin layer of Ag, using an electroless plating technique, and their plasmonic properties were investigated.

2. Experimental Details

A bare c-sapphire piece with the size of $1 \times 1 \text{ cm}^{-1}$ was cleaned in a piranha solution at 90°C for 30 min to produce a hydrophilic surface, rinsed by DI- H_2O , and dried under a flow of nitrogen. Commercial silica nanospheres (NSs) slurry, with a diameter of 300 nm, was further diluted in a mixture of the surfactant Triton X-100 and methanol (1 : 400 by volume), with a dilution fraction of 1 : 3. NS lithography was performed on the sapphire surface by spin-coating the diluted silica nanosphere at a speed of 3600 rpm for 60 s. The sapphire surface, having a single layer of closely packed NS, was then covered by 10 nm of gold, using an FC-2000 Temescal e-beam metal evaporation system, at a rate of 0.5 \AA/s . After the gold deposition, the NS were removed by sonicating in DI- H_2O for 1-2 minutes. Well-ordered gold particles in hexagonal patterns were left on the sapphire surface, and they served as a catalyst during the vertical ZnO growth.

Using the sapphire substrate prepared above, the growth of the vertical ZnO NWs was carried out in a horizontal furnace via the vapor-liquid-solid (VLS) growth mechanism. The mixture powder of ZnO : C (1 : 1 by weight) used as the source was placed at one end of an alumina boat, and the substrate with the gold pattern was put directly above the material sources, face down. The furnace was heated to 900°C while flowing simultaneously a mixture of argon and oxygen gases in a ratio of 25 : 1 through the tube.

For the formation of the Si NW arrays, commercial p-type Si (100) wafer with narrow resistivity range of 6.3–7.0 $\Omega\text{-cm}$ was cleaned by piranha solution for 30 min at 90°C and then rinsed by DI water. Then 5% HF aqueous solution was used to remove the oxide layer for 2 min, which generated a fresh Si surface passivated with H-termination. The resulting clean Si wafer was put into a mixture of 4.8 M HF and 0.005 M AgNO_3 solution for 1 min. Then the wafer with a layer of silver was taken out of the solution, rinsed with DI water, and immediately immersed into wet etching chemicals of 4.8 M HF and 0.4 M H_2O_2 in the dark. After 30 min, the wafer was taken out, rinsed with DI water, and immersed in dilute HNO_3 (1 : 1 v/v) to dissolve the extra Ag catalyst. Finally the wafer was washed with 5% HF again to remove the oxide layer, cleaned with DI water, and dried under a flow of N_2 . All was carried out at room temperature.

An electroless silver plating approach was employed to produce ZnO or Si NWs core/Ag sheath composites for the SERS investigations. The detailed procedure has been well demonstrated in our previous report [11, 12]. Briefly silver mirror reaction was used to produce neutral Ag in solution, and the freshly formed Ag nanoparticles were simultaneously deposited on NW surface, coating the whole surface of the nanowires.

A LEO scanning electron microscope (SEM) with energy dispersive X-ray (EDX) was used to investigate the topographies of NS patterned surface, growth of the vertical ZnO NWs, etching of the Si NWs, and electroless silver plating of the vertical ZnO or Si NWs. The SERS measurements of ZnO NWs were carried out utilizing a well-known SERS molecule, benzene thiol (BT), and a confocal μ -Raman system which

consisted of a Mitutoyo Microscope and an Ocean Optics QE65000 spectrometer equipped with a thermoelectrically cooled CCD. The 514.5 nm line of an Ar ion laser was used as the excitation source. The microscope utilized a 100x 0.7 NA objective for focusing the laser light and was coupled to the spectrometer through a fiber optic cable. The spectra were collected with low laser power of 0.75 mW at the sample. This was done to prevent desorption and damage to the SERS-active molecules, benzene thiol, and to prevent alterations to the Ag layer. The SERS behavior of Si NWs arrays was performed using a Delta Nu system which consists of an Olympus Microscope and a Raman spectrometer equipped with a thermoelectrically cooled CCD. The 785 nm line of Ti : Sapphire laser was used as the excitation source to detect the SERS strength dependence on a single NW/silver composite. The microscope utilized a 50x 0.75 NA objective for focusing the laser light. The spectra were collected with a laser power of 3 mW at the sample.

3. Results and Discussion

A single layer of closely packed silica nanospheres produced by self-assembly is shown in Figures 1(a) and 1(b). By this simple and high throughput way, the NS patterned area tens of microns in size can be easily produced. After the deposition of 10 nm of gold, the liftoff was performed in DI- H_2O by sonicating. Hexagonal periodic Au particle arrays were obtained, as shown in Figure 1(c). When performing the sonicating lift-off process, 1-2 minutes was used. Longer sonication time usually led to the loss of the hexagonal gold patterns, while a shorter time resulted in incomplete liftoff of the nano-spheres from the substrate. Figure 1(d) shows an SEM image after the patterned sample was lifted off and annealed at 500°C for 10 min. The distance between two nearest nanoparticle centers is around 170 nm. Considering the 3D structure of the gold particles, the spacing may even be smaller, down to less than 100 nm, which provides one way to obtain ordered ZnO NW arrays for further plasmonic studies.

For the vertical ZnO nanowire growth, the well-known vapor-liquid-solid (VLS) growth mechanism was used. Due to the need to form a eutectic with the Au dots for NW growth, high selectivity of the growth resulted, and well-ordered ZnO NW arrays were obtained, as shown in Figure 2(a). Since the NW growth rate depends on the size of the initial Au catalyst, some differences in the NW total lengths were noted. However, the hexagonal patterns are quite recognizable. To produce the patterned nanowire arrays required, we optimized the growth time to 10 minutes in order to control the nanowire growth length, as shown in Figure 2(a). In the case of longer NWs, the detailed information is discussed in what follows. In addition, the distance between the gold catalyst can be controlled by varying the size of the nanospheres, which provides a way to control the spacing between the vertical NWs. A representative image of the vertical ZnO NW covered with a thin layer of silver using the electroless plating approach is shown in Figure 2(b), by which the roughness of the silver-coated NW surface is visible.

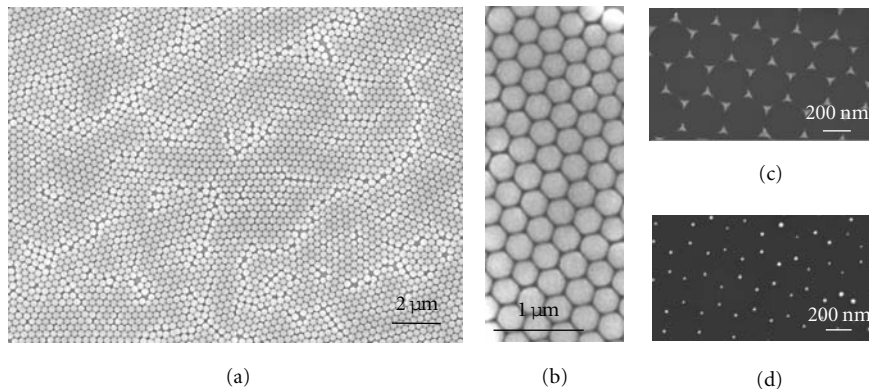


FIGURE 1: SEM images of monolayer of 300 nm silica nanospheres (a, b), hexagonal patterns after liftoff by sonicating (c, d).

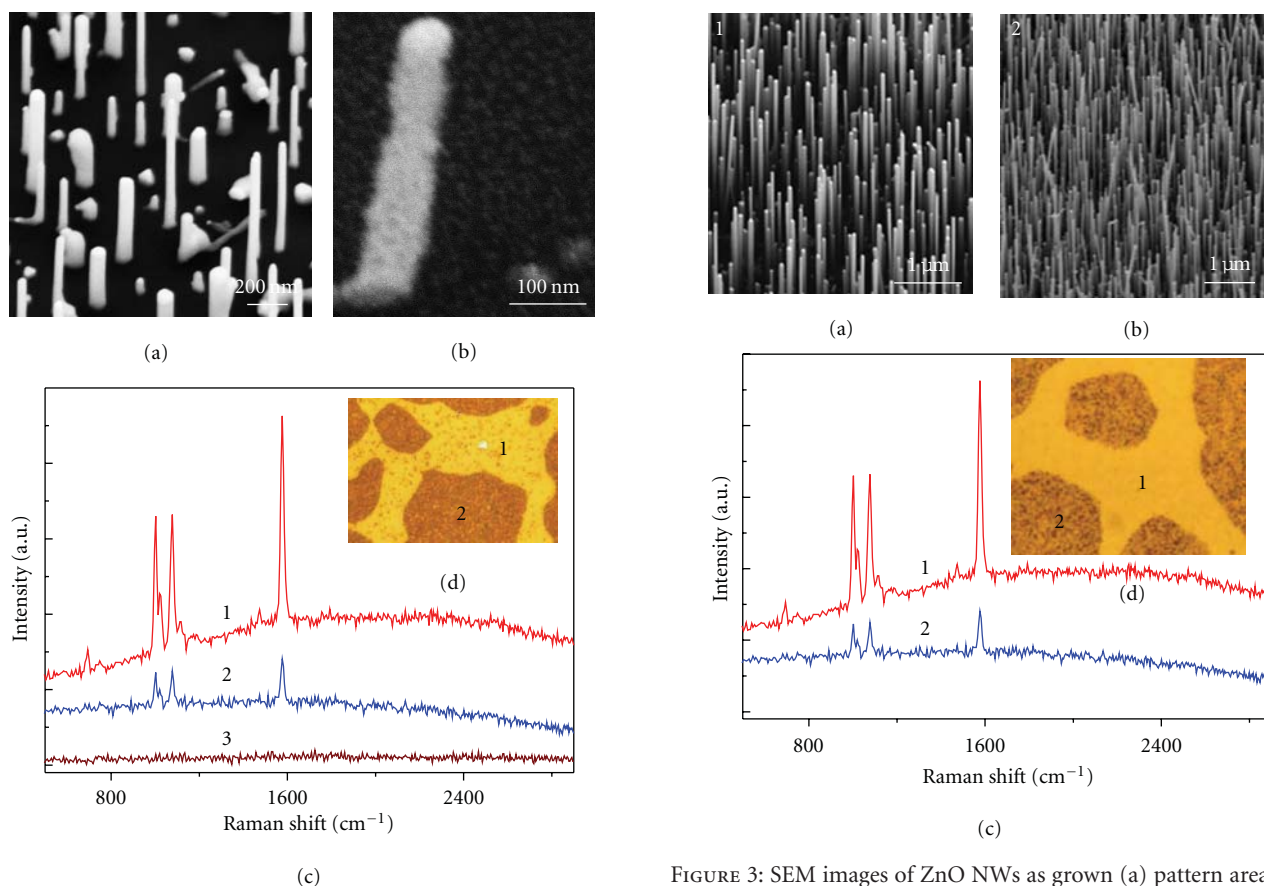


FIGURE 2: SEM images of short ZnO NWs as grown (a) and after silver coating on ZnO NWs surface (b); surface-enhanced Raman spectra (c) on silver-coated NWs at patterned area (red line 1), random area (blue line 2), and no NWs area (brown line 3) microscope image of SERS measurement sample (d).

Representative surface-enhanced Raman scattering (SERS) spectra of three regions are shown in Figure 2(c), including a well-ordered NWs area, random NWs area, and no NWs area. Figure 2(d) is a corresponding optical microscope image, showing the different areas. The major Raman peaks at 1002, 1071, and 1576 cm^{-1} can, respectively,

FIGURE 3: SEM images of ZnO NWs as grown (a) pattern area and (b) random area; surface-enhanced Raman spectra (c); (d) microscope image of SERS measurements of area 1 and 2.

be assigned to symmetric ring breathing, in plane C–H bending and in plane C–C stretching of the phenyl ring from the active molecules, benzene thiol (BT), which are in good agreement with those reported previously [28–33]. It is obvious that the strongest SERS signal is obtained on the well-ordered vertical NWs arrays area, while no enhancement is received on the area without NWs, further confirming the important effect of dielectric ZnO NW on SERS mechanism, as reported previously [10]. The intensity of the 1567 cm^{-1}

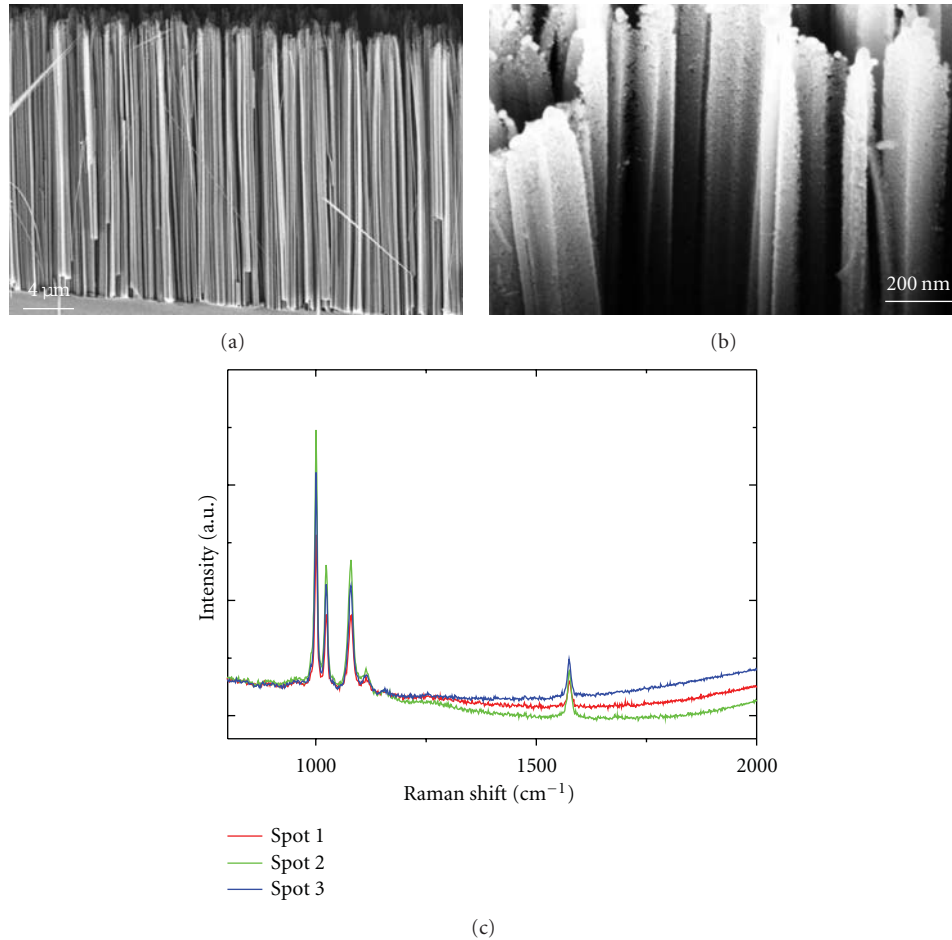


FIGURE 4: Representative SEM images of Si NWs produced by wet chemical etching (a), and silver-coated Si NWs (b). The sample stage was tilted 45° when imaging. (c) Surface-enhanced Raman spectroscopy (SERS) patterns at different spots.

SERS band on the patterned vertical NW area is about 4 times stronger than those of the random NW area. This observation can be attributed to the reproducibility of the well-patterned NWs, while the NWs on the random area are stochastic. It has been demonstrated that the randomly distributed dielectric NW core/Ag sheath composite lying on the surface can also produce notable SERS signal due to the interactions between silver-silver particles and silver-NW substrate [11, 12]. In addition, there may be plasmonic coupling in the well-ordered area because of the close distance between the adjacent aligned NWs. Since this effect increases with the number of aligned NWs, this may also be contributing to the enhanced SERS measured. It is well known that the SERS effect relies on enhanced electric fields that are created because of light-induced plasmons in the silver nanoparticles. As reported earlier [11], the plasmons in closely spaced metal nanostructures are coupled to form regions of very high field, further enhancing the SERS response.

The strongest SERS enhancement displayed above was obtained using the short vertical ZnO NWs with the length of less than 700 nm. In fact, we also investigated the SERS behavior on the well-ordered and patterned sample with longer NWs. Several-microns-long vertical ZnO NWs of

patterned area and unpatterned area are, respectively, shown in Figures 3(a) and 3(b). As shown in Figure 3(c), the SERS intensity is moderately greater in the aligned case than in the nonaligned case. Figure 3(d) is an optical microscope image of the measured surface area with ordered or random ZnO NWs. It is well known that SERS signals depend on density, size, morphology, and thickness of the coated material. However, in the case of closely packed and vertically aligned random NWs, the silver particle coverage is gradually decreasing as a function of depth, from the NWs top to the bottom, which can be attributed to the well-known capillary effect since we introduced solutions to perform the electroless silver plating. This defect of the silver particles coverage on NWs could affect the strength of SERS due to lack of “hot spots.” In fact, the NW density of unpatterned area is greater than in the patterned case. This is logical, since in the unpatterned area, a continuous Au film is used as a catalyst, and thus, in the VLS growth, a large number of catalyst islands form to grow NWs. In the patterned area, however, only a very small fraction of the substrate is covered in Au islands, since most of the area is taken up by the nanospheres, which of course get removed prior to growth, leaving only the small triangular regions of Au, as shown in Figure 1(c).

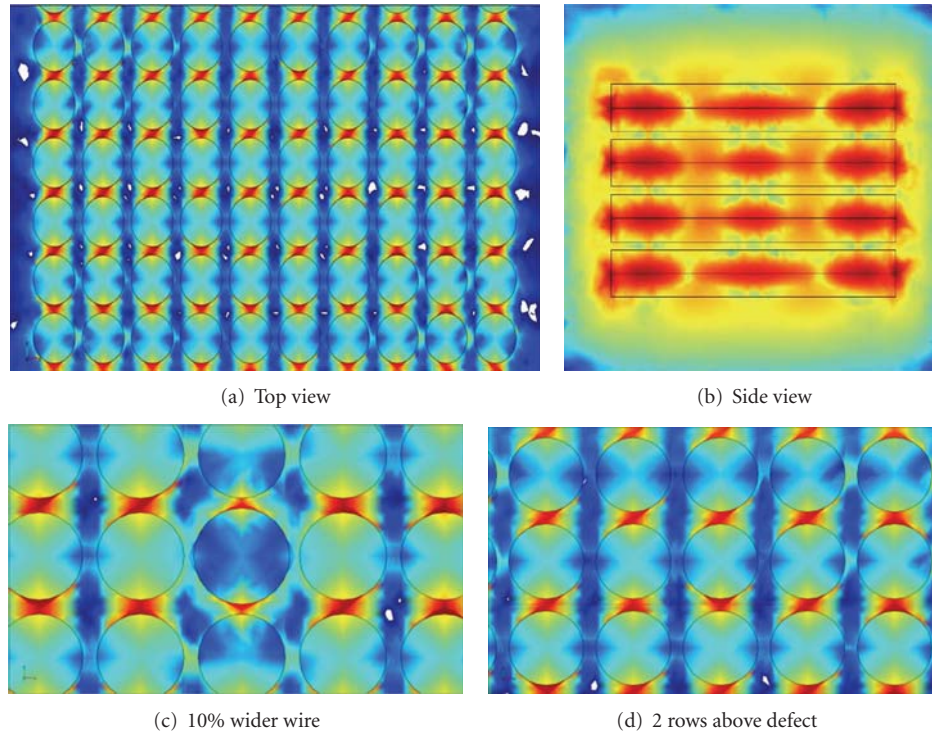


FIGURE 5: COMSOL simulations of the plasmonic coupling of parallel Si NWs; (a) top view; (b) side view, (c) local enhancement decrease (less intense red regions) with larger NW diameter “defect” and (d) no effect on SERS enhancement of the NW arrays two rows away from NW “defect.”

Since, as noted above, it is harder to get a high coverage of the silver particles along the whole length of the NW in closely spaced random NW arrays due to the capillary effect, one might expect a reduction in the SERS response, although a higher total NW density is present. In the case of the patterned area, the NWs result in better Ag coverage due to the lower NW density and thus a more open structure. It is also noted that increasing the plating time or concentration of the plating solution does not help to improve the silver plating of closely packed NWs and usually results in NW breakage or a pileup of silver nanostructures on the tip of the NWs, blocking the way to further silver plating of the NWs parting depth.

It is hard to investigate the detailed morphology of the nanostructures at high-resolution SEM due to the charging issue of sapphire substrate, on which vertical ZnO nanowires were usually grown. Thus, we employed semiconductor Si NWs, which was produced by chemical wet etching and has similar vertically aligned nanostructures to ZnO NWs. A typical side view SEM image of Si NWs is shown in Figure 4(a), indicating that the NWs are uniform with a high density and close spacing. The lengths of the NWs are close to $30\ \mu\text{m}$. As shown in Figure 4(b), the vertical Si NWs were covered by a thin layer of silver nanoparticles by electroless plating as described above. The SERS measurements at different spots were performed. As shown in Figure 4(c), the SERS intensity is very uniform across Si NWs array sample, demonstrating that the wet chemical etching and electroless plating results in repeatable and uniform plasmonic NW large area arrays. The

lines for the SERS-active molecules, BT, are very similar to those reported previously [28–33]. When the SERS intensity of the Si NW arrays was compared to the ZnO NW arrays using the 514 nm laser line, an order of magnitude greater signal was noted for the Si NWs. This is most likely to a much higher density of wires, which are also more closely spaced, leading to greater plasmon coupling.

Vertical NWs with smaller separation distance can result in the formation of hot spots corresponding to very intense electric field. Kottmann and Martin [34] have shown that coupled parallel metallic wires lead to a significantly enhanced coupled plasmon resonance in the overall structure. Finite element COMSOL simulation of the NW array plasmonic properties is shown in Figure 5. As can be seen in Figure 5(a), parallel and closely packed NWs/Ag composites induced high electric field along the whole length of the nanowires, which result in the very large enhancement of the observed SERS signals. Figure 5(b) is a side view of the parallel NW/Ag composites, clearly demonstrating the strong plasmonic coupling between the NW/Ag composites. Furthermore, on average, the strong plasmonic coupling is not dramatically influenced by small variations in the nanowire diameters. Figure 5(c) shows the influence of a 10% increase in the thickness of the central nanowire. The local fields around the nanowire are reduced leading to a factor of 4 decrease in the very local SERS enhancement. However, note that areas that are only several nanowires away from our defect show virtually no change in the SERS enhancement. In fact as shown in Figure 5(d), the line of nanowires that

are two rows above the defect are not impacted by the defect at all. Thus, the plasmonic fields behave similarly to semiconductor bands that have local densities of states from impurities that are isolated from the semiconductor conduction or valence bands. This analogy further suggests that even in the “amorphous” case, which is random distributions of aligned nanowires, there should still be a high SERS uniformity across the array, as shown in Figure 4.

4. Conclusion

We have successfully produced ordered, parallel ZnO and Si nanowire arrays on c-sapphire and Si substrates, respectively. The area of periodic ZnO NWs exhibits 4 times stronger SERS signal than those of random ZnO NWs, demonstrating the feasibility of using metal/dielectric nanowire periodic arrays to enhance the SERS signal. The wet chemically etched Si NWs were also studied, demonstrating the strong plasmonic coupling between the parallel NWs/Ag composites. These results are in good agreement with our COMSOL simulations of the closely packed vertical NWs/Ag composites. Since large SERS enhancements and SERS uniformity and repeatability are important issues, this study provides potential for the development of reliable, remotely deployable, and more sensitive optically based sensors.

Acknowledgments

We are thankful for the support of the Office of Naval Research (ONR), the American Society for Engineering Education program, the National Basic Research Program (2011CB933101) and Nanoscience Institute at Naval Research Lab (NRL).

References

- [1] Y. Sun and J. A. Rogers, “Fabricating semiconductor nanowires and transfer printing ordered arrays of them onto plastic substrates,” *Nano Letters*, vol. 4, no. 10, pp. 1953–1959, 2004.
- [2] T. Mårtensson, C. P. T. Svensson, B. A. Wacaser et al., “Epitaxial III-V nanowires on silicon,” *Nano Letters*, vol. 4, no. 10, pp. 1987–1990, 2004.
- [3] P. Mohan, J. Motohisa, and T. Fukui, “Controlled growth of highly uniform, axial/radial direction-defined, individually addressable InP nanowire arrays,” *Nanotechnology*, vol. 16, no. 12, pp. 2903–2907, 2005.
- [4] S. D. Hersee, X. Sun, and X. Wang, “The controlled growth of GaN nanowires,” *Nano Letters*, vol. 6, no. 8, pp. 1808–1811, 2006.
- [5] M. T. Björk, C. Thelander, A. E. Hansen et al., “Few-electron quantum dots in nanowires,” *Nano Letters*, vol. 4, no. 9, pp. 1621–1625, 2004.
- [6] R. Gunawidjaja, S. Peleshanko, H. Ko, and V. V. Tsukruk, “Bimetallic nanocobs: decorating silver nanowires with gold nanoparticles,” *Advanced Materials*, vol. 20, no. 8, pp. 1544–1549, 2008.
- [7] S. J. Seung, J. M. Baik, and M. Moskovits, “Polarization-dependent surface-enhanced Raman scattering from a silver nanoparticle-decorated single silver nanowire,” *Nano Letters*, vol. 8, no. 10, pp. 3244–3247, 2008.
- [8] H. Wei, F. Hao, Y. Huang, W. Wang, P. Nordlander, and H. Xu, “Polarization dependence of surface-enhanced Raman scattering in gold nanoparticle-nanowire systems,” *Nano Letters*, vol. 8, no. 8, pp. 2497–2502, 2008.
- [9] C. Fang, A. Agarwal, E. Widjaja et al., “Metallization of silicon nanowires and SERS response from a single metallized nanowire,” *Chemistry of Materials*, vol. 21, no. 15, pp. 3542–3548, 2009.
- [10] S. M. Prokes, O. J. Glembocki, R. W. Rendell, and M. G. Ancona, “Enhanced plasmon coupling in crossed dielectric/metal nanowire composite geometries and applications to surface-enhanced Raman spectroscopy,” *Applied Physics Letters*, vol. 90, no. 9, Article ID 093105, 2007.
- [11] H. Qi, D. Alexson, O. Glembocki, and S. M. Prokes, “Plasmonic coupling on dielectric nanowire core-metal sheath composites,” *Nanotechnology*, vol. 21, no. 8, Article ID 085705, 2010.
- [12] H. Qi, D. Alexson, O. Glembocki, and S. M. Prokes, “The effect of size and size distribution on the oxidation kinetics and plasmonics of nanoscale Ag particles,” *Nanotechnology*, vol. 21, no. 21, Article ID 215706, 2010.
- [13] S. M. Prokes, D. A. Alexson, O. J. Glembocki, H. D. Park, and R. W. Rendell, “Effect of crossing geometry on the plasmonic behavior of dielectric core/metal sheath nanowires,” *Applied Physics Letters*, vol. 94, no. 9, Article ID 093105, 2009.
- [14] O. J. Glembocki, R. W. Rendell, S. M. Prokes, D. A. Alexson, A. Fu, and M. A. Mastro, “Dielectric-Substrate interactions with metal/dielectric nanowires composites in surface-enhanced Raman spectroscopy,” *Physical Reviews B*, vol. 80, no. 1, 2009.
- [15] R. R. W. Pease, “Nanolithography and its prospects as a manufacturing technology,” *Journal of Vacuum Science & Technology B*, vol. 10, no. 1, pp. 278–285, 1992.
- [16] M. A. McCord, “Electron beam lithography for 0.13 μm manufacturing,” *Journal of Vacuum Science and Technology B*, vol. 15, no. 6, pp. 2125–2129, 1997.
- [17] J. Melngailis, A. A. Mondelli, I. L. Berry, and R. Mohondro, “A review of ion projection lithography,” *Journal of Vacuum Science and Technology B*, vol. 16, no. 3, pp. 927–957, 1998.
- [18] H. I. Smith and M. L. Schattenburg, “X-ray lithography, from 500 to 30 nm: X-ray nanolithography,” *IBM Journal of Research and Development*, vol. 37, no. 3, pp. 319–329, 1993.
- [19] J. P. Silverman, “X-ray lithography: status, challenges, and outlook for 0.13 μm ,” *Journal of Vacuum Science and Technology B*, vol. 15, no. 6, pp. 2117–2124, 1997.
- [20] Y. S. Kim, K. Lee, J. S. Lee, G. Y. Jung, and W. B. Kim, “Nanoimprint lithography patterns with a vertically aligned nanoscale tubular carbon structure,” *Nanotechnology*, vol. 19, no. 36, Article ID 365305, 2008.
- [21] I. W. Moran, A. L. Briseno, S. Loser, and K. R. Carter, “Device fabrication by easy soft imprint nano-lithography,” *Chemistry Letters*, vol. 20, no. 14, pp. 4595–4601, 2008.
- [22] S. Manne, P. K. Hansma, J. Massie, V. B. Elings, and A. A. Gewirth, “Atomic-resolution electrochemistry with the atomic force microscope: copper deposition on gold,” *Science*, vol. 251, no. 4990, pp. 183–186, 1991.
- [23] W. T. Müller, D. L. Klein, T. Lee, J. Clarke, P. L. McEuen, and P. G. Schultz, “A Strategy for the chemical synthesis of nanostructures,” *Science*, vol. 268, no. 5208, pp. 272–273, 1995.
- [24] G. H. Chan, J. Zhao, E. M. Hicks, G. C. Schatz, and R. P. Van Duyne, “Plasmonic properties of copper nanoparticles fabricated by nanosphere lithography,” *Nano Letters*, vol. 7, no. 7, pp. 1947–1952, 2007.

- [25] C. L. Haynes and R. P. Van Duyne, "Nanosphere lithography: a versatile nanofabrication tool for studies of size-dependent nanoparticle optics," *Journal of Physical Chemistry B*, vol. 105, no. 24, pp. 5599–5611, 2001.
- [26] J. C. Hulteen, D. A. Treichel, M. T. Smith, M. L. Duval, T. R. Jensen, and R. P. Van Duyne, "Nanosphere lithography: size-tunable silver nanoparticle and surface cluster arrays," *Journal of Physical Chemistry B*, vol. 103, no. 19, pp. 3854–3863, 1999.
- [27] M. L. Zhang, K. Q. Peng, X. Fan et al., "Preparation of large-area uniform silicon nanowires arrays through metal-assisted chemical etching," *Journal of Physical Chemistry C*, vol. 112, no. 12, pp. 4444–4450, 2008.
- [28] C. Jiang, W. Y. Lio, and V. V. Tsukruk, "Surface enhanced raman scattering monitoring of chain alignment in freely suspended nanomembranes," *Physical Review Letters*, vol. 95, no. 11, Article ID 115503, pp. 1–4, 2005.
- [29] J. Ding, V. I. Birss, and G. Liu, "Formation and properties of polystyrene-block-poly(2-cinnamoyl ethyl methacrylate) brushes studied by surface-enhanced raman scattering and transmission electron microscopy," *Macromolecules*, vol. 30, no. 5, pp. 1442–1448, 1997.
- [30] W. M. Sears, J. L. Hunt, and J. R. Stevens, "Raman scattering from polymerizing styrene. I. Vibrational mode analysis," *The Journal of Chemical Physics*, vol. 75, no. 4, pp. 1589–1598, 1981.
- [31] V. Zucolotto, M. Ferreira, M. Cordeiro et al., "Unusual interactions binding iron tetrasulfonated phthalocyanine and poly(allylamine hydrochloride) in layer-by-layer films," *Journal of Physical Chemistry B*, vol. 107, no. 16, pp. 3733–3737, 2003.
- [32] R. Aroca and A. Theedchanamoorthy, "Vibrational studies of molecular organization in evaporated phthalocyanine thin solid films," *Chemistry of Materials*, vol. 7, no. 1, pp. 69–74, 1995.
- [33] M. Lütt, M. R. Fitzsimmons, and D. Li, "X-ray reflectivity study of self-assembled thin films of macrocycles and macromolecules," *Journal of Physical Chemistry B*, vol. 102, no. 2, pp. 400–405, 1998.
- [34] J. P. Kottmann and O. J. F. Martin, "Plasmon resonant coupling in metallic nanowires," *Optics Express*, vol. 8, no. 12, pp. 655–663, 2001.

Research Article

Carbon Nanotubes/Gold Nanoparticles Composite Film for the Construction of a Novel Amperometric Choline Biosensor

Baoyan Wu,¹ Zhongmin Ou,¹ Xiaojuan Ju,² and Shihua Hou³

¹MOE Key Laboratory of Laser Life Science & Institute of Laser Life Science, College of Biophotonics, South China Normal University, Guangzhou 510631, China

²University Hospital, South China Normal University, Guangzhou 510631, China

³School of Electronic and Information Engineering, South China University of Technology, Guangzhou 510641, China

Correspondence should be addressed to Shihua Hou, shhou@scut.edu.cn

Received 17 July 2011; Revised 26 September 2011; Accepted 3 October 2011

Academic Editor: Yanqiu Zhu

Copyright © 2011 Baoyan Wu et al. This is an open access article distributed under the Creative Commons Attribution License, which permits unrestricted use, distribution, and reproduction in any medium, provided the original work is properly cited.

This study develops a facile method to fabricate a novel choline biosensor based on multiwalled carbon nanotubes (MWCNTs) and gold nanoparticles (AuNPs). Chitosan, a natural biocompatible polymer, was used to solubilize MWCNTs for constructing the aqueous Chit-MWCNTs solution. Then Chit-MWCNTs were first dropped on the surface of a cleaned platinum electrode. Finally, a thiolated silica sol containing AuNPs and choline oxidase (ChOx) was immobilized on the surface of the Chit-MWCNTs-modified electrode. The MWCNTs/AuNPs/Pt electrode showed excellent electrocatalytic activity for choline. The resulting choline biosensor showed high sensitivity of choline ($3.56 \mu\text{A}/\text{mM}$), and wide linear range from 0.05 to 0.8 mM with the detection limit of $15 \mu\text{M}$. In addition, good reproducibility and stability were obtained.

1. Introduction

Choline, a precursor of acetylcholine and phosphatidylcholine, is an essential nutrient required by the body for healthy cell membrane function [1–3]. Without choline, many fat-based nutrients and waste products could not pass in and out of our cells [4]. There is undisputed need for the measurement of neurochemical substances [5]. However, the measurement of choline is difficult because the concentrations of choline in the samples are quite low [6].

As the most promising alternative technique of choline determination, enzyme-based biosensors have attracted wide attention because they can offer simple and reliable means for the analysis [4, 6]. For example, Bai et al. provided a sensitive and anti-interference choline biosensor based on a biocomposite composed of chitosan hydrogel, choline oxidase (ChOx), and MnO_2 nanoparticles [4]. Another example is that presented by Song et al. [7]. They provided a choline biosensor based on the immobilization of ChOx into a sol-gel silicate film on the multiwall carbon nanotubes (MWCNTs) modified platinum electrode, exhibiting good sensitivity and stability. Recently, Frey et al. developed

a novel functionalisation method for the deposition of ChOx and anti-interference layers on the microelectrodes, providing the evidence of adequate biosensor performances for the detection of choline in the physiologically relevant concentration ranges [5].

The physical and chemical properties of the materials used in the construction of biosensors have got significant influence on their performance [8]. The application of carbon nanotubes in enzyme-based biosensors has attracted the attention of many researchers due to their unique physical and chemical properties, which provided high surface areas for enzyme loading and a compatible microenvironment, and its ability to promote the electron transfer between the biomolecules and electrode surface has been extensively studied [9–11]. Meanwhile, gold nanoparticles (AuNPs) are one of the most intensively studied and applied metal nanoparticles in amperometric biosensors owing to its stable physical and chemical properties, catalytic activity, and small dimensional size [12–14]. Therefore, the composite composed of carbon nanotubes and AuNPs, an area of intense research, has been widely used for the fabrication of biosensors. It has been demonstrated that the carbon nanotubes

and AuNPs composite can not only conserve or enhance the intrinsic properties of the particles, but also offer an effective approach to enhance the properties of biosensors [10, 15–17]. For example, our group developed an amperometric glucose biosensor based on self-assembly of multilayer films composed of MWCNTs, AuNPs, and glucose oxidase for the specific detection of glucose, providing a promising alternative mode to design amperometric biosensors [10]. Hu et al. also demonstrated that MWCNTs/AuNPs composite is particularly promising for novel, highly efficient photo-electrochemical cells and sensor devices [16]. More recently, Zhang et al. introduced the deposition of AuNPs on a MWCNT-based composite film immobilized on an electrode interface and found that the modified electrode exhibited a variety of good electrochemical characteristics including a relatively high sensitivity and long-term stability [17].

Taking account of the advantages of MWCNTs and AuNPs, the main focus of the present study was to construct a novel choline biosensor based on MWCNTs and AuNPs composite film. To meet the desired requirements, Chit-MWCNTs were first dropped on the surface of a Pt electrode, and then a thiolated silica sol containing AuNPs and ChOx was immobilized on the surface of the Chit-MWCNTs modified electrode to construct a MWCNTs/AuNPs/Pt-based amperometric choline biosensor. The electrocatalytic behaviors of the resulting choline biosensor are investigated and discussed.

2. Experimental

2.1. Reagents. Choline oxidase (EC 1.1.3.17, 17 units/mg protein, from *alcaligenes species*), (3-mercaptopropyl) trimethoxy silane (MPTMOS) and chitosan (low molecular weight, 75–85% deacetylated) were purchased from Sigma-Aldrich. MWCNTs (>50 nm diameter, length 0.5–1 μm , and >95% purity) were obtained from Chengdu Institute of Organic Chemistry, Chinese Academy of Science (China). Chloroauric acid hydrated ($\text{HAuCl}_4 \cdot 4\text{H}_2\text{O}$) were purchased from Sinopharm Chemical Reagent Co. (China). All the reagents were of analytical grade and used without further purification. The high-purity deionized water (resistance > 18 $\text{M}\Omega \cdot \text{cm}$) was used throughout this work. Phosphate-buffered saline (PBS, pH 8.0) buffer was employed as supporting electrolyte. All experiments were performed in PBS at room temperature, approximately 25°C.

2.2. Preparation of the Biosensor

2.2.1. Preparation of Chit-MWCNTs. MWCNTs (1 g/L) were sonicated in chitosan solution (2 g/L, in acetate buffer, pH 5.0), and centrifuged at 10,000 rpm for 10 min. The sediment comprising of impurities aggregates and bundles of nanotubes at the bottom of the centrifuge tube was discarded, and the supernatant containing Chit-MWCNTs was collected and filtrated through a 100 KDa filter (Millipore) to remove excess chitosan.

2.2.2. Preparation of AuNPs. All glassware used in the following procedure was cleaned in a bath of freshly prepared

solution (3 : 1 $\text{HNO}_3\text{-HCl}$), thoroughly washed with water, and dried prior to use. The AuNPs were prepared according to the literature [18] by adding sodium citrate to a boiling HAuCl_4 aqueous solution. The solution was kept boiling for 15 min under vigorous stirring, then allowed to cool down to room temperature, and stored at 4°C.

2.2.3. Preparation of Silica Sol. Silica sol was prepared according to the literatures [19, 20]. Briefly, MPTMOS with water at a 1 : 4 ratio, 10% of ethanol, and 3.3% of 0.1 M hydrochloric acid were mixed and sonicated for 30 min until a clear and homogenous solution resulted and was subsequently stored at room temperature for 2–3 h.

2.2.4. Configuration of Choline Biosensor. Prior to the experiment, the bare Pt electrode was polished with chamois leather containing 0.05 μm alumina slurry, rinsed thoroughly with water, sonicated in water and absolute ethanol, and dried at room temperature. Then, 5 μL of Chit-MWCNTs was dropped on the surface of a cleaned Pt electrode and allowed to dry at room temperature. A casting solution was prepared by mixing sol-gel solution with ChOx and AuNPs at a 1 : 2 : 2 volume ratio. After carefully mixing, 10 μL of the freshly prepared casting solution was dropped immediately on the surface of bare and Chit-MWCNTs modified Pt electrodes, regarded as AuNPs/Pt electrode and MWCNTs/AuNPs/Pt electrode, respectively, and allowed to dry at 4°C.

2.3. Scanning Electron Microscope (SEM) Measurements. Surface image of the substrate modified by Chit-MWCNTs was obtained by SEM (QUANTA 200, FEI Co.) measurement operated at an accelerating voltage of 25.0 kV.

2.4. Transmission Electron Microscope (TEM) Measurements. To examine the size of AuNPs, the sample was observed by a JEM-2100HR TEM by dropping 5 μL of the solution on the top of a TEM grid.

2.5. Optical Spectra Measurements. The absorption spectrum of AuNPs was obtained using a UV/VIS spectrometer (Lambda 35, Perkin-Elmer, USA).

2.6. Electrochemical Measurements. Electrochemical measurements were carried out by a Potentiostat-Galvanostat (EG & G PARC Model 283 with a software M270). All electrochemical experiments were carried out using a conventional three-electrode system comprising the AuNPs and MWCNTs modified Pt electrode as the working electrode, a Pt wire as the auxiliary electrode, and Ag/AgCl (saturated KCl) as the reference electrode in an electrochemical cell filled with 20 mL of PBS at room temperature. In steady-state amperometric experiment, the potential was set at +600 mV under gently magnetic stirring.

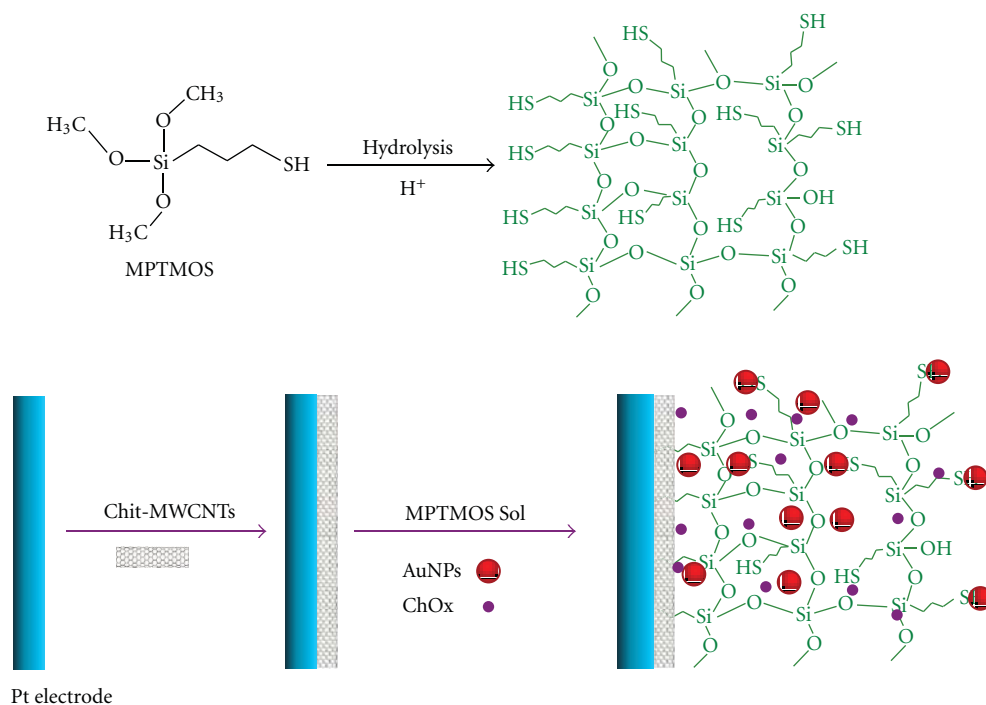
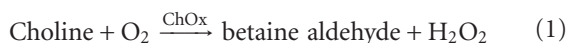


FIGURE 1: Scheme of preparation of the ChOx amperometric biosensor for choline based on AuNPs, MWCNTs, and silica sol-gel of MPTMOS.

3. Results and Discussion

Biomedical application potentials of carbon nanotubes-based materials have been investigated intensively in recent years [21]. In this work, a novel amperometric choline biosensor based on MWCNTs, AuNPs, and silica sol-gel of MPTMOS has been developed, as shown in Figure 1. Firstly, MWCNTs were sonicated in chitosan solution and dropped on the surface of a cleaned Pt electrode. Then, the sol-gel solution composed of AuNPs and ChOx was dropped on the surface of the Chit-MWCNTs modified Pt electrode. The working mechanism of the resulting choline biosensor for choline is based on the following sequential biochemical reactions:



In the presence of oxygen, ChOx converts choline into betaine and hydrogen peroxide (H₂O₂). Hydrogen peroxide, an electrochemically active product, is easily oxidized on electrode. The oxidation current of hydrogen peroxide can be used as a measure of choline.

The microscopic morphology of Chit-MWCNTs prepared by strong stirring and ultrasonication was shown in Figure 2(a), which can be stable for at least 1 month at room temperature without visible flocculation, evidenced by the homogeneous black color of Chit-MWCNTs solution (Figure 2(d)). The diameter of AuNPs was about 15 nm, as shown in Figure 2(b), which was confirmed by the UV-vis absorption spectrum (Figure 2(c)). AuNPs presented an

absorption peak at 520 nm in the range from 400 to 600 nm, which is the characteristic absorbance of AuNPs.

MPTMOS is a bifunctional molecule that contains both trimethoxysilane and thiol functional groups. Trimethoxysilane groups can undergo hydrolysis and condensation reaction to form a covalently linked siloxane network which is used for physical encapsulation of ChOx and AuNPs. Meanwhile, the thiol groups can be used for the covalent attachment of AuNPs to sol-gel network. It has been demonstrated that AuNPs with the diameter of 20 nm can be both diffused into and on the surface of the sol-gel network [22] and can generate a continuous array of AuNPs throughout the sol-gel network [23]. In view of the fact that the diameter of AuNPs used in this work was about 15 nm, AuNPs can be immobilized both inside and on the surface of the sol-gel, providing a necessary conduction pathway between the immobilized ChOx and the surface of the Pt substrate. Therefore, the resulting choline biosensor will exhibit the benefits of sol-gel, nanoparticles, and enzyme-based amperometric biosensor.

Figure 3 shows cyclic voltammograms of AuNPs (a and c), MWCNTs/AuNPs (b and d) modified Pt electrode in PBS containing no choline (a and b), and 1.6 mM choline (c and d) in the applied potential range from 0 to 600 mV with a scan rate of 50 mV/s, respectively. The response of AuNPs/Pt electrode and MWCNTs/AuNPs/Pt electrode in PBS displayed a low background current. Upon addition of 1.6 mM choline in PBS, a large oxidation current was observed, confirming that ChOx catalyzed the oxidation reaction of choline and the resultant H₂O₂ was electrooxidized at the electrodes. The current of MWCNTs/AuNPs/Pt electrode was

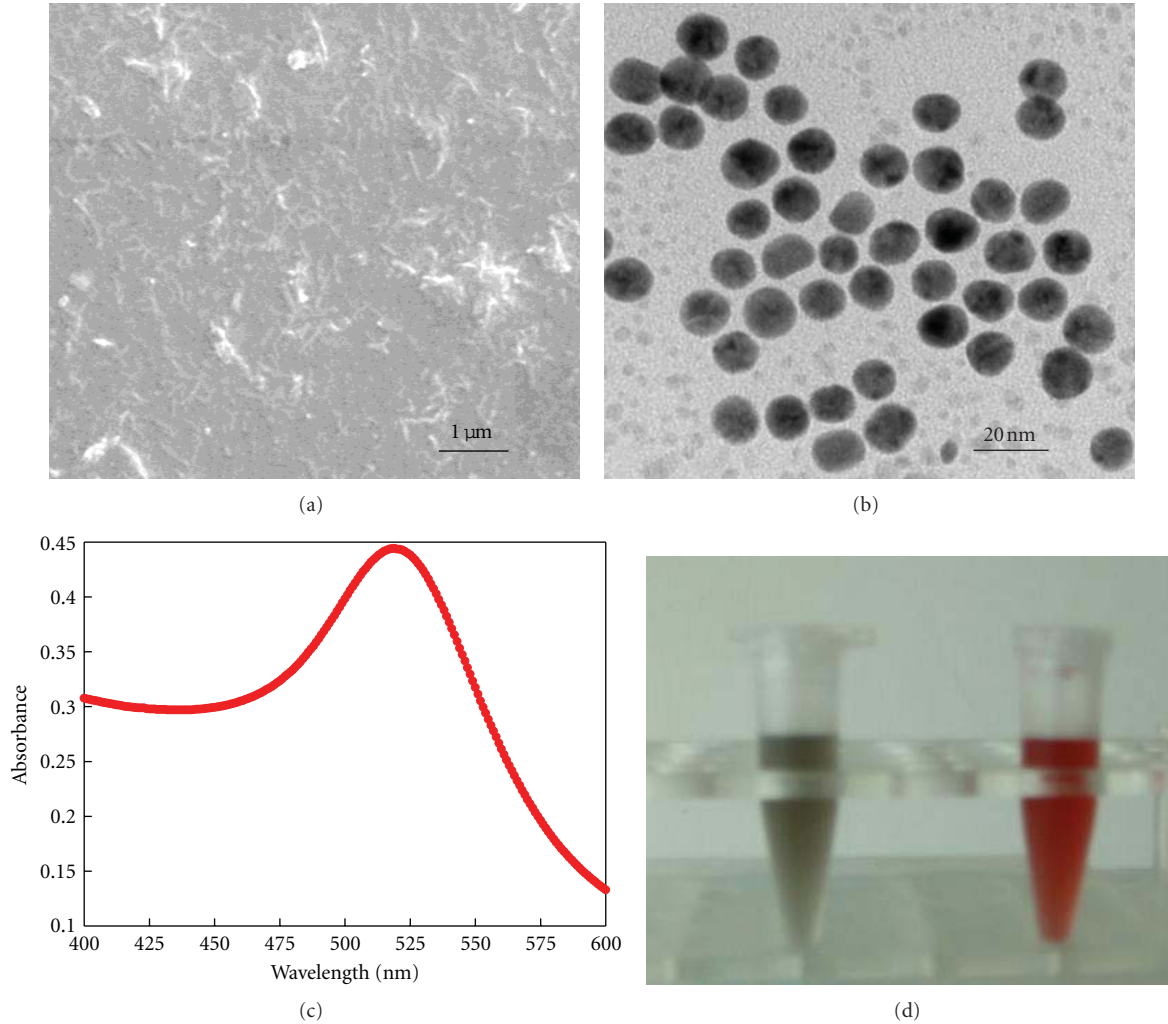


FIGURE 2: SEM image of Chit-MWCNTs (a), TEM image and UV-visible absorbance spectrum of AuNPs with an average diameter of about 15 nm (b and c), and a photo of Chit-MWCNTs solution (d, left) and AuNPs (d, right).

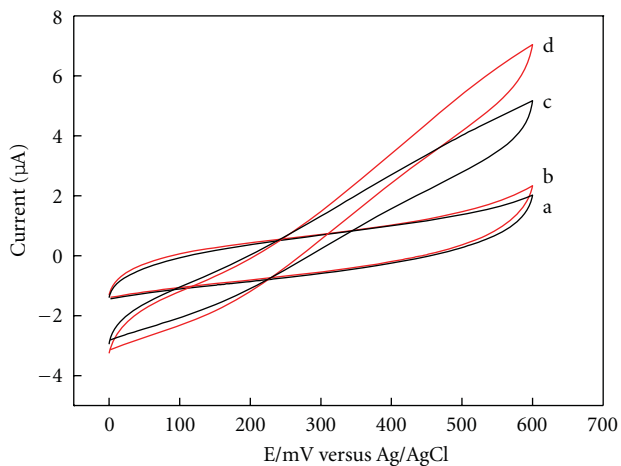


FIGURE 3: Cyclic voltammograms of AuNPs (a and c), MWCNTs/AuNPs (b and d) modified Pt electrode in PBS containing no choline (a and b), and 1.6 mM choline (c and d). The scan rate is 50 mV/s.

much higher than that of AuNPs/Pt electrode, indicating that MWCNTs and AuNPs in the biosensing interface efficiently improved the electron transfer between analyte and electrode surface.

Figure 4 shows a typical current-time plot of AuNPs/Pt electrode (a) and MWCNTs/AuNPs/Pt electrode (b) on successive addition of choline, which are 0.05, 0.1, 0.2, 0.4, 0.8, and 1.6 mM, respectively. These amperometric data were consistent with the results obtained from cyclic voltammograms experiments, demonstrating that MWCNTs/AuNPs/Pt electrode exhibited higher activity for the enzymatic product H_2O_2 than that of AuNPs/Pt electrode. The performance of the MWCNTs/AuNPs/Pt electrode was better than that reported for MWCNTs/sol-gel modified Pt electrode and ChOx/sol-gel modified Pt electrode [7]. So among the resulting biosensors, MWCNTs/AuNPs/Pt electrode was the best one, which was attributed to the MWCNT-AuNPs composite film. The amperometric response of MWCNTs/AuNPs/Pt electrode was in accordance with that reported for nanocomposite modified electrodes [24].

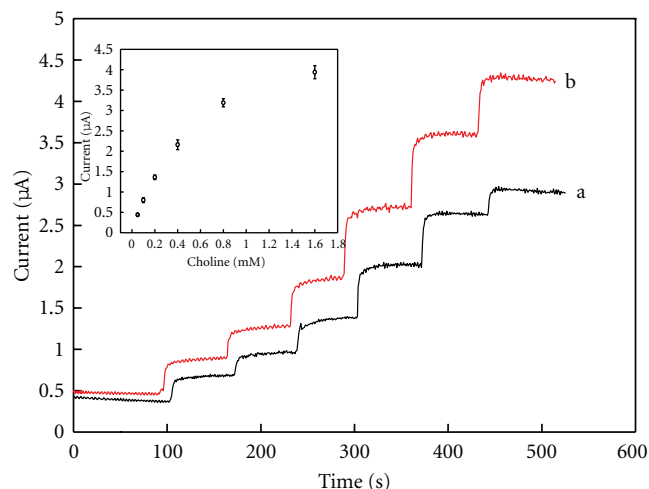


FIGURE 4: Amperometric response of AuNPs (a), MWCNTs/AuNPs (b) modified Pt electrodes upon successive addition of choline. Inset: the calibration curve of MWCNTs/AuNPs/Pt electrode. Error bars = \pm standard deviation and $n = 5$.

The calibration curve (Figure 4, inset) shows the current reached a saturation value at high choline concentration, showing the characteristics of the Michaelis-Menten kinetics. A linear relationship between the current and the choline concentration within the range from 0.05 to 0.8 mM for MWCNTs/AuNPs/Pt electrode was $Y(\mu\text{A}) = 0.49 + 3.56X$ (choline, mM), with a correlation coefficient of 0.9833. The sensitivity of the electrode was $3.56 \mu\text{A}/\text{mM}$ with the detection limit of $15 \mu\text{M}$ when signal-to-noise ratio was 3. In addition, five successive measurements of choline on MWCNTs/AuNPs/Pt electrode yielded an R.S.D. of 4.7%. The stability of the MWCNTs/AuNPs/Pt electrode is evaluated by examining the current of 0.4 mM choline. After each experiment, the electrode was washed with PBS and stored at 4°C when not in use. The current only decreased slightly after one month. The high stability should be attributed to the natural features of sol-gel film, MWCNTs, and AuNPs. The sol-gel film not only can prevent ChOx from leaking out of the electrode, but also together with MWCNTs and AuNPs can provide a favorable microenvironment for retaining the biocatalytic activity of ChOx.

4. Conclusions

A novel choline biosensor based on immobilization of ChOx on a thiolated silica sol-gel, AuNPs, and Chit-MWCNTs interface was successfully developed. The MWCNTs/AuNPs-based Pt electrode generated a significant catalytic oxidation current compared with other ChOx electrodes modified with MWCNTs alone or AuNPs alone. The resulting choline biosensor showed a high sensitivity of choline, wide linear concentration range, acceptable reproducibility, and good stability. Significant advantages of the proposed choline biosensor include simplicity of fabrication and the benefits of sol-gel, MWCNTs, AuNPs, and enzyme-based amperometric biosensor.

Acknowledgments

This research is supported by the National Natural Science Foundation of China (30800261), the Scientific Research Foundation for the Returned Overseas Chinese Scholars, State Education Ministry ([2009]8), the Scientific Research Foundation of the State Human Resource Ministry for Returned Chinese Scholars (2008), and the Department of Education of Guangdong Province (Breeding Program, 2008).

References

- [1] K. M. Mitchell, "Acetylcholine and choline amperometric enzyme sensors characterized in vitro and in vivo," *Analytical Chemistry*, vol. 76, no. 4, pp. 1098–1106, 2004.
- [2] A. Guerrieri and F. Palmisano, "An acetylcholinesterase/choline oxidase-based amperometric biosensor as a liquid chromatography detector for acetylcholine and choline determination in brain tissue homogenates," *Analytical Chemistry*, vol. 73, no. 13, pp. 2875–2882, 2001.
- [3] S. M. Babb, Y. Ke, N. Lange, M. J. Kaufman, P. F. Renshaw, and B. M. Cohen, "Oral choline increases choline metabolites in human brain," *Psychiatry Research: Neuroimaging*, vol. 130, no. 1, pp. 1–9, 2004.
- [4] Y. H. Bai, Y. Du, J. J. Xu, and H. Y. Chen, "Choline biosensors based on a bi-electrocatalytic property of MnO_2 nanoparticles modified electrodes to H_2O_2 ," *Electrochemistry Communications*, vol. 9, no. 10, pp. 2611–2616, 2007.
- [5] O. Frey, T. Holtzman, R. M. Mcnamara et al., "Enzyme-based choline and l-glutamate biosensor electrodes on silicon microprobe arrays," *Biosensors and Bioelectronics*, vol. 26, no. 2, pp. 477–484, 2010.
- [6] X. Ren, F. Tang, R. Liao, and L. Zhang, "Using gold nanorods to enhance the current response of a choline biosensor," *Electrochimica Acta*, vol. 54, no. 28, pp. 7248–7253, 2009.
- [7] Z. Song, J. D. Huang, B. Y. Wu, H. B. Shi, J. I. Anzai, and Q. Chen, "Amperometric aqueous sol-gel biosensor for low-potential stable choline detection at multi-wall carbon nanotube modified platinum electrode," *Sensors and Actuators B*, vol. 115, no. 2, pp. 626–633, 2006.
- [8] R. B. Rakhi, K. Sethupathi, and S. Ramaprabhu, "A glucose biosensor based on deposition of glucose oxidase onto crystalline gold nanoparticle modified carbon nanotube electrode," *Journal of Physical Chemistry B*, vol. 113, no. 10, pp. 3190–3194, 2009.
- [9] M. Belesi, I. Panagiotopoulos, S. Pal et al., "Decoration of carbon nanotubes with CoO and Co nanoparticles," *Journal of Nanomaterials*, vol. 2011, Article ID 320516, 2011.
- [10] B. Y. Wu, S. H. Hou, F. Yin et al., "Amperometric glucose biosensor based on multilayer films via layer-by-layer self-assembly of multi-wall carbon nanotubes, gold nanoparticles and glucose oxidase on the Pt electrode," *Biosensors and Bioelectronics*, vol. 22, no. 12, pp. 2854–2860, 2007.
- [11] S. Hrapovic, Y. Liu, K. B. Male, and J. H. T. Luong, "Electrochemical biosensing platforms using platinum nanoparticles and carbon nanotubes," *Analytical Chemistry*, vol. 76, no. 4, pp. 1083–1088, 2004.
- [12] C. Wang, G. Wang, and B. Fang, "Electrocatalytic oxidation of bilirubin at ferrocenecarboxamide modified MWCNT-gold nanocomposite electrodes," *Microchimica Acta*, vol. 164, no. 1–2, pp. 113–118, 2009.

- [13] B. Y. Wu, S. H. Hou, F. Yin et al., "Amperometric glucose biosensor based on layer-by-layer assembly of multilayer films composed of chitosan, gold nanoparticles and glucose oxidase modified Pt electrode," *Biosensors and Bioelectronics*, vol. 22, no. 6, pp. 838–844, 2007.
- [14] V. Pavlov, Y. Xiao, and I. Willner, "Inhibition of the acetylcholine esterase-stimulated growth of Au nanoparticles: nanotechnology-based sensing of nerve gases," *Nano Letters*, vol. 5, no. 4, pp. 649–653, 2005.
- [15] D. N. Ventura, R. A. Stone, K. S. Chen et al., "Assembly of cross-linked multi-walled carbon nanotube mats," *Carbon*, vol. 48, no. 4, pp. 987–994, 2010.
- [16] X. Hu, T. Wang, X. Qu, and S. Dong, "In situ synthesis and characterization of multiwalled carbon nanotube/Au nanoparticle composite materials," *Journal of Physical Chemistry B*, vol. 110, no. 2, pp. 853–857, 2006.
- [17] H. Zhang, Z. Meng, Q. Wang, and J. Zheng, "A novel glucose biosensor based on direct electrochemistry of glucose oxidase incorporated in biomediated gold nanoparticles-carbon nanotubes composite film," *Sensors and Actuators B*, vol. 158, no. 1, pp. 23–27, 2011.
- [18] H. D. Hill and C. A. Mirkin, "The bio-barcode assay for the detection of protein and nucleic acid targets using DTT-induced ligand exchange," *Nature Protocols*, vol. 1, no. 1, pp. 324–336, 2006.
- [19] B. Wang, B. Li, Q. Deng, and S. Dong, "Amperometric glucose biosensor based on sol-gel organic-inorganic hybrid material," *Analytical Chemistry*, vol. 70, no. 15, pp. 3170–3174, 1998.
- [20] J. Jia, B. Wang, A. Wu, G. Cheng, Z. Li, and S. Dong, "A method to construct a third-generation horseradish peroxidase biosensor: self-assembling gold nanoparticles to three-dimensional sol-gel network," *Analytical Chemistry*, vol. 74, no. 9, pp. 2217–2223, 2002.
- [21] X. Cheng, J. Zhong, J. Meng et al., "Characterization of multiwalled carbon nanotubes dispersing in water and association with biological effects," *Journal of Nanomaterials*, vol. 2011, Article ID 938491, 2011.
- [22] S. Bharathi, M. Nogami, and S. Ikeda, "Novel electrochemical interfaces with a tunable kinetic barrier by self-assembling organically modified silica gel and gold nanoparticles," *Langmuir*, vol. 17, no. 1, pp. 1–4, 2001.
- [23] P. Kalimuthu and S. A. John, "Size dependent electrocatalytic activity of gold nanoparticles immobilized onto three dimensional sol-gel network," *Journal of Electroanalytical Chemistry*, vol. 617, no. 2, pp. 164–170, 2008.
- [24] D. Du, S. Chen, D. Song, H. Li, and X. Chen, "Development of acetylcholinesterase biosensor based on CdTe quantum dots/gold nanoparticles modified chitosan microspheres interface," *Biosensors and Bioelectronics*, vol. 24, no. 3, pp. 475–479, 2008.

Research Article

Electromagnetic Wave Interactions with 2D Arrays of Single-Wall Carbon Nanotubes

Taha A. Elwi and Hussain M. Al-Rizzo

Department of Systems Engineering, George W. Donaghey College of Engineering and Information Technology,
University of Arkansas at Little Rock, Little Rock, AR 72204, USA

Correspondence should be addressed to Taha A. Elwi, taelwi@ualr.edu

Received 13 June 2011; Revised 7 September 2011; Accepted 26 September 2011

Academic Editor: Raymond Whitby

Copyright © 2011 T. A. Elwi and H. M. Al-Rizzo. This is an open access article distributed under the Creative Commons Attribution License, which permits unrestricted use, distribution, and reproduction in any medium, provided the original work is properly cited.

We report, for the first time, the scattering, absorption, and reflection characteristics of 2D arrays of finite-length, armchair, single-walled carbon nanotubes (SWNTs) in the visible frequency regime. The analysis is based on the Finite-Element-Method formulation of Maxwell's equations and a 3D quantum electrical conductivity function. Three geometrical models have been considered: solid cylinder, hollow cylinder, and honeycomb. We demonstrate that classical electromagnetic theory is sufficient to evaluate the scattering and absorption cross sections of SWNTs, which revealed excellent agreement against measurements without the need to invoke the effective impedance boundary conditions. The solid and hollow cylindrical models fail to provide accurate results, when *both* scattering and absorption are considered. Finally, it is shown that reflection and transmission characteristics of both individual and arrays of SWNTs, which are essential for solar cell applications, are strongly influenced by the length and the phenomenological parameters of the SWNT.

1. Introduction

Since arrays of SWNTs were introduced as trapping and absorbing layers to receive light from different angles, they became one of the most promising candidates for solar cell technology [1]. It is well known that the efficiency of solar cells decreases when the incident light deviates away from the normal to the cell's surface where a mechanical rotary system is required [2]. Therefore, enormous research efforts have been devoted to place SWNTs on top of photovoltaic cells to maintain efficient performance even when the sun is not directly overhead [3]. This is important for spacecraft applications to avoid mechanical aiming systems with minimum feature sizes and improved reliability [2].

The proper configuration of SWNT arrays, in terms of spacing and orientation, enables localization of light with minimum reflection and scattering losses, which is essential for increasing the conversion efficiency of solar cells [4]. For example, ultra-low refractive index films based on vertical SWNT arrays leading to reduced reflectance from solar cell substrates were recently demonstrated [5, 6].

SWNTs, which possess a ballistic conductivity, transport electrical charges over at least micrometer lengths [7]. One of the most celebrated theories on the ballistic conductivity of SWNT is the π -electron, tight-binding quantum conductance, and the effective impedance boundary conditions (EIBC) [8], which were subsequently used to evaluate the electromagnetic (EM) interaction with carbon nanotubes [9–16]. The classical Hallén-type integral equation was invoked to solve the dipole antenna problem and evaluate the scattering cross section (σ_{sca}) from an individual SWNT [9, 10]. The current distribution on an infinitely long carbon nanotube antenna fed by a delta-gap generator is reported in [11] using a Fourier transform technique. In [10], a model consisting of infinite 2D arrays of finite-length SWNT was presented to calculate the scattering cross section (σ_{sca}) based on a periodic Green's function. In [13], the Leontovich-Levin equation was formulated to evaluate scattering by a carbon nanotube of finite length, both numerically and analytically. In [14], the σ_{sca} of an infinite 2D array of SWNTs was studied using periodic Green's function and the Born approximation. In [15], the normalized σ_{sca} was calculated in the Rayleigh

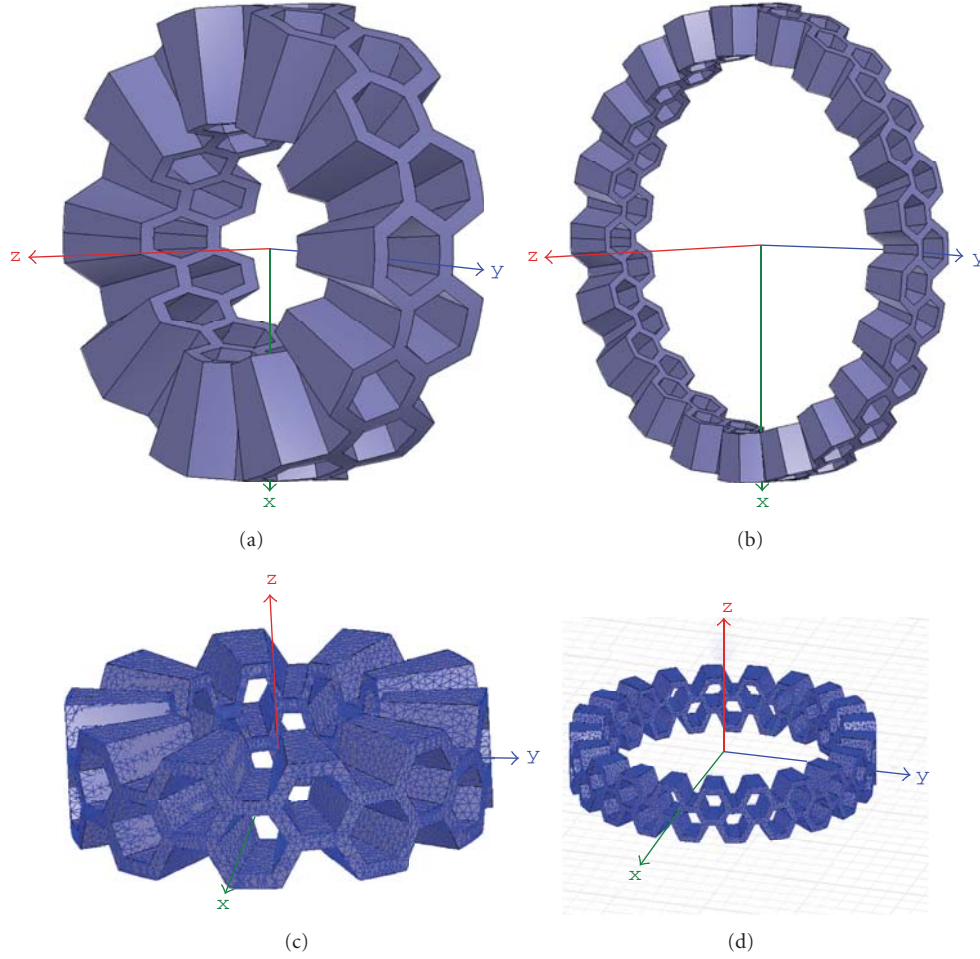


FIGURE 1: The numerical models of the HS for (10, 10) and (21, 21) armchair SWNT: (a) and (b) 3D geometrical models for (10, 10) and (21, 21) of SWNT; (c) and (d) are the mesh view for (10, 10) and (21, 21) of SWNT.

region based on a closed-form expression derived for an infinitely long, hollow cylindrical (HC) SWNT model of zero thickness and compared to experimental results. In [16], the absorption cross section (σ_{abs}) was calculated for an individual and bundles of parallel, finite-length SWNTs. The analyses were based on the Fredholm integral equation of the first kind in the near-field region at different orientations and locations from the EM sources.

Two assumptions were common among previously reported studies [8–16]. First, the SWNT is modeled as a solid wire or as a thin cylindrical shell, both of which do not provide realistic values for σ_{abs} . Second, only the axial surface current has been considered for the solid and hollow model. It should be noted that the phenomenological parameters in the research reported in [9–16] were determined based on comparing the calculated σ_{sca} versus measurements without considering σ_{abs} .

To the best of the authors' knowledge, we consider for the first time a realistic honeycomb-shaped (HS) model of two armchair SWNTs using 3D full wave numerical simulations to evaluate the EM interactions with SWNT in single and array configurations without invoking the EIBC. The σ_{sca}

and σ_{abs} of (10, 10) and (21, 21) SWNTs obtained from the HS, SC, and HC models are compared against the measured results published in [17, 18]. Next, the reflection spectra from 2D arrays of SWNTs are considered for the SC, HC, and HS models in both horizontal and vertical orientations. Finally, the reflection spectra from the (10, 10) SWNT arrays are provided at different lengths of the HS model in both horizontal and vertical orientations.

2. Theoretical Treatment

We start from the ballistic, 1D quantum conductance model of SWNT based on the π -electron tight-binding quantum conductance defined below [8]

$$\begin{aligned} \sigma_{cn}(\omega) &= \frac{je^2\omega}{\pi^2\hbar a} \left\{ \frac{1}{\omega(\omega - j\nu)} \sum_{s=1}^m \int_{1^{\text{st}}\text{BZ}} \frac{\partial F_c}{\partial p_z} \frac{\partial \varepsilon_c}{\partial p_z} dp_z \right. \\ &\quad \left. + 2 \sum_{s=1}^m \int_{1^{\text{st}}\text{BZ}} \varepsilon_c |R_{vc}|^2 \frac{F_c - F_v}{\hbar^2 \omega(\omega - j\nu) - 4\varepsilon_c^2} dp_z \right\}, \end{aligned} \quad (1)$$

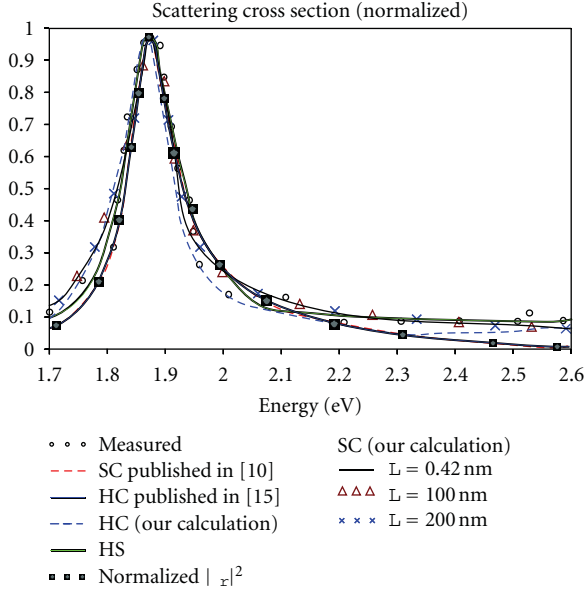


FIGURE 2: The σ_{sca} of SC, HC, and HS models of a SWNT compared against measured data in [10, 15].

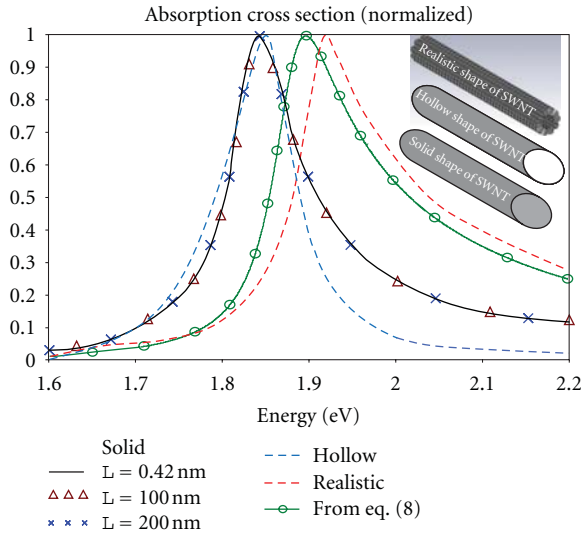


FIGURE 3: Comparison of σ_{abs} of the armchair (10, 10) SWNT for three different geometries.

where $\nu = \tau^{-1}$ is the relaxation frequency, \hbar is the normalized Planck's constant, 1.05457×10^{-34} J.s, e is the electron charge, 1.602×10^{-19} C, ϵ_c and $F_{c,\nu}$ are the Fermi dispersion and electron dispersion relation function of the carbon nanotube, respectively, and $R_{\nu c}$ is the matrix element for the SWNT.

The 1D conductance of (1) is converted to a 3D conductivity (σ_{3d}) in (S/m) to properly represent the 3D SWNT model in our simulations. The impedance of a solid cylindrical conductor is given by [19]

$$Z_i = \frac{\gamma_i J_0(\alpha \gamma_i)}{2\pi a \sigma_{3d}(\omega) J_1(\alpha \gamma_i)}, \quad (2)$$

where a is radius, $a = 0.678$ nm for (10, 10) and $a = 1.424$ nm for (21, 21), ω is the radian frequency, and γ_i is the skin depth, given by [10]

$$\gamma_i = (1 - j) \sqrt{\frac{\omega \mu \sigma_{3d}}{2}}. \quad (3)$$

Using the asymptotic forms of Bessel functions of the first and second order for small arguments, (2) can be approximated as

$$Z_i = \frac{1}{\pi a^2 \sigma_{3d}(\omega)}. \quad (4)$$

The expression of the impedance per unit length of a SWNT is given by [11]

$$Z_{cn} = \frac{1}{2\pi a \sigma_{cn}(\omega)}. \quad (5)$$

Taking the ratio (Z_i/Z_{cn}), σ_{3d} can be determined from σ_{cn} defined in (1) using the following formula

$$\sigma_{3d}(\omega) = \frac{2}{a} \sigma_{cn}(\omega). \quad (6)$$

In our numerical analysis, we used the complex relative permittivity to compute σ_{sca} and σ_{abs} of the individual SWNTs. It can be shown that the real and imaginary parts of the relative permittivity (ϵ_r) can be expressed as

$$\epsilon_r' = 1 + \frac{\sigma_r'}{\omega \epsilon_0}, \quad (7)$$

$$\epsilon_r'' = \frac{\sigma_r''}{\omega \epsilon_0},$$

where σ_r' , σ_r'' , ϵ_r' , and ϵ_r'' are the real and imaginary parts of the conductivity and permittivity, respectively.

3. Comparison of Model Results with Measurements

The σ_{sca} of (10, 10) and (21, 21) armchair SWNTs are evaluated from Ansoft's High Frequency Structure Simulator (HFSS) [20] and compared to the measured data reported in [17] and [18], respectively. The SWNT is surrounded by an air box, the six faces of which are set as perfectly matched layer (PML) [21]. The incident field is a plane wave of unity amplitude, and the magnetic field is perpendicular to the SWNT axis similar to the measurement setup reported in [17, 18].

The complex relative permittivity of each geometry is generated from (7) by adjusting the phenomenological parameters (γ and τ) in (1) in order to match the σ_{sca} results generated from HFSS to the measured σ_{sca} reported in [17, 18] for the (10, 10) and (21, 21) SWNTs, respectively. The numerical model of the HS is implemented in HFSS by building a single graphene layer from 20 honeycomb cells for the (10, 10) SWNT and from 42 honeycomb cells for the (21, 21) SWNT that is folded around the z -axis. The numerical 3D models of the (10, 10) and (21, 21) SWNTs are presented

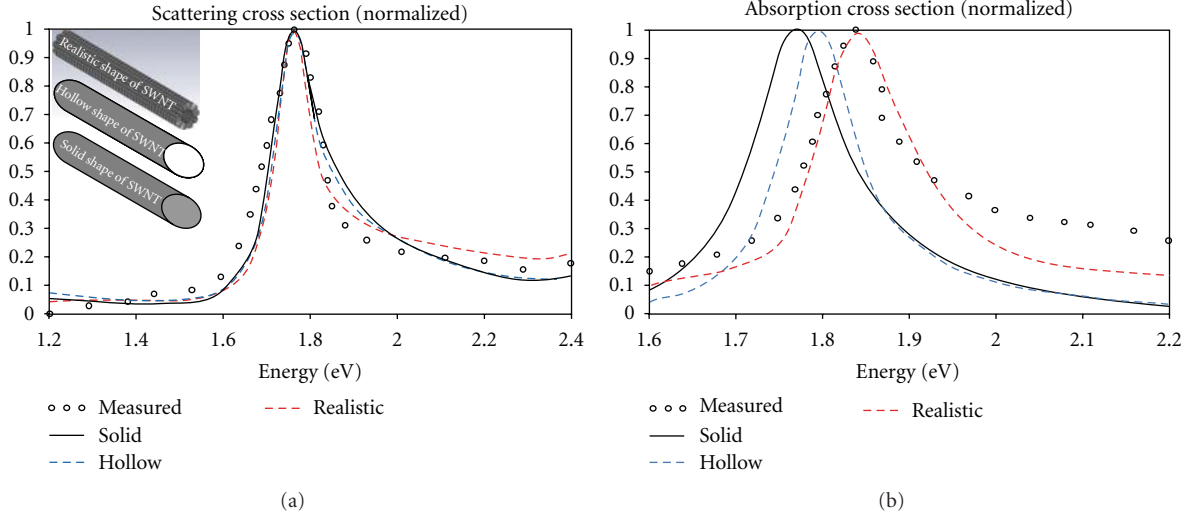


FIGURE 4: σ_{sca} and σ_{abs} of the armchair (21, 21) SWNT for three different geometries (SC, HC, HS) compared to measured results in [18]: (a) σ_{sca} and (b) σ_{abs} .

in Figures 1(a) and 1(b), respectively. Results presented in this paper are based on the convergence criterion that the relative deviation of the computed σ_{sca} and σ_{abs} between at least two consecutive mesh passes should be below 2 percent. The mesh chosen is tetrahedral with typical mesh distributions shown in Figures 1(c) and 1(d) for the (10, 10) and (21, 21) SWNTs, respectively.

3.1. Phenomenological Parameters from the Scattering Cross Section. To estimate γ and τ for the SC, HC, and HS models of the SWNT, HFSS is used to simulate σ_{sca} of the (10, 10) SWNT, which is compared to the measured results reported in [17]. Next we compare σ_{sca} for the three models to demonstrate the effect of the geometry on the estimated γ and τ . By varying $\gamma \approx 2.5\text{--}3.1$ e.V and $\tau \approx 0.005\text{--}0.015$ ps, we calculated the constitutive parameters of the respective SWNT geometry. We started by simulating the SC since both γ and τ are reported in [10] to validate our computational procedure. Figure 2 displays the normalized σ_{sca} for the (10, 10) SC armchair SWNT for three different lengths: 0.42 nm, 100 nm, and 200 nm, along with the results reported in [10] and those measured in [17]. It can be seen from Figure 2 that the profile of the normalized σ_{sca} is independent of length. This is explained in [10, 14] based on the quantum effects associated with interband transitions.

However, the independence of the σ_{sca} profile on length can also be described in terms of the classical Rayleigh scattering theory, which is applicable when the maximum linear dimension of the object is much smaller than the wavelength of the minimum frequency considered, as can be seen from the results depicted in Figure 2. In this case, σ_{sca} is proportional to the oscillating dipoles induced inside the object. The oscillatory dipole moments are proportional to the electric permittivity of the object [22]. The normalized σ_{sca} for both the HC and HS models of a SWNT 0.42 nm in length and 0.678 nm in radius are also presented in Figure 2. For the HC-shaped SWNT, the extracted γ and τ are

TABLE 1: Comparison of γ and τ against the published values for the three models (SC, HC, and HS) for (10, 10) SWNT.

Model	Our calculated values	Published values
SC	$\gamma = 3.03$ e.V, $\tau = 0.01$ ps	$\gamma = 3.01$ e.V, $\tau = 0.01$ ps [10]
HC	$\gamma = 3.05$ e.V, $\tau = 0.0097$ ps	$\gamma = 3.035$ e.V, $\tau = 0.0097$ ps [15]
HS	$\gamma = 3.059$ e.V, $\tau = 0.011$ ps	—

compared to those published in [15]. Results from simulated σ_{sca} of the HS model are also shown in Figure 2.

It should be noted that the normalized σ_{sca} reported in [10, 15] can be simply obtained from the normalized value of $|\epsilon_r|^2$ as described in [22]. Therefore, results presented in [10, 15] can be simply obtained by normalizing the square value of the modulus of the complex permittivity versus energy, as can be seen in Figure 2. At low frequencies, σ_{sca} obtained from the modulus of complex permittivity is closer to the measured results than at high frequencies. Moreover, this approximation is valid only in the Rayleigh region. However, when using HFSS, the calculated results produce better agreement with the measured σ_{sca} for the three geometrical models and, furthermore, can be extended well above the Rayleigh region.

3.2. Absorption Cross Section. In general, the simulated σ_{sca} for the three geometrical models provided an excellent agreement with the measured results reported in [17]. However, each individual model exhibits different γ and τ as seen in Table 1. These differences in γ and τ and the geometrical model of the SWNT strongly influence the computed σ_{abs} spectra as depicted in Figure 3.

In Figure 3, we present the spectrum of σ_{abs} computed by HFSS for the SC model with different lengths: 0.42 nm,

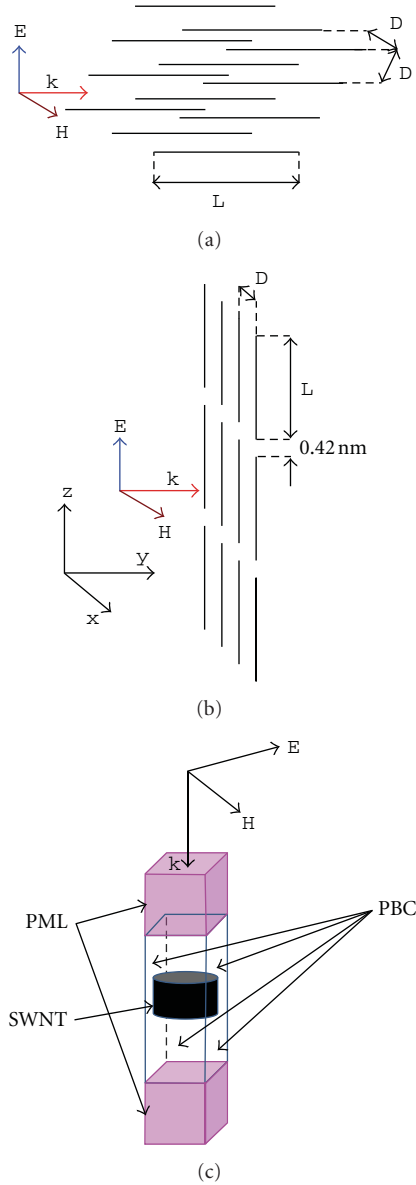


FIGURE 5: Alignments of the infinite 2D arrays of finite length SWNT; (a) vertical alignment, (b) horizontal alignment, and (c) the numerical setup of the 2D arrays of SWNTs as implemented in HFSS.

100 nm, and 200 nm, and for both HC, and HS models computed from the following expression [16]:

$$\sigma_{\text{abs}} = \text{Normalized} \left[\frac{8\pi^2 aL}{c} \text{Re}(\sigma_{cn}) \right], \quad (8)$$

where L is the length of the SWNT and c is the speed of light in vacuum. The normalized σ_{abs} is not very sensitive to the length of the SWNT, as is seen in Figure 3. The effect of the geometry of the SWNT is revealed in Figure 3 when comparing the σ_{abs} of the SC, HC and HS models. This observation reveals the geometrical dispersion introduced by the honeycomb shape of the SWNT, which is not captured by the SC and HC models. In Figure 3, it is observed that

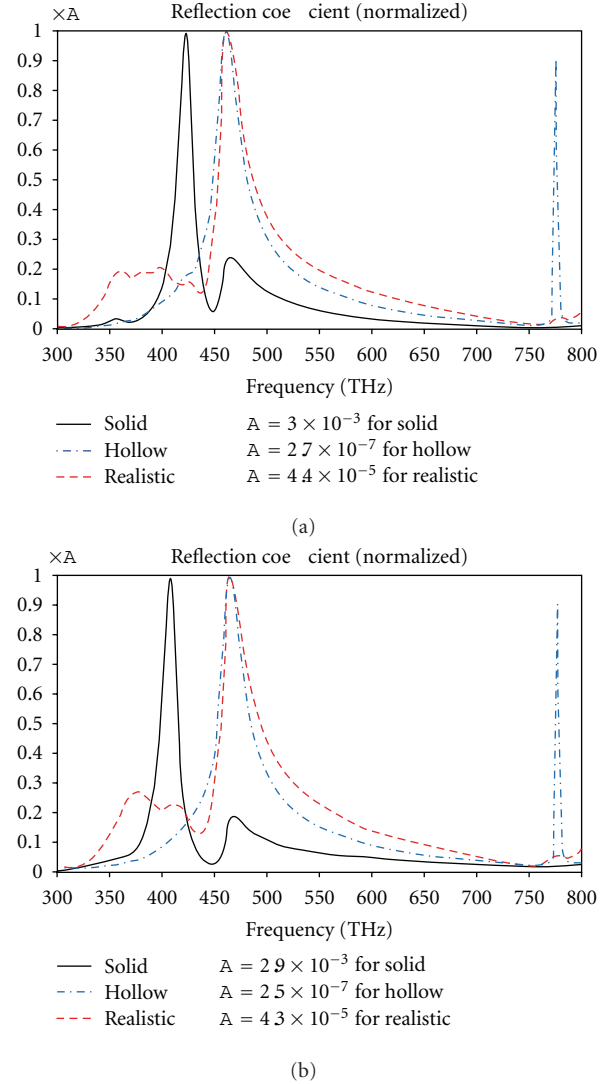


FIGURE 6: The reflection spectra of the 2D arrays of armchair (10, 10) SWNT using three geometrical models (SC, HC, and HS); (a) for vertical arrays and (b) for horizontal arrays.

σ_{abs} peaks at different frequencies for the three models. The spectral characteristics of σ_{abs} are different too.

Due to the differences observed in Figure 3, we performed additional studies to emphasize the effects of the geometrical model on the absorption characteristics of SWNTs. The measurements of the σ_{sca} and σ_{abs} reported in [18] for the armchair SWNT of index (21, 21) are used to further confirm the observations inferred from Figure 3. We started by simulating σ_{sca} to find γ and τ by using the same approach outlined in the previous section. The measured and simulated spectra of σ_{sca} and σ_{abs} for the (21, 21) armchair SWNT are presented in Figures 4(a) and 4(b), respectively.

4. Numerical Analysis for the 2D Arrays of SWNT

For the numerical results presented in this section, we used the complex permittivity for the (10, 10) armchair SWNT

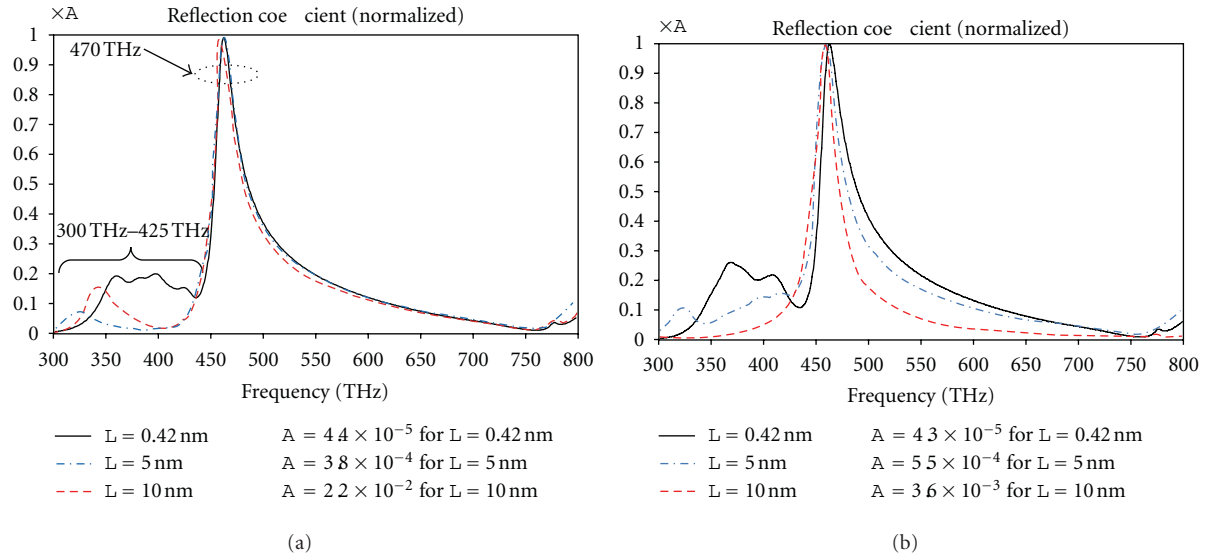


FIGURE 7: The reflection spectra of the 2D arrays of armchair (10, 10) SWNT of HS shape: (a) for vertical arrays and (b) for horizontal arrays.

developed in Section 2. The infinite array of finite-length SWNTs situated in the x - z plane and the simulation setup used in HFSS are depicted in Figure 5. Two orientations of the SWNT array are considered. Vertical orientation is defined when the array is normal to the x - z plane as seen in Figure 5(a). Horizontal orientation refers to the case in which the array is parallel to the x - z plane as shown in Figure 5(b). The direction of propagation of the incident field is set to be normal to the x - z plane as illustrated in Figures 5(a) and 5(b). The SWNTs are separated by a distance $D = 2a + 0.34 \text{ nm} \approx 1.7 \text{ nm}$, (0.34 nm corresponds to the Van der Waal's gap [22]) with three lengths, $L = 0.42 \text{ nm}$, 5 nm , and 10 nm . Short carbon nanotubes have been chosen since the synthesis of arrays of short carbon nanotubes is much easier than with long carbon nanotubes [23]. Furthermore, long carbon nanotubes are vulnerable to bending, and the cost and time for growing short carbon nanotube are much less than for long tubes [24]. The 2D arrays of SWNTs are considered to be infinite in extent; however, for practical purposes, the dimensions of SWNTs arrays are finite. Since the length of an individual SWNT is much smaller than the arrays' dimensions, the diffraction effects from the arrays' edges can be ignored [14]. Following the standard procedure for the modeling of infinite periodic arrays of arbitrarily shaped scatterers as outlined in [21], an air box is used to surround the scatterer, and the four faces parallel to the direction of propagation are set as periodic boundary conditions (PBC). The remaining two faces are assigned as PML as shown in Figure 5(c).

Results are presented first for vertical and horizontal SWNT arrays with $D = 1.7 \text{ nm}$ and $L = 0.42 \text{ nm}$ for the SC, HC, and HS models to demonstrate the effect of the geometry on the reflection characteristics. Next, the effects of the length and orientation of the SWNT on the performance of arrays based on the HS model are reported. In general, it is found that the maximum reflection from the SWNT arrays occurs at frequencies ranging from 400 THz to 470 THz as depicted in Figure 6. The simulated reflection coefficients

are normalized by a constant, A . The magnitude of A is presented in Figure 6 with the normalized reflection coefficients for the vertical and horizontal arrays. It can be seen that maximum reflection occurs for the SC model and the minimum for HC model. This is because the volumetric density of the SC model is much larger than the volumetric density of the HC model. It is found that for the two alignments, the effect is observed only on the magnitude of the reflection coefficient.

Next, the effect of length of the HS SWNT model on the performance of the SWNT arrays is investigated. For solar cells applications, the intrinsic thickness of SWNT layers may vary up to 50 nm, and the separation distance should be very small such as to maximize the quantum efficiency [25]. Therefore, in our simulations we assumed L to range from 0.42 nm to 10 nm and $D = 1.7 \text{ nm}$. The reflection coefficients for vertical and horizontal alignments are presented in Figure 7.

It can be seen that the reflection coefficients of the SWNT array decrease when the length of SWNT increases. However, the bandwidth and resonant frequency are not affected for all cases considered. Therefore, the reflection of light from arrays consisting of short SWNTs is less than that from arrays with long SWNTs. This is because the volumetric losses increase as the length of SWNTs increases. The bandwidth of modes excited from 300 THz to 425 THz decreases when the length of the SWNTs increases. The bandwidth around 470 THz decreases when the length of the SWNTs increases only when the SWNTs are aligned horizontally as seen in Figure 7(b). Also, we found that the reflection coefficients for the SWNT arrays are proportional to the complex relative permittivity.

5. Conclusion

In this paper, the fundamental properties of EM interactions with SC, HC, and HS 3D models of SWNTs, both individual

and in infinite array configurations, are investigated in the visible frequency range using the finite-element formulation of Maxwell's equations combined with a quantum conductivity function. The scattering and absorption cross sections of two armchair SWNTs are examined. It is found that only the HS model is capable of providing accurate results for the spectrum of both σ_{sca} and σ_{abs} as compared against measured results. As far as SWNT arrays are concerned, maximum reflection is observed for frequencies ranging from 400 THz to 470 THz, which occurs for the SC model, whereas the minimum is observed for the HC model. For the horizontally and vertically aligned SWNTs, only the magnitude of the reflection coefficient has been affected. The reflection of light from arrays consisting of short SWNTs is found to be less than that from arrays with long SWNTs. The bandwidth of the excited modes decreases when the length of the SWNTs increases. The bandwidth decreases as the length of the SWNTs increases when the SWNTs are aligned horizontally. Finally, the reflection coefficients for the SWNT arrays are proportional to the complex relative permittivity.

Acknowledgments

The authors would also like to thank Dr. Said M. Mikki and Dr. M.V. Shuba for their valuable discussions and comments. Finally, the authors thank Dr. George W. Hanson for his helpful discussions.

References

- [1] Y. Jia, P. Li, X. Gui et al., "Encapsulated carbon nanotube-oxide-silicon solar cells with stable 10% efficiency," *Applied Physics Letters*, vol. 98, no. 13, Article ID 133115, 2011.
- [2] X. Dang, H. Yi, M. H. Ham et al., "Virus-templated self-assembled single-walled carbon nanotubes for highly efficient electron collection in photovoltaic devices," *Nature Nanotechnology*, vol. 6, no. 6, pp. 377–384, 2011.
- [3] H. Zhou, A. Colli, A. Ahnood et al., "Arrays of parallel connected coaxial multiwall-carbonnanotube-amorphous-silicon solar cells," *Advanced Materials*, vol. 21, no. 38–39, pp. 3919–3923, 2009.
- [4] I. A. Levitsky, "Hybrid solar cells based on carbon nanotubes and nanoporous silicon," *IEEE Nanotechnology Magazine*, vol. 4, no. 4, Article ID 5599964, pp. 24–25, 2010.
- [5] H. Zhou, A. Colli, T. Butler et al., "Carbon nanotube arrays for optical design of amorphous silicon solar cells," *International Journal of Material Forming*, vol. 1, no. 2, pp. 113–116, 2008.
- [6] Y. Wang, K. Kempa, B. Kimball et al., "Receiving and transmitting light-like radio waves: antenna effect in arrays of aligned carbon nanotubes," *Applied Physics Letters*, vol. 85, no. 13, pp. 2607–2609, 2004.
- [7] S. Reich, C. Thomsen, and J. Maultzsch, *Carbon Nanotubes: Basic Concept and Physical Properties*, John Wiley and Sons, Hoboken, NJ, USA, 3rd edition, 2004.
- [8] G. Y. Slepyan, S. A. Maksimenko, A. Lakhtakia, O. Yevtushenko, and A. V. Gusakov, "Electrodynamics of carbon nanotubes: dynamic conductivity, impedance boundary conditions, and surface wave propagation," *Physical Review B*, vol. 60, no. 24, pp. 17136–17149, 1999.
- [9] G. W. Hanson, "Fundamental transmitting properties of carbon nanotube antennas," *IEEE Transactions on Antennas and Propagation*, vol. 53, no. 11, pp. 3426–3435, 2005.
- [10] J. Hao and G. W. Hanson, "Infrared and optical properties of carbon nanotube dipole antennas," *IEEE Transactions on Nanotechnology*, vol. 5, no. 6, pp. 766–775, 2006.
- [11] G. W. Hanson, "Current on an infinitely-long carbon nanotube antenna excited by a gap generator," *IEEE Transactions on Antennas and Propagation*, vol. 54, no. 1, pp. 76–81, 2006.
- [12] J. Hao and G. W. Hanson, "Electromagnetic scattering from finite-length metallic carbon nanotubes in the lower IR bands," *Physical Review B*, vol. 74, no. 3, Article ID 035119, pp. 1–6, 2006.
- [13] G. Y. Slepyan, M. V. Shuba, S. A. Maksimenko, and A. Lakhtakia, "Theory of optical scattering by achiral carbon nanotubes and their potential as optical nanoantennas," *Physical Review B*, vol. 73, no. 19, Article ID 195416, pp. 1–11, 2006.
- [14] J. Hao and G. W. Hanson, "Optical scattering from a planar array of finite-length metallic carbon nanotubes," *Physical Review B*, vol. 75, no. 16, Article ID 165416, pp. 1–7, 2007.
- [15] S. M. Mikki and A. A. Kishk, "Theory of optical scattering by carbon nanotubes," *Microwave and Optical Technology Letters*, vol. 49, no. 10, pp. 2360–2364, 2007.
- [16] M. V. Shuba, S. A. Maksimenko, and G. Y. Slepyan, "Absorption cross-section and near-field enhancement in finite-length carbon nanotubes in the terahertz-to-optical range," *Journal of Computational and Theoretical Nanoscience*, vol. 6, no. 9, pp. 2016–2023, 2009.
- [17] M. Y. Sfeir, T. Beetz, F. Wang et al., "Optical spectroscopy of individual single-walled carbon nanotubes of defined chiral structure," *Science*, vol. 312, no. 5773, pp. 554–556, 2006.
- [18] F. Wang, D. J. Cho, B. Kessler et al., "Observation of excitons in one-dimensional metallic single-walled carbon nanotubes," *Physical Review Letters*, vol. 99, no. 22, Article ID 227401, pp. 1–4, 2007.
- [19] R. W. P. King and T. T. Wu, "The imperfectly conducting cylindrical transmitting antenna," *IEEE Transactions on Antennas and Propagation*, vol. AP-14, no. 15, pp. 524–534, 1966.
- [20] "Ansoft's High Frequency Structure Simulator HFSS," 13th version, 2011, <http://www.ansoft.com>.
- [21] D. Perry, "HFSS- antennas arrays and FSS'S," Ansoft, <http://www.ansoft.com/hfworkshop02/perry.pdf>.
- [22] L. Tsang, J. A. Kong, and K. Ding, *Scattering of Electromagnetic Waves*, John Wiley and Sons, New York, NY, USA, 2000.
- [23] H. Li and K. Banerjee, "High-frequency analysis of Carbon Nanotube interconnects and implications for on-chip inductor design," *IEEE Transactions on Electron Devices*, vol. 56, no. 10, pp. 2202–2214, 2009.
- [24] M. S. Dresselhaus and G. Dresselhaus, *Carbon Nanotubes: Synthesis, Structure, Properties and Applications*, Springer, New York, NY, USA, 2001.
- [25] M. Vaezzadeh, M. R. Saeedi, T. Barghi, and M. R. Sadeghi, "The necessary length of carbon nanotubes required to optimize solar cells," *Chemistry Central Journal*, vol. 1, no. 1, article 22, 2007.

Research Article

Carbide Nanoparticles Encapsulated in the Caves of Carbon Nanotubes by an In Situ Reduction-Carbonization Route

Chunli Guo,¹ Yitai Qian,² and Pengju Han³

¹ College of Materials Science and Engineering, Taiyuan University of Technology, Taiyuan 030024, China

² Key Laboratory of Colloid and Interface Chemistry, Shandong University, Ministry of Education, Jinan 250100, China

³ College of Architecture and Civil Engineering, Taiyuan University of Technology, Taiyuan 030024, China

Correspondence should be addressed to Chunli Guo, gcl@sdu.edu.cn

Received 11 July 2011; Revised 23 September 2011; Accepted 26 September 2011

Academic Editor: Renzhi Ma

Copyright © 2011 Chunli Guo et al. This is an open access article distributed under the Creative Commons Attribution License, which permits unrestricted use, distribution, and reproduction in any medium, provided the original work is properly cited.

Carbides (TiC, WC, and NbC) nanoparticles fully encapsulated in the caves of carbon nanotubes (CNTs) were synthesized via an in situ reduction-carbonization route at 600°C in an autoclave. The structural features and morphologies of as-obtained products were investigated using X-ray diffraction, scanning electron microscopy, and high-resolution transmission electron microscopy (HRTEM). HRTEM studies showed that the average diameter of CNTs encapsulated with carbide nanoparticles are in the range of 15–40 nm. The reaction temperature, the reaction time, and the metal catalyst are found to play crucial roles to the product morphology. The growth mechanism of carbide nanoparticles encapsulated in CNTs was discussed in detail.

1. Introduction

Transition metal carbides are important materials because they possess some desired properties such as thermal stability, corrosion, and wear resistance, electronic, magnetic, and catalytic characteristics [1–4]. Among them, titanium carbide (TiC), tungsten carbide (WC), and niobium carbide (NbC) are three kinds of important transition metal carbides, which are applied as cutting tools, ceramics, and wear-resistance materials [5–7]. Furthermore, WC shows excellent catalyst properties similar to platinum [8]. However, their widespread applications have been limited due to their inherent brittleness, catastrophic failure mode, and gathering [9]. Carbon nanotubes (CNTs) highlighted by the work of Iijima [10] in 1991 are now a major component of nanotechnology, which have attracted increasing attention because of their unusual properties and numerous potential applications [11]. The encapsulation of these carbides in CNTs has also attracted widespread attention, not only because CNTs can be used as protecting shells to environmental effects, but also because they exhibit more excellent properties than individual materials such as magnetic, catalytic, electronic,

and optical properties [12–15]. The reported encapsulation phases inside CNTs were mainly metals and oxides but scarcely carbides. The encapsulation of carbides nanoparticles in CNTs can compensate for the defect of each other and make better. For transition metal carbides, it can increase their specific surface area and decrease their aggregation. Simultaneously, the CNTs properties such as field emission properties, electrical conductivity, and quantum transport behavior can be improved better. All these will extremely enlarge their applications compared to single material.

To date, some synthetic methods about TiC, WC, and NbC nanoparticles encapsulated in CNTs systems have been investigated. Pan et al. [16] reported TiC nanoparticles coated with CNTs prepared by CVD had good field emission properties. WC-CNTs composites were synthesized by the reduction and carbonization process [17] and the shape memory synthesis method [18]. NbC nanoparticles encapsulated in CNTs were produced by arcing electrodes of graphite-metal mixtures, and its susceptibility property was also studied [19]. Most reports described that carbides located either on the inner surface or on the outer surface of CNTs to form composite materials. However, to our knowledge, there

have been few reports about TiC, WC, and NbC nanoparticles fully encapsulated in the caves of CNTs up to now.

Pyrolysis of ferrocene has been proved to be the most promising way to prepare not only CNTs but also carbon-encapsulated ferromagnetic nanoparticles [20–22]. Distinct from other approaches, ferrocene can supply both iron as catalyst of CNTs growth and carbon sources in the synthetic strategy. Therefore, we present a way to fabricate TiC, WC, and NbC nanoparticles fully encapsulated in CNT caves by an in-situ reduction-carbonization route at 600°C in an autoclave, and the growth mechanisms of as-obtained samples were discussed in detail.

2. Experimental Section

TiC, WC, and NbC nanoparticles encapsulated in the CNT caves were prepared as follows. In a typical experimental procedure, 2 g ferrocene, 1 g metal oxide (TiO_2 , WO_3 , or Nb_2O_5), and 1 g Mg powder were mixed and placed in a 50 mL stainless-steel autoclave. The autoclave was sealed and put into an electronic furnace which was heated to 600°C for 10 h, then cooled to room temperature in the air. The black powder products were collected and washed with distilled water, dilute HCl, and absolute ethanol in turn several times. Finally, the products were dried under vacuum at 50°C for 6 h. In addition, the final products of WC-CNTs were treated with ammonia to remove W_2C impurities.

X-ray powder diffraction (XRD) measurements were carried out using a Bruker D8 advanced X-ray diffractometer equipped with graphite monochromatized $\text{Cu K}\alpha$ radiation ($\lambda = 1.5418 \text{ \AA}$). Field emission scanning electron microscopy (FESEM) images were taken by a JSM-6700F scanning electron microscope. The transmission electron microscopy (TEM) images were obtained by a Hitachi model H-7000 TEM. The high-resolution (HRTEM) images were recorded on a JEOL 2100 transmission electron microscope.

3. Results and Discussion

The XRD pattern of as-obtained samples is shown in Figure 1, which confirms that the three samples were composed of two phases: the broad peaks with relatively low peak intensity could be ascribed to the diffraction of graphite (marked with “o”); the other sharp peaks with relatively high peak intensity could be indexed as carbides. From Figure 1(a), the sharp and high-intensity diffraction peaks can be indexed to face-centered cubic TiC (JCPDS card no. 65-8417). The XRD pattern of Sample 2 is shown in Figure 1(b), which reveals that the diffraction peaks are indexed as hexagonal WC (JCPDS card no. 65-4539). Figure 1(c) shows the typical XRD pattern of Sample 3, which can be indexed as face-centered cubic NbC (JCPDS card no. 65-8784). The CNT-related graphite peaks are detected at 22.6° and 44.9° for the graphite (002) and (102) planes, respectively.

Figure 2(a) is HRTEM image of Sample 1, which shows that TiC nanoparticles are encapsulated in CNTs with a diameter range of 15–25 nm at some intervals. The inset of Figure 2(a) is a single CNT encapsulated with some TiC nanoparticles. It is clear that the CNT is not one-dimen-

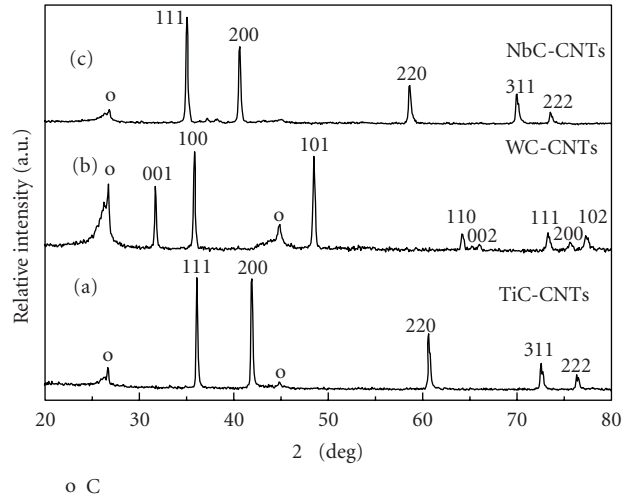


FIGURE 1: XRD patterns of the as-obtained samples: (a) TiC-CNTs, (b) WC-CNTs, and (c) NbC-CNTs.

sion smooth, but bamboo-like and TiC nanoparticles are encapsulated in small caves of bamboo-like CNTs, which are different from previous reports that TiC nanoparticles were located on the surface of CNTs. Detailed structural analysis of the core-sheath nanostructures was carried out with HRTEM (shown in Figure 2(b)). The HRTEM image of the core indicates clearly resolved interplanar distances of 0.201 nm, corresponding to the (200) lattice spacing of TiC. In addition, it can be seen that there is a layered structure which the d-spacing of 0.32 nm corresponds well to the (200) lattice spacing of graphite. In contrast, with well-crystallized graphite layers in CNTs, there are many stacking faults in the bamboo-like carbon wall. There are some TiC nanoparticles outside of CNTs. Those sizes are larger than that of inside CNTs possibly due to their easy aggregation property. Figure 2(c) shows the HRTEM images of Sample 2. Sample 2 is also consisted of nanoparticles and CNT with a diameter range of 20–40 nm, and nanoparticles lie on the inner channels of the CNT. The inset SEM image shows that a knot in the middle of the CNT suggests that the WC nanoparticle is wrapped in graphite. The crystal plane distances of the nanoparticle inside the cave of CNT is 0.188 nm (shown in Figure 2(d)), which is almost equal to that of WC (101) plane. Figure 2(e) shows the typical HRTEM image of Sample 3, which indicates that Sample 3 is mainly composed of nanotubes with a diameter range of 30–40 nm and lengths up to ten micrometers. In addition, a few nanoparticles were located on the outside surface of the CNT. The inset of Figure 2(e) is a SEM image of a closed CNT tumid end, implying that the NbC nanoparticles were encapsulated in the CNTs. HRTEM image (shown in Figure 2(f)) indicates that the d-spacing of 0.157 nm corresponds well to the (220) lattice spacing of NbC, and the fringe interplanar spacing was close to those of graphite.

In order to explain the growth mechanism, a series of controlled experiments were carried out. The experimental

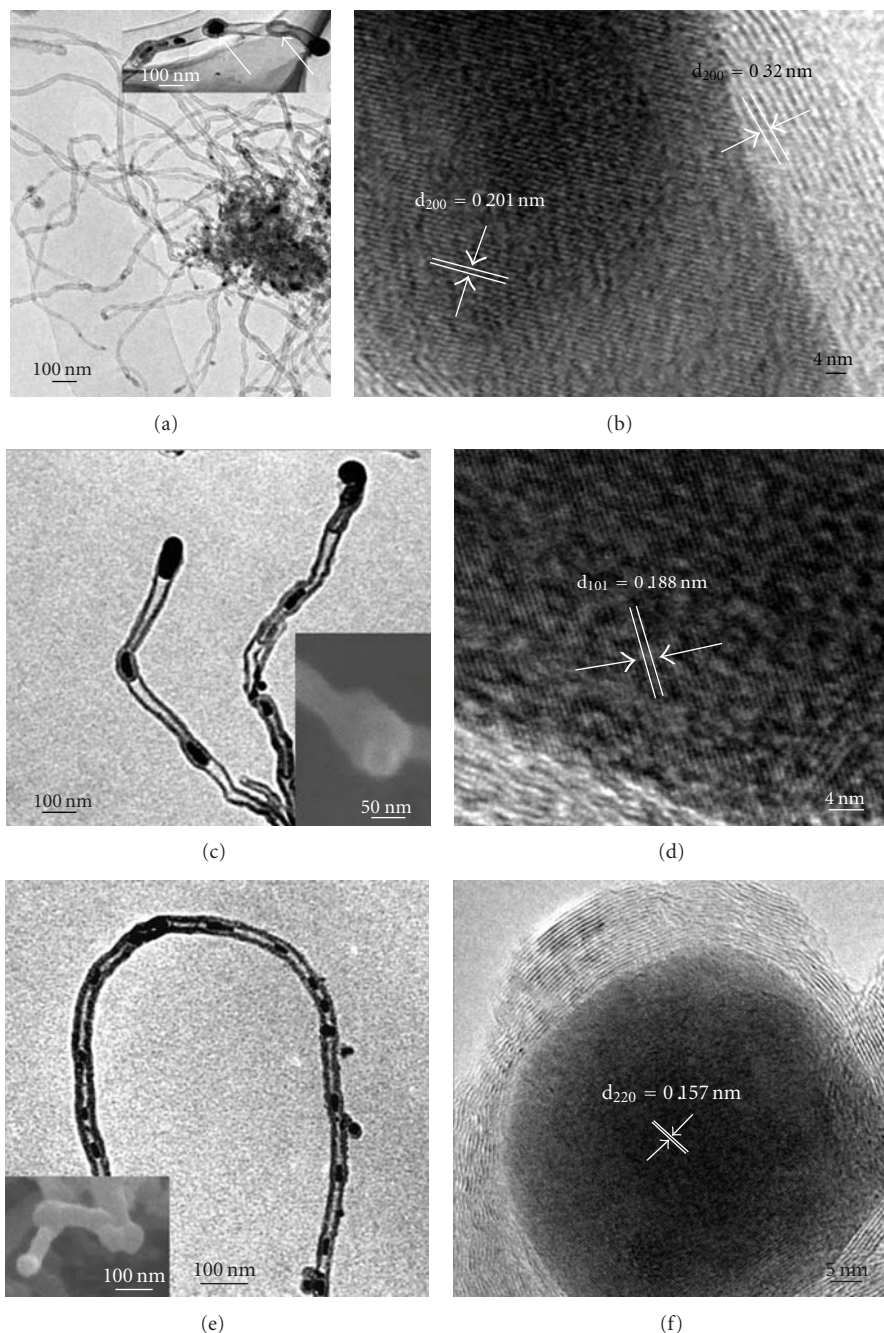


FIGURE 2: Typical HRTEM and SEM images of the as-obtained samples: (a,b) TiC-CNTs, (c,d) WC-CNTs, and (e,f) NbC-CNTs.

results proved that Mg powder played a key role in the formation of CNTs. When heating pure ferrocene or the mixture of ferrocene and TiO_2 , the morphologies of the final products are symmetrical spiral carbon nanofibers (Figure 3(a)) and oxhorn-like (Figure 3(b)). Leonhardt et al. obtained carbon nanotubes when heating pure ferrocene [14], which is different from our results. The possible reason of forming symmetrical spiral carbon nanofibers was that the magnetic Fe particles (arrowed in Figure 3(c)) were attracted mutually to cause two sections of textile fibers to curve and approach in the sealed system. As adding Mg powder to pure ferrocene,

straightforward CNTs instead of flexural carbon nanofibers were obtained in the final products. The catalyst particle located in the top of both the CNTs (Figure 3(d)) was observed in the untreated samples, which were used as the catalyst to promote the 1-D carbon nanomaterials formation corresponding to vapor-liquid-solid growth mechanism [23]. Moreover, the amount of Mg powder also has a great influence on the formation of CNTs. As the amount of Mg powders is less than 0.1 g, only carbon nanofibers can be found in the final products. If increasing it to 0.3 g, carbon nanofibers and CNTs along with a small quantity of carbon

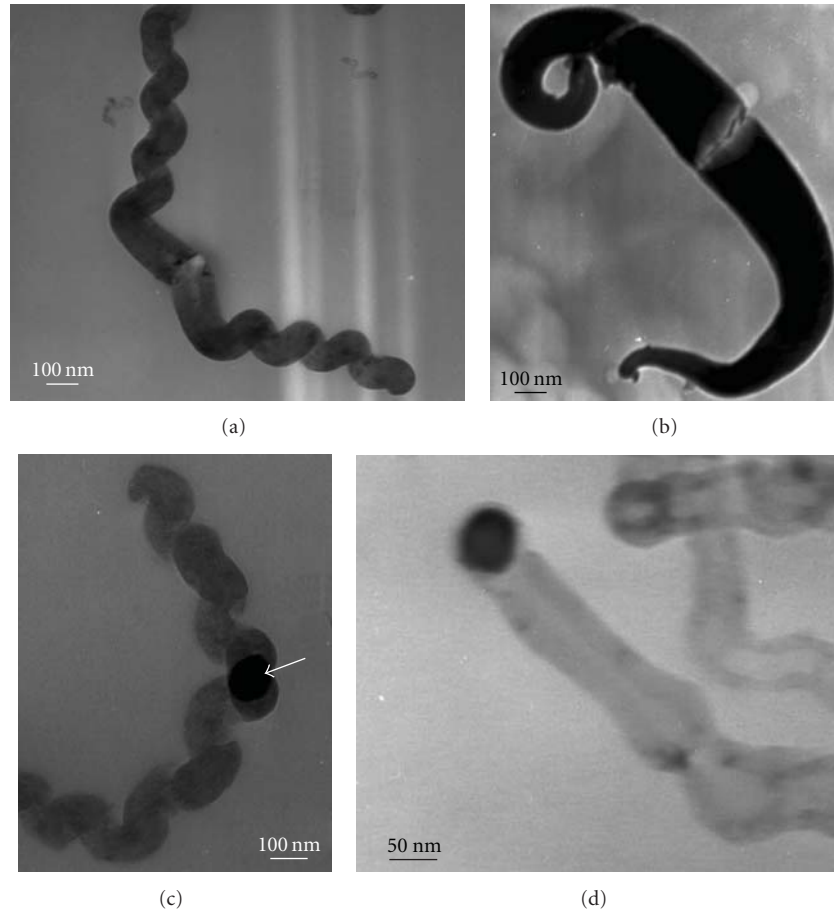


FIGURE 3: Typical HRTEM images showing the reaction progress. (a) Heated ferrocene, (b) heated mixture of ferrocene and TiO_2 , and (c,d) metal particles located on the 1-D carbon nanomaterials.

hollow spheres coexisted in the sample. Only above 0.5 g, the final products were the straight CNTs entirely. In the route of carbides encapsulated in CNTs, Mg powder was used both as catalyst to CNTs formation and as reducing agent. Carbon particles deposited on the surface of the fresh Ti obtained from the reaction between TiO_2 and Mg at 600°C to form carbides, which were wrapped up by excessive carbon to form the encapsulation subsequently.

In addition, the effect of reaction temperature, reaction time, different oxides, and metal reducing agents on the final formation of carbides encapsulated in CNTs was also investigated. Only CNTs were produced if reaction temperature was lower than 600°C . The experimental data also indicated that the reaction would be incomplete if reaction time was shorter than 2 h. As the reaction time prolonged, the amount of carbides nanoparticles encapsulated in CNTs increased. It is found that no carbides formed if oxides were substituted by SiO_2 or B_2O_3 . The possible reason was that the reaction between SiO_2 or B_2O_3 and Mg needed higher temperature. As other metals such as Na, Zn, Ca, Fe, Ni, Co, and Cr were substituted for Mg powder, there were no carbides existing in the final products. If the oxides (TiO_2 and WO_3) were replaced with the corresponding metals, there were also no

carbides because the activity of the fresh Ti or W was lower than the commercial products.

4. Conclusions

In summary, TiC, WC, and NbC nanoparticles fully encapsulated in the caves of CNTs have been prepared via in situ reduction carbonization at 600°C in an autoclave. HRTEM studies show that TiC, WC, or NbC nanoparticles are located in the caves of CNTs, and a spot of carbides particles exists outside of CNTs. The average diameters of the prepared CNTs are in the range of 15–40 nm. The reaction temperature, the reaction time, and the metal catalyst are key influencing factors to the product morphology. The growth mechanism of carbides encapsulated in CNTs was discussed in detail.

Acknowledgments

Financial support from the National Natural Science Foundation of China (no. 20671058) and the Talent Introduction Funding of Taiyuan University of Technology are greatly

appreciated. The authors thank Dr. Pamela Holt for editing the manuscript for English.

References

- [1] C. C. Yu, S. Ramanathan, B. Dhandapani, J. G. Chen, and O. S. Ted, "Bimetallic Nb-Mo carbide hydroprocessing catalysts: synthesis, characterization, and activity studies," *The Journal of Physical Chemistry B*, vol. 101, no. 4, pp. 512–518, 1997.
- [2] D. R. Sadoway, "Electrochemical processing of refractory metals," *Journal of the Minerals Metals & Materials Society*, vol. 47, no. 7, pp. 15–19, 1991.
- [3] S. Niu and M. B. Hall, "Theoretical studies on reactions of transition-metal complexes," *Chemical Reviews*, vol. 100, no. 2, pp. 353–406, 2000.
- [4] M. M. Rohmer, M. Bénard, and J. M. Poblet, "Structure, reactivity, and growth pathways of metallocarbohedrenes M_8C_{12} and transition metal/carbon clusters and nanocrystals: a challenge to computational chemistry," *Chemical Reviews*, vol. 100, no. 2, pp. 495–542, 2000.
- [5] Y. Liang and S. P. Dutta, "Application trend in advanced ceramic technologies," *Technovation*, vol. 21, no. 1, pp. 61–65, 2001.
- [6] S. H. Jhi, S. G. Louie, M. L. Cohen, and J. Ihm, "Vacancy hardening and softening in transition metal carbides and nitrides," *Physical Review Letters*, vol. 86, no. 15, pp. 3348–3351, 2001.
- [7] B. F. Dal, S. G. Hardin, D. G. Hay, and T. W. Turney, "Selective, low-temperature synthesis of niobium carbide and a mixed (niobium/tungsten) carbide from metal oxide-polyacrylonitrile composites by carbothermal reduction," *Journal of Materials Science*, vol. 28, no. 24, pp. 6657–6664, 1993.
- [8] F. H. Ribeiro, R. A. Dalla Betta, M. Boudart, J. Baumgartner, and E. Iglesia, "Reactions of neopentane, methylcyclohexane, and 3 3-dimethylpentane on tungsten carbides: the effect of surface oxygen on reaction pathways," *Journal of Catalysis*, vol. 130, no. 1, pp. 86–105, 1991.
- [9] A. Biedunkiewicz, N. Gordon, J. Straszko, and S. Tamir, "Kinetics of thermal oxidation of titanium carbide and its carbon nano-composites in dry air atmosphere," *Journal of Thermal Analysis and Calorimetry*, vol. 88, no. 3, pp. 717–722, 2007.
- [10] S. Iijima, "Helical microtubules of graphitic carbon," *Nature*, vol. 354, no. 12, pp. 56–58, 1991.
- [11] M. M. J. Treacy, T. W. Ebbesen, and J. M. Gibson, "Exceptionally high Young's modulus observed for individual carbon nanotubes," *Nature*, vol. 381, no. 6, pp. 678–680, 1996.
- [12] C. Y. Zhi, D. Y. Zhong, and E. G. Wang, "GaN-filled carbon nanotubes: synthesis and photoluminescence," *Chemical Physics Letters*, vol. 381, no. 5-6, pp. 715–719, 2003.
- [13] P. M. Ajayan and J. M. Tour, "Materials science: nanotube composites," *Nature*, vol. 447, pp. 1066–1068, 2007.
- [14] A. Leonhardt, M. Ritschel, D. Elefant et al., "Enhanced magnetism in Fe-filled carbon nanotubes produced by pyrolysis of ferrocene," *Journal of Applied Physics*, vol. 98, no. 7, Article ID 074315, 5 pages, 2005.
- [15] H. Park, M. H. Kim, Y. K. Hwang, J. S. Chang, and Y. U. Kwon, "Sonochemical syntheses and catalytic properties of oxide and carbide nanocomposites on carbon nanotubes," *Chemistry Letters*, vol. 34, no. 2, pp. 222–223, 2005.
- [16] L. Pan, T. Shoji, A. Nagataki, and Y. Nakayama, "Field emission properties of titanium carbide coated carbon nanotube arrays," *Advanced Engineering Materials*, vol. 9, no. 7, pp. 584–587, 2007.
- [17] X. Shi, H. Yang, P. Sun, G. Shao, X. Duan, and X. Zhen, "Synthesis of multi-walled carbon nanotube-tungsten carbide composites by the reduction and carbonization process," *Carbon*, vol. 45, no. 9, pp. 1735–1742, 2007.
- [18] N. Keller, B. Pietruszka, and V. Keller, "A new one-dimensional tungsten carbide nanostructured material," *Materials Letters*, vol. 60, no. 13-14, pp. 1774–1777, 2006.
- [19] M. Terrones, W. K. Hsu, A. Schilder et al., "Novel nanotubes and encapsulated nanowires," *Applied Physics A*, vol. 66, no. 3, pp. 307–317, 1998.
- [20] C. N. R. Rao, R. Sen, B. C. Sathishkumar, and A. Govindaraj, "Large aligned-nanotube bundles from ferrocene pyrolysis," *Chemical Communications*, no. 15, pp. 1525–1526, 1998.
- [21] Y. Lu, Z. Zhu, and Z. Liu, "Carbon-encapsulated Fe nanoparticles from detonation-induced pyrolysis of ferrocene," *Carbon*, vol. 43, no. 2, pp. 369–374, 2005.
- [22] J. Huo, H. Song, X. Chen, and W. Lian, "Formation and transformation of carbon-encapsulated iron carbide/iron nanorods," *Carbon*, vol. 44, no. 13, pp. 2849–2852, 2006.
- [23] K. Jiang, C. Feng, K. Liu, and S. Fan, "A vapor-liquid-solid model for chemical vapor deposition growth of carbon nanotubes," *Journal of Nanoscience and Nanotechnology*, vol. 7, no. 4-5, pp. 1494–1504, 2007.

Research Article

Fabrication and Optical Property of Periodic $\text{Sn}_{1-x}\text{Ti}_x\text{O}_2$ Nanostructures Patterned by the Polystyrene Microsphere Templates

Shutian Chen, Zhengcao Li, and Zhengjun Zhang

Advanced Materials Laboratory, Department of Materials Science and Engineering, Tsinghua University, Beijing 100084, China

Correspondence should be addressed to Zhengcao Li, zcli@tsinghua.edu.cn

Received 28 June 2011; Revised 31 August 2011; Accepted 13 September 2011

Academic Editor: Yanqiu Zhu

Copyright © 2011 Shutian Chen et al. This is an open access article distributed under the Creative Commons Attribution License, which permits unrestricted use, distribution, and reproduction in any medium, provided the original work is properly cited.

Regular arrays of $\text{Sn}_{1-x}\text{Ti}_x\text{O}_2$ nanostructures were fabricated by glancing angle sputter deposition onto self-assembled close-packed arrays of 200 nm diameter, 500 nm diameter, and 1 μm diameter polystyrene microspheres, respectively. The morphology of the nanostructures could be modulated by the variation of the sputtering power of Ti target and the size of polystyrene microspheres templates. Accordingly, the performance of reflection which was dependent on the morphology of nanostructures could be tuned by optimizing the parameters. The anisotropic morphology of nanoflakes achieved by adjusting the sputtering power of Ti target could generate the anisotropism of reflectance. With the increase of the PS sphere size, the anisotropism of nanostructures weakened; however, they exhibited excellent antireflection effects by creating a smaller gradient of refractive index.

1. Introduction

Much attention has been attracted to the design of nanoscale semiconductor oxide materials with controlled morphology and novel morphology-dependent properties. Recently, subwavelength grating (SWG) structures with a moth-eye profile have aroused the interest of researchers [1–3]. The surface of the moth eye is covered by highly packed protuberances, which reduce the reflection and thus improve the visual efficiency. The operation of SWG structures is similar to the moth eye. From the viewpoint of the effective medium theory, the nanostructures can be considered as a homogeneous medium with a graded refractive index which varies gradually from 1.0 (air) to that of the bulk material [4]. Therefore, the reflection can be reduced significantly by SWG structures with tapered features. The antireflection structures exhibit great potentials in the applications of solar cells, LEDs, photodetectors, transparent glasses, and so on [5–8].

Tin dioxide (SnO_2) is an n-type semiconductor with a wide band gap ($E_g = 3.6\text{ eV}$ at 300 K) that is well known for its promising applications in gas sensing [9], lithium-ion batteries [10], photocatalysis [11], and dye-sensitized solar cells (DSCs) [12]. Similar to other highly transparent

semiconductors, SnO_2 is also expected to be a competitive candidate for optical devices [13–15]. Due to the isostructure (rutile type) and close lattice parameters of TiO_2 and SnO_2 , the metal cations can be replaced by each other in a wide concentration region. Hence, Ti is an appealing alternative of doping, compared with other elements whose contents are restricted to a low level since the emergence of the second phase [16]. In our study, we have successfully yielded periodic arrays of $\text{Sn}_{1-x}\text{Ti}_x\text{O}_2$ nanostructures by glancing angle sputter deposition onto self-assembled close-packed arrays of polystyrene spheres. The morphology of the $\text{Sn}_{1-x}\text{Ti}_x\text{O}_2$ nanostructures could be controlled by changing the sputtering power of Ti target and the size of polystyrene microspheres templates. Accordingly, their optical properties could be tuned by adjusting the parameters. Such unique structures with modulated morphology and designed optical performance are promising to be applied in optical devices.

2. Experimental Details

The $\text{Sn}_{1-x}\text{Ti}_x\text{O}_2$ nanostructures were prepared in an ultra-high vacuum magnetron sputter deposition system on Si

(001) substrates that were patterned with 200 nm diameter, 500 nm diameter, and 1 μm diameter hexagonal close-packed polystyrene microspheres, respectively. $\text{Sn}_{1-x}\text{Ti}_x\text{O}_2$ depositions were carried out using a 6 cm diameter Ti target (99.99% pure) and a 6 cm diameter SnO_2 target (99.9% pure) mounted at an angle of 120° with respect to each other, and with the Ti target back to the substrate. The deposition angle α (the angle between the trajectory of the incident vapor flux and the substrate normal), which was controlled by the substrate position with respect to the Ti target, was selected to be 85° . Sputtering was carried out at 0.15 Pa which was held constant during all depositions in 99.999% pure Ar. No external substrate heating was applied. Power-regulated DC and RF power supplies were used to provide the discharge currents of 0.20 A, 0.25 A, 0.30 A, and 0.35 A, respectively, at 340 V for Ti, and a radio frequency current of 130 mA at 500 V for SnO_2 . The $\text{Sn}_{1-x}\text{Ti}_x\text{O}_2$ nanostructures were obtained with the simultaneous deposition from the sputtering sources of Ti and SnO_2 onto a stationary substrate. The morphology of all samples was examined by a scanning electron microscope (SEM), with their structure identified by X-ray diffraction (XRD) analysis, and the reflectance was measured by a spectrophotometer.

3. Results and Discussion

The $\text{Sn}_{1-x}\text{Ti}_x\text{O}_2$ nanostructures were prepared on Si (001) substrates that were patterned with 200 nm diameter, 500 nm diameter, and 1 μm diameter hexagonal close-packed polystyrene microspheres, respectively. In the depositions, the power of RF sputtering was fixed while the power of DC sputtering was regulated at the discharge currents = 0.20 A, 0.25 A, 0.30 A, and 0.35 A, respectively, for each size of PS microsphere templates. Correspondingly the prepared samples were named 1#, 2#, 3#, and 4#. The structures of films were identified by X-ray diffraction (XRD), indicating the amorphous state in all the samples.

The morphology and optical properties of the $\text{Sn}_{1-x}\text{Ti}_x\text{O}_2$ nanostructures with different PS sphere sizes were studied, respectively. First, Figure 1 shows typical SEM micrographs of 1# and 2# grown on 200 nm, 500 nm, and 1 μm PS microspheres. Arrays of well-separated $\text{Sn}_{1-x}\text{Ti}_x\text{O}_2$ nanostructures were produced. The regular hexagonal arrays replicate the close-packed pattern of the polystyrene spheres, attributed to the limited adatom surface diffusion and atomic shadowing effects in the process of GLAD. The films deposited on 200 nm diameter PS spheres exhibit anisotropic morphology of melon seed-shape nanoflakes, as shown in Figures 1(a) and 1(b). The formation of nanoflakes can be explained by the mechanism of GLAD. As GLAD is a physical vapor deposition process in which the incident flux impinges the substrate from an oblique angle, causing atomic shadowing and the resulting highly porous nanostructures [17–19], the morphology of nanostructures is closely related to the direction of the incident flux. With the incident flux from lateral SnO_2 target, the direction of the growth front is changed from straight up to lateral growth, leading to an increase of the growth rate in the direction parallel to the SnO_2 flux and a decrease in the perpendicular

direction [20]. As a result, the nanostructures are deformed by the anisotropic lateral growth and exhibit the anisotropic morphology of melon seed-shaped nanoflakes. From Figures 1(a) and 1(b), the height of nanostructures is 400 nm approximately with the diameter of PS spheres deducted, which is comparable with respect to the scale of PS spheres. When the size of PS microspheres is increased to 500 nm, it indicates that the films still exhibit the anisotropy to some extent, as shown in Figures 1(c) and 1(d), though less distinctly compared with that deposited on 200 nm diameter PS spheres. As the size of the template is further increased, the nanostructures become “spheric shells” covering the polystyrene microspheres, which is shown in Figures 1(e) and 1(f).

Comparing the films with different PS sphere sizes, it can be concluded that the anisotropy of morphology degenerates gradually with the increase of the template size. When grown on 200 nm diameter PS microspheres, the anisotropic nanoflakes are yielded in the film 1# and 2#. With the size of PS microspheres increased, the nanostructures degenerate to asymmetric “spheric shells” gradually. This result matches well with the growing mechanism of the nanoflakes. For the deposition layer is relatively thin, the anisotropic lateral growth is overwhelmed by the effect of templates gradually with the increase of the template size, causing the degeneration from nanoflakes to asymmetric “spheric shells”.

The morphology of film 3# and 4# with various PS sphere sizes is shown in Figure 2. As discussed before, the morphology of nanostructures is influenced by the anisotropic lateral growth deriving from the incident flux. Therefore, with the increased sputtering rate of Ti target, the effect of lateral SnO_2 flux was outweighed by the Ti flux, resulting in the transition of the nanostructures from nanoflakes to nanopillars, as shown in Figures 2(a) and 2(b). Similarly, the film 3# and 4# turn to short nanopillars when deposited on 500 nm diameter PS spheres, and symmetric “spheric shells” on 1 μm diameter PS spheres, which is indicated in Figures 2(c)–2(f). Besides, there is an interesting phenomenon worth noticing. Both as nanopillars, it is clear that the surface of film 4# is coarser than film 3# with the increase of the sputtering power, as shown in Figures 2(a) and 2(b). With the size of PS microspheres increased to 500 nm, there are subrods protruding out from the tips of nanopillars in film 4#; when the size of the template is increased to 1 μm , more subrods are formed both in the film 3# and 4#, as shown in Figures 2(c)–2(f).

The effect of templates to the subrods is noteworthy. The nucleation of subrods is caused by surface mounds that capture, due to atomic shadowing, a larger fraction of the deposition flux than the surrounding surface. With the elevated sputtering power, the adatom mobility is limited with respect to the high-speed deposition, which leads to kinetic roughening [21, 22]. Once one or multiple surface mounds have developed on a single nanostructure, atomic shadowing favors the growth of the mounds, leading to the formation of subrods on the top ultimately. For the films deposited on 200 nm diameter PS microspheres, the roughening of the surface of nanostructures is observed, when the sputtering current is lifted to 0.35 A. However, there

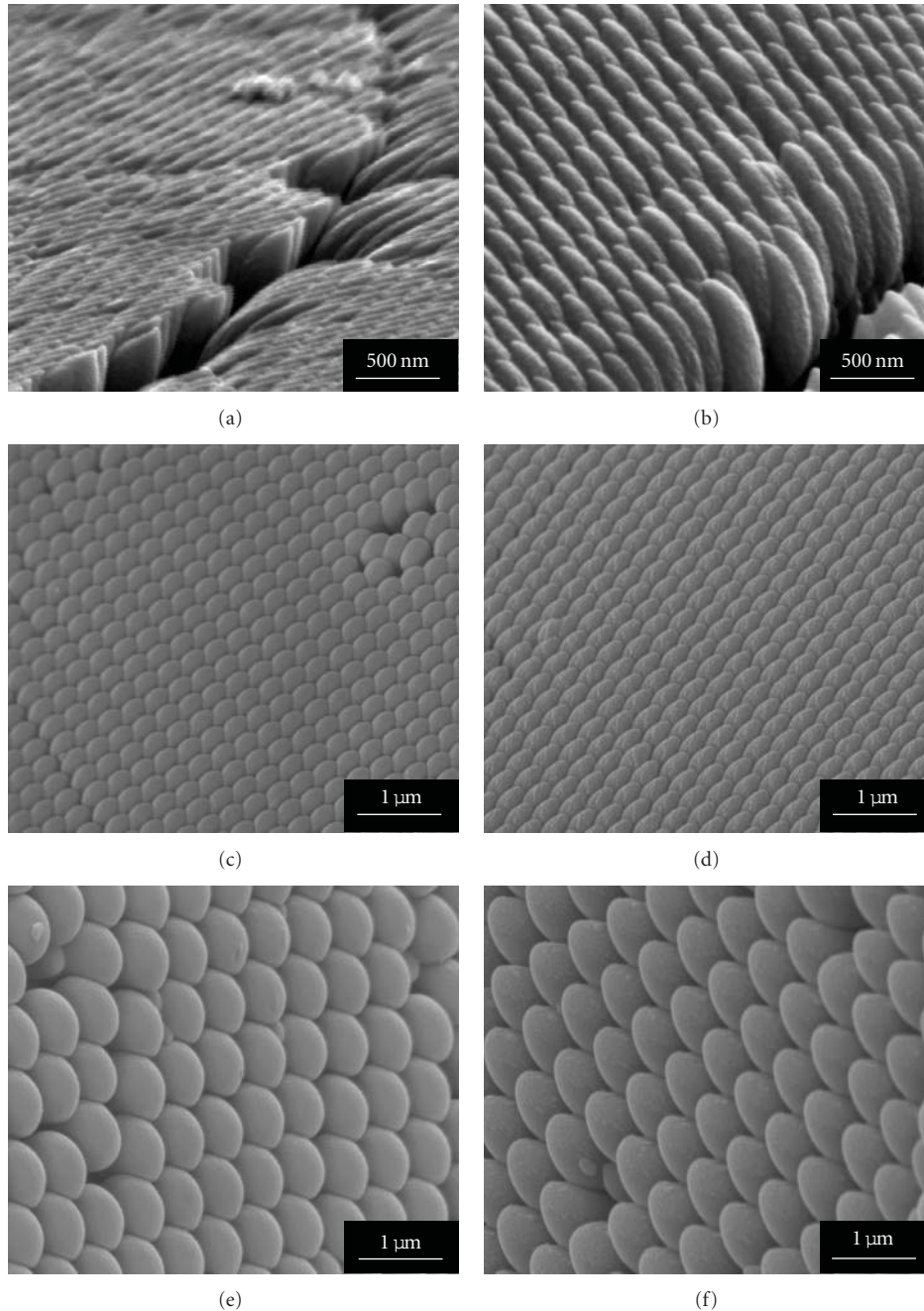


FIGURE 1: Scanning electron microscopic images of $\text{Sn}_{1-x}\text{Ti}_x\text{O}_2$ films deposited on 200 nm, 500 nm, and $1\ \mu\text{m}$ PS spheres at I (the discharge currents) of Ti target 0.20 A and 0.25 A (a) film 1# at $I = 0.20$ A on 200 nm PS spheres; (b) film 2# at $I = 0.25$ A on 200 nm PS spheres; (c) film 1# at $I = 0.20$ A on 500 nm PS spheres; (d) film 2# at $I = 0.25$ A on 500 nm PS spheres; (e) film 1# at $I = 0.20$ A on $1\ \mu\text{m}$ PS spheres; (f) film 2# at $I = 0.25$ A on $1\ \mu\text{m}$ PS spheres.

are not any subrods existing. The subrods begin appearing in the film 4# with a PS sphere size of 500 nm, and increase significantly in the film 3# and 4# with a PS sphere size of $1\ \mu\text{m}$. It is in agreement with the preceding discussion. Because the nanostructures replicate the close-packed array of the initial surface pattern, the size of templates is required to be larger than the surface mound separation for the nucleation of subrods. Therefore, the subrods cannot

form when grown on 200 nm diameter PS microspheres. Conversely, the probability of subrods is expected to increase substantially with the increase of the template size, ascribed to more surface mounds.

Because the optical properties of films are dependent on the morphology of nanostructures, which is quite related with the size of PS microspheres templates, the comparison of the reflectance between the films with different PS sphere

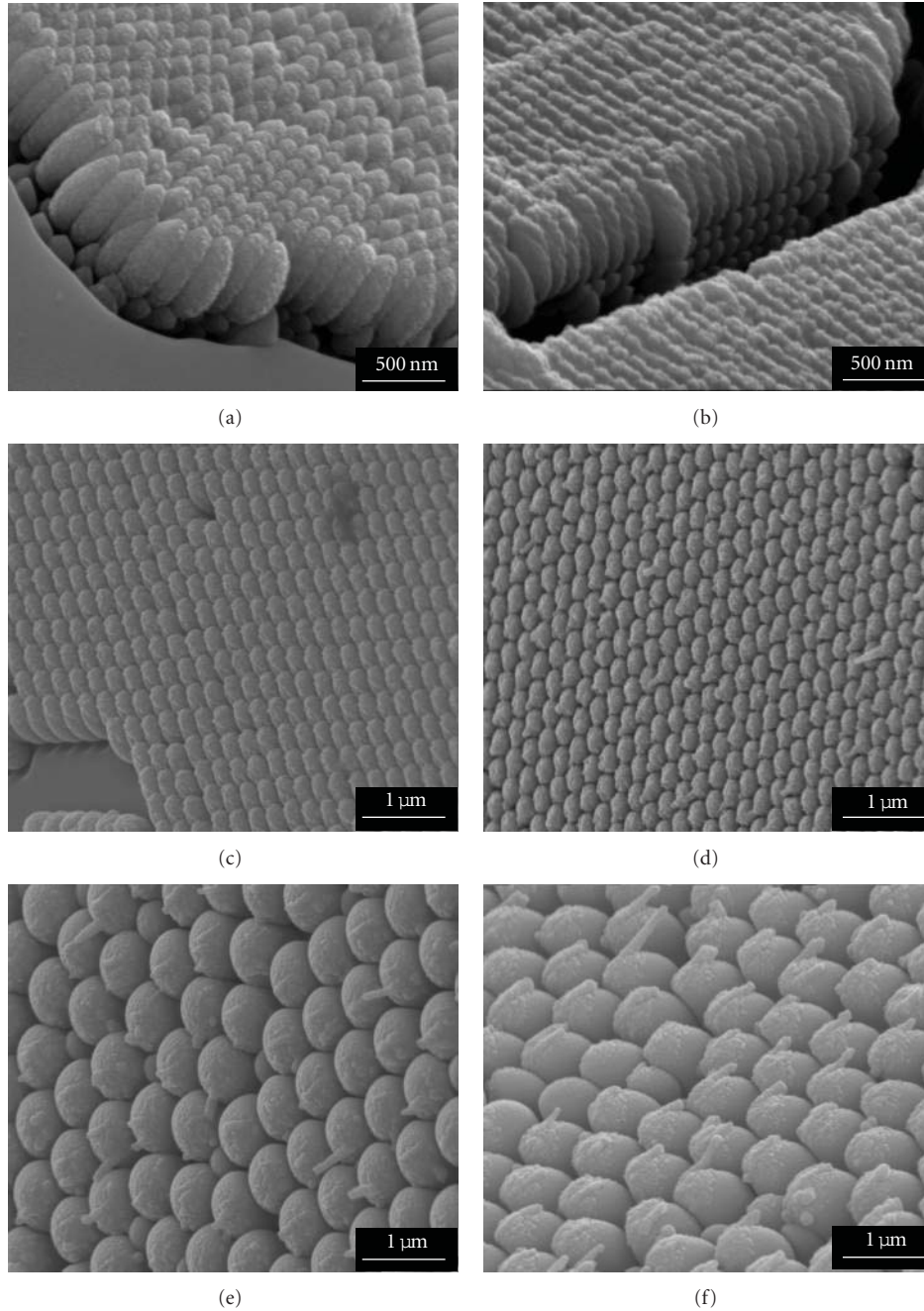


FIGURE 2: Scanning electron microscopic images of $\text{Sn}_{1-x}\text{Ti}_x\text{O}_2$ films deposited on 200 nm, 500 nm and $1\ \mu\text{m}$ PS spheres at I (the discharge currents) of Ti target 0.30 A and 0.35 A (a) film 3# at $I = 0.30$ A on 200 nm PS spheres; (b) film 4# at $I = 0.35$ A on 200 nm PS spheres; (c) film 3# at $I = 0.30$ A on 500 nm PS spheres; (d) film 4# at $I = 0.35$ A on 500 nm PS spheres; (e) film 3# at $I = 0.30$ A on $1\ \mu\text{m}$ PS spheres; (f) film 4# at $I = 0.35$ A on $1\ \mu\text{m}$ PS spheres.

sizes was conducted. The reflectance of films was measured by a spectrophotometer. Figure 3(a) shows the directions of incident light. The reflectance in the direction parallel to the surface of the nanoflakes is marked as R_{\parallel} while the reflectance in the other direction is marked as R_{\perp} . The definition of R_{\parallel} and R_{\perp} is consistent for the films with various PS sphere sizes. Figures 3(b) and 3(c) provide the R_{\parallel} and R_{\perp} of film 1# and 2# in the spectral range 300–750 nm. It is evident that for the film 1# and 2# deposited on 200 nm

diameter PS spheres, R_{\parallel} is considerably lower than R_{\perp} . However, the anisotropy of reflectance for the films with a PS sphere size of 500 nm lowers significantly; the reflectance for the films with a PS sphere size of $1\ \mu\text{m}$ is all fairly low in the whole spectral region, and no apparent anisotropy is observed. This result is consistent with the trend of the anisotropy of the morphology.

Figures 4(a) and 4(b) provide the R_{\parallel} and R_{\perp} of film 3# and 4# with various PS sphere sizes. It indicates that,

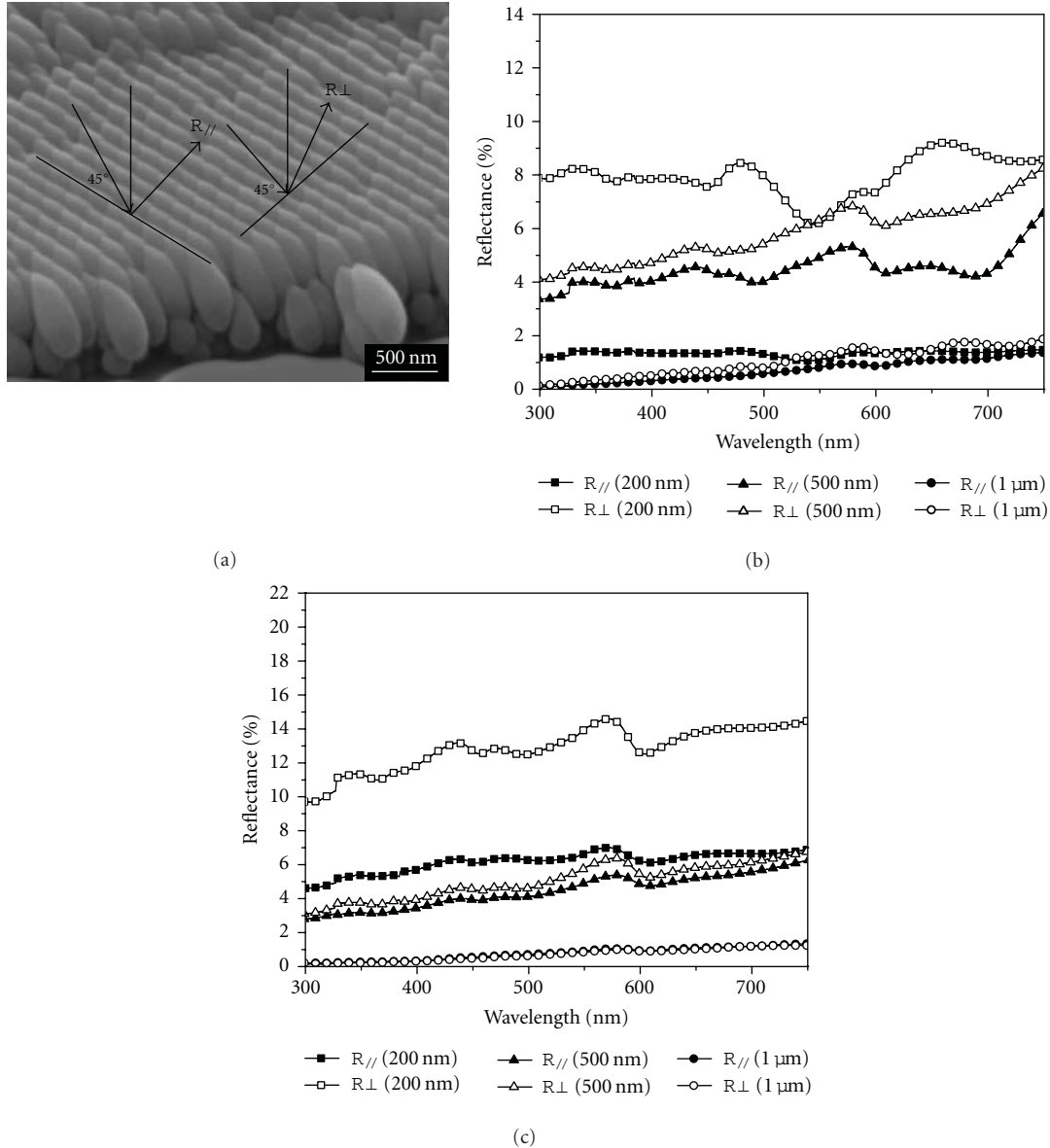


FIGURE 3: The sketch of the incident and reflected light, with the reflectance in two directions marked as $R_{//}$ and R_{\perp} , respectively (a), and the $R_{//}$ and R_{\perp} of film 1# (b) and 2# (c) with various PS sphere sizes at the wavelength range of 300–750 nm.

compared with film 1# and 2#, the reflectance of these films is almost isotropic except for the film 4# deposited on 500 nm PS spheres, probably owing to the subrods on the surface. However, the subrods-induced anisotropy is not observed for the film 3# and 4# with a PS sphere size of 1 μm , though there are even more subrods obtained, which is likely because the reflectance is too low to be differentiated. On the other hand, it can be concluded that the reflectance of films shows a decrease trend with the increase of the PS sphere size from Figures 3 and 4.

The result of reflectance can be explained by the model of two-dimensional submicrometer antireflection coatings. Since the application of conventional single-layer antireflection coatings is limited at a single wavelength only, the gradient-refractive index antireflection coating inspired biologically by moth eyes becomes a desirable alternative. The

“moth eye” antireflection surface consisting of submicron structure arrays, with refractive index varying monotonically from the air to the substrate along its thickness, can be thought of as a set of multilayers with minimal difference in the refractive index according to effective medium theory and effectively suppress the specular reflectance at the interface of the two media [23, 24]. Therefore, periodic nanostructures which could lead to an effective refractive index gradient were designed to diminish the reflection [25–27]. The nanostructures we prepared, with tapered profile, can be approximately equivalent to a gradient-refractive index submicrometer coating. The effect of “moth eye” antireflection surface depends on the height and profile of the submicron structures. Accordingly, the reflectance can be tuned by the sputtering parameters and the size of PS microsphere templates, which have a great influence

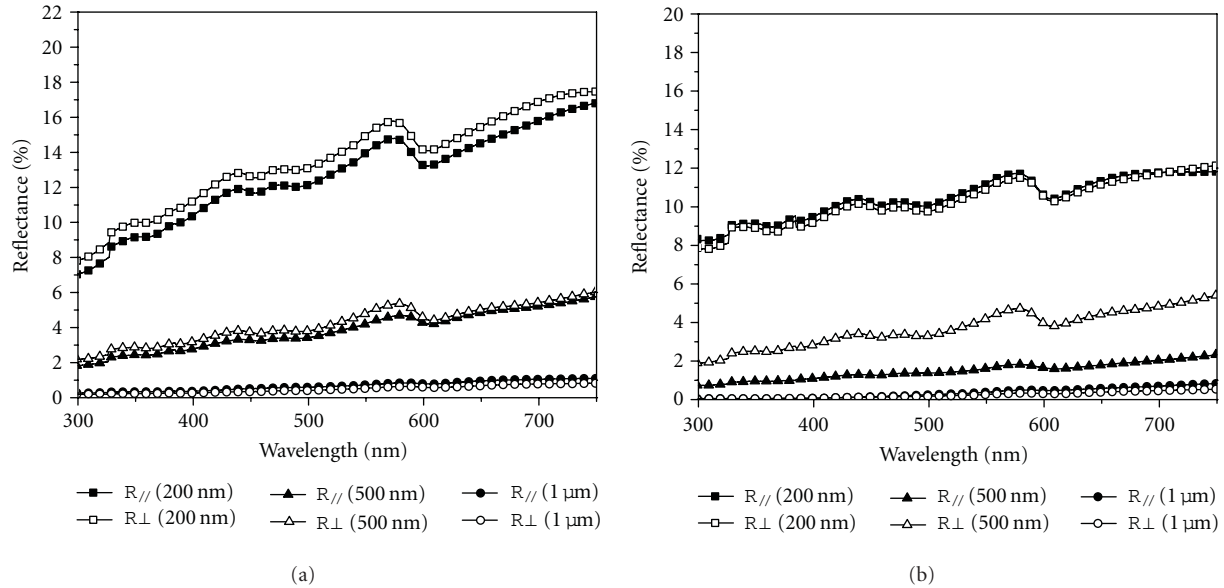


FIGURE 4: The $R_{//}$ and R_{\perp} of film 3# (a) and 4# (b) with various PS sphere sizes at the wavelength range of 300–750 nm.

on the height and shape of periodic structures. On one hand, the sputtering parameter is correlated with the interaction of the incident flux and impacts the morphology of nanostructures. As the anisotropy of the morphology plays a crucial role in the anisotropy of reflectance, the anisotropy of reflectance weakens with the increase of sputtering power of Ti target. On the other hand, the periodicity of nanostructure arrays is also a critical factor. The nanostructure array with a smaller periodicity displays apparent anisotropy of reflectance, while a larger periodicity is not beneficial for it, resulting from the effect of templates on the anisotropic lateral growth. However, the films grown on $1\ \mu\text{m}$ diameter PS spheres render a better antireflection effect in comparison to that grown on 200 nm diameter, and 500 nm diameter PS spheres. Because the increase of the height of nanostructures generates smaller effective-index gradient, the reflection is progressively reduced with increased height and the film deposited on $1\ \mu\text{m}$ PS spheres demonstrates superior antireflection performance [28, 29].

In summary, the preparation method of glancing angle sputter deposition we proposed can accomplish the adjustment to the morphology of nanostructures, and ultimately the tuning to the optical property. Porous and textured surfaces with a graded refractive index can be generated by obliqueness of the incident flux. It is worth to mention its advantages over the top-down method. As the most popular technique to fabricate antireflection films, the top down method, including wet or dry etching, is preferred as the precise control over the nanostructures. However, this method has some limitations: it is difficult to achieve smaller diameter or period and too costly for the multiple complicated and time-consuming process steps. Compared to the top down method, the glancing angle sputter deposition shows great potential in optical device applications.

4. Conclusions

We have demonstrated closely packed and morphology-controlled $\text{Sn}_{1-x}\text{Ti}_x\text{O}_2$ nanostructures on patterned Si substrates by glancing angle sputter deposition, indicating unique optical properties in the visible region. The shape of the $\text{Sn}_{1-x}\text{Ti}_x\text{O}_2$ nanostructures could be controlled by adjusting the sputtering power of Ti target and the periodicity of nanostructure arrays, which was dominated by the size of PS sphere templates. The anisotropic morphology of nanoflakes achieved by adjusting the sputtering power of Ti target could generate the anisotropism of reflectance, a phenomenon that was of interest for applications. A smaller periodicity was preferable to the anisotropism of morphology and reflectance, while a larger periodicity was not beneficial for it. However, they provided substantially reduced reflectance as the smaller effective-index gradient. These nanostructures with controlled morphology and optical properties are expected to open up application areas as optical devices.

Acknowledgments

The authors are grateful to the financial support by the National Basic Research Program of China (973 program, 2010CB731600) and the National Natural Science Foundation of China (51072094 and 61076003).

References

- [1] S. A. Boden and D. M. Bagnall, "Tunable reflection minima of nanostructured antireflective surfaces," *Applied Physics Letters*, vol. 93, no. 13, Article ID 133108, 2008.

- [2] Z. Yu, H. Gao, W. Wu, H. Ge, and S. Y. Chou, "Fabrication of large area subwavelength antireflection structures on Si using trilayer resist nanoimprint lithography and liftoff," *Journal of Vacuum Science and Technology B*, vol. 21, no. 6, pp. 2874–2877, 2003.
- [3] K. Kintaka, J. Nishii, A. Mizutani, H. Kikuta, and H. Nakano, "Antireflection microstructures fabricated upon fluorine-doped SiO₂ films," *Optics Letters*, vol. 26, no. 21, pp. 1642–1644, 2001.
- [4] J. Huang, X. Wang, and Z. L. Wang, "Bio-inspired fabrication of antireflection nanostructures by replicating fly eyes," *Nanotechnology*, vol. 19, no. 2, Article ID 025602, 2008.
- [5] P. Lalanne and G. M. Morris, "Antireflection behavior of silicon subwavelength periodic structures for visible light," *Nanotechnology*, vol. 8, no. 2, pp. 53–56, 1997.
- [6] Y. F. Huang, S. Chattopadhyay, Y. J. Jen et al., "Improved broadband and quasi-omnidirectional anti-reflection properties with biomimetic silicon nanostructures," *Nature Nanotechnology*, vol. 2, no. 12, pp. 770–774, 2007.
- [7] Y. Peichen, C. H. Chang, C. H. Chiu et al., "Efficiency enhancement of gas photovoltaics employing antireflective indium tin oxide nanocolumns," *Advanced Materials*, vol. 21, no. 16, pp. 1618–1621, 2009.
- [8] T. Lohmüller, M. Helgert, M. Sundermann, R. Brunner, and J. P. Spatz, "Biomimetic interfaces for high-performance optics in the deep-UV light range," *Nano Letters*, vol. 8, no. 5, pp. 1429–1433, 2008.
- [9] K. M. Li, Y. J. Li, M. Y. Lu, C. I. Kuo, and L. J. Chen, "Direct conversion of single-layer SnO nanoplates to multi-layer SnO₂ nanoplates with enhanced ethanol sensing properties," *Advanced Functional Materials*, vol. 19, no. 15, pp. 2453–2456, 2009.
- [10] H. X. Zhang, C. Feng, Y. C. Zhai, K. L. Jiang, Q. Q. Li, and S. S. Fan, "Cross-stacked carbon nanotube sheets uniformly loaded with SnO₂ nanoparticles: a novel binder-free and high-capacity anode material for lithium-ion batteries," *Advanced Materials*, vol. 21, no. 22, pp. 2299–2304, 2009.
- [11] M. Niu, F. Huang, L. Cui, P. Huang, Y. Yu, and Y. Wang, "Hydrothermal synthesis, structural characteristics, and enhanced photocatalysis of SnO₂/α-Fe₂O₃ semiconductor nanoheterostructures," *ACS Nano*, vol. 4, no. 2, pp. 681–688, 2010.
- [12] S. Gubbala, V. Chakrapani, V. Kumar, and M. K. Sunkara, "Band-edge engineered hybrid structures for dye-sensitized solar cells based on SnO₂ nanowires," *Advanced Functional Materials*, vol. 18, no. 16, pp. 2411–2418, 2008.
- [13] Z. Weichang, L. Ruibin, W. Qiang et al., "Bound exciton and optical properties of SnO₂ One-Dimensional nanostructures," *Journal of Physical Chemistry C*, vol. 113, no. 5, pp. 1719–1726, 2009.
- [14] J. H. He, T. H. Wu, C. L. Hsin et al., "Beaklike SnO₂ nanorods with strong photoluminescent and field-emission properties," *Small*, vol. 2, no. 1, pp. 116–120, 2006.
- [15] S. Mathur and S. Barth, "Molecule-based chemical vapor growth of aligned SnO₂ nanowires and branched SnO₂/V₂O₅ heterostructures," *Small*, vol. 3, no. 12, pp. 2070–2075, 2007.
- [16] T. Hirata, K. Ishioka, M. Kitajima, and H. Doi, "Concentration dependence of optical phonons in the TiO₂-SnO₂ system," *Physical Review B*, vol. 53, no. 13, pp. 8442–8448, 1996.
- [17] Q. Zhou, Z. Li, Y. Yang, and Z. Zhang, "Arrays of aligned, single crystalline silver nanorods for trace amount detection," *Journal of Physics D: Applied Physics*, vol. 41, no. 15, Article ID 152007, 2008.
- [18] Q. Zhou, Y. Yang, J. Ni, Z. Li, and Z. Zhang, "Rapid recognition of isomers of monochlorobiphenyls at trace levels by surface-enhanced Raman scattering using Ag nanorods as a substrate," *Nano Research*, vol. 3, no. 6, pp. 423–428, 2010.
- [19] Q. Zhou, Z. Li, J. Ni, and Z. Zhang, "A simple model to describe the rule of glancing angle deposition," *Materials Transactions*, vol. 52, no. 3, pp. 469–473, 2011.
- [20] S. V. Kesapragada and D. Gall, "Anisotropic broadening of Cu nanorods during glancing angle deposition," *Applied Physics Letters*, vol. 89, no. 20, Article ID 203121, 2006.
- [21] C. M. Zhou and D. Gall, "Branched Ta nanocolumns grown by glancing angle deposition," *Applied Physics Letters*, vol. 88, no. 20, Article ID 203117, 2006.
- [22] C. M. Zhou and D. Gall, "The structure of Ta nanopillars grown by glancing angle deposition," *Thin Solid Films*, vol. 515, no. 3, pp. 1223–1227, 2006.
- [23] H. Sankur and W. H. Southwell, "Broadband gradient-index antireflection coating for ZnSe," *Applied Optics*, vol. 23, no. 16, pp. 2770–2773, 1984.
- [24] S. Chattopadhyay, Y. F. Huang, Y. J. Jen, A. Ganguly, K. H. Chen, and L. C. Chen, "Anti-reflecting and photonic nanostructures," *Materials Science and Engineering R*, vol. 69, no. 1–3, pp. 1–35, 2010.
- [25] M. A. Ray, N. Shewmon, S. Bhawalkar, L. Jia, Y. Yang, and E. S. Daniels, "Submicrometer surface patterning using interfacial colloidal particle self-assembly," *Langmuir*, vol. 25, no. 13, pp. 7265–7270, 2009.
- [26] A. Čampa, O. Isabella, R. van Erven et al., "Optimal design of periodic surface texture for thin-film a-Si:H solar cells," *Progress in Photovoltaics: Research and Applications*, vol. 18, no. 3, pp. 160–167, 2010.
- [27] Y. M. Song, E. S. Choi, J. S. Yu, and Y. T. Lee, "Light-extraction enhancement of red AlGaInP light-emitting diodes with antireflective subwavelength structures," *Optics Express*, vol. 17, no. 23, pp. 20991–20997, 2009.
- [28] Y. M. Song, S. Y. Bae, J. S. Yu, and Y. T. Lee, "Closely packed and aspect-ratio-controlled antireflection subwavelength gratings on GaAs using a lenslike shape transfer," *Optics Letters*, vol. 34, no. 11, pp. 1702–1704, 2009.
- [29] Y. M. Song and Y. T. Lee, "Investigation of geometrical effects of antireflective subwavelength grating structures for optical device applications," *Optical and Quantum Electronics*, vol. 41, no. 10, pp. 771–777, 2009.

Research Article

Electrocatalytic Activity for CO, MeOH, and EtOH Oxidation on the Surface of Pt-Ru Nanoparticles Supported by Metal Oxide

Kwang-Sik Sim, Sin-Mook Lim, Hai-Doo Kwen, and Seong-Ho Choi

Department of Chemistry, Hannam University, Daejeon 305-811, Republic of Korea

Correspondence should be addressed to Seong-Ho Choi, shchoi@hnu.kr

Received 15 June 2011; Accepted 14 September 2011

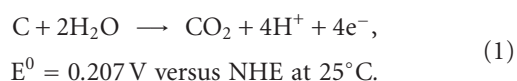
Academic Editor: Steve Acquah

Copyright © 2011 Kwang-Sik Sim et al. This is an open access article distributed under the Creative Commons Attribution License, which permits unrestricted use, distribution, and reproduction in any medium, provided the original work is properly cited.

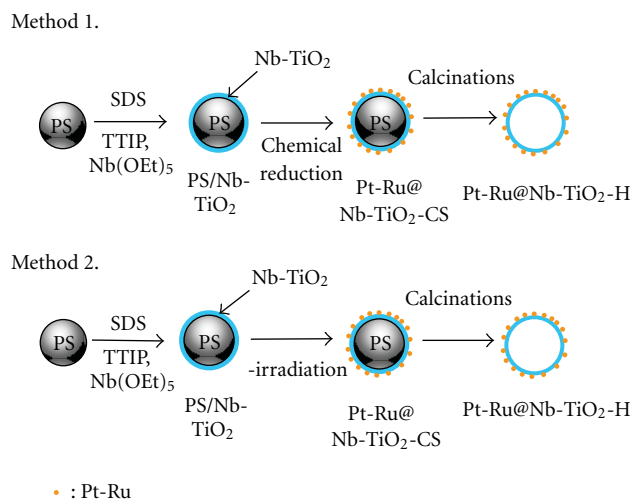
This paper describes the electrocatalytic activity for CO, MeOH, and EtOH oxidation on the surface of Pt-Ru nanoparticles supported by metal oxide (Nb-TiO₂-H) prepared for use in a fuel cell. To prepare Nb-TiO₂-supported Pt-Ru nanoparticles, first, the Nb-TiO₂ supports were prepared by sol-gel reaction of titanium tetraisopropoxide with a small amount of the niobium ethoxide in polystyrene (PS) colloids. Second, Pt-Ru nanoparticles were then deposited by chemical reduction of the Pt⁴⁺ and Ru³⁺ ions onto Nb-TiO₂ supports (Pt-Ru@Nb-TiO₂-CS). Nb element was used to reduce electrical resistance to facilitate electron transport during the electrochemical reactions on a fuel cell electrode. Finally, the Pt-Ru@Nb-TiO₂-H catalysts were formed by the removal of core-polystyrene ball from Pt-Ru@TiO₂-CS at 500°C. The successfully prepared Pt-Ru electrocatalysts were confirmed via TEM, XPS, and ICP analysis. The electrocatalytic efficiency of Pt-Ru nanoparticles was evaluated via CO, MeOH, and EtOH oxidation for use in a direct methanol fuel cell (DMFC). As a result, the Pt-Ru@Nb-TiO₂-H electrodes showed high electrocatalytic activity for the electrooxidation of CO, MeOH, and EtOH.

1. Introduction

Many researcher efforts have been devoted to improving the catalytic performance of carbon supported Pt-Ru catalysts [1–3]. In a colloidal method, dispersion and adsorption of catalytic nanoparticles on the surface of carbon supports is done in the presence of protecting agents to avoid aggregation of particles. It should be noted that the protecting agent is likely to reduce the catalytic activities of catalyst particles. In another method known as the impregnation method, a metal precursor is reduced by the carbon supports dispersed in the solution [4–6]. Carbon supports should be dispersed well without interference of a protecting agent in the suspension. In previous papers [7, 8], the Pt-Ru nanoparticles were deposited on various carbon supports using γ -irradiation to use as anode catalysts in a direct methanol fuel cell (DMFC). However, the life time of the electrode was reduced, since the carbon supports were slowly oxidized in the fuel cell, as shown in



In general, the support materials should possess the following properties: (1) a high surface area for a high level of dispersion of the nanosized catalysts, (2) low electrical resistance to facilitate electron transport during the electrochemical reactions, (3) a pore structure suitable for fuel or oxidant contact and by product release, and (4) strong interaction between the catalyst nanoparticles and the supports. Oxide materials are widely used as a support in heterogeneous catalyst, since they possess those properties. They have inherently higher stability compared to carbon in oxidizing environments [9, 10]. The use of titanium dioxide support in a fuel cell operation has been of great interest due to its stability, low cost, commercial availability in water, and ease to control size and structure [11, 12]. The potential applications of hollow nanomaterials, especially TiO₂ hollow (TiO₂-H) spheres, have been explored in various areas, such as light-trapping, chemical separation, photocatalysts, biomedicine, and optical devices [13, 14]. Compared to general core-shell nanostructures, TiO₂-H spheres are exceptional for their special internal cavity, high specific surface area, high mobility, and low density [15–17]. However, to our knowledge, little work has been reported



SCHEME 1: Preparation procedure of the Pt-Ru@Nb-TiO₂-H catalysts by two methods.

on the application of hollow oxide spheres as a support, especially in fuel cells.

In this study, the Nb-doped TiO₂ supports were prepared with core-polystyrene and shell-Nb-TiO₂, (Nb-TiO₂-CS), for use as fuel cell anode catalysts. The Pt-Ru@Nb-TiO₂-CS was then obtained by deposition of the Pt-Ru nanoparticles on the surface of the Nb-TiO₂-CS using γ -irradiation and chemical reducing agents in aqueous solution, respectively. Finally, the Pt-Ru@Nb-TiO₂-H was fabricated via removal of the core-polystyrene from Nb-TiO₂-CS at 500°C. The electrocatalytic activity of Pt-Ru nanoparticles on metal oxide supports was evaluated via CO, methanol, and ethanol oxidation in a 0.5 M H₂SO₄ electrolyte in order to use for fuel cell anode electrode.

2. Experiment

2.1. Reagents. Styrene, sodium dodecyl sulfate (SDS), and 2-propanol (99%) were obtained from Samchun Chemical Co (Korea). Titanium tetraisopropoxide, niobium ethoxide, hydrogen hexachloroplatinate(IV) hydrate, potassium persulfate, and ruthenium(III) chloride hydrate were purchased from Sigma-Aldrich Co. (USA). Formalin and ethyl alcohol were obtained from Jin Chemical pharmaceutical Co., Ltd. (Korea). All other chemicals were in reagent grade and were used without further purification.

2.2. Synthesis of Polystyrene as Core-Ball via Surfactant-Free Emulsion Polymerization. Polystyrene nanoparticles (PS) as core-ball were prepared as follows: potassium persulfate (KPS) was dissolved completely in deionized (D.I.) water with stirring of 350 rpm for 60 min under nitrogen atmosphere. Styrene monomer was added to the above-prepared solution and polymerized at 75°C for 24 hours under nitrogen atmosphere.

2.3. Preparation of the Pt-Ru@Nb-TiO₂-H Catalysts. The Nb-TiO₂ supports were prepared by sol-gel method. SDS

(0.5 g) as an anchoring agent was dissolved in the prepared PS colloids (10 mL) and stirred for 60 min under nitrogen atmosphere. Titanium tetraisopropoxide (1.2 mL) and niobium ethoxide (45 μ L) were dissolved in 25 mL ethanol. The ethanol solution was slowly added to PS colloids, and the polymerization was processed while stirring (350 rpm) at 75°C for 24 hours under nitrogen atmosphere.

Scheme 1 shows the preparation procedure of Pt-Ru@Nb-TiO₂-H catalysts by chemical reduction method and γ -irradiation. In Method 1, the core-PS and shell-Nb-TiO₂ supports (0.5 g) were well dispersed in 182 mL D.I. water, and pH was adjusted to 9.0 using NaOH. Hydrogen hexachloroplatinate(IV) hydrate (0.21 g) and ruthenium(III) chloride hydrate (0.205 g) were then added to the above-prepared colloids. To reduce the Pt⁴⁺ and Ru³⁺ ions, the formalin, as a reducing agent, was added to the above-prepared colloids. After the Pt⁴⁺ and Ru³⁺ ions were reduced by ultrasonic irradiation for 60 min, the prepared Pt-Ru@Nb-TiO₂-CS nanoparticles were filtered (Whatman-2) and dried in a vacuum oven at 50°C for 8 h. Upon calcination at 500°C for 4 hrs in air, the Pt-Ru@Nb-TiO₂-H catalysts were obtained.

In Method 2, Pt-Ru@Nb-TiO₂-CS nanostructure was prepared by radiolytic reduction of Pt⁴⁺ and Ru³⁺ ions in the presence of the core-PS and shell-Nb-TiO₂. H₂PtCl₆xH₂O (0.21 g) and RuCl₃xH₂O (0.205 g) were dissolved in the Nb-TiO₂ colloids (182 mL) that contained 2-propanol (12.0 mL) as the radical scavenger. Nitrogen was bubbled for 30 min through the solution to remove oxygen, and the solution was then irradiated (Co-60 source) under atmospheric pressure and ambient temperature. A total dose of 30 kGy (a dose rate = 6.48 \times 10⁵/h) were applied. Pt-Ru@Nb-TiO₂-CS nanoparticles were filtered (Whatman-2) and dried in a vacuum oven at 50°C for 8 h. The Pt-Ru@Nb-TiO₂-H catalysts were also obtained by the method described above.

2.4. Characterization. Particle size and morphology of the Pt-Ru@Nb-TiO₂-CS and Pt-Ru@Nb-TiO₂-H catalysts were analyzed by FE-SEM (Hitachi, S-4700, Japan) and HR-TEM (JEOL, JEM-2010, USA). The content of Pt and Ru in

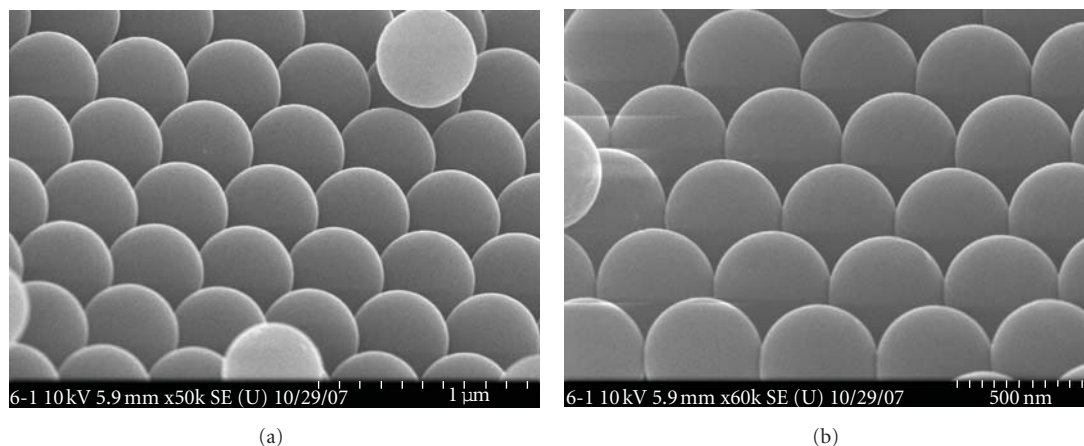


FIGURE 1: SEM images of PS spheres as template prepared by emulsion-free polymerization.

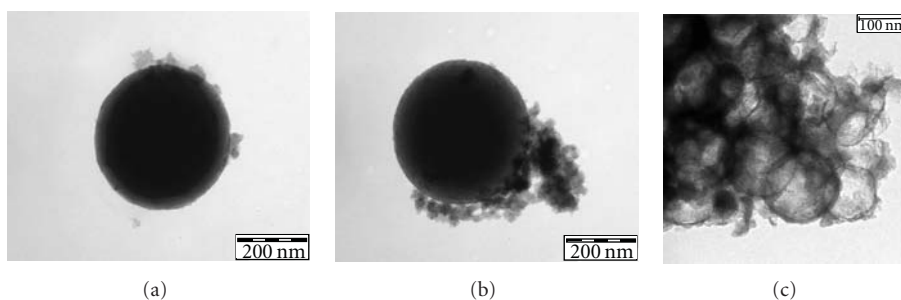


FIGURE 2: TEM images of the PS/Nb-TiO₂ (a), Pt-Ru@Nb-TiO₂-CS (b), and Pt-Ru@Nb-TiO₂ (c) prepared by Method 1 in Scheme 1.

samples was measured by inductively coupled plasma-atomic emission spectrometer (ICP-AES) (Jobin-Yvon, Ultima-C, USA). The X-ray photoelectron spectra of the samples were obtained using Thermo Fisher Scientific, MultiLab. ESCA2000, (USA). X-ray diffraction (XRD) patterns were obtained using a Japanese Rigaku D/max γ A X-ray diffractometer equipped with graphite monochromatized Cu K α radiation ($\lambda = 0.15414$ nm). The scanning range was 5–80° with a scanning rate of 5°/min.

To evaluate the catalytic efficiency of Pt-Ru@Nb-TiO₂-H catalysts for the electro-oxidation of CO, MeOH, and EtOH, the Pt-Ru@Nb-TiO₂-H catalyst electrode was prepared as follows: firstly, the catalytic inks were prepared by mixing of Pt-Ru@Nb-TiO₂-H catalysts (5.0 mg) and 5% Nafion solution (0.05 mL) and stirred for 24 h. Secondly, the catalytic inks were applied on a glass carbon (0.02 cm²) by wet coating and dried in a vacuum oven at 50°C under nitrogen gas. The electro-oxidation of CO, MeOH, and EtOH was examined using the Pt-Ru@Nb-TiO₂-H catalyst electrode, submerged in 0.5 M H₂SO₄ electrolyte by cyclic voltammetry (EG&G INSTRUMENTS, Potentiostat/Galvanostat model 283, USA).

3. Results and Discussion

3.1. Characterization of Pt-Ru@Nb-TiO₂-H Catalysts. As mentioned above, the oxide supports for fuel cell electrode

have high surface area, low electrical resistance, uniform porous structure, and interaction between catalysts and supports. In particular, surface area and electrical conductivity are very important factors in electrocatalytic reactions. The Nb-TiO₂ powder has been attractive as supports due to its high conductivity [18]. The conductivity of the Nb-TiO₂ ($\sim 0.1 \Omega^{-1} \text{cm}^{-1}$) is superior to that of the pure TiO₂ ($10^{-6} \Omega^{-1} \text{cm}^{-1}$) and commercial Vulcan XC-72 carbon supports. However, the Nb-TiO₂ powder is insufficient as fuel cell supports because of low surface area. To increase surface area, the supports require nanostructure such as core-shell nanostructure or the ordered uniform porous structure.

In a previous paper [19], the PS particles of 450 nm in diameter and poly(styrene-*co*-styrene sulfonate), PSS, particles of 140–160 nm in diameter were prepared by emulsifier-free emulsion polymerization. The surfaces of the PS and PSS particles were coated with Ag nanoparticles as antimicrobial agents via reduction of Ag ions using γ -irradiation. In this study, PS particles were used as template for preparing nanostructure supports as shown in Scheme 1. Figure 1 shows SEM images of PS spheres as a template prepared by emulsion-free polymerization. The diameter of the monodispersed PS particles was 450 nm. The surface of the monodispersed PS ball possess hydrophobic properties; therefore, in order to deposit Nb-TiO₂ with hydrophilic properties, anchoring agents such as SDS, poly(N-vinylpyrrolidone), and PVP were used.

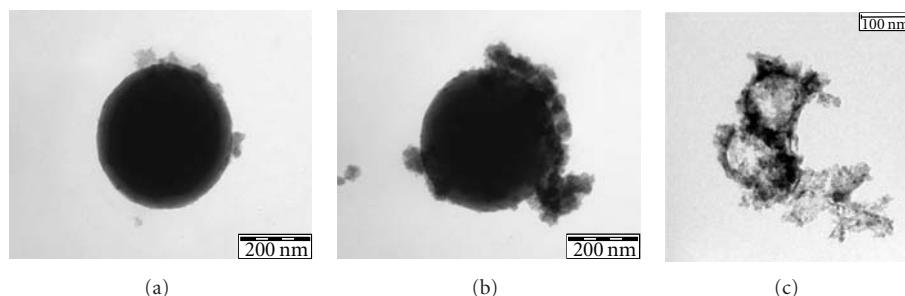


FIGURE 3: TEM images of the PS/Nb-TiO₂ (a), Pt-Ru@Nb-TiO₂-CS (b), and Pt-Ru@Nb-TiO₂ (c) prepared by Method 2 in Scheme 1.

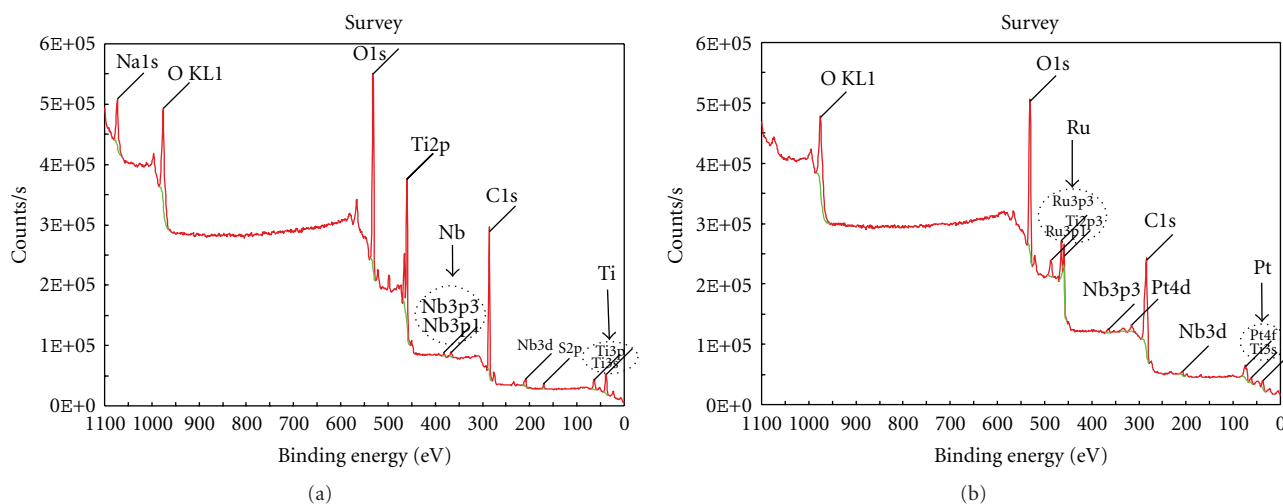


FIGURE 4: X-ray photoelectron spectroscopy (XPS) spectra of the PS/Nb-TiO₂ (a) and Pt-Ru@Nb-TiO₂-H (b) prepared by Method 1 in Scheme 1.

Figure 2 shows TEM images of the sphere with core-PS and shell-Nb-TiO₂, PS/Nb-TiO₂ (a), Pt-Ru@Nb-TiO₂-CS (b), and Pt-Ru@Nb-TiO₂-H (c) prepared by chemical reduction, as shown in Scheme 1. In Figure 2(a), Nb metals were deposited on the surface of TiO₂ shell wall. As shown in Figures 2(b) and 2(c), the Pt-Ru nanoparticles do not completely appear in TEM images. On the other hand, the nanostructure form (hollow form) with thickness of ~15 nm was successfully prepared as shown in Figure 2(c). Figure 3 also shows the TEM images of PS/Nb-TiO₂ (a), Pt-Ru@Nb-TiO₂-CS (b), and Pt-Ru@Nb-TiO₂-H (c) prepared by γ -irradiation as shown in Scheme 1. In Figure 3(b), after deposition of Pt-Ru nanoparticle on the surface of Nb-TiO₂ supports using γ -irradiation, the Pt-Ru nanoparticles were well dispersed on the surface of Nb-TiO₂. However, the Pt-Ru nanoparticles do not appear in TEM image. After calcinations, the patterns of Pt-Ru@Nb-TiO₂-H catalysts are different compared to that of Pt-Ru@Nb-TiO₂-H catalysts prepared by chemical reduction. This might be caused by the radiation damage of TiO₂ shell.

As mentioned above, the Pt-Ru nanoparticles cannot clearly be determined by TEM images. For clear evaluation of the existence of Pt-Ru nanoparticles, the core-PS and shell-Nb-TiO₂ supports, PS/Nb-TiO₂, and Pt-Ru@Nb-TiO₂-H were analyzed via XPS spectroscopy. Figure 4 shows the

XPS data of the PS/Nb-TiO₂ (a) and Pt-Ru@Nb-TiO₂-H catalysts (b) prepared by chemical reduction. The peaks Nb and Ti element are assigned, as shown in Figure 4(a), and the Pt and Ru elements of the Pt-Ru@Nb-TiO₂-H prepared by chemical reduction were determined, as shown in Figure 4(b). These results clearly indicate that the Pt-Ru nanoparticles were successfully deposited on the surface of PS/Nb-TiO₂ by chemical reduction method. Figure 5 also shows the XPS spectra of the PS/Nb-TiO₂ nanostructure (a) and Pt-Ru@Nb-TiO₂-H catalysts (b) prepared by γ -irradiation method. The peaks Nb and Ti element are also assigned in Figure 5(a), and the Pt and Ru elements of the Pt-Ru@Nb-TiO₂-H prepared by γ -irradiation were also determined in Figure 5(b). From these results, Pt-Ru nanoparticles were successfully loaded on the surface of PS/Nb-TiO₂ nanostructure by γ -irradiation.

Figure 6 presents XRD patterns of the Pt-Ru@Nb-TiO₂-H catalysts prepared by Method 1 (a) and by Method 2 (b). Figure 6(a) shows the crystallinity of the Pt-Ru nanoparticles, and peaks are present at 39.9°, 46.2°, and 67.4°. These peaks are assigned to Pt-(111), -(200), and -(220), respectively. The (*) mark represents XRD patterns of Nb-TiO₂ nanosized supports. This means that Nb-TiO₂ supports were interpreted dominant rutile crystal structure of TiO₂. On the other hand, in Figure 6(b), the peaks of Pt-Ru nanoparticles

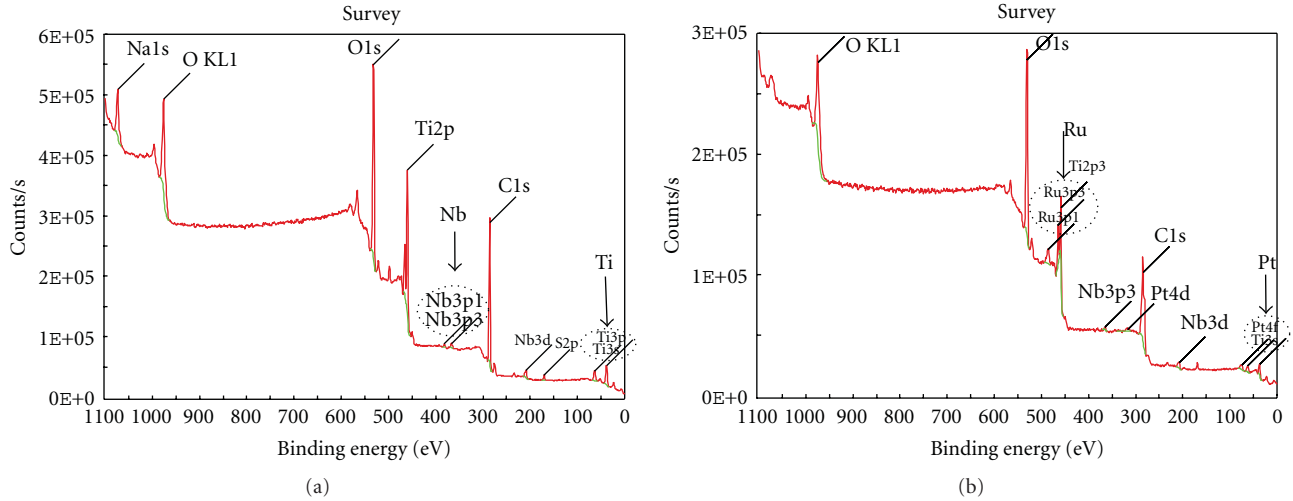


FIGURE 5: X-ray photoelectron spectroscopy (XPS) spectra of the PS/Nb-TiO₂ (a) and Pt-Ru@Nb-TiO₂-H (b) prepared by method 2.

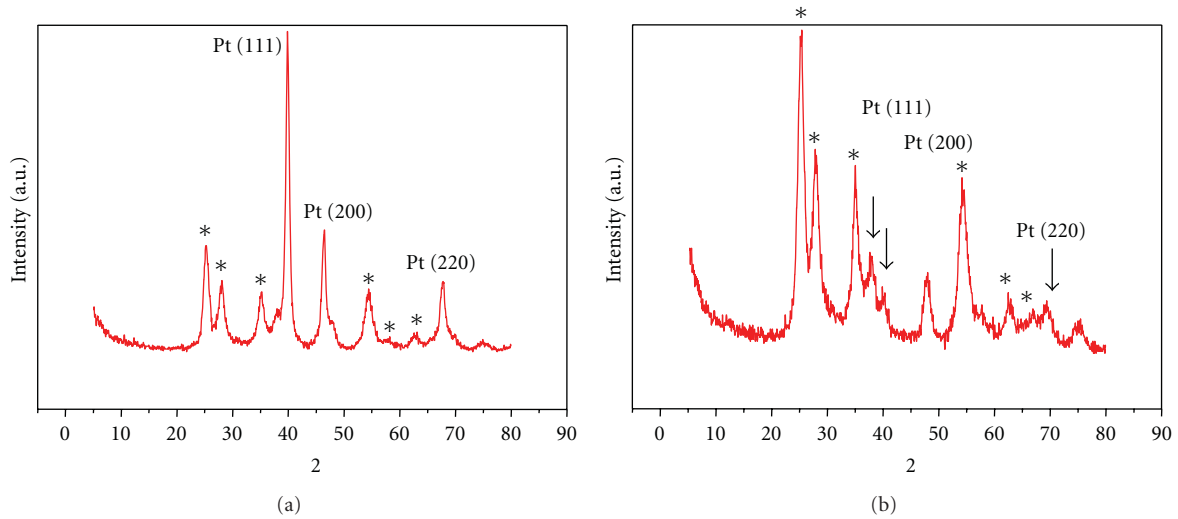


FIGURE 6: X-ray diffraction patterns of Pt-Ru@Nb-TiO₂-H catalyst prepared by Method 1 (a) and by Method 2 (b). The (*) marked represents XRD patterns of Nb-TiO₂ nanosized support.

on Pt-Ru@Nb-TiO₂-H catalysts shows very broad patterns compared to that of Pt-Ru nanoparticle on Pt-Ru@Nb-TiO₂-H catalysts prepared by chemical reduction. The size of Pt-Ru nanoparticle was very small compared to that of Pt-Ru@Nb-TiO₂ catalyst prepared by chemical reduction.

Table 1 presents the contents (wt-%) of Pt and Ru element in the Pt-Ru@Nb-TiO₂-H catalysts prepared by chemical reduction and γ -irradiation. When Pt-Ru alloy nanoparticles are deposited on Nb-TiO₂ supports, γ -irradiation generates slightly higher Pt content than that of Ru content, while chemical reduction produces significantly higher Ru content than that of Pt content. This may be due to the difference in the reduction potential of the two metal ions. The reduction potential of Pt ion, [(PtCl)₄]²⁻ (aq) + 2e⁻ → Pt(s) + 4Cl⁻ (aq), E⁰ = 0.73 V], is higher than that of Ru ion. In chemical reduction, a metal ion is reduced by accepting an electron from a reducing agent. On the other hand, when the

TABLE 1: Contents of the containing elements in Pt-Ru@Nb-TiO₂-H prepared by Method 1 and 2 analyzed by ICP.

Sample name	Contents (wt-%)			
	Nb	Pt	Ru	TiO ₂
Pt-Ru@Nb-TiO ₂ -H (Method 1)	2.80	0.98	6.44	40.6
Pt-Ru@Nb-TiO ₂ -H (Method 2)	2.78	14.4	9.40	39.4

Pt-Ru alloy nanoparticle is deposited on Nb-TiO₂ support by γ -irradiation irradiation, the hydrated electron (e_{aq}⁻) is generated in aqueous solution. This hydrated electron may hold lower reduction potential, so the Pt ions are quickly reduced to that of Ru ions. The hydrated electron

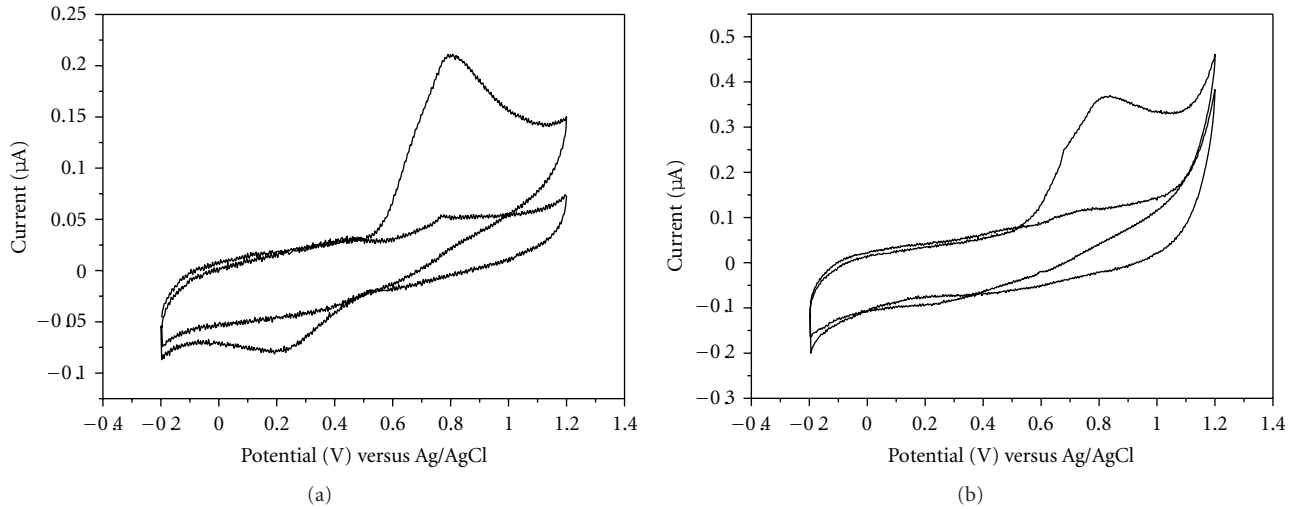


FIGURE 7: CO stripping voltammograms recorded in 0.5 M H_2SO_4 for Pt-Ru@Nb-TiO₂-H catalyst prepared by Method 1 (a) and Method 2 (b).

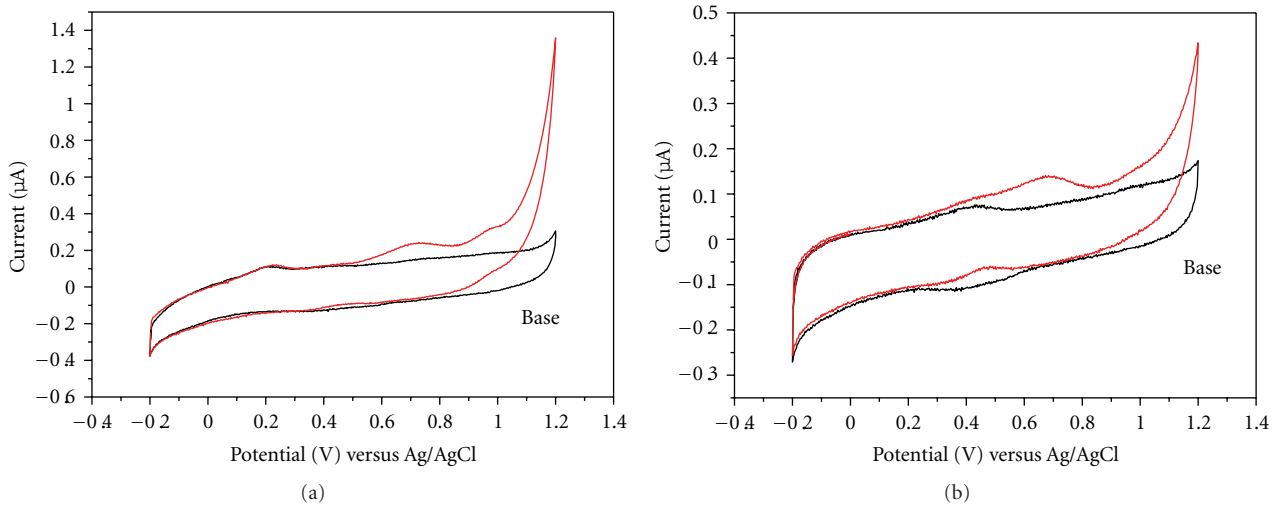


FIGURE 8: CV curves recorded in 0.5 M H_2SO_4 to 1.0 M MeOH oxidation for Pt-Ru@Nb-TiO₂-H catalysts prepared by Method 1 (a) and Method 2 (b).

produced in aqueous solution affects the yield of Pt-Ru alloy nanoparticles.

3.2. Electrocatalytic Efficiency of CO, MeOH, and EtOH Oxidation on the Surface of Pt-Ru Nanoparticles on Nb-TiO₂-H Supports. The efficiency of these catalysts toward the electrochemical oxidation of carbon monoxide (CO) was tested. Figure 7 presents the cyclic voltammograms (CVs) of electro-oxidation of CO oxidation on the Pt-Ru@Nb-TiO₂-H catalyst electrodes. Peak of stripping CO could be seen at 0.8 V for the Pt-Ru@Nb-TiO₂-H catalyst electrodes prepared by chemical reduction (a) and γ -irradiation (b). These peaks signify that CO oxidation is energetically favorable at these electrodes. The electrochemically active specific area (SEAS) of the catalysts was calculated by using the charges deduced from the CV of CO adsorption and desorption electro-

oxidation process, and using the following equation [7]

$$\text{SEAS} = \frac{Q_{\text{CO}}}{G} \times 420, \quad (2)$$

where Q_{CO} is the charge for CO desorption electro-oxidation in microcoulomb (μC), G represents the summation of Pt + Ru metal loading (μg) on the electrode, and 420 is the charge required to oxidize a monolayer of CO on the catalysts in $\mu\text{C cm}^{-2}$. The electrochemical SEASs are 58 and $36 \text{ m}^2 \text{ g}^{-1}$ for the Pt-Ru@Nb-TiO₂-H catalyst prepared by chemical reduction (a) and γ -irradiation (b), respectively. It may be considered that the higher SEAS for Pt-Ru@Nb-TiO₂-H catalyst is obtained due to the smaller particle size, even distribution, and the large loading of Pt-Ru alloy nanoparticles on the surface of Nb-TiO₂ supports.

Figure 8 presents the CVs recorded at the Pt-Ru@Nb-TiO₂-H catalyst electrodes for electro-oxidation of methanol

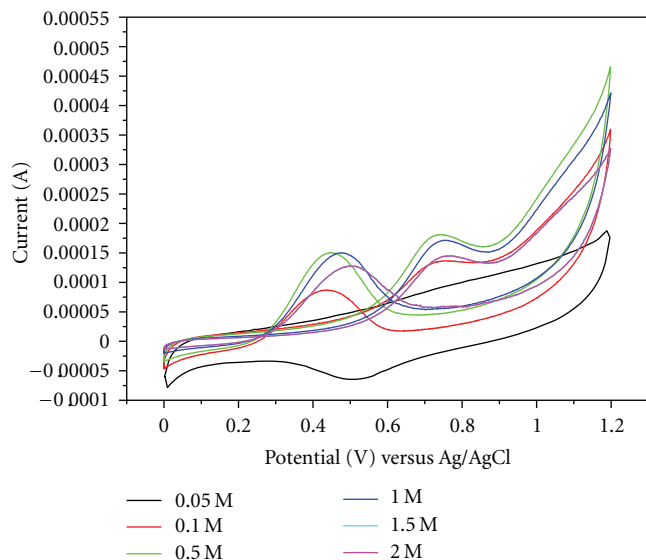


FIGURE 9: CV curves recorded in 0.5 M H_2SO_4 to EtOH oxidation for Pt-Ru@Nb-TiO₂-H catalysts.

in 0.5 M H_2SO_4 . The peak current values at 0.7 V (versus Ag/AgCl) corresponding to the oxidation of methanol shows variation between the catalysts prepared by different routes. A larger peak current was noticed at 0.7 V (versus Ag/AgCl) for the Pt-Ru@Nb-TiO₂-H catalyst prepared by γ -irradiation (Figure 8(b)). We conclude that a higher content of Pt (wt%) in Pt-Ru@Nb-TiO₂-H catalysts (γ -irradiation) determines the catalytic efficiency towards methanol oxidation. However, as one can see in Figure 3(c), the TiO₂ supports was destroyed during γ -irradiation. Therefore, the chemical reduction assisted with ultrasonic irradiation for the deposition of Pt-Ru nanoparticles onto Nb-TiO₂ supports was better than that of γ -irradiation method as stability of metal oxide supports.

Figure 9 shows the CVs for EtOH oxidation with various concentrations onto the surface of Pt-Ru nanoparticles deposited with Nb-TiO₂ supports in 0.5 M H_2SO_4 electrolyte. The peak current values at 0.8 V (versus Ag/AgCl) corresponding to the oxidation of ethanol. The maximum catalytic efficiency was appeared in 0.5 M EtOH concentration. As a result, the prepared Pt-Ru nanoparticles onto metal oxide supports can be used in fuel cell anode electrode.

4. Conclusion

This study describes the preparation of Pt-Ru@Nb-TiO₂-H catalysts by chemical reduction assisted with ultrasonic irradiation and γ -irradiation for fuel cell anode electrode. The conclusion was as follows.

- (1) The Pt-Ru@Nb-TiO₂-H catalyst was successfully prepared by chemical reduction assisted with ultrasonic irradiation and γ -irradiation.

- (2) The size, morphology, and composition of Pt-Ru@Nb-TiO₂-H catalysts were determined via TEM, XRD, and elemental analysis.
- (3) The Pt-Ru@TiO₂-H electrodes showed the high electrocatalytic activity for electro-oxidation of CO, MeOH, and EtOH. As a result, the catalyst prepared by chemical reduction assisted with ultrasonic irradiation can be used in a fuel cell electrode.

Acknowledgments

This research was supported by the Nano R&D program through the Korea Science and Engineering Foundation funded by the Ministry of Science and Technology. In particular, the authors would like to thank the Korea Basic Science Institute (KBSI) for FETEM measurements.

References

- [1] Z. Liu, L. M. Gan, L. Hong, W. Chen, and J. Y. Lee, "Carbon-supported Pt nanoparticles as catalysts for proton exchange membrane fuel cells," *Journal of Power Sources*, vol. 139, no. 1-2, pp. 73-78, 2005.
- [2] G. Chai, S. B. Yoon, S. Kang et al., "Ordered uniform porous carbons as a catalyst support in a direct methanol fuel cell," *Electrochimica Acta*, vol. 50, no. 2-3, pp. 823-826, 2004.
- [3] D. F. Silva, A. O. Neto, E. S. Pino, M. Linardi, and E. V. Spinacé, "PtRu/C electrocatalysts prepared using γ -irradiation," *Journal of Power Sources*, vol. 170, no. 2, pp. 303-307, 2007.
- [4] W. Chen, J. Y. Lee, and Z. Liu, "Preparation of Pt and PtRu nanoparticles supported on carbon nanotubes by microwave-assisted heating polyol process," *Materials Letters*, vol. 58, no. 25, pp. 3166-3169, 2004.
- [5] K. W. Park, Y. E. Sung, S. Han, Y. Yun, and T. Hyeon, "Origin of the enhanced catalytic activity of carbon nanocoil-supported PtRu alloy electrocatalysts," *Journal of Physical Chemistry B*, vol. 108, no. 3, pp. 939-944, 2004.
- [6] Z. Liu, J. Y. Lee, W. Chen, M. Han, and L. M. Gan, "Physical and electrochemical characterizations of microwave-assisted polyol preparation of carbon-supported PtRu nanoparticles," *Langmuir*, vol. 20, no. 1, pp. 181-187, 2004.
- [7] K.-D. Seo, S.-D. Oh, S.-H. Choi, S.-H. Kim, H. G. Park, and Y. P. Zhang, "Radiolytic loading of the Pt-Ru nanoparticles onto the porous carbons," *Colloids and Surfaces A*, vol. 313-314, pp. 393-397, 2008.
- [8] H.-B. Bae, J.-H. Ryu, B.-S. Byun, S.-H. Choi, S.-H. Kim, and C.-G. Hwang, "Radiolytic deposition of Pt-Ru catalysts on the conductive polymer coated MWNT and their catalytic efficiency for CO and MeOH," *Advanced Materials Research*, vol. 47-50, pp. 1478-1481, 2008.
- [9] H. Chhina, S. Campbell, and O. Kesler, "An oxidation-resistant indium tin oxide catalyst support for proton exchange membrane fuel cells," *Journal of Power Sources*, vol. 161, no. 2, pp. 893-900, 2006.
- [10] N. Zheng and G. D. Stuck, "A general synthetic strategy for oxide-supported metal nanoparticle catalysts," *Journal of the American Chemical Society*, vol. 128, no. 44, pp. 14278-14280, 2006.
- [11] H. Einaga and M. Harada, "Photochemical preparation of poly(N-vinyl-2-pyrrolidone)-stabilized platinum colloids and their deposition on titanium dioxide," *Langmuir*, vol. 21, no. 6, pp. 2578-2584, 2005.

- [12] M. Hepel, I. Kumarihamy, and C. J. Zhong, "Nanoporous TiO₂-supported bimetallic catalysts for methanol oxidation in acidic media," *Electrochemistry Communications*, vol. 8, no. 9, pp. 1439–1444, 2006.
- [13] J. H. Pan, X. W. Zhang, A. J. Du, D. D. Sun, and J. O. Leckie, "Self-etching reconstruction of hierarchically mesoporous F-TiO₂ hollow microspherical photocatalyst for concurrent membrane water purifications," *Journal of the American Chemical Society*, vol. 130, no. 34, pp. 11256–11257, 2008.
- [14] H. J. Koo, Y. J. Kim, Y. H. Lee, W. I. Lee, K. Kim, and N.-G. Park, "Nano-embossed hollow spherical TiO₂ as bifunctional material for high-efficiency dye-sensitized solar cells," *Advanced Materials*, vol. 20, no. 1, pp. 195–199, 2008.
- [15] S. S. K. Kamal, P. K. Sahoo, M. Premkumar et al., "Synthesis of cobalt nanoparticles by a modified polyol process using cobalt hydrazine complex," *Journal of Alloys and Compounds*, vol. 474, no. 1-2, pp. 214–218, 2009.
- [16] J. G. Yu, W. Liu, and H. G. Yu, "A one-pot approach to hierarchically nanoporous titania hollow microspheres with high photocatalytic activity," *Crystal Growth and Design*, vol. 8, no. 3, pp. 930–934, 2008.
- [17] Y. Wang, F. B. Su, J. Y. Lee, and X. S. Zhao, "Crystalline carbon hollow spheres, crystalline carbon-SnO₂ hollow spheres, and crystalline SnO₂ hollow spheres: synthesis and performance in reversible Li-ion storage," *Chemistry of Materials*, vol. 18, no. 5, pp. 1347–1353, 2006.
- [18] J. Chen, S. R. Bare, and T. E. Mallouk, "Development of supported bifunctional electrocatalysts for unitized regenerative fuel cells," *Journal of the Electrochemical Society*, vol. 149, no. 8, pp. A1092–A1099, 2002.
- [19] S.-D. Oh, B.-S. Byun, S. Lee, and S.-H. Choi, "Preparation of Ag-PS and Ag-PSS particles by γ -irradiation and their antimicrobial efficiency against *Staphylococcus aureus* ATCC 6538 and *Klebsiella pneumonia* ATCC 4352," *Macromolecular Research*, vol. 14, no. 2, pp. 194–198, 2006.

Research Article

ZnO Nanowire Formation by Two-Step Deposition Method Using Energy-Controlled Hollow-Type Magnetron RF Plasma

Hideki Ono and Satoru Iizuka

Department of Electrical Engineering, Graduate School of Engineering, Tohoku University, Miyagi, Sendai 980-8579, Japan

Correspondence should be addressed to Satoru Iizuka, iizuka@ecei.tohoku.ac.jp

Received 14 June 2011; Accepted 16 September 2011

Academic Editor: Renzhi Ma

Copyright © 2011 H. Ono and S. Iizuka. This is an open access article distributed under the Creative Commons Attribution License, which permits unrestricted use, distribution, and reproduction in any medium, provided the original work is properly cited.

ZnO nanowire was produced in RF (radio frequency) discharge plasma. We employed here a two-step deposition technique. In the 1st step, zinc atoms were sputtered from a zinc target to create zinc nuclei on a substrate before the growth of ZnO nanostructure. Here, we used pure argon plasma for physical sputtering. In the 2nd step, we employed an oxygen discharge mixed with argon, where oxygen radicals reacted with zinc nuclei to form ZnO nanostructures. Experimental parameters such as gas flow ratio and target bias voltage were controlled in O₂/Ar plasma. Properties of the depositions were analysed by SEM and Raman spectroscopy. We found that many folded and bundled nanowires formed in the 2nd step. The diameter of wires was typically 10–100 nm. We also discussed a growth mechanism of ZnO nanowires.

1. Introduction

ZnO is an oxide semiconductor with a wide band gap of 3.37 eV at room temperature and has a large exciton binding energy of 60 meV in comparison with GaN [1–3]. Therefore, ZnO was expected to develop a light emitting device, especially for a blue-light emission diode, instead of GaN.

ZnO nanostructures such as nanowires and nanorods are expected to make nanophotonic devices [4]. ZnO nanowires and nanorods have been believed to grow via vapour-liquid-solid (VLS) process [5, 6]. However, several other techniques for the growth have been reported. For example, molecular beam epitaxy (MBE) and pulsed-laser deposition (PLD) are generally employed for the growth processes of ZnO thin layers. These techniques take an advantage for the formation of high-quality ZnO crystals. Metal organic chemical vapour deposition (MOCVD) process is also one of the remarkable processes nowadays [7, 8].

Here, the growth process of ZnO by a plasma processing was studied. This is superior to the other processes for low-temperature and large-area deposition. Moreover, when we control the energy of plasma, we would make ZnO thin films

or ZnO nanoparticle, selectively. However, very few studies referred to the energy-controlled plasma.

In this study, we investigated how zinc, sputtered from a zinc target, reacted with oxygen in O₂/Ar plasma when discharge parameters such as gas pressure, gas flow ratio, and target bias voltage were changed. We employed a two-step deposition technique for the formation of ZnO nanostructures. In the 1st step, zinc atoms were sputtered from a zinc target to create zinc nuclei for the base of ZnO nanostructure growth. Here, we used pure argon plasma for physical sputtering. In the 2nd step, we employed an oxygen discharge with argon, where oxygen radical reacted with zinc nuclei on a substrate to form ZnO nanostructures. Dependence on the deposition time was investigated in O₂/Ar plasma.

2. Experimental Setup

Experimental apparatus [9, 10] is schematically shown in Figure 1. Plasma was generated by a hollow-type magnetron (HTM) RF plasma source at frequency of 13.56 MHz [11, 12]. The HTM consists of powered electrode made of stainless cylinder of 4.8 cm in diameter and 5.5 cm height,

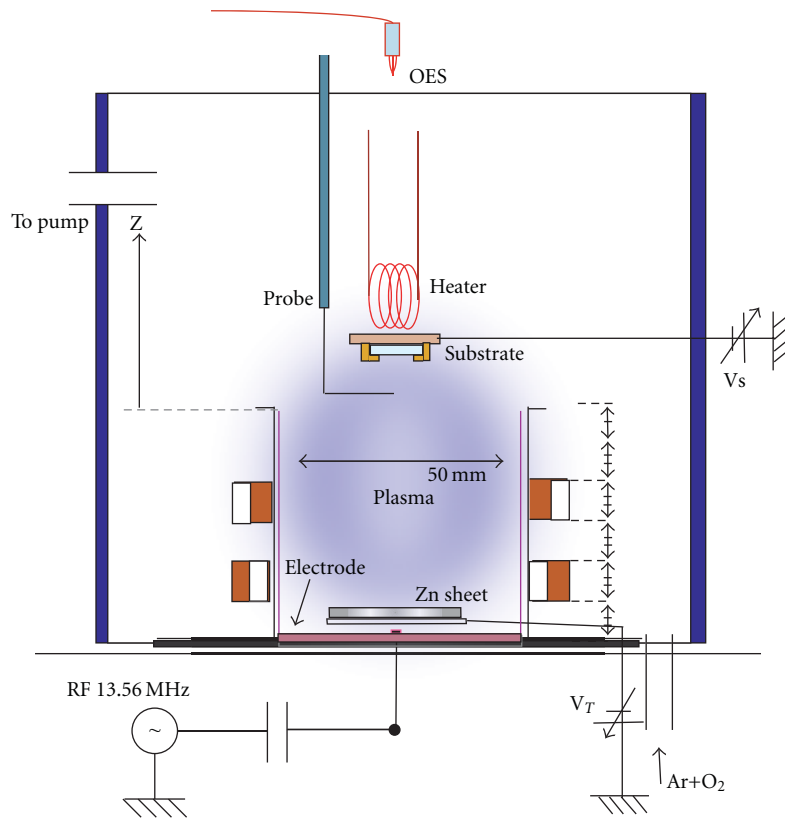


FIGURE 1: Experimental apparatus.

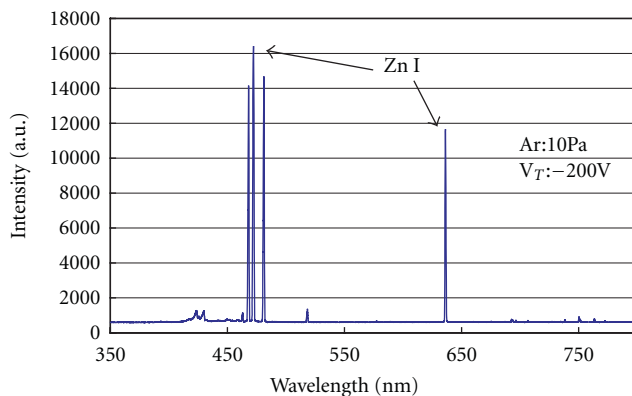


FIGURE 2: Typical optical emission spectrum.

which is covered by a grounded stainless steel cylinder of 5.2 cm diameter and 6.0 cm height. Furthermore, two magnet rings are wound around outside of a grounded cylinder with spacing of 2 cm to confine the plasma and to prevent the electrode from sputtering by deep self-bias voltage.

A zinc target was set on a bottom plate. Target DC bias voltage V_T controlled the Zn sputtering. We can change gas pressure ratio O_2/Ar and target DC voltage V_T . In this experiment a grid used for the electron temperature control was removed. Plasma parameters were measured by a Langmuir probe. Wavelength of optical emission from the

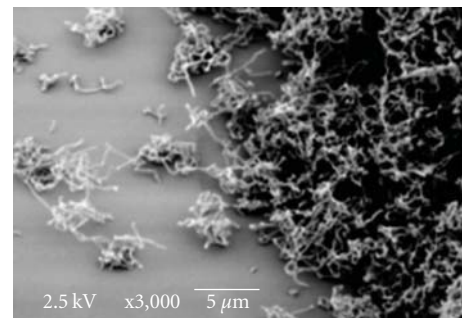


FIGURE 3: Typical SEM image of nanowires.

plasma was measured by a spectroscope (OES). Substrate was fixed at 2.5 cm above the top of the electrode. Deposition of ZnO on the substrate was estimated by scanning electron microscope (SEM) and Raman spectroscopy.

3. Experimental Results

3.1. Growth of ZnO Nanowires. Blue-light emission from Zn neutrals produced in the plasma was found to be one of the most important factors for a deposition of ZnO nanowires. Typical spectrum of the optical emission is shown in Figure 2. The spectrum can be characterized by a strong blue emission line of zinc neutral around 460 nm. However, the blue-light emission diminished drastically when O_2 gas

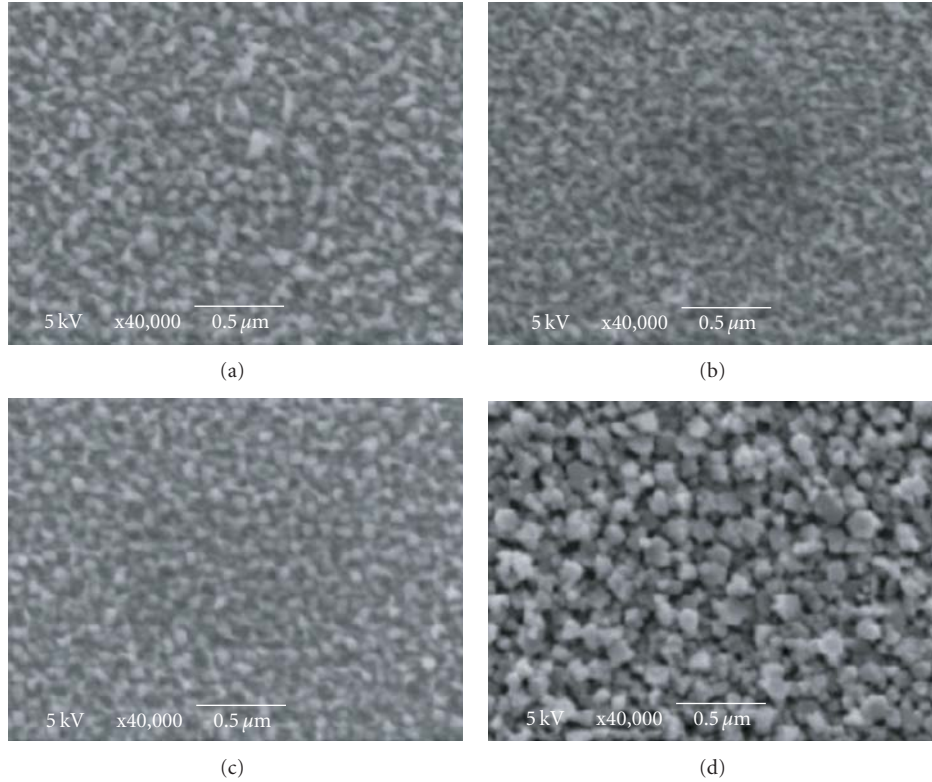


FIGURE 4: SEM images with deposition time T_{ZnO} as a parameter in case of $T_{\text{Zn}} = 60$ s: $T_{\text{ZnO}} =$ (a) 0 s, (b) 60 s, (c) 300 s, and (d) 600 s.

was slightly mixed with Ar. This phenomenon markedly influenced ZnO deposition. In case of weak blue-light emission, we could not detect materials consisting of ZnO nanowires on the substrate.

In case of simultaneous processing with Zn sputtering and its oxidization by using a mixed gas of O_2 and Ar, we clearly observed a formation of nanowires. After turning on the plasma with blue-light emission, the substrate was inserted into the plasma for the deposition of ZnO. Deposition period was varied in a range 10–600 sec. Typical SEM image of the materials deposited under strong blue-light emission is shown in Figure 3. We found many folded nanowires bundled on the substrate. The diameter of wires was of the order of 100 nm. From Raman spectroscopy, we found that these wires consisted of ZnO.

Almost all nanowires were bent and twisted complicatedly as shown in Figure 3. The structure was in principle one dimensional, but the shape was complicated, which might be preferably available for an increment of effective surface area of ZnO materials. Total surface area could be much larger than that of flat and smooth ZnO surface. However, from a viewpoint of practical application in industries, it would be better for these nanowires to grow straight in one direction on the substrate. One-dimensionally grown nanowires will make it easy to produce an electronic device like PN junction for blue-light emission. Therefore, we intended to investigate the mechanism by which nanowires were bundled on the substrate. In order to clarify the growth process the deposition period was varied under various conditions.

3.2. Dependence on Deposition Time. We tried first to examine initial growth process of ZnO nanowires. From a comparison with Raman spectrum, we confirmed that Zn stacked up first on the substrate to form thin Zn layer, then oxygen reacted with zinc to construct nanowires. Thickness of Zn layer was an important factor for ZnO nanowire growth. If Zn layer was too thin, for example, we could not obtain nanowires. Even when oxygen reacted with Zn, the reaction could not result in construction of nanowires. So, next we tried to find out a dependence of the growth of ZnO nanowires on the thickness of Zn layer deposited initially.

Therefore, for this reason, we separated processing procedures, that is, Zn deposition process and its oxidization process. So, the deposition period T_{Zn} for Zn layer formation was separated from the period T_{ZnO} for oxygen reaction. We can control reaction time of oxygen, independently. Then, we would find a mechanism of the growth of ZnO nanowires.

In the experiments we fixed RF power at 100 W and substrate temperature at 150°C . In the deposition period of Zn layer (1st period) Ar gas pressure was fixed at 10 Pa. No oxygen gas was fed in, and the target bias voltage was fixed at -200 V for zinc sputtering. In the oxygen reaction period (2nd period), however, Ar gas pressure was fixed at 9.5 Pa under fixed O_2 gas pressure at 0.5 Pa. No target bias voltage was applied in this case. The 1st period T_{Zn} was varied in a range of 5–600 sec, and the 2nd period T_{ZnO} was varied in a range of 0–600 sec.

When the deposition period of Zn is short ($T_{\text{Zn}} = 60$ s), thin film including only Zn was generated on the substrate, instead of ZnO nanowires. Figure 4(a) shows a typical SEM

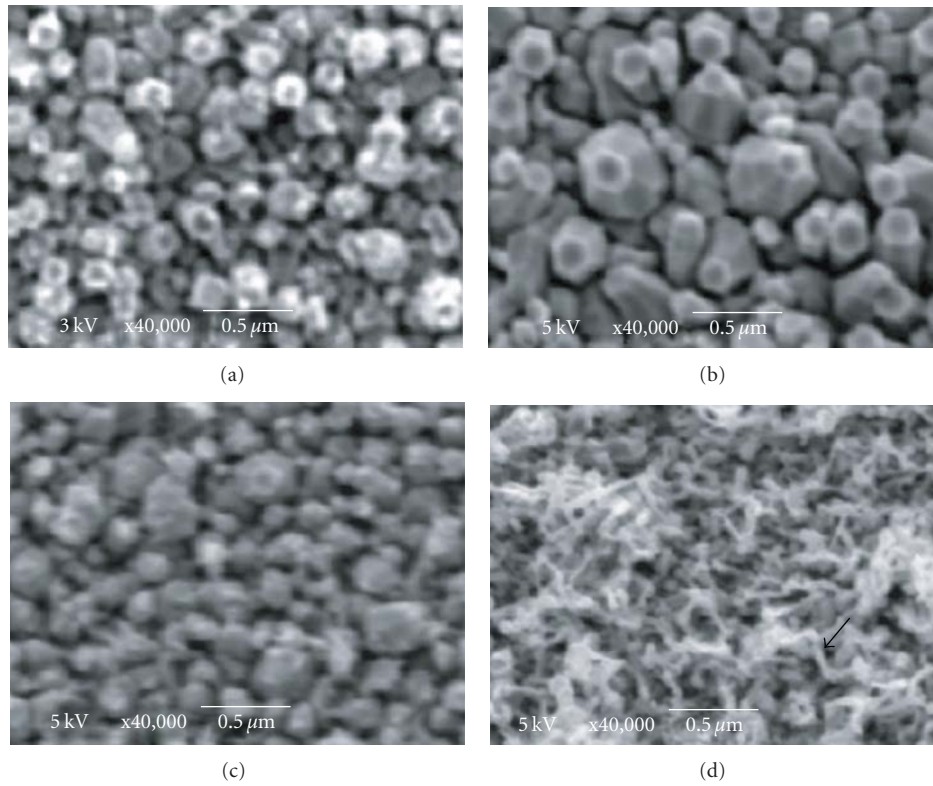


FIGURE 5: SEM images with deposition time T_{ZnO} as a parameter in case of $T_{\text{Zn}} = 300$ s: $T_{\text{ZnO}} =$ (a) 0 s, (b) 30 s, (c) 60 s, and (d) 90 s. The nanowire is pointed by arrow in (d).

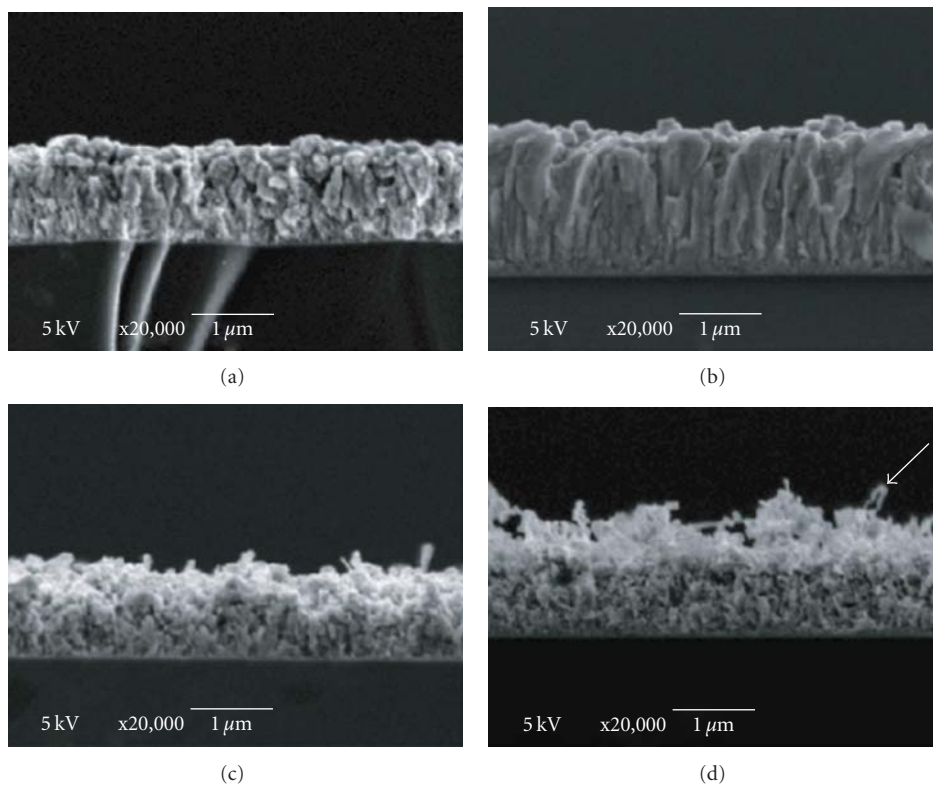


FIGURE 6: SEM images of cross-section with deposition time T_{ZnO} as a parameter in case of $T_{\text{Zn}} = 300$ s: $T_{\text{ZnO}} =$ (a) 0 s, (b) 30 s, (c) 60 s, and (d) 90 s. The nanowire is pointed by arrow in (d).

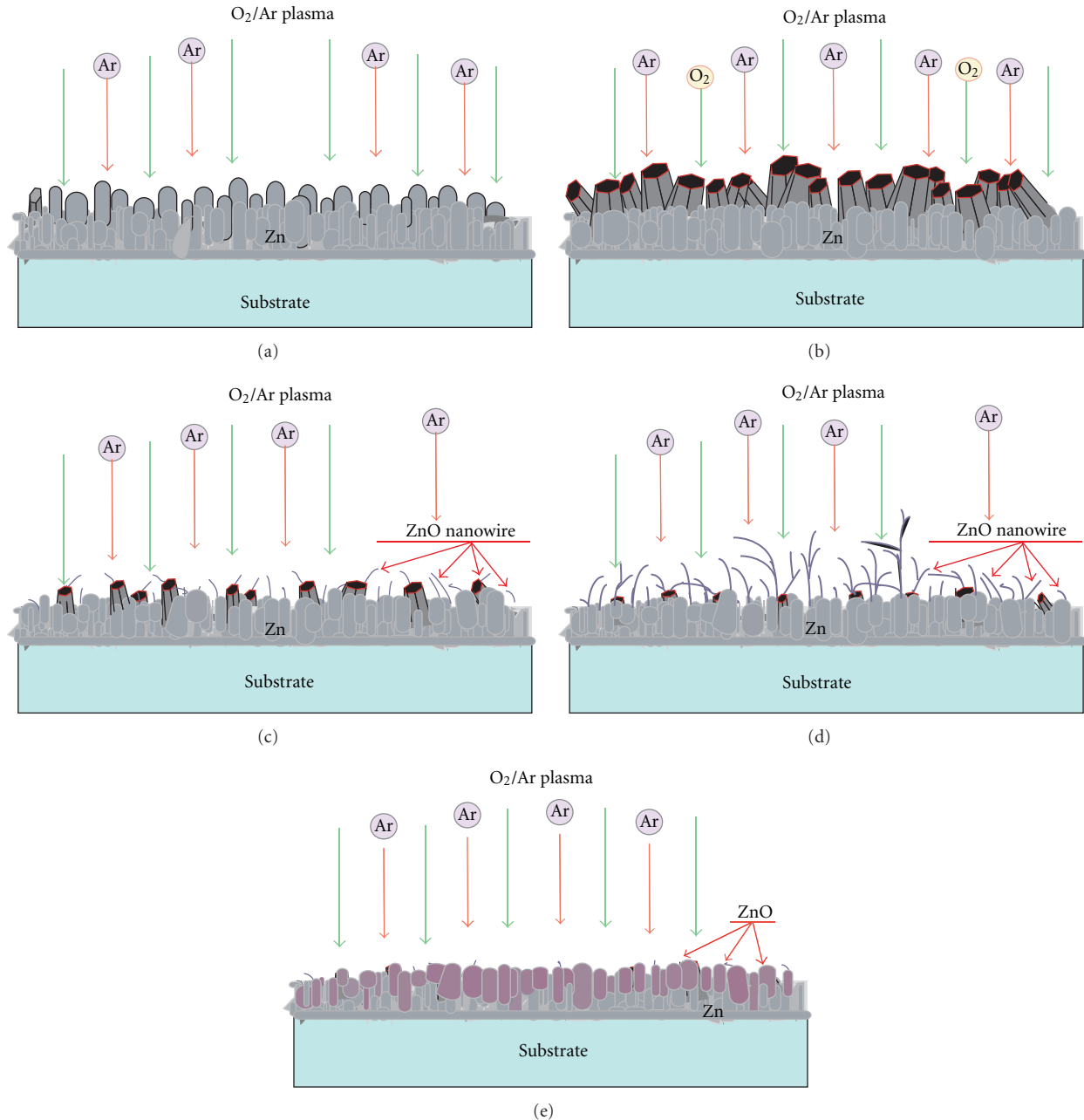


FIGURE 7: Growth model of ZnO nanowires in case of Figure 5. (a) Irregular surface of Zn layer with particulate and pillar-like structures is formed in the 1st step. (b) Particulate and pillar-like structures are changed to hexagonal pillars, growing with time, by oxidation in the 2nd step. (c) Then, the hexagonal pillars start shrinking by Ar ion sputtering, which triggers a start of ZnO nanowire growth. (d) ZnO nanowires grow and bend in the presence of Ar ion bombardment. (e) The nanowire growth stops and decays with time by the ion sputtering, and finally smooth surface of ZnO layer comes out.

image taken from the top of the substrate after deposition period of $T_{Zn} = 60$ s. From a detailed observation, we confirmed that the layer consisted of many small-size zinc particles. The size was 50–100 nm, and the particles were distributed almost randomly on the surface.

In the 2nd period we introduced oxygen to oxidize the surface of Zn particles and oxygen reaction period T_{ZnO} was varied. Then, thin layer including ZnO was generated on the top of Zn particles, as shown in Figures 4(b) and

4(c), where we found many small pillows. After oxidation period of 600 s, that is, $T_{ZnO} = 600$ s, many pillars changed their shape to something like hexagon pillars, as shown in Figure 4(d). These pillars grew in time and were distributed on the surface of the substrate. These pillars seem to grow from the bottom of the deposited Zn particles. The hexagonal structure indicates that these were consisting of ZnO crystal [13]. Increasing oxidation period the shape of hexagon structure gradually disappeared, and more smooth structure

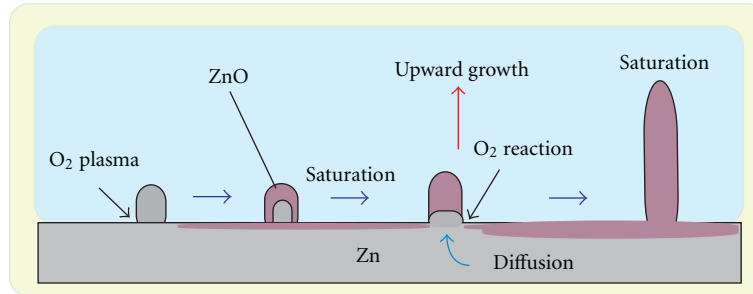


FIGURE 8: Growth model of ZnO nanowires, corresponding to the phase (c) in Figure 7. Zn pillar of small size, formed initially on Zn thin film, is oxidized from its surface. Crystallization of ZnO occurs first at the tip of the pillar, and excess oxygen extracts Zn from the Zn layer. Then, ZnO nanowire extends upward, being accompanied with the Zn supply from the Zn layer. Finally, the growth of ZnO nanowire is completed because of a limit of Zn diffusion from the Zn layer.

came out, eventually. The size was also gradually decreased by the effect of Ar sputtering. We could not observe nanowire formation in this case.

We have checked similar oxidization in case of $T_{Zn} = 300$ s. Figure 5 shows SEM images for the case of $T_{Zn} = 300$ s. As shown in Figure 5(a), we clearly found many pillars after the deposition of Zn layer. The pillars grew in length and in diameter, and the cross-section of the top turned to a hexagonal structure as shown in Figure 5(b). However, then, the shape was gradually changed and more smaller hexagon pillars were generated as shown in Figure 5(c). The size was decreased to about 50–100 nm and the shape was changed to something like a pillar again. Then, finally, further oxidization caused an evolution of thin nanowires, growing from the dwindled hexagon pillars, as shown by the arrow in Figure 5(d). We find clearly characteristic structures of ZnO nanowires, though the hexagon pillars shrink simultaneously by the effect of oxidization and Ar sputtering. The condition for the growth of nanowires seemed to correspond to a production of smaller size structure like shrunken hexagon pillars.

Since no additional Zn was supplied from the plasma, the growth of nanowires came to an end finally. Therefore, the diameter of wires remained thin compared with that in Figure 3. After further oxidization such nanowires were almost completely removed by Ar sputtering and only homogeneous thin film of ZnO was left instead of the nanowires.

Figure 6 shows cross sectional view of deposited layers in case of $T_{Zn} = 300$ s. The growth of nanowires was found in Figures 6(c) and 6(d). In case of initial growth, most of the wires looked straight as one-dimensional needles, as shown in Figure 6(c). However, the direction of the growth was quite random because of an irregularity of the background zinc layers. With increasing the length, the wires had a tendency to bend, as shown by the arrow in Figure 6(d). This might be due to a stoichiometric unbalance between Zn and O. Therefore, the crystallization was not enough in this growth phase.

4. Discussion

Formation process of ZnO nanowires was studied by using two-step deposition technique. The growth processes were

schematically shown in Figure 7. In the 1st step, only Zn layers were deposited as shown in Figure 7(a). The shape of Zn layer was something like particulates and pillars. In the 2nd period, though no additional zinc was supplied on the substrate, growth of ZnO nanowires took place. This means that oxygen could be taken into Zn layer to provide oxidization layer near the surface.

The shape of deposited zinc surface was changed to hexagonal pillar, which had grown in time, as shown in Figure 7(b). In this case the pillars might consist of crystallized ZnO. The shape of this structure was straight with no bending component. We could not observe nanowires at this moment. The beginning time of nanowire growth seemed to be related with the initial size of hexagonal pillars. Though ZnO pillars grew first, they finally shrunk due to Ar sputtering. So, the size of pillars diminished in time (Figure 7(c)). The start point of nanowire growth was related with this timing. As the size was reduced, the growth of ZnO nanowires started as shown in Figures 7(c) and 7(d). However, after further oxidization, the nanowire growth stopped and decayed in time. Finally, such nanowires were almost completely removed by Ar sputtering and smooth surface of ZnO layer came out (Figure 7(e)).

As another important mechanism, it should be pointed out that a supply of Zn took place from the bottom of nanowires. Ar ions impinging on the substrate could heat Zn surface to provide a liquid-solid state, in which Zn atoms could move and react with oxygen to form the structure of ZnO. Therefore, the growth point of ZnO should be the bottom end of nanowires as shown in Figure 8. Zn pillar of small size, formed initially on Zn thin film, was oxidized from its surface. Therefore, ZnO crystallization started first at the tip of the pillar. Since Zn could be supplied from the Zn layer to the region of excess oxygen, the crystallized part of ZnO extended upward as a form of nanowire, being accompanied with diffusion of Zn from the Zn layer. Finally, the growth of ZnO nanowire would be completed because of a limit of Zn diffusion. Initial zinc layer played as a kind of catalysis, which promoted not only the growth of ZnO hexagonal pillars but also the growth of ZnO nanowires. Two-step growth technique is quite important for investigating and controlling the growth of ZnO nanostructures.

In case of one-step growth by using a mixed gas of O_2 and Ar, typical spectrum of Raman shifts revealed that the intensity of ZnO signal clearly increased with deposition time. However, before and even during the growth of ZnO, we always observed another peak at 540 cm^{-1} , which always appeared in case of zinc deposition. This indicated that supply of Zn atom on the substrate dominated the supply of oxygen for ZnO production. In other words, the amount of oxygen radicals O^* might be lacked relatively. For this reason, nanowires contained not only ZnO component but also metallic Zn. The reason why the wires were bending would come from an irregularity in one-dimensional growth of ZnO crystal because of excess Zn supply during the growth.

5. Conclusions

Here, we employed a two-step deposition method for the formation of ZnO nanostructures. We separated the zinc deposition from its oxidization process, that is, the deposition period T_{Zn} for Zn layer formation was separated from the period T_{ZnO} for oxygen reaction. This method makes it possible to control the time of oxygen reaction.

By separating the period of ZnO nanowire formation from the period of Zn layer formation, we found ZnO nanowires grown in the 2nd step in O_2/Ar RF plasma. We found also that the size of Zn pillars formed in the 1st step was crucial for the nucleation and growth of ZnO nanowires in the 2nd step. A formation model of ZnO nanowires was proposed. We also observed a formation of thin homogeneous ZnO film, as a result of further oxidization, accompanied with Ar sputtering. The method proposed here would be useful for understanding the growth mechanism of ZnO nanostructures.

Acknowledgment

The work was supported by a Grant-in-Aid for Scientific Research from the Ministry of Education, Culture, Sports, Science and Technology, Japan.

References

- [1] K. Hüemmer, "Interband magnetoreflexion of ZnO," *Physica Status Solidi B*, vol. 56, no. 1, pp. 249–260, 1973.
- [2] A. Ohtomo, K. Tamura, M. Kawasaki et al., "Room-temperature stimulated emission of excitons in ZnO/(Mg, Zn)O superlattices," *Applied Physics Letters*, vol. 77, no. 14, Article ID 2204, 3 pages, 2000.
- [3] M. H. Huang, Y. Wu, H. Feick, N. Tran, E. Weber, and P. Yang, "Catalytic growth of zinc oxide nanowires by vapor transport," *Advanced Materials*, vol. 13, no. 2, pp. 113–116, 2001.
- [4] F. Patolsky, G. Zheng, and C. M. Lieber, "Nanowire sensors for medicine and the life sciences," *Nanomedicine*, vol. 1, no. 1, pp. 51–65, 2006.
- [5] R. S. Wagner and W. C. Ellis, "Vapor-liquid-solid mechanism of single crystal growth," *Applied Physics Letters*, vol. 4, no. 5, pp. 89–90, 1964.
- [6] A. M. Morales and C. M. Lieber, "A laser ablation method for the synthesis of crystalline semiconductor nanowires," *Science*, vol. 279, no. 5348, pp. 208–211, 1998.
- [7] X. Liu, X. Wu, H. Cao, and R. P. H. Chang, "Growth mechanism and properties of ZnO nanorods synthesized by plasma-enhanced chemical vapor deposition," *Journal of Applied Physics*, vol. 95, no. 6, pp. 3141–3147, 2004.
- [8] S. Choopun, H. Tabata, and T. Kawai, "Self-assembly ZnO nanorods by pulsed laser deposition under argon atmosphere," *Journal of Crystal Growth*, vol. 274, no. 1-2, pp. 167–172, 2005.
- [9] H. Ono and S. Iizuka, "Growth of ZnO nanowires in hollow-type magnetron O_2/Ar RF plasma," *Thin Solid Films*, vol. 518, no. 3, pp. 1016–1019, 2009.
- [10] K. Kumeta, H. Ono, and S. Iizuka, "Formation of ZnO nanostructures in energy-controlled hollow-type magnetron RF plasma," *Thin Solid Films*, vol. 518, no. 13, pp. 3522–3525, 2010.
- [11] J. Emi, K. Kato, T. Abe, and S. Iizuka, "Formation of nanoparticles by control of electron temperature in hollow-typed magnetron radio frequency CH_4/H_2 plasma," *Japanese Journal of Applied Physics*, vol. 45, no. 10, pp. 8071–8074, 2006.
- [12] J. Emi and S. Iizuka, "Characteristics of carbon-related materials deposited in electron-energy controlled CH_4/H_2 RF discharge plasmas," *Diamond and Related Materials*, vol. 20, no. 4, pp. 568–572, 2011.
- [13] K. Prabakar and H. Kim, "Growth control of ZnO nanorod density by sol-gel method," *Thin Solid Films*, vol. 518, no. 24, pp. e136–e138, 2010.

Research Article

Direct Deposition of Micron-Thick Aligned Ceramic TiO₂ Nanofibrous Film on FTOs by Double-Needle Electrospinning Using Air-Turbulence Shielded Disc Collector

T. Krishnamoorthy,^{1,2} V. Thavasi,² V. Akshara,³ A. Senthil Kumar,⁴ D. Pliszka,² S. G. Mhaisalkar,¹ and S. Ramakrishna^{2,4,5}

¹ School of Materials Science and Engineering, Nanyang Technological University, 50 Nanyang Avenue, Singapore 639798

² NUS Nanoscience and Nanotechnology Initiative (NUSNNI), Faculty of Engineering, National University of Singapore, Singapore 117576

³ Amity Institute of Nanotechnology, Amity University, Sector-125, Noida 201301, India

⁴ Department of Mechanical Engineering, National University of Singapore, Engineering Drive 3, Singapore 117576

⁵ King Saud University, Riyadh 11451, Saudi Arabia

Correspondence should be addressed to V. Thavasi, velnanotech@gmail.com

Received 30 June 2011; Accepted 22 August 2011

Academic Editor: Renzhi Ma

Copyright © 2011 T. Krishnamoorthy et al. This is an open access article distributed under the Creative Commons Attribution License, which permits unrestricted use, distribution, and reproduction in any medium, provided the original work is properly cited.

One-dimensional (1D) metal oxides, typically nanowires and nanorods, have unique electronic and optical properties due to quantum phenomena that find applications in modern energy and electronic devices. We present here the electrospinning method that produces the aligned TiO₂ nanofibres directly on the fluorine-doped tin oxide (FTO) substrates mounted rotating disc collector. The aligned TiO₂ ceramic nanofibres mat of 6 μm thickness is achieved in 4 h using a nonconductive enclosed-air-shield with air-hood design over the FTO mounted rotating disc collector. The aligned TiO₂ nanofibers are found to retain its integrity and binding on FTO surface even after sintering at 500°C. SIMON 8 modeling package is used to determine the behaviour of the charged polymer/TiO₂ jet when single and double needles are used for electrospinning process. The simulation study reveals that the repulsive force of the charged fibers from the double needle exerts stronger electric field distribution along the flow of stream that results in the reduction of the fibers diameter, which is about 28 nm than that of using single-needle system.

1. Introduction

Metal oxide semiconductors exhibit unique electronic and optical properties in its one-dimensional (1D) morphology as the self-organization of charges occurs in 1D form via interaction energy minimization. A highly ordered 1D nanostructure is preferred to enhance the performance of electronic and photonic devices. It has been reported that the ordered 1D nanostructure enabled for larger current generation by improving the charge separation and electron transport in polymers and oxides [1–4]. For example, the ordered nanostructure has improved the gas sensing property of ZnO compared to that of random structure [5]. Likewise, the orderly aligned SnO₂ nanoboxes have improved the electron transport [6]. Numerous methods such as electric

field directed assembly, flow-assisted alignment, selective chemical patterning, laser, photolithography [7], self-assembly [8–10], and Langmuir-Blodgett (LB) technique [11] have been explored to align the metal oxides and polymers.

Electrospinning is another competent technique that has also been employed to produce 1D polymers and metal oxides [12–16]. The simple electrospinning often produces intertangled nanofibres after deposition which could cause the insufficient exposure of the faces and edges of fibres. Furthermore, a film made by simple electrospinning contains random arrangement of fibres, with different length, which might impose poor reproducibility when prepared as electroactive layer. Alignment of materials as nanofibres creates greater compactness, and the aligned architecture could accommodate more quantity of material per unit area that

support for the miniaturisation of the electronic devices. The aligned nanofibres were successfully produced by researchers in electrospinning using the rotating disc as collector and at higher speed. However, available electrospinning methods are limited by their capability to produce aligned metal oxide nanofibers of higher thickness. For instance, the nano TiO_2 film should possess the thickness of 0.5–2.0 μm and 8–30 μm for solid state and liquid state dye sensitized solar cells (DSSC), respectively, because such thick film supports for significant electron diffusion [17–20]. In literatures, the maximum thickness of the aligned nanofibres obtained using electrospinning so far was only about 250 nm [21]. Hence, there is a great demand for the production of aligned metal oxide nanofibers with the higher thickness, in shorter time, and with good reproducibility. Aligning the nanofibers directly on the conductive fluorine-doped tin oxide (FTO) substrate for various applications such as optoelectronic and photovoltaics are preferred as such technique shortens two conventional steps in electrospinning: preparation of well-ordered fibres and the deposition of these fibres on FTO using doctor blade/or dip casting. However, currently available techniques impose major challenge due to complexity in the steps that convert the composite fibers into ceramic fibers. Sintering at 400–550°C, an important process that converts TiO_2 /polymer nanofibres into ceramic structure by bridging between the grains, is believed to enhance electron/charge carrier mobility in the film. The stress is developed on the nanofibers during sintering, and when exceeding the internal resistance of the nanofibers, the peeling-off FTO occurs. Therefore, in addition to the better alignment, the bondage of ceramic nanofibers onto the conductive substrate is critical for device applications.

In this work, the TiO_2 nanofibres have been produced and aligned directly on FTO using the modified electrospinning setup. A nonconductive air-shield has been introduced in electrospinning setup that facilitated for the production of micron thick ceramic TiO_2 nanofibres film. The method developed in this study can be extended to control the alignment and thickness in large scale for metal-oxide-based solar cells and sensors.

2. Experimental

The precursor for TiO_2 was prepared by dissolving 0.2 g of polyvinylpyrrolidone (PVP, MW of 1.6×10^6 g/mol) and 0.5 g of titanium tetra-isopropoxide (Aldrich) in 3.5 mL of ethanol (AR grade). 1 mL of acetic acid was added into the solution. The solution was then loaded into a plastic syringe equipped with a 27 1/2 gauge needle (Becton Dickson). The diameter of the rotating disc was 20 cm. To obtain more samples, six FTOs (1 mm-thick, Asahi Glass) with a sheet resistance of 15 Ω were mounted over the six plastic holders affixed using scotch tape on the edge of the disc at equal space (Figure 1). A small $1 \times 1 \text{ cm}^2$ of aluminium foil was attached such that it wrapped both the back of the holders and the top side of FTO. The conductive wire was hooked to the foil using double-side tape, which made FTO grounded. This allowed the nanofibres to be collected directly onto

TABLE 1: Effect of design modification in electrospinning.

Electrospinning	Design modification	Collection time (h)	Thickness of sintered aligned TiO_2 nanofibres (μm)
Single needle	Without shield	4	0.5
	Top-air-shield	4	1.5
	Enclosed-air-shield	4	4
	Enclosed-air-shield and air-hood	4	4
Double needle	Enclosed-air-shield and air-hood	4	6

the FTOs. The syringe pump flow rate of 0.2 mL/h was set up. A distance of 10 cm between the needle tip and the edge of rotating disc was set up, and the potential of 15 kV was applied between them. The speed of the rotating disc was held constant at 750 rpm for all the experiments. All the electrospinning experiments were performed at room temperature. A nonconductive block of size 24 cm \times 24 cm was designed and introduced as top-air-shield over the rotating disc collector (Figure 1(b)) and compared the effect of alignment and thickness of film obtained using the setup without any shield. For another study, an enclosed-air-shield (24 cm \times 24 cm) with the slit dimension of 22 cm \times 3.5 cm was fabricated and positioned as shown in Figure 1(c). For the third set of experiment, an air-hood of size (14 cm \times 3.5 cm) was affixed just behind the slit of the enclosed shield (Figures 1(d) and 1(e)).

3. Results and Discussion

Better the alignment of fibers is, the larger will be the quantity of materials per unit area as illustrated in Figure 2, which are beneficial for device applications. For example, dye adsorption on the nanosized TiO_2 is the critical factor in improving the performance because anchored dye molecules absorb more photons thus results in larger photocurrent. The aligned nanofibres architecture could improve the photon conversion efficiency and charge separation.

Figure 3(a) shows the SEM images of TiO_2 nanofibres obtained when rotating the disc at 750 rpm, but without air-shield. The average diameter of the green nanofibres (TiO_2 /PVP) was found to be 180 ± 20 nm. The collected nanofibres on each FTO substrate were first hot pressed at 120°C and for 15 min as a pretreatment to sintering. Then the samples were introduced for sintering in the tubular furnace at 500°C for 3 h with the ramp rate of 1°C/min and cooled down to 30°C with the rate of 1°C/min. The sintered TiO_2 nanofibres were observed to possess the diameter of 98 ± 20 nm. All the film thicknesses reported in this work are the measurement of the ceramic TiO_2 nanofibers after sintering (Table 1).

During electrospinning without air shield, it was observed that the majority of the TiO_2 /PVP nanofibres were

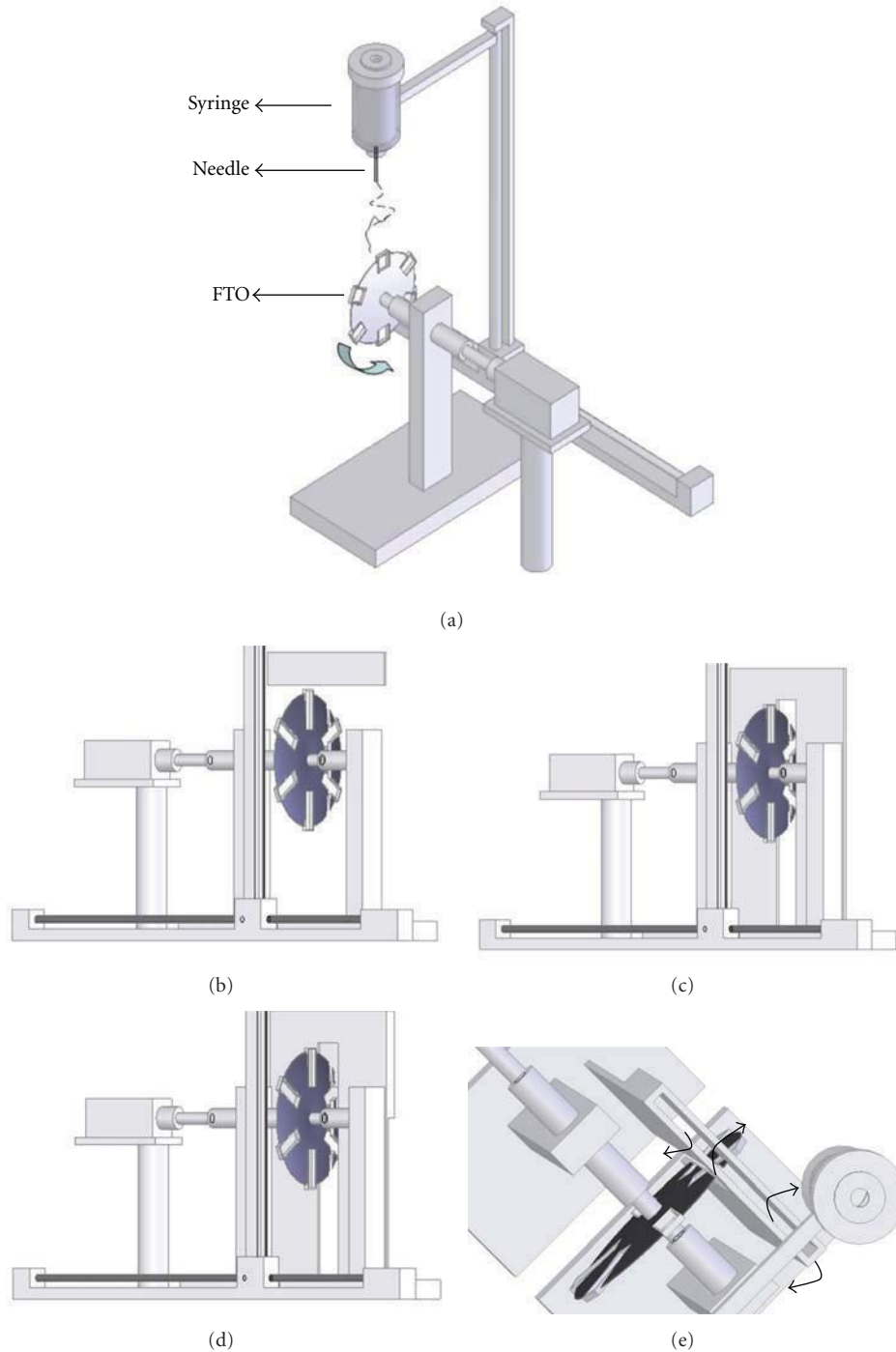


FIGURE 1: (a) Experimental setup of electrospinning. The metal oxide precursor is taken in a syringe. 1-mm-thick six FTOs are fixed on the holder mounted on rotating disc at equal space. The rotating disc of diameter 20 cm with (b) top-shield, (c) enclosed-air-shield, (d) enclosed-air-shield with air-hood (front view), and (e) air-hood arrangement (top view) for the turbulent air to escape.

flown away from the deposition area (FTO). This was due to the velocity of the rotating disk. Rotation at 750 rpm guided for better alignment of nanofibres; however, the disk at such speed generates the turbulent wind inward direction that carries the nanofibres away from the deposition area as the fibres were nano in size, which results in more wastage of

TiO₂, and also affects its alignment. This yielded the poor thickness of the collected aligned nanofibres for 4 h, which was about 500 nm.

The nanofibres shown in Figure 3(b) were collected at 750 rpm with top-air shield. With top-air-shield arrangement, the rate of nanofibres deposition was improved to

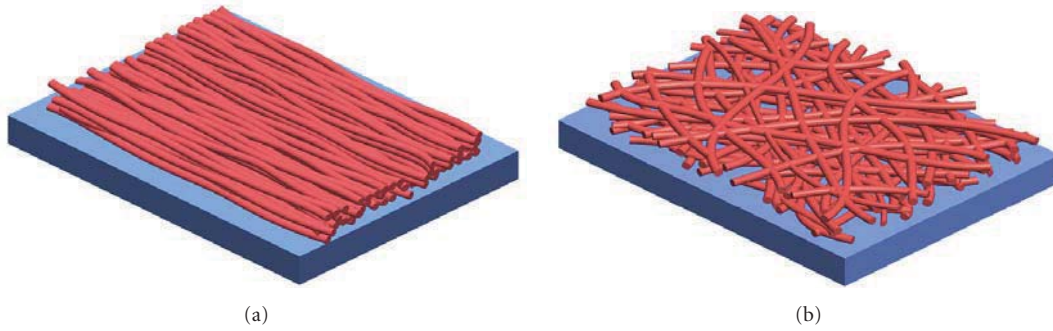


FIGURE 2: Schematic of (a) aligned TiO_2 nanofibres and (b) random TiO_2 fibres.

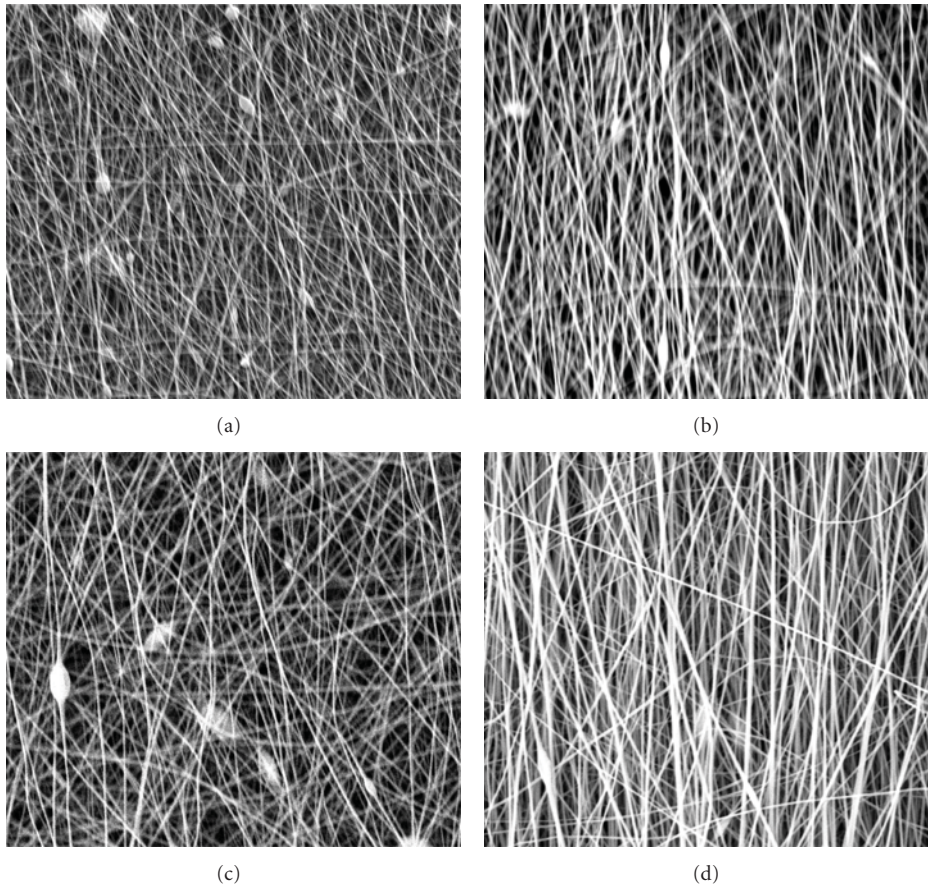


FIGURE 3: The TiO_2 ceramic nanofibres of diameter 98 ± 20 nm were collected using the rotating disc at 750 rpm; (a) without air shield, (b) using top-air shield, (c) using enclosed-air-shield, (d) using enclosed-air-shield with air-hood.

$1.5 \mu\text{m}$ in 4 h compared to the electrospinning without any shield. The alignment was substantially improved by the insertion of the top-air shield, and the nanofibres were nearly bead-free. The top-air-shield reduced the wind generated by the rotating disc, in turn enabled to align the nanofibres over the FTOs. The nanofibres alignment was found to be decreased gradually after hours of electrospinning. The poorer alignment was observed mainly due to the turbulence wind from the disc that disturbs the nanofibres deposition onto the target.

Figure 3(c) shows the fibres collected in the presence of enclosed-air-shield. Electrospinning with enclosed-air-shield improved the thickness of aligned nanofibres film to $4 \mu\text{m}$ and in 4 h, but the alignment was found to be poorer than that of obtained with top-air-shield as well as without shield setup. This result indicated that air flow exclusively towards the deposition area was influencing the alignment significantly. The installation of air-hood within the enclosed-air-shield as shown in Figure 1(d) allows collection of aligned nanofibres onto FTOs without much air

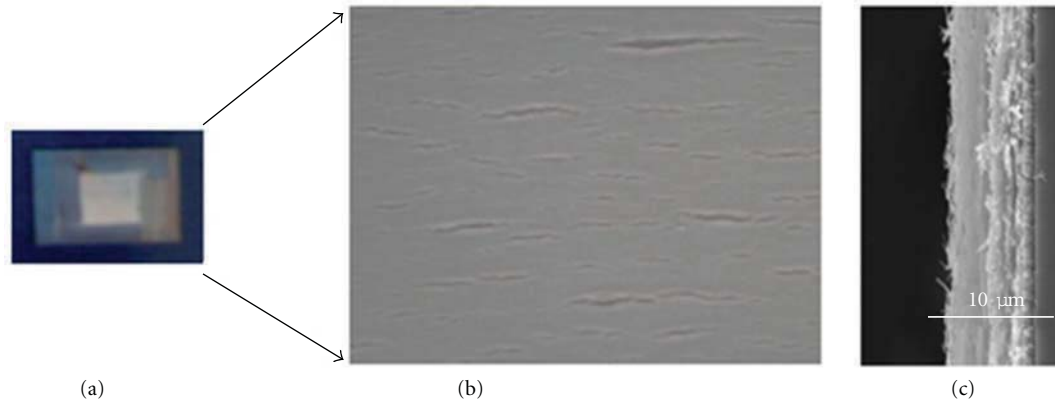


FIGURE 4: Sintered-aligned TiO_2 ceramic nanofibres. (a) Photo image, (b) optical microscope image (50x), and (c) SEM cross-sectional view of TiO_2 ceramic nanofibres.

disturbance. This configuration yielded two benefits: $4\ \mu\text{m}$ thick nanofibres were produced in 4 h, and better alignment.

A higher degree of fibres alignment was achieved by air-hood as shown in the SEM micrographs (Figure 3(d)). SEM Figure 3(d) shows that more than 80% were aligned to within $15\text{--}20^\circ$ of the average orientation. This could be attributed to the charges that each nanofibre acquires during the electrospinning. The distribution of the fibres across the gap became more stable. The enclosed air shield with air-hood produced the aligned TiO_2 nanofibres of $4\ \mu\text{m}$ thickness in 4 h. Earlier our group reported that time period of 8 h was required to obtain $4\ \mu\text{m}$ thick ZnO random nanofibres on FTO by simple electrospinning [22]. The shield not only reduced the collection time for obtaining same film thickness, but also allowed for well alignment of TiO_2 fibres on FTO substrates. The $4\ \mu\text{m}$ thick sintered TiO_2 nanofibres under microscope showed that there was no peeling-off problem upon sintering even after the thickness was increased higher, but few cracks along the fiber alignment direction (Figures 4(a) and 4(b)). It was also realized that the alignment of TiO_2 nanofibres at 750 rpm onto FTO itself increased the firmness to the fibres and adhesiveness to FTO. This was confirmed upon comparing the same thick but random TiO_2 nanofibres prepared on FTO without disc rotation. The fibers were found to be flaked off the FTO substrate upon annealing at 500°C . Investigation under SEM revealed that the alignment of the TiO_2 nanofibres was retained even at higher thickness after sintering at 500°C , indicating that the relaxation of residual stresses could be evenly distributed upon aligning the fibers.

Poor thickness of nanofibrous film is also connected to the lower flow rate of the precursor solution in electrospinning. Flow rate can be scaled up by increasing the needle diameter; however, it leads to large diameter fibres. Researchers have explored the possibility of both using multiple needles [23] and creating multiple holes in the single needle [24] in electrospinning. In this work, double-needle setup was fabricated for the collection of aligned TiO_2 nanofibres (Figure 5). In double-needle electrospinning, the distance between two needles is critical in producing the

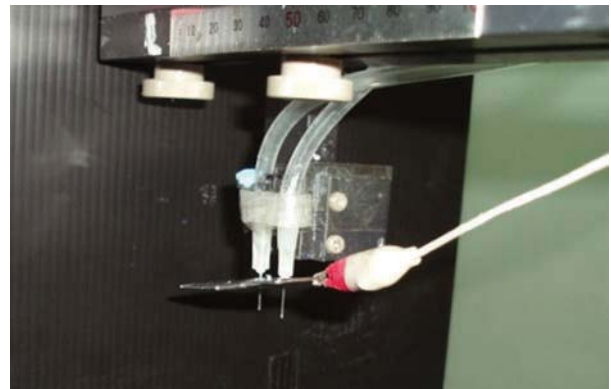


FIGURE 5: Photo image of double-needle arrangement for electrospinning.

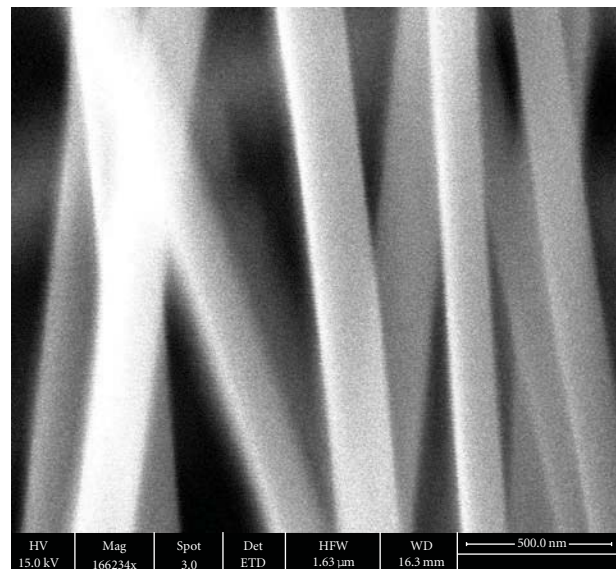


FIGURE 6: SEM image of aligned ceramic TiO_2 nanofibres using double-needle electrospinning.

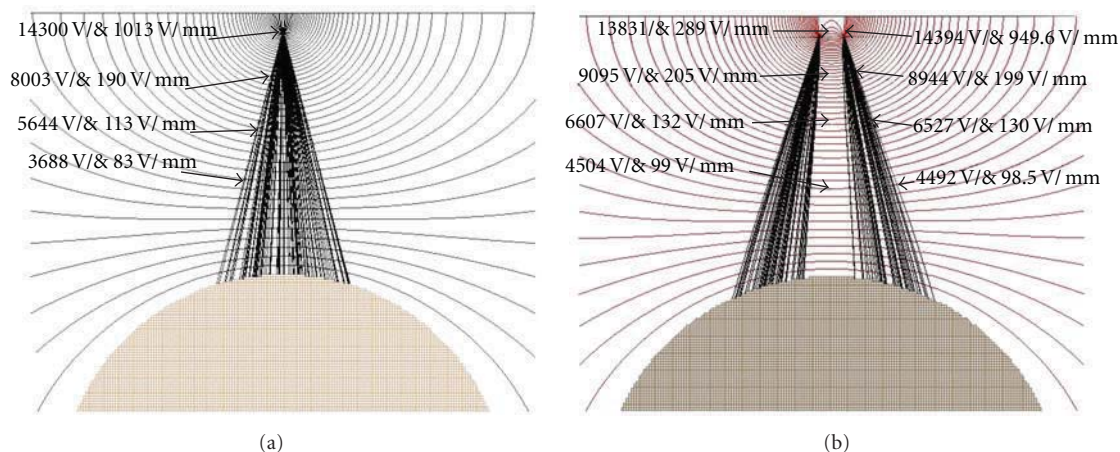


FIGURE 7: Theoretical prediction of flow of stream calculated based on 15 kV and the distance of 10 cm between needle tip and disc collector for (a) single-needle system and (b) double-needle system.

uniform nanofibres. In our study, the distance between the needles was optimized to 1 cm such that the repelling force between jets from two needles could be minimal. The same electrospinning condition was adopted for double-needle setup. The study using double needle with enclosed air-shield and air-hood yielded 6 μm thick and aligned TiO_2 nanofibres in 4 h. TiO_2 nanofibres obtained using double-needle-based electrospinning were quite uniform in diameter (Figure 6), but was found to be smaller than that of fibres produced using a single-needle-based electrospinning. The diameter of the sintered fibres from the double needle was about 70 ± 12 nm, whereas the sintered fibres obtained using the single needle possessed 98 ± 20 nm. The difference in diameter could be due to following effects: the repulsive force from the two charged jet might involve in pulling of the nanofibres and secondly, stronger electric field leads to greater stretching of the jet and resulting in thin fibres.

Theoretical studies were carried out to correlate the difference in fibres diameter obtained from experiments. SIMION 8, an ion modeling package, was adopted to interpret the electrospinning jet based on the electric field distribution by estimating equipotential lines distribution around the electrodes as well as collector. For the same 15 kV potential and distance of 10 cm between the needle and disc collector, the simulation profiles on electrical distribution of the jet stream from both single-needle and double-needle system were obtained. Figure 7 shows the electric field distribution along the jet path for both single-needle and double-needle systems.

For the identical voltage, the electric field lines at the tip of the needle in double-needle arrangement was estimated to be lower compared to single-needle setup, indicating that the repulsive field plays a critical role in the double-needle system. At the area just below the needle tip, the electric field intensity for the double-needle setup was higher than that of single-needle setup. In the mid distance between the needle and collector, the electric field intensity was measured as 98.5 V/mm for double needle, and 83 V/mm for a single needle. The intensity of the electric field (V/m) at the various

position of the flow stream was measured to be stronger in double-needle system, suggesting that overstretching of the nanofibres were possible in double needle before deposition. Thus, the simulation study conveyed that the repulsive force of the charged fibers and the stronger electric field distribution along the flow of stream should play an influential role in reducing the fibers diameter.

4. Conclusions

Highly aligned ceramic TiO_2 nanofibres of diameter 98 nm on FTOs were directly prepared using rotating disc-based electrospinning. With the ease of design, control over deposition, and the potential for continuous electrospinning, this study demonstrated the substantial improvement in the alignment (over 80%) of nanofiber by introducing an enclosed-air-shield and air-hood. Aligned nanofiberous film with the thickness adjustable from 100 nm upto 6 μm was demonstrated. We believe that the ability to prepare aligned and controlled thickness of nanofibres directly on the conductive substrates opens up potential opportunities in the domain of energy and electronics. There are still challenges that must be addressed in our approach: to reach above 80% alignment, thickness above 10 μm in shorter time (<4 h), and better understanding of the physics underlying alignment.

Acknowledgments

Authors acknowledge Singapore NRF-Technion Grant (WBS no: R-398-001-065-592) and Singapore NRF-NTU CRP Grant for the funding support.

References

- [1] M. Law, L. E. Greene, J. C. Johnson, R. Saykally, and P. Yang, "Nanowire dye-sensitized solar cells," *Nature Materials*, vol. 4, no. 6, pp. 455–459, 2005.
- [2] S. I. Na, S. S. Kim, W. K. Hong et al., "Fabrication of TiO_2 nanotubes by using electrodeposited ZnO nanorod template

- and their application to hybrid solar cells," *Electrochimica Acta*, vol. 53, no. 5, pp. 2560–2566, 2008.
- [3] T. Krishnamoorthy, V. Thavasi, G. M. Subodh, and S. Ramakrishna, "A first report on the fabrication of vertically aligned anatase TiO₂ nanowires by electrospinning: preferred architecture for nanostructured solar cells," *Energy & Environmental Science*, vol. 4, no. 8, pp. 2807–2812, 2011.
- [4] H. S. Shim, S. I. Na, S. H. Nam et al., "Efficient photovoltaic device fashioned of highly aligned multilayers of electrospun TiO₂ nanowire array with conjugated polymer," *Applied Physics Letters*, vol. 92, no. 18, Article ID 183107, 2008.
- [5] S. H. Choi, G. Ankonina, D. Y. Youn et al., "Hollow ZnO nanofibers fabricated using electrospun polymer templates and their electronic transport properties," *ACS Nano*, vol. 3, no. 9, pp. 2623–2631, 2009.
- [6] Y. Liu, J. Dong, and M. Liu, "Wll-aligned "nano-box-beams" of SnO₂," *Advanced Materials*, vol. 16, no. 4, pp. 353–356, 2004.
- [7] S. S. Kim, J. Jo, C. Chun, J. C. Hong, and D. Y. Kim, "Hybrid solar cells with ordered TiO₂ nanostructures and MEH-PPV," *Journal of Photochemistry and Photobiology A*, vol. 188, no. 2-3, pp. 364–370, 2007.
- [8] K. O. Hill and G. Meltz, "Fiber Bragg grating technology fundamentals and overview," *Journal of Lightwave Technology*, vol. 15, no. 8, pp. 1263–1276, 1997.
- [9] M. Lončar, T. Doll, J. Vučković, and A. Scherer, "Design and fabrication of silicon photonic crystal optical waveguides," *Journal of Lightwave Technology*, vol. 18, no. 10, pp. 1402–1411, 2000.
- [10] S. M. Yang and G. A. Ozin, "Opal chips: vectorial growth of colloidal crystal patterns inside silicon wafers," *Chemical Communications*, no. 24, pp. 2507–2508, 2000.
- [11] P. Katta, M. Alessandro, R. D. Ramsier, and G. G. Chase, "Continuous electrospinning of aligned polymer nanofibers onto a wire drum collector," *Nano Letters*, vol. 4, no. 11, pp. 2215–2218, 2004.
- [12] S. A. Theron, A. L. Yarin, E. Zussman, and E. Kroll, "Multiple jets in electrospinning: experiment and modeling," *Polymer*, vol. 46, no. 9, pp. 2889–2899, 2005.
- [13] A. L. Yarin and E. Zussman, "Upward needleless electrospinning of multiple nanofibers," *Polymer*, vol. 45, no. 9, pp. 2977–2980, 2004.
- [14] V. Thavasi, G. Singh, and S. Ramakrishna, "Electrospun nanofibers in energy and environmental applications," *Energy & Environmental Science*, vol. 1, no. 2, pp. 205–221, 2008.
- [15] J. A. Matthews, G. E. Wnek, D. G. Simpson, and G. L. Bowlin, "Electrospinning of collagen nanofibers," *Biomacromolecules*, vol. 3, no. 2, pp. 232–238, 2002.
- [16] D. Li and Y. Xia, "Direct fabrication of composite and ceramic hollow nanofibers by electrospinning," *Nano Letters*, vol. 4, no. 5, pp. 933–938, 2004.
- [17] K. Tennakone, G. R. R. A. Kumara, and K. G. U. Wijayantha, "The suppression of the recombination of photogenerated carriers in a dye-sensitized nano-porous solid-state photovoltaic cell," *Semiconductor Science and Technology*, vol. 11, no. 11, pp. 1737–1739, 1996.
- [18] B. O'Regan and D. T. Schwartz, "Large enhancement in photocurrent efficiency caused by UV illumination of the dye-sensitized heterojunction TiO₂/RuLL'NCS/CuSCN: initiation and potential mechanisms," *Chemistry of Materials*, vol. 10, no. 6, pp. 1501–1509, 1998.
- [19] U. Bach, D. Lupo, P. Comte et al., "Solid-state dye-sensitized mesoporous TiO₂ solar cells with high photon-to-electron conversion efficiencies," *Nature*, vol. 395, no. 6702, pp. 583–585, 1998.
- [20] J. Krüger, R. Plass, M. Grätzel, P. J. Cameron, and L. M. Peter, "Charge transport and back reaction in solid-state dye-sensitized solar cells: a study using intensity-modulated photovoltage and photocurrent spectroscopy," *Journal of Physical Chemistry B*, vol. 107, no. 31, pp. 7536–7539, 2003.
- [21] H. S. Shim, S. I. Na, S. H. Nam et al., "Efficient photovoltaic device fashioned of highly aligned multilayers of electrospun TiO₂ nanowire array with conjugated polymer," *Applied Physics Letters*, vol. 92, no. 18, Article ID 183107, 2008.
- [22] W. Zhang, R. Zhu, X. Liu, B. Liu, and S. Ramakrishna, "Facile construction of nanofibrous ZnO photoelectrode for dye-sensitized solar cell applications," *Applied Physics Letters*, vol. 95, no. 4, Article ID 043304, 2009.
- [23] F. L. Zhou, R. H. Gong, and I. Porat, "Mass production of nanofibre assemblies: by electrostatic spinning," *Polymer International*, vol. 58, no. 4, pp. 331–342, 2009.
- [24] F. L. Zhou, R. H. Gong, and I. Porat, "Three-jet electrospinning using a flat spinneret," *Journal of Materials Science*, vol. 44, no. 20, pp. 5501–5508, 2009.

Review Article

Design Modifications in Electrospinning Setup for Advanced Applications

Rahul Sahay,^{1,2} Velmurugan Thavasi,¹ and Seeram Ramakrishna¹

¹ NUS Nanoscience and Nanotechnology Initiative, National University of Singapore, Singapore 117576

² School of Materials Science and Engineering, Nanyang Technological University, 50 Nanyang Avenue, Singapore 639798

Correspondence should be addressed to Velmurugan Thavasi, velnanotech@gmail.com

Received 12 July 2011; Accepted 28 August 2011

Academic Editor: Yanqiu Zhu

Copyright © 2011 Rahul Sahay et al. This is an open access article distributed under the Creative Commons Attribution License, which permits unrestricted use, distribution, and reproduction in any medium, provided the original work is properly cited.

The paper deals with the modification made to the general electrospinning setup. The emphasis is given to characterize the designs based on their applicability. Four basic categories are identified, namely, patterned fibers, fiber yarns, multicomponent, and deposition area of the fiber mat obtained. The mathematical modeling to better understand the physics behind the modification made to the general electrospinning setup is presented. Emphasis is given to critically analyse these categories on the basis of the applications served by them. Each of these categories is found to serve a specific pool of advanced application enabling the researchers to make a calculated choice for the design of the electrospinning setup for particular application.

1. Introduction

Electrospinning is one of the most widely used processes for the production of nanofibers. This technique of producing nanofibers employs electrostatic forces for stretching the viscoelastic fluid. The fiber diameters obtained are found to be one or two orders of magnitude smaller than the conventional spinning techniques. As the process is capable of achieving large surface to volume ratios with desirable physical and chemical properties, it has been considered for a wide variety of applications, ranging from sensors [1], antibacterial surfaces [2], scaffolds [3], photocatalyst [4], nanofilters [5], anti-counterfeiting application [6], water-proof fabric [7], and solar energy applications [8].

Electrospinning is a simple process employing a syringe pump, high voltage direct current (HVDC) supply, and a grounded collector. The syringe pump connected to the syringe is employed to control the flow rate of the polymer solution as depicted in Figure 1. HVDC power supply is connected to the metallic needle. This metallic needle, on the other hand, is connected to the syringe. When the high voltage is applied to a polymer drop emanating from the metallic needle, the charged particles start to concentrate on the surface of the polymer drop, thus resulting in the excess buildup of charged particles at the tip of the drop. At some

critical value of the applied electric field proposed by Taylor [9], applied electric field surpasses the surface tension and results in jetting from the polymer drop. The trajectory of polymer jet is a straight line before it starts to curl and spiral in space. This curling and spiraling of polymer jet are responsible for the reduction of its diameter to the order of nanometers resulting in nanofibers as depicted in Figure 2. These fibers later get deposited on the grounded surface. It is advisable to make a brief note of the mathematical modeling pertaining electrospinning as it will help to better understand the physics behind the modification made to the general electrospinning setup.

2. Mathematical Modeling of the Electrospinning Process

Although vast majorities of work related to electrospinning were of an experimental nature, nevertheless, some theoretical studies had been proposed. The theoretical studies could be divided into two broad categories. The first category dealt with the mathematical analysis related to straight section of electrospun jet. On the other hand, the second category was related to the bending instabilities suffered by the electrospun jet. Spivak et al. [10, 11] proposed a one-dimensional (1D)

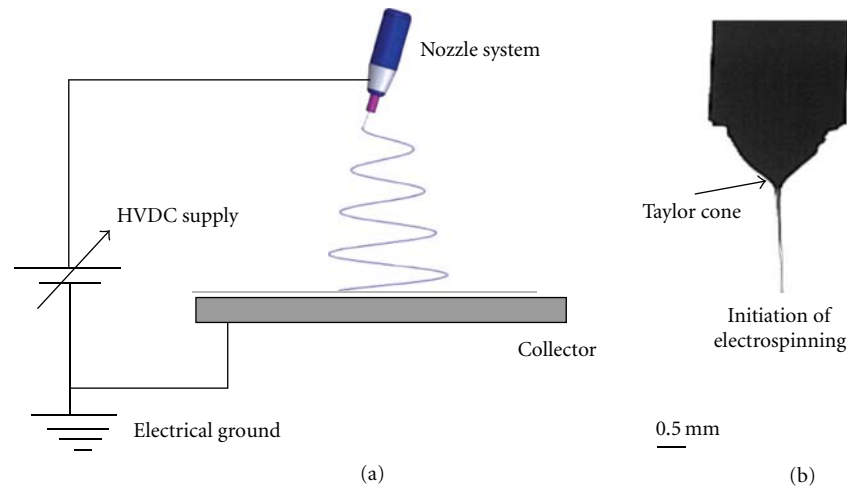


FIGURE 1: (a) The schematic of basic electrospinning. The nozzle system usually consists of a needle and a syringe pump. Where HVDC stands for high voltage direct current. (b) The figure depicts the formation of Taylor cone required for the initiation of electrospinning. The images were obtained with the help of high speed camera at 2000 f/s.

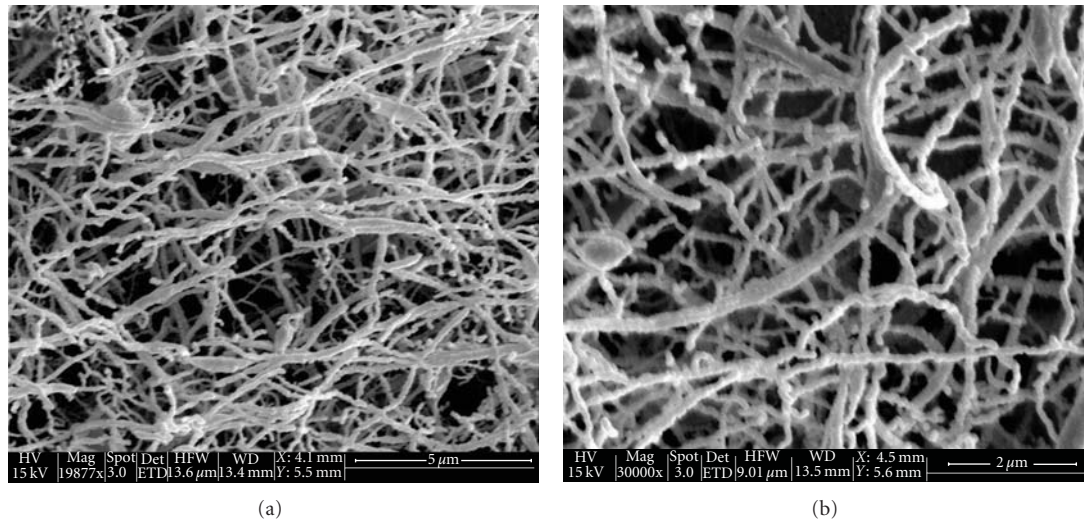


FIGURE 2: CuO fibers fabricated through electrospinning. (a) Composite fibers: the chemical reagents (copper acetate and water) were dissolved in 10 wt% aqueous poly(vinyl) alcohol solution. The polymer solution was employed to achieve appreciable viscosity required for the initiation of electrospinning. The electrospinning was performed at flow rate of 0.25 mL/h with the applied electric field strength of 1.33 kV/cm. (b) Annealed fibers: the composite fibers obtained were annealed at 500°C to remove polymer as water vapor and CO₂ resulting in pure CuO fibers.

model for the electrospun jet, with fluid behavior represented by a nonlinear power law rheological constitutive equation. Yarin et al. [12, 13] modeled the jet as a series of charged beads connected by viscoelastic dumbbell elements. Hohman et al. [14, 15] proposed a model, which accounted for the influence of the charge density of the jet on the surrounding electric field. The fluid employed, was considered as Newtonian in nature. Feng [16, 17] reformulated the Hohman et al. treatment, accounting for viscoelastic polymeric rheological behavior. The viscoelastic behavior was employed by incorporating the Giesekus constitutive equation into the jet-governing equations. Carroll and Joo [18] modeling of the electrospinning process closely followed the work of Feng, with the introduction of Oldroyd-B and FENE-P constitutive

equations for modeling the rheological behavior of Boger fluids.

The second phase of electrospinning had been studied by Reneker et al. [19]. They proposed that the electrically driven bending instabilities of an electrospun jet as the particular case of the general Earnshaw theorem in electrostatics. On the other hand, Hohman et al. [14] proposed instability models to describe the phenomena observed during electrospinning. Models related to higher order instabilities such as “branches on electrospun jet” was also proposed by Yarin et al. [20].

2.1. *Straight Section of Electrospun Jet.* Spivak et al. [10, 11] modeled the motion of a weakly conductive infinite viscous

jet accelerated by an external electric field taking into account the inertial, hydrostatic, viscous, electrical, and surface tension forces. The polymer fluid was described by a nonlinear power law rheological constitutive equation. The linear momentum, mass, and electric charge conservation equations were obtained by averaging over the jet cross-section to give the resultant equation along the jet flow direction. The asymptotic momentum equation in its dimensionless form was given by the expression

$$\left\{ \tilde{R}^{-4} + We\tilde{R}^{-1} - Y\tilde{R}^2 - \frac{1}{Re} \left(\frac{1}{2} \frac{d}{d\tilde{z}} (\tilde{R}^{-2}) \right)^m \right\} = \tilde{Z} + C, \quad (1)$$

where dimensionless jet radius $\tilde{R} = R/R_0$, where R_0 was the characteristic jet radius. Dimensionless axial coordinate $\tilde{Z} = Z/Z_0$, where $Z_0 = \rho Q^3 / 2\pi^2 R_0^4 E_0 I$. The nondimensional parameters were Weber number $We = (2\pi^2 R_0^3 \sigma_s) / (\rho Q^2)$ represented the ratio of the surface tension forces to the inertial forces. $Y = \pi^2 I^2 R_0^6 / (4\epsilon_0 \rho Q^4)$ represented the ratio of the electrical to inertial forces. The effective Reynolds number for the fluid is given by $Re = (Q^2 \rho) / (2\pi^2 R_0^2 \mu [4\pi E_0 I R_0^2 / (Q^2 \rho)]^{-m})$. All the symbols have their usual meaning, and m is the flow index in the rheological constitutive equation. The constant C was evaluated with the help of the imposed boundary conditions. Substituting power law asymptotic approximation of the jet radius ($\tilde{R} \sim \tilde{z}^{-\alpha}$) in the integrated form of the asymptotic momentum equation (1) results

$$\tilde{z}^{-4\alpha} + We\tilde{z}^{-1\alpha} - Y\tilde{z}^{-2\alpha} - \frac{\alpha^m}{Re} \tilde{z}^{(2\alpha-1)m} - \tilde{Z} = O(1). \quad (2)$$

Spivak et al. [10, 11] numerically integrated asymptotic momentum (2) and compared it with the experimental measurements obtained for a 4 wt% aqueous solution of poly(ethylene) oxide ($M_w = 1,450,000$) electrospun at an electric field strength of 0.4 kV/cm. Spivak et al. [10, 11] observed good agreement between numerical and experimental values over a distance of 15 mm from the initiation of the spinning process.

Yarin et al. [12, 13] derived quasi-one-dimensional equations for the conservation of mass, momentum, and electrical charge describing the dynamics of the electrospun jet

$$\lambda f = \lambda_0 f_0, \quad (3)$$

$$\rho \lambda_0 f_0 \frac{\partial V}{\partial \tau} = \tau \frac{\partial p}{\partial s} + \lambda |\kappa| p n - \rho_g \lambda_0 f_0 k \quad (4)$$

$$+ \lambda |\kappa| \times \left(\pi a \sigma - e^2 \ln \frac{l}{a} \right) n - \lambda_\epsilon \frac{U_0}{h} k, \quad (5)$$

$$e\lambda = e_0 \lambda_0,$$

where “ s ” was a Lagrangian parameter “frozen” into the jet elements. Equation (3) represents conservation of mass, where λ was the geometrical stretching ratio such that $\lambda ds = d\zeta$, and the $f = \pi a^2$ being the cross-sectional area. Subscript zero denotes the parameter values at the time $t = 0$. Equation (4) was momentum balance equation with ρ being the

liquid density, V its velocity, p the longitudinal force in the jet cross section, and g is acceleration due to gravity. U_0 being the value of electrical potential at the jet origin and “ h ” the distance between the origin and the collecting plate. Equation (5) represents the conservation of charges. In Cartesian coordinates, the kinematics relations were given as $\partial R / \partial \tau = V$, where R was the radius vector of a point on the axis of the jet. Substituting the kinematics relations in (4), a system of scalar equations was obtained. The simplest version of the upper-convected Maxwell model of viscoelasticity was assumed to describe the behavior of electrospun jet. This system of the equations allowed Yarin et al. to obtain the jet configuration in space at any particular instance of time. Comparisons were made between experimental and theoretical results for a 6 wt% poly(ethylene) oxide solution dissolved in 60/40 v/v water/ethanol mixture. The applied electric field strength was 1 kV/cm. The predicted motion of the jet was found to be in good agreement with the experimental data until about 3 ms after jet initiation.

Hohman et al. [14, 15] modeled the electrospinning process based on the approach that the instabilities occurred on a length scale much longer than the jet radius. As a result, the jet was represented as a long, slender object. The polymer fluid was considered Newtonian and incompressible. The three-dimensional variables considered were radial velocity (V_r), axial velocity (V_z), radial electric field (E_r), and axial electric field (E_z). Taylor series expansions in r (instantaneous radius of the jet) of these four variables were substituted into three-dimensional equations for conservation of mass, conservation of charge, and momentum balance. Only the leading terms of the expansions were retained. The resulting hydrodynamic equations were made nondimensional by employing length scale r_0 , where r_0 was the diameter of the capillary; time scale $t_0 = \sqrt{\rho r_0^3 / \gamma}$, where γ was the surface tension and ρ was the density of the fluid; an electric field strength $E_0 = \sqrt{\gamma / (\epsilon - \bar{\epsilon})} r_0$, where ϵ and $\bar{\epsilon}$ were the permittivity of the fluid and air, respectively, and surface charge density was given by $\sqrt{\gamma / (\bar{\epsilon})} / r_0$. The material properties of the fluid were characterized by dimensionless parameters $\beta = \epsilon / \bar{\epsilon} - 1$, the dimensionless viscosity $\nu^* = \sqrt{\nu^2 / (\rho \gamma r_0)}$, the viscous scale $l_\nu = \rho \nu^2 / \gamma$. The other nondimensional parameters are dimensionless gravity $g^* = g \rho r_0^2 / \gamma$ and the dimensionless conductivity $K^* = K \sqrt{\rho r_0^3 / (\beta \gamma)}$. The nondimensionalized equations for conservation of mass and charge and the Navier-Stokes equation for the conservation of momentum were given as follows:

$$\begin{aligned} \partial_t (h^2) + (h^2 \nu)' &= 0, \\ \partial_t (\sigma h) + \left(\sigma h \nu + \frac{K^*}{2} h^2 E \right) &= 0, \\ \partial_t \nu + \nu \nu' &= - \left(\frac{1}{h} - h'' - \frac{E^2}{8\pi} - 2\pi \sigma^2 \right) \\ &\quad + \frac{2\sigma E}{h\sqrt{\beta}} + g^* + \frac{3\nu^{*2}}{h^2} (h^2 \nu)', \end{aligned} \quad (6)$$

where $h(z)$ was the radius of the jet at axial coordinate z ; $V(z)$ was the axial velocity of the jet and was assumed to be constant across the jet cross-section; $\sigma(z)$ was the surface charge density; $E(z)$ was the electric field in the axial direction. The prime on the variables denotes differentiation with respect to z . The nondimensionalized tangential field inside the jet, was expressed as

$$E = E_\infty + \int ds \frac{\lambda(s)}{|x - r(s)|} \approx E_\infty + \ln \frac{r}{L} \left(\frac{\beta}{2} (h^2 E)' - \frac{4\pi}{\bar{\epsilon}} h\sigma \right), \quad (7)$$

where $\lambda(s)$ was the linear charge density along the jet, parameterized by the arc length “ s ,” which varied over the length scale “ L ” much larger than the jet radius.

Feng [16, 17] simplified the Hohman et al. [14, 15] formulation by making it insensitive to the initial charge density, except inside a tiny “boundary layer” at the capillary end. They integrated viscoelastic polymeric rheological behavior by incorporating the Giesekus constitutive equation into the governing equations given as

$$\frac{\bar{\eta}^+}{3\eta_s} = \begin{cases} \exp\{p[1 - \cos(\gamma^2/\gamma_s^2)]\} & \text{if } \gamma \leq \gamma_s \\ \exp(2p) & \text{if } \gamma > \gamma_s \end{cases}. \quad (8)$$

The governing equation for the unknown parameters $R, v, E,$ and σ were given by the (9)–(12). The characteristic qualities length R_0 , velocity $v_0 = Q/(\pi R_0^2)$, electric field $E_0 = I/(\pi R_0^2 k)$, and surface charge density $\sigma_0 = \bar{\epsilon} E_0$ were used for scaling the governing equations. The resultant governing equations were

$$vR^2v' = 1, \quad (9)$$

$$R^2E + PeRv\sigma = 1, \quad (10)$$

$$vv' = \frac{1}{Fr} + \frac{3}{ReR^2} \frac{d}{dz} (\eta R^2 v') + \frac{1}{WeR^2} + \Xi \left(\sigma\sigma' + \beta EE' + \frac{2\sigma E}{R} \right), \quad (11)$$

$$E = E_\infty - \ln \chi \left(\frac{d(\sigma R)}{dz} - \frac{\beta}{2} \frac{d^2(ER^2)}{dz^2} \right), \quad (12)$$

where the nondimensional groups are given as $Fr = v_0^2/gR_0$, $Pe = 2\bar{\epsilon}v_0/KR_0$, $Re = \rho v_0 R_0/\eta_0$, $We = \rho v_0^2 R_0/\gamma$, $E = \bar{\epsilon} E_0^2/\rho v_0^2$, $De = \lambda v_0/R_0$, $r_\eta = \eta_p/\eta_0$, and $\beta = \epsilon/\bar{\epsilon} - 1$, $\chi = L/R_0$. The other symbols have their usual meaning. Feng [16, 17] documented that strain hardening promoted jet thinning at the beginning but suppressed it further downstream to produce thicker fibers. In addition, the Giesekus model also predicted earlier onset of strain hardening at higher strain rate. Though definitive comparisons with experiments were not performed, the theory appeared to predict jet thinning on the right order of magnitude.

Carroll and Joo [18] modeled the electrospinning process that closely followed the work of Feng [16, 17]. The model consisted of steady state equations for mass, charge, momentum conservation, as well as an electric field equation with the introduction of Oldroyd-B and FENE-P constitutive

equations for modeling the rheological behavior of Boger fluids. The nondimensional governing equations were

$$vR^2v' = 1, \quad (13)$$

$$R^2E + PeRv\sigma = 1, \quad (14)$$

$$vv' = \frac{1}{Fr} + \frac{3}{ReR^2} \frac{d}{dz} (\eta R^2 v') + \frac{1}{WeR^2} + \Xi \left(\sigma\sigma' + \beta EE' + \frac{2\sigma E}{R} \right), \quad (15)$$

$$E = E_\infty - \ln \chi \left(\frac{d(\sigma R)}{dz} - \frac{\beta}{2} \frac{d^2(ER^2)}{dz^2} \right). \quad (16)$$

For the special case of the infinitely extensible polymer chain, the polymeric stress components reduce to the Oldroyd-B model were

$$\tau_{pzz} + De(v\tau'_{pzz} - 2v'\tau_{pzz}) = 2(1 - B)v', \quad (17)$$

$$\tau_{prrr} + De(v\tau'_{prrr} + v'\tau_{prrr}) = -(1 - B)v'. \quad (18)$$

The momentum and electric field equations, (15) and (16), were both second order ordinary differential equations, which were rewritten as a set of four first order ODEs. The polymeric stress (17) and (18) add two first order ODE. To solve this system of equations, six boundary conditions were formulated as also performed by Feng [16, 17]. Carroll and Joo [18] demonstrated that the one-dimensional model for electrically driven jet had correctly captured the initial straight-line motion of jet. The resultant simulation had given good quantitative jet radius profiles plotted against parameters such as the electrical conductivity, fluid viscoelasticity, and volumetric flow rate, which were in good agreement with experimental results.

2.2. Bending Instabilities of Electrospun Jet. Reneker et al. [19] considered the electrically driven bending instabilities of an electrospun jet as the particular case of the general Earnshaw theorem in electrostatics. The theorem states that it is impossible to create a stable structure in which the elements interact only by Coulomb’s law. The result of the phenomenon will be a lateral force component that will cause the jet to deviate from its original initiated path into a looping spiraling trajectory.

Hohman et al. [14, 15] performed linear instability analysis to better understand the phenomenon of bending instabilities of the electrospun jet. Three different types of instabilities were predicted, two of which were axisymmetric whereas, third was non-axisymmetric in nature. The first axisymmetric mode was stated to be associated with the Raleigh instability, which was dominated by surface tension. The Raleigh instability was suppressed at high electric fields and was considered irrelevant for electrospinning. The other two modes were electrically driven and referred to as “conducting” modes. These conductive modes were primarily sensitive to fluid conductivity and insensitive to surface tension at high electric fields. The one of these conductive modes was

axisymmetric, while the second was non-axisymmetric in nature. The competition between the two conducting modes was of importance at high electric fields of the electrospinning process. The mode that will dominate depends on both the surface charge density and the radius of the jet as it thins away from the tip of the needle.

3. Effect of Applied Forces on the Trajectory of Electrospun Jet

Although the electrostatic force is the dominant force experienced by the electrospun jet, it is beneficial to compare qualitatively the forces acting on the electrospun jet. As can be seen from (12) and (16), the electric field acting on the jet in the axial direction is the sum of external applied electric field and the electric field induced by the total free charge on the jet surface. The total free charge on the jet is given by the (10) and (14). This total charge is the sum of conductive and convective charges. It is observed that conductive charge transfer dominates the charge transfer mode inside the Taylor cone [12]. This conductive charge gives way to convective charge as the jet thins away from the Taylor cone to the collector surface. This implies that contribution to the total electric field from the free charge reduces as the jet moves away from the needle exit. This implies that the total electric field near the collector surface is approximately same to the external applied electric field. This is theoretically an order of magnitude reduction in the total electric as the jet moves from the needle tip to the collector surface.

The total electric field can be increased either by increasing the external applied electric field or by increasing the total charge density. Salt (NaCl) is considered as one of the widely used additive to increase the charge density of the polymer solution [21]. The other additives used for increasing the charge density are ionic surfactant [22], which has the dual purpose of increasing the conductivity while reducing the surface tension of the polymer solution. This increase in the charge density, as predicted by Hohman et al. [14, 15], will aggravate non-axisymmetric instabilities colloquially known as the bending instabilities making it difficult to control the trajectory of the jet.

For the initiation of electrospun jet the electrostatic force has to overtake surface tension. This happens at the tip of the Taylor cone, where charge density is the maximum. Ironically, the surface tension is maximum at the tip of the Taylor cone due to the infinitesimally small radius at the tip. This large charge density at the tip of Taylor cone increases the total electric field by an order of magnitude greater than the applied electric field, thus enabling the initiation of the jet from the tip of Taylor cone. After the initiation of electrospun jet, high viscoelastic force of polymer jet suppresses the surface tension, resulting in uniform diameter electrospun jet. Surface tension becomes relevant again with the decrease in the jet radius as the jet thins away from the metallic needle to the collector surface. In cases where the surface tension surpasses viscoelastic forces, it results in the formation of beads [23]. The beads are the local increase in the jet diameter, which results from axisymmetric nonconducting instability

better known as Rayleigh Plateau instability [24]. Beads are considered as defects as it reduces the large surface area of the electrospun fibers as shown in Figure 3. Increase in the free charge density results in an increase in the stretching of jet and thus reduces the bead formation [25]. Increase in the viscoelastic forces by increasing the viscosity [26] of the polymer solution is the other way of surpassing bead formation. The viscosity of the polymer solution can be increased by either increasing the molecular weight or concentration of the polymer solution. Nevertheless, beaded fibers were obtained with an increase in the polymer concentration in case of polymer blend as shown in Figure 4. This may be due to the nonlinear interaction of polymer component in the polymer blend resulting in variable viscosity profile.

Inertia and aerodynamic drag force were considered negligible in comparison to electrostatic force during the initiation of electrospun jet from a polymer drop. Upward need-
less electrospinning [27] is one of the examples which confirms the given argument. Nevertheless, these forces (aerodynamic drag and inertia) start to become significant as the jet gets close to the collector surface due to the reduction of total electric force near the collector surface as discussed earlier. For instance, the fiber mat collected by the upward electrospinning setup will be more porous and loosely bound together as compared to the normal electrospinning setup due to the inertial effect of nanofibers. These forces (aerodynamic drag and inertia) also tend to play an important role during the patterning of electrospun jet. For instance, the most common collector device used for the collection of aligned fibers is the rotating mandrel. As the electrospun jet comes near to the fast rotating mandrel, it experiences a drag force due to the rapid displacement of air near the mandrel surface, which affects its alignment. The analysis pertaining to the drag force experienced by the electrospun jet due to the rotating mandrel will appear elsewhere.

4. Need for Modifications in the Electrospinning Setup

It has been observed that the electrostatic force is the driving force behind the bending instability of electrospun jet. This bending instability is responsible for the reduction of jet diameter to the order of nanometer. This particular instability is also responsible for the randomness of the resultant product obtained. This makes it obvious that manipulating electric field lines will help to control the trajectory of the electrospun jet and so does the architecture of the final product.

Possible configurations of electric field lines between the needle system and the collector are shown in Figure 5. From herein and hereafter the term “needle system” will comprise of the syringe pump, HVDC supply, and metallic needle connected to the syringe. Figure 5(a) shows the electric field lines for point-plate system. Here, “point” is represented by the needle system, whereas “plate” is the infinitely long collector surface with respect to the needle system. These electric field lines depict the configuration for general electrospinning setup. In practice, the “plate” collector configuration can be

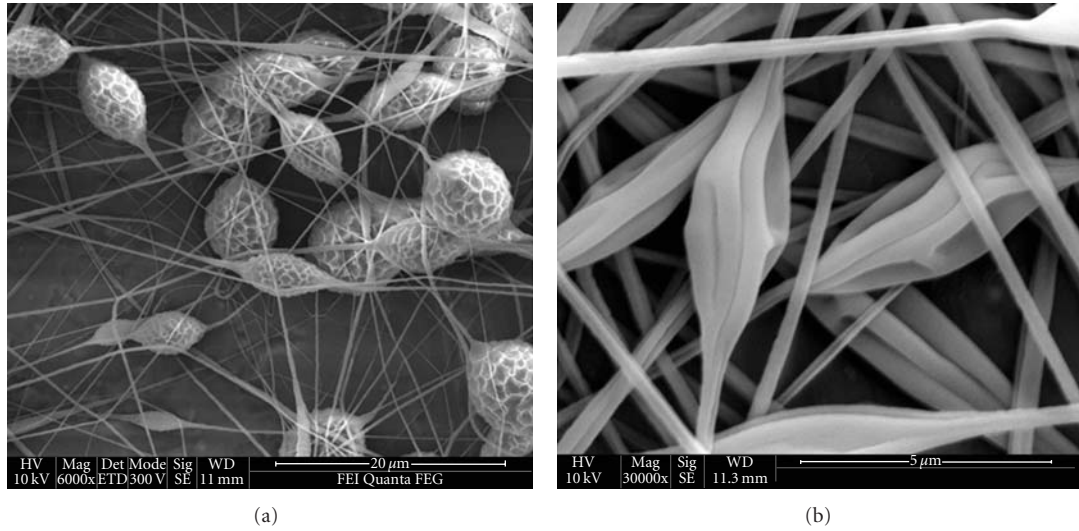


FIGURE 3: Formation of beads on electrospun fibers prepared using 10% polyvinyl pyrrolidone (PVP) dissolved in dimethylformamide (DMF) with the applied electric field strength of 2.0 kV/cm.

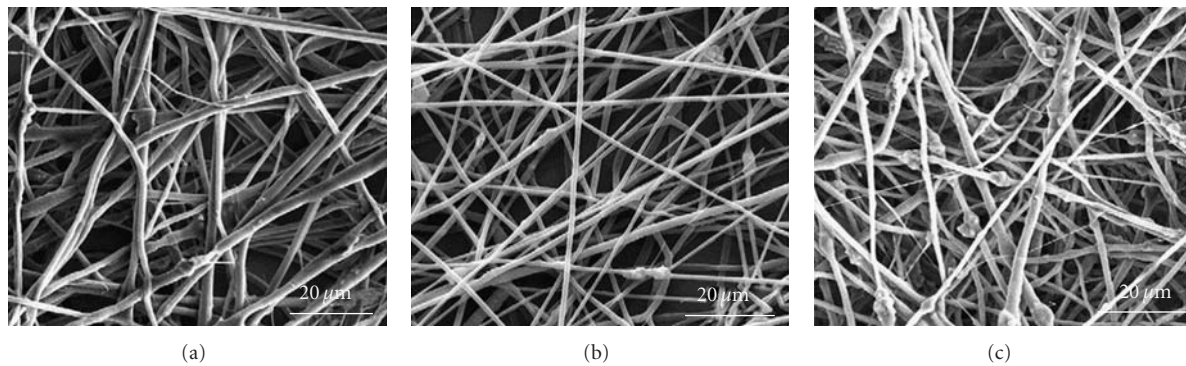


FIGURE 4: The figure depicts the effect of the concentration of the polymer solution on fiber morphology. The fibers were fabricated from poly(ethylene) oxide (PEO) blended with (a) 6%, (b) 12%, and (c) 19% PANi. The blended polymer was dissolved in chloroform. The electrospinning was performed at flow rate of 0.3 mL/h with the applied electric field strength of 1.25 kV/cm.

represented by a conducting plate, rotating mandrel, and so forth. Figure 5(b) shows electric field lines for point-point system. Here, the “point” collector represented by sharp-pointed surfaces. These surfaces may include a tip of a sharp pointed knife, sharp edges of plate, thin metallic wires, and so forth. As it seems from the Figure 5(b), the purpose of point collector is to concentrate the electric field lines and thus the trajectory of the jet at an infinitesimally small point. Figure 5(c) depicts the highly uniform electric field lines for plate-plate system. This setup though will produce a uniform jet profile is seldom employed as it requires higher externally applied electric field strength as compared to the point-plate system for the initiation of electrospinning.

As will be seen later, the large number of electrospinning setups employ components to concentrate electric field lines at a certain given point or a given area. This confinement, though helps in achieving controlled deposition of nanofibers, hinders the possible trajectory of electrospun jet. This hindered trajectory of electrospun jet will subsequently hin-

der the reduction of jet diameter as it moves from the needle tip to the collector surface. It is noted later during the discussion of electrospinning setups that this phenomenon resulted in micron or submicron diameter fibers. Nevertheless, these possible configurations of electric field lines will help us in understanding the mechanism behind the fiber alignment.

In this paper, the emphasis has been given to characterize the configurations of electrospinning setups on their usage. This is done to help the reader make a calculated choice regarding design of their electrospinning setup. Four basic categories were identified, namely, patterned fibers, fiber yarns, and multicomponent and rate and area of deposition of electrospun mat.

4.1. Patterned Fibers. The patterning of nanofibers was found important as ordered architecture finds applications in fields such as electronics [28], skeletal muscle regeneration [29], and polarized luminescence [30]. These configurations

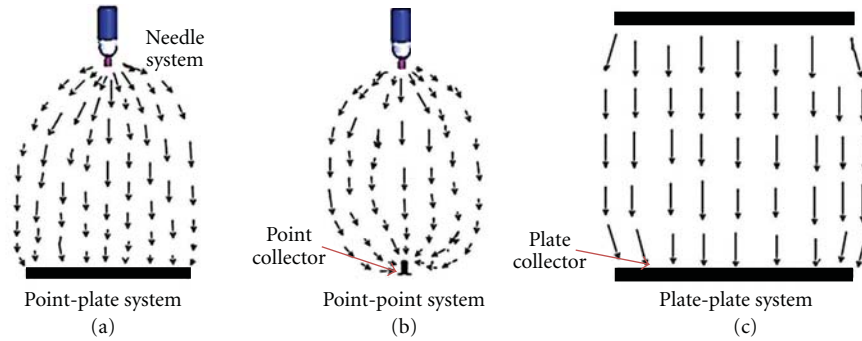


FIGURE 5: Possible configurations of electric field lines between the needle system and the collector.

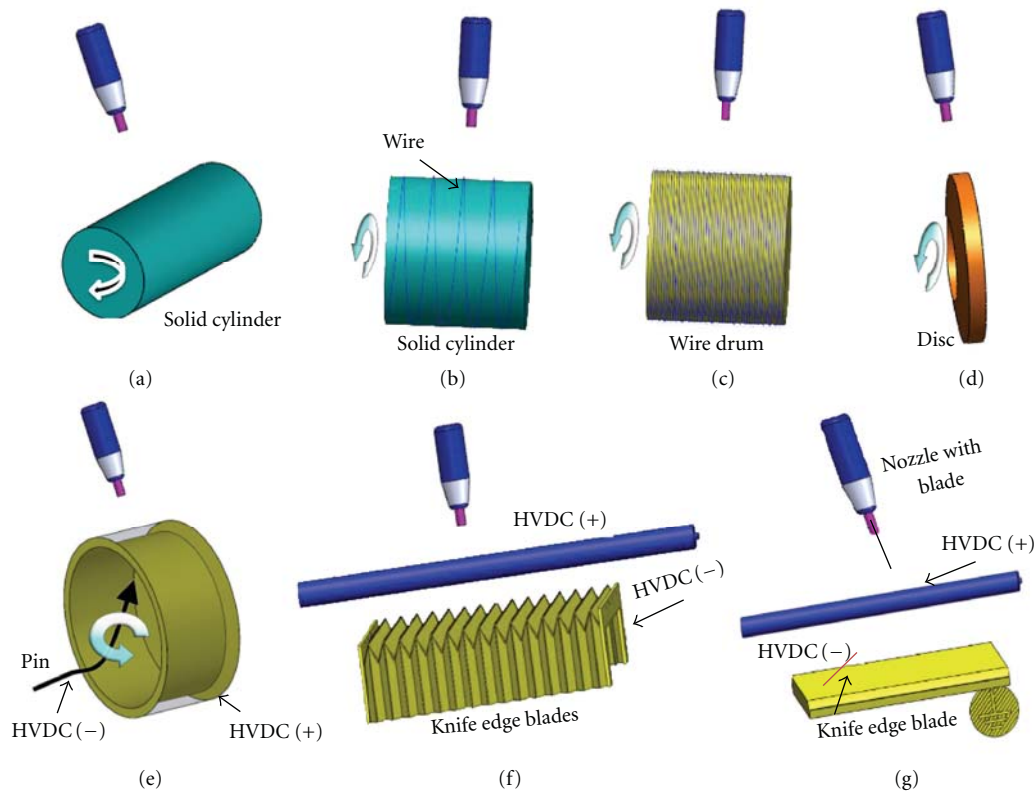


FIGURE 6: Category of electrospinning setups based on rotating device. These configurations include (a) solid cylindrical, (b) wire wound on an insulated cylinder, (c) wired drum, (d) disc collector, (e) sharp pin inside the rotating collector, (f) knife-edged electrodes, and (g) knife-edged electrode and needle system.

include 1D- as well as 3D-aligned structures. Other specific-patterned structures have been configured so as to fulfill the desired requirements. The configurations can be broadly divided based on the manipulations in the subsystems. These subsystems include the needle system and the collector. The collector can be further divided into the rotating device or a configuration of electrodes.

The major category of electrospinning setups configuring aligned nanofibers employs a rotating device as the collector. The purpose of the rotating device is to mechanically stretch the fibers, thus helping it to align along the periphery of the mandrel. The mandrel can transverse along its axis in order to obtain aligned fiber mat. These configurations include

a solid cylindrical collector [31], which can rotate about its axis, shown in Figure 6(a). The aligned fibers obtained with the help of solid rotating drum are shown in Figure 7. The other variations include a conducting wire wound on an insulated cylinder by Bhattarai et al. [32] as shown in Figure 6(b). These conducting wires act as the electric field concentrator as shown in Figure 5(b). As expected, a highly aligned fiber bundle was obtained on and in near vicinity of wires. It was also noted that the size of the fiber bundle directly correlates with the thickness of the wire. Similarly, in case of wired drum [33] in Figure 6(c), each wire acts as the electric field concentrator, resulting in aligned fiber at the low speed of the drum. On the similar lines, Sundaray et al. [34]

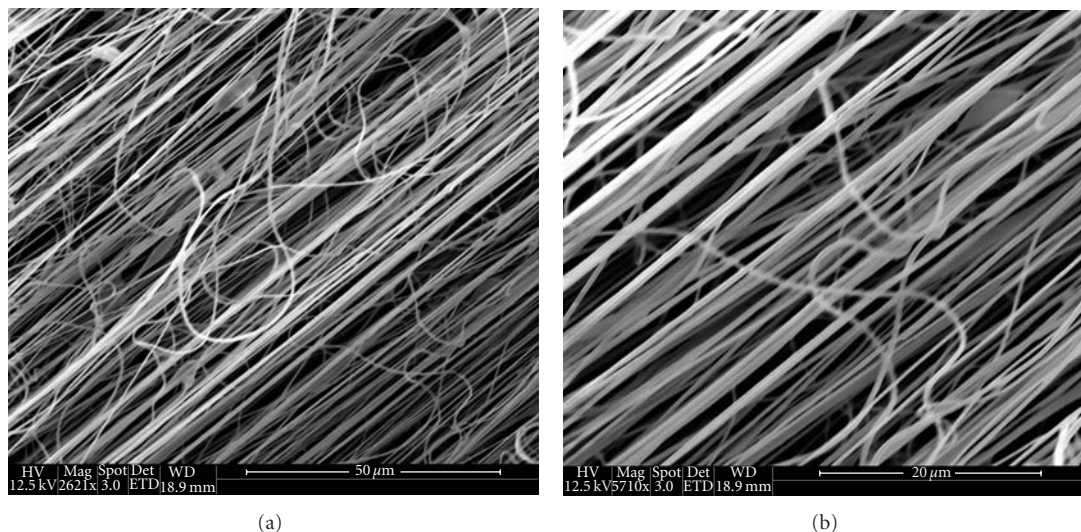


FIGURE 7: Aligned nanofibers of 10 wt% polyacrylonitrile (PAN) dissolved in dimethylformamide (DMF) collected on a rotating drum. The rotation speed of the drum was kept at 2000 rpm. The electrospinning was performed at the flow rate of 1.2 mL/h with the applied electric field strength of 1.5 kV/cm.

placed a sharp pin inside the rotating collector as an electric field concentrator shown in Figure 6(e). As the drum was given translational motion, it resulted in large deposition area of the aligned nanofibers. Nevertheless, cross-bar pattern (instead of uniaxially aligned fibers) is resulted due to the translation motion of the drum. Other configurations employing electric field concentrator include knife-edged electrodes (Figures 6(f) and 6(g)) employed by Teo et al. [35, 36]. Appreciable degree of alignment was obtained with the provisions to control the direction of aligned fibers. One of the notable collector configurations based on disc collector [37] depicted in Figure 6(d), is Zussman et al.'s [38] collector system. The collector system consists of rotating disc and a small aluminum table attached to the disk edge. Double- and triple-layer highly aligned crossbar structures were obtained. The only drawback of the setup was the manual rotation of aluminum table for the deposition of the subsequent nanofibrous array. Similar setup was designed in the laboratory to fabricate aligned fibers as shown in Figure 8(a). It was noted that alignment of the fibers improved with an increase in the rotation speed of the disc from 800 rpm (Figure 8(b)) to 2000 rpm (Figure 8(d)).

The collector configurations shown in Figure 9 are based upon a group of counter electrodes placed in certain configuration. Appreciable degree of alignment was obtained from these proposed setups. Figures 9(a) and 9(b) show a setup consisting of parallel electrodes and an array of counter electrodes designed by Li et al. [39, 40], as expected edges of electrodes act as the electric field concentrator. These electric field concentrators thereby exert tensional electrostatic force on electrospun jet resulting in the stretching of the jet to the linear array between two given edges. On the similar lines, Teo and Ramakrishna [35] configured the collector system from two steel blades placed with a gap between them, shown in Figure 9(c). This system enabled to align fibers between the tip of steel blades. It was also observed that the postproc-

essing resulted in the improvement of the alignment of the electrospun fibers. Similarly, Lee et al. [41] designed a collector system composed of two pieces of conductive substrates separated by a gap. This particular setup helped to obtain uniaxial aligned fibers between the gap. On the similar lines, Kakade et al. [42] employed a set of electrically charged aluminum plates with a variable gap as a collector. The electrical polarity of the aluminum plates was kept negative with respect to the one applied to the syringe system. Kakade et al. [42] successfully aligned nanofibers between two electrically charged aluminum plates. Similarly, Shin et al. [43] designed a parallel electrode system consisting of aluminum and gold electrodes as shown in Figure 9(d) to obtain aligned fiber mat. The gold electrodes were patterned to have a single trench placed between a pair of subelectrodes. The subelectrodes made of a rectangular aluminum foil and insulating plates were placed parallel to each other. Both the main collectors and the subelectrodes were grounded.

Although these configurations can achieve a high degree of orientation in nanofibers, they suffer from the low throughput as compared to rotating drum. Kakade et al. [42] compared the aligned fibers obtained from a rotating mandrel with the fibers collected between the electrically charged plates. It was noted that polymer chains within the nanofibers were oriented only in case of electrically charged plates. The electric charge on the aluminum plates was found to be responsible for the phenomenon as compared to the grounded mandrel.

The particular setup shown in Figure 9(e) consists of the usual needle system consisting of a syringe pump and HVDC supply connected to a metallic needle. The collector for this particular setup consists of two pieces of stainless steel collectors (collector 1 and collector 2). The provision was made in the setup to selectively connect the collectors to HVDC power supply. This particular provision helped Ishii et al. [44] obtain straight fiber forms between the collectors.

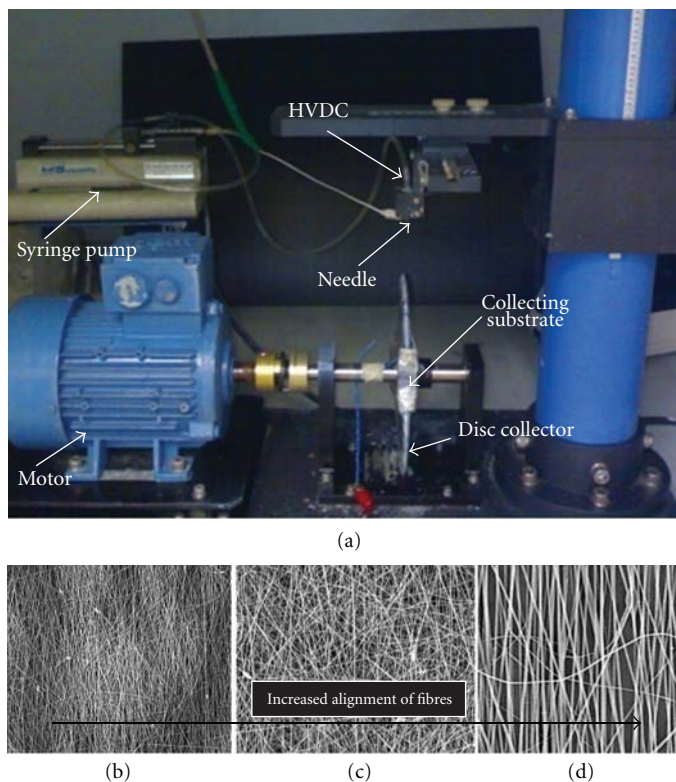


FIGURE 8: (a) The electrospinning setup for the fabrication of aligned TiO_2 fibers. The increase in the alignment of the fiber was observed with the increase in the rotation speed of the disc collector. The speed of the disc was increased from (b) 800, (c) 1000 to (d) 2000 rpm to obtain aligned fibers. The electrospinning was performed at flow rate of 0.1 mL/h with the applied electric field strength of 1 kV/cm.

Nevertheless, the diameter of the fibers obtained was in sub-micron range thus reducing the applicability of the fibers obtained. Chuangchote's and Supaphol's [45] collector system consists of dual vertical stainless steel wires as the secondary electrodes with grounded aluminum foil as the primary electrodes as shown in Figure 9(f). These vertical steel wires were mounted along the center line between the tip of the needle system and the grounded aluminum foil. Chuangchote and Supaphol [45] was able to achieve simultaneous collection of aligned fibers between the parallel vertical wires and a random fiber mat on the aluminum foil. Nevertheless, aligned fibers were observed between the vertical wires at short collection times, whereas a further increase in the collection time resulted in random fiber mat. Liu et al. [46] employed external magnetic field in the collector region to achieve aligned fibers as shown in Figure 9(g). It was observed that fiber diameter further decreased due to the application of external applied magnetic field near the surface of collector. The percentage decreases in fiber diameter were found to be at least 40% due to the application of external applied magnetic field. Liu et al. [46] also observed highly uniform nanofibers with minimal splitting.

This particular category shown in Figure 10 deals with the setups in which dispensing system of the electrospinning setup is modified to obtain aligned fibers. In one of the setup [47] shown in Figure 10(a), the dispensing system consists of a triangular aluminum tip without any solution supply

system. The grounded upright coin act as the collector placed a certain distance away from the triangular tip. The triangular tip is dipped in electrospinning solution to form a small droplet on its tip. When a high voltage is applied to the tip, a bundle of electrospun fibers were then formed between the tip and the collector. Wu et al. [47] successfully fabricated ultralong highly oriented fiber bundles. Nevertheless, as the bending instabilities were totally suppressed, the fiber diameter obtained was in micron range. On the other hand, Rafique et al. [48] configured a collector system comprising a tip collector, and a support plate shown in Figure 10(b). Tip collector is assembled from the grounded wire electrode with wooden holder. The needle system was placed at an angle to the tip collector. By controlling the flow rate, Rafique et al. [48] were able to align individual nanofibers. It was noted that the collector tip resulted in the convergence of electric field lines as in Figure 5(b). This resulted in the dragging of nanofibers to the collect tip. The repelling force between similarly charged fibers resulted in the highly aligned fiber mat. Nevertheless, the fibers obtained were broken with their diameter being in submicron range.

4.2. Rate and Area of Deposition of Electrospun Mat. As mentioned, the electrospun jet follows a spiraling path with increasing radius. This phenomenon results in the deposition area of the order or few square centimeters. It has been

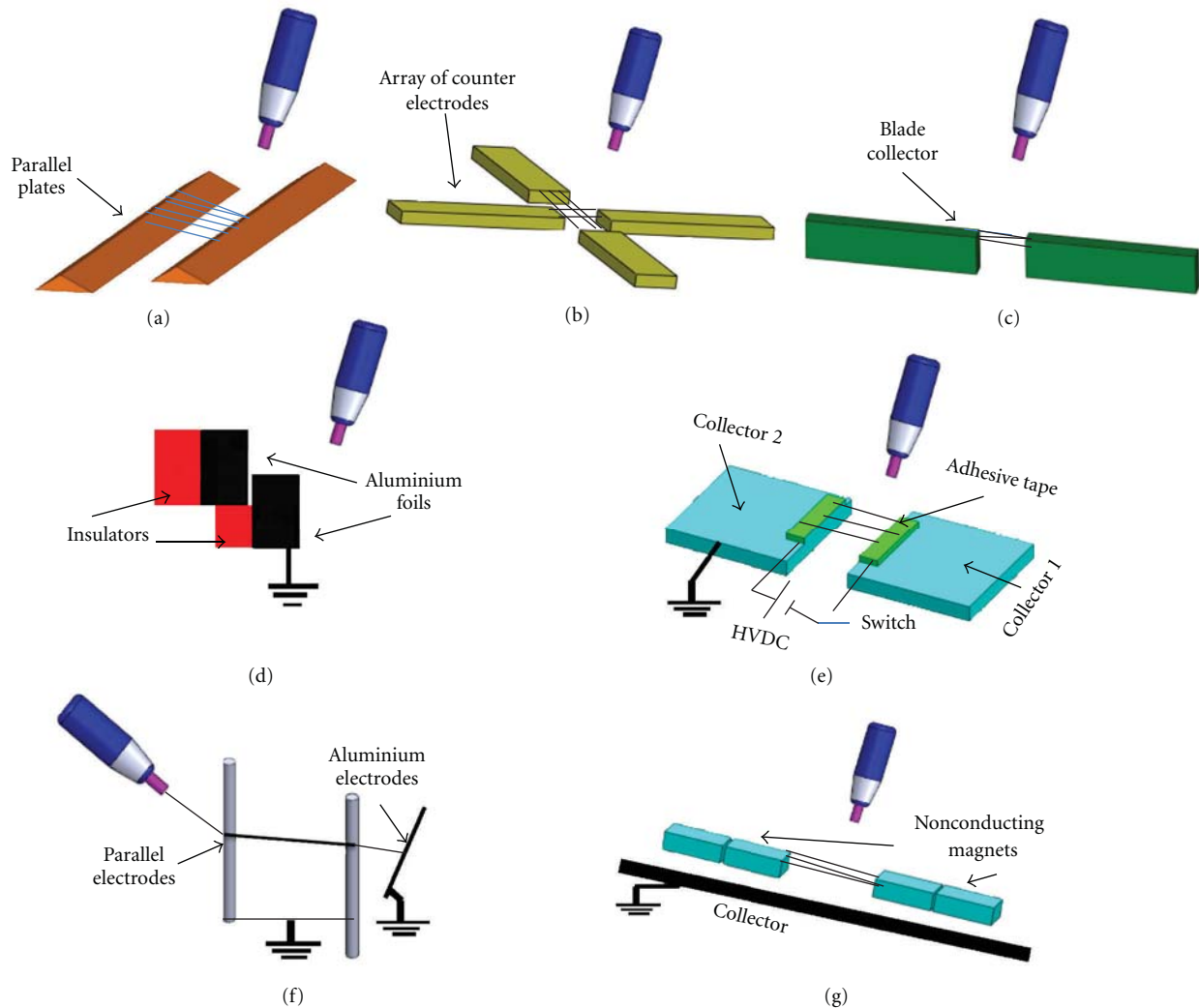


FIGURE 9: Collector configurations are mainly based upon a group of counter electrodes placed in certain configuration: (a) parallel electrodes: (b) array of counter electrodes: (c) two steel blades placed with a gap: (d) parallel electrode system consisting of aluminum and gold electrodes: (e) two pieces of stainless steel electrodes with the provision to selectively connect to HVDC power supply: (f) collector system consisted of dual vertical stainless steel wires as the secondary electrodes with grounded aluminum foil as the primary electrode: (g) external magnets as auxiliary electrodes.

noticed by the researches that controlling the deposited area and density of electrospun fiber mat will widen the application spectrum of these fibers. Yang et al. [49] designed a regular hexagon distribution multineedle system as shown in Figure 11(a). The setup has the provision of enclosing the needle system inside an iron ring. This particular enclosure helps in the concentration of electric field lines and thus controlling the deposited area. This multineedle system as expected also increase the deposition density of the fiber mat. On the similar lines, Kim [50] modified the electrospinning setup with the introduction of an electrically charged cylindrical electrode connected to the needle system and a field-controllable target electrode. Both the electrically charged cylindrical electrode and needle system connected to single HVDC supply through a copper wire. Kim [50] noted the convergence of the applied electric field along the spinning

axis. This convergence of electric field lines results in a very stable spinning process. The notable feature of the setup was the reduction of the deposited area. This may be due to the suppressing of bending instabilities of electrospun jet by the cylindrical electrode. Due to the application of the field-controllable target electrode, appreciable degree of alignment of nanofibers was also obtained. These field-controllable target electrodes consist of parallel electrodes [50] and circular, interdigitated, and parallel targets [51] connected to HVAC supply. Ying et al. [52] on the other hand controlled the deposition of electrospun fibers by placing an insulating tube around the needle system as shown in Figure 11(b). This is made possible by the static charges developed on the surface of the insulating tube helping in the reduction of the extend of bending instabilities and thus the deposited area. Similar results were obtained by the configuration employing dual rings [53] (Figure 11(d)) and three rings [54] (Figure 11(e))

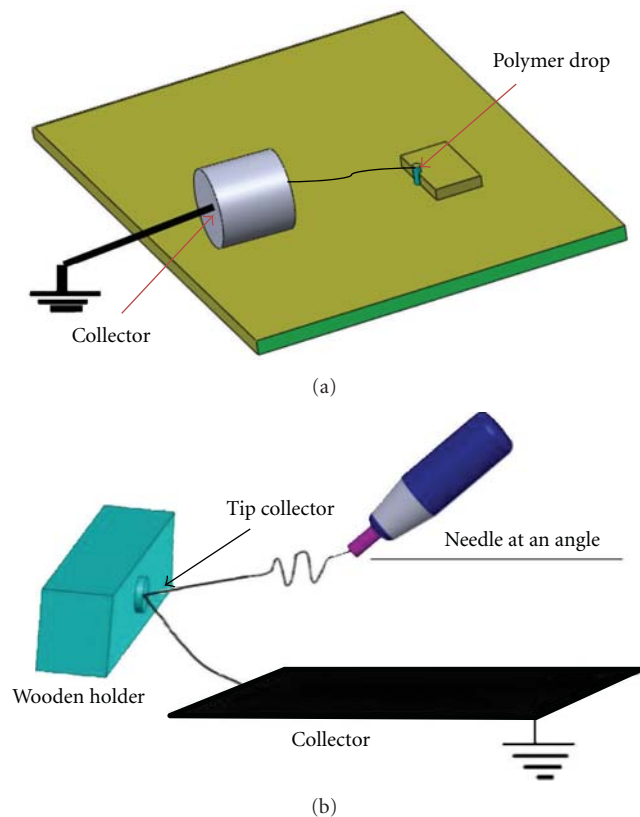


FIGURE 10: This category deals with the setups in which dispensing system of the electrospinning designs is modified to obtain aligned fibers, (a) dispensing system consists of a triangular aluminum tip, (b) needle system was placed at an angle to the tip collector to control the flow rate.

as auxiliary electrodes. Bellan and Craighead [55] employed a group of focusing and steering electrodes placed close to collecting substrate as shown in Figure 11(c). A constant voltage is applied to two focusing electrodes, whereas time-varying voltage is applied to the other two steering electrodes. Employing this setup, Bellan and Craighead [55] were able to focus and steer an electrospinning jet into a patterned structure. Nevertheless, small intricate patterns were not possible due to the limited electronics of the setup.

Li et al. [56] devised 2 needles system with rotating drum as a collector as shown in Figure 11(f). These needle systems were given opposite polarities with respect to each other. This particular configuration resulted in highly intertwined and three-dimensional isotropic network structure. As expected, Li et al. [56] were able to achieve 170 times increase in the throughput compared to the conventional single needle system. Vaseashta [57] was able to achieve a large deposition area by configuring multiple Taylor cone from a single needle system. This is achieved by manipulating the electric field lines near the collector as shown in Figure 11(g). Vaseashta [57] also noted that clogging of the passageway of the needle system from polymer solution may also result in the splitting of the polymer drop and hence formation of more than one Taylor cone. Dosunmu et al. [58] employed porous walled

cylindrical tube as the dispensing system depicted in Figure 11(h). In this particular dispensing system, air pressure is applied to push the fluid through the pores. Electrostatic force applied on the drops coming out from the pores resulted in the formation of jets. This particular setup will result in the considerable increase in throughput of the electrospun fibers. Lukas et al. [59] designed a multijet electrospinning setup as shown in Figure 11(i), thus improving the throughput from the process. Lukas et al. [59] observed that sawlike pattern was not the main field concentration, whereas electrospinning jets are created from crests of the exponentially growing wave on the liquid surface.

4.3. Multicomponent Electrospun Fibers. The approach of the modified setup is to produce multicomponent fibers. These components are important for their application in areas such as nanosprings [60], superhydrophobic surfaces [61], sensor [62], and drug delivery [63]. The most prominent in the multicomponent structures are the core-shell structures. These structures may include a core and any number of shells thus resulting in the formation of bicomponent to multicomponent structures. Figure 12(a) depicts the schematic of core-shell structure. The phenomenon mainly comprised of coaxially pumping out two chemically dissimilar solutions. The phenomenon needs precise control of the system and process parameters for achieving core-shell structure. Sun et al. [64] noted that entrainment of nonspinnable core material inside a spinnable shell material is one of the advantages of this particular arrangement. The other variation of this configuration [65] depicted in Figure 12(b) includes gas as a shell material. The gas flow applies additional drawing action on the polymer jet during the electrospinning process. Lin et al. [65] observed a decrease in the fiber diameter with the increase in the gas flow rate. Varesano et al. [66] on other hand, was able to spin crimped fibers by employing an air flow around a needle system. It was noted that the air flows spiraling downward in the electrospinning chamber impedes the development of the bending instabilities suffered by the electrospun jet. Due to this impeded bending instabilities, Varesano et al. [66] was only able to obtain submicron ranged fibers.

One of the innovative approaches was employed by the Bazilevsky et al. [67] for producing core-shell fibers. Bazilevsky et al. [67] employed a single needle system to electrospin emulsions. It was observed that the dissolved phase undergoes ordinary electrospinning, whereas the dispersion phase gets trapped as a drop at the base of Taylor cone depicted in Figure 12(c). It was observed that the drop stretches due to the force acting on it by the outer fluid. This stretching of drop results in the formation of core-shell fibers. The morphology was also found to be similar to coannular needle electrospinning setups. The other notable configuration designed by Gupta and Wilkes [68] employ dispensing system having two chambers for two given polymer solutions as depicted in Figure 12(d). The dispensing system disperses two solutions from a single needle, thus fabricating bicomponent nanofibers. The other configuration [69] shown in Figure 12(e) includes a rotating drum between two needle systems. Each of these needle systems disperses a desired solution. This configuration allowed for the production

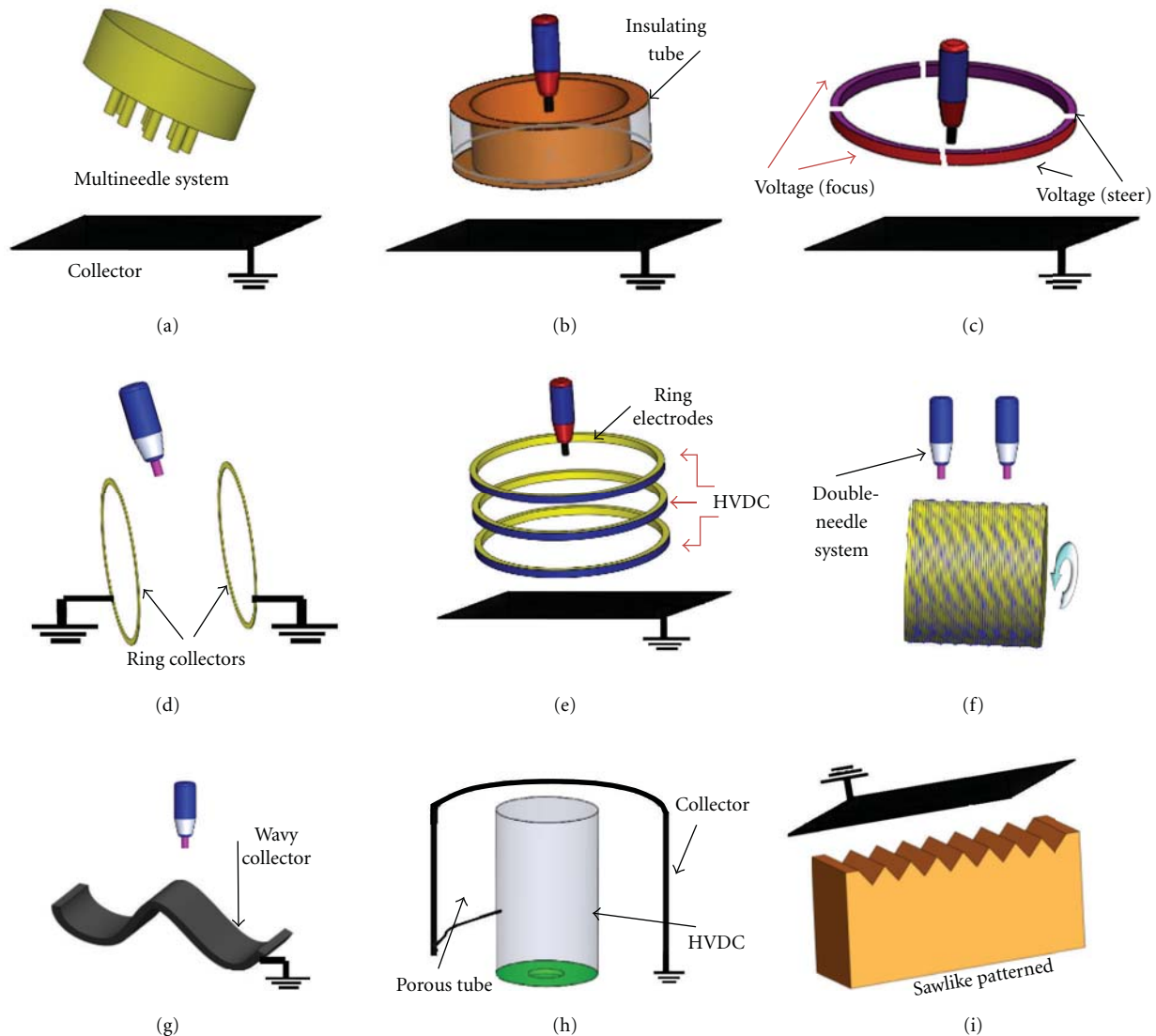


FIGURE 11: Setups to control the deposited area and density of electrospun fiber, (a) regular hexagon multineedle system enclosed inside an iron ring, (b) insulating tube around the needle system, (c) group of focusing and steering electrodes placed close to collecting substrate, (d) dual rings, (e) three rings, (f) 2-needle system, (g) wavy-shaped collector, (h) porous-walled cylindrical tube as the dispensing system, and (i) sawlike-patterned dispensing system.

of homogeneously mixed superhydrophobic composite nanofibers. Duan et al. [69] on the other hand, was able to configure mechanically stable highly hydrophilic membranes with the similar electrospinning setup.

In-house designed core-shell setup was employed for the production of core-shell as well as hollow fibers shown in Figure 13. These fibers are being employed for the advanced application such as photocathodes in dye-synthesized solar cells, gas sensors, and regenerative medicine applications. Hollow fibers obtained were employed as photocathodes in DSSCs due to their large surface area to the volume ratio. This large surface area of the hollow fibers results in the improved dye loading of the photocathode and thus improved performance of the solar cells. The abovementioned work will appear elsewhere. Work is also in the process to employ core-shell fiber in the solid state solar cells, web guides, gas sensors, and so forth.

Though the core-shell and bicomponent nanofibers are quite promising, the final fiber morphology largely depends upon the fluid dynamics in the boundary layer at the interface of the dissimilar fluid components. A thick boundary layer at the interface will imply a large drag force acting on the inner fluid component. This large drag force will impede the flow of inner fluid component resulting in predominately single component nanofibers, thus defying the purpose of the designed setup. This implies that proper control of process and system parameters such as flow rate and chemical composition of the solutions is required for the production of core-shell fibers.

Composite nanofibers are also being obtained through chemical synthesis by employing electrospun fibers as the base material. For instance, Sebastian et al. [70] (co-researcher at NUSNNI, NUS, Singapore) fabricated efficient catalytic filter membrane employing nanofibers as shown in

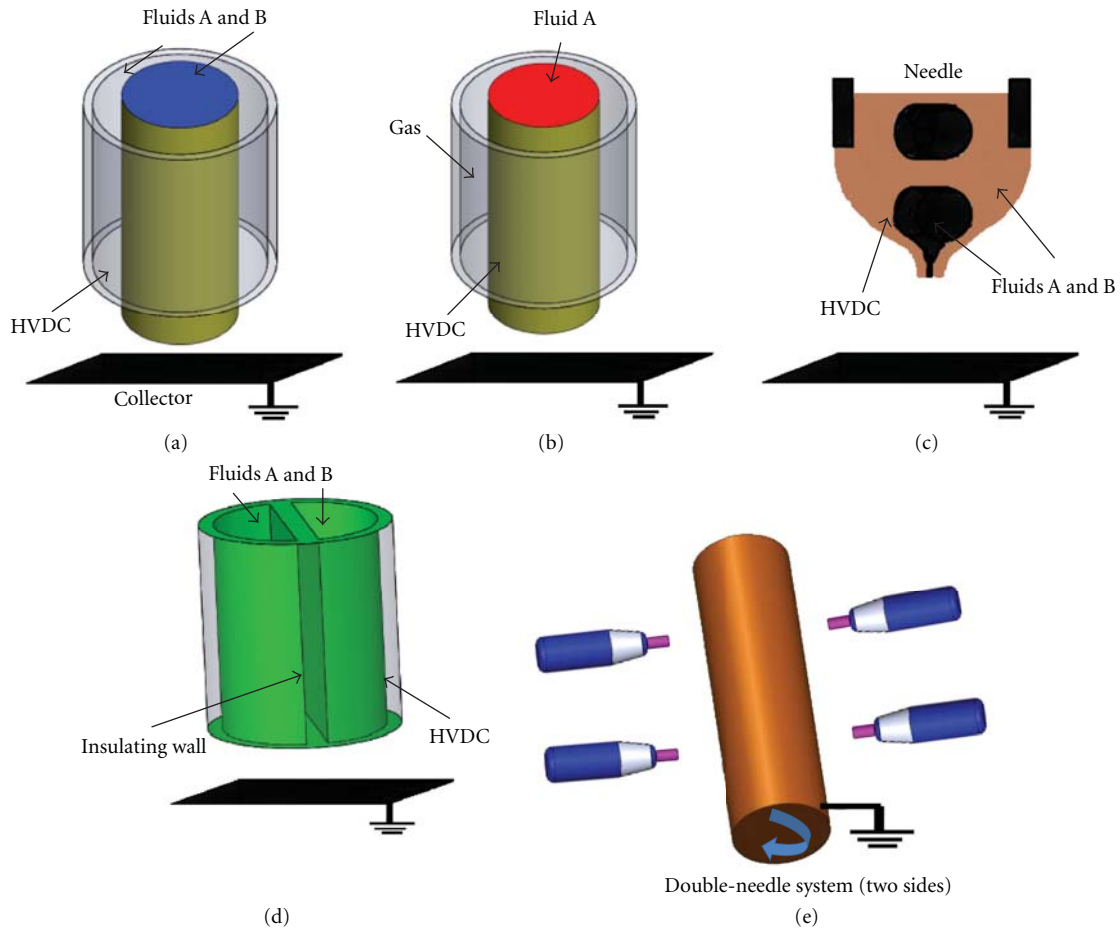


FIGURE 12: The function of the modified setup is to produce multicomponent fibers, (a) core shell, (b) gas as a shell material in core-shell structure, (c) single-needle core shell structure, (d) bicomponent electrospinning system, and (e) rotating drum between two needle systems as electrospinning setup.

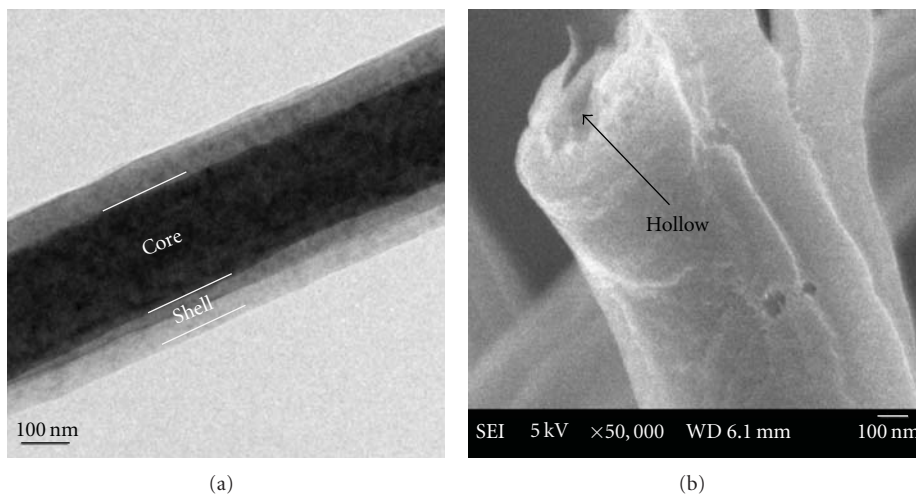


FIGURE 13: (a) TEM of core-shell fibers prepared by coaxial electrospinning. 10 wt% aqueous polyvinyl alcohol (PVA) was employed as the core, whereas 8 wt% polyvinylpyrrolidone (PVP) dissolved in dimethylformamide (DMF) as the shell. The electrospinning was performed at the applied electric field strength of 1.5 kV/cm, (b) SEM image of the hollow TiO₂ nanofibers.

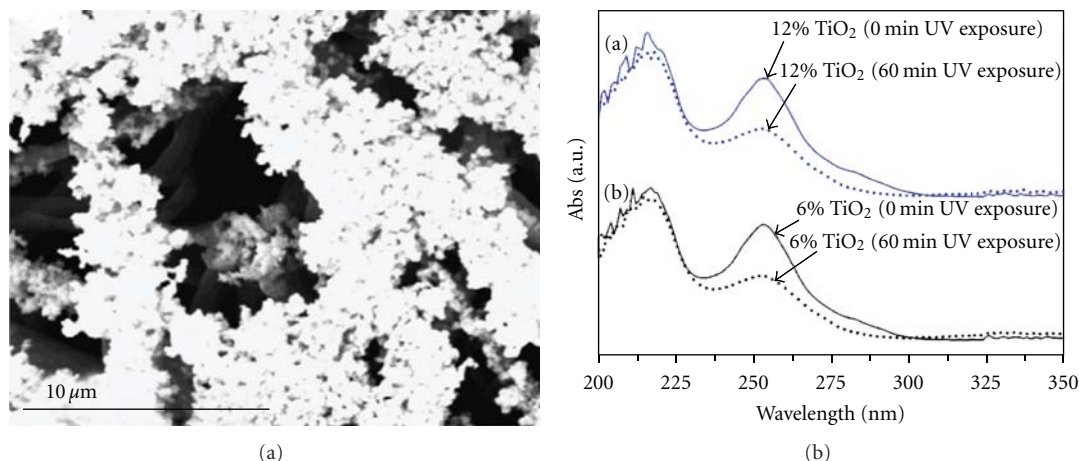


FIGURE 14: (a) TiO₂ nanoparticles deposited on 12 wt% PANi/PEO-blended nanofibrous mat. (b) Increase in the catalytic activity of the composite fiber with the increase in the concentration of the TiO₂ deposited on the conductive PANi/PEO-blended nanofibers.

Figure 14(a). The catalytic filter membrane was fabricated by electrospinning TiO₂ nanoparticles on electrically conductive PANi-PEO nanofibrous membrane. It was noted that blended PANi-PEO nanofibrous membrane as the collecting substrate resulted in the uniform deposition of TiO₂ on its surface as compared to fiber mat placed on aluminum foil. It can be seen from the Figure 14(b) that the catalytic activity of the membrane improved with an increase in the concentration of TiO₂ nanoparticles. The obtained membrane was found to be highly stable against ultrasonic sonication, thus making it viable for large-scale industrial production.

4.4. Yarns. These twisted nanofibers that can emulate organic material such as collagen and DNA are being readily exploited in the field such as tissue engineering [71] to p-n junction [72]. A number of electrospinning configurations are being analyzed related to configuring nanofibrous yarn. One of these configurations shown in Figure 15(a) depicts the phenomenon of self-bundling electrospinning employed for the generation of continuous electrospun yarn. An external electrode is employed to initiate self-bundling of the nanofibers, which is later collected on the rotating mandrel. Wang et al. [73] observed that the conductivity played a major role in the production of continuous self-bundled yarns. It was noted that the increment in the conductivity of the polymer solution resulted in the self-bundling of the fiber without the need of the external electrode. Aggravated bending instability due to the increase in the conductivity of polymer solution was considered responsible for the above phenomenon. The particular setup [74] shown in Figure 15(b) consists of electrospinning nanofibers in a liquid container. This is done to neutralize the free charges available on the surface of the fibers. These neutralized fibers were later collected as the fiber yarn via a rotating mandrel. Gu et al. [75] proposed a novel configuration for the production of yarn shown in Figure 15(c). This setup consists of four auxiliary electrodes with a usual ground electrode. The purpose of these electrodes is to help in the twisting of nanofibers.

These electrodes are electrically activated in sequence to allow the 360° rotation of electrospun jet. The yarn was later collected on the grounded surface. Gu et al. [75] were also able to control the twist length of the yarn by controlling the rotation time of the amplitude of electric field on the auxiliary electrode.

The other setup [53] consists of two grounded stainless steel rings placed at a certain distance apart, shown in Figure 15(d). These fibers get suspended between the collector rings. One of these collector rings is allowed to rotate about its axis thus producing twisted nanofibers. This setup though simple results in the low throughput. The other setup [76] depicted in Figure 15(e) consists of two needles systems placed in the horizontal direction facing each other. Each of these needle systems consists of a syringe pump with a HVDC supply. These syringe systems were given opposite polarities with respect to each other. These opposite polarities help in the sticking of the oppositely charged fibers originating from the needles. The fiber yarn thus obtained is considered to be electrically neutral, thus not attracted to any of the electrically charged needles. Pan et al. [76] observed that it was easier to align this electrically neutral yarn with the help of a rotating collector. The shortcoming of this particular setup may be the manual towing of fiber yarn to the rotating collector.

5. Conclusions

Various electrospinning setups have been discussed based on their applications. This is done for the researchers to make a calculated choice regarding design of their electrospinning setup. Four basic categories were identified, namely, patterned fibers, fiber yarns, and multicomponent and rate and area of deposition of electrospun mat. These categories help to analyze the limitations of the electrospinning process, that is, what need to be done to better utilize the inherent capabilities of the electrospinning process? Nevertheless, we hope that this analysis will shed some light on one of the highly researched nanofiber production techniques.

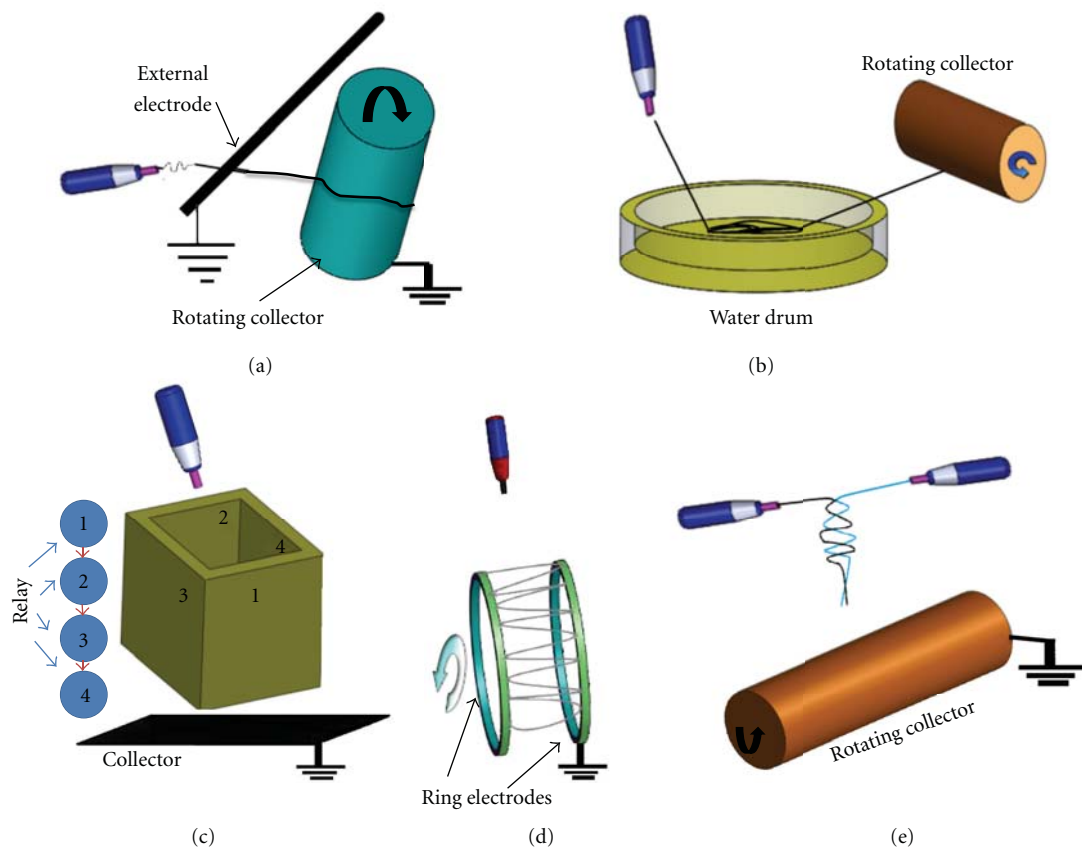


FIGURE 15: These setups are employed to produce twisted nanofibers, (a) self-bundling electrospinning, (b) electrospinning in a liquid container to neutralize the free charges, (c) twisting by four auxiliary electrodes, (d) ring collector, and (e) two horizontal needles systems.

Acknowledgments

The authors gratefully acknowledge National University of Singapore, Nanyang Technological University, and National Research Foundation, Singapore, for funding support of the research Grant (NRF-CRP-4-2008-03).

References

- [1] J. S. Im, S. C. Kang, S. H. Lee, and Y. S. Lee, "Improved gas sensing of electrospun carbon fibers based on pore structure, conductivity and surface modification," *Carbon*, vol. 48, no. 9, pp. 2573–2581, 2010.
- [2] J. Yuan, J. Geng, Z. Xing, J. Shen, I. K. Kang, and H. Byun, "Electrospinning of antibacterial poly(vinylidene fluoride) nanofibers containing silver nanoparticles," *Journal of Applied Polymer Science*, vol. 116, no. 2, pp. 668–672, 2010.
- [3] S. Y. Chew, R. Mi, A. Hoke, and K. W. Leong, "The effect of the alignment of electrospun fibrous scaffolds on Schwann cell maturation," *Biomaterials*, vol. 29, no. 6, pp. 653–661, 2008.
- [4] S. Chuangchote, J. Jitputti, T. Sagawa, and S. Yoshikawa, "Photocatalytic activity for hydrogen evolution of electrospun TiO₂ nanofibers," *ACS Applied Materials & Interfaces*, vol. 1, no. 5, pp. 1140–1143, 2009.
- [5] Y. C. Ahn, S. K. Park, G. T. Kim et al., "Development of high efficiency nanofilters made of nanofibers," *Current Applied Physics*, vol. 6, no. 6, pp. 1030–1035, 2006.
- [6] C. Barrera, K. Hyde, J. P. Hinestroza, T. Gould, G. Montero, and C. Rinaldi, "Electrospun magnetic nanofibers with anti-counterfeiting applications," in *Proceedings of the ASME International Mechanical Engineering Congress and Exposition (IMECE '05)*, pp. 467–473, New York, NY, USA, November 2005.
- [7] Y. K. Kang, C. H. Park, J. Kim, and T. J. Kang, "Application of electrospun polyurethane web to breathable water-proof fabrics," *Fibers and Polymers*, vol. 8, no. 5, pp. 564–570, 2007.
- [8] M. Grätzel, "Dye-sensitized solid-state heterojunction solar cells," *MRS Bulletin*, vol. 30, no. 1, pp. 23–27, 2005.
- [9] R. E. Taylor, "Electrically Driven Jets," *Proceedings—Royal Society of London, A*, vol. 313, pp. 453–475, 1969.
- [10] A. F. Spivak and Y. A. Dzenis, "Asymptotic decay of radius of a weakly conductive viscous jet in an external electric field," *Applied Physics Letters*, vol. 73, no. 21, pp. 3067–3069, 1998.
- [11] A. F. Spivak, Y. A. Dzenis, and D. H. Reneker, "Model of steady state jet in the electrospinning process," *Mechanics Research Communications*, vol. 27, no. 1, pp. 37–42, 2000.
- [12] A. L. Yarin, S. Koombhongse, and D. H. Reneker, "Taylor cone and jetting from liquid droplets in electrospinning of nanofibers," *Journal of Applied Physics*, vol. 90, no. 9, pp. 4836–4846, 2001.
- [13] A. L. Yarin, S. Koombhongse, and D. H. Reneker, "Bending instability in electrospinning of nanofibers," *Journal of Applied Physics*, vol. 89, no. 5, pp. 3018–3026, 2001.
- [14] M. M. Hohman, M. Shin, G. Rutledge, and M. P. Brenner, "Electrospinning and electrically forced jets. I. Stability theory," *Physics of Fluids*, vol. 13, no. 8, pp. 2201–2220, 2001.

- [15] M. M. Hohman, M. Shin, G. Rutledge, and M. P. Brenner, "Electrospinning and electrically forced jets. II. Applications," *Physics of Fluids*, vol. 13, no. 8, pp. 2221–2236, 2001.
- [16] J. J. Feng, "The stretching of an electrified non-Newtonian jet: a model for electrospinning," *Physics of Fluids*, vol. 14, no. 11, pp. 3912–3926, 2002.
- [17] J. J. Feng, "Stretching of a straight electrically charged viscoelastic jet," *Journal of Non-Newtonian Fluid Mechanics*, vol. 116, no. 1, pp. 55–70, 2003.
- [18] C. P. Carroll and Y. L. Joo, "Electrospinning of viscoelastic Boger fluids: modeling and experiments," *Physics of Fluids*, vol. 18, no. 5, Article ID 053102, 14 pages, 2006.
- [19] D. H. Reneker, A. L. Yarin, H. Fong, and S. Koombhongse, "Bending instability of electrically charged liquid jets of polymer solutions in electrospinning," *Journal of Applied Physics*, vol. 87, no. 9, pp. 4531–4547, 2000.
- [20] A. L. Yarin, W. Kataphinan, and D. H. Reneker, "Branching in electrospinning of nanofibers," *Journal of Applied Physics*, vol. 98, no. 6, Article ID 064501, pp. 1–12, 2005.
- [21] L. Huang, K. Nagapudi, P. R. Apkarian, and E. L. Chaikof, "Engineered collagen—PEO nanofibers and fabrics," *Journal of Biomaterials Science, Polymer Edition*, vol. 12, no. 9, pp. 979–993, 2001.
- [22] T. Lin, H. Wang, H. Wang, and X. Wang, "The charge effect of cationic surfactants on the elimination of fibre beads in the electrospinning of polystyrene," *Nanotechnology*, vol. 15, no. 9, pp. 1375–1381, 2004.
- [23] K. H. Lee, H. Y. Kim, M. S. Khil, Y. M. Ra, and D. R. Lee, "Characterization of nano-structured poly(ϵ -caprolactone) non-woven mats via electrospinning," *Polymer*, vol. 44, no. 4, pp. 1287–1294, 2003.
- [24] L. Rayleigh, "On the instability of a cylinder of viscous liquid under capillary forces," *Philosophical Magazine Series 5*, vol. 34, no. 207, pp. 145–154, 1982.
- [25] H. Fong, I. Chun, and D. H. Reneker, "Beaded nanofibers formed during electrospinning," *Polymer*, vol. 40, no. 16, pp. 4585–4592, 1999.
- [26] M. G. McKee, G. L. Wilkes, R. H. Colby, and T. E. Long, "Correlations of solution rheology with electrospun fiber formation of linear and branched polyesters," *Macromolecules*, vol. 37, no. 5, pp. 1760–1767, 2004.
- [27] A. L. Yarin and E. Zussman, "Upward needleless electrospinning of multiple nanofibers," *Polymer*, vol. 45, no. 9, pp. 2977–2980, 2004.
- [28] S. W. Lee, H. J. Lee, J. H. Choi et al., "Periodic array of polyelectrolyte-gated organic transistors from electrospun poly(3-hexylthiophene) nanofibers," *Nano Letters*, vol. 10, no. 1, pp. 347–351, 2010.
- [29] K. J. Aviss, J. E. Gough, and S. Downes, "Aligned electrospun polymer fibres for skeletal muscle regeneration," *European Cells & Materials*, vol. 19, pp. 193–204, 2010.
- [30] M. Campoy-Quiles, Y. Ishii, H. Sakai, and H. Murata, "Highly polarized luminescence from aligned conjugated polymer electrospun nanofibers," *Applied Physics Letters*, vol. 92, no. 21, Article ID 213305, 2008.
- [31] J. A. Matthews, G. E. Wnek, D. G. Simpson, and G. L. Bowlin, "Electrospinning of collagen nanofibers," *Biomacromolecules*, vol. 3, no. 2, pp. 232–238, 2002.
- [32] N. Bhattarai, D. Edmondson, O. Veisoh, F. A. Matsen, and M. Zhang, "Electrospun chitosan-based nanofibers and their cellular compatibility," *Biomaterials*, vol. 26, no. 31, pp. 6176–6184, 2005.
- [33] P. Katta, M. Alessandro, R. D. Ramsier, and G. G. Chase, "Continuous electrospinning of aligned polymer nanofibers onto a wire drum collector," *Nano Letters*, vol. 4, no. 11, pp. 2215–2218, 2004.
- [34] B. Sundaray, V. Subramanian, T. S. Natarajan, R. Z. Xiang, C. C. Chang, and W. S. Fann, "Electrospinning of continuous aligned polymer fibers," *Applied Physics Letters*, vol. 84, no. 7, pp. 1222–1224, 2004.
- [35] W. E. Teo and S. Ramakrishna, "Electrospun fibre bundle made of aligned nanofibres over two fixed points," *Nanotechnology*, vol. 16, no. 9, pp. 1878–1884, 2005.
- [36] W. E. Teo, M. Kotaki, X. M. Mo, and S. Ramakrishna, "Porous tubular structures with controlled fibre orientation using a modified electrospinning method," *Nanotechnology*, vol. 16, no. 6, pp. 918–924, 2005.
- [37] C. Y. Xu, R. Inai, M. Kotaki, and S. Ramakrishna, "Aligned biodegradable nanofibrous structure: a potential scaffold for blood vessel engineering," *Biomaterials*, vol. 25, no. 5, pp. 877–886, 2004.
- [38] E. Zussman, A. Theron, and A. L. Yarin, "Formation of nanofiber crossbars in electrospinning," *Applied Physics Letters*, vol. 82, no. 6, pp. 973–975, 2003.
- [39] D. Li, Y. Wang, and Y. Xia, "Electrospinning nanofibers as uniaxially aligned arrays and layer-by-layer stacked films," *Advanced Materials*, vol. 16, no. 4, pp. 361–366, 2004.
- [40] D. Li, Y. Wang, and Y. Xia, "Electrospinning of polymeric and ceramic nanofibers as uniaxially aligned arrays," *Nano Letters*, vol. 3, no. 8, pp. 1167–1171, 2003.
- [41] S. J. Lee, N. I. Cho, and D. Y. Lee, "Effect of collector grounding on directionality of electrospun titania fibers," *Journal of the European Ceramic Society*, vol. 27, no. 13–15, pp. 3651–3654, 2007.
- [42] M. V. Kakade, S. Givens, K. Gardner, K. H. Lee, D. B. Chase, and J. F. Rabolt, "Electric field induced orientation of polymer chains in macroscopically aligned electrospun polymer nanofibers," *Journal of the American Chemical Society*, vol. 129, no. 10, pp. 2777–2782, 2007.
- [43] M. K. Shin, S. I. Kim, and S. J. Kim, "Controlled assembly of polymer nanofibers: from helical springs to fully extended," *Applied Physics Letters*, vol. 88, no. 22, 3 pages, 2006.
- [44] Y. Ishii, H. Sakai, and H. Murata, "A new electrospinning method to control the number and a diameter of uniaxially aligned polymer fibers," *Materials Letters*, vol. 62, no. 19, pp. 3370–3372, 2008.
- [45] S. Chuangchote and P. Supaphol, "Fabrication of aligned poly (vinyl alcohol) nanofibers by electrospinning," *Journal of Nanoscience and Nanotechnology*, vol. 6, no. 1, pp. 125–129, 2006.
- [46] Y. Liu, X. Zhang, Y. Xia, and H. Yang, "Magnetic-field-assisted electrospinning of aligned straight and wavy polymeric nanofibers," *Advanced Materials*, vol. 22, no. 22, pp. 2454–2457, 2010.
- [47] H. Wu, D. Lin, R. Zhang, and W. Pan, "Oriented nanofibers by a newly modified electrospinning method," *Journal of the American Ceramic Society*, vol. 90, no. 2, pp. 632–634, 2007.
- [48] J. Rafique, J. Yu, J. Yu et al., "Electrospinning highly aligned long polymer nanofibers on large scale by using a tip collector," *Applied Physics Letters*, vol. 91, no. 6, Article ID 063126, 3 pages, 2007.
- [49] Y. Yang, Z. D. Jia, Q. Li, L. Hou, and Z. C. Guan, "Electrospun uniform fibres with a special regular hexagon distributed multi-needles system," *Journal of Physics: Conference Series*, vol. 142, no. 1, Article ID 012027, pp. 1–6, 2008.
- [50] G. H. Kim, "Electrospinning process using field-controllable electrodes," *Journal of Polymer Science, Part B*, vol. 44, no. 10, pp. 1426–1433, 2006.

- [51] G. Kim and W. Kim, "Nanofiber spraying method using a supplementary electrode," *Applied Physics Letters*, vol. 89, no. 1, pp. 013111–013111-3, 2006.
- [52] Y. Ying, J. Zhidong, and G. Zhicheng, "Controlled deposition of electrospun poly (ethylene oxide) fibers via insulators," in *Proceedings of the 15th IEEE International Conference on Dielectric Liquids (ICDL '05)*, pp. 457–460, Coimbra, Portugal, July 2005.
- [53] P. D. Dalton, D. Klee, and M. Möller, "Electrospinning with dual collection rings," *Polymer*, vol. 46, no. 3, pp. 611–614, 2005.
- [54] J. M. Deitzel, J. Kleinmeyer, D. Harris, and N. C. Beck Tan, "The effect of processing variables on the morphology of electrospun nanofibers and textiles," *Polymer*, vol. 42, no. 1, pp. 261–272, 2001.
- [55] L. M. Bellan and H. G. Craighead, "Control of an electrospinning jet using electric focusing and jet-steering fields," *Journal of Vacuum Science and Technology B*, vol. 24, no. 6, pp. 3179–3183, 2006.
- [56] M. Li, Y. D. He, C. L. Xin et al., "Dual electrode mode electrospinning of biodegradable polymers," *Applied Physics Letters*, vol. 92, no. 21, 3 pages, 2008.
- [57] A. Vaseashta, "Controlled formation of multiple Taylor cones in electrospinning process," *Applied Physics Letters*, vol. 90, no. 9, Article ID 093115, 3 pages, 2007.
- [58] O. O. Dosunmu, G. G. Chase, W. Kataphinan, and D. H. Reneker, "Electrospinning of polymer nanofibres from multiple jets on a porous tubular surface," *Nanotechnology*, vol. 17, no. 4, pp. 1123–1127, 2006.
- [59] D. Lukas, A. Sarkar, and P. Pokorny, "Self-organization of jets in electrospinning from free liquid surface: a generalized approach," *Journal of Applied Physics*, vol. 103, no. 8, Article ID 084309, 7 pages, 2008.
- [60] C. Shuiliang, H. Haoqing, H. Ping, J. H. Wendorff, A. Greiner, and S. Agarwal, "Polymeric nanosprings by bicomponent electrospinning," *Macromolecular Materials and Engineering*, vol. 294, no. 4, pp. 265–271, 2009.
- [61] A. Borrás, A. Barranco, and A. R. González-Elipé, "Reversible superhydrophobic to superhydrophilic conversion of Ag@TiO₂ composite nanofiber surfaces," *Langmuir*, vol. 24, no. 15, pp. 8021–8026, 2008.
- [62] S.-W. Choi, J. Y. Park, and S. S. Kim, "Synthesis of SnO₂-ZnO core-shell nanofibers via a novel two-step process and their gas sensing properties," *Nanotechnology*, vol. 20, no. 46, Article ID 465603, 2009.
- [63] H. H. Huang, C. L. He, H. S. Wang, and X. M. Mo, "Preparation of core-shell biodegradable microfibers for long-term drug delivery," *Journal of Biomedical Materials Research—Part A*, vol. 90, no. 4, pp. 1243–1251, 2009.
- [64] Z. Sun, E. Zussman, A. L. Yarin, J. H. Wendorff, and A. Greiner, "Compound core-shell polymer nanofibers by co-electrospinning," *Advanced Materials*, vol. 15, no. 22, pp. 1929–1932, 2003.
- [65] Y. Lin, Y. Yao, X. Yang et al., "Preparation of poly (ether sulfone) nanofibers by gas-jet/electrospinning," *Journal of Applied Polymer Science*, vol. 107, no. 2, pp. 909–917, 2008.
- [66] A. Varesano, A. Montarsolo, and C. Tonin, "Crimped polymer nanofibres by air-driven electrospinning," *European Polymer Journal*, vol. 43, no. 7, pp. 2792–2798, 2007.
- [67] A. V. Bazilevsky, A. L. Yarin, and C. M. Megaridis, "Co-electrospinning of core-shell fibers using a single-nozzle technique," *Langmuir*, vol. 23, no. 5, pp. 2311–2314, 2007.
- [68] P. Gupta and G. L. Wilkes, "Some investigations on the fiber formation by utilizing a side-by-side bicomponent electrospinning approach," *Polymer*, vol. 44, no. 20, pp. 6353–6359, 2003.
- [69] B. Duan, L. Wu, X. Yuan et al., "Hybrid nanofibrous membranes of PLGA/chitosan fabricated via an electrospinning array," *Journal of Biomedical Materials Research—Part A*, vol. 83, no. 3, pp. 868–878, 2007.
- [70] N. Sebastian, P. Damian, T. Velmurugan, E. Wintermantel, and S. Ramakrishna, "Conductive electrospun PANi-PEO/TiO₂ fibrous membrane for photo catalysis," *Materials Science and Engineering B*, vol. 176, no. 8, 7 pages, 2011.
- [71] W. E. Teo, S. Liao, C. K. Chan, and S. Ramakrishna, "Remodeling of three-dimensional hierarchically organized nanofibrous assemblies," *Current Nanoscience*, vol. 4, no. 4, pp. 361–369, 2008.
- [72] A. F. Lotus, S. Bhargava, E. T. Bender et al., "Electrospinning route for the fabrication of p-n junction using nanofiber yarns," *Journal of Applied Physics*, vol. 106, no. 1, Article ID 014303, 2009.
- [73] X. Wang, K. Zhang, M. Zhu et al., "Continuous polymer nanofiber yarns prepared by self-bundling electrospinning method," *Polymer*, vol. 49, no. 11, pp. 2755–2761, 2008.
- [74] E. Smit, U. Buttner, and R. D. Sanderson, "Continuous yarns from electrospun fibers," *Polymer*, vol. 46, no. 8, pp. 2419–2423, 2005.
- [75] B. K. Gu, M. K. Shin, K. W. Sohn et al., "Direct fabrication of twisted nanofibers by electrospinning," *Applied Physics Letters*, vol. 90, no. 26, Article ID 263902, 2007.
- [76] H. Pan, L. Li, L. Hu, and X. Cui, "Continuous aligned polymer fibers produced by a modified electrospinning method," *Polymer*, vol. 47, no. 14, pp. 4901–4904, 2006.

Research Article

Room Temperature Ferromagnetism of (Mn,Fe) Codoped ZnO Nanowires Synthesized by Chemical Vapor Deposition

Yongqin Chang,¹ Pengwei Wang,² Qingling Sun,¹ Yongwei Wang,¹ and Yi Long¹

¹ School of Materials Science and Engineering, University of Science and Technology Beijing, Beijing 100083, China

² Department of Physics, National Key Laboratory of Mesoscopic Physics, Peking University, Beijing 100871, China

Correspondence should be addressed to Yongqin Chang, chang@ustb.edu.cn

Received 28 March 2011; Accepted 28 August 2011

Academic Editor: Steve Acquah

Copyright © 2011 Yongqin Chang et al. This is an open access article distributed under the Creative Commons Attribution License, which permits unrestricted use, distribution, and reproduction in any medium, provided the original work is properly cited.

(Mn,Fe) codoped ZnO nanowires were synthesized on silicon substrates in situ using a chemical vapor deposition method. The structure and property of the products were investigated by X-ray, electron microscopy, Raman, photoluminescence, and superconducting quantum interference device magnetometer. The doped nanowires are of pure wurtzite phase with single crystalline, and the elements distribute homogeneously in the doped nanowires. Photoluminescence spectrum of the doped nanowires is dominated by a deep-level emission with a negligible near-band-edge emission. The magnetic hysteresis curve with a coercive field of 35 Oe is clearly observed at 300 K, resulting from room-temperature ferromagnetic ordering in the (Mn,Fe) codoped ZnO nanowires, which has great potential applications for spintronics devices.

1. Introduction

Diluted magnetic semiconductors (DMSs) have stimulated great interest in recent years due to their potential applications in spintronics devices, where the spin degree of freedom of the electron is utilized in addition to its carrier concentration [1–3]. A promising technique is to use DMS to inject spin-polarized carriers into nonmagnetic semiconductor, and it is very important that the DMS materials have room temperature ferromagnetic property for the practical applications. ZnO doped with transition metals is one of the most promising DMS candidates, as it was predicted to be ferromagnetic above room temperature [1, 4], and some room temperature ferromagnetic materials have been successfully synthesized by several groups [5–7]. To integrate the ZnO-based DMSs into present electronics, it is reasoned that the combination of low dimensionality and room-temperature ferromagnetism in diluted magnetic oxides would generate new functional nanomaterials useful for future spintronics nanodevices. Some efforts have been focused on this kind of material, such as the fabrication of Mn-doped ZnO nanorods arrays [8] and Co-doped ZnO nanowire arrays [9]. Recently, several codoped DMS materials

have been reported with the expectation that codoping can lead to remarkable improvement in the properties of DMS [10, 11]. Chakrabarti et al. reported that the saturation magnetic field can be enhanced by doping addition 2% Fe in the Mn-doped ZnO system [12]. Codoped Mn and Fe in ZnO nanostructures may contribute the local magnetic moments and enhancement of the charge carrier density. To the best of our knowledge, there was no research presented on Mn- and Fe-codoped ZnO nanostructures. In this letter, magnetization above room temperature has been achieved in (Mn,Fe) codoped ZnO nanowires prepared by a chemical vapor deposition (CVD) route.

2. Experiments

The fabrication process of the chemical vapor deposition is similar to our previous reports [13]. A gold film with thickness of 2 nm acting as catalyst was sputtered on a cleaned silicon substrate. In a typical synthesis, Zn, Mn, and Fe powders were put in a small alumina boat to serve as source materials. Silicon wafer was placed above the source at a vertical distance of 5 mm with its gold side facing downwardly. Then, the alumina boat was transferred into

the center of a horizontal alumina furnace. Argon with a flow rate of 30 sccm (standard-state cubic centimeter per minute) was supplied as the carrier gas in the furnace during heating. When the temperature at the center of the furnace reached 810°C, 5 sccm of oxygen was introduced. The furnace was held at 810°C for 2 h to synthesize the nanowires. During the whole growth process, the pressure of the system was maintained at atmospheric pressure without using pumping system. After the furnace was cooled down to room temperature, a yellowish film was observed on the silicon substrate. ZnO nanowires were synthesized at the similar condition only with Zn powder as the evaporation source.

X-ray diffraction (XRD) experiments were carried out with a X'pert MRD-Philips diffractometer using CuK α radiation. The micromorphology, structure, and composition of the products were studied using transmission electron microscopy (TEM, JEM-2010) and energy dispersive X-ray spectroscopy (EDXS). Elemental mapping was investigated by JEM-2100F microscope. Photoluminescence (PL) spectroscopy was performed at room-temperature, using a He-Cd laser of 325 nm wavelength as the excitation source. Room-temperature unpolarized Raman spectra were excited with a 514.5 nm Ar⁺ laser, taken under backscattering geometry. Magnetization measurements were checked by means of a superconducting quantum interference device (SQUID, MPMS XL-7) magnetometer.

3. Results and Discussion

Figure 1 displays the indexed XRD pattern of the products, and the position and relative intensity of the diffraction peaks of both (Mn,Fe) codoped ZnO and pure ZnO nanowires are indexed to wurtzite ZnO structure. The XRD results of the (Mn,Fe) codoped ZnO nanowires demonstrate that the structure of the ZnO matrix is not changed by doping of Mn and Fe. The lattice constants measured from the XRD of the products are $a = 0.3252$ nm and $c = 0.5211$ nm, which are a little larger than those of pure ZnO ($a = 0.3250$ nm and $c = 0.5206$ nm). The ionic radius of Zn²⁺, Mn²⁺, Mn³⁺, Fe²⁺, and Fe³⁺ are 0.74, 0.80, 0.66, 0.74, and 0.64 nm, respectively. Zn ions replaced with Fe and Mn may result in the changing in lattice constants, and it also indicates that there is few Mn³⁺ and Fe³⁺ in the (Mn,Fe) codoped ZnO nanowires, because the lattice constants increase slightly compared with those of pure ZnO.

Figure 2(a) shows the typical TEM image of the (Mn,Fe) codoped ZnO nanowires, and it reveals that the mean diameter of the nanowires is around 65 nm with lengths up to several micrometers. High-resolution TEM (HRTEM) images show that the doped nanowires are of single-crystalline nature, and the lattice fringe spacing of 0.247 nm corresponds to the d value of (101) planes (Figure 2(b)). No any particle-like features were observed in the examined nanowires. The EDXS analysis reveals the existence of Mn and Fe ions in the ZnO samples, and the content of Mn and Fe are 6 at.% and 2 at.%, respectively. Elemental mapping was carried out to investigate the element distribution in the doped nanowires. The typical EDX elemental mapping

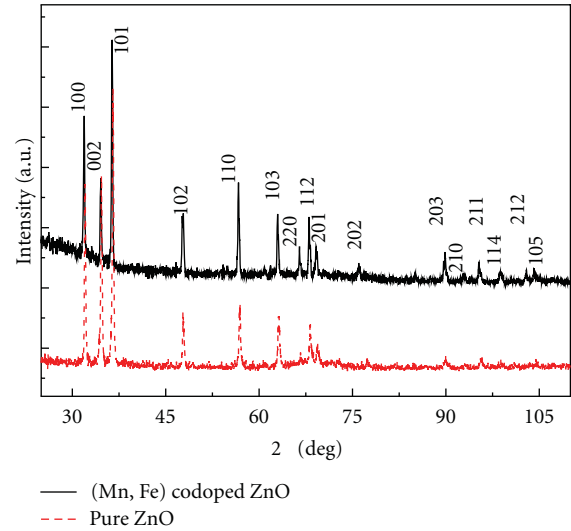


FIGURE 1: XRD pattern of the (Mn,Fe) codoped ZnO (solid line) and pure ZnO nanowires (dash line).

images of an individual (Mn,Fe) codoped ZnO nanowire were illustrated in Figure 3. These results show the shape of nanowire without any partial aggregation, which means that Mn and Fe distribute homogeneously in the nanowire instead of forming any oxide fine particles. Figure 3(d) shows that the profile of O is broader than those of the other elements, the reason is that O element was also absorbed by the supporting carbon film on the TEM grid and displaced in the profile.

The wurtzite ZnO structure belongs to the spaced group C_{6V}^4 , and the optical phonon irreducible representation is $2A_1 + 2B_1 + 2E_1 + 2E_2$. Both the A_1 and E_1 modes are polar and split into transverse optical (TO) and longitudinal optical (LO) phonons. Nonpolar E_2 modes are Raman active, while B_1 modes are Raman inactive. Their phonon frequencies of the Raman spectra in ZnO are $A_{1(TO)} = 380$ cm⁻¹, $A_{1(LO)} = 574$ cm⁻¹, $E_{1(TO)} = 407$ cm⁻¹, $E_{1(LO)} = 583$ cm⁻¹, $E_{2(High)} = 437$ cm⁻¹, and $E_{2(Low)} = 101$ cm⁻¹ [14], respectively. The frequency of 330 cm⁻¹ is the second-order spectrum arising from zone-boundary phonons $2-E_2(M)$ of ZnO [15]. The room temperature Raman spectra ranging from 200 to 850 cm⁻¹ was presented in Figure 4. For the pure ZnO nanowires, the mode at 436.9 cm⁻¹ with the strongest intensity is ascribed as $E_{2(high)}$ phonon mode, which is the typical Raman peak of ZnO bulk. $E_{2(high)}$ mode was usually used to understand the stress-induced phenomena in wurzite ZnO structures. As it is well known, an increase in the $E_{2(high)}$ phonon frequency is ascribed to compressive stress, whereas a decrease in the $E_{2(high)}$ phonon frequency is ascribed to tensile stress [16]. Compared with the frequency branch of $E_{2(high)}$ phonon of ZnO (436.9 cm⁻¹), the line center position of $E_{2(high)}$ phonon for the (Mn,Fe) codoped ZnO nanowires is observed at 434.9 cm⁻¹, a Raman shift of 2.0 cm⁻¹ had taken place, which indicates that a tensile stress was introduced in the nanowires because of the difference ionic radius between Mn, Fe, and

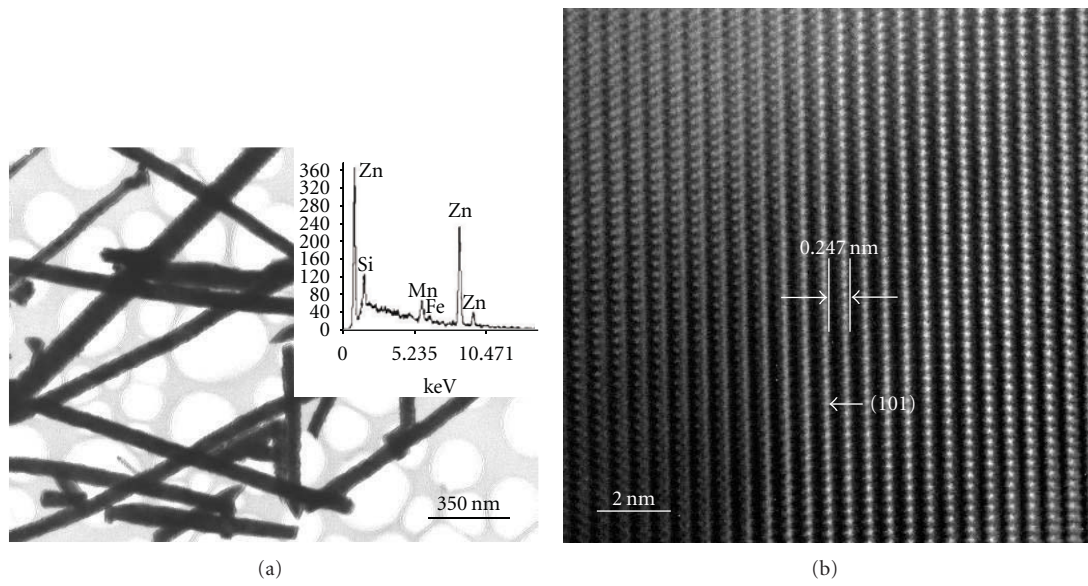


FIGURE 2: (a) Typical TEM image of the (Mn,Fe) codoped nanowires, and the inset is the EDS pattern. (b) HRTEM image of the (Mn,Fe) codoped ZnO nanowires, revealing the single crystalline.

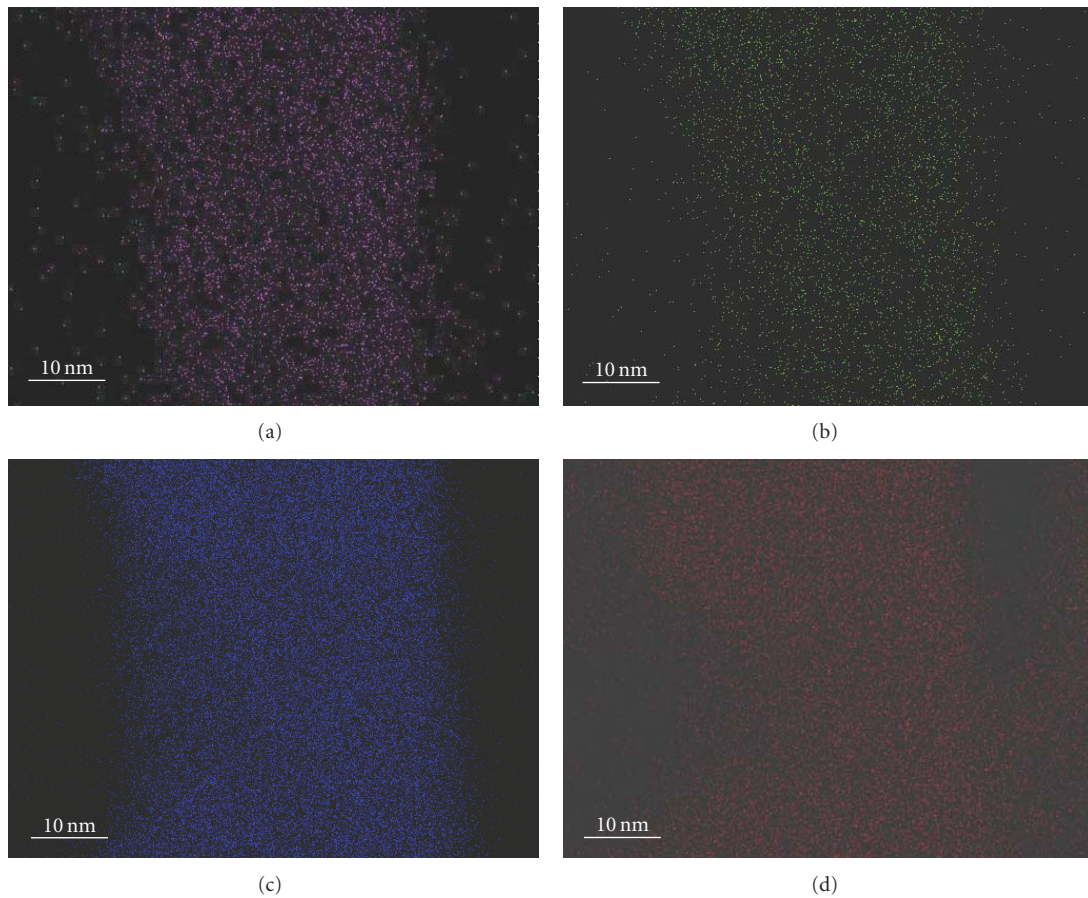


FIGURE 3: Elemental mapping images for the nanowire with Mn (a), Fe (b), Zn (c), and O (d).

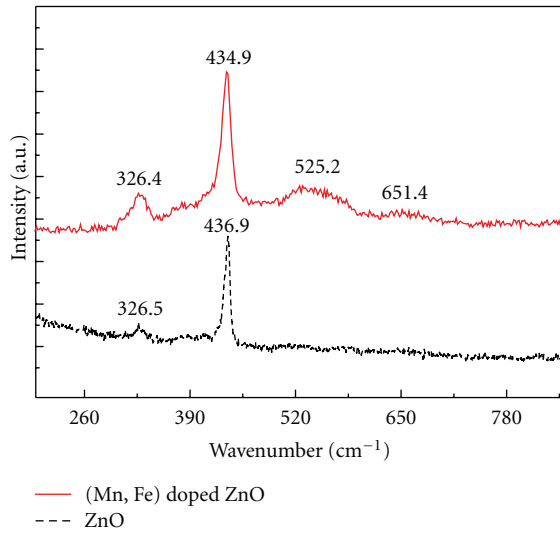


FIGURE 4: Raman spectra of the (Mn,Fe) codoped ZnO nanowires and pure ZnO nanowires.

Zn. The strongest intensity of $E_{2(\text{high})}$ phonon frequency for the (Mn,Fe) codoped ZnO nanowires also means that the wurtzite structure is preserved in spite of the inclusion of the Mn and Fe ions, which is consistent with the XRD results. The phonon mode centered at 326.5 cm^{-1} for ZnO and 326.4 cm^{-1} for (Mn,Fe) codoped ZnO are second-order spectra feature, which originates from the zone-boundary phonons of $2-E_2(\text{M})$ for ZnO [15]. In the Raman spectrum of the (Mn,Fe) codoped ZnO nanowires, there are two additional broad Raman bands at around 525.2 cm^{-1} and 651.4 cm^{-1} , respectively. The vibration mode at 651.4 cm^{-1} was not presented in the ZnO films and single crystals, while it has been observed in Mn doped ZnO materials, where it was ascribed as local vibrational modes due to the intrinsic host-lattice defects [17]. In our experiments, when Mn and Fe atoms occupy the Zn sites, some new lattice defects are introduced or intrinsic host-lattice defects become activated due to the difference radius of Mn, Fe, and Zn. So, we guess that the vibration mode at 651.4 cm^{-1} associated with the defects was induced by Mn and Fe substitution. The mode at 525.2 cm^{-1} was also detected in other Mn single and Mn codoped with other magnetic ions ZnO films and nanostructures prepared by other groups [18, 19], and this mode has been reported correlated with Mn-related local vibration. The above Raman analysis shows that only ZnO phase is obtained, and a tensile stress is introduced because of the doping of Mn and Fe.

Room temperature photoluminescence spectra of the as-synthesized products were measured with excitation wavelength of 325 nm. As shown in Figure 5, the PL spectrum of the (Mn,Fe) codoped ZnO nanowires is similar to many reported data of ZnO. The luminescence band centered at 384 nm assigns to the ultraviolet (UV) excitonic emission, corresponding to the band emission of ZnO. The green luminescence band was generally attributed to the single ionized oxygen vacancies [20]. Up to now, we have not seen

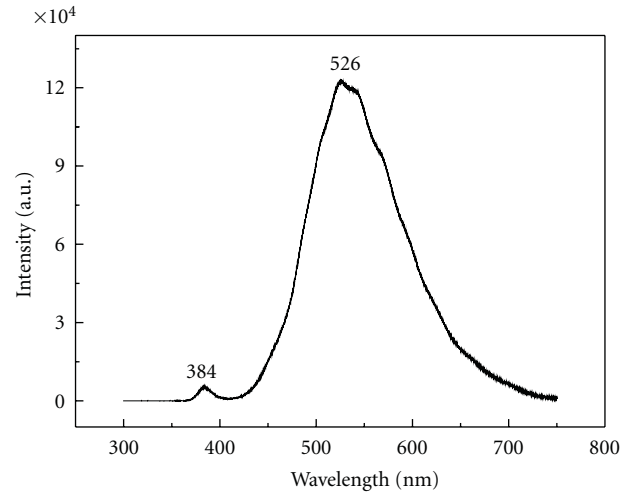


FIGURE 5: PL spectrum of the (Mn,Fe) codoped ZnO nanowires excited at room temperature.

any reports on the photoluminescence of FeO, Fe_2O_3 , Fe_3O_4 , Mn_2O_3 , and Mn_3O_4 . A published report showed that MnO crystal shows the excitation spectra of the emission bands centered at 1.25 eV (992 nm) and 1.66 eV (747 nm) [21]. Figure 5 obviously shows that the green emission (526 nm) of the (Mn,Fe) codoped ZnO nanowires is not originated from MnO. From above results, we can conclude that the strong green emission (526 nm) was merely due to defects in the doped ZnO nanowires instead of from secondary inclusions. The broad band with the strong intensity of the green emission indicates that there exist many oxygen vacancies in the doped materials. The doping of Mn and Fe may affect the emission of ZnO. The high emission intensity of the near band emission only is observed in high crystal quality of ZnO [22]. If the material is of degraded quality, the exciton lifetime would be very short due to the additional scattering by defects, and the PL spectrum would be dominated by deep level emission. Mn and Fe dopants may introduce some defects and stress, which have been confined by the Raman spectra (Figure 4). The strong green emission in Figure 5 may result from the high quantity of oxygen vacancies and the defects originated from the dopants and the growth process.

The magnetic behavior of the doped materials is of critical importance for spintronics applications. Applied field-dependent magnetization (M - H) measurements of the (Mn,Fe) codoped ZnO nanowires were performed at 5 and 300 K, respectively. The diamagnetic response of the silicon substrate was subtracted from the magnetization plots. In Figure 6(a), the appearance of a well-defined loop with a coercive field of about 115 Oe signifies the (Mn,Fe) codoped ZnO nanowires being ferromagnetic at 5 K. Figure 6(b) shows the magnetic hysteresis curve measured at 300 K. The saturated magnetization M_s and coercive field H_c are 0.4 emu g^{-1} and 35 Oe, respectively. Although the magnetization at 300 K is relatively weak compared with the value measured at 5 K, the hysteresis loop was clearly observed at 300 K, resulting from room-temperature ferromagnetic ordering in the (Mn,Fe) codoped ZnO nanowires. Recent

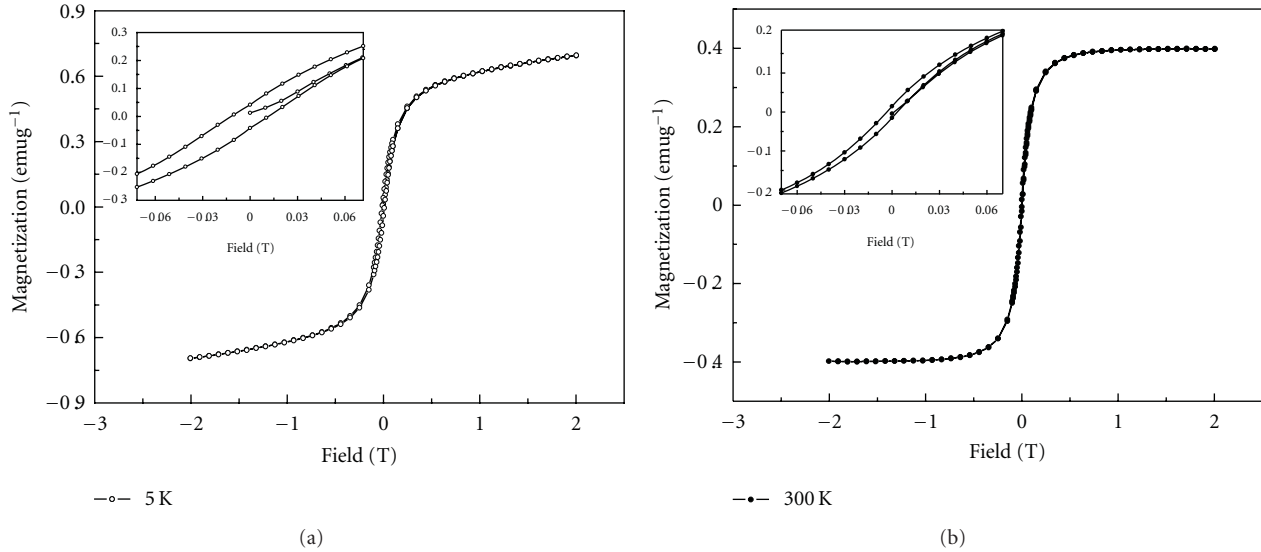


FIGURE 6: Hysteresis loops for the (Mn,Fe) codoped ZnO nanowires measured at 5 (a) and 300 K (b), and the corresponding insets show the enlarged parts of the M - H curves.

works reported that the ferromagnetism in the ZnO-based DMS controlled by the concentration of oxygen vacancies [23], and the enhancement of ferromagnetism was strongly correlated with the increase of oxygen vacancies in ZnO [24]. The PL measurements in our case demonstrate that there exist many oxygen vacancies in the doped materials. The room-temperature ferromagnetism of the (Mn,Fe) doped ZnO nanowires might originate from the super exchange interaction between nearest neighbor distance of magnetic ions (via oxygen vacancies). The role of Mn and Fe will be further investigated in the future.

4. Conclusions

This paper reported on the synthesis, characterization, and magnetic property of the (Mn,Fe) codoped ZnO nanowires through a chemical vapor deposition method. The XRD and Raman results show that the products are composed of pure wurtzite ZnO phase. HRTEM image indicates that the nanowires are of single crystalline, and the elemental mapping profiles of the single nanowires show that the elements distribute homogeneously along the doped nanowires. Ferromagnetic behavior was obtained in the (Mn,Fe) codoped ZnO nanowires at low temperature as well as at room temperature. Our experimental results reveal that Mn and Fe incorporated into ZnO develop a room-temperature diluted magnetic semiconductor, which represents an important method for fabrication of transition metal-doped ZnO nanostructures with room-temperature ferromagnetic behavior.

Acknowledgments

This project is financially supported by Beijing Natural Science Foundation (no. 1092014), Open Project of Key Laboratory for Magnetism and Magnetic Materials of the Ministry

of Education, Lanzhou University (LZUMMM2010002), and Metallurgy Foundation of University of Science and Technology Beijing. Y. Q. Chang is supported by Program for New Century Excellent Talents in University (no. NCET-07-0065) and Beijing Novel Program.

References

- [1] A. H. Macdonald, P. Schiffer, and N. Samarth, "Ferromagnetic semiconductors: moving beyond (Ga,Mn)As," *Nature Materials*, vol. 4, no. 3, pp. 195–202, 2005.
- [2] J. B. Yi, H. Pan, J. Y. Lin et al., "Ferromagnetism in ZnO nanowires derived from electro-deposition on AAO template and subsequent oxidation," *Advanced Materials*, vol. 20, no. 6, pp. 1170–1174, 2008.
- [3] N. H. Hong, J. Sakai, N. Poirot, and V. Brizé, "Room-temperature ferromagnetism observed in undoped semiconducting and insulating oxide thin films," *Physical Review B*, vol. 73, no. 13, Article ID 132404, 4 pages, 2006.
- [4] T. Dietl, H. Ohno, F. Matsukura, J. Cibert, and D. Ferrand, "Electric-field control of ferromagnetism," *Science*, vol. 287, no. 6815, pp. 1019–1022, 2000.
- [5] P. Sharma, A. Gupta, K. V. Rao et al., "Ferromagnetism above room temperature in bulk and transparent thin films of Mn-doped ZnO," *Nature Materials*, vol. 2, no. 10, pp. 673–677, 2003.
- [6] T. S. Heng, D. C. Qi, T. Berlijn et al., "Room-temperature ferromagnetism of Cu-doped ZnO films probed by soft X-ray magnetic circular dichroism," *Physical Review Letters*, vol. 105, no. 20, Article ID 207201, 2010.
- [7] X. G. Xu, H. L. Yang, Y. Wu et al., "Intrinsic room temperature ferromagnetism in boron-doped ZnO," *Applied Physics Letters*, vol. 97, no. 23, Article ID 232502, 2010.
- [8] H. L. Yan, X. L. Zhong, J. B. Wang et al., "Cathodoluminescence and room temperature ferromagnetism of Mn-doped ZnO nanorod arrays grown by chemical vapor deposition," *Applied Physics Letters*, vol. 90, no. 8, Article ID 082503, 2007.

- [9] L. R. Shah, W. Wang, H. Zhu et al., "Role of dopant, defect, and host oxide in the observed room temperature ferromagnetism: Co-ZnO versus Co-CeO₂," *Journal of Applied Physics*, vol. 105, no. 7, Article ID 07C515, 3 pages, 2009.
- [10] L. Q. Liu, B. Xiang, X. Z. Zhang, Y. Zhang, and D. P. Yu, "Synthesis and room temperature ferromagnetism of FeCo-codoped ZnO nanowires," *Applied Physics Letters*, vol. 88, no. 6, Article ID 063104, 2006.
- [11] D. Rubi, J. Fontcuberta, A. Calleja, L. Aragonès, X. G. Capdevila, and M. Segarra, "Reversible ferromagnetic switching in ZnO:(Co, Mn) powders," *Physical Review B*, vol. 75, no. 15, Article ID 155322, 2007.
- [12] M. Chakrabarti, S. Dechoudhury, D. Sanyal, T. K. Roy, D. Bhowmick, and A. Chakrabarti, "Observation of room temperature ferromagnetism in Mn-Fe doped ZnO," *Journal of Physics D*, vol. 41, no. 13, Article ID 135006, 2008.
- [13] Y. Q. Chang, D. B. Wang, X. H. Luo et al., "Synthesis, optical, and magnetic properties of diluted magnetic semiconductor Zn_{1-x}MnxO nanowires via vapor phase growth," *Applied Physics Letters*, vol. 83, no. 19, pp. 4020–4022, 2003.
- [14] Z. C. Zhang, B. B. Huang, Y. Q. Yu, and D. L. Cui, "Electrical properties and Raman spectra of undoped and Al-doped ZnO thin films by metalorganic vapor phase epitaxy," *Materials Science and Engineering B*, vol. 86, no. 2, pp. 109–112, 2001.
- [15] J. M. Calleja and M. Cardona, "Resonant Raman scattering in ZnO," *Physical Review B*, vol. 16, no. 8, pp. 3753–3761, 1977.
- [16] Y. Huang, M. Liu, Z. Li, Y. Zeng, and S. Liu, "Raman spectroscopy study of ZnO-based ceramic films fabricated by novel sol-gel process," *Materials Science and Engineering B*, vol. 97, no. 2, pp. 111–116, 2003.
- [17] L. W. Yang, X. L. Wu, G. S. Huang, T. Qiu, and Y. M. Yang, "In situ synthesis of Mn-doped ZnO multileg nanostructures and Mn-related Raman vibration," *Journal of Applied Physics*, vol. 97, no. 1, Article ID 014308, pp. 1–14308, 2005.
- [18] C. L. Du, Z. B. Gu, M. H. Lu et al., "Raman spectroscopy of (Mn, Co)-codoped ZnO films," *Journal of Applied Physics*, vol. 99, no. 12, Article ID 123515, 2006.
- [19] J. B. Wang, G. J. Huang, X. L. Zhong, L. Z. Sun, Y. C. Zhou, and E. H. Liu, "Raman scattering and high temperature ferromagnetism of Mn-doped ZnO nanoparticles," *Applied Physics Letters*, vol. 88, no. 25, Article ID 252502, 2006.
- [20] X. L. Wu, G. G. Siu, C. L. Fu, and H. C. Ong, "Photoluminescence and cathodoluminescence studies of stoichiometric and oxygen-deficient ZnO films," *Applied Physics Letters*, vol. 78, no. 16, pp. 2285–2287, 2001.
- [21] S. Mochizuki, B. Piriou, and J. Dexpert-Ghys, "Spin-wave-assisted photoluminescence in MnO crystals," *Journal of Physics: Condensed Matter*, vol. 2, no. 23, pp. 5225–5232, 1990.
- [22] Y. Q. Chang, D. P. Yu, G. H. Li et al., "Photoluminescence characterization of nanocrystalline ZnO array," *Chinese Physics Letters*, vol. 21, no. 11, pp. 2301–2304, 2004.
- [23] S. Ramachandran, J. Narayan, and J. T. Prater, "Effect of oxygen annealing on Mn doped ZnO diluted magnetic semiconductors," *Applied Physics Letters*, vol. 88, no. 24, Article ID 242503, 2006.
- [24] H. S. Hsu, J. C. A. Huang, Y. H. Huang et al., "Evidence of oxygen vacancy enhanced room-temperature ferromagnetism in Co-doped ZnO," *Applied Physics Letters*, vol. 88, no. 24, Article ID 242507, 2006.

Research Article

The Synthesis of Highly Aligned Cupric Oxide Nanowires by Heating Copper Foil

Jianbo Liang,¹ Naoki Kishi,¹ Tetsuo Soga,¹ and Takashi Jimbo²

¹Department of Frontier Materials, Nagoya Institute of Technology, Nagoya 4668555, Japan

²Department of Electrical and Electronics Engineering, Nagoya Institute of Technology, Nagoya 4668555, Japan

Correspondence should be addressed to Jianbo Liang, liangjianbo1980@yahoo.co.jp

Received 16 June 2011; Revised 8 August 2011; Accepted 22 August 2011

Academic Editor: Yanqiu Zhu

Copyright © 2011 Jianbo Liang et al. This is an open access article distributed under the Creative Commons Attribution License, which permits unrestricted use, distribution, and reproduction in any medium, provided the original work is properly cited.

We have investigated the effects of grain size and orientation of copper substrates for the growth of cupric oxide nanowires by thermal oxidation method. Long, less-roughness, high-density, and aligned cupric oxide nanowires have been synthesized by heating (200) oriented copper foils with small grain size in air gas. Long and aligned nanowires of diameter around 80 nm can only be formed within a short temperature range from 400 to 700°C. On the other hand, uniform, smooth-surface, and aligned nanowires were not formed in the case of larger crystallite size of copper foils with (111) and (200) orientation. Smaller grain size of copper foil with (200) orientation is favorable for the growth of highly aligned, smooth surface, and larger-diameter nanowires by thermal oxidation method.

1. Introduction

Nanostructured materials have attracted much scientific attention due to their interesting size-dependent chemical and physical properties and potential technological applications. One-dimensional (1D) nanostructures such as nanowires, nanobelts, nanorods, and nanotubes have become the focus of intensive research as a result of their unique properties and potential usages [1]. Nanowires and nanorods of various semiconductor materials including Si, Ge, GaN, ZnO, and so forth, have been the focus of intense studies in the past years. Different approaches, such as vapor-liquid-solid [2], vapor-solid [1], and template-mediated [3] growth methods, have been used for the preparation of 1D nanostructures of semiconducting materials.

Cupric oxide (CuO) with a known band gap of 1.2 eV has an interesting monoclinic crystal structure belonging to the Mott insulator material class whose electronic structure cannot be described by conventional band theory [4]. There has been increasing interest in developing 1D nanostructures of CuO for device applications such as gas sensor [5, 6], magnetic storage media [7], catalysts [8–10], and field emitters [11]. During the last couple of years, 1D nanowires, nanorods, nanowhiskers, and nanosheets of CuO have been

synthesized by various growth techniques such as thermal decomposition of Cu_2O_4 precursors [12], hydrothermal decomposition route [13], self-catalytic growth processes [14], and so forth. Important factors in synthesizing 1D nanostructure are control of composition, size, and crystallinity. Moreover, from the point of view of studying fundamental properties of nanowires as well as their applications, the method of preparation of the 1D nanostructures should be simple for producing bulk quantities and amenable to control diameter and length. In comparison to complex chemical methods, thermal annealing or thermal oxidation of copper foil is a simple, convenient, and fast method for synthesizing CuO nanowires. This method is becoming an increasingly attractive method for synthesizing nanostructures. Many studies on synthesizing CuO nanowires by thermal annealing of the copper foils in oxygen atmosphere have been reported up to now [15–26]. However, recent studies on CuO nanowires have focused on the influence of growth time, temperature, and oxidative environment on the growth rate, size distribution, and a real density of CuO nanowires [11, 22]. It has been shown that the growth time can be used to control nanowire length distribution [11], the growth temperature can be used to control the nanowire

diameter distribution, and the O₂ and H₂O partial pressures strongly affect areal density of nanowires [22]. The surface condition of the copper substrate was also shown to affect growth of nanowires significantly [14, 16]. But, the growth of long, high-density, and aligned cupric oxide nanowires has rarely been reported in the literature. It is due to the fact that the effects of copper substrates on the structure of cupric oxide nanowires have not studied until now. According to previous investigations, it seems very difficult to grow uniform and aligned vertical cupric oxide nanowires from pure metal thin films just by thermal oxidation, and very few approaches have been reported about this matter. In this study, we report a simple process for growing high-density, uniform, and vertically aligned cupric oxide nanowires by thermal oxidation. We have investigated the effects of the grain size, orientation of grains, and surface roughness of substrates for the growth of cupric oxide nanowires.

2. Experimental Procedure

In order to investigate the effect of grain size and orientation of copper substrates for cupric oxide nanowire formation during thermal oxidation, four copper foils (purchased from Nilaco Co. Ltd.) were used as substrates. Foils were cut into standard sizes of 1 cm × 1 cm. The substrates were washed by dilute hydrochloric acid to remove the native oxide layer and adsorbed impurities followed by cleaning with acetone, methanol, and deionized water under an ultrasonic bath for 5 min and, finally, dried by N₂ flow. The cleaned samples were placed in a quartz boat. The quartz boat was positioned in the center of a quartz tube, and the quartz tube was mounted in the middle of a horizontal tube furnace. The air humidity is unstable in ambient air; it may be affect the growth of nanowires, so we use stability cylinder air. The cylinder air was firstly introduced into the quartz tube at a flow rate of 1 L/min for 20 min to remove the ambient air from the system, and then it was adjusted to 0.5 L/min for oxidation of copper foils. The tube furnace was heated to the set-point temperature (300, 400, 500, and 600°C at atmospheric pressure). After reaching the set-point temperature, the air gas flow was stopped and the N₂ gas flow was employed at a rate of 1 L/min. The film was allowed to cool naturally to room temperature to prevent the thin film from cracking by thermal stress and further oxidation by atmospheric air (arise due to rapid cooling). The substrate was pulled out of the furnace for further analysis.

The crystal structure and phase composition were identified by X-ray diffraction (XRD, Rigaku RINT-2100) using a 40 kV, 30 mA, Cu-K α X-ray. A scanning step of degree of 0.02° was applied to record the XRD patterns in the 2 θ range of degree of 40–55°. The morphology of the CuO nanowires were characterized by scanning electron microscope (SEM, Hitachi S-3000H) operated at 15 kV. Transmission electron microscopy (TEM) and electron diffraction observation were carried out using a JEOL JEM-4000 EXII.

3. Results

3.1. Effect of Crystallite Size. In order to know the crystal structure and the corresponding grain size of copper foils,

X-ray diffraction was performed immediately after cleaning the substrate. There were a set of Bragg peaks in the XRD that could readily be indexed to the *fcc* structure of metal copper (Fm $\bar{3}$ m, *a* = 3.615 Å, JCPDF no. 85-1326) (Figure 1). The diffraction profiles of the copper foil A, C and B, D show very distinctive features. In Figure 1 there are two peaks on the copper foil A and C at 2 θ = 50.50° and 2 θ = 43.36° corresponding to (200) plane and (111) plane of copper structures. Compared with the XRD pattern of the copper foil A and C, only the peak at 2 θ = 50.50° corresponding to (200) reflection of the crystals in the sample B and D appeared. Such a feature indicates that copper crystals in the sample B and D are predominantly oriented with their *a*-axes perpendicular to the support surface. The average grain size can be calculated using the Scherrer equation [22]:

$$D = \frac{0.9\lambda}{W \cos \theta}, \quad (1)$$

where λ is the X-ray wavelength, θ is the Bragg diffraction angle, and W is the full width at half maximum (FWHM) of the peak corresponding to θ . When calculated by using the peak corresponding to the (200) plane of copper, the resultant grain size in copper foil A is about 72.2 nm, in copper foil B is about 35.6 nm, in copper foil C is about 64.5 nm, and in copper foil D are about 34.3 nm. The size of the grain in the copper foil A and C is about two times larger than that in the copper B and D. So the number of grain in the copper foil B and D is larger than that in the copper A and C. The properties of copper foil A, B, C, and D are summarized in Table 1.

3.2. Effect of Oxidizing Temperature. Figure 2 shows SEM images of surface morphologies after heating the copper foil A, B, C, and D at 300°C for 2 h in an air gas flow of 0.5 L/min., respectively. As can be seen, oxide grains are observed on four substrates. Oxide grains on copper A and C are less compact than the others on the copper B and D. The measured oxide grain size on copper A and C are about 250 and 300 nm. The grains on the copper foil B and D are denser, and the size is about 160 and 170 nm, without nanowires on the surface of the specimen. The oxide grains become larger as temperature increases. The oxide grains formed on copper foil B and D (smaller grain size) are much smaller than those formed on copper foil A and C (larger grain size) at the early stage of oxidation. It is due to a large number of nucleation sites on the smaller grain size of copper foils. From the morphology of the samples grown at 400°C (Figure 3), it is observed that nanowires formed at this temperature. High-density, more uniform, and longer nanowires are formed on copper foil B and D compared with copper foil A and C. As the temperature was increased to 500°C, a large amount of nanowires formed on the copper B and D (Figures 4(B) and 4(D)). It can be seen that long and uniform nanowires are formed on the entire surface, and nanowires are mostly vertical along the substrate surface. The average diameters of nanowires on copper foil B and D are about 80 and 100 nm, and average length of nanowires on the same substrates are about 7 and 8 μ m, respectively. Nevertheless, large-area

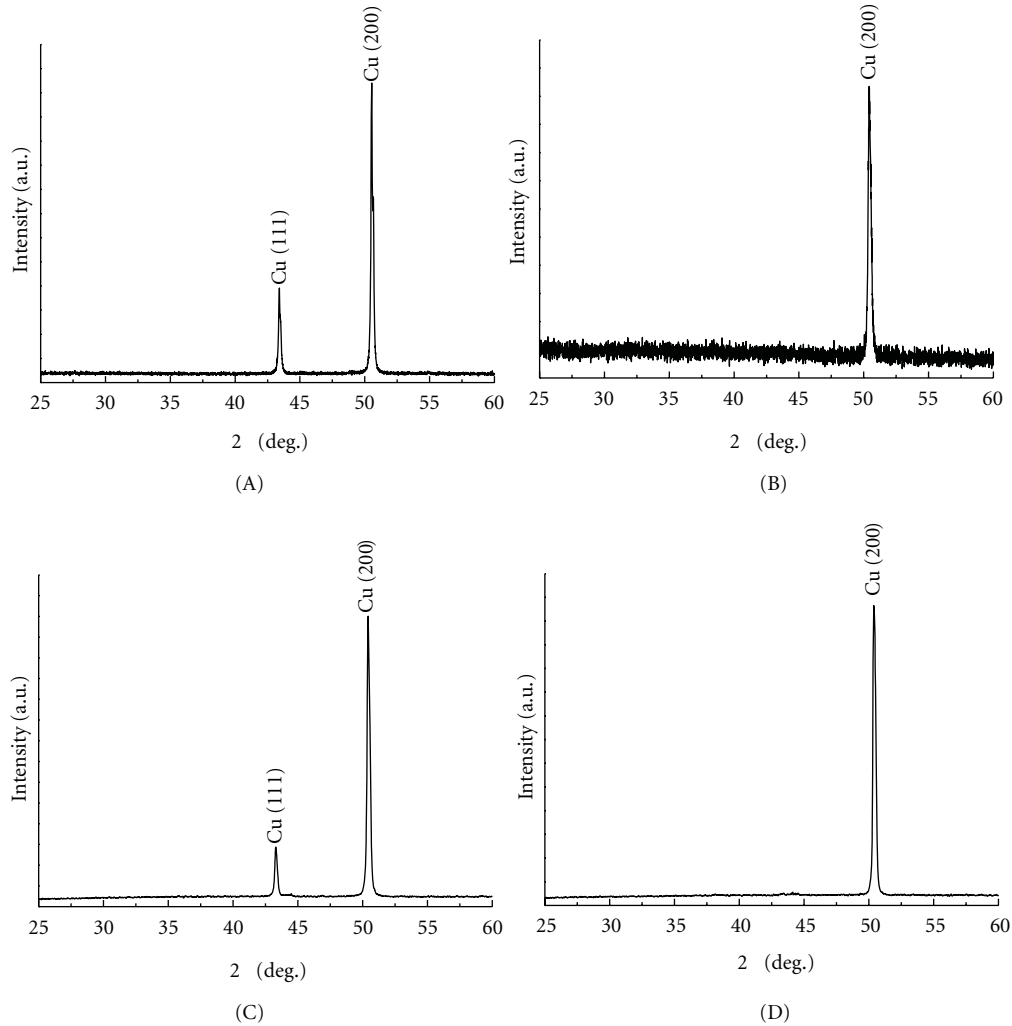


FIGURE 1: XRD patterns of (A) copper foil A, (B) copper foil B, (C) copper foil C, and (D) copper foil D.

and high density CuO nanowires can also grow from the copper A and C substrates under an air gas flow as shown in Figures 4(A) and 4(C). The as-prepared nanowires on the copper foil A and C were not well vertically aligned along the substrate surface with the lengths of about 4 and 5 μm and the diameter of about 50 and 62 nm. It is desirable to grow large-area, uniform, and vertically aligned CuO nanowires along the copper substrate surface for the applications in field emission emitters [23] and realization of nanosized CuO/Al-based energetic materials [24]. At 600°C, a high-density and uniform nanowires formed on copper foil B and D as shown in Figures 5(B) and 5(D). However, these nanowires are longer than those nanowires on copper foil A and C, with the length ranging from 5 to 15 μm and the diameter about 180 nm as shown in Figure 5. A large amount of nanowires of low density were observed on copper foil A and C prepared at 600°C with the length of 3 to 6 μm and the diameter from 100 to 400 nm. We can conclude that the grain size and crystal orientation of copper foil have a great effect on the growth of nanowires. The smaller grain size with (200) oriented copper foil is favourable for the growth of nanowires.

TABLE 1: Properties of four copper foils. The grain size and orientation of copper foils were characterized by XRD measurement.

	Grain size (nm)	Orientation of copper foils
Copper foil A	72.2	(111) and (200) orientation
Copper foil B	35.6	(200) orientation
Copper foil C	64.5	(111) and (200) orientation
Copper foil D	34.3	(200) orientation

3.3. Cross-Sectional Characterization of CuO Nanowire Samples. Figure 6 shows the SEM images of the cross sections of oxidized the copper foil A and B at 500°C for 2 h. In order to measure the oxide layer thickness, an oxide flake was carefully removed from a copper substrate. When copper foil is oxidized, at first the major product is Cu₂O, and it is expected that CuO is formed through a second step of oxidation of Cu₂O [15, 27]. In this case, Cu₂O serves as a precursor to CuO. The outmost layer is always of CuO if the oxide consists of both Cu₂O and CuO. In this bilayer

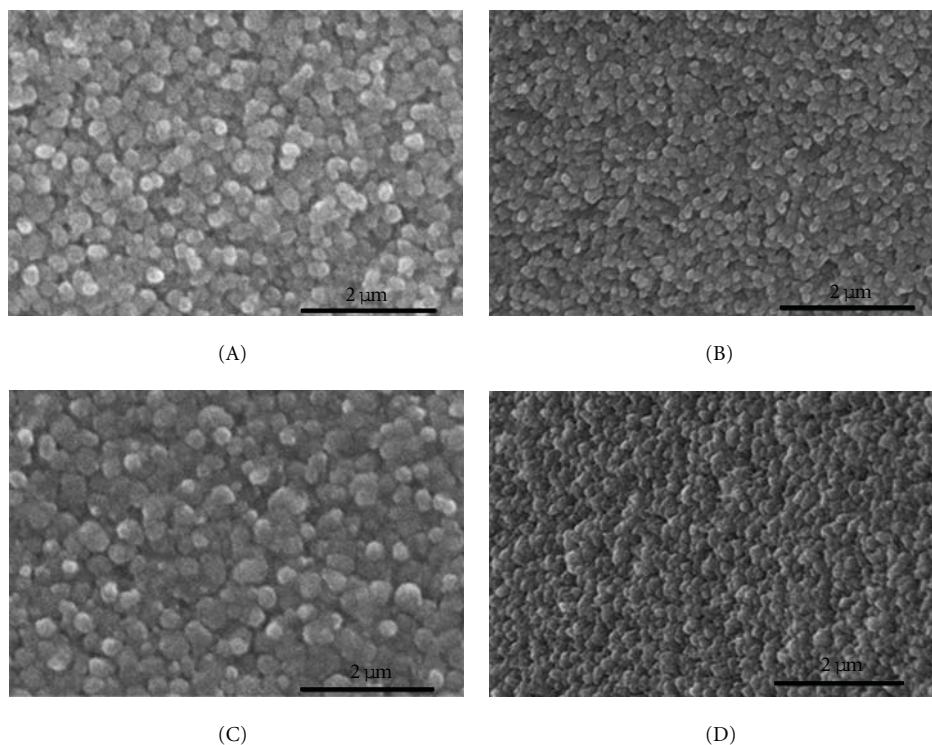


FIGURE 2: SEM images of copper foil (A) A, (B) B, (C) C, and (D) oxidized at 300°C for 2 h in an air gas flow of 0.5 L/min.

oxide, fractional thickness of outmost layer mainly depends on annealing temperature. In the Figure 6(A), the oxide layer is divided into the bottom layer of Cu_2O and the outermost layer of CuO [28]. By EDX measurement, the CuO layer was found about $0.9 \mu\text{m}$ thick and Cu_2O layer about $4.2 \mu\text{m}$ for copper foil A. For copper foil B, the outermost CuO layer is thicker than that of foil A which is about $1.8 \mu\text{m}$ thick (Figure 6(B)). The bottom Cu_2O layer is evidently thicker (about $5.8 \mu\text{m}$). The total thickness of the layer on the copper substrate B is about $7.6 \mu\text{m}$, which is thicker than that of copper foil A (about $5.1 \mu\text{m}$). The thicker oxide layer on the copper foil B is due to the higher oxidation rate. In principle, the copper ions and oxygen ions can diffuse across the scales much faster along the grain boundaries than through the bulk. The high oxidation rate of copper foil B would be due to the smaller grain size, resulting in faster overall rates of scale growth.

3.4. TEM Characterization of CuO Nanowires. We further characterized the size, structure, and crystal of these nanowires using TEM and selected area diffraction (SAD) pattern. The selected sample was prepared at 500°C for 2 h. Figures 7 and 8 display TEM diffraction patterns of an individual nanowire of the copper foil A and B oxidized at 500°C for 2 h. In Figure 8(A), it is observed that the nanowire of the copper foil B has wire-like shape of very smooth surface with the diameter of about 70 nm. In comparison with the nanowires of foil B, the surface of nanowire of copper foil A has roughness and diameter of about 45 nm (Figure 7(A)). Larger diameter of nanowire (in Figure 8(A))

is observed for copper foil B compared to Cu foil A (Figure 7(A)), which may be due to larger number of grain boundaries of the copper foil B. Figure 7(B) shows a TEM diffraction pattern of an individual nanowire from copper foil A. It would be typically observed when the electron beam was focused on an individual nanowire along the [001] direction. The double diffraction is due to the twin plane within a nanowire. Figure 8(B) also shows a TEM diffraction pattern of an individual nanowire from copper foil B prepared at 500°C. Similarly, the double diffraction is caused by the twin plane within the nanowire, each set diffraction spot is a single crystal and corresponds to monoclinic structure of CuO with the lattice constants, $a = 0.469 \text{ nm}$, $b = 0.343 \text{ nm}$, $c = 0.513 \text{ nm}$, and $\beta = 99.55^\circ$.

4. Discussion

The formation of nanowires occurs when two layers of copper oxides are gradually formed by oxidation of copper [15, 26–28]. We examine our results based on mechanisms of nanowire growth reported in the literature. Gonçalves et al. suggested that CuO nanowires growth occurs via grain boundary diffusion of copper ions through the Cu_2O layer and the oxygen ions through the outmost CuO layer [25]. Xu et al. also suggested that nanowire growth is via grain boundary diffusion [26]. This idea shares similarities with the model proposed recently for Fe_2O_3 nanowire formation [29]. However, Park et al. and Shao et al. reported that the mechanism of nanowires growing in this case is due to the relaxation of compressive stress [27, 28]. Here, we

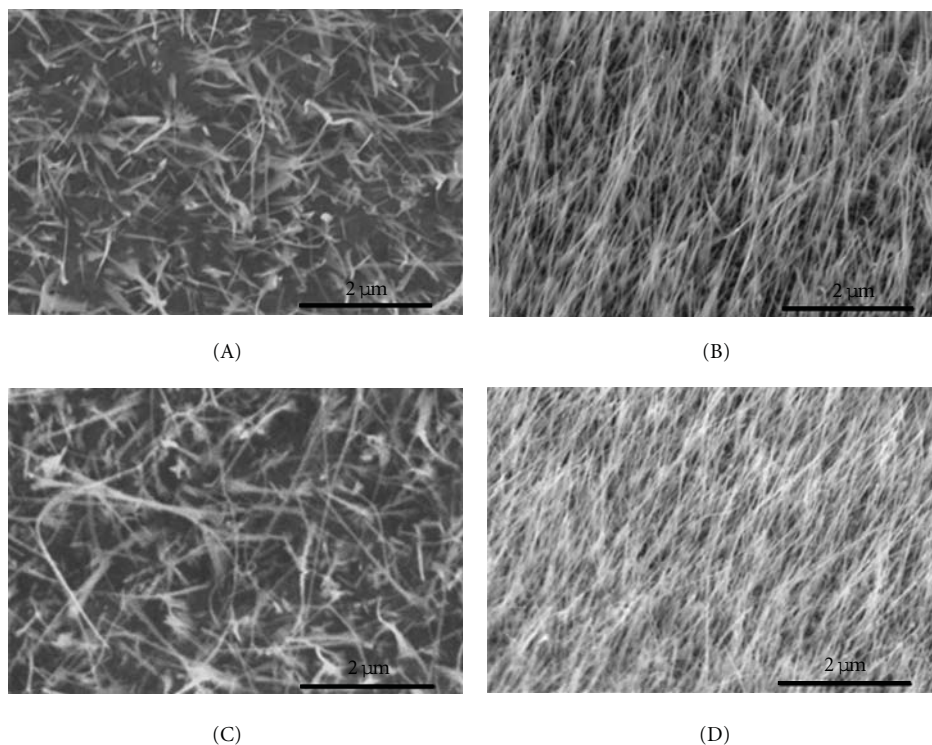


FIGURE 3: SEM images of copper foil (A) A, (B) B, (C) C, and (D) oxidized at 400°C for 2 h in an air gas flow of 0.5 L/min.

believe that the growth of nanowire occurs to reduce the stress generated during oxidation of copper by the grain boundary diffusion process [20]. Now, we shall discuss how the proposed model can be explained by our obtained results. Long, high-density and aligned cupric oxide nanowires observed in Figures 3, 4, 5(B), and 5(D) can be attributed to grain boundary and the crystal direction with the effective relaxation of compressive stress. It is well known that the initial oxidation rate of a metal at intermediate temperatures (300–600°C for copper) is too rapid to be attributed solely to lattice diffusion of the various ionic species in its oxide film [30]. The oxidation of copper at low temperatures is dominated by grain boundaries. The smaller grain size and the higher grain boundary energy can play an important role in increasing the effective diffusion coefficient of copper ions and oxygen in smaller crystallite size at intermediate temperatures as a result of grain boundary diffusion [31]. Oxidation of Cu foil to Cu_2O and Cu_2O to CuO leads to a compressive stress on the interface due to volume and structural change. The compressive stress drives outward diffusion of copper cations along grain boundaries, resulting in CuO nanowire growth on CuO grains [27]. Therefore, a high density of nanowires is observed in Figures 3, 4, 5(B), and 5(D) compared to Figures 3, 4, 5(A), and 5(C) as the large numbers of grain boundaries increase the relaxation of the compressive stresses at the CuO and Cu_2O layer interface. The oriented direction is favorable to the diffusion of copper cations along grain boundaries in the copper film. It may affect the surface of nanowire. The TEM images presented in Figure 8 indicate a large diameter of nanowire

and smooth-surface nanowire formed on copper foil B. This is also attributed to the relaxation of compressive stress by effective grain boundary diffusion. Depending on the oxidation temperature, the diffusion of the atoms or ions may take place within the lattice, through grain boundaries in the oxide layer. As a result nanowire density decreases as temperature increases, as seen in the sequence of SEM images of Figure 5. The oxide grains become larger as temperature increases in our experiment. Although we have tried to raise the heating temperature to 800°C, large oxide grains are observed, but no nanowires appeared on the surface of substrate. When the temperature is higher than 800°C, copper oxidation is dominated by lattice diffusion of copper ions; the influence of grain boundary diffusion would finally become small compared to lattice diffusion. This explains the absence of nanowires for oxidations at 800°C. The relative importance of grain boundary transport through a scale depends on the grain size of the oxide and on temperature and tends to become negligible at sufficiently high temperatures [32]. By heating the copper foil with the smaller grain size with (200) oriented in an air gas flow, the large numbers of grain boundaries are favorable to the relaxation of compressive stress, resulting in the growth of high-density and smooth-surface nanowires.

5. Conclusion

High-density, smooth-surface, and aligned cupric oxide nanowires have been synthesized by heating copper foils

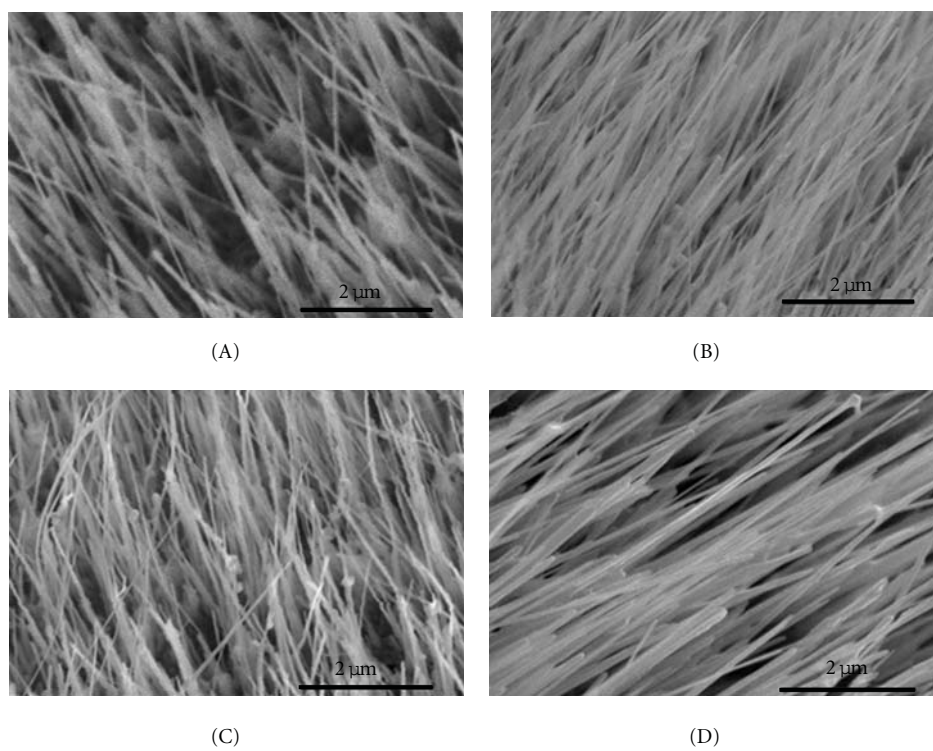


FIGURE 4: SEM images of copper foil (A) A, (B) B, (C) C, and (D) oxidized at 500°C for 2 h in an air gas flow of 0.5 L/min.

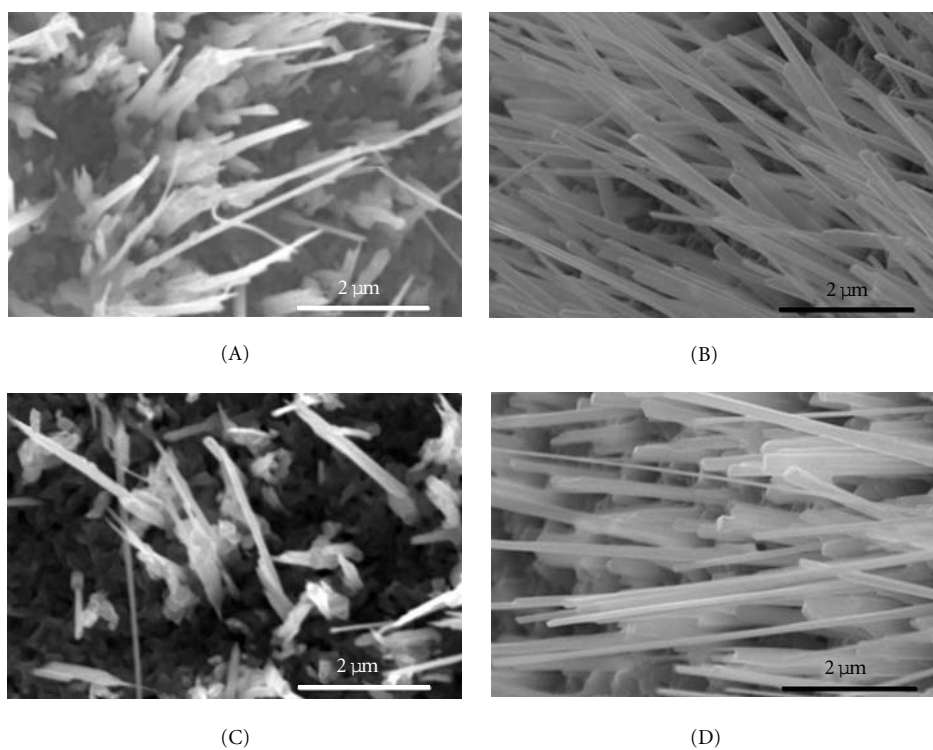


FIGURE 5: SEM images of copper foil (A) A, (B) B, (C) C, and (D) oxidized at 600°C for 2 h in an air gas flow of 0.5 L/min.

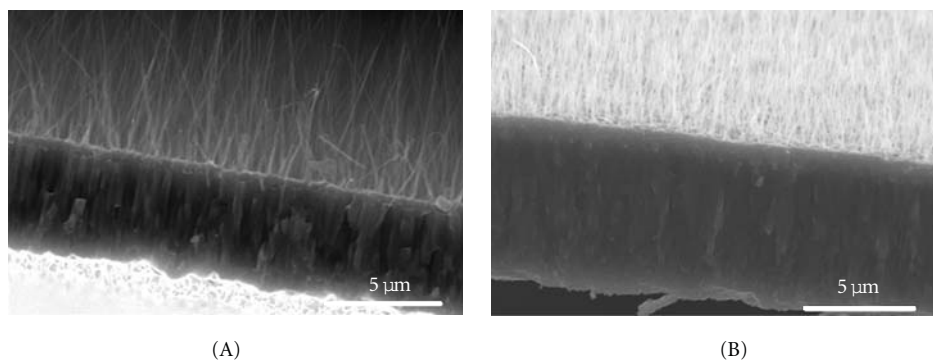


FIGURE 6: SEM images of the cross section of nanowires on (A) the copper foil A and (B) B. The nanowires were synthesized at 500°C for 2 h.

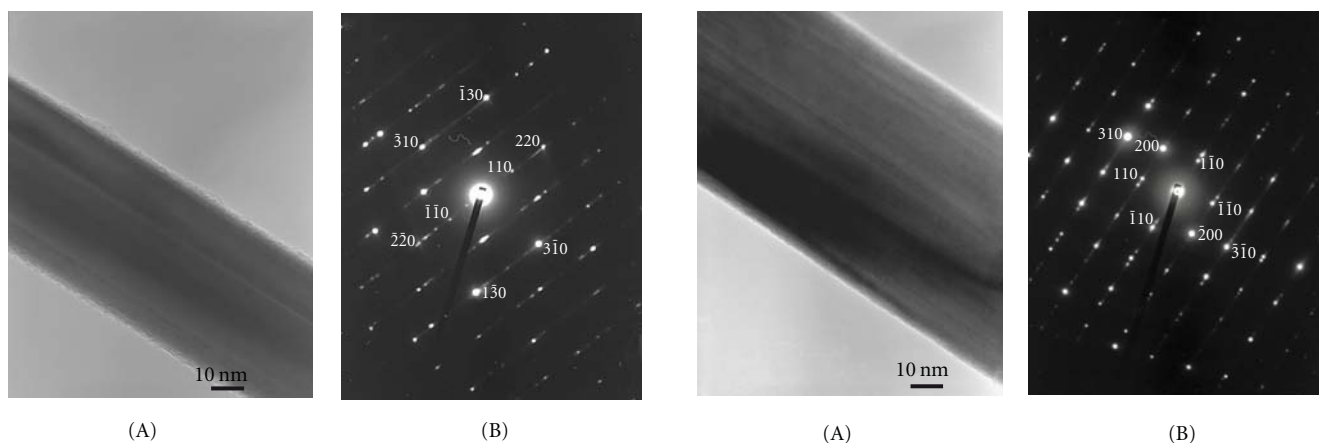


FIGURE 7: (A) TEM images and (B) SAD pattern of a single CuO nanowire of copper foil A prepared at 500°C for 2 h in air gas flow of 0.5 L/min.

FIGURE 8: (A) TEM images and (B) SAD pattern of a single CuO nanowire of copper foil B prepared at 500°C for 2 h in air gas flow of 0.5 L/min.

with the smaller grain size and (200) oriented in an air gas flow. On the other hand, uniform, smooth-surface, and aligned nanowires cannot be obtained by heating copper foils with the larger grain size and two crystal orientations. The difference is attributed to the faster relaxation of compress stress by outward diffusion of copper ions and inward diffusion of oxygen along the grain boundaries (both in the metal and in the layer for the smaller grain size of copper substrate). The small grain size of the copper foil B and C is favorable to the growth of nanowires due to the larger number of grain boundaries. Aligned cupric oxide and smooth-surface nanowires could be produced by heating the (200) oriented copper foil.

References

- [1] Y. Xia, P. Yang, Y. Sun et al., "One-dimensional nanostructures: synthesis, characterization, and applications," *Advanced Materials*, vol. 15, no. 5, pp. 353–389, 2003.
- [2] R. S. Wagner and W. C. Ellis, "Vapor-liquid-solid mechanism of single crystal growth," *Applied Physics Letters*, vol. 4, no. 5, pp. 89–90, 1964.
- [3] K. S. Shankar and A. K. Raychaudhuri, "Fabrication of nanowires of multicomponent oxides: review of recent advances," *Materials Science and Engineering C*, vol. 25, no. 5-8, pp. 738–751, 2005.
- [4] P. A. Cox, *Transition Metal Oxides: An Introduction to Their Electronic Structure and Properties*, Oxford University Press, New York, NY, USA, 1992.
- [5] A. Cruccolini, R. Narducci, and R. Palombari, "Gas adsorption effects on surface conductivity of nonstoichiometric CuO," *Sensors and Actuators, B*, vol. 98, no. 2-3, pp. 227–232, 2004.
- [6] V. R. Katti, A. K. Debnath, K. P. Muthe et al., "Mechanism of drifts in H₂S sensing properties of SnO₂:CuO composite thin film sensors prepared by thermal evaporation," *Sensors and Actuators, B*, vol. 98, no. 1-2, pp. 245–252, 2003.
- [7] H. Fan, L. Yang, W. Hua et al., "Controlled synthesis of monodispersed CuO nanocrystals," *Nanotechnology*, vol. 15, no. 1, pp. 37–42, 2004.
- [8] A. Santos, P. Yustos, A. Quintanilla, G. Ruiz, and F. Garcia-Ochoa, "Study of the copper leaching in the wet oxidation of phenol with CuO-based catalysts: causes and effects," *Applied Catalysis B*, vol. 61, no. 3-4, pp. 323–333, 2005.
- [9] A. A. Ponce and K. J. Klabunde, "Chemical and catalytic activity of copper nanoparticles prepared via metal vapor

- synthesis," *Journal of Molecular Catalysis A*, vol. 225, no. 1, pp. 1–6, 2005.
- [10] G. Larsen and S. Noriega, "Dendrimer-mediated formation of Cu-CuOx nanoparticles on silica and their physical and catalytic characterization," *Applied Catalysis A*, vol. 278, no. 1, pp. 73–81, 2004.
- [11] C. T. Hsieh, J. M. Chen, H. H. Lin, and H. C. Shih, "Field emission from various CuO nanostructures," *Applied Physics Letters*, vol. 83, no. 16, pp. 3383–3385, 2003.
- [12] F. Lanza, R. Feduzi, and J. Fuger, "Effects of lithium oxide on the electrical properties of CuO at low temperatures," *Journal of Materials Research*, vol. 5, no. 8, pp. 1739–1744, 1990.
- [13] D. Chen, G. Shen, K. Tang, and Y. Qian, "Large-scale synthesis of CuO shuttle-like crystals via a convenient hydrothermal decomposition route," *Journal of Crystal Growth*, vol. 254, no. 1-2, pp. 225–228, 2003.
- [14] C. T. Hsieh, J. M. Chen, H. H. Lin, and H. C. Shih, "Synthesis of well-ordered CuO nanofibers by a self-catalytic growth mechanism," *Applied Physics Letters*, vol. 82, no. 19, pp. 3316–3318, 2003.
- [15] J. Liang, N. Kishi, T. Soga, and T. Jimbo, "Cross-sectional characterization of cupric oxide nanowires grown by thermal oxidation of copper foils," *Applied Surface Science*, vol. 257, no. 1, pp. 62–66, 2010.
- [16] K. Zhang, C. Rossi, C. Tenailleau, P. Alphonse, and J.-Y. Chane-Ching, "Synthesis of large-area and aligned copper oxide nanowires from copper thin film on silicon substrate," *Nanotechnology*, vol. 18, no. 27, article 275607, 2007.
- [17] R. C. Wang and C. H. Li, "Improved morphologies and enhanced field emissions of CuO nanoneedle arrays by heating ZnO coated copper foils improved morphologies and enhanced field emissions of CuO nanoneedle arrays by heating ZnO coated copper foils," *Crystal Growth and Design*, vol. 9, no. 5, pp. 2229–2234, 2009.
- [18] K. Zhang, Y. Yang, E. Y.B. Pun, and R. Shen, "Local and CMOS-compatible synthesis of CuO nanowires on a suspended microheater on a silicon substrate," *Nanotechnology*, vol. 21, no. 23, p. 7, 2010.
- [19] J. Chen, B. J. Hansen, and G. Lu, "Direct oxidation growth of CuO nanowires from copper-containing substrates," *Journal of Nanomaterials*, vol. 2008, no. 1, Article ID 830474, 7 pages, 2008.
- [20] A. M.B. Gonçalves, L. C. Campos, A. S. Ferlauto, and R. G. Lacerda, "On the growth and electrical characterization of CuO nanowires by thermal oxidation," *Journal of Applied Physics*, vol. 106, no. 3, article 34303, 5 pages, 2009.
- [21] X. Jiang, T. Herricks, and Y. Xia, "CuO Nanowires Can Be Synthesized by Heating Copper Substrates in Air," *Nano Letters*, vol. 2, no. 12, pp. 1333–1338, 2002.
- [22] C. H. Xu, C. H. Woo, and S. Q. Shi, "The effects of oxidative environments on the synthesis of CuO nanowires on Cu substrates," *Superlattices and Microstructures*, vol. 36, no. 1–3, pp. 31–38, 2004.
- [23] C. T. Hsieh, J. M. Chen, H. H. Lin, and H. C. Shih, "Field emission from various CuO nanostructures," *Applied Physics Letters*, vol. 83, no. 16, pp. 3383–3385, 2003.
- [24] C. Rossi, K. Zhang, D. Esteve et al., "Nano energetic materials for MEMS: a review IEEE/ASME," *Journal of Microelectromechanical Systems*, vol. 16, no. 4, pp. 919–931, 2007.
- [25] A. M. B. Gonçalves, L. C. Campos, A. S. Ferlauto, and R. G. Lacerda, "On the growth and electrical characterization of CuO nanowires by thermal oxidation," *Journal of Applied Physics*, vol. 106, no. 3, Article ID 034303, 2009.
- [26] C. H. Xu, C. H. Woo, and S. Q. Shi, "Formation of CuO nanowires on Cu foil," *Chemical Physics Letters*, vol. 399, no. 1–3, pp. 62–66, 2004.
- [27] Y. W. Park, N. J. Seong, H. J. Jung, A. Chanda, and S. G. Yoon, "Growth mechanism of the copper oxide nanowires from copper thin films deposited on CuO-buffered silicon substrate," *Journal of the Electrochemical Society*, vol. 157, no. 6, pp. K119–K124, 2010.
- [28] P. Shao, S. Deng, J. Chen, and N. Xu, "Large-scale fabrication of ordered arrays of microcontainers and the restraint effect on growth of CuO nanowires," *Nanoscale Research Letters*, vol. 6, no. 86, pp. 1–4, 2011.
- [29] A. G. Nasibulin, S. Rackauskas, H. Jiang et al., "Simple and rapid synthesis of α -Fe₂O₃ nanowires under ambient conditions," *Nano Research*, vol. 2, no. 5, pp. 373–379, 2009.
- [30] J. M. Perrow, W. W. Smeltzer, and J. D. Embury, "The role of structural defects in the growth of nickel oxide films," *Acta Metallurgica*, vol. 16, no. 10, pp. 1209–1218, 1968.
- [31] Z. Han, L. Lu, H. W. Zhang, Z. Q. Yang, F. H. Wang, and K. Lu, "Comparison of the oxidation behavior of nanocrystalline and coarse-grain copper," *Oxidation of Metals*, vol. 63, no. 5-6, pp. 261–275, 2005.
- [32] Y. Niu, F. Gesmundo, G. Farnè, Y. S. Li, P. Matteazzi, and G. Randi, "The air oxidation of a nanocrystalline Cu-10 wt%Ni alloy at 800°C," *Corrosion Science*, vol. 42, no. 10, pp. 1763–1777, 2000.

Research Article

Carbon Nanostructures Production by AC Arc Discharge Plasma Process at Atmospheric Pressure

Shenqiang Zhao,^{1,2,3} Ruoyu Hong,² Zhi Luo,² Haifeng Lu,² and Biao Yan¹

¹ College of Material Science and Engineering, Tongji University, Shanghai 201804, China

² Chemical Engineering and Material Science & Key Laboratory of Organic Synthesis of Jiangsu Province, College of Chemistry, Soochow University, SIP, Suzhou 215123, China

³ Modern Experiment and Technology Center, Anhui University, Hefei 230039, China

Correspondence should be addressed to Ruoyu Hong, rhong@suda.edu.cn and Biao Yan, yanbiao2002@yahoo.com.cn

Received 6 July 2011; Accepted 22 August 2011

Academic Editor: Yanqiu Zhu

Copyright © 2011 Shenqiang Zhao et al. This is an open access article distributed under the Creative Commons Attribution License, which permits unrestricted use, distribution, and reproduction in any medium, provided the original work is properly cited.

Carbon nanostructures have received much attention for a wide range of applications. In this paper, we produced carbon nanostructures by decomposition of benzene using AC arc discharge plasma process at atmospheric pressure. Discharge was carried out at a voltage of 380 V, with a current of 6 A–20 A. The products were characterized by scanning electron microscopy (SEM), high-resolution transmission electron microscopy (HRTEM), powder X-ray diffraction (XRD), and Raman spectra. The results show that the products on the inner wall of the reactor and the sand core are nanoparticles with 20–60 nm diameter, and the products on the electrode ends are nanoparticles, agglomerate carbon particles, and multiwalled carbon nanotubes (MWCNTs). The maximum yield content of carbon nanotubes occurs when the arc discharge current is 8 A. Finally, the reaction mechanism was discussed.

1. Introduction

Carbon nanomaterials, which usually are carbon blacks (CBs), fullerenes, and carbon nanotubes, carbon fibres, have a privileged position in all applications related to nanotechnology. Current and potential applications of carbon nanomaterials cover all segments of the energy and materials sectors [1]. Carbon black belongs to the first nanomaterials produced on an industrial scale in the early 20th century [2]. Production of CB is about 8 million tons per year in the world. Fullerenes are considered a versatile building block in organic chemistry for molecular engineering and practical application (photovoltaics, medicine, etc.). Carbon fibres and CBs are large-scale products used as reinforcement structures in polymers and metals. Carbon nanotubes have been proposed for many applications, including electronic devices, field emitters, hydrogen storage, scanning microscope probe tips, and composites [3].

This work focused on CBs, fullerenes, and carbon nanotubes.

Historically, the synthesis of these nanocarbons is closely related to plasma processes, particularly arc discharge. Initial papers claiming fullerenes and CNT production to gram scale were based on it [4]. In addition, carbon nanotubes discovery was associated with microscopic characterization of samples produced by the arc technique [5]. However, CB and fullerenes are currently produced at industrial scale in flame reactors [6, 7]. This technique, which is classified within the gas-phase synthesis method, consists of the continuous production of carbon nanostructures by employing the flame heat to initiate chemical reactions producing condensable monomers. The flame is usually produced by burning a fraction of the carbon precursor, usually a hydrocarbon. The principle of the plasma process consists in replacing the incomplete combustion by directly cracking the hydrocarbon into carbon black and hydrogen owing to an external electric energy supply. Plasma processes provide a reasonable alternative to flame aerosol technology due to their number of advantages with respect to combustion [8]. At first, plasma processes are allothermal: the energy input is

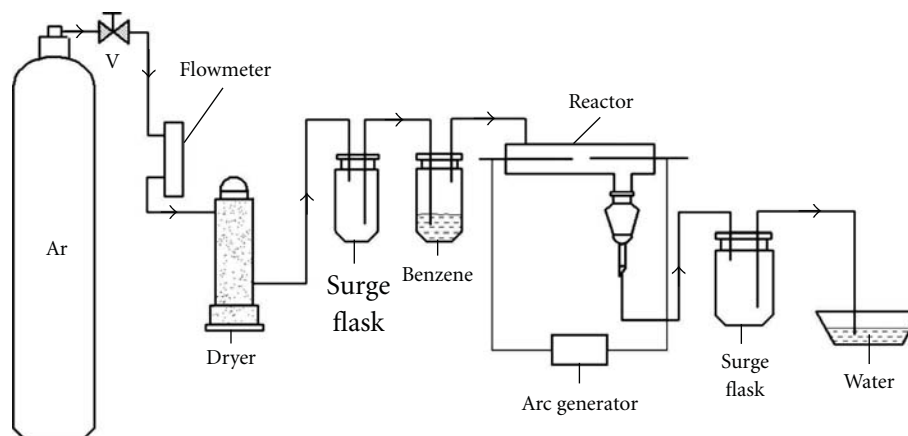


FIGURE 1: Schematic diagram of an AC arc plasma reactor system.

independent of chemical reactions happening in the reactor. Secondly, plasma techniques are usually environmentally clean processes since they are not a primary greenhouse gas emitter. Thirdly, the conversion efficiency is close to 100%. Finally, hydrocarbon plasma conversion leads to the formation of hydrogen, a highly valuable by product considered today the most feasible energetic vector of the future.

In the conventional arc discharge processes used in producing fullerenes and carbon nanotubes, the electrodes are two graphite rods and the origin of the carbon precursor comes from the ablation of a graphite electrode. In this work, the two graphite electrodes were substituted with two tungsten electrodes, and the origin of the carbon precursor was the carbon black which comes from the decomposition of the benzene in the reactor. Benzene was used as the origin of the carbon precursor because the hydrocarbon (benzene, methane, acetylene, ethylene) has no influence on the products' properties [9] and the experimental device can be simplified.

2. Experimental

A schematic diagram of the carbon nanomaterials synthesis by benzene decomposition is shown in Figure 1. The thermal plasma was produced by an electric arc between tungsten electrodes with 6 mm in diameter connected to AC power supply, which allows a maximum power input of 8 kW. The frequency of the electrical source is 50 Hz. Argon (purity 99.99%, Jinhong Gas Co., Ltd., China) was used as plasma gas, and benzene (AR, Sinopharm Chemical Reagent Co., Ltd., China) was used as carbon source. Benzene was carried into the reactor by argon flow. Plasma gas and benzene were injected simultaneously at atmospheric pressure with flow rates of 80 l/h. Discharge was carried out at a voltage of 380 V, with a current of 6 A, 8 A, 14 A, and 20 A, respectively.

In this experiment, the products were deposited on the internal wall of the reactor, the sand core, and the tungsten electrode ends. The products on the electrode ends showed radial, others evenly distributed on the surface of the reactor internal wall and sand core. These carbon nanostructures were characterized using a scanning electron microscopy

(S-4800, FE-SEM), a high-resolution transmission electron microscopy (JEM-2100, HRTEM-200 KV), powder X-ray diffraction (DX-2700, XRD), and laser Raman spectra (HR800, Raman). SEM was performed at 0.5–30 kV with no metallisation of the samples. For TEM analysis, the collected products were first sonicated in alcohol. Then, the prepared suspension was deposited onto copper microgrids coated with amorphous lacey carbon membranes. Once dried, the microgrids were observed by HRTEM.

3. Results and Discussions

3.1. SEM and HRTEM Studies. A study conducted by SEM and TEM is conclusive to characterize the texture (elemental particles and their aggregating) as well as the structure (crystallinity) of the deposited carbon. It shows that the AC arc discharge plasma process is a versatile process for growing a wide range of carbon black.

SEM images were obtained on a film, deposited on a silicon wafer. Figures 2 and 3 show morphology of the sample obtained from benzene in argon plasma medium. Figures 2(a), 2(b), 2(c), and 2(d) illustrate the typical micrographs of the deposited carbon on the inner wall of the reactor and the sand core which correspond to the arc discharge current of 6 A, 8 A, 14 A, and 20 A, respectively. It was observed that the carbon particles exhibit a spherical particle with nanosized diameter. The diameter of the carbon particle varied from 20 to 60 nm, and the mean diameter was about 30 nm. Figures 3(a), 3(b), 3(c), and 3(d) illustrate the typical micrographs of the deposited carbon on the electrode ends, which correspond to the arc discharge current of 6 A, 8 A, 14 A, and 20 A, respectively. It was clear that carbon nanotubes (CNTs), aggregate carbon nanoparticles, and agglomerate carbon particles are formed in all cases, and yield content of CNTs depends on the arc discharge current. The production rate of CNTs begins to increase and then decrease while the arc discharge current increased. The maximum, which is roughly about 80%, was obtained while the current is up to 8 A. The solid phase theory for carbon nanotubes may help us to understand the phenomena [10]. The temperature of the electrode ends needs to reach high temperature, on

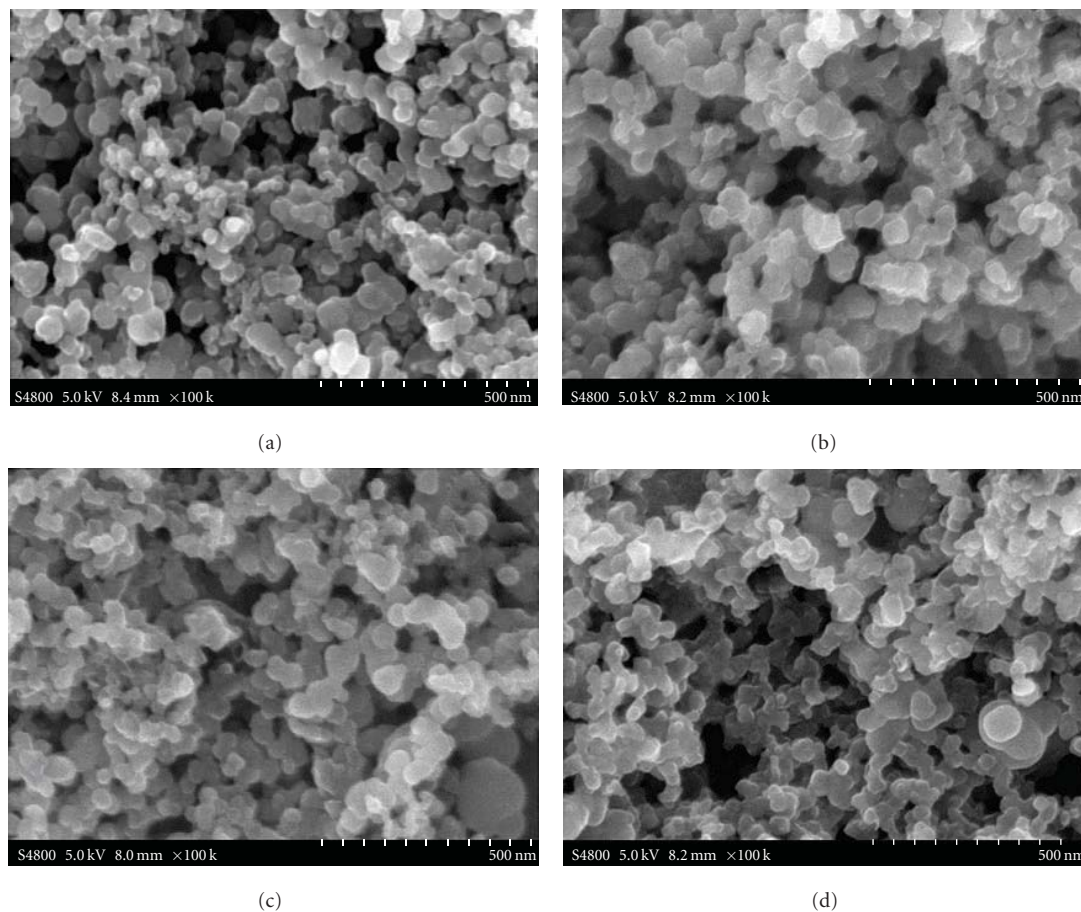


FIGURE 2: SEM micrographs of the deposited carbon on the internal wall of the reactor and the sand core (a) 6 A, (b) 8 A, (c) 14 A, and (d) 20 A.

which nanotube growth can occur. However, the excessively high temperature will cause sintering of the nanotubes. The temperature increases along with the arc discharge electric current elevates. Therefore, the 8 A current is ideal for the growth of nanotube.

A HRTEM image displayed in Figure 4 shows clearly that the deposited carbon on the inner wall of the reactor and the sand core is the turbostratic structure of graphite; that is, the deposited carbon is partially graphitized, not in a complete graphite phase. Figure 5 clearly shows well-graphitized layers of the multiwall nanotubes, the hollow shell morphology, and turbostratic structure deposited on the electrode ends. These CNTs consist of more than ten concentric carbon shells with a spacing of 0.34 nm, which is consistent with that of graphite, only a little bit of carbonaceous material attached to its surface. The hollow shell structures can be considered as “giant fullerene”: graphene layers are extended, their curvatures are related to pentagons, and no graphene edges can be observed.

3.2. X-Ray Diffraction Studies of Various Nanostructures. The measured diffraction patterns are shown in Figure 6. The inserted labels are Miller indices corresponding to the peaks of pure graphite. Only (002) peak appears in all patterns, (100) peak is visible in (e), and other weak peaks are invisible

in all cases. The observed intensities for deposited carbon and their d-spacings seem to match those of the graphite-2H structure [11] with slightly expanded lattice parameters. The observed d-spacings of 0.3482, 0.3440, 0.3424, 0.3421, and 0.3419 nm, corresponding to (a), (b), (c), (d), and (e), respectively, are wider than that of an ideal graphite crystal (0.3354 nm). This slight expansion in d_{002} is attributed to the turbostratic character in the carbon structure [5, 12–14]. In other words, graphitization degree of the carbon structure is inversely with d-spacing.

3.3. Raman Studies of Various Carbon Nanostructures. Raman measurements were performed using a 632.8 nm He-Ne laser on the surface of the deposited carbon material. The Raman spectra of the deposited carbon (a) on the inner wall of the reactor and the sand core, and on the electrode ends of (b) 6 A, (c) 8 A, (d) 14 A, (e) 20 A, are shown in Figure 7. All spectra show mainly two Raman bands at 1328 and 1582 cm^{-1} corresponding to graphite’s D- and G-bands, respectively. Generally speaking, for any carbon material, the peaks around 1328 cm^{-1} indicate the disorder in the sample due to carbon nanoparticles and the random orientation of the tubes, and the peaks around 1582 cm^{-1} are associated with the graphitic nature of the carbon materials [15]. Relative intensity ratio of D and G

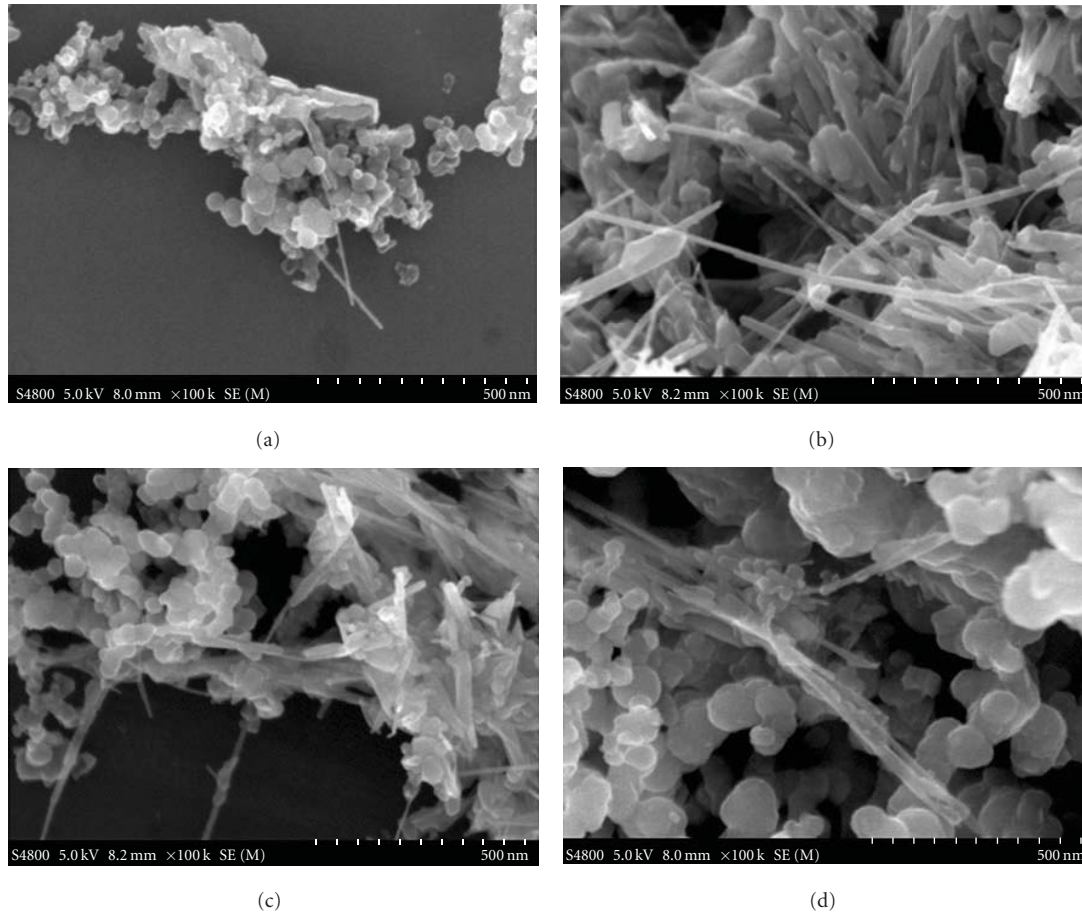


FIGURE 3: SEM micrographs of the deposited carbon on the electrode ends (a) 6 A, (b) 8 A, (c) 14 A, and (d) 20 A.

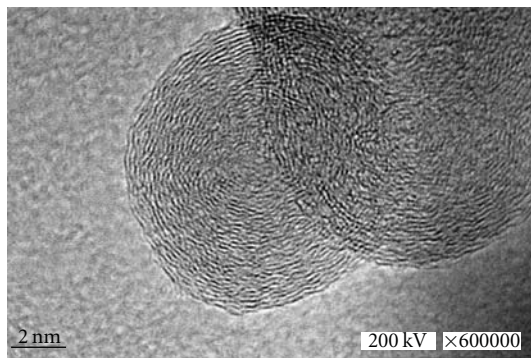


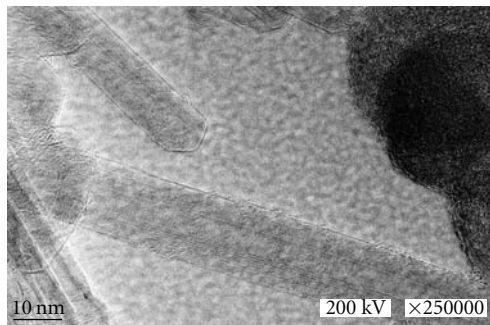
FIGURE 4: HRTEM micrographs of the deposited carbon on the inner wall of the reactor and the sand core.

peaks (I_D/I_G) is a measure of the amount of disorder in the crystallinity [16]. Higher intensity of G band indicates the higher degree of crystallinity/graphitization. The value of I_D/I_G decreases from 1.2 to 0.6 with the increasing arc discharge current. From these observations, it is concluded that the graphitization degree of the samples increases with the arc discharge current. The Raman results are nicely consistent with XRD analysis in which the crystallinity of

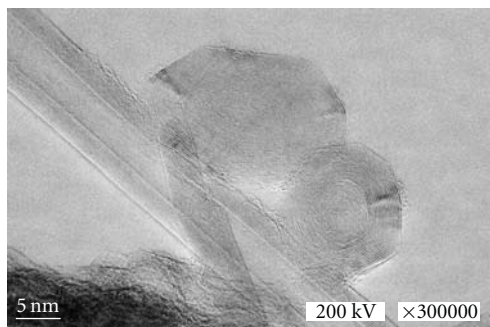
graphitic sheets improves progressively as the arc discharge current increases.

3.4. Reaction Mechanism. A better understanding of the growth mechanism for nanotubes would help in the development of new efficient production methods. Many different theories have been proposed for the growth of nanotubes. Most theories rely on the presence of a metal catalyst [17–19]. However, for the growth of CNTs without catalysts, the majority of theories describe the formation of nanotubes from a carbon vapor comprised of carbon atoms, ions, and molecules within the plasma [20–22]. At the same time, other theories believe that a carbon vapor is not necessary for the growth of multiwalled nanotubes [3, 23]. Nanotubes can be made by the heat treatment of disordered carbons.

In this paper, we present the following explanation for our observations. Firstly, carbon vapor comprising of carbon atoms, ions, and molecules was obtained from benzene by pyrolysis of plasma torch. Then, nucleation process results in the transformation of a molecular system to a particulate system. Thirdly, aggregation due to collisions of nanometer-sized particles (results of the nucleation process) forms 20–60 nm spherical particles (see Figure 3). The spherical particles were deposited on the inner wall of the reactor, sand core and electrode ends, which is of an aggregate of semispherical



(a)



(b)

FIGURE 5: HRTEM micrographs of the deposited carbon on the electrode ends.

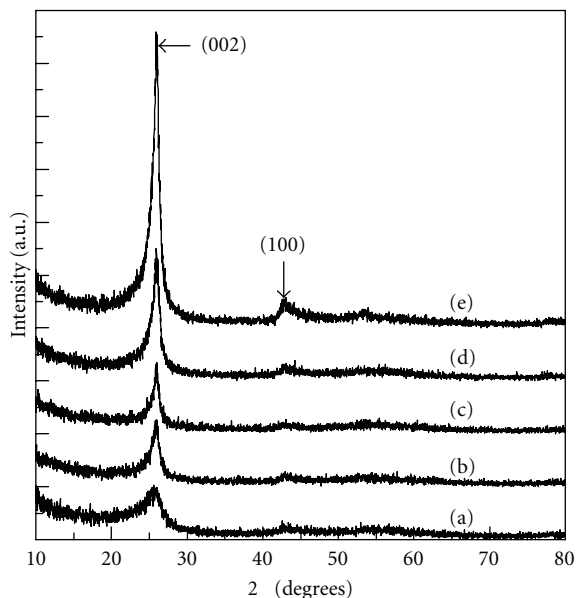


FIGURE 6: X-ray diffraction patterns of the deposited carbon (a) on the inner wall of the reactor and the sand core, and on the electrode ends of (b) 6 A, (c) 8 A, (d) 14 A, and (e) 20 A.

carbon-onion-like structures, built up by concentric carbon-layers around a defect-fullerene nucleus [24] (see Figure 5). After that, graphitization of the spherical particles deposited on the electrode ends begins with carbon self-diffusion by the heat treatment, leading to order in the planes of graphite

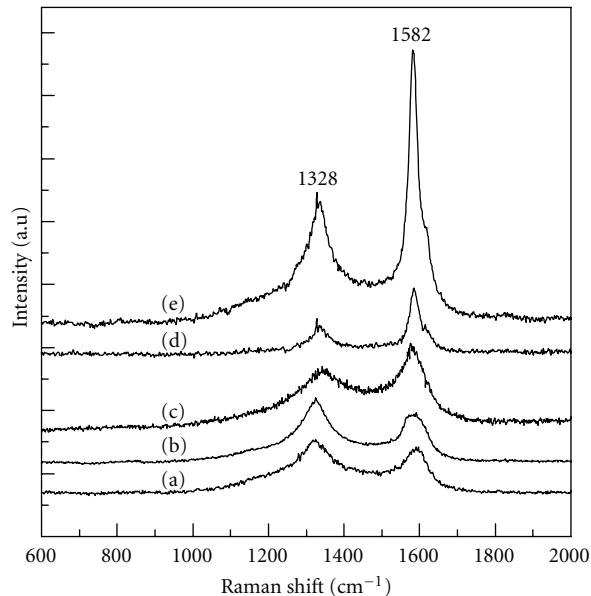


FIGURE 7: Raman spectra of the deposited carbon (a) on the inner wall of the reactor and the sand core, and on the electrode ends of (b) 6 A, (c) 8 A, (d) 14 A, and (e) 20 A.

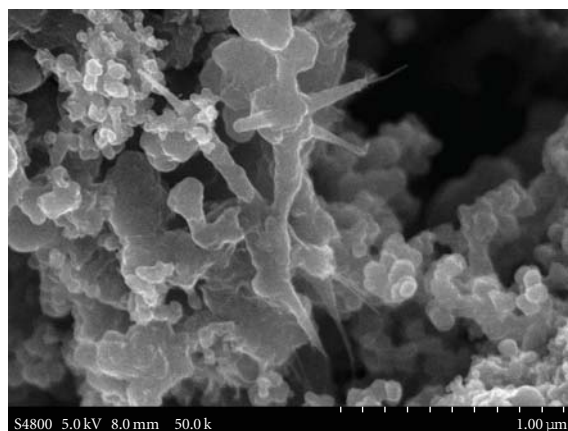


FIGURE 8: Schematic diagram of the formation of carbon nanotubes and agglomerate.

[25]. However, defects (pentagon, heptagon, and pentagon-heptagon pairs) initially present in nongraphitizable carbons cannot be removed completely, which is necessary for the transformation of spherical particles to nanotubes [26–28]. The thermally generated tensile forces result in the formation of short nanotubes (no more than 1 μm), and agglomerate bulk formed by the melt of the particles simultaneously (see Figure 8).

4. Conclusions

Direct thermal decomposition of benzene was carried out using an AC arc discharge plasma process which is an environmentally favorable process.

The carbon particles deposited on the inner wall of reactor and the sand core exhibit a spherical particle with

nanosized diameter. The diameter of the carbon particle varied from 20 to 60 nm, and the mean diameter was about 30 nm.

The carbon product deposited on the electrode ends is comprised of MWCNTs, aggregate carbon nanoparticles, and agglomerate carbon particles. The maximum yield content of CNTs occurs at an arc discharge current of 8 A.

Further study is necessary in order to design a better plasma system and to produce larger quantities of nanotubes or carbon black.

Acknowledgments

The authors gratefully acknowledge Zhongqing Lin (Modern Experiment and Technology Center, Anhui University, China) for the SEM analysis, Yonglong Zhuang (Modern Experiment and Technology Center, Anhui University, China) for the HRTEM analysis. This work was supported by the National Natural Science Foundation of China (NSFC, nos. 20876100 and 20736004) the National Basic Research Program of China (973 Program, no. 2009CB219904).

References

- [1] O. Vohler, G. Nutsch, G. Collin, F. von Sturm, and E. Wege, "Carbon," in *Ullmann's Encyclopedia of Industrial Chemistry*, vol. 6, pp. 281–292, Wiley-VCH, Weinheim, Germany, 2002.
- [2] G. Kühner and M. Voll, *Manufacture of Carbon Black in Carbon Black Science and Technology*, Marcel Dekker, New York, NY, USA, 2nd edition, 1993.
- [3] S. P. Doherty and R. P. H. Chang, "Synthesis of multiwalled carbon nanotubes from carbon black," *Applied Physics Letters*, vol. 81, no. 13, pp. 2466–2468, 2002.
- [4] R. E. Haufler, J. Conceicao, L. P. F. Chibante et al., "Efficient production of C60 (Buckminsterfullerene), C60H36, and the solvated buckide ion," *Journal of Physical Chemistry*, vol. 94, no. 24, pp. 8634–8636, 1990.
- [5] S. Iijima, "Helical microtubules of graphitic carbon," *Nature*, vol. 354, no. 6348, pp. 56–58, 1991.
- [6] A. Gutsch, M. Krämer, G. Michael, H. Mühlenweg, M. Pridöhl, and G. Zimmermann, "Gas-phase production of nanoparticles," *KONA*, no. 20, pp. 24–37, 2002.
- [7] H. Murayama, S. Tomonoh, J. M. Alford, and M. E. Karpuk, "Fullerene production in tons and more: from science to industry," *Fullerenes Nanotubes and Carbon Nanostructures*, vol. 12, no. 1-2, pp. 1–9, 2004.
- [8] J. Gonzalez-Aguilar, M. Moreno, and L. Fulcheri, "Carbon nanostructures production by gas-phase plasma processes at atmospheric pressure," *Journal of Physics D*, vol. 40, no. 8, article S16, pp. 2361–2374, 2007.
- [9] K. Schmidt-Szalowski, T. Opalinska, J. Sentek et al., "Methane conversion into C2 hydrocarbons and carbon black in dielectric-barrier and gliding discharges," *Journal of Advanced Oxidation Technologies*, vol. 7, no. 1, pp. 39–50, 2004.
- [10] P. J. F. Harris, "Solid state growth mechanisms for carbon nanotubes," *Carbon*, vol. 45, no. 2, pp. 229–239, 2007.
- [11] I. Sanc, "Pattern: 00-041-1478, Graphite-2H, Polytechna," Foreign Trade Corporation, Panska, Czechoslovakia, ICDD Grant-in-Aid, 1990.
- [12] L. Dobiasova, M. Stary, P. Glogar, and V. Valvoda, "Analysis of carbon fibers and carbon composites by symmetric X-ray diffraction technique," *Carbon*, vol. 37, no. 3, pp. 421–425, 1999.
- [13] Y. Saito, T. Yoshikawa, S. Bandow, M. Tomita, and T. Hayashi, "Interlayer spacings in carbon nanotubes," *Physical Review B*, vol. 48, no. 3, pp. 1907–1909, 1993.
- [14] K. Tohji, M. Sugano, A. Kasuya, Y. Nishina, Y. Saito, and H. Takahashi, "Resonant Raman scattering from single-walled nanotubes of small diameters," *Applied Surface Science*, vol. 144-145, pp. 657–662, 1999.
- [15] R. Saito, G. Dresselhaus, and M. S. Dresselhaus, *Physical Properties of Carbon Nanotubes*, Imperial College Press, London, UK, 1998.
- [16] M. Kumar and Y. Ando, "Single-wall and multi-wall carbon nanotubes from camphor—a botanical hydrocarbon," *Diamond and Related Materials*, vol. 12, no. 10-11, pp. 1845–1850, 2003.
- [17] S. Iijima and T. Ichihashi, "Single-shell carbon nanotubes of 1 nm diameter," *Nature*, vol. 363, no. 6430, pp. 603–605, 1993.
- [18] D. S. Bethune, C. H. Kiang, M. S. De Vries et al., "Cobalt-catalysed growth of carbon nanotubes with single-atomic-layer walls," *Nature*, vol. 363, no. 6430, pp. 605–607, 1993.
- [19] C. Journet, W. K. Maser, P. Bernier et al., "Large-scale production of single-walled carbon nanotubes by the electric-arc technique," *Nature*, vol. 388, no. 6644, pp. 756–758, 1997.
- [20] E. G. Gamaly and T. W. Ebbesen, "Mechanism of carbon nanotube formation in the arc discharge," *Physical Review B*, vol. 52, no. 3, pp. 2083–2089, 1995.
- [21] T. Guo, P. Nikolaev, A. G. Rinzler, D. Tománek, D. T. Colbert, and R. E. Smalley, "Self-assembly of tubular fullerenes," *Journal of Physical Chemistry*, vol. 99, no. 27, pp. 10694–10697, 1995.
- [22] J. C. Charlier, A. De Vita, X. Blase, and R. Car, "Microscopic growth mechanisms for carbon nanotubes," *Science*, vol. 275, no. 5300, pp. 646–649, 1997.
- [23] A. A. Setlur, S. P. Doherty, J. Y. Dai, and R. P. H. Chang, "A promising pathway to make multiwalled carbon nanotubes," *Applied Physics Letters*, vol. 76, no. 21, pp. 3008–3010, 2000.
- [24] V. I. Berezkin, "Fullerenes as nuclei of carbon black particles," *Physics of the Solid State*, vol. 42, no. 3, pp. 580–585, 2000.
- [25] L. E. Jones and P. A. Thrower, "Influence of boron on carbon fiber microstructure, physical properties, and oxidation behavior," *Carbon*, vol. 29, no. 2, pp. 251–269, 1991.
- [26] W. A. de Heer and D. Ugarte, "Carbon onions produced by heat treatment of carbon soot and their relation to the 217.5 nm interstellar absorption feature," *Chemical Physics Letters*, vol. 207, no. 4–6, pp. 480–486, 1993.
- [27] P. J. F. Harris, S. C. Tsang, J. B. Claridge, and M. L. H. Green, "High-resolution electron microscopy studies of a microporous carbon produced by arc-evaporation," *Journal of the Chemical Society, Faraday Transactions*, vol. 90, no. 18, pp. 2799–2802, 1994.
- [28] D. B. Geohegan, H. Schittenhelm, X. Fan et al., "Condensed phase growth of single-wall carbon nanotubes from laser annealed nanoparticulates," *Applied Physics Letters*, vol. 78, no. 21, pp. 3307–3309, 2001.

Research Article

Toward 3D Integration of 1D Conductors: Junctions of InAs Nanowires

Phillip M. Wu, Lars Samuelson, and Heiner Linke

*Division of Solid State Physics and The Nanometer Structure Consortium (nmC@LU), Lund University,
P.O. Box 118, 221 00 Lund, Sweden*

Correspondence should be addressed to Phillip M. Wu, phillip.wu@ftf.lth.se

Received 5 July 2011; Accepted 23 August 2011

Academic Editor: Raymond Whitby

Copyright © 2011 Phillip M. Wu et al. This is an open access article distributed under the Creative Commons Attribution License, which permits unrestricted use, distribution, and reproduction in any medium, provided the original work is properly cited.

A vision and one of the next challenges in nanoelectronics is the 3D integration of nanowire building blocks. Here we show that capillary forces associated with a liquid-air meniscus between two nanowires provides a simple, controllable technique to bend vertical nanowires into designed, interconnected assemblies. We characterize the electric nature of the junctions between crossed nanowires in a lateral geometry, which is one type of basic unit that can be found in interconnected-bent vertical nanowires. The crossed nanowire junction is capacitive in nature, and we demonstrate that one nanowire can be used to field effect gate the other nanowire, allowing for the possibility to develop extremely narrow conducting channels in nanowire planar or 3D electronic devices.

1. Introduction

Advances in fabrication techniques over the last decade have allowed researchers to exercise full creativity in developing novel nanometer size devices. One of the primary issues concerning nanostructures, however, is the ability to upscale to allow for more complex systems with specific function and easy integration with devices of larger dimensions. There have been promising results recently in this direction with the demonstration of controlled synthesis of self-assembled three-dimensional (3D) networks of interconnected one-dimensional (1D) nanowires, termed “nanotree” networks [1, 2]. These networks have the potential for upscaling into complex, integrated 3D nanoelectronics devices.

Networked nanowires present a natural system for studying electronic behavior in complex 3D junctions of 1D components. These 3D networks of 1D components could give rise to novel and unexpected collective transport properties. This expectation is reasonable as self-assembled junctions of two nanowires have been shown to exhibit unusual nonlinear electrical characteristics and signatures of ballistic transport [3, 4]. Understanding the electronic and spin behavior in such systems will be critical to further develop applications for nanoelectronic devices.

In this paper we report steps to achieve and characterize networked nanowires. We present a simple, controllable technique to bend vertical nanowires into contact. Positioning nanowire seed particles with lithography allows one to design various interconnected nanowire array geometries. Then we discuss transport measurements performed on crossed nanowires in a lateral geometry, which is one type of basic unit that can be found in interconnected-bent vertical networks of nanowires. We find that the crossed nanowire junction is capacitive in nature and demonstrate that one nanowire can be used to field-effect gate the other nanowire, allowing for the possibility to develop extremely short gates in nanowire planar or 3D electronic devices.

2. Experimental Methods

InAs nanowires were grown in a high vacuum chemical beam epitaxy (CBE) unit on InAs (111) B wafers [5]. Gold (Au) aerosol particles or electron beam lithography (EBL) defined Au dots acted as catalysts to seed the growth. Tertiarybutylarsine (TBA) was thermally cracked into As and the growth chamber maintained at As ambient of 1.5 mbar. At the growth temperature of 425°C, 0.15 mbar of

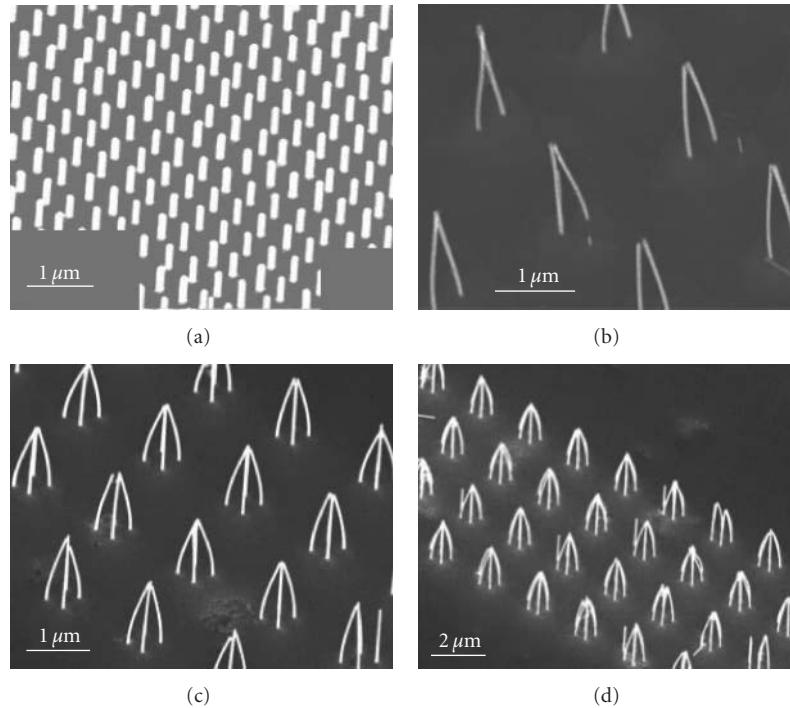


FIGURE 1: (a) Array of nanowires that remain vertical after PMMA/acetone treatment. (b) Patterned “doublet” of nanowires. (c) “Tetrapod” arrangement of four nanowires placed at the vertices of a parallelogram. (d) “Hexapod” arrangement of six nanowires, with nanowire centered at the vertices of a hexagon. The individual nanowires shown here are all approximately 80 nm in diameter, and lengths for those in (b)–(d) are from 3 to 3.5 μm .

TrimethylIndium (TMIn) was introduced to initiate growth. The growth rate was typically 60 nm/minute [6]. Once the targeted nanowire length was achieved, the TMIn flow to chamber was shut, and sample allowed to cool to nearly room temperature in As ambient background. The nanowires were then removed from the CBE unit.

To connect nanowires, we dropped a single droplet of PMMA 950A5 onto the growth substrate. After 1 minute, the sample was spun at 3000 rpm in a spincoater to smooth the PMMA layer. Nanowires were observed to be bent after this process. Then the PMMA was removed by soaking in acetone. Simply dropping the PMMA, leaving for 1 minute, then removing the PMMA by soaking the sample in acetone for 10 minutes was also enough to bend and aggregate nanowires.

For the transport characterization, good ohmic contacts must be made to the nanowires. We chose a lateral contact geometry as it was simpler to fabricate. Nanowires were picked up from the growth substrate with cleanroom tissue paper, then brushed onto Si/SiO₂ chips with 110 nm thick oxide. We searched for crossed nanowire geometries optically and determined the location of the nanowires with predefined Au alignment marks on the SiO₂ chips. Contacts to the crossed nanowires were fabricated via standard e-beam lithography processes [7]. Briefly, 950A5 PMMA was spun onto the sample at 5000 rpm for 60 s and baked at 180°C for 5 minutes. After the contact pattern exposure, the resist was developed in MIBK : IPA (1 : 3) for 30 s. To ensure ohmic

contacts to the nanowires, we passivated the nanowires in (NH₄)₂S_x solution at 40°C prior to thermal evaporation of metal contacts Ti : Au (25 nm : 75 nm) [8].

3. Results and Discussions

EBL-based seeding of nanowire growth is quite versatile, and seed-spacing, seed patterns, and nanowire length can be used to control the resulting 3D, interconnected geometry (Figure 1). Figure 1(a) is an image of an array of ~ 80 nm diameter InAs nanowires, with lengths of 760 nm and separation distance between nanowires of 400 nm. Figures 1(b)–1(d) show images of nanowires that have been brought into contact by the PMMA drop/acetone rinse procedure. These nanowires have diameter ~ 80 nm and lengths longer than 3 micron. In contrast, the nanowires of Figure 1(a) do not meet after the rinse procedure. We believe that the nanowires here are not long enough, such that the external forces and torques are not sufficient to overcome the inherent nanowire stiffness. Figure 1(b) presents the simplest structure beyond single vertical nanowires, that is a doublet of two bent and connected nanowires, while Figure 1(c) shows a parallelogram arrangement of four nanowires, which we call “tetrapod,” and Figure 1(d) shows a hexagonal arrangement of six nanowires, or “hexapod.”

We observed bent and aggregated nanowires after spin-coating a PMMA layer on the growth substrate. During the spin process, the PMMA is flattened out such that

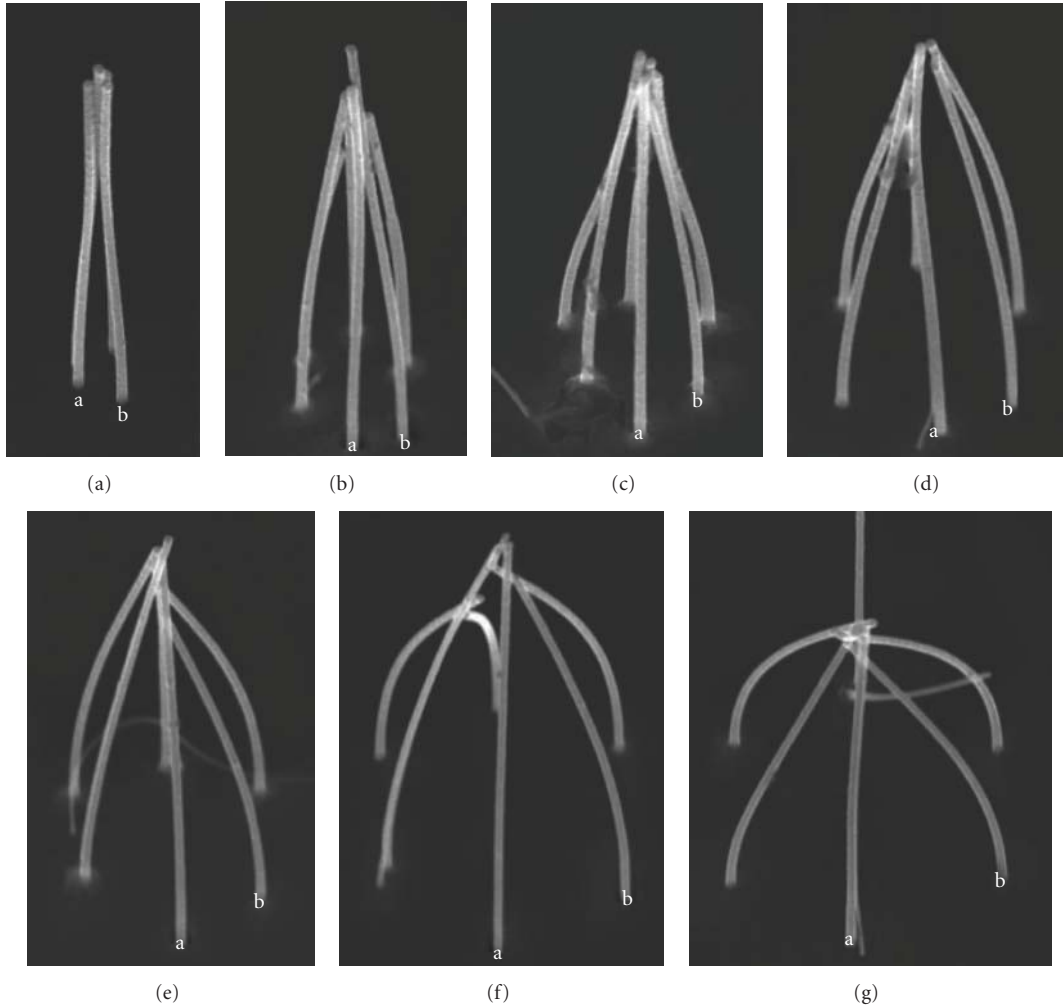


FIGURE 2: Controllability of bending technique: measured separation between points a and b in SEM for hexapod InAs. (a) 237 nm; (b) 322 nm; (c) 413 nm; (d) 500 nm; (e) 650 nm; (f) 850 nm; (g) 970 nm. The nanowires here are approximately 40 nm in diameter and 2.5–3 μm in length.

the upper parts of the nanowires are exposed, and the upper surface of the PMMA curves in relation to the nanowires, forming a meniscus (much like the upper surface of water in a test tube). The capillary action of the curved PMMA on the nanowire causes the nanowires to bend. Essentially, the nanowires bend as a result of a competition between intranowire elasticity and internanowire adhesion forces. The surface tension at the liquid-nanowire-air interface, γ , must be large enough to overcome the inherent rigidity of the nanowire [9]. We further observed that nanowires can be bent without the need for a spin step. A meniscus can also be formed by a drying or evaporative process, such as when the PMMA is removed by acetone and the sample then blown dry, instead of relying on spinning the liquid [10].

Nanowires have a bending stiffness which depends roughly on E^*r^4 , where E is the Young's modulus and r the radius of the nanowire. Here we assume that one end of the nanowire is clamped to the substrate, and the forces in play occur where the meniscus is formed [10, 11]. The maximum adhesive torques occur when the meniscus is at the top of the

nanowire (or at the beginning of the evaporative process). The force required to bend the nanowires then goes as $F_{\text{bend}} \sim d^*E^*r^4/L^3$, where d is the internanowire distance and L the length of the nanowire. For InAs nanowires, Young's modulus is ~ 70 GPa, which is slightly lower than the bulk theoretical value of 97 GPa [12]. For 500 nm nanowire separation, lengths of about 2 μm and 40 nm radius, bending forces are in the tens of nN range. The critical factor determining whether the nanowire bends or not, as seen when comparing the situations in Figures 1(a) or 1(b)–1(d), is the length of the nanowire. We can estimate a critical length, $L_C \sim (E^*d/\gamma)^{1/3}r \sim 4 \mu\text{m}$, for 500 nm nanowire separation, 40 nm radius, and PMMA-air surface tension $\gamma = 33$ mN/m [13]. Nanowires longer than the critical length will bend, while those shorter will remain upright. This estimate is in the ballpark of what is experimentally observed—2 μm length or longer InAs nanowires are needed for the bending to be possible for 40 nm or larger diameter nanowires. This model is simple and works but is far from complete, as we have ignored the contributions from electrostatic repulsive

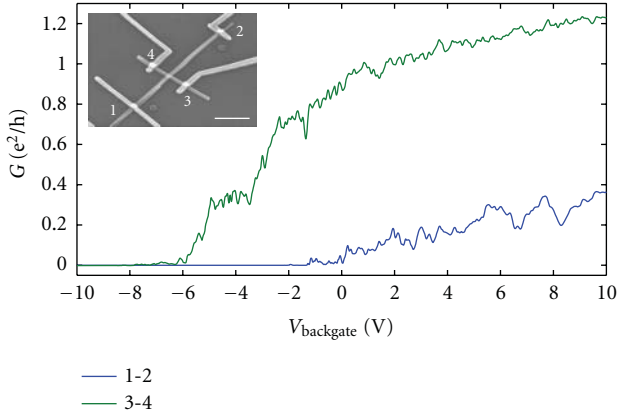


FIGURE 3: Current versus backgate voltage for individual nanowires. AC voltage is applied on electrode 1(3) with the resulting current measured out of 2(4) for the blue (green) curve, which corresponds to measuring the linear conductance of the top (bottom) nanowire. While measuring 1-2, the contact to 3-4 is left floating (and vice versa). Inset is a SEM image of the device with scale bar of 1 μm . These traces were measured at He3 cryostat base temperature of 300 mK.

forces from charge buildup on the nanowires [11]. We also have ignored the fact that for InAs nanowires grown in the CBE with the diameters discussed here, the crystal structure tends towards Wurtzite [14]. In this case, it is better to approximate the nanowire shape as hexagonal and not circular. The key point though is that longer nanowires can better bend to accommodate the attractive capillary force. Once the nanowires come into contact, they likely remain in contact due to short-range van der Waal's forces [15].

To demonstrate the controllability of this process, Figure 2 shows hexapod arrangements with the spacing between adjacent nanowires varied from ~ 200 nm to 1 μm . The individual nanowires have diameters around 40 nm. In all cases, bending and connecting of nanowires is possible. The images show nanowires from the same substrate. Nanowires on a separate substrate during the same growth also exhibit the same behavior.

To realize functional devices with these structures, it is important to know the nature of the junction between two nanowires joined in such a way. In particular, a native oxide forms on the surface of the InAs nanowires once exposed to air. Crossed nanowires effectively would form a semiconductor-oxide-semiconductor junction. To understand the transport characteristics through such a contact, we prepared nanowire junctions with metal contact electrodes as shown in the inset of Figure 3. Here, the nanowire contacted with electrodes 3 and 4 lies flat on the substrate surface (bottom nanowire). The nanowire, connected through electrodes 1-2, lies on top of this nanowire. From the linear conductance, Figure 3, it is evident that the two nanowires conduct, though the behavior is quite different. Conductance through the nanowire contacted by electrodes 1-2, the top nanowire, is ~ 3 times lower than that in the bottom nanowire. This factor of 3 is about the difference in lengths of the contacted region for the bottom and top nanowires.

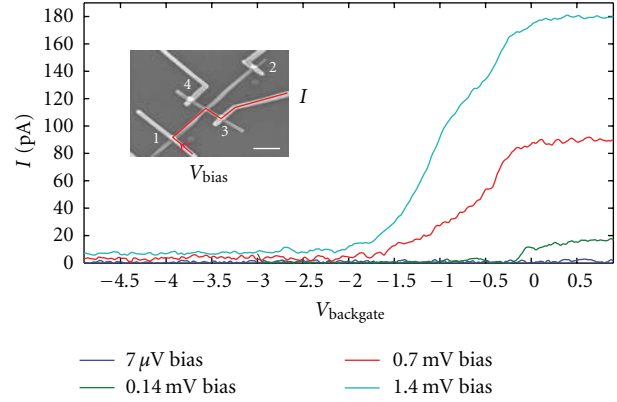


FIGURE 4: Current versus backgate voltage through the cross junction, with different bias voltage applied on electrode 1. The frequency used was 17.3 Hz. The current is measured from electrode 3 (current path is indicated in red in inset figure of device, which has scale bar of 1 μm), and contacts 2 and 4 are floating. Traces were measured at 300 mK.

However, the pinchoff voltage, V_{pinch} , which is where the nanowire is completely shut and no further current flows, is also at more negative voltage for the bottom nanowire. The pinchoff voltage is related to the density of carriers in the nanowire, and comparing the pinchoff voltages of the top and bottom nanowires reveals that the charge density of the bottom nanowire is larger, requiring more negative gate voltages to fully drive away all electronic charge. This suggests that there may be a kink or bend in the top nanowire right at the junction, which may affect the charge density. Surprisingly, the pinchoff voltage shifts to more positive voltage at higher temperature. This is unusual, as the pinchoff voltage tends to shift more negative with increasing temperature. It is possible that the junction geometry and the floating voltage on the other nanowire during the conductance measurement may play a role. Further studies with nanowire contact regions with nearly equal length to better understand the effect of the bend are in progress.

An alternating electrical current (AC) can be driven through the junction as seen in Figure 4. On the other hand, for up to ± 5 V DC bias, no DC current passes through, which points to the capacitive nature of the junction. Applying a backgate voltage tunes the allowed current through the crossed junction. When both nanowires are shut at $V_{\text{backgate}} < -6$ V, see Figure 3, the junction is “off.” At gate voltages greater than 0 V, both nanowires are open, putting the junction in an “on” state.

The capacitive nature of the junction also suggests that one nanowire could be used to gate the other. In Figure 5 we demonstrate that this is possible, by applying a voltage, V_{nw} , to the top nanowire, which then modulates the amount of current in the bottom nanowire, see Figure 5 right inset for a schematic. The backgate voltage is set to 1.9 V such that both nanowires are slightly open. The arrow in inset of Figure 5 shows the voltage the bottom nanowire is set to. Pushing $V_{\text{nw}} > 2$ V enhances the amount of current through the bot-

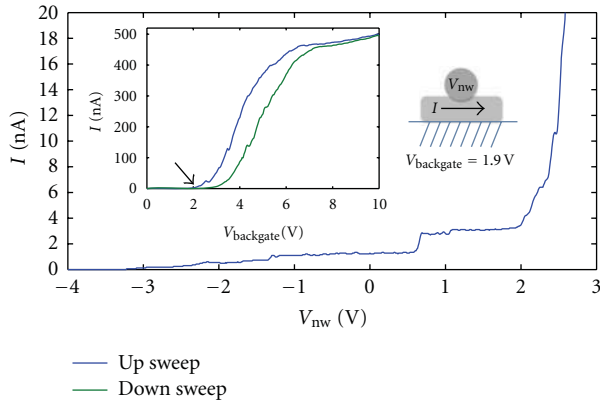


FIGURE 5: Top nanowire as gate for field effect control of bottom nanowire. Voltage, V_{nw} , is applied to electrodes 1 and 2 simultaneously. A bias voltage of 0.65 V on electrode 3 drives the bottom nanowire. Left inset shows the linear conductance of the bottom nanowire at this bias, with arrow pointing to the voltage the backgate is set in the main image measurement. Right inset is a profile view schematic of the setup. The field effect from the top nanowire and backgate modulate the current in the bottom nanowire. These measurements were performed at 4 K.

tom nanowire, while going to < -3 V shuts the conducting channel beneath the top nanowire gate. The diameter of the top nanowire effectively determines the conducting channel length, and it would be interesting to investigate whether smaller diameter nanowires gate as effectively.

4. Conclusions

In conclusion, we have demonstrated a versatile and simple technique to bend and connect vertically free-standing nanowires and have separately characterized the transport properties of junctions formed by crossing one nanowire on top of another. By controlling the internanowire spacing with lithography and undergoing a rinse procedure, nanowire doublet, tetrapod, and hexapod assemblies can be formed. A key factor for allowing the nanowires to meet is to grow wires longer than a critical length so that capillary forces arising from the rinse procedure can overcome the nanowire's inherent stiffness. Separately, as the nanowires have a native oxide, we have determined that junctions of two crossed nanowires would be capacitive in nature. A nanowire was then used to field effect control another nanowire in this crossed junction geometry. This points to the potential to use an all-nanowire circuit, as both channel and gate, in nanoelectronic devices.

Acknowledgments

The authors acknowledge support from nmC@LU, the Swedish Research Council, the Strategic Foundation, and Knut and Alice Wallenberg Foundation.

References

- [1] K. A. Dick, K. Deppert, M. W. Larsson et al., "Synthesis of branched "nanotrees" by controlled seeding of multiple branching events," *Nature Materials*, vol. 3, no. 6, pp. 380–384, 2004.
- [2] K. A. Dick, K. Deppert, L. S. Karlsson, W. Seifert, R. Wellenberg, and L. Samuelson, "Position-controlled interconnected InAs nanowire networks," *Nano Letters*, vol. 6, no. 12, pp. 2842–2847, 2006.
- [3] D. B. Suyatin, J. Sun, A. Fuhrer et al., "Electrical properties of self-assembled branched inas nanowire junctions," *Nano Letters*, vol. 8, no. 4, pp. 1100–1104, 2008.
- [4] Y. Cui, U. Banin, M. T. Bjork, and A. P. Alivisatos, "Electrical transport through a single nanoscale semiconductor branch point," *Nano Letters*, vol. 5, no. 7, pp. 1519–1523, 2005.
- [5] A. I. Persson, M. W. Larsson, S. Stenstrom, B. J. Ohlsson, L. Samuelson, and L. R. Wallenberg, "Solid-phase diffusion mechanism for GaAs nanowire growth," *Nature Materials*, vol. 3, no. 10, pp. 677–681, 2004.
- [6] L. E. Jensen, M. T. Bjork, S. Jeppesen, A. I. Persson, B. J. Ohlsson, and L. Samuelson, "Role of surface diffusion in chemical beam epitaxy of InAs nanowires," *Nano Letters*, vol. 4, no. 10, pp. 1961–1964, 2004.
- [7] C. Thelander, M. T. Bjork, M. W. Larsson, A. E. Hansen, L. R. Wallenberg, and L. Samuelson, "Electron transport in InAs nanowires and heterostructure nanowire devices," *Solid State Communications*, vol. 131, no. 9–10, pp. 573–579, 2004.
- [8] D. B. Suyatin, C. Thelander, M. T. Bjork, I. Maximov, and L. Samuelson, "Sulfur passivation for ohmic contact formation to InAs nanowires," *Nanotechnology*, vol. 18, no. 10, Article ID 105307, 2007.
- [9] P. A. Kralchevsky, V. N. Paunov, N. D. Denkov, I. B. Ivanov, and K. Nagayama, "Energetical and force approaches to the capillary interactions between particles attached to a liquid-fluid interface," *Journal of Colloid And Interface Science*, vol. 155, no. 2, pp. 420–437, 1993.
- [10] B. Pokroy, S. H. Kang, L. Mahadevan, and J. Aizenberg, "Self-organization of a mesoscale bristle into ordered, hierarchical helical assemblies," *Science*, vol. 323, no. 5911, pp. 237–240, 2009.
- [11] J. J. Hill, K. Haller, B. Gelfand, and K. J. Ziegler, "Eliminating capillary coalescence of nanowire arrays with applied electric fields," *ACS Applied Materials & Interfaces*, vol. 2, no. 7, pp. 1992–1998, 2010.
- [12] M. Lexholm, I. Karlsson, F. Boxberg, and D. Hessman, "Optical determination of young's modulus of InAs nanowires," *Applied Physics Letters*, vol. 95, no. 11, Article ID 113103, 2009.
- [13] K. Kostourou, D. Peschka, A. Munch, B. Wagner, S. Herminghaus, and R. Seemann, "Interface morphologies in liquid/liquid dewetting," *Chemical Engineering and Processing*, vol. 50, no. 5–6, pp. 531–536, 2011.
- [14] P. Caroff, K. A. Dick, J. Johansson, M. E. Messing, K. Deppert, and L. Samuelson, "Controlled polytypic and twin-plane superlattices in III-V nanowires," *Nature Nanotechnology*, vol. 4, no. 1, pp. 50–55, 2009.
- [15] K. J. Ziegler, D. M. Lyons, J. D. Holmes et al., "Bistable nanoelectromechanical devices," *Applied Physics Letters*, vol. 84, no. 20, pp. 4074–4076, 2004.

Research Article

Surface Effects on the Vibration and Buckling of Double-Nanobeam-Systems

Dong-Hui Wang and Gang-Feng Wang

Department of Engineering Mechanics, SVL, Xi'an Jiaotong University, Xi'an 710049, China

Correspondence should be addressed to Gang-Feng Wang, wanggf@mail.xjtu.edu.cn

Received 13 June 2011; Accepted 18 August 2011

Academic Editor: Raymond Whitby

Copyright © 2011 D.-H. Wang and G.-F. Wang. This is an open access article distributed under the Creative Commons Attribution License, which permits unrestricted use, distribution, and reproduction in any medium, provided the original work is properly cited.

Surface effects on the transverse vibration and axial buckling of double-nanobeam-system (DNBS) are examined based on a refined Euler-Bernoulli beam model. For three typical deformation modes of DNBS, we derive the natural frequency and critical axial load accounting for both surface elasticity and residual surface tension, respectively. It is found that surface effects get quite important when the cross-sectional size of beams shrinks to nanometers. No matter for vibration or axial buckling, surface effects are just the same in three deformation modes and usually enhance the natural frequency and critical load. However, the interaction between beams is clearly distinct in different deformation modes. This study might be helpful for the design of nano-optomechanical systems and nanoelectromechanical systems.

1. Introduction

Nanowires hold a wide variety of potential applications, such as sensors, actuators, transistors, probes, and resonators in nanoelectromechanical systems (NEMSs) [1]. In the design of nanowire-based components, it is of great importance to acquire the mechanical behaviors of nanowires accurately. Owing to the increasing ratio of surface area to volume in nanostructured components, the influence of surfaces gets important in their mechanical performance. To account for surface energy in solids, Gurtin et al. [2] established the surface elasticity theory, and recently its applications in nanosized structural element agree reasonably well with atomistic simulations and experimental measurements [3–6]. For example, Miller and Shenoy [3] investigated the size-dependent elastic properties of nanoscale beams and plates by both surface elasticity and atomic simulation. Ru [4] explained the difference and essence of various versions of Gurtin's surface elastic theory. A core-shell model was developed by Chen et al. [5] to explain the size-dependent Young's modulus of ZnO nanowires. Through Laplace-Young equation, Wang and Feng [7, 8] addressed both the impacts of residual surface stress and surface elasticity on the vibration and buckling of nanobeams. He and Lilley

[9] analyzed the static bending of nanowires, and explained its size-dependent elastic modulus. Using this model, Wang [10] considered the transverse vibration of fluid-conveying nanotube, Fu et al. [11] studied the nonlinear static and dynamic behaviors of nanobeams, and Assadi and Farshi [12] investigated the size-dependent stability and self-stability of circular nanoplates.

Most of above analyses addressed surface effects on single nanowire. Recently, the double-nanobeam-system (DNBS) has been utilized in nano-optomechanical systems [13–18]. The DNBS can be modeled by two one-dimensional nanobeams connected by coupling medium (i.e., van der Waals force, electrostatic force, capillary force, or Casimir force). Frank et al. [14] used electrostatic forces to tune the reconfigurable filters based on two coupled nanobeams model. Karabalin et al. [18] studied the nonlinear dynamics of two elastically coupled nanomechanical resonators and demonstrated that one oscillator could be modified by driving the second oscillator.

In the present paper, we will analyze surface effects on the transverse vibration and axial buckling of DNBS. Our solutions would provide more accurate predictions on the mechanical properties of DNBS and a more reliable

mechanical model for the design of coupled photonic crystal nanobeams [16].

2. Surface Effects on Beam Deformation

The creation of a free surface in a solid leads to excess free energy, which is referred as surface energy, thereby the increase in surface area during deformation will require external work. In addition, the atoms or molecules near a free surface experience a different local environment than that in the interior of the material. As a consequence, the energy density, atom density, and other physical properties in the surface layer will be distinct from those in the bulk.

Surface effects on the mechanical behavior of nanosized elements and nanomaterials can be examined by considering surface energy and/or surface stresses. According to Gibbs [19] and Cammarata [20], the surface stress tensor $\sigma_{\alpha\beta}^s$ is related to the surface energy density γ through the surface strain tensor $\varepsilon_{\alpha\beta}^s$ by

$$\sigma_{\alpha\beta}^s = \gamma \delta_{\alpha\beta} + \frac{\partial \gamma}{\partial \varepsilon_{\alpha\beta}^s}. \quad (1)$$

For the deformation of microbeam, only surface stress and surface strain along the longitude direction are of importance, and the one-dimensional and linear form of (1) is

$$\sigma^s = \tau^0 + E^s \varepsilon^s, \quad (2)$$

where $\tau^0 = \gamma + \partial\gamma/\partial\varepsilon^s|_{\varepsilon^s=0}$ is the residual surface stress when the bulk is under unstrained and E^s is the surface Young's modulus and can be determined either by atomic simulations or experimental measurements [3, 6]. The ratio of surface energy, surface stress, and surface modulus to the bulk elastic modulus is usually on the order of nanometers. For macroscopic structures, the influence of surface effects can be neglected. However, for nanosized structural elements, the contribution of surface effects becomes quite important and should be accounted for.

According to Laplace-Young equation [7, 9], the residual surface stress induces a distributed normal pressure $q(x)$ spanning the beam (as shown in Figure 1(a)), which is given by

$$q(x) = H \frac{d^2 w(x)}{dx^2}, \quad (3)$$

where $w(x)$ is deflection at the position x . H is a constant related to the residual surface stress and the cross-sectional shape. For a rectangular cross section with width b and height h or a circular cross section with diameter D as shown in Figures 1(b) and 1(c), respectively, one has [7, 9]

$$H = \begin{cases} 2\tau^0 b & (\text{rectangular}), \\ 2\tau^0 D & (\text{circular}). \end{cases} \quad (4)$$

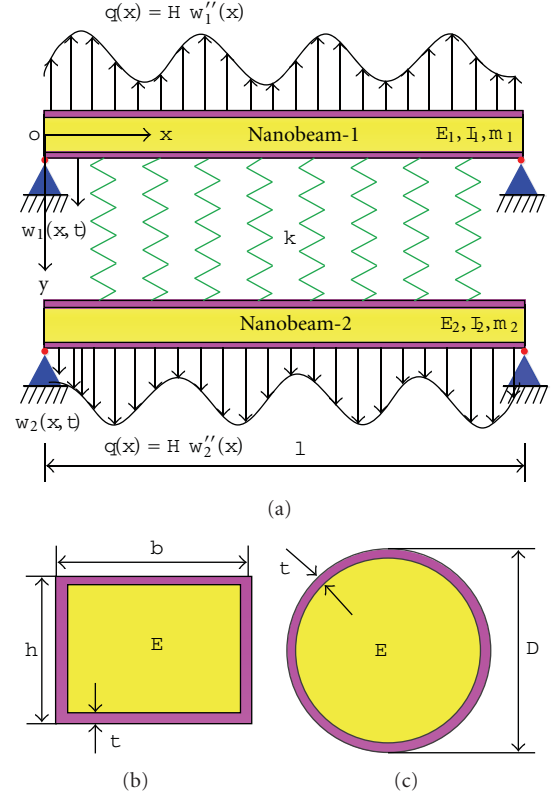


FIGURE 1: (a) A double-nanobeam-system, (b) a rectangular cross section with a surface layer, and (c) a circular cross section with a surface layer.

The influence of the second term in (2) can be accounted for by the effective flexural rigidity $(EI)^*$ [7, 9]

$$(EI)^* = \begin{cases} \frac{1}{12} E b h^3 + \frac{1}{2} E^s b h^2 + \frac{1}{6} E^s h^3 & (\text{rectangular}), \\ \frac{\pi}{64} E D^4 + \frac{\pi}{8} E^s D^3 & (\text{circular}), \end{cases} \quad (5)$$

where E is the Young's modulus of the bulk of beam. In what follows, we will consider the vibration and buckling of DNBS by this surface model.

3. Vibration of Double-Nanobeam-System

Consider a double-nanobeam-system as illustrated in Figure 1(a). Two nanobeams with identical length l are connected by distributed springs with stiffness k . In physical nature, the springs could represent the effects of electrostatic force, nano-optomechanical-induced force, van der Waals force, or elastic medium, which can be adjusted by the electrical potential difference or the distance between two nanobeams [14]. Denote the elastic modulus, mass density, cross-section area, and second moment of inertia of the i th beam by E_i , ρ_i , A_i , and I_i ($i = 1, 2$), respectively. Since the DNBS usually has a large length/depth ratio ($l/D \gg 10$) [13], it is reasonable to neglect the effect of shear deformation and

rotary inertia, and adopt the Euler-Bernoulli beam theory to predict its mechanical behaviors.

Denote the deflections of two nanobeams by $w_1(x, t)$ and $w_2(x, t)$, respectively. Account for surface effects in Section 2, the differential equations of the free vibration of DNBS can be obtained as

for nano-beam-1,

$$(E_1 I_1)^* \frac{\partial^4 w_1}{\partial x^4} - H \frac{\partial^2 w_1}{\partial x^2} + k(w_1 - w_2) + \rho_1 A_1 \frac{\partial^2 w_1}{\partial t^2} = 0, \quad (6)$$

and for nano-beam-2,

$$(E_2 I_2)^* \frac{\partial^4 w_2}{\partial x^4} - H \frac{\partial^2 w_2}{\partial x^2} + k(w_2 - w_1) + \rho_2 A_2 \frac{\partial^2 w_2}{\partial t^2} = 0. \quad (7)$$

In practical applications, the two nanobeams in DNBS are usually identical; therefore, in present paper we assume

$$E_1 I_1 = E_2 I_2 = EI, \quad (E_1 I_1)^* = (E_2 I_2)^* = (EI)^*, \quad (8)$$

$$\rho_1 A_1 = \rho_2 A_2 = m.$$

It should be noted that more general cases can also be achieved but in a more complicated form [21].

For convenience in analysis, we introduce the relative movement of two beams as [22]

$$w(x, t) = w_1(x, t) - w_2(x, t). \quad (9)$$

Then

$$w_1(x, t) = w(x, t) + w_2(x, t). \quad (10)$$

Subtracting (6) from (7) gives

$$(EI)^* \frac{\partial^4 w}{\partial x^4} - H \frac{\partial^2 w}{\partial x^2} + 2kw + m \frac{\partial^2 w}{\partial t^2} = 0, \quad (11)$$

$$(EI)^* \frac{\partial^4 w_2}{\partial x^4} - H \frac{\partial^2 w_2}{\partial x^2} + m \frac{\partial^2 w_2}{\partial t^2} = kw. \quad (12)$$

When surface effects are ignored ($H = E^s = 0$) and single beam ($k = 0$) is considered, (12) reverts to the vibration equations of a single Euler beam.

In order to display the surface effects, we consider a simple case, in which both beams are simply supported at their ends. The boundary conditions are given by

$$w_1(0, t) = w_2(0, t) = 0, \quad w_1(l, t) = w_2(l, t) = 0, \quad (13)$$

$$\frac{\partial^2 w_1(0, t)}{\partial x^2} = \frac{\partial^2 w_2(0, t)}{\partial x^2} = 0, \quad (14)$$

$$\frac{\partial^2 w_1(l, t)}{\partial x^2} = \frac{\partial^2 w_2(l, t)}{\partial x^2} = 0.$$

Thus, the boundary conditions associated with (11) become

$$w(0, t) = 0, \quad w(l, t) = 0, \quad (15)$$

$$\frac{\partial^2 w(0, t)}{\partial x^2} = 0, \quad \frac{\partial^2 w(l, t)}{\partial x^2} = 0. \quad (16)$$

Assuming that the relative motion $w(x, t)$ is one of its natural modes of vibration of DNBS, the boundary condition (16) can be satisfied by the following vibration displacement:

$$w^{(n)}(x, t) = \sin\left(\frac{n\pi x}{l}\right) [C \cos(p_n t) + D \sin(p_n t)], \quad n = 1, 2, 3, \dots, \quad (17)$$

where p_n is the natural frequency of n th mode.

To discuss the vibration and buckling of DNBS, three typical cases including out-of-phase sequence, in-phase sequence, and one-beam being stationary as shown in Figures 2(a), 2(b), and 2(c), are considered, respectively.

3.1. Out-of-Phase Vibration. In this case, both nanobeams vibrate out-of-phase, and $w_1(x, t) - w_2(x, t) \neq 0$, as shown in Figure 2(a). Substituting (17) into (11), one can obtain the natural frequency of DNBS in the out-of-phase vibration as

$$p_n = \sqrt{\frac{n^4 \pi^4 (EI)^*}{l^4} + \frac{n^2 \pi^2 H}{l^2} + \frac{2k}{m}}, \quad n = 1, 2, 3, \dots \quad (18)$$

When surface effects are neglected ($H = E^s = 0$), the natural frequency reduces to the classical double Euler beam solution P_n^0 [22],

$$P_n^0 = \sqrt{\frac{n^4 \pi^4 EI}{l^4} + \frac{2k}{m}}, \quad n = 1, 2, 3, \dots \quad (19)$$

3.2. In-Phase Vibration. In the case of in-phase vibration as shown in Figure 2(b), two nanobeams vibrate synchronously, thus the relative displacement between them disappears ($w_1(x, t) - w_2(x, t) = 0$). Therefore, any one of the two beams could represent the vibration of the coupled vibration system. Following a similar procedure as that in out-of-phase vibration, one can determine the frequency as

$$p_n = \sqrt{\frac{n^4 \pi^4 (EI)^*}{l^4} + \frac{n^2 \pi^2 H}{l^2}}, \quad n = 1, 2, 3, \dots \quad (20)$$

It is seen that the interaction between nanobeams does not affect the natural frequency of DNBS for in-phase vibration, since two beams vibrate synchronously. For this vibrating mode, the vibration frequency is just as the same as that of the single Euler beam with surface effects [7].

3.3. One Nanobeam Being Stationary. Another vibrating mode of interest is one nanobeam being stationary (i.e., $w_2(x, t) = 0$), as shown in Figure 2(c). In this case, the vibration equation (11) reduces to

$$(EI)^* \frac{\partial^4 w}{\partial x^4} - H \frac{\partial^2 w}{\partial x^2} + kw + m \frac{\partial^2 w}{\partial t^2} = 0. \quad (21)$$

In this context, the DNBS behaves as if nanobeam-1 is supported on an elastic medium. Similarly, one obtains the natural frequency of beam as

$$p_n = \sqrt{\frac{n^4 \pi^4 (EI)^*}{l^4} + \frac{n^2 \pi^2 H}{l^2} + \frac{k}{m}}, \quad n = 1, 2, 3, \dots \quad (22)$$

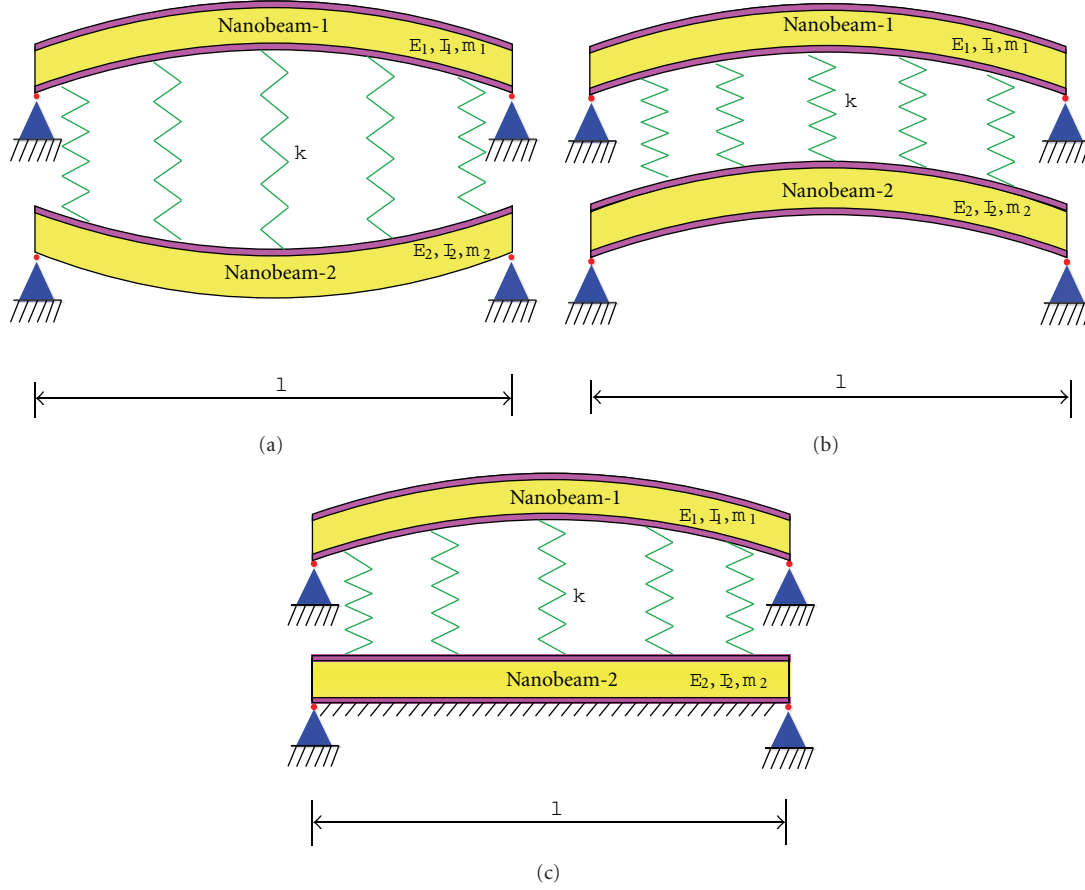


FIGURE 2: Three different deformation modes of DNBS: (a) out-of-phase deformation, (b) in-phase deformation, and (c) one beam being stationary.

Comparing (18), (20), and (22), it is noticed that surface effects have the same contribution to these three vibration modes, but the influence of beam interaction is distinct in different vibration modes. The interaction between beams tends to increase the natural frequency for vibration modes other than in-phase vibration.

3.4. Example and Discussion. To illustrate surface effects on the vibration of DNBS quantitatively, we consider a DNBS consisting of two silver nanowires with circular cross section. The material constants of nanowires are $E = 76$ GPa, $\nu = 0.3$, and the surface properties $\tau^0 = 0.89$ N/m and $E^s = 1.22$ N/m [9]. To examine the influence of beam interaction, the spring stiffness has been taken from 2×10^4 N/m² to 2×10^7 N/m² [23]. We also take a length/diameter aspect ratio as $l/D = 20$ in the following analysis.

Since surface effects are just the same in three vibration modes, here we consider surface effects and beam interaction on only the out-of-phase vibration. Figure 3 displays the variation of normalized first-order natural frequency P_1/P_1^0 with respect to the wire diameter. It is seen that when the diameter reduces to nanometers, the vibration frequency depends on the absolute size of nanobeam, which is clearly distinct from the prediction of conventional elasticity. As the diameter

decreases, the contribution of surface effects gets important and tends to increase the natural frequency. It is also noticed that surface effects are more prominent for a small spring constant corresponding to a weak beam interaction. With the spring constant increasing, the influence of surface effects becomes relatively unimportant compared to the beam interaction. The higher-order natural frequency of DNBS is also plotted in Figure 4, in which the spring stiffness k is taken as 2×10^4 N/m². It is found that surface effects are more significant for low-order natural frequency and declines dramatically for high-order frequency.

4. Axial Buckling of Double-Nanobeam-System

It is also of interest to consider the axial buckling of DNBS. Accounting for surface effects stated in Section 2, the buckling equations of two nanobeams subjected to axial compressive forces N_1 and N_2 can be expressed as for beam one,

$$(E_1 I_1)^* \frac{\partial^4 w_1}{\partial x^4} + (N_1 - H) \frac{\partial^2 w_1}{\partial x^2} + k(w_1 - w_2) = 0, \quad (23)$$

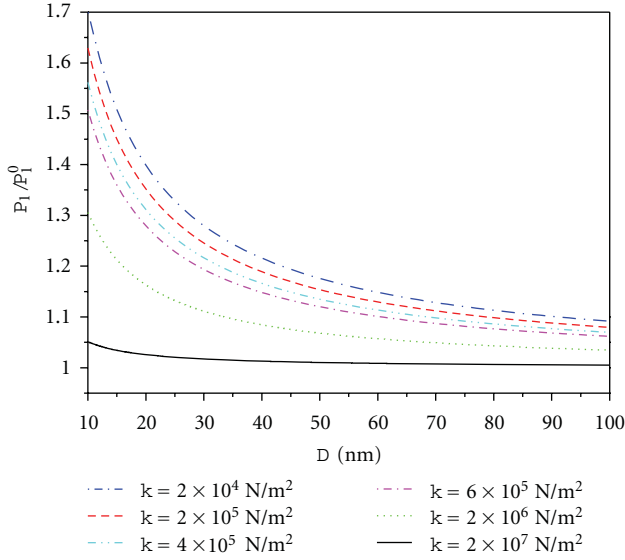


FIGURE 3: Normalized first-order natural frequency of DNBS versus the wire diameter.

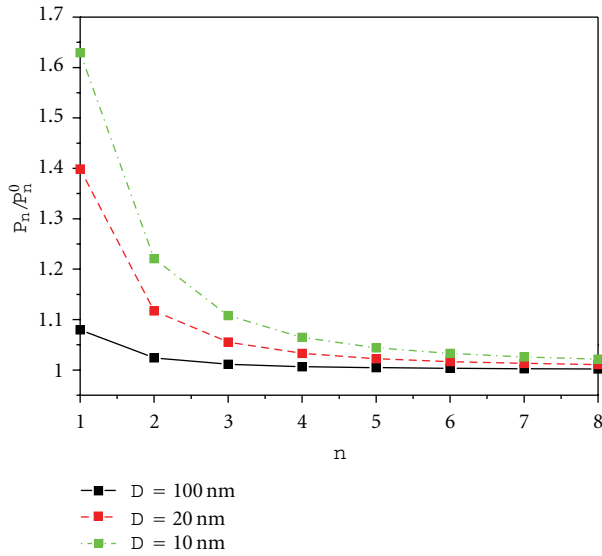


FIGURE 4: Normalized natural frequency of different modes for out-of-phase vibration.

and for beam two,

$$(E_2 I_2)^* \frac{\partial^4 w_2}{\partial x^4} + (N_2 - H) \frac{\partial^2 w_2}{\partial x^2} + k(w_2 - w_1) = 0. \quad (24)$$

Assume the two beams are identical for simplification and $N_1 = N_2$, we get

$$(EI)^* \frac{\partial^4 w}{\partial x^4} + (N - H) \frac{\partial^2 w}{\partial x^2} + 2kw = 0, \quad (25)$$

$$(EI)^* \frac{\partial^4 w_2}{\partial x^4} + (N - H) \frac{\partial^2 w_2}{\partial x^2} = kw. \quad (26)$$

Similar to those of vibration modes, the buckling of DNBS can also be categorized into the out-of-phase buckling, in-phase buckling, and buckling with one beam being stationary. We also consider only the boundary conditions for ends of two beams being simply supported, as described by (16). The following buckling mode satisfies the boundary condition

$$w = W \sin\left(\frac{n\pi x}{l}\right). \quad (27)$$

For out-of-phase buckling, substitution of (27) into (25) yields

$$(EI)^* \left(\frac{n\pi}{l}\right)^4 + (H - N) \left(\frac{n\pi}{l}\right)^2 + 2k = 0. \quad (28)$$

Consequently, the critical buckling load is derived as

$$N_{cr} = \frac{n^2 \pi^2 (EI)^*}{l^2} + \frac{2kl^2}{n^2 \pi^2} + H, \quad n = 1, 2, 3, \dots \quad (29)$$

For the case without surface effects ($H = E^s = 0$), the critical load reduces to the classical solution

$$N_{cr}^0 = \frac{n^2 \pi^2 EI}{l^2} + \frac{2kl^2}{n^2 \pi^2}, \quad n = 1, 2, 3, \dots \quad (30)$$

Similarly, the critical load of buckling for in-phase buckling can be readily given as

$$N_{cr} = \frac{n^2 \pi^2 (EI)^*}{l^2} + H, \quad n = 1, 2, 3, \dots \quad (31)$$

This coincides with the solution of axial buckling of a single nanowire [8].

Also, for the case of buckling with one beam being stationary, the critical load is expressed as

$$N_{cr} = \frac{n^2 \pi^2 (EI)^*}{l^2} + \frac{kl^2}{n^2 \pi^2} + H, \quad n = 1, 2, 3, \dots \quad (32)$$

For the axial buckling of DNBS, it is found again that the influence of surface effects is just the same in three buckling modes. For in-phase buckling, the beam interaction has no influence on the critical load, while for other buckling modes, the beam interaction will enhance the critical load of DNBS.

To demonstrate surface effects on the buckling of NDBS, we consider two circular silver nanowires with $E = 76$ GPa, $\nu = 0.3$, and surface properties $\tau^0 = 0.89$ Nm and $E^s = 1.22$ Nm [9]. The interaction between them is modeled by the coupling stiffness k varying from 2×10^4 N/m² to 2×10^7 N/m² [23]. For out-of-phase buckling, Figure 5 displays the critical compressive force N_{cr}/N_{cr}^0 with respect to the wire diameter. The normalized critical force of buckling exhibits a distinct dependence on the characteristic size of the nanowires, which is different from the conventional elasticity. The influence of surface effects become significant as the diameter decreases in the range of nanometers and usually raises the critical buckling load of DNBS. Moreover, surface effects are more prominent for weak beam interaction than for stiff interaction.

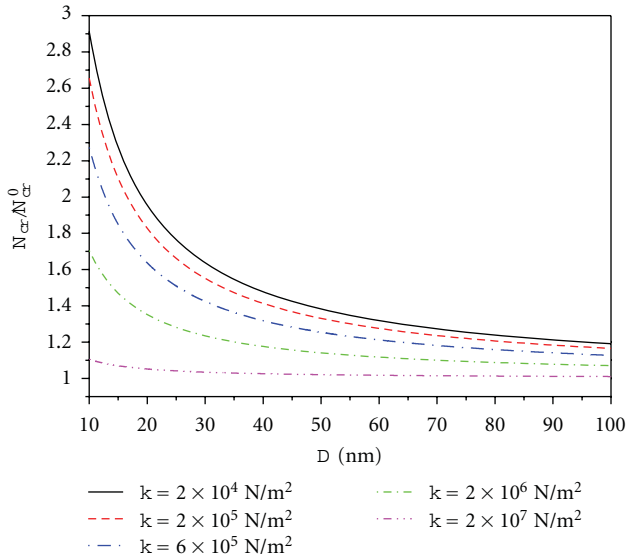


FIGURE 5: Normalized critical load of DNBS versus the nanowire diameter.

5. Conclusions

Based on a modified Euler-Bernoulli beam theory, we have analyzed surface effects on the transverse vibration and axial buckling of DNBS. The natural frequency and critical compression force are obtained analytically. The results show that both surface elasticity and residual surface tension affect the natural frequency and buckling load of DNBS when the cross section of nanowires shrinks to nanometers. Surface effects play the same impact in three deformation modes no matter for vibration or axial buckling and evidently enhance the natural frequency and critical load. In contrast, the influence of beam interaction is clearly distinct in different deformation modes. The present study might be helpful for the design of double-nano-beam-based nano-optomechanical systems and nanoelectromechanical systems.

Acknowledgments

The supports from the National Natural Science Foundation (Grant no. 11072186) and the NCET program and SRF for ROCS of MOE are acknowledged.

References

- [1] Y. Cui, Q. Wei, H. Park, and C. M. Lieber, "Nanowire nanosensors for highly sensitive and selective detection of biological and chemical species," *Science*, vol. 293, no. 5533, pp. 1289–1292, 2001.
- [2] M. E. Gurtin, J. Weissmüller, and F. Larché, "A general theory of curved deformable interfaces in solids at equilibrium," *Philosophical Magazine A*, vol. 78, no. 5, pp. 1093–1109, 1998.
- [3] R. E. Miller and V. B. Shenoy, "Size-dependent elastic properties of nanosized structural elements," *Nanotechnology*, vol. 11, no. 3, pp. 139–147, 2000.
- [4] C. Q. Ru, "Simple geometrical explanation of Gurtin-Murdoch model of surface elasticity with clarification of its related versions," *Science China*, vol. 53, no. 3, pp. 536–544, 2010.
- [5] C. Q. Chen, Y. Shi, Y. S. Zhang, J. Zhu, and Y. J. Yan, "Size dependence of Young's modulus in ZnO nanowires," *Physical Review Letters*, vol. 96, no. 7, Article ID 075505, pp. 1–4, 2006.
- [6] S. Cuenot, C. Frétiigny, S. Demoustier-Champagne, and B. Nysten, "Surface tension effect on the mechanical properties of nanomaterials measured by atomic force microscopy," *Physical Review B*, vol. 69, no. 16, Article ID 165410, 5 pages, 2004.
- [7] G.-F. Wang and X.-Q. Feng, "Effects of surface elasticity and residual surface tension on the natural frequency of microbeams," *Applied Physics Letters*, vol. 90, no. 23, Article ID 231904, 2007.
- [8] G.-F. Wang and X.-Q. Feng, "Surface effects on buckling of nanowires under uniaxial compression," *Applied Physics Letters*, vol. 94, no. 14, Article ID 141913, 2009.
- [9] J. He and C. M. Lilley, "Surface effect on the elastic behavior of static bending nanowires," *Nano Letters*, vol. 8, no. 7, pp. 1798–1802, 2008.
- [10] L. Wang, "Vibration analysis of fluid-conveying nanotubes with consideration of surface effects," *Physica E*, vol. 43, no. 1, pp. 437–439, 2010.
- [11] Y. Fu, J. Zhang, and Y. Jiang, "Influences of the surface energies on the nonlinear static and dynamic behaviors of nanobeams," *Physica E*, vol. 42, no. 9, pp. 2268–2273, 2010.
- [12] A. Assadi and B. Farshi, "Size dependent stability analysis of circular ultrathin films in elastic medium with consideration of surface energies," *Physica E*, vol. 43, no. 5, pp. 1111–1117, 2011.
- [13] M. Eichenfield, R. Camacho, J. Chan, K. J. Vahala, and O. Painter, "A picogram- and nanometre-scale photonic-crystal optomechanical cavity," *Nature*, vol. 459, no. 7246, pp. 550–555, 2009.
- [14] I. W. Frank, P. B. Deotare, M. W. McCutcheon, and M. Lončar, "Programmable photonic crystal nanobeam cavities," *Optics Express*, vol. 18, no. 8, pp. 8705–8712, 2010.
- [15] M. W. McCutcheon, P. B. Deotare, Y. Zhang, and M. Lončar, "High- Q transverse-electric/transverse-magnetic photonic crystal nanobeam cavities," *Applied Physics Letters*, vol. 98, no. 11, Article ID 111117, 3 pages, 2011.
- [16] P. B. Deotare, M. W. McCutcheon, I. W. Frank, M. Khan, and M. Lončar, "Coupled photonic crystal nanobeam cavities," *Applied Physics Letters*, vol. 95, no. 3, Article ID 031102, 3 pages, 2009.
- [17] Q. Lin, J. Rosenberg, D. Chang et al., "Coherent mixing of mechanical excitations in nano-optomechanical structures," *Nature Photonics*, vol. 4, no. 4, pp. 236–242, 2010.
- [18] R. B. Karabalin, M. C. Cross, and M. L. Roukes, "Nonlinear dynamics and chaos in two coupled nanomechanical resonators," *Physical Review B*, vol. 79, no. 16, Article ID 165309, 5 pages, 2009.
- [19] J. W. Gibbs, *The Scientific Papers of J. Willard Gibbs. Vol 1: Thermodynamics*, Longmans and Green, New York, NY, USA, 1993.
- [20] R. C. Cammarata, "Surface and interface stress effects in thin films," *Progress in Surface Science*, vol. 46, no. 1, pp. 1–38, 1994.
- [21] S. G. Kelly and S. Srinivas, "Free vibrations of elastically connected stretched beams," *Journal of Sound and Vibration*, vol. 326, no. 3–5, pp. 883–893, 2009.
- [22] H. V. Vu, A. M. Ordonez, and B. H. Karnopp, "Vibration of a double-beam system," *Journal of Sound and Vibration*, vol. 229, no. 4, pp. 807–822, 2000.

- [23] J. Zhu, C. Q. Ru, and A. Mioduchowski, "Instability of a large coupled microbeam array initialized at its two ends," *Journal of Adhesion*, vol. 83, no. 3, pp. 195–221, 2007.

Research Article

Effect of Applied Potential on the Formation of Self-Organized TiO₂ Nanotube Arrays and Its Photoelectrochemical Response

Chin Wei Lai and Srimala Sreekantan

School of Materials and Mineral Resources Engineering, Universiti Sains Malaysia Engineering Campus, Seberang Perai Selatan, Pulau Pinang, 14300 Nibong Tebal, Malaysia

Correspondence should be addressed to Srimala Sreekantan, srimala@eng.usm.my

Received 13 July 2011; Accepted 11 August 2011

Academic Editor: Renzhi Ma

Copyright © 2011 C. W. Lai and S. Sreekantan. This is an open access article distributed under the Creative Commons Attribution License, which permits unrestricted use, distribution, and reproduction in any medium, provided the original work is properly cited.

Self-organized TiO₂ nanotube arrays have been fabricated by anodization of Ti foil in an electrochemical bath consisting of 1 M of glycerol with 0.5 wt% of NH₄F. The effects of applied potential on the resulting nanotubes were illustrated. Among all of the applied potentials, 30 V resulted in the highest uniformity and aspect ratio TiO₂ nanotube arrays with the tube's length approximately 1 μm and pore's size of 85 nm. TiO₂ nanotube arrays were amorphous in as-anodized condition. The anatase phase was observed after annealing at 400°C in air atmosphere. The effect of crystallization and effective surface area of TiO₂ nanotube arrays in connection with the photoelectrochemical response was reported. Photoelectrochemical response under illumination was enhanced by using the annealed TiO₂ nanotube arrays which have larger effective surface area to promote more photoinduced electrons.

1. Introduction

Since titanium oxide (TiO₂) is a commercial product in the early twentieth century, it is believed to be the most promising photocatalyst, due to its great capacity for oxidation, wide band gap, nontoxicity, low-cost, widespread availability, and long term stability [1–5]. Due to its wide range of functions, TiO₂ photocatalyst can be applied to the field of environmental cleanup including deodorization, antibacterial protection, antifouling protection, water treatment, emission gas treatment, dye-sensitized solar cells, hydrogen generation by water photoelectrolysis, gas sensors, and so on [4–8]. These applications can be roughly divided into “environmental” and “energy” categories. In this context, simple anodization method has caught the attention of the scientific community because vertically oriented and highly ordered TiO₂ nanotube arrays can be produced via this method [2, 9–12].

Heterogeneous photocatalysis is a well-known process in which a combination of photochemistry and catalysis are operating together [5, 13]. It implies that both light and catalyst are necessary to bring out the chemical reaction. Upon absorption of photons with energy larger than the

band gap of TiO₂, electrons are excited from the valence band to the conduction band, creating electron-hole pairs [4, 13–15]. The valence band holes are powerful oxidants (+1 to +3.5 V versus NHE depending on the semiconductor and pH), while the conduction band electrons are good reductants (+0.5 to –1.5 V versus NHE). During photocatalytic hydrogen production, an essential photogeneration of electron-hole pairs is required. When photocatalysis is applied to perform water splitting process for hydrogen production, the reducing conduction band electrons become important as their role is to reduce protons to hydrogen molecules [14, 16–18].

The photocatalytic hydrogen production of TiO₂ is largely controlled by (i) the light absorption properties, (ii) reduction and oxidation rates on the surface by the electron and hole, and (iii) the electron-hole recombination rate [14, 19]. However, the main barriers of these activities are the rapid recombination of photogenerated electron-hole pairs as well as the backward reaction and the poor activation of TiO₂ by visible light [15, 20]. Shifting the threshold of its photoresponse into the visible region would definitely enhance its potential for solar energy conversion [14, 21].

In response to these problems, continuous efforts have been made to fabricate a highly efficient photocatalyst with a suitable architecture that could minimize the recombination of photogenerated electron-hole pairs. Therefore, in this paper, a detailed study has been performed to evaluate the morphology of the anodized Ti foil in different applied potential. The one-dimensional (1D) structure of nanotube arrays provides a high surface-to-volume ratio and excellent charge transfer properties if the precise design and control of the geometrical features are determined [21–24]. Such a mechanistic understanding is very important for the controlled growth of ordered TiO₂ nanotube structure that finds potential use in the development of viable hydrogen fuel cell for sustainable energy system.

2. Experimental

TiO₂ nanotube arrays were grown by anodic oxidation of titanium foils (4 cm × 1 cm) with 99.6% purity and 0.127 mm in thickness. Prior to anodization, the Ti foils were degreased by sonication in ethanol for 30 min. The foils were then rinsed in deionized water and dried with nitrogen stream. The anodization was performed in a two-electrode configuration bath with the Ti foil as the anode and the platinum rod as the counterelectrode. The electrolyte was homogenized via magnetic stirring. An experiment was done by adapting optimum condition for TiO₂ nanotubes formation, that is, anodization of Ti foil is performed at the feed rate of 0.1 V/sec, and the electrolyte is 0.5 wt% of NH₄F in 1 M of glycerol (85% glycerol and 15% water) for 30 minutes. The applied potential was varied from 10 to 50 V. The anodized Ti foils were cleaned using acetone and dried in nitrogen stream. After the cleaning and drying treatments, the as-anodized samples were annealed at 400°C for 2 hours in air atmosphere to convert to the TiO₂ anatase phase.

The morphology of the anodized Ti foils was viewed using a field emission scanning electron microscope (FESEM) Zeiss SUPRA 35 VP at a working distance of around 1 mm. In order to obtain the thickness of the anodic oxide formed, cross-sectional measurements were carried out on mechanically bent samples, where a partial liftoff of the anodic layer occurred. On top of that, the elemental analysis, that is, atomic percentage of the TiO₂, can be determined with EDX (energy dispersion X-ray) which is equipped in the FESEM. Phase determination of the anodic layer was determined by an X-ray diffraction (XRD) using Philips, PW 1729, operated at 45 kV and 40 mV.

The photoelectrochemical response of the samples were characterized using a three-electrode photoelectrochemical cell with TiO₂ nanotube arrays as the working photoelectrode, platinum rod as the counterelectrode, and saturated calomel electrode (SCE) was used as the reference electrode. 1 M KOH with 1 wt% of ethylene glycol solution was used as the electrolyte in this experiment. All of the three electrodes were connected to a potentiostat (μ Autolab III). A Xenon lamp with an intensity of 800 W/m² (Zolix LSP-X150) was used to produce a largely continuous and uniform spectrum, and 100% transmittance of the light was permitted by the quartz glass as the xenon lamp shined on the TiO₂ nanotube

arrays (photoanode). The Xenon lamp was switched on after the three electrodes were connected to the potentiostat. Then, a linear sweep potentiometry (LSP) was swept from –0.5 V to 1.0 V at a scan rate of 5 mV/s. During the voltage sweeping, the corresponding photocurrent was measured.

3. Results and Discussion

3.1. Surface Morphology of TiO₂ Nanotube Arrays. In this part of the experiment, the effect of applied potential on the morphology of the TiO₂ nanotube arrays is discussed. The formation of TiO₂ nanotube arrays in fluorinated electrolyte was the result of three simultaneously occurring processes: (1) field-assisted oxidation of Ti metal to form TiO₂, (2) field-assisted dissolution of Ti metal ions into electrolyte, and (3) chemical dissolution of Ti and TiO₂ in the presence of H⁺ and F[–] ions. In general, it can be concluded that the electrochemical condition is an important factor for the formation of well-aligned TiO₂ nanotube arrays [25, 26].

Figure 1 shows the FESEM images of surface morphology of the anodized Ti foils in electrolyte composed of 1 M of glycerol with 0.5 wt% of dissolved NH₄F for 30 minutes, and potential was varied from 10 V to 50 V. Insets are the cross-section morphology of the oxides. From these images, the appearance of the anodic oxides on the Ti foils was dependent on the applied potential in the fluorinated electrolyte. At low anodizing potential (10 V), pits started to form on the TiO₂ surface (Figure 1(a)). Upon increasing the potential to 20 V, 30 V, and 40 V, well-aligned TiO₂ nanotubes were observed (Figures 1(b)–1(d)). It is also apparent that the diameter of the pores increased from 50 nm to 110 nm when potential was raised from 20 V to 40 V. At 50 V, the intertubes' spacing was filled, and discrete nanotubes became more interconnected to form a nanoporous-like structure (Figure 1(e)). The average diameter, length, and surface area of the tube anodized at different applied potential are summarized in Table 1.

The diameter of the tubes was found to increase with the applied potential. The main reason may be attributed to the severe electric field dissolution which accelerates the formation of pits during the early stage of anodization. These pits were etched to form larger pore in higher potential. In addition, the increase in nanotube's length is attributed to the increased driving force for ionic species (H⁺, F[–], and O^{2–}) to transport through the barrier layer at the bottom of the nanotube under electric field, which results in faster movement of the Ti/TiO₂ interface into the Ti metal. This improves the pore deepening and results in longer nanotube length. With the increase of applied potential, the rate of the fluoride (F[–]) ions and the chemical dissolution at the barrier layer inside the nanotubes were increased, hence, allowing more oxygen (O^{2–}) to enter and oxidize the underlying Ti. This condition disrupts the self-ordering of nanotubular structure due to the imbalance reaction between the chemical dissolution, electric field dissolution, and oxidation process [7, 27, 28]. Besides, the anodic layer induces polarization of the Ti–O bond under higher applied potential and, hence, destroying the nanotubular structure. As a result, shorter

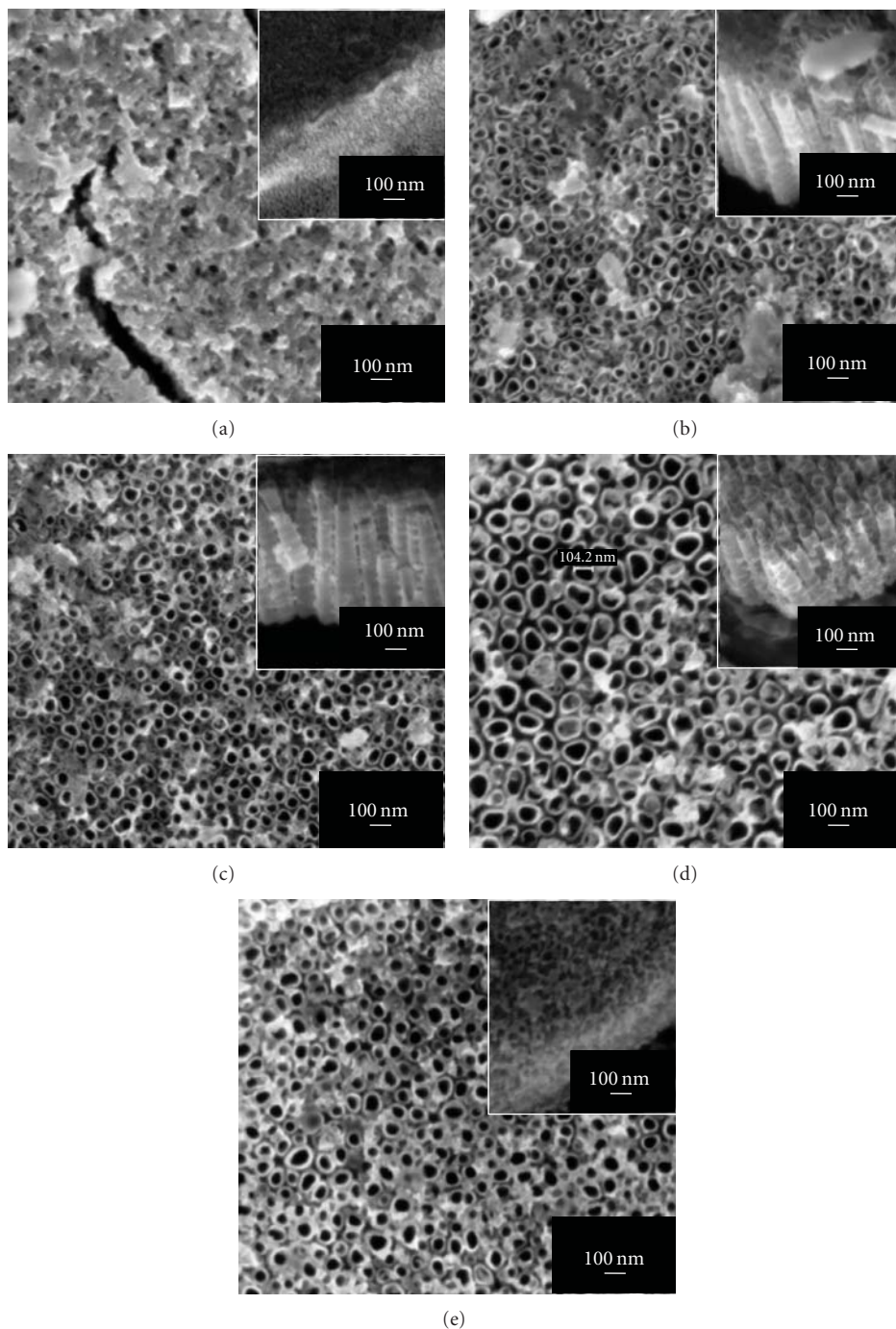


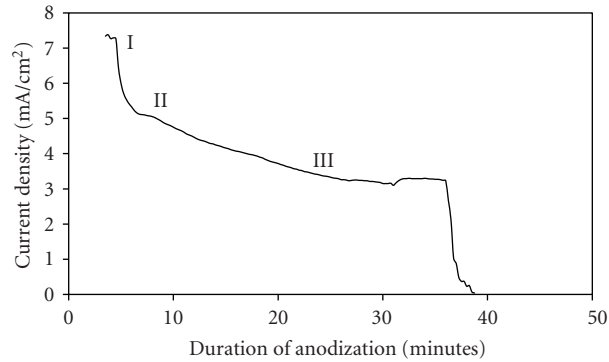
FIGURE 1: FESEM images of TiO_2 nanotube arrays fabricated at different applied potential in 1 M of glycerol electrolyte containing 0.5 wt% NH_4F for 30 minutes at (a) 10 V, (b) 20 V, (c) 30 V, (d) 40 V, and (e) 50 V. Insets are the cross-section morphology of the TiO_2 nanotube arrays.

length of irregular nanotubular structure was observed at higher applied potential. The dimensions and uniformity of the morphology of TiO_2 nanotube arrays were a function of applied potential in anodization process. Based on this study, 30 V was found to be the optimum potential for the formation of uniform circular nanotubes with lengths approaching $1 \mu\text{m}$.

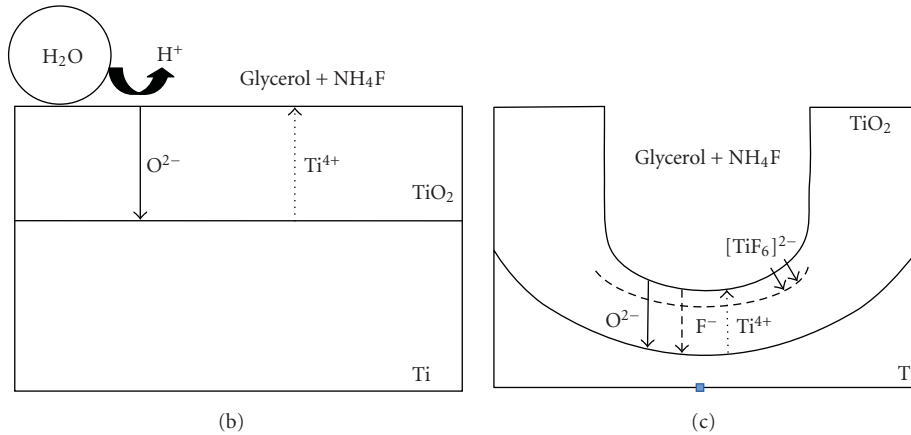
3.2. Formation Mechanism of TiO_2 Nanotube Arrays. In order to obtain the electrochemical information during the formation of TiO_2 nanotube arrays, a curve of current density versus time transient was plotted. Figure 2(a) shows the current density versus time curve recorded during anodization of Ti in 1 M of glycerol electrolyte containing 0.5 wt% NH_4F with a sweep rate of 0.1 V/s to 30 V for 30

TABLE 1: Dimension of the TiO₂ nanotube arrays anodized at different applied potential.

Potential (V)	Surface morphology	Length (nm)	Diameter (nm)	Average aspect ratio (L/D)
10	Nanoporous	275	—	—
20	Nonuniform nanotubes	750	Smaller tube = 50 Larger tube = 100	10
30	Uniform nanotubes	1000	~85	11.8
40	Nonuniform nanotubes	550	Smaller tube = 70 Larger tube = 110	6.1
50	Nonuniform nanotubes	250	Smaller tube = 40 Larger tube = 100	4.2



(a)

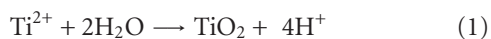


(b)

(c)

FIGURE 2: (a) Current density against time plot for anodized Ti foils at 30 V for 30 minutes in 1 M glycerol electrolyte containing 0.5 wt% NH₄F, (b) schematic illustration to explain the formation of oxide layer (region I), and (c) schematic illustration to explain the dissolution of the barrier layer (region II).

minutes. Such plot is important to explain the mechanism of TiO₂ nanotube formation. Initially, there is an abrupt decrease of current as compact oxide layer is formed, which induces the potential drop between the Ti foil and the electrolytes. The existence of 15 wt% of water in the glycerol will contribute O²⁻ ions. The migration of O²⁻ ions towards the Ti/TiO₂ interface induces further growth of the barrier layer. This is the passivation process of Ti (region I), and a schematic illustration leading to the oxide layer formation is shown in Figure 2(b). The reaction occurred is depicted in the following equation:



In the second stage (region II), a slight increase in current was observed. As mentioned previously, high electric field across the thin layer will induce electric field dissolution. This is accompanied by breakdown of the passivated layer. Random pits are formed on the surface of the oxide due to polarization of Ti–O bond assisted by electric field across the sample. These random pits will grow into pores of various sizes and depths as the pits react with F⁻ ions to produce [TiF₆]²⁻ complex ions as shown in (2). The chemical etching would slightly increase the current density as marked in region II. A schematic illustration regarding the dissolution of the barrier layer is exhibited in Figure 2(c) as follows:



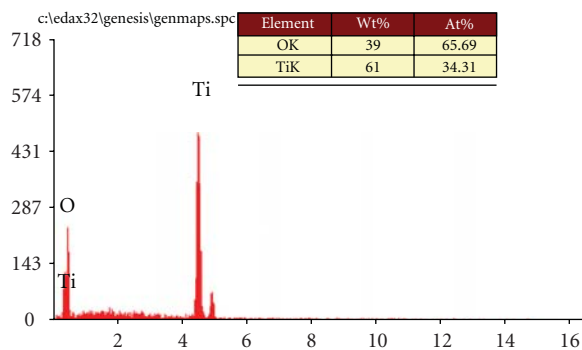


FIGURE 3: EDX spectra of TiO₂ nanotube arrays formed in glycerol electrolyte containing 0.5 wt% NH₄F at 30 V for 30 minutes.

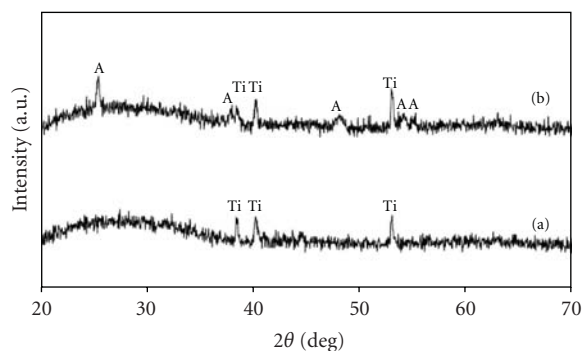


FIGURE 4: X-ray diffraction pattern of TiO₂ nanotubes (a) as anodized and (b) annealed at 400°C in air atmosphere for the sample formed in 1 M of glycerol electrolyte containing 0.5 wt% NH₄F at 30 V for 30 minutes (Ti = Titanium; A = Anatase).

In the third stage (region III), constant equilibrium was maintained with increasing anodization time whilst current density slightly reduced due to the change in pore's depth of the pits. The growth of pores is due to the competition between electrochemical oxide formation and chemical dissolution by F⁻ ions. Thus, the nanotube structure will grow inwards [27].

3.3. EDX Analysis of the Anodized TiO₂ Nanotube Arrays.

The energy dispersive X-ray analysis (EDX) was employed to investigate the chemical stoichiometry of the Ti anodized and subsequently annealed at 400°C under the air atmosphere. From Figure 3, it can be concluded that the atomic ratio of Ti to O was approximately 1 : 2, indicating that only Ti and O elements were present without any impurities.

3.4. XRD Analysis of the Anodized TiO₂ Nanotube Arrays.

It is well known that surface morphology change is closely related to crystal growth and phase transition. Therefore, XRD was used to investigate the effect of crystal growth and phase transition on the change in surface morphology of the TiO₂ nanotube arrays. Figure 4 depicts the XRD patterns of as-anodized and annealed TiO₂ nanotubes fabricated at 30 V in glycerol containing 0.5 wt% NH₄F. The presence of Ti phase was detected in the as-anodized sample, which represents

the amorphous phase of TiO₂ (Figure 4(a)). On the other hand, the presence of anatase phase was detected in the sample subjected to annealing at 400°C in air atmosphere (Figure 4(b)). It can be seen that the diffraction peaks of the entire samples are ascribed to the TiO₂ with anatase phase [JCPDS no. 21-1272]. The diffraction peaks allocated at 25.37°, 38.67°, 48.21°, 54.10°, and 55.26° are corresponding to (101), (112), (200), (105), and (211) crystal planes for the anatase phase, respectively.

3.5. Photoelectrochemical Response of the TiO₂ Nanotube Arrays.

In order to evaluate the effect of surface area and crystallization of TiO₂ nanotube arrays on its photoelectrochemical response, the as-anodized and annealed samples fabricated from different applied potentials were used as photoelectrodes in the photoelectrochemical process. The photocurrent density-voltage transient was recorded under darkness and illuminated conditions, with a light intensity of approximately 800 W/m². Linear sweep potentiometry (LSP) was firstly applied to investigate the photoelectrochemical behaviors of TiO₂ nanotube samples. The corresponding experimental results are presented in Figure 5.

All of the samples exhibited insignificant photocurrents less than 10⁻⁶ A/cm² under dark condition (without illumination). This indicates inactive photoreaction of TiO₂ without generating photoinduced electrons under dark condition. However, the photocurrent density increased under illumination. This situation implies that TiO₂ is a good photoresponse semiconductor for the transfer and decay of photoinduced electrons through the sample [19]. Based on the photocurrent density-voltage (*I*-*V*) characteristic, the photocurrent density increased when the voltage was increased from -0.5 V to 1 V under illumination.

A maximum photocurrent density of up to 0.85 mA/cm² was observed from the TiO₂ nanotubes fabricated at 30 V; this is relatively high among all of the samples (Figure 5(a)). On the contrary, the as-anodized TiO₂ nanotube (without annealing) had the lowest photocurrent density compared with the annealed TiO₂ nanotube arrays, having a minimum photocurrent density as low as 0.02 mA/cm² (Figure 5(f)). The TiO₂ nanotubes fabricated at 20 V, 40 V, 50 V, and 10 V exhibited decreased photocurrent densities, approximately 0.70 mA/cm² (Figure 5(b)), 0.50 mA/cm² (Figure 5(c)), 0.40 mA/cm² (Figure 5(d)), and 0.20 mA/cm² (Figure 5(e)), respectively. These results clearly indicate that the differences in crystallization and surface area of the anodic samples influence the photoelectrochemical performance of TiO₂ nanotube.

In Figure 5, the TiO₂ nanotubes were amorphous in the as-anodized condition, which showed poor photocurrent density. However, the photocurrent density was found to increase for annealed TiO₂ nanotube arrays. Transformation of amorphous structure into crystalline phase was observed after annealing at 400°C in air atmosphere. The increase in photocurrent density is likely attributed to the higher photogenerated electron/hole pairs caused by higher content of anatase phase, whereas the presence of amorphous phase reduces the content of electron/hole pairs due to the existence of more recombination centers in amorphous phase [29].

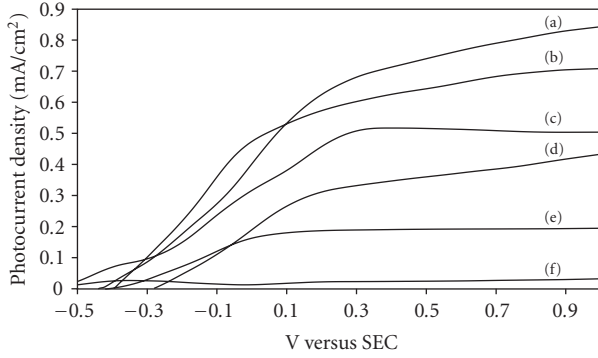


FIGURE 5: The I - V characteristics of TiO_2 nanotubes with different applied potentials, (a) 30 V, (b) 20 V, (c) 40 V, (d) 50 V, (e) 10 V, and (f) as-anodized sample.

The photocurrent density-voltage (I - V) characteristic shows that the higher photocurrent densities of the higher aspect ratio TiO_2 nanotube arrays are strongly dependent upon the availability of larger active surface area for photoelectrochemical reaction. Larger active surface area have better photon absorption as more photoinduced electrons have been effectively transported from TiO_2 nanotube photoanode to counterelectrode through the external circuit under illumination. In addition, photocurrent density can be enhanced by improving the uniformity of the nanotube's size due to the effectively triggered interfacial electron shift, which eventually leads to a more significant promotion of photocurrent [19, 30]. The highly uniform morphology of TiO_2 nanotube arrays provides a high degree of electron mobility along the tube axis. This is because the grains of uniform TiO_2 nanotubes are stretched in the tube growth direction, thus, results in better charge transfer properties compared to nonuniform TiO_2 nanoporous structure.

To estimate the quantitative correlation of light absorption to the different surface area and crystallization of the TiO_2 nanotubes, the photoconversion efficiency (η) of light-to-hydrogen energy was measured (Figure 6) and calculated based on the following equation:

$$\eta (\%) = \left[\frac{(\text{total power output} - \text{electrical power output})}{\text{light power input}} \right] \times 100\% = j_p \left[\frac{(E_{\text{rev}}^0 - |E_{\text{app}}|)}{I_o} \right] \times 100, \quad (3)$$

where j_p is the photocurrent density (mA/cm^2), $j_p E_{\text{rev}}^0$ is the total power output; $j_p |E_{\text{app}}|$ is the electrical power input, I_o is the power density of the incident light (mW/cm^2), E_{rev}^0 is the standard reversible potential (1.23 V/SHE), $E_{\text{app}} = E_{\text{mean}} - E_{\text{aoc}}$, E_{mean} is the electrode potential (versus SCE) of the working electrode where the photocurrent was measured

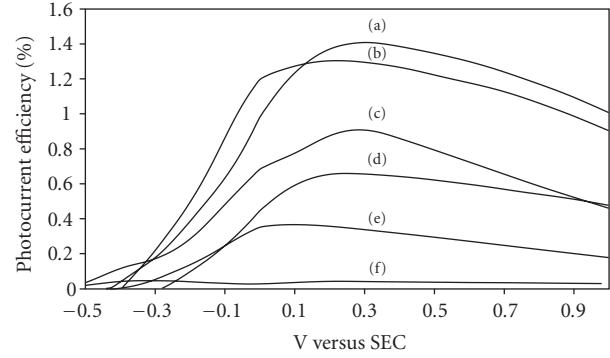


FIGURE 6: The corresponding photoconversion efficiencies of TiO_2 nanotubes with different anodization potentials, (a) 30 V, (b) 20 V, (c) 40 V, (d) 50 V, (e) 10 V, and (f) as-anodized sample.

under illumination, and E_{aoc} is the potential (versus SCE) of the working electrode at open circuit condition.

Based on the photoconversion efficiency curve shown in Figure 6, the highest visible spectrum efficiency (about 1.4%) was obtained from the nanotube arrays fabricated at 30 V. The decrease in photocurrent efficiency was as follows: 1.30%, 0.90%, 0.65%, 0.38%, and 0.05%, which correspond to the anodic samples fabricated at 20 V, 40 V, 50 V, 10 V, and as-anodized TiO_2 nanotube arrays, respectively. The results clearly indicate that the photoelectrochemical properties are dependent on the crystal structure, surface morphology, and surface area of the nanotubular structure. The increase in number of charge carrier plays an important role on improving the efficiency of the water-splitting process.

4. Conclusion

The effect of applied potential on the surface morphology of TiO_2 nanotube arrays formed in glycerol electrolyte containing 0.5 wt% of NH_4F was investigated. TiO_2 nanotubes having a tube's length of approximately $1 \mu\text{m}$ and a uniform diameter of 85 nm have been successfully synthesized by anodization of Ti at 30 V. At lower applied potential, the Ti surface consisted of oxide layer with random pits whereas, at higher applied potential, irregular structure was formed as the balance between the chemical dissolution and electric field dissolution, and oxidation process was interrupted. The higher aspect ratio of TiO_2 nanotubes arrays produced at 30 V shows higher photocurrent response among all of the samples. It can be concluded that the effective surface area and crystallization of TiO_2 nanotube arrays are important factors influencing the efficiency of photoelectrochemical performance.

Acknowledgment

The authors would like to thank Universiti Sains Malaysia for sponsoring this work under RU Grant 814075, Fellowship USM, and Research University Postgraduate Research Grant Scheme (Grant no. 80430146).

References

- [1] A. Ghicov and P. Schmuki, "Self-ordering electrochemistry: a review on growth and functionality of TiO₂ nanotubes and other self-aligned MOx structures," *Chemical Communications*, no. 20, pp. 2791–2808, 2009.
- [2] C. A. Grimes, "Synthesis and application of highly ordered arrays of TiO₂ nanotubes," *Journal of Materials Chemistry*, vol. 17, no. 15, pp. 1451–1457, 2007.
- [3] J. Wan, X. Yan, J. Ding, M. Wang, and K. Hu, "Self-organized highly ordered TiO₂ nanotubes in organic aqueous system," *Materials Characterization*, vol. 60, no. 12, pp. 1534–1540, 2009.
- [4] J. F. Chen, J. Lin, and X. F. Chen, "Self-assembled TiO₂ nanotube arrays with U-shaped profile by controlling anodization temperature," *Journal of Nanomaterials*, vol. 2010, Article ID 753253, 4 pages, 2010.
- [5] M. Kitano, M. Matsuoka, M. Ueshima, and M. Anpo, "Recent developments in titanium oxide-based photocatalysts," *Applied Catalysis A*, vol. 325, no. 1, pp. 1–14, 2007.
- [6] X. Quan, S. Yang, X. Ruan, and H. Zhao, "Preparation of titania nanotubes and their environmental applications as electrode," *Environmental Science & Technology*, vol. 39, no. 10, pp. 3770–3775, 2005.
- [7] D. Wang, Y. Liu, B. Yu, F. Zhou, and W. Liu, "TiO₂ nanotubes with tunable morphology, diameter, and length: synthesis and photo-electrical/catalytic performance," *Chemistry of Materials*, vol. 21, no. 7, pp. 1198–1206, 2009.
- [8] K. S. Raja, M. Misra, and K. Paramguru, "Formation of self-ordered nano-tubular structure of anodic oxide layer on titanium," *Electrochimica Acta*, vol. 51, no. 1, pp. 154–165, 2005.
- [9] M. Paulose, H. E. Prakasam, O. K. Varghese et al., "TiO₂ nanotube arrays of 1000 μm length by anodization of titanium foil: phenol red diffusion," *The Journal of Physical Chemistry C*, vol. 111, no. 41, pp. 14992–14997, 2007.
- [10] S. Y. Ok, K. K. Cho, K. W. Kim, and K. S. Ryu, "Structure and dye-sensitized solar cell application of TiO₂ nanotube arrays fabricated by the anodic oxidation method," *Physica Scripta*, vol. T139, article 014052, 2010.
- [11] S. Li, G. Zhang, D. Guo, L. Yu, and W. Zhang, "Anodization fabrication of highly ordered TiO₂ nanotubes," *The Journal of Physical Chemistry C*, vol. 113, no. 29, pp. 12759–12765, 2009.
- [12] D. Gong, C. A. Grimes, O. K. Varghese et al., "Titanium oxide nanotube arrays prepared by anodic oxidation," *Journal of Materials Research*, vol. 16, no. 12, pp. 3331–3334, 2001.
- [13] A. Fujishima, X. Zhang, and D. A. Tryk, "TiO₂ photocatalysis and related surface phenomena," *Surface Science Reports*, vol. 63, no. 12, pp. 515–582, 2008.
- [14] M. Ni, M. K. H. Leung, D. Y. C. Leung, and K. Sumathy, "A review and recent developments in photocatalytic water-splitting using TiO₂ for hydrogen production," *Renewable and Sustainable Energy Reviews*, vol. 11, no. 3, pp. 401–425, 2007.
- [15] C. A. Grimes, O. K. Varghese, and S. Ranjan, *Light, Water, Hydrogen: The Solar Generation of Hydrogen by Water Photoelectrolysis*, Springer, New York, NY, USA, 2008.
- [16] Z. Liu, B. Pesic, K. S. Raja, R. R. Rangaraju, and M. Misra, "Hydrogen generation under sunlight by self ordered TiO₂ nanotube arrays," *International Journal of Hydrogen Energy*, vol. 34, no. 8, pp. 3250–3257, 2009.
- [17] A. Fujishima and K. Honda, "Electrochemical photolysis of water at a semiconductor electrode," *Nature*, vol. 238, no. 5358, pp. 37–38, 1972.
- [18] G. K. Mor, K. Shankar, O. K. Varghese, and C. A. Grimes, "Photoelectrochemical properties of titania nanotubes," *Journal of Materials Research*, vol. 19, no. 10, pp. 2989–2996, 2004.
- [19] Y. Xie, L. Zhou, and J. Lu, "Photoelectrochemical behavior of titania nanotube array grown on nanocrystalline titanium," *Journal of Materials Science*, vol. 44, no. 11, pp. 2907–2915, 2009.
- [20] Z. Zhang, M. F. Hossain, and T. Takahashi, "Photoelectrochemical water splitting on highly smooth and ordered TiO₂ nanotube arrays for hydrogen generation," *International Journal of Hydrogen Energy*, vol. 35, no. 16, pp. 8528–8535, 2010.
- [21] W. Zhu, X. Liu, H. Liu, D. Tong, J. Yang, and J. Peng, "An efficient approach to control the morphology and the adhesion properties of anodized TiO₂ nanotube arrays for improved photoconversion efficiency," *Electrochimica Acta*, vol. 56, no. 6, pp. 2618–2626, 2011.
- [22] R. L. D. Whitby, S. F. A. Acquah, R. Z. Ma, and Y. Q. Zhu, "1D nanomaterials," *Journal of Nanomaterials*, vol. 2010, Article ID 597851, 3 pages, 2010.
- [23] W. J. Lee, M. Alhoshan, and W. H. Smyrl, "Titanium dioxide nanotube arrays fabricated by anodizing processes: electrochemical properties," *Journal of the Electrochemical Society*, vol. 153, no. 11, pp. B499–B505, 2006.
- [24] K. Yu and J. Chen, "Enhancing solar cell efficiencies through 1-D nanostructures," *Nanoscale Research Letters*, vol. 4, no. 1, pp. 1–10, 2009.
- [25] G. K. Mor, O. K. Varghese, M. Paulose, N. Mukherjee, and C. A. Grimes, "Fabrication of tapered, conical-shaped titania nanotubes," *Journal of Materials Research*, vol. 18, no. 11, pp. 2588–2593, 2003.
- [26] A. Jaroenworarluck, D. Regonini, C. R. Bowen, R. Stevens, and D. Allsopp, "Macro, micro and nanostructure of TiO₂ anodised films prepared in a fluorine-containing electrolyte," *Journal of Materials Science*, vol. 42, no. 16, pp. 6729–6734, 2007.
- [27] G. K. Mor, O. K. Varghese, M. Paulose, and C. A. Grimes, "Transparent highly ordered TiO₂ nanotube arrays via anodization of titanium thin films," *Advanced Functional Materials*, vol. 15, no. 8, pp. 1291–1296, 2005.
- [28] S. Yoriya, M. Paulose, O. K. Varghese, G. K. Mor, and C. A. Grimes, "Fabrication of vertically oriented TiO₂ nanotube arrays using dimethyl sulfoxide electrolytes," *Journal of Physical Chemistry C*, vol. 111, no. 37, pp. 13770–13776, 2007.
- [29] V. K. Mahajan, M. Misra, K. S. Raja, and S. K. Mohapatra, "Self-organized TiO₂ nanotubular arrays for photoelectrochemical hydrogen generation: effect of crystallization and defect structures," *Journal of Physics D*, vol. 41, no. 12, Article ID 125307, 2008.
- [30] Y. B. Liu, J. H. Li, B. X. Zhou et al., "Comparison of photoelectrochemical properties of TiO₂-nanotube- array photoanode prepared by anodization in different electrolyte," *Environmental Chemistry Letters*, vol. 7, no. 4, pp. 363–368, 2009.

Research Article

Acoustic Phonons in Nanowires with Embedded Heterostructures

Hussein M. Ayedh^{1,2} and Andreas Wacker¹

¹Mathematical Physics, Lund University, Box 118, 22100 Lund, Sweden

²Physics Department, Faculty of Science, Thamar University, Box 87246, Dhamar, Yemen

Correspondence should be addressed to Andreas Wacker, andreas.wacker@fysik.lu.se

Received 30 June 2011; Accepted 10 August 2011

Academic Editor: Raymond Whitby

Copyright © 2011 H. M. Ayedh and A. Wacker. This is an open access article distributed under the Creative Commons Attribution License, which permits unrestricted use, distribution, and reproduction in any medium, provided the original work is properly cited.

Acoustic phonons are studied in finite nanowires based on the elastic continuum model. The phonon dispersion relations are compared for different types of approximations both for pure nanowires and nanowire heterostructures including cubic and wurtzite materials. We find that the isotropic approximation highly underestimates the frequency of torsional modes. The impact of heterostructures on the lowest modes is rather weak and can be described by an average of the different structure parameters.

1. Introduction

The phonon spectrum for semiconductor nanowires is important for a variety of applications. On the one hand, nanowires are of high interest for thermoelectric applications [1, 2], where the energy transport by phonons deteriorates the performance [3]. Furthermore, the phonon scattering is an important feature for all sorts of electronic devices [4]. This interaction could recently be directly experimentally accessed [5, 6].

Currently, most calculations of the phonon spectrum are done either within the isotropic approximations for ideal (e.g., [7]) and coupled [8] quantum wires or using atomistic approaches (e.g., [3, 9]). Here, we present corresponding calculations using the commercial COMSOL package [10], which allows to treat both the correct cubic material properties and nanowires with embedded heterostructures in a straightforward way. This enables us to check the quality of the approximation by an isotropic material and the impact of heterostructures [11] on the acoustic branches, which is most important for the broadening of the zero photon line [12].

Our paper is organized as follows: in Section 2, we show how we extract the phonon dispersion relation from simulations of a finite nanowire length. Here, we consider the isotropic approximation, where one has easy access to analytical results for comparison. Section 3 focuses on the cubic

material properties of GaAs wires, where we analyze the differences for the acoustic branches. Nanowire heterostructures are considered in Section 4, where we show that the acoustic branches are only weakly affected. The application to wurtzite structures, see also [13], is demonstrated in Section 5.

2. Obtaining the Phonon Spectrum from Finite Nanowires

Throughout this work, we apply the elastic continuum model, which treats the crystal as a continuum. Thus, the internal vibrations that give rise to the optical modes cannot be considered in this model [14]. It is valid as long as the wavelength of the phonon mode is much longer than the lattice dimension.

The linear relation between stress T and strain S has the general form

$$T_i = \sum_{j=1}^6 c_{ij} S_j, \quad (i = 1, 2, \dots, 6). \quad (1)$$

Here, c_{ij} are the elastic *stiffness* constants with 36 elements in Voigt notation. These stiffness constants can be reduced depending on the symmetries of the material. Many common semiconductors having diamond structure (e.g., silicon and germanium) or zincblende structure (e.g., GaAs and InAs)

exhibit cubic symmetry. The matrix of elastic constants for such materials has only three independent elements [15, 16], c_{11} , c_{12} , and c_{44} .

For isotropic approximation these three independent elastic moduli for the cubic materials can be decreased into two moduli, and they have been expressed by *Lamé* constants λ and μ

$$\begin{aligned}\lambda &= c_{12}, \\ \mu &= \frac{(c_{11} - c_{12})}{2}.\end{aligned}\quad (2)$$

Then, the elastic moduli matrix in the isotropic approximation will only include both of *Lamé* constants as distinct constants

$$c = \begin{bmatrix} 2\mu + \lambda & \lambda & \lambda & 0 & 0 & 0 \\ \lambda & 2\mu + \lambda & \lambda & 0 & 0 & 0 \\ \lambda & \lambda & 2\mu + \lambda & 0 & 0 & 0 \\ 0 & 0 & 0 & \mu & 0 & 0 \\ 0 & 0 & 0 & 0 & \mu & 0 \\ 0 & 0 & 0 & 0 & 0 & \mu \end{bmatrix}.\quad (3)$$

As most of the materials have their elastic properties described in terms of *Young's* modulus E and *Poisson's* ratio ν [17], the two *Lamé* constants λ and μ can be written in terms of E and ν [17]

$$\begin{aligned}\lambda &= \frac{E\nu}{(1+\nu)(1-2\nu)}, \\ \mu &= \frac{E}{2(1+\nu)}.\end{aligned}\quad (4)$$

Here, we approximate the actual shape of the nanowires by a cylinder with radius R , length l , and homogeneous mass density ρ . The acoustic vibrational modes of an infinite cylinder can be classified into three types: longitudinal modes, torsional modes, and flexural modes [17].

The longitudinal modes represent the vibrations of the atoms around their equilibrium positions, where the displacements of the atoms are mostly parallel to the direction of the nanowire [17]. In contrast to bulk longitudinal modes, there is also a small radial component due to the *Poisson's* ratio. The angular frequency ω of each mode is related to its wavevector k by the following relation:

$$\omega = ck, \quad (5)$$

this relation is called the dispersion relation and the proportionality constant is the mode velocity. The longitudinal modes velocity c_{long} have the form

$$c_{\text{long}} = \sqrt{\frac{E}{\rho}}.\quad (6)$$

In the torsional vibrations, the radial displacement of the atoms about their equilibrium positions is perpendicular to

the direction of the wave propagation. The torsional modes also have linear dispersion relation as in (5), and the torsional modes velocity c_{tor} has the following form:

$$c_{\text{tor}} = \sqrt{\frac{\mu}{\rho}}.\quad (7)$$

The flexural modes are more complicated than the previous modes. The dispersion relation of the flexural modes is quadratic

$$\omega = f_{\text{flex}}k^2, \quad (8)$$

where the proportionality factor of the flexural modes reads

$$f_{\text{flex}} = \sqrt{\frac{ER^2}{4\rho}}.\quad (9)$$

Simulating a finite nanowire by COMSOL, we obtain directly the set of eigenfrequencies. From the spatial structure, see Figure 1, we determine the character of the modes and determine the wavevector $k = 2\pi/\lambda$ by a close inspection of the spatial periodicity of the mode (with period λ) in the wire direction. One can clearly identify the different branches from the infinite wire. Figure 2 shows the calculated lowest frequencies for GaAs nanowire with isotropic approximation of length 225 nm and radius 20 nm. In this way, we obtain the dispersion relations (5), (8). From the data in Figure 2, we extract the velocities $c_{\text{long}} = 3890$ m/s and $c_{\text{tor}} = 2484$ m/s. These values are very close to the theoretical values given by (6) and (7), $c_{\text{long}} = 4020$ m/s, $c_{\text{tor}} = 2484$ m/s. The extracted proportionality factor of the flexural modes $f_{\text{flex}} = 4.7 * 10^{-5}$ m²/s also agrees roughly with the theoretical value given by (9), $f_{\text{flex}} = 4 * 10^{-5}$ m²/s. We conclude that our procedure allows to obtain reliable data for the dispersion relations.

3. Isotropic Approximation versus Cubic Nanowire

In this section, the isotropic symmetry, which manifests the same result at any direction, will be compared to the actual cubic symmetry of GaAs. As is well known and mentioned above, the cubic symmetry has three distinct elastic moduli whereas the isotropic material has only two independent elastic constants. The question that arises currently is how the dispersion relations of phonon modes, in material with cubic symmetry, will differ from those that have been displayed previously with isotropic symmetry. The COMSOL simulation tool allows for a treatment of both types of symmetries, which are directly compared in this section. For this purpose, we study the phonon modes in GaAs nano-wires along [001] direction. In Figure 3, one can easily notice the difference between the dispersion relations of the two kinds of symmetries. The longitudinal modes have similar dispersion relations in both, and they have almost identical longitudinal velocities in the both symmetries. The dispersion relation of the flexural modes in the two types of symmetries are similar at lower frequencies, but they

TABLE 1: The density (ρ) and the elastic properties *Young's modulus* (E) and *Poisson's ratio* (ν) of materials of zincblende structure that considered in this work as isotropic material.

Material	ρ (kg/m ³)	E (GPa)	ν
GaAs ^a	5318 ^b	85.9	0.31
AlAs ^a	3598	83.5	0.32
InAs ^c	5667 ^b	51.4	0.35
InP ^d	4810	61.1	0.36

^a: Elastic properties are from [18].

^b: [17].

^c: Elastic properties are from [19].

^d: [20].

TABLE 2: The elastic moduli of materials with cubic symmetry.

Material	c_{11} (GPa)	c_{12} (GPa)	c_{44} (GPa)
GaAs ^a	118.8	53.8	59.4
AlAs ^a	120.2	57	58.9

^a: [21].

manifest a divergence at high frequencies. More noticeable, the torsional modes exhibit a significant difference in their dispersion relations, as shown in Figure 3. For the cubic material, we extract $c_{\text{tor}} = 3343$ m/s, while the isotropic approximation provides $c_{\text{tor}} = \sqrt{\mu/\rho} = 2484$ m/s as addressed above. This difference can be elucidated by the fact that the *Lamé* coefficients extracted from the material parameters in Table 1 by (4) satisfy $\lambda = c_{12}$ and $\mu = (c_{11} - c_{12})/2$ for the cubic parameters from Table 2. Now, the isotropic approximation, see (3), requires $c_{44} = (c_{11} - c_{12})/2$, which, however, does not hold exactly for cubic materials; see Table 2. In contrast, the observed velocity c_{tor} for the torsional modes equals $\sqrt{c_{44}/\rho}$ in this case. As $c_{44} > (c_{11} - c_{12})/2$, the isotropic approximation underestimates the torsional velocity in [001] direction.

4. Acoustic Phonons in Nanowire Heterostructure

Now, we consider acoustic phonons in nanowire heterostructures in order to compare the results to those of simpler pure nanowires. We consider structures, where the wires consist of segments of different materials stacked in the wire direction as experimentally realized in [11]. Note that the interfaces between the materials are perpendicular to the wire direction in contrast to the case intensively studied by Balandin and coworkers [22], where the interfaces are parallel to the wire direction. Due to the lacking translational invariance in the wire direction, k is not an exact quantum number for the phonon modes in our case. Nevertheless, we can still extract an average distance λ between nodes or maxima in the mode profile as discussed above, and thus obtain an effective $k = 2\pi/\lambda$ for comparison with the ideal wires.

We consider a nanowire of total length 225 nm. In the middle, there is GaAs region with length 35 nm, embedded between two barriers of AlAs of thickness 5 nm. The outer

TABLE 3: The density (ρ) and the elastic moduli of materials with wurtzite symmetry.

Material	ρ (kg/m ³)	c_{11} (GPa)	c_{12} (GPa)	c_{13} (GPa)	c_{33} (GPa)	c_{44} (GPa)
GaN ^{a,d}	6095 ^b	390	145	106	398	105
AlN ^{c,d}	3255 ^b	410	148	99	388	130

^a: Elastic moduli are from [23].

^b: [17].

^c: Elastic moduli are from [24].

^d: [16].

regions are again GaAs. This structure constitutes the prototype of an electron resonant tunneling nanowire device. The acoustic phonons in the AlAs/GaAs/AlAs nanowire heterostructure display the same behavior as in the pure GaAs nanowire of the same length; see Figure 4(a). Very slight differences in the eigenfrequencies of the phonon modes are observed due to existence of another material, and we checked that these differences are getting larger by increasing the amount of the other material. Consequently, the dispersion relations of all phonon modes are essentially the same in a nanowire and a nanowire heterostructure. For the heterostructure, we extract the values $c_{\text{long}} = 3898$ m/s, $c_{\text{tor}} = 2494$ m/s, and $f_{\text{flex}} = 4.75 \times 10^{-5}$ m²/s in the isotropic approximation, which are slightly larger than the corresponding values for pure GaAs wires are $c_{\text{long}(\text{GaAs})} = 3881$, $c_{\text{tor}(\text{GaAs})} = 2484$ m/s, and $f_{\text{flex}(\text{GaAs})} = 4.7 \times 10^{-5}$. The main difference can be accounted for by considering an average material of 95.556% GaAs and 4.444% AlAs, corresponding to the composition of the finite wire. Then, we expect

$$c_{\text{long}(\text{av})} = \frac{95.556 * c_{\text{long}(\text{GaAs})} + 4.444 * c_{\text{long}(\text{AlAs})}}{100} \quad (10)$$

$$= 3915 \text{ m/s,}$$

and similarly $c_{\text{tor}(\text{av})} = 2505$ m/s and $f_{\text{flex}(\text{av})} = 4.8 \times 10^{-5}$ m²/s, which all slightly overestimate the increase.

Similar results have been obtained from the comparison between phonon modes in nanowire and nanowire heterostructure with the cubic symmetry. The dispersion relations of phonon modes in a cubic pure GaAs nanowire are in full accord with those in a cubic GaAs/AlAs nanowire heterostructure, as it is illustrated in Figure 4(b). The phonon modes in these two kind of nanostructures have also very small variances in their eigenfrequencies due to the existence of small part of another material which has different elastic properties.

Indium arsenide (InAs) and indium phosphide (InP) also have a zincblende structure with three independent elastic constants. But for simplicity, we have used the isotropic approximation to study the phonon modes in InAs/InP heterostructure. Then, the dispersion relations of the acoustic phonon modes in InAs/InP heterostructure have been compared to those in a pure InAs nanowire; see Figure 5. It is difficult to distinguish the difference in the frequencies of the modes in a nanowire and a nanowire heterostructure by just looking at Figure 5, due to the smallness of these variances. These small variances arise from usage of different

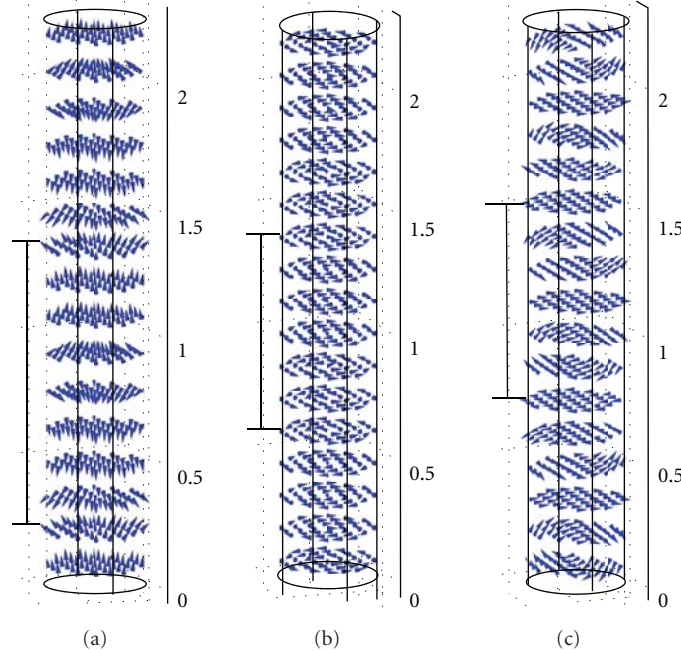


FIGURE 1: Examples of the vibrational mode shapes. (a) Longitudinal mode, (b) Torsional mode, and (c) Flexural mode. The vertical axis displays the nanowire height in units of 100 nm.

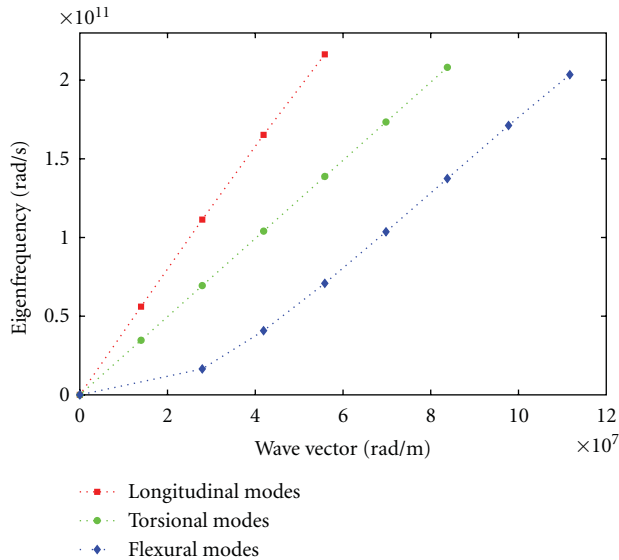


FIGURE 2: Dispersion relations of the acoustic phonons in pure GaAs nanowires with isotropic approximation.

material and it depends on the percentage contribution of each substance in the nanoheterostructure size. We extract the values $c_{\text{long}} = 2960$ m/s, $c_{\text{tor}} = 1842$ m/s, and $f_{\text{flex}} = 3.5 \times 10^{-5}$ m²/s for the heterostructure wire. Here, the assumption of an average material provides $c_{\text{long(av)}} = 2961$ m/s, $c_{\text{tor(av)}} = 1844$ m/s, and $f_{\text{flex(av)}} = 3.32 \times 10^{-5}$ m²/s. This approximation works much better for the InAs/InP material system than for the GaAs/AlAs case discussed above (except for the flexural modes, where the coefficient is difficult to extract).

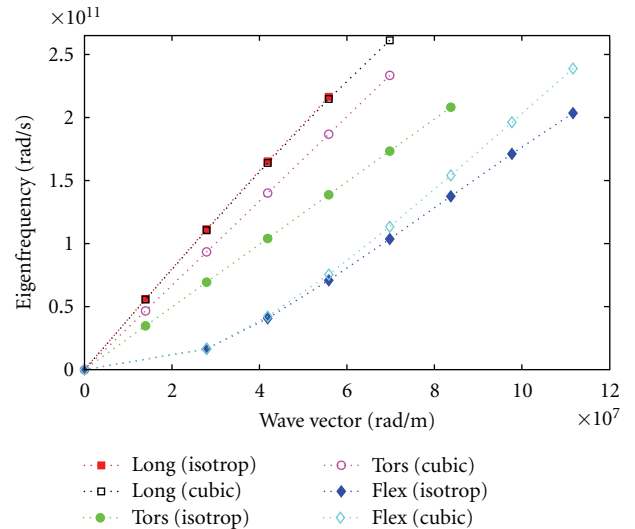


FIGURE 3: Dispersion relations of the acoustic phonons in pure GaAs nanowires with isotropic and cubic symmetries along [001] direction. The results for the longitudinal modes fall on top of each other.

Another way to prove the similarities of the acoustic phonon modes, with small wavevectors, in both pure InAs nanowire and InAs/InP nanoheterostructure are the comparisons of the strain components in both structures. Figure 6 illustrate the likeness of normal strains for the longitudinal modes and the shear strains for the flexural modes in both pure InAs nanowire and InAs/InP nanoheterostructure regardless of the discontinuities of the strain components at the interfaces between InAs and InP segments. One can see mirror reflections around z-axis of some modes in

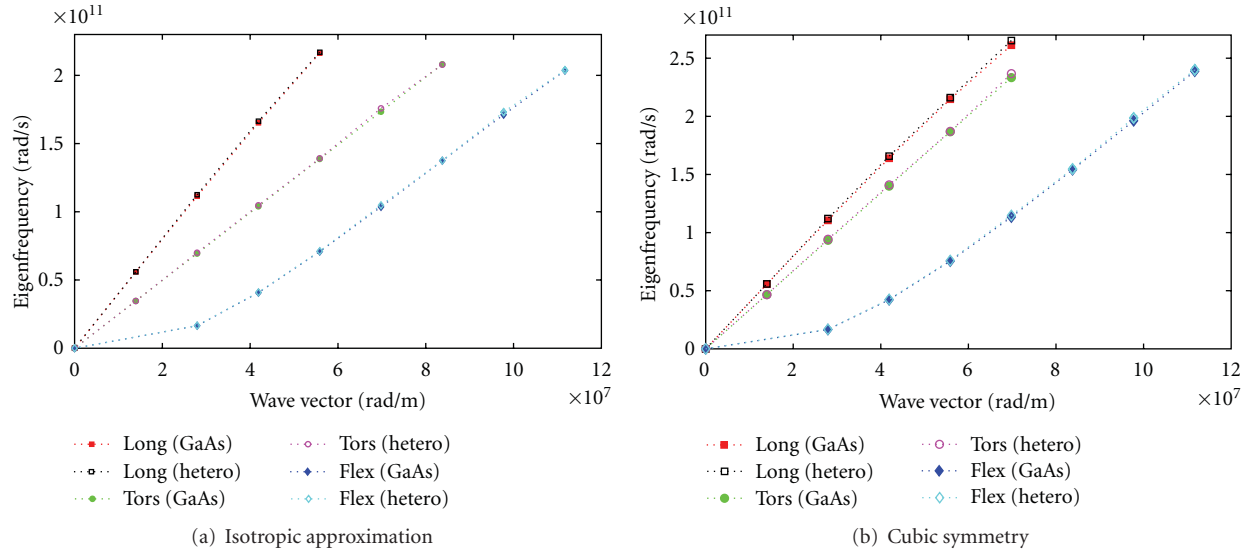


FIGURE 4: These figures illustrate that the phonon dispersion relations in pure GaAs nanowire and GaAs/AlAs nanowire-heterostructures are almost identical. (a) GaAs nanowire and GaAs/AlAs nanowire-heterostructure with isotropic approximation. (b) Same structures calculated with cubic symmetry. The wire length is 225 nm in all cases.

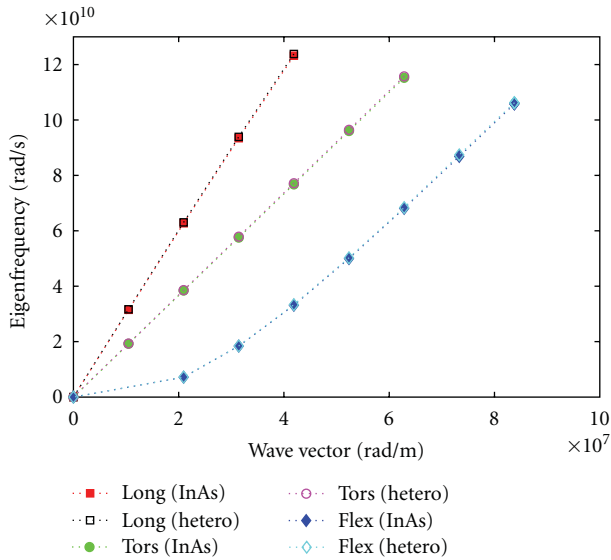


FIGURE 5: Dispersion relations of phonons in both InAs nanowire and InAs/InP nanowire heterostructure with the same length 300 nm, which are almost equal to each other.

the figures, but with the same strain values. The reason is that the solver in COMSOL multiphysics is solving for the absolute value which may take positive or negative values. Taking this into account, we conclude that the strain profiles are only weakly affected by the presence of the heterostructure.

5. Acoustic Phonons in a Nitride Heterostructure

Another kind of structure has been used in this work, the wurtzite structure. The materials that have wurtzite struc-

ture, such as Gallium nitride (GaN) and aluminum nitride (AlN), manifest symmetry in the elastic moduli matrix with five independent constants c_{11} , c_{12} , c_{13} , c_{33} , and c_{44} [14, 16, 17]; see Table 3. The motivation of studying acoustic phonons in plenty of materials with different structures is to explore whether acoustic phonons might show different behavior in different structures. The dispersion relations of acoustic phonon modes have been drawn in a pure GaN nanowire in Figure 7(a) and a GaN/AlN nanoheterostructure in Figure 7(b). In these structures the longitudinal and torsional modes have linear dispersion relations, as it is observed above for the isotropic and zincblende materials. The flexural modes have two components due to bending of the nanostructure toward (x -axis) and (y -axis). While these are exactly degenerate for cubic materials addressed in preceding sections, these two flexural components become non-degenerate for higher frequencies in the pure GaN nanowire as well as in the GaN/AlN heterostructure. The acoustic phonon eigenfrequencies in the GaN/AlN heterostructure are slightly higher than those in a pure GaN nanowire, and the approximation of an average material again slightly overestimates the trend.

6. Conclusion

The phonon dispersion relation, $\omega(k)$, that holds for an infinite wire, has been extracted from COMSOL calculations in finite nanostructures made of different III-V semiconductors such as GaAs, InAs, and GaN. We find that the dispersion relation of torsional modes has changed significantly during the switching between the isotropic and cubic symmetries, while the longitudinal modes are not influenced at all for a [001] wire direction. For heterostructures, we demonstrated, that the phonon spectrum is only weakly modified and the strain components do not vary essentially. This suggests that

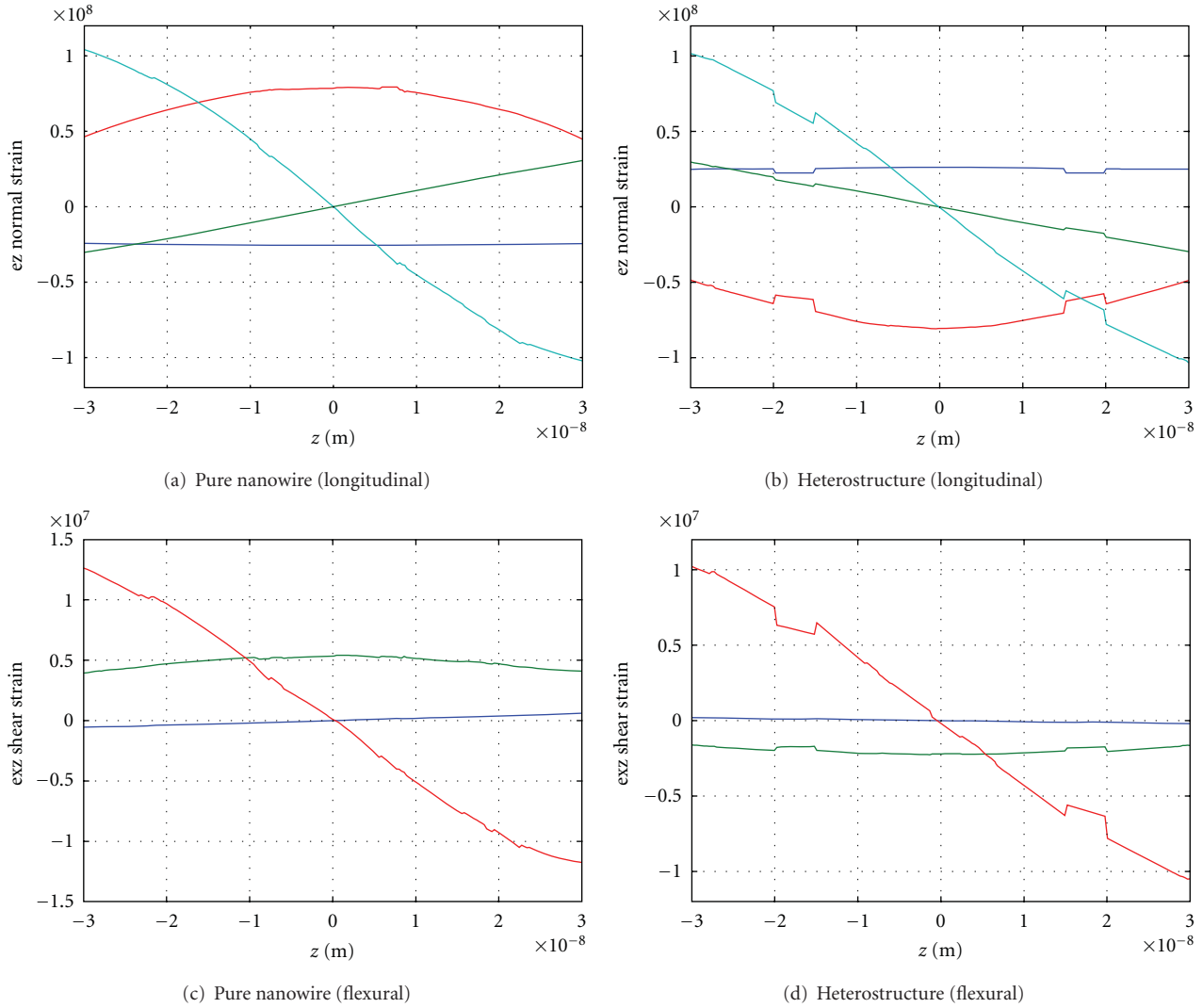


FIGURE 6: The normal and shear strains e_z and e_{xz} of the lowest longitudinal and flexural modes respectively in a cross-section taken in the middle of an InAs nanowire and an InAs/InP nanowire heterostructure with $l = 60$ nm along z -axis, where the region shown includes two barriers and the quantum well in the heterostructures (calculations in isotropic approximation).

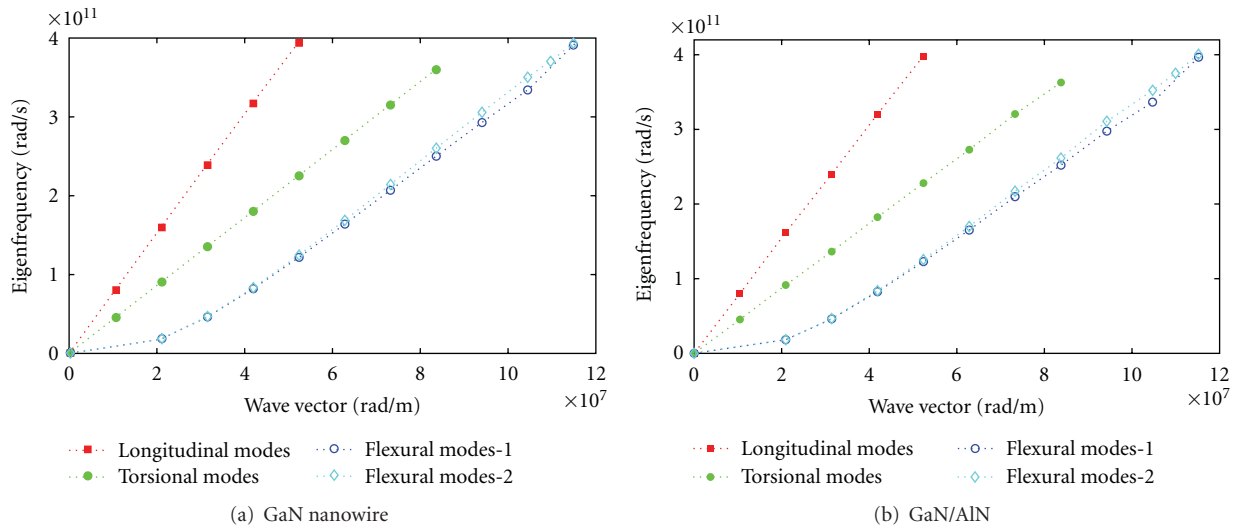


FIGURE 7: Dispersion relation of phonons in a GaN nanowire and a GaN/AlN nanowire heterostructure with the same length 300 nm using the wurtzite symmetry.

one can safely ignore the presence of heterostructures if the lowest phonon branches are needed in calculations for electron scattering processes.

Acknowledgments

Financial support from the Erasmus Mundus program and the Swedish Research Council (VR) is gratefully acknowledged.

References

- [1] M. S. Dresselhaus, G. Chen, M. Y. Tang et al., “New directions for low-dimensional thermoelectric materials,” *Advanced Materials*, vol. 19, no. 8, pp. 1043–1053, 2007.
- [2] A. I. Boukai, Y. Bunimovich, J. Tahir-Kheli, J. K. Yu, W. A. Goddard, and J. R. Heath, “Silicon nanowires as efficient thermoelectric materials,” *Nature*, vol. 451, no. 7175, pp. 168–171, 2008.
- [3] N. Mingo, “Calculation of Si nanowire thermal conductivity using complete phonon dispersion relations,” *Physical Review B*, vol. 68, no. 11, pp. 1133081–1133084, 2003.
- [4] C. Thelander, P. Agarwal, S. Brongersma et al., “Nanowire-based one-dimensional electronics,” *Materials Today*, vol. 9, no. 10, pp. 28–35, 2006.
- [5] C. Weber, A. Fuhrer, C. Fasth, G. Lindwall, L. Samuelson, and A. Wacker, “Probing confined phonon modes by transport through a nanowire double quantum dot,” *Physical Review Letters*, vol. 104, no. 3, Article ID 036801, 2010.
- [6] P. Roulleau, S. Baer, T. Choi et al., “Coherent electron-phonon coupling in tailored quantum systems,” *Nature Communications*, vol. 2, no. 1, 2011.
- [7] M. A. Stroscio, K. W. Kim, S. Yu, and A. Ballato, “Quantized acoustic phonon modes in quantum wires and quantum dots,” *Journal of Applied Physics*, vol. 76, no. 8, pp. 4670–4675, 1994.
- [8] W.-Q. Huang, M.-L. Zou, G.-F. Huang, J.-J. Yao, and W. Hu, “Material properties dependence of ballistic phonon transmission through two coupled nanocavities,” *Journal of Applied Physics*, vol. 105, no. 12, 2009.
- [9] T. Thonhauser and G. D. Mahan, “Phonon modes in Si [111] nanowires,” *Physical Review B*, vol. 69, no. 7, Article ID 075213, pp. 752131–752135, 2004.
- [10] COMSOL, “Multiphysics user’s guide,” comsol 3.5 ed., 2008, <http://www.comsol.com/>.
- [11] M. T. Björk, B. J. Ohlsson, T. Sass et al., “One-dimensional heterostructures in semiconductor nanowhiskers,” *Applied Physics Letters*, vol. 80, no. 6, p. 1058, 2002.
- [12] G. Lindwall, A. Wacker, C. Weber, and A. Knorr, “Zero-phonon linewidth and phonon satellites in the optical absorption of nanowire-based quantum dots,” *Physical Review Letters*, vol. 99, no. 8, Article ID 087401, 2007.
- [13] E. P. Pokatilov, D. L. Nika, and A. A. Balandin, “Acoustic-phonon propagation in rectangular semiconductor nanowires with elastically dissimilar barriers,” *Physical Review B*, vol. 72, no. 11, pp. 1–4, 2005.
- [14] M. A. Stroscio and M. Dutta, *Phonons in Nanostructures*, Cambridge University Press, Cambridge, UK, 2001.
- [15] C. Kittel, *Introduction to Solid State Physics*, John Wiley & Sons, Toronto, Canada, 7th edition, 1996.
- [16] P. Yu and M. Cardona, *Fundamentals of Semiconductors Physics and Materials Properties*, Springer, Berlin, Germany, 3rd edition, 2003.
- [17] A. N. Cleland, *Foundations of Nanomechanics from Solid-State Theory to Device Applications*, Springer, Berlin, Germany, 2003.
- [18] S. Adachi, “GaAs, AlAs, and $\text{Al}_x\text{Ga}_{1-x}\text{As}$,” *Journal of Applied Physics*, vol. 58, no. 3, pp. R1–R29, 1985.
- [19] Y. A. Burenkov, S. Y. Davydov, and S. P. Nikanorov, “Elastic properties of indium-arsenide,” *Soviet Physics.Solid State*, vol. 17, p. 1446, 1975.
- [20] D. N. Nichols, D. S. Rimai, and R. J. Sladek, “Elastic anharmonicity of inP: its relationship to the high pressure transition,” *Solid State Communications*, vol. 36, no. 8, pp. 667–669, 1980.
- [21] S. Adachi, *Properties of Aluminium Gallium Arsenide*, The Institution of Electrical Engineers, London, UK, 3rd edition, 1993.
- [22] A. A. Balandin, E. P. Pokatilov, and D. L. Nika, “Phonon engineering in hetero- and nanostructures,” *Journal of Nanoelectronics and Optoelectronics*, vol. 2, no. 2, pp. 140–170, 2007.
- [23] A. Polian, M. Grimsditch, and I. Grzegory, “Elastic constants of gallium nitride,” *Journal of Applied Physics*, vol. 79, no. 6, pp. 3343–3344, 1996.
- [24] L. E. McNeil, M. Grimsditch, and R. H. French, “Vibrational spectroscopy of Aluminum Nitride,” *Journal of the American Ceramic Society*, vol. 76, no. 5, pp. 1132–1136, 1993.

Review Article

Synthesis and Characterization of 1D Ceria Nanomaterials for CO Oxidation and Steam Reforming of Methanol

Sujan Chowdhury and Kuen-Song Lin

Department of Chemical Engineering and Materials Science and Fuel Cell Center, Yuan Ze University, Chung-Li 320, Taiwan

Correspondence should be addressed to Kuen-Song Lin, kslin@saturn.yzu.edu.tw

Received 12 June 2011; Accepted 29 July 2011

Academic Editor: Yanqiu Zhu

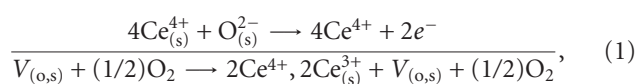
Copyright © 2011 S. Chowdhury and K.-S. Lin. This is an open access article distributed under the Creative Commons Attribution License, which permits unrestricted use, distribution, and reproduction in any medium, provided the original work is properly cited.

Novel one-dimensional (1D) ceria nanostructure has been investigated as a promising and practical approach for the reforming of methanol reaction. Size and shape of the ceria nanomaterials are directly involved with the catalytic activities. Several general synthesis routes as including soft and hard template-assemble phenomenon for the preparation of 1D cerium oxide are discussed. This preparation phenomenon is consisting with low cost and ecofriendly. Nanometer-sized 1D structure provides a high-surface area that can interact with methanol and carbon-monoxide reaction. Overall, nanometer-sized structure provides desirable properties, such as easy recovery and regeneration. As a result, the use of 1D cerium has been suitable for catalytic application of reforming. In this paper, we describe the 1D cerium oxide syntheses route and then summarize their properties in the field of CO oxidation and steam reforming of methanol approach.

1. Introduction

Modern society insists on a new energy carrier with the chemical conversion of fuels to minimize the environmental disaster. Recently, hydrogen production processes have applied effectively for environmental impact and energy generation issues. Hydrogen is usually generated through the organics mainly based on hydrocarbon waste treatment and is extremely renowned as a clean energy carrier [1–6]. Nowadays, it is an important environmental issue on the case of an atmospheric condition. Methanol is one of the most promising sources of hydrogen for fuel cell applications included with the advantages of high-energy density, easy availability, and safe handling/storage materials [3]. In the literatures, several types of catalyst are frequently used for hydrogen generation by steam reforming of methanol (SRM) [1, 5, 6]. SRM is the main reforming reaction that provides the stoichiometric conversion of methanol to hydrogen. The overall methanol decomposition reaction can be regarded as the effect of the conversion of CO, CO₂, H₂O, and water gas shift (WGS) reaction. SRM is one of the attractive approaches on the rise owing to higher-energy density and relatively low-reforming temperatures (200–300°C). Combination of SRM and partial oxidation of methanol (POM) is effectively

known as autothermal reforming (ATR) process and is attenuated with decreasing the reactor volume and design [3, 7, 8]. SRM is the main reforming reaction that provides the stoichiometric conversion of methanol to hydrogen. In addition, methanol steam reforming produces a relatively small amount of carbon monoxide at a low temperature, whereas carbon monoxide is known to be very poisonous for Pt catalyst in a proton exchange membrane fuel cell (PEMFC) system [5]. Therefore, there has been considerable interest in the development of catalytic performance of methanol decomposition. The catalytic reaction for SRM and ATRM is generally based on copper or palladium. As well, cerium-promoted copper catalyst existed for the recovery of hydrogen from methanol with the optimization of carbon monoxide concentration [2–4]. Cerium is often referred to as the rare-earth element or lanthanide ($Z = 57–71$). As an important component in catalysts, ceria ($Z = 58$) promotes high oxygen storage capacity (OSC), oxygen ion conductivity, and oxygen vacancy. The formation of oxygen vacancy can be expressed by the following equation:



where $V_{(O,s)}$ represents an empty position (anion-vacant site) originating from the removal of O^{2-} from the lattice. Charge balance is maintained by the reduction of two cerium cations from +4 to +3. The radius of the Ce^{3+} ion (1.14 Å) is larger than that of Ce^{4+} (0.97 Å), and hence the lattice expansion is a consequence of the reduction of Ce^{4+} ions to Ce^{3+} . There is a gradual decrease in the concentration of oxygen vacancies extended from the surface to the bulk. Such gradient enables the outward diffusion of lattice oxygen to the surface. Therefore, the reduction of Ce^{4+} to Ce^{3+} by oxygen ion leads to the generation of surface oxygen vacancy. These oxygen vacancies can be acted as promoting sites for NO and CO conversion [1–9].

As well, cerium oxide (CeO_2) is commonly known as cerium dioxide, ceria, or ceric oxide, visualized as pale yellow-white powder and slightly hygroscopic in nature at the atmospheric conditions. Usually ceria are obtained through the calcinations of cerium oxalate or cerium hydroxide. In the room temperature and pressure, CeO_2 represents much more stable form than cerium (III) oxide (Ce_2O_3). CeO_2 has consisted of FCC crystal fluorite structure, and their Ce^{4+} ions are closed packed and O ions in the space of a tetrahedron. It has been evident that doped metal ions onto the ceria material are still showing the FCC crystal structure [10, 11]. Novel structure of 1D ceria nanostructure with various morphologies such as nanorods, nanowires, nanotubes, and nanopolyhedrons has been successfully fabricated by a variety of methods [12–28]. Nanoscale ceria materials of 1D structure are represented with surface morphologies, allowing attractive applications for catalytic reactions [12, 13]. Moreover, ceria nanomaterial research has focused on the scheme of the physical treatment, based on the controlling of the reaction time, temperature, pressure, and so forth.

Ceria is belonging to higher oxygen ion conductivity and one-dimensional ceria, and doped ceria have wide applications in the electrochemistry, catalysis, optics, and different fields [14–23, 27, 28]. Therefore, as synthesized one-dimensional ceria nanomaterials are particularly attained an attraction for the catalytic behavior on the chemical reaction of carbon monoxide and methanol, which are overviewed in this paper. General physical and chemical properties of the ceria nanomaterials are specifically enhanced through the dimension of the nanostructure and doped material with respect to their bulk-like materials.

2. Nucleation and Growth

Bulk- or nanometer-sized different dimensional crystal structure growth is readily involved in the process of precipitation of solid phase from solution. Simultaneous process of nucleation and following growth phenomenon govern the crystal morphology (as including size and shape) in the precipitation reaction. At the initial stage, numerous small crystallites are formed to refer to as the nucleation process. Consequently, small crystallites are aggregated together to form thermodynamically stable structure and referred to as a growth process. An effective process control is leading to the formation of the desired solid crystal structure.

Thus, the formation of crystal structure is essential to consider the nucleation and growth of structure. Initially, surface energy plays an important role to increase the size of the nuclei where nucleation is a spontaneous process, and large crystals have lower surface energy. Surfactant, solvent, concentration, pH, reaction temperature, and time are readily involved in the surface energy of the crystal growth. In the thermodynamic point of view, addition of surfactants is used to control the process of nucleation and the size of the resulting nucleus. Nucleation process is readily involved in heterogeneous nucleation, secondary nucleation and homogeneous nucleation. Presence of suspended particles may provide the start of the nucleation, and thus insists the heterogeneous nucleation with the requirement of less energy. Heterogeneous nucleation obtains more often than homogeneous nucleation. Secondary nucleation is involved in the formation of nuclei with the recombination of existing crystal. On the other hand, homogeneous nucleation occurs spontaneously and randomly in the absence of solid interface by a combination of solute molecules. The growth process of crystal occurs for dissolving the solute in the solution at higher temperatures and then cooling to low temperature or by adding the necessary reactants to produce a supersaturated solution during the reaction. This overall crystal growth phenomenon is belonging to the consumption of smaller particle by larger particle to form larger stabilized structure, and it has been referred to as Ostwald ripening also known as coarsening [29]. Lifshitz and Slyozov first developed mathematical derivation of Ostwald ripening process and independently by Wagner; their combined models today are referred to as LSW theory. The relationship between monomer concentration and crystal size is established by the Gibbs-Thomson equation with the Fick's First Law and Einstein-Stokes equation as follows:

$$\begin{aligned}\bar{r}^3 - \bar{r}_0^3 &= Kt, \\ \bar{r}^3 - \bar{r}_0^3 &= \frac{8\gamma V_m^2 C_{r=\alpha} D}{9R_g T} t, \\ \bar{r}^3 - \bar{r}_0^3 &= \frac{8\gamma V_m^2 C_{r=\alpha}}{54\pi\eta a N_A} t,\end{aligned}\quad (2)$$

where \bar{r} is an average particle radius, \bar{r}_0 is an initial average particle radius, $C_{r=\alpha}$ is the solubility of the particle material, V_m is the molar volume of the particle material, D is the diffusion coefficient ($k_B T/6\pi\eta a$) of the particle material, R_g is the ideal gas constant, T is the absolute temperature, t is the time, k_B is Boltzmann's constant (R_g/N_A), η is the viscosity, a is the ionic radius of the particle, and N_A is the Avogadro constant. Thus, cubic of the average radius of the precipitate particles is a function of time, that is, $\bar{r}^3 = Kt$, where K is the coarsening rate constant that can be obtained from the slopes of the linear regions of the plots of \bar{r}^3 versus time and increases with the aging temperature. The activation energy is obtained from the slope with the plots of coarsening rate constant versus inverse of absolute temperature, and it would be a straight line. Nuclei formation that precedes crystal growth can occur by solid-state restructuring of the gel or precipitation from the supersaturated solution [30, 31].

In the last decade, nuclear magnetic resonance (NMR), small-angle and wide-angle X-ray, Raman spectroscopy, and neutron scattering spectroscopy techniques have provided the details information about the nucleation process [30, 31]. Recently, Pan et al. elaborately studied specifically addressing, the coarsening of one-dimensional ceria nanoparticle growth [32].

3. Synthesis of One-Dimensional Structured Cerium Oxides

One-dimensional cerium oxides can be produced via a simple hydrothermal and precipitation route using ammonia solution and precursor. In addition, most synthesis methods for 1D structured cerium oxides employ templates (soft and hard), which assist in obtaining a uniform morphology and the desired morphological phenomenon. Crystal's structure formation is basically involved with the precipitation process then basically consists of a nucleation step followed by particle growth stages where surface tension (γ) and saturation ratio (S) are influenced by surfactants, solvent, concentration, pH ratios, and so forth. In other words, surfactant on the surface of the nucleus directly reduced the surface tension and thus caused smaller critical radius with critical energy. The presence of micelles in solution also affects the process of nucleation and growth of the crystal where micelles solubilise the molecules of the material, thus affecting the relative supersaturation towards the nucleation and growth of the crystal.

3.1. Soft-Template Techniques. Surfactant plays an effective role in the preparation of 1D nanophase compounds and has been adversely observed in the past decades [14–24, 33]. Most commonly used soft templates are surfactants, such as cetyl trimethyl ammonium bromide (CTAB), polyvinylpyrrolidone (PVP), tetrabutylammonium bromide (TBAB), and polyethylene glycol (PEG). Cerium salts (either chloride or nitrate) under basic conditions react with ammonia at room temperature which results in the precipitation of gelatinous and hydrous cerium oxide. It is well evident that the geometry of the monomer will determine the size and shape of the surfactant aggregates. The desired size and shape of this aggregation are based on the packing parameter (P) concept $P = v/a_0l$, where packing properties of surfactant depend on the volume v of the hydrocarbon chain, average area of a hydrophilic head group a_0 (defined by the equilibrium between hydrocarbon tail attraction and head group repulsion), and the critical chain length l . The packing parameter values in the range of $1/3 < P < 1/2$ form cylindrical micelles, values of $P < 1/3$ lead to spherical micelles, and $P > 1/2$ favors flat bilayers (lamellar sheet) as represented in Figure 1. The formation of micelle is usually nonsphericity and consists of ellipsoidal shape, oblate shape, acetabuliform, or claviform. Usually claviform shape (cylindrical micelles) is obtained in the case when the concentration of surfactant reaches ten times that of critical micelles concentration (CMC). There are many methods available in literature for the determination of the CMC:

surface tension, spectrophotometric, kinetics, conductivity, osmotic pressure, and so forth [30–35]. Fluorescence spectroscopy is a sensitive technique for accurately determining the CMC. Halder used the fluorescence spectroscopy for the determination of CMC of cetyl trimethyl-ammonium bromide (CTAB) [30]. It is well known that CMC of CTAB is around 0.90–0.98.

The size and shape of the 1D nanostructure are greatly influenced through the reaction time, reaction temperature, and surfactant/ Ce^{3+} ratio in the initial solution [18, 36–40]. Triangular and rhombic shape ceria nanoparticles are attained with the influence of surfactant/ Ce^{3+} ratio, carbamide concentration, and reaction temperature [41, 42]. Guo et al. [42] synthesized $\text{Ce}(\text{OH})\text{CO}_3$ triangular microplate by a thermal decomposition-oxidation process at 150°C for 16 h using surfactant/ Ce^{3+} molar ratio 2:1, and calcination process produces straw-yellow triangular ceria microplate in air at 650°C for 7 h. Later on, Zhang et al. [41] reported the synthesis of the rhombic $\text{Ce}(\text{OH})\text{CO}_3$ nanostructure by a sonochemical method using surfactant/ Ce^{3+} molar ratio 1:10. Finally, rhombic ceria nanostructure is obtained by calcination at 500°C in air for 0.5 h and to remove the CTAB. They investigate that reaction temperature is lower than the boiling point of water (100°C) that can be formed the mixture of nanoparticles nanorods and irregular microrods. Therefore, reaction temperature and time also play an important role in the formation of rhombic microplates. After that, Riccardi et al. [43] used similar surfactant/ Ce^{3+} concentration and conditions as proposed by Guo et al. with a slight modification of reaction environment and time. They synthesized the cerium carbonate hydroxide (orthorhombic $\text{Ce}(\text{OH})\text{CO}_3$) hexagonal-shaped microplates with a domestic microwave (2.45 GHz, maximum power of 800 W) at 150°C for 30 min with a fixed heating rate of $10^\circ\text{C min}^{-1}$ and then converted into ceria cubic/rhombus shape after a thermal decomposition oxidation process at 500°C for 1 h. They conclude that microwave method increases the kinetics of crystallization by one or two orders of magnitude compared to the conventional hydrothermal [29, 43–48]. Similarly, ceria nanocube is obtained in the presence of ethylene glycol, oleic acid, and *tert*-butylamine at the different temperatures of microwave radiation for 60 min [49]. The high-frequency electromagnetic radiation interacts with the permanent dipole of the existing liquid to initiate rapid heating from the resultant molecular rotation. Thus, the effects of the superheating environment within a short period of time concern and facilitate the crystal growth. Instead of surfactant (CTAB), there is a significant effect of urea (or carbamide) solution on the synthesis of ceria nanomaterial, and we will explain this effect in the nontemplate technique section. Vantomme et al. [17] and Pan et al. [18] reported the formation of CeO_2 nanorods with a diameter of 10–25 nm at 80 – 160°C by the presence of CTAB. Pan and coworkers [18] also synthesized the CeO_2 nanoplates by hydrothermal reactions with CTAB. They controlled the conversion of nanoplates into nanotubes and nanorods by using changing CTAB/ Ce^{3+} ratio values, reaction time, temperature, and ammonia solution instead of carbamide. Higher temperature and higher concentration

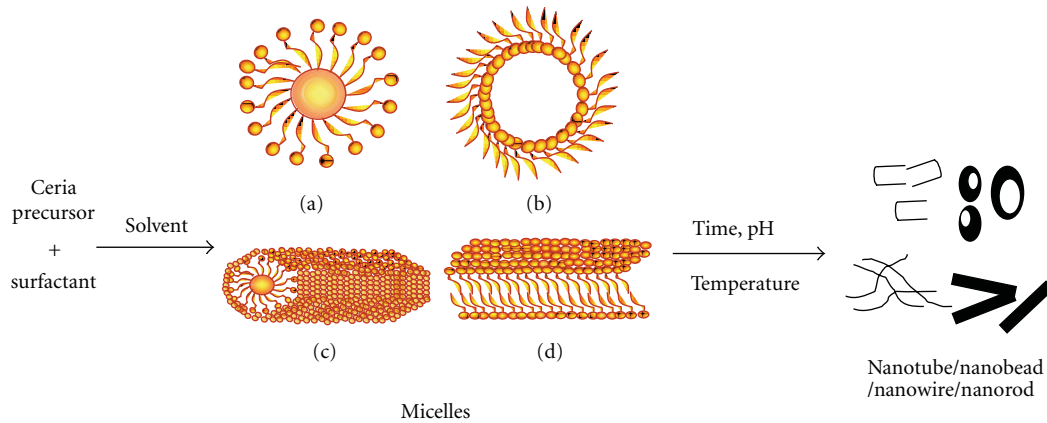


FIGURE 1: Different types of micelle: (a) normal, (b) reverse, (c) rodlike, and (d) bilayer structures for the formation of nanotubes, nanobeads, nanowires, and nanorods.

of CTAB as a surfactant are controlled by the synthesis of Ce-NT in the two-step procedure. In the first step, a higher concentration of the CTAB led to an increase in the absorption force between the CTA^+ and $\text{Ce}^{3+/4+}$ ion pairs and accelerated the formation of lamellar sheet as represented by the packing parameter $P > 1/2$. In the second step, Ce-NT was formed by rolling up the lamellar sheets. In addition, the lower concentration of CTAB can appear into a cubic plate-like structure, where reaction temperature and time controls the cubic platelike to nanoplate, hexagon, and nanorod structure, respectively. By using a precipitation method, Vantomme et al. [17] and Yan et al. [39] carried out the ceria nanowire preparation with the presence of easily available CTAB. Furthermore, Zhang et al. [24] prepared 1D ceria nanorods at room temperature in a one-step process through polyethylene glycol (PEG) surfactant and alkali solution. They confirmed that vigorous agitation without ultrasound at various temperatures (25, 40, and 60°C) would form only nanoparticles as the sole products, even with a longer reaction time. Concentration of the surfactant (e.g., PEG or CTAB) significantly affects the formation of 1D nanostructures [17, 18, 24]. Moreover, the transformation from one structure to the next is caused by intermolecular interactions between surfactant monomers. According to Ho et al. [15], ethylene glycol-mediated synthesis has been widely used for the following physical properties: (1) a high-dielectric constant, which enhances the solubility of inorganic salts; (2) a high boiling point (195°C at an atmospheric pressure), which makes it possible to carry out the preparation of inorganic compounds at relatively high temperatures; (3) its strong reducing power. Additionally, Ho et al. [15] observed that a higher precursor concentration with lower reaction time provides spherical-shaped cerium oxide increasing the reaction time, consequently extended the spherical shape into 1D rod structures. In addition, with similar experimental conditions and a lower precursor concentration, they obtained the spindle-shaped nanostructure.

Surfactants were frequently used for the fabrication of cerium oxide 1D nanowire/nanofibers. Qi et al. [22] first time demonstrated the electrospinning technique for

the formation of PVP/ $\text{Ce}(\text{NO}_3)_3$ composite fibers. They fabricated the cerium oxide hollow nanofibers with calcining the composite fibers at 600–800°C for 10 h. According to the FE-SEM microphotographs, the diameters of CeO_2 hollow nanofibers (300 nm at 600°C and 600 nm at 800°C, resp.) were smaller than those of PVP/ $\text{Ce}(\text{NO}_3)_3$ composite fibers (1–2 μm), with the length of greater than 50 μm . They observed, through TG-DTA and FTIR data analysis, that the calcination temperatures largely influenced the formation of CeO_2 hollow nanofibers. In addition, cationic surfactant played an important role in the preparation of nanowire and nanotube. Yang and Guo [40] also employed octadecylamine ($\text{C}_{18}\text{H}_{37}\text{NH}_2$) (cationic surfactants) as the structure-directing agent to synthesize CeO_2 nanowires with a diameter of 10–25 nm in the presence of nitric acid and water, where nitric acid was used for the transformation of octadecylamine into octadecylammonium nitrate to dissolve in water. They explained that octadecylammonium cations ($\text{C}_{18}\text{H}_{37}\text{NH}_3^+$) in aqueous solution could form claviform micelles by the self-assembly. Cerium hydroxide is combined by the hydrated Ce^{+4} ions with H_2O molecules or OH^- ions and then polymerized at the micelles-solution interface to form the nanowire structure as diameters ranging between 10 and 25 nm. Yang and Guo [50] also synthesized the $\text{Ce}(\text{OH})\text{CO}_3$ to fluorite-type Ce-NT with an outer diameter of 10–20 nm and inner diameter of 5–6 nm. $\text{Ce}(\text{OH})\text{CO}_3$ was attained by a hydrothermal method using $\text{Ce}(\text{NH}_4)_2(\text{NO}_3)_6$ as the Ce source, octadecylamine as a surfactant template, and urea as a precipitation agent. On the other hand, cationic surfactants (i.e., alkyltrimethylammonium salts, CTAB, octadecylamine, or ethylenediamine ($\text{C}_2\text{H}_4(\text{NH}_2)_2$)), hydrous cerium oxide can incorporate the organic molecule by exchange with surface OH^- groups with the formation or reverse micelle. This approach follows the observation that hydrous oxides can exchange either cations or anions, depending on the pH of the medium [36, 37]. If the pH is higher than that of the isoelectric point of hydrous cerium oxide (6.75–8, depending on the environment), then incorporation of cationic surfactants takes place.

Reverse micelle is another process to the synthesis of different structure in the presence of the reaction media. Significant surfactant solutions in organic solvents are capable of solubilizing water in the polar core and are called as reverse micelles as shown in Figure 1. It seems that water can be readily incorporated in the core of the micelle, with the radius of the micelle increasing as the water/surfactant ratio increases. Reverse micelles provide spontaneous self-assembly of surfactants in solution for the formation of nanorods as specially in the presence of anionic surfactant sodium bis(2-ethylhexy) sulfosuccinate (AOT). Kuiry et al. [51] reported that the cylindrical supra-aggregates and their subsequent growth occurred by preferential assembling of ceria nanorods along the longitudinal direction with the addition of AOT/toluene/water and H_2O_2 /AOT/toluene/water microemulsions after a few weeks of aging. Such nanorods have an aspect ratio of 6 with a diameter of approximately 40 nm. In addition, according to the TEM analysis, it was proposed that the abrupt change in surface-free energy in the micelle might form the cone-shaped portions at both ends of the nanorods. Sun et al. [38] synthesized CeO_2 nanowires, 30–120 nm in diameter, by a precipitation method combined with thermostatic treatment using AOT as a template. Yada et al. [37] prepared different types of 1D nanowire structures with the presence of different-order alcohol and AOT as anions at 700°C or above. In the presence of AOT, adding lower-order alcohol such as alkyl or butyl alcohol and higher-order alcohol (octyl or dodecyl alcohol) only produced nanowire and the nanoring shape nanowire (diameter of ~280 nm and width of ~80 nm), respectively.

Lundberg et al. [52] prepared the mesoporous cerium dioxide flakes by using a copolymer surfactant (Pluronic 123) at ambient conditions in alcohol as a solvent. The material was produced via a direct calcination step, without the necessity of a gelling stage. According to the small angle X-ray scattering (SAXS) analysis, they observed that in the pluronic-ethanol mixture the surfactants were in a random coil state with no short-range or long-range order between them and combined with the cerium chloride precursor before the formation of pure CeO_2 mesoporous flakes. Son et al. [53] synthesized the ceria nanocubes through the reverse micelle method as the presence of aqueous solution of poly(oxyethylene) nonylphenyl ether (Igepal CO-520), cyclohexane, and hydrazine hydrate as a reducing agent. In a typical procedure, Gu et al. [27] successfully synthesized mesoporous ceria nanofibers, nanobelts, and rodlike nanoparticles using a reverse micelle method. They synthesized the mesoporous ceria nanofibers at the lower aging temperature at 30°C with a diameter of 50–200 nm and length of more than 50 μm with the presence of nonionic surfactant Triton X-100. On the other hand, nanobelts materials with the length of a few tens of μm , widths ranging from 0.5 to 5 μm , and the thicknesses ranging from 20 to 100 nm have been prepared at the slightly higher aging temperature at 40°C and constant time of 48 h, where BET surface area and pore volume of the nanobelts (114.9 m^2g^{-1} and 0.1470 cm^3g^{-1} , resp.) are about twice as high as those of the nanofibers (54.41 m^2g^{-1} and 0.09051 cm^3g^{-1} , resp.).

In the presence of hexadecylamine and aqueous ethanol, solution may form hexagonal type comet structure. On the other hand, the presence of hexadecylamine and aqueous toluene solution can provide ceria nanocubic structure at 180°C for 24 h [54]. Bouchara et al. [55] investigated the coral-like, helical, or macroporous sieve morphologies with the presence of poly-g-benzyl-L-glutamate (PBLG) of organically functionalised CeO_2 crystalline nanoparticles. As an increase of the molar ratio $s = \text{nanoparticles/PBLG}$, phenyl-functionalized nanoparticles lead to the formation of coral-like structure ($s = 15$), helical ($10 < s < 60$), and macroporous where $s > 60$, respectively. Zhang et al. [56] formed the three-dimensional inverse opal type mesoporous structure by the presence of poly(methyl methacrylate) (PMMA) in cerous nitrates solution ($\text{Ce}(\text{NO}_3)_3 \cdot 6\text{H}_2\text{O}$) with alcohol (0.5 molL^{-1}), after drying and calcination at 350 to 800°C temperature. Similarly, Chen et al. [6] reported that novel ceria hollow nanocubes were synthesized through a solvothermal method using peroxyacetic acid (PAA) in anhydrous ethanol for 9 h at 160°C. Crystal growth of ceria hollow nanocubes was obtained through Oswald ripening method. It is observed that the prepared CeO_2 hollow nanocubes exhibit a higher catalytic activity toward CO oxidation. Andreescu et al. [57] investigated that thermal calcination process in the presence of air converts the initial precipitate amorphous spherical particles that consist of a complex mixture of ceria, ceria hydrate, cerium hydroxide, cerium glycolate complex, and residual propylene glycol, PG, to crystalline ceria. Similarly, the formation of monodispersed ceria particles was favored when polyethylene glycols (PEGs) of higher molecular weight were used [57–59]. Amino acid surfactant such as L-asparagine in the presence of KBrO_3 acts as OH provider and is followed by oxidizer to form hollow ceria sphere with a mean diameter of 1.5 μm and as shell thickness of 90 nm [60]. On the other hand, preparation of ceria aerogel is a novel technique to obtain higher-surface area ($>200 \text{ m}^2\text{g}^{-1}$) for further water gas shift reaction, electrical conductivity analysis, and oxidation of propane application [61–63]. Recently, Gasser-Ramirez and coworkers synthesized the ceria aerogel in the presence of aqueous solution of 2-methoxyethanol and cerium(IV) methoxyethoxide through hydrolysis reaction [63].

3.2. Hard Template Techniques. Generally, the tubular structure itself may consist of higher thermal, chemical, and structural stability [50, 64–67]. Various preparation conditions have been employed to synthesize 1D Ce-NT materials, such as the use of different surfactants and templates, ultrasound treatment, hydrothermal method with different temperatures, aging effect, and acidic treatment. The template synthesis method is an effective way for preparation of the nanomaterials in the presence of polymeric filtration membrane and similar materials [50, 64–67]. Carbon nanotube (CNT) as a template plays a significant role in the formation of 1D ceria nanostructures. It was reported that the surface of the template was covered with ceria nanomaterials and possesses Ce-NT in the presence of pyridine. However, a homogeneous and continuous layer of ceria nanoparticles on CNTs is important for the formation

of Ce-NT. It should be noted that it is impossible to fabricate Ce-NT if the pyridine is replaced by DMF [68]. In addition, higher-temperature treatment was carried out for the removal of the templates [66–70]. The CNTs were refluxed in a mixture of concentrated KOH and NaOH at 450°C and that could be coated with CeO₂ for the formation of 1D nanotubular structures [69, 70]. The formation of Ce-NT is assisted with different methods just like ultrasonication, facile solvothermal method, and boiling reflux of ethylene glycol [66, 67, 71–74]. The preparation of Ce-NT is composed of several tiny interconnected nanocrystallites of about 10 nm in size. The pretreatment of CNTs and calcination temperature have been considered as crucial factors for determining the formation of Ce-NT. Metal ion doping is a promising technique to control the properties of material. Doping of metallic ion on the nanomaterials can influence the surface morphology, nanocrystal shape, and growth in solution. Laha and Ryoo [75] prepared the mesoporous cerium using the hexagonal p6mm and cubic Ia3d symmetries of the silica templates. Later on, Shen et al. [76] used the similar types of ordered mesoporous silica KIT-6 as a hard template for the formation of mesoporous ceria and doped CuO structure by wet impregnation technique. Hydrothermal method is a significant approach to synthesize the hollow ceria microspheres with around 70–100 nm shell thickness. On the other hand, polystyrene latex spheres as the template can be an influence on the formation of hollow ceria nanospheres in the two-step procedure [77, 78]. Fuentes et al. [64] obtained the mixed Zr-Ce-NT oxide in the presence of polycarbonate film through the microwave radiation at 800 W. The ordered CeO₂ nanowire arrays embedded in anodic alumina membranes (AAM) fabrication are also a novel technique. La et al. [28] and Wu et al. [79] fabricated CeO₂ nanowires with a diameter of 60–70 nm by using AAM as templates. As it showed in Figure 2, anions and cations are conversely migrated into the hexagonally ordered nanochannels of the AAM and are reacted inside the channels to form 1D nanostructures.

3.3. Nontemplate Techniques. The solvent composition and the cerium source precursor are of importance in the final product morphology [14–18]. The reaction temperature, concentration of the cerium precursor, and reaction time have a significant influence on the yield of CeO₂ nanorods [14]. Tang and coworkers [16] successfully obtained needle-shaped nanostructures at an environment with a higher amount of oxidizing agent and a higher concentration of the precursor. The surface area of the 1D cerium oxide was increased significantly with the calcination, attributable to the higher-temperature treatment initiating the crystallization into the nanostructures. Urea has a significant effect for the formation of one-dimensional nanostructure [80, 81]. In the presence of urea, Hirano and Kato [81] showed that the angular nanocrystalline ceria with a cubic fluorite structure were hydrothermally synthesized in the presence of three different types of cerium source cerium(III) chloride (CeCl₃·7H₂O), and cerium(III) sulfate (Ce₂(SO₄)₃·8H₂O), cerium(III) nitrate (Ce(NO₃)₃·6H₂O). Later on, Wang and Lu [82] significantly investigated the

concentration effect of urea for the formation of CeOHCO₃ at 160°C. At the lower urea concentration (0.05 M), a small amount of ceria with angular CeOHCO₃ is found with lower pH value from the unused urea solution. After an increase of the urea solution concentration from 0.1 to 1 M, the morphology of the CeOHCO₃ changes to rhomboidal platelets to prismatic shape with simultaneously increasing the pH value from the unused urea solution. They further explained that deprotonation of hydrated metal ions is accelerated at elevated temperatures. Once protons are released into the solution, the pH value of the solution will be lowered after the hydrothermal reaction, but at the increasing of urea concentration, a large amount of carbonate and hydroxyl ion is dissociated onto the solution to increase the pH [82]. In addition, phase transformation from orthorhombic CeOHCO₃ to cubic ceria takes place at the calcination temperature 500°C. Similar calcination temperature, in the presence of 2 mL of 0.01 M Ce(NO₃)₃ in 40 mL of distilled water and 1.0 g of urea at 150°C for 12 h in the hydrothermal process, can form spindle-type ceria structure [80]. Spindle ceria nanomaterial is effective for optoelectrical application. Sequentially, morphology of metallic-doped ceria one-dimensional structure has the significant effect in optoelectrical and chemical conversion reaction. Huang et al. [20] synthesized Au/CeO₂ nanorods with the wet chemical reducing system in the presence of NaBH₄ solution, as a reducing agent. They also observed that hydrothermal temperatures influenced the nucleation and crystal growth of the CeO₂ nanorod. Morphological transformation of the nanorod was not completed with hydrothermal temperatures below 150°C at 5 or 10 M KOH solution. Consequently, higher-alkaline concentration provides thicker nanorod structures. Therefore, it would be considered that higher-alkaline concentration is involved in increasing the width of the nanostructures rather than the nucleation of length of the samples. Similar to this approach, it was also confirmed for the formation of different shape of cerium oxide 1D nanostructures with the presence of different concentrations of alkali [21]. At lower precipitation concentrations, the shape of nanopolyhedra, and at the higher concentrations, a mixture of rods and polyhedral shapes were provided, respectively. On the other hand, the precipitant mainly formed the cubic and rod-shaped structure at higher temperature and higher concentrations, respectively. Zhou et al. [19] obtained the CeO₂ nanorods of 15–30 nm in diameter and lengths of up to tens of micrometers by a precipitation method combined with the hydrothermal treatment with the presence of alkali solution. Ge et al. [83] successfully used the emulsion liquid membrane system to synthesize CeO₂ sponge-like rods with diameters of 170–810 nm and lengths of 5–10 μm, which were successfully fabricated through a route of liquid emulsion membrane followed by heat treatment. Recently, Macedo et al. [84] developed the ceria nanorod in the presence of higher concentration of NaOH (12 M) and in the presence of Ce₂(SO₄)₃·9H₂O at 135°C for 15 h. They observed that pretreatment of CeNR with H₂O₂ or *t*-BuOOH prior to reaction of PhEt with *t*-BuOOH leads to faster reaction than CeNR. He et al. [85] investigated

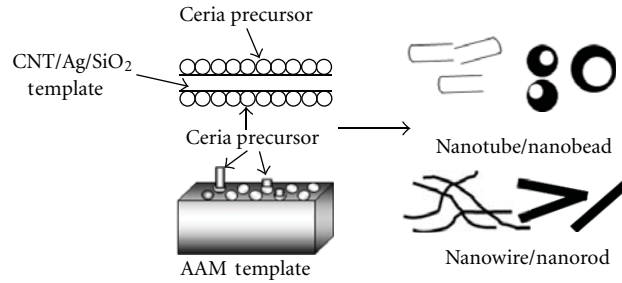


FIGURE 2: Schematic illustration for the formation of one-dimensional nanostructures using hard template methods.

the correlations between the shape and size of ceria nanostructure and the mechanical performance of composite with the presence of epoxy resin. They found that epoxy resins made with high-aspect-ratio ceria nanorods show the four-times-higher-impact strength up to 17.27 kJ m^{-2} , where size and shape are influenced to enhance the strength of composite materials. The one-step synthesis of CeO_2 nanorods is still a challenge. In this case, ultrasonication methods have been successfully used to prepare nanorods. In the previous reports, the synthesis methods of CeO_2 nanorods were relatively complicated and always needed high-temperature, high-pressure, or long-time treatments [22–24]. In addition, Qi et al. [22] synthesized the thicker CeO_2 microrod (200–250 nm in diameter and 600–1200 nm in length) by an ultrasonication process than surfactant-assisted hydrothermal method.

Recently, Gao et al. [25] approached the microwave-hydrothermal method for the facile, rapid synthesis of higher yields of 1D CeO_2 with average sizes of $\sim 1.6 \text{ nm}$ to $\sim 20 \text{ nm}$. Compared with a conventional hydrothermal method, the microwave-assisted hydrothermal method shows advantages of rapidity, convenience, and cost effectiveness and could be potentially extended to the synthesis of other nanoparticles and nanorods. On the other hand, Tang et al. [16] simply used the hydrothermal method to achieve nanowires with nonsurfactant-assisted method. They observed that the presence of acidic precipitant H_2O_2 with $0.1 \text{ M Ce}(\text{NO}_3)_3$ produces the nanowire and nanocubes, whereas a lower concentration of the precursor ($0.05 \text{ M Ce}(\text{NO}_3)_3$) formed only nanowire diameters of 20–70 nm and lengths up to $40 \mu\text{m}$ in the hydrothermal process at 250°C for 3 h. Furthermore, aggregated nanoneedles have been formed as the absence of oxidizing agent H_2O_2 . Nanowires were structurally uniform and single crystalline. The interplane distance in this research was obtained as 0.28 nm, corresponding to the separation between the (200) lattice planes of cubic CeO_2 . It is evident that complete and controlled conversion of CeO_2 nanostructures through templates is not readily achievable. Additionally, fabrication and removal of the template have been achieved as very troublesome techniques for the Ce-NT synthesis process. Therefore, the formation of 1D nanotubes with the absence of templates has been attractive owing to simple, quick, and economical considerations. On an important low-cost basis, Miao et al. [86] developed the procedure of ultrasound irradiations, in

order to prepare Ce-NT from ceria nanoparticles at room temperature. In addition, Dos Santos et al. [87] explained that the calcined temperature readily affected the crystallinity and morphology of the CeO_2 nanostructure. Thus, the development of a facile and controllable formation of Ce-NT with proper crystalline structure is of great significance.

One of the most notable characterizations of the fluorite Ce-NT has been recently developed by a hydrothermal method. Han et al. [88] synthesized the yellowish CeO_{2-x} nanotubes, nanowire, and nanoparticles in two steps. At the beginning, the samples were prepared at 100°C in the presence of 7 mL of 5% ammonia hydroxide solution and then aged at 0°C for 45 days. This procedure is time consuming. Tang et al. [89] proposed the lamellar rolling of the $\text{Ce}(\text{OH})_3$ crystal nanotubes through the alkali treatment of the trivalent ceria salt CeCl_3 at 120°C under an oxygen-free environment with the hydrothermal method. They observed that 1D Ce-NT was obtained from the annealing of $\text{Ce}(\text{OH})_3$ crystal nanotubes in the reducing atmosphere. Pan and coworkers [32] observe that cerium oxide nanorods are easily obtained under a higher concentration of alkali treatment (10–15 M) at room temperature to up to 100°C temperature with the presence of $\text{Ce}(\text{NO}_3)_3$ as a precursor. When $\text{Ce}(\text{NO}_3)_3$ is replaced by $(\text{NH}_4)_2\text{Ce}(\text{NO}_3)_6$, CeO_2 nanorods are not obtained. According to the LSW theory and analysis, nitrate from $(\text{NH}_4)_2\text{Ce}(\text{NO}_3)_6$ has noncomplexing characteristics for the formation of one-dimensional ceria nanostructure. In addition, they explained that accumulation of the Ce^{3+} ion for 72 h on the cerium oxide nanorod surface would provide Ce-NT in the hydrothermal condition around 100°C . As well, at increasing temperature, the deposition of Ce^{3+} ion occurred at the tip of the nanorod and formed the nanowire and subsequently nanocubes. It was also shown that a larger surface area was achieved by the lower-temperature nanorod preparation. However, this method is an effective way for the preparation of Ce-NT in the case of the template-free controlled conversion system.

Chen et al. [90] synthesized Ce-NT with a simple solid liquid interface reaction route in the absence of any surfactants by employing $\text{Ce}(\text{OH})\text{CO}_3$ nanorods as precursors. Recently, Wang et al. [91] synthesized the nanospheres, and nanowires, and nanorods can be obtained through a surfactant and template-free solution simply by varying the anionic composition or the type of counter ion, such as chloride, nitrate, and phosphate in solution before the hydrothermal

treatment. As a synthesis of hydrothermal method, Zhou et al. [92] converted CeO₂ nanorods into nanotubes in an acidic treatment like H₂O₂ solution assisted by ultrasonication. The converted Ce-NT has a higher reducible property, which was due to the higher activity of CeO₂ surface (100) than that of common surface (111) [92, 93]. In addition, CeO₂ nanorods consisted of Ce⁴⁺ as a surface material and Ce³⁺ as inside [92]. On the other side, Han et al. [88] obtained the opposite phenomenon, since the fraction of Ce³⁺ is significantly larger than that of CeO_{2-x} nanoparticles with the same diameter. Thus, Ce³⁺ ions remained on the surface of the 1D Ce-NT. Chen and coworkers [94], through the Kirkendall effect, obtained 1D Ce-NT in which Zr⁴⁺ ions may act as the catalyst to promote the diffusion rate of Ce³⁺/Ce⁴⁺ ions inside the nanorod as shown in Figure 3. According to a partial oxidation of Ce³⁺ ions and differential rate of diffusion between Ce⁴⁺ and Ce³⁺ ions inside the material, the metal hydroxide nanorods gradually decompose to form Zr_xCe_{1-x}O₂ nanotubes. Chen et al. [65] studied three different ways for the formation of ceria nanotube on the basis of the Kirkendall effect (denoted as K-type), template (T-type), and lamellar rolling (L-type). The K-type Ce-NT had been prepared by congregating Kirkendall voids, and subsequent calcinations were acquired in the presence of air at 600°C for 4 h. In addition, T-type and L-type nanotubes had been obtained without any calcination. Precipitant and the reaction temperature are implicated in the formation of the K-type ceria nanotube. Furthermore, Martin et al. [95] used the atomistic simulation techniques based on the Born model of solids to observe multilayer Ce-NT with a wall thickness of 5.5 nm and a lumen diameter of 4.8 nm. Besides, the 1D ceria nanostructure was achieved with the electrochemically synthesized route through change of the electric field, strength, and direction by Fu et al. [96]. They acquired the morphologies of ceria nanomaterials from nanoparticles and nanorods to nanowire by simply changing the potential direction and time of anodic oxidation. Tuning the ammonium acetate concentration through the precipitation method, Bugayeva and Robinson [97] controlled the particle size, shape, and agglomeration of the 1D nanowire. The hydrated CeO₂ nanowires as thin as 5 nm in diameter and nanoneedles with various aspect ratios were obtained via a chemical precipitation technique in the presence of ammonium acetate. However, Tang et al. [16] proposed and explained that the concentration of an oxidant such as H₂O₂ would significantly affect to impose the cone type or needle-like phenomenon in the 1D cerium structure.

4. Applications

In recent years, oxidation catalysts are receiving considerable attention because of their potential role in the environmentally important fuel cell technologies. As an important component in catalysts, ceria promote high oxygen storage capacity (OSC) and high oxygen ion conductivity. Several morphological structures of CeO₂ such as nanorod, nano-sponge single or multiwall, hollow structure, mesoporous, spindle have been investigated widely for the selective

oxidation of mainly carbon monoxide, nitrogen oxides, sulfur oxide, and so on, due to OSC of ceria.

4.1. Advantage of 1D Structured Cerium Oxide for Carbon-Monoxide Oxidation Reaction. The catalytic performance of the 1D CeO₂ nanomaterials is affected with the structure and surface area as shown in Table 1. As well, surface area, structural defects, and oxygen vacancy have a positive effect on CO oxidation [15]. Zhang et al. [2] have compared the two different kinds of 1D nanomaterials to exhibit the CO oxidation, where they derived that CeO₂ single/multiwall hollow microspheres may provide CO total conversion at 230°C and for bulk CeO₂ is 500°C, respectively. Hollow microspheres afford more available oxygen and oxygen deficiency for CO oxidation [1, 2, 99]. In addition, high catalytic activity on CO oxidation was obtained for CeO₂ single/multiwall hollow microspheres and consisted of similar activity at 240°C for T₁₀₀ in the second and the third runs, which revealed its excellent thermal stability and recycling performance [2]. Similar tendency of the CO oxidation was followed for the hollow nanobeads and hollow nanocubes [6, 99]. CNT templates in the CeO₂ hollow nanobeads may be formed by CeO_{2-x}C and thus increase the catalytic activity [99]. According to Chen et al. [6], the CO conversion of CeO₂ hollow nanocubes is 56% and almost 3.5 times higher than that of the CeO₂ powder at 270°C. They explained that the interconnected hollow structure enables better contact with the gas molecule owing to the existence of interior spaces: penetrable shell and that influenced to exhibit effective performance. The stability and recycling performance of CeO₂ catalyst are important factors for the practical applications. According to TEM analyses, they demonstrated that the hollow structure has not been collapsed at a high temperature (300°C), and the catalytic operation has been conducted after the reactor cooled down to room temperature, which demonstrated its excellent stability and recycling performance [1, 6]. On the other hand, the overall catalytic activity and the BET specific surface area are affected with the preparation method of the catalyst [18, 100]. Masui et al. [100] reported that the CeO₂/Al₂O₃ catalyst prepared by the microemulsion method shows higher activity for carbon monoxide oxidation although CeO₂/Al₂O₃ catalyst surface area is as low as that prepared by the coprecipitation method. Pan and coworkers [18] have explained that nanomaterials consist with similar BET-specific area are greatly influenced by the crystal surface to represent the catalytic activity. They also observed that CeO₂ nanorods, nanoplate, and nanotubes are exhibited with higher BET surface area: 52.5, 37.2, and 80.1 m²g⁻¹, respectively, in addition, nanoplates consisted of higher crystal surface (100) and that contributes to create enormous oxygen vacancies and thus favors the higher catalytic performance.

Most recently, Zhang et al. [11, 13, 101, 102] synthesized various ceria micro/nanostructures such as spheres, spindles, columns, spheres, and rods and then investigated the catalytic activity in the oxidation of carbon monoxide. Regarding the several types of nanostructures such as spindle, rod the effect of carbon monoxide oxidization of CeO₂

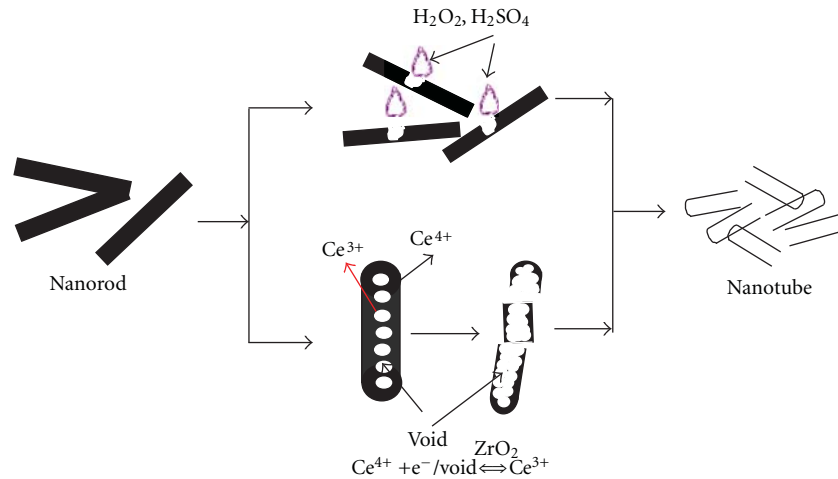


FIGURE 3: Schematic illustration of Kirkendall effect for the formation of one-dimensional structures.

TABLE 1: Carbon-monoxide oxidation onto several ceria nanostructures.

Sample	T_{50} ($^{\circ}C$)	T_{100} ($^{\circ}C$)	BET (m^2g^{-1})	Reference
Bulk Ceria	300–435	500	5–15	[9, 67]
Nanoparticle	220–305	300–380	30–115	[15, 19, 32, 51, 67]
Nanorod	190–290	205–345	50–128	[15, 18, 19, 32]
Nanotube	223–265	230–325	44–98	[2, 18, 32, 67]
Nanowire	245	N.A.	79.8	[32]
Nanocube/bead	240–315	300	87–115	[2, 6, 32, 51, 76]
Metal/ CeO_2 nanostructure	110–270	130–320	70–165	[9, 20, 76, 103]

“N.A.” denotes “not available”.

was revealed by Ho et al. [15]. The spindle-like sample shows the highest CO conversion rate $0.861 \mu\text{mol g}^{-1}\text{s}^{-1}$, which is almost 4.5 times higher than CeO_2 particles (as referred to), $0.189 \mu\text{mol g}^{-1}\text{s}^{-1}$. According to XRD analysis, they observed that the order of the lattice cell volume was strongly related to the degree of Ce^{4+} reduction and the extent of oxygen vacancy. Interestingly, the surface area and pore volume of the samples were significantly increased after calcinations and affected the CO oxidation. The same result for the effects of surface area was also demonstrated for the ceria nanorod and sponge nanorod [19, 83]. Zhou et al. [19] have attained that CeO_2 nanorods are three times more active than CeO_2 nanoparticles for CO oxidation and found that the T_{100} (the temperature at which the CO conversion is 100%) for the CeO_2 nanorods and CeO_2 nanoparticles catalysts approaches to 275 and $300^{\circ}C$, respectively. In addition, using CeO_2 sponge-like rods as a catalyst, the T_{100} is only $205^{\circ}C$, which shows that catalytic property of CeO_2 sponge-like rods has an advantage over that of CeO_2 nanorods and CeO_2 nanoparticles [83]. The sponge nanorod may provide a larger percentage of atoms onto the surface and would create structural defects and generate pronounced oxygen vacancies than nanorod or nanoparticles [19, 64, 83]. Similar tendency is also observed for the case of ceria nanotube [67], therefore it could provide the three times higher catalytical activity than bulk ceria and ceria nanoparticle.

Recently, Pan et al. [32] explained that 1D ceria nanorods synthesized at a low temperature with enough aging time possess a large BET-specific area and thus provide a perfect crystalline form and have a high performance for CO oxidation. The physical and chemical properties of ceria could be tuned by doping with different metals to obtain low-temperature reducibility (Au, Cu, Pr, and Sn). Metallic doping with tetravalent cations, (such as Zr and Hf) onto the ceria nanostructures, may enhance the OSC and consequently archive high ionic conductivities with trivalent cations (such as La, Sm, Gd, and Y) [8, 9, 103]. Sunder and Deevi [8] observed that the catalytic activity of the CO oxidation with Cu-CeO nanocomposite may significantly increase due to the addition of CuO. A similar research was also observed by Sun et al. [9]. They have seen that the quickly accelerated CO conversion starts below $120^{\circ}C$, and complete CO oxidation is achieved at about $220^{\circ}C$ over the catalysts containing more than 10 wt% CuO onto the 3-D flower-like CeO_2 nanomaterials. The performance of the flower-like CeO_2 microspheres loaded with 20 wt% CuO became worse, and 15 wt% CuO sample had the best catalytic activity for CO oxidation. It may be affected with higher content of the CuO or surface-volume ratio of the catalyst [8, 9]. However, Shen et al. [76] observed that up to 20% of molar ratio CuO loaded onto mesoporous ceria nanostructure has higher catalytic activity for CO oxidation.

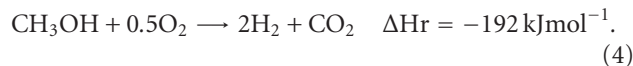
The role of the support and the oxygen supply for the catalytic reaction remains controversial. Although it is accepted that factors, such as gold particle size, synthesis method, pretreatment conditions, and support, influence the reactivity of the supported gold catalysts the nature of the active sites and the reaction mechanism for CO oxidation are still subjects of debate. According to Raman spectroscopic analyses, Guzman et al. [103] indicated that nanocrystalline CeO₂ in the presence of gold catalyst, supplies reactive oxygen in the form of surface η^1 superoxide species and peroxide adspecies. The conventionally precipitated CeO₂ tends to stabilize O₂^{δ-} ($0 < \delta < 1$) adspecies and molecular O₂ onto the surface. Thus, both cationic and metallic gold are attributed in nanocrystalline CeO₂ to accelerate CO oxidation at low temperatures. The formation of the surface chemisorbed oxygen species can be facilitated by defects in the catalyst structure. Therefore, Sun et al. [9] demonstrated the 2.77 wt%, of Au-loaded flower-like CeO₂ microsphere catalysts highly active with CO gas conversion into CO₂ above 80% at room temperature, and T₁₀₀ is observed at 130°C. On the other hand, around 81% CO conversion is achieved at 220°C for Au/CeO₂ nanorod as a catalyst, while only 20–22% CO conversion is obtained at the same temperature for pure CeO₂ nanorods and nanoparticles as a catalyst [20]. The catalytic activities of Au/CeO₂ flower, nanorods, and nanoparticles are much higher than those of pure CeO₂ nanorods and nanoparticles, consequently [9, 20].

4.2. Advantage of One-Dimensional Cerium Oxide for CH₃OH/SRM Reaction. Several researchers to optimize the catalysts for a carbon monoxide oxidation reaction have investigated the effect of different structure of ceria nanomaterials and the impact of metal loading. In addition, the ceria and doped ceria nanomaterial would also be used for the SRM reaction, whereas the preparation procedure, size, and shape are effectively influenced by the SRM reaction. Several synthesis techniques have been applied to obtain the different structure of ceria [98, 104–107]. Porosity and surface structure of the ceria nanomaterials facilitate to obtain the utmost performance for the catalytic reaction. These properties can also be changed by the concentration differences for presols and the treatment procedures of the drying and calcinations temperatures. There are three process alternatives to produce hydrogen through the conversion of methanol: (1) decomposition, (2) partial oxidation and (3) steam reforming. Different reactions were involved in a reactor with different enthalpies to achieve hydrogen-rich gas from methanol at standard condition [98, 104–106]. The decomposition reaction is the simplest process from a chemical point of view as solely methanol is used as feedstock as shown below [98, 104–107]:

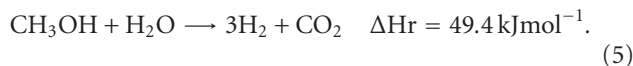


However, the reaction is strongly endothermic, which means that it requires a lot of energy for operating. Furthermore, the decomposition yields product gas containing up to 67% of hydrogen and 33% of carbon monoxide. The

high content of the CO clean-up system is regarded to be the most complicated part in the fuel cell system. Because of these drawbacks, the decomposition of methanol is found to be unsuitable for fuel cell applications. This shortcoming could be overcome with the CO oxidation through the promising catalyst ceria. In contrast to the decomposition reaction, partial oxidation is a fast and exothermic reaction as represented below:



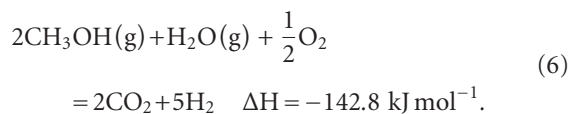
Several studies on this reaction have been published in the last few years [104]. The advantage of this process with respect to the exothermic nature is that an additional energy supply for the reaction is not necessary. However, the exothermic behavior should be taken into account when designing the reactor. The fast increase of temperature in the reactor can form hot spots, which can cause the deactivation of the oxidation catalyst through sintering of the metal particles. The hydrogen concentration up to 67% in a product stream can be achieved when methanol is partially oxidized with pure oxygen in the feed. The oxygen required for the automobile application would most likely be supplied from air. Due to the high content of nitrogen in the air, this causes dilution of the product gas with nitrogen. As a result, the maximum theoretical hydrogen content in such a system is lowered to 41%. The decrease of the hydrogen content in the product stream influences strongly the performance of the electricity production in fuel cell [104]. The steam reforming of methanol (SRM) is known as a reverse reaction of methanol synthesis as follows:



SRM is considered to be the most favorable process of hydrogen production in comparison to the decomposition and partial oxidation of methanol. This is because of the ability to produce gas with high hydrogen concentration (75%) and high selectivity for carbon dioxide. SRM is an endothermic reaction. Another additional alternative to produce hydrogen from methanol is to combine the partial oxidation with the steam reforming. The advantage of this process is that heat requirement for the reaction can be supplied by the reaction itself (autothermal reaction). However, the concentration of hydrogen in gas product and methanol conversion is lower than that in the SRM [108]. Yi and coworkers found that small amount of gold-doped one-dimensional ceria nanomaterial was significantly more active and selective towards CO₂ at temperatures below 250°C [109]. Strong-bonded Au_n-O-Ce species are the active sites for the SRM reaction, and the apparent activation energies are not dependent on the shape of the ceria. The catalytic properties of these catalysts, such as activity, CO₂ selectivity, were studied by means of a fixed bed reactor. In order to evaluate the catalytic properties of the different-dimensional ceria and dope catalysts, a commercial ceria catalyst was used as a reference. A kinetic study for the synthesis of the different structure of the ceria nanomaterial is also performed in this

work. They pointed out that the 1% Au-ceria (rod) catalyst shows excellent activity for the water-gas shift reaction, comparable to Au-ceria nanopowders, including Au-ceria with a high surface area of $250 \text{ m}^2 \text{ g}^{-1}$, while the Au-ceria (cube) is inactive.

The SRM produces a relatively small amount of carbon monoxide at low temperatures whereas carbon monoxide is known to be very poisonous for Pt catalysts in a proton exchange membrane fuel cell (PEMFC) system [113]. In addition, autothermal reforming of the methanol (ATRM) process leads to produce a higher amount of hydrogen and consists with CO as a by-product which has the negative impact on PEMFC operation. Therefore, there is great interest in developing highly selective catalysts as follows:



The catalytic reaction for SRM and ATRM is generally based on copper or palladium, where Pd has consisted of higher thermal stability and the production of large content of CO with lower selectivity from methanol decomposition. On the other hand, Cu-based catalyst has consisted of low cost, higher reactivity, and selectivity [114, 115]. Copper catalyst is effectively dispersed in ZnO or ZnO/Al₂O₃ to generate mesoporosity, with high-surface area and good thermal stability, exhibited interesting catalytic activity in the CO preferential oxidation reaction. Thus, CuO/ZnO-Al₂O₃ is one of the most used catalysts for hydrogen generation by ATRM in a microchannel reactor [116, 117]. Cerium-promoted copper catalyst existed for the recovery of hydrogen from methanol with the optimization of carbon monoxide concentration [118]. Furthermore, ceria hindered Cu sintering in Cu/Al₂O₃ catalysts and increased thermal stability and catalytical reactivity [112]. According to our recent work in Figure 4 and Table 2 [98], we observe that ceria accompanied with the copper metal complexes formation is influenced by the catalytic activities on the ATRM reaction in the microchannel reactor to generate hydrogen for further application of a fuel cell system, where as-synthesized homogeneous sol was prepared by adding 20 g as-synthesized catalyst (CuO 40%, ZnO 50%, and Al₂O₃ 10%) to form the catalyst slurry (S20) and combined with the CeO₂ sol (B) 1 to 10 wt.% of solid content, respectively. Ceria promote to reduce the poisonous carbon monoxide to carbon-dioxide. According to the XRD and XPS data analyses, we confirmed that catalyst content copper species strongly interact with CeO₂ to form Cu–O–Ce. Moreover, a hydrogen production rate of 2.16 Lh^{-1} is obtained, and the corresponding methanol conversion is 100% at 270°C for ceria sol washcoat catalysts. After the activation of the catalyst (S20-B2), methanol started to decompose, and the conversion was above 95% at 240°C. In addition, a higher temperature was required for higher methanol conversion but decreasing with the increase of feed flow rate and was related with the steam to carbon (methanol) ratio [107, 111, 119]. According to the Seo et al. [107], methanol conversion was achieved 90% at 260°C, and the feed flow rate was

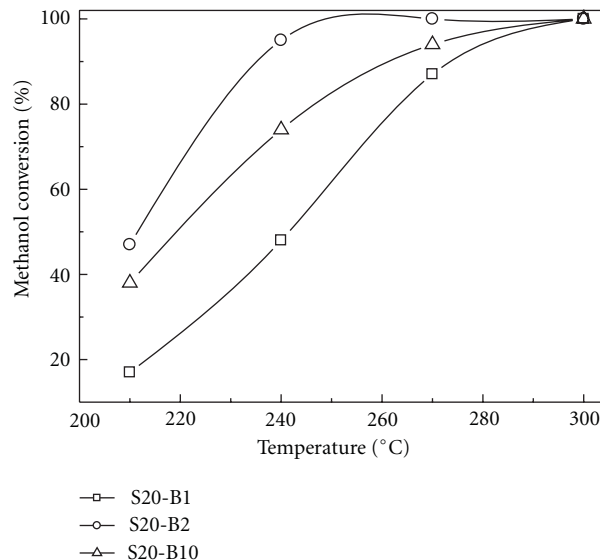


FIGURE 4: Methanol conversion of Cu/ZnO-Al₂O₃ catalyst with CeO₂ binder washcoats of (a) S20-B1, (b) S20-B2, and (c) S20-B10, respectively, for the steam reforming of methanol in a microreactor (steam/MeOH = 1.3; WHSV = $16.2 \text{ g}_{\text{MeOH}} \text{ h}^{-1} \text{ g}_{\text{cat}}^{-1}$; loading weight of washcoat catalyst = 20 mg/plate) [98].

$0.2 \text{ cm}^3 \text{ min}^{-1}$. A hydrogen production rate of 2.16 Lh^{-1} was obtained at a feed rate of methanol liquid mixtures of $0.05\text{--}0.2 \text{ mL min}^{-1}$ with a WHSV of $16.2 \text{ g}_{\text{MeOH}} \text{ h}^{-1} \text{ g}_{\text{cat}}^{-1}$. Moreover, the selectivity of hydrogen and carbon dioxide was high enough, and a typical dry gas composition of the present system was 73–74% H₂, 24–25% CO₂, and <0.1% CO gas products, respectively. Nevertheless, $T_r > 260 \pm 10^\circ \text{C}$ were also required in the cases to achieve high methanol conversion [112, 120–124]. The addition of ceria caused the synergistic effect to give the activity enhancement. However, methanol conversion was decreased to 95% at 270°C for S20-B10. Avgouropoulos and coworkers [110] studied the effect of methanol decomposition (MD), SRM, and ATRM reaction on the noble metal/ceria catalysts process. They observed that catalytic activity increases in the order of $\text{Rh} < \text{Pt} < \text{Pd/Ceria}$ for all three processes, where H₂ and CO are the major products, while ethylene, ethane, and propylene are formed only over Rh/CeO₂ at $T \geq 270^\circ \text{C}$ with selectivities lower than 0.5%. The H₂ yield and CO selectivity increase with the temperature. Due to the morphology and porosity, BET surface area significantly affects the catalytic activity. This confirms that ceria-based catalyst is suitable for ATRM reaction with the integrated PEMFC application on energy generation.

5. Conclusions

In this paper, we have shown how one-dimensional ceria nanomaterial synthesizes on the template and nontemplate methods. The key issue for large scale of one-dimensional ceria nanostructure for further catalytical applications is the development of the synthesis methods that implies for

TABLE 2: Comparison of the MD/SRM/ATRM performances over different metal-doped CeO₂ catalysts in literatures.

Catalyst	S/C ^a	WHSV ^b (GHSV) ^b	S _{CO} ^c (%)	T ^d (°C)	Reference
Pt/CeO ₂ ^e	N.A.	(42,000)	1.41	270 (100)	[110]
Pd/CeO ₂ ^e	N.A.	(42,000)	0.589	270 (100)	[110]
Rh/CeO ₂ ^e	N.A.	(42,000)	44.6	270 (100)	[110]
Pt/CeO ₂ ^f	1.5	(42,000)	0.86	270 (100)	[110]
Pd/CeO ₂ ^f	1.5	(42,000)	20.46	250 (100)	[110]
Rh/CeO ₂ ^f	1.5	(42,000)	19.89	270 (100)	[110]
Ceria (nanorods) ^f	1.3	(42,000)	N.A.	450 (95)	[109, 111]
Ceria (nanocubes) ^f	1.3	(42,000)	N.A.	500 (95)	[109, 111]
1% Au-ceria (rod) ^f	1.3	(42,000)	N.A.	300 (95)	[109, 111]
1% Au-ceria (cube) ^f	1.3	(42,000)	N.A.	380 (95)	[109, 111]
Pt/CeO ₂ ^g	1.5	(42,000)	0.729	270 (100)	[110]
Pd/CeO ₂ ^g	1.5	(42,000)	22.27	250 (100)	[110]
Rh/CeO ₂ ^g	1.5	(42,000)	2.52	270 (100)	[110]
Cu ₄₀ Zn ₅₀ Al ₁₀ -CeO ₂ ^g	1.3	16.2	0.58	300 (95)	[98, 105]
Cu ₄₀ Zn ₅₀ Al ₁₀ -CeO ₂ ^g	1.3	16.2	0.40	240 (95)	[98, 105]
Cu ₄₀ Zn ₅₀ Al ₁₀ -CeO ₂ ^g	1.3	16.2	0.35	270 (95)	[98, 105]
Cu ₅₀ Zn ₃₃ Al ₈ -Al ₂ O ₃ ^g	1.1	54.0	2.90	260 (99)	[98, 105]
Cu ₅₀ Zn ₃₃ Al ₈ -Al ₂ O ₃ ^g	1.5	14.8	1.10	270 (80)	[98, 105]
Cu ₆₅ Zn ₂₈ Ce ₇ -Al ₂ O ₃ ^g	1.3	8.3	2.05	292 (97)	[98, 105, 112]
Cu ₄₈ Zn ₄₈ Ce ₄ -Al ₂ O ₃ ^g	1.3	8.3	1.30	292 (98)	[98, 105, 112]
Cu ₃₈ Zn ₅₈ Ce ₄ -Al ₂ O ₃ ^g	1.3	8.3	1.60	292 (91)	[98, 105, 112]
Cu ₄₈ Zn ₄₈ Ce ₄ -Al ₂ O ₃ ^g	1.3	8.3	2.10	292 (88)	[98, 105, 112]

S/C^a: steam-to-carbon ratio; WHSV^b: weight hourly space velocity in mass methanol per time and mass of catalyst ($\text{g}_{\text{MeOH}} \text{h}^{-1} \text{g}_{\text{cat}}^{-1}$); (GHSV)^b: (gas hourly space velocity at NTP (h^{-1})); S_{CO}^c (%): CO selectivities; T^d (°C): temperatures required for conversion of methanol at different percentage; ^e: methanol decomposition; ^f: steam reforming reaction; ^g: autothermal reforming of methanol; N.A.: not available.

the production of one-dimensional structure with large-surface areas. Current investigation through this work directed towards the application of ceria nanomaterials readily involved the size, shape, and structure, which are likely to display higher-catalytic phenomenon.

Acknowledgment

The financial supports of the National Science Council (Contract no. NSC-97-2221-E-155-005) of Taiwan are gratefully acknowledged.

References

- [1] S. S. Deshmukh, M. Zhang, V. I. Kovalchuk, and J. L. D'Itri, "Effect of SO₂ on CO and C₃H₆ oxidation over CeO₂ and Ce_{0.75}Zr_{0.25}O₂," *Applied Catalysis B*, vol. 45, no. 2, pp. 135–145, 2003.
- [2] Y. Zhang, T. Cheng, Q. Hu, Z. Fang, and K. Han, "Study of the preparation and properties of CeO₂ single/multiwall hollow microspheres," *Journal of Materials Research*, vol. 22, no. 6, pp. 1472–1478, 2007.
- [3] M. Y. Cui, J. X. He, N. P. Lu et al., "Morphology and size control of cerium carbonate hydroxide and ceria micro/nanostructures by hydrothermal technology," *Materials Chemistry and Physics*, vol. 121, no. 1-2, pp. 314–319, 2010.
- [4] Z. Sun, H. Zhang, G. An, G. Yang, and Z. Liu, "Supercritical CO₂-facilitating large-scale synthesis of CeO₂ nanowires and their application for solvent-free selective hydrogenation of nitroarenes," *Journal of Materials Chemistry*, vol. 20, no. 10, pp. 1947–1952, 2010.
- [5] Z. Guo, F. Jian, and F. Du, "A simple method to controlled synthesis of CeO₂ hollow microspheres," *Scripta Materialia*, vol. 61, no. 1, pp. 48–51, 2009.
- [6] G. Chen, C. Xu, X. Song, S. Xu, Y. Ding, and S. Sun, "Template-free synthesis of single-crystalline-like CeO₂ hollow nanocubes," *Crystal Growth and Design*, vol. 8, no. 12, pp. 4449–4453, 2008.
- [7] P. Fornasiero, R. Dimonte, G. R. Rao et al., "Rh-loaded CeO₂-ZrO₂ solid-solutions as highly efficient oxygen exchangers: dependence of the reduction behavior and the oxygen storage capacity on the structural-properties," *Journal of Catalysis*, vol. 151, no. 1, pp. 168–177, 1995.
- [8] R. S. Sundar and S. Deevi, "CO oxidation activity of Cu-CeO₂ nano-composite catalysts prepared by laser vaporization and controlled condensation," *Journal of Nanoparticle Research*, vol. 8, no. 3-4, pp. 497–509, 2006.
- [9] C. Sun, H. Li, and L. Chen, "Study of flowerlike CeO₂ microspheres used as catalyst supports for CO oxidation reaction," *Journal of Physics and Chemistry of Solids*, vol. 68, no. 9, pp. 1785–1790, 2007.
- [10] H. Mai, D. Zhang, L. Shi, T. Yan, and H. Li, "Highly active Ce_{1-x}Cu_xO₂ nanocomposite catalysts for the low

- temperature oxidation of CO," *Applied Surface Science*, vol. 257, no. 17, pp. 7551–7559, 2011.
- [11] D. Zhang, H. Mai, L. Huang, and L. Shi, "Pyridine-thermal synthesis and high catalytic activity of CeO₂/CuO/CNT nanocomposites," *Applied Surface Science*, vol. 256, no. 22, pp. 6795–6800, 2010.
- [12] K. S. Lin and S. Chowdhury, "Synthesis, characterization, and application of 1-D cerium oxide nanomaterials: a review," *International Journal of Molecular Sciences*, vol. 11, no. 9, pp. 3226–3251, 2010.
- [13] F. Niu, D. Zhang, L. Shi et al., "Facile synthesis, characterization and low-temperature catalytic performance of Au/CeO₂ nanorods," *Materials Letters*, vol. 63, no. 24-25, pp. 2132–2135, 2009.
- [14] C. Sun, H. Li, H. Zhang, Z. Wang, and L. Chen, "Controlled synthesis of CeO₂ nanorods by a solvothermal method," *Nanotechnology*, vol. 16, no. 9, pp. 1454–1463, 2005.
- [15] C. Ho, J. C. Yu, T. Kwong, A. C. Mak, and S. Lai, "Morphology-controllable synthesis of mesoporous CeO₂ nano- and microstructures," *Chemistry of Materials*, vol. 17, no. 17, pp. 4514–4522, 2005.
- [16] B. Tang, L. Zhuo, J. Ge, G. Wang, Z. Shi, and J. Niu, "A surfactant-free route to single-crystalline CeO₂ nanowires," *Chemical Communications*, no. 28, pp. 3565–3567, 2005.
- [17] A. Vantomme, Z. Y. Yuan, G. Du, and B. L. Su, "Surfactant-assisted large-scale preparation of crystalline CeO₂ nanorods," *Langmuir*, vol. 21, no. 3, pp. 1132–1135, 2005.
- [18] C. Pan, D. Zhang, and L. Shi, "CTAB assisted hydrothermal synthesis, controlled conversion and CO oxidation properties of CeO₂ nanoplates, nanotubes, and nanorods," *Journal of Solid State Chemistry*, vol. 181, no. 6, pp. 1298–1306, 2008.
- [19] K. Zhou, X. Wang, X. Sun, Q. Peng, and Y. Li, "Enhanced catalytic activity of ceria nanorods from well-defined reactive crystal planes," *Journal of Catalysis*, vol. 229, no. 1, pp. 206–212, 2005.
- [20] P. X. Huang, F. Wu, B. L. Zhu et al., "CeO₂ nanorods and gold nanocrystals supported on CeO₂ nanorods as catalyst," *Journal of Physical Chemistry B*, vol. 109, no. 41, pp. 19169–19174, 2005.
- [21] H. X. Mai, L. D. Sun, Y. W. Zhang et al., "Shape-selective synthesis and oxygen storage behavior of ceria nanopolyhedra, nanorods, and nanocubes," *Journal of Physical Chemistry B*, vol. 109, no. 51, pp. 24380–24385, 2005.
- [22] R. J. Qi, Y. J. Zhu, G. F. Cheng, and Y. H. Huang, "Sonochemical synthesis of single-crystalline CeOHCO₃ rods and their thermal conversion to CeO₂ rods," *Nanotechnology*, vol. 16, no. 11, pp. 2502–2506, 2005.
- [23] D. E. Zhang, X. M. Ni, H. G. Zheng, X. J. Zhang, and J. M. Song, "Fabrication of rod-like CeO₂: characterization, optical and electrochemical properties," *Solid State Sciences*, vol. 8, no. 11, pp. 1290–1293, 2006.
- [24] D. Zhang, H. Fu, L. Shi et al., "Synthesis of CeO₂ nanorods via ultrasonication assisted by polyethylene glycol," *Inorganic Chemistry*, vol. 46, no. 7, pp. 2446–2451, 2007.
- [25] F. Gao, Q. Lu, and S. Komarneni, "Fast synthesis of cerium oxide nanoparticles and nanorods," *Journal of Nanoscience and Nanotechnology*, vol. 6, no. 12, pp. 3812–3819, 2006.
- [26] Q. Cui, X. Dong, J. Wang, and M. Li, "Direct fabrication of cerium oxide hollow nanofibers by electrospinning," *Journal of Rare Earths*, vol. 26, no. 5, pp. 664–669, 2008.
- [27] F. Gu, Z. Wang, D. Han, C. Shi, and G. Guo, "Reverse micelles directed synthesis of mesoporous ceria nanostructures," *Materials Science and Engineering B*, vol. 139, no. 1, pp. 62–68, 2007.
- [28] R. J. La, Z. A. Hu, H. L. Li, X. L. Shang, and Y. Y. Yang, "Template synthesis of CeO₂ ordered nanowire arrays," *Materials Science and Engineering A*, vol. 368, no. 1-2, pp. 145–148, 2004.
- [29] G. J. Wilson, A. S. Matijasevich, D. R. G. Mitchell, J. C. Schulz, and G. D. Will, "Modification of TiO₂ for enhanced surface properties: finite ostwald ripening by a microwave hydrothermal process," *Langmuir*, vol. 22, no. 5, pp. 2016–2027, 2006.
- [30] M. Halder, "Determination of the critical micellar concentration (CMC) of a cationic micelle from stokes shift data," *The Chemical Educator*, vol. 12, no. 1, pp. 33–36, 2007.
- [31] R. J. Hunter, *Fundamentals of Colloid Science*, vol. 1-2, Clarendon, Oxford, UK, 1989.
- [32] C. Pan, D. Zhang, L. Shi, and J. Fang, "Template-free synthesis, controlled conversion, and CO oxidation properties of CeO₂ nanorods, nanotubes, nanowires, and nanocubes," *European Journal of Inorganic Chemistry*, no. 15, pp. 2429–2436, 2008.
- [33] S. Yang and L. Gao, "Controlled synthesis and self-assembly of CeO₂ nanocubes," *Journal of the American Chemical Society*, vol. 128, no. 29, pp. 9330–9331, 2006.
- [34] P. W. Atkins, *Physical Chemistry*, Freeman, 1998.
- [35] K. Kalyanasundaram, *Photochemistry in Microheterogeneous Systems*, 1987.
- [36] D. Terribile, A. Trovarelli, J. Llorca, C. De Leitenburg, and G. Dolcetti, "The synthesis and characterization of mesoporous high-surface area ceria prepared using a hybrid organic/inorganic route," *Journal of Catalysis*, vol. 178, no. 1, pp. 299–308, 1998.
- [37] M. Yada, S. Sakai, T. Torikai, T. Watari, S. Furuta, and H. Katsuki, "Cerium compound nanowires and nanorings templated by mixed organic molecules," *Advanced Materials*, vol. 16, no. 14, pp. 1222–1226, 2004.
- [38] C. Sun, H. Li, Z. Wang, L. Chen, and X. Huang, "Synthesis and characterization of polycrystalline CeO₂ nanowires," *Chemistry Letters*, vol. 33, no. 6, pp. 662–663, 2004.
- [39] L. Yan, X. Xing, R. Yu, J. Deng, J. Chen, and G. Liu, "Facile alcoholthermal synthesis of large-scale ceria nanowires with organic surfactant assistance," *Physica B*, vol. 390, no. 1-2, pp. 59–64, 2007.
- [40] R. Yang and L. Guo, "Synthesis of cubic fluorite CeO nanowires," *Journal of Materials Science*, vol. 40, pp. 1305–1307, 2005.
- [41] D. Zhang, L. Huang, J. Zhang, and L. Shi, "Facile synthesis of ceria rhombic microplates," *Journal of Materials Science*, vol. 43, no. 16, pp. 5647–5650, 2008.
- [42] Z. Guo, F. Du, G. Li, and Z. Cui, "Synthesis and characterization of single-crystal Ce(OH)CO₃ and CeO₂ triangular microplates," *Inorganic Chemistry*, vol. 45, no. 10, pp. 4167–4169, 2006.
- [43] C. S. Riccardi, R. C. Lima, M. L. dos Santos, P. R. Bueno, J. A. Varela, and E. Longo, "Preparation of CeO₂ by a simple microwave-hydrothermal method," *Solid State Ionics*, vol. 180, no. 2-3, pp. 288–291, 2009.
- [44] Y. Ikuma, H. Oosawa, E. Shimada, and M. Kamiya, "Effect of microwave radiation on the formation of Ce₂O(CO₃)₂·H₂O in aqueous solution," *Solid State Ionics*, vol. 151, no. 1-4, pp. 347–352, 2002.
- [45] S. Komarneni, Q. H. Li, and R. Roy, "Microwave-hydrothermal processing for synthesis of layered and network

- phosphates," *Journal of Materials Chemistry*, vol. 4, no. 12, pp. 1903–1906, 1994.
- [46] S. Komarneni, R. Pidugu, Q. H. Li, and R. Roy, "Microwave-hydrothermal processing of metal powders," *Journal of Materials Research*, vol. 10, no. 7, pp. 1687–1692, 1995.
- [47] S. Komarneni, R. Roy, and Q. H. Li, "Microwave-hydrothermal synthesis of ceramic powders," *Materials Research Bulletin*, vol. 27, no. 12, pp. 1393–1405, 1992.
- [48] C. H. Lu and H. C. Wang, "Formation and microstructural variation of cerium carbonate hydroxide prepared by the hydrothermal process," *Materials Science and Engineering B*, vol. 90, no. 1-2, pp. 138–141, 2002.
- [49] Y. Tao, F. H. Gong, H. Wang, H. P. Wu, and G. L. Tao, "Microwave-assisted preparation of cerium dioxide nanocubes," *Materials Chemistry and Physics*, vol. 112, no. 3, pp. 973–976, 2008.
- [50] R. Yang and L. Guo, "Synthesis of the nanotubular cubic fluorite CeO₂," *Chinese Journal of Inorganic Chemistry*, vol. 20, no. 2, pp. 152–158, 2004.
- [51] S. C. Kuiry, S. D. Patil, S. Deshpande, and S. Seal, "Spontaneous self-assembly of cerium oxide nanoparticles to nanorods through supraaggregate formation," *Journal of Physical Chemistry B*, vol. 109, no. 15, pp. 6936–6939, 2005.
- [52] M. Lundberg, B. Skårman, F. Cesar, and L. Reine Wallenberg, "Mesoporous thin films of high-surface-area crystalline cerium dioxide," *Microporous and Mesoporous Materials*, vol. 54, no. 1-2, pp. 97–103, 2002.
- [53] J. H. Son, S. W. Kim, D. S. Bae et al., "Synthesis and characterization of CeO₂-doped SiO₂ nanoparticles by a reverse micelle and sol-gel processing," *Materials Science and Engineering A*, vol. 498, no. 1-2, pp. 2–4, 2008.
- [54] L. Qian, J. Zhu, W. Du, and X. Qian, "Solvothermal synthesis, electrochemical and photocatalytic properties of monodispersed CeO₂ nanocubes," *Materials Chemistry and Physics*, vol. 115, no. 2-3, pp. 835–840, 2009.
- [55] A. Bouchara, G. J. D. A. Soler-Illia, J. Y. Chane-Ching, and C. Sanchez, "Nanotectonic approach of the texturation of CeO₂ based nanomaterials," *Chemical Communications*, no. 11, pp. 1234–1235, 2002.
- [56] X. Y. Zhang, T. W. Wang, W. Q. Jiang, D. Wu, L. Liu, and A. H. Duan, "Preparation and characterization of three-dimensionally ordered crystalline macroporous CeO₂," *Chinese Chemical Letters*, vol. 16, no. 8, pp. 1109–1112, 2005.
- [57] D. Andreescu, E. Matijević, and D. V. Goia, "Formation of uniform colloidal ceria in polyol," *Colloids and Surfaces A*, vol. 291, no. 1-3, pp. 93–100, 2006.
- [58] N. Uekawa, M. Ueta, Y. J. Wu, and K. Kakegawa, "Synthesis of CeO₂ spherical fine particles by homogeneous precipitation method with polyethylene glycol," *Chemistry Letters*, no. 8, pp. 854–855, 2002.
- [59] N. Uekawa, M. Ueta, Y. J. Wu, and K. Kakegawa, "Characterization of CeO₂ fine particles prepared by the homogeneous precipitation method with a mixed solution of ethylene glycol and polyethylene glycol," *Journal of Materials Research*, vol. 19, no. 4, pp. 1087–1092, 2004.
- [60] Z. Yang, L. Liu, H. Liang, H. Yang, and Y. Yang, "One-pot hydrothermal synthesis of CeO₂ hollow microspheres," *Journal of Crystal Growth*, vol. 312, no. 3, pp. 426–430, 2010.
- [61] J. M. Herrmann, C. Hoang-Van, L. Dibansa, and R. Harivololona, "An in situ electrical conductivity study of a CeO₂ aerogel supported palladium catalyst in correlation with the total oxidation of propane," *Journal of Catalysis*, vol. 159, no. 2, pp. 361–367, 1996.
- [62] C. Laberty-Robert, J. W. Long, E. M. Lucas et al., "Sol-gel-derived ceria nanoarchitectures: synthesis, characterization, and electrical properties," *Chemistry of Materials*, vol. 18, no. 1, pp. 50–58, 2006.
- [63] J. L. Gasser-Ramirez, B. C. Dunn, D. W. Ramirez et al., "A simple synthesis of catalytically active, high surface area ceria aerogels," *Journal of Non-Crystalline Solids*, vol. 354, no. 52–54, pp. 5509–5514, 2008.
- [64] R. O. Fuentes, L. M. Acuña, M. G. Zimic et al., "Formation and structural properties of Ce-Zr mixed oxide nanotubes," *Chemistry of Materials*, vol. 20, no. 23, pp. 7356–7363, 2008.
- [65] G. Chen, S. Sun, X. Sun, W. Fan, and T. You, "Formation of CeO₂ nanotubes from Ce(OH)CO₃ nanorods through kirkendall diffusion," *Inorganic Chemistry*, vol. 48, no. 4, pp. 1334–1338, 2009.
- [66] D. Zhang, H. Fu, L. Shi, J. Fang, and Q. Li, "Carbon nanotube assisted synthesis of CeO₂ nanotubes," *Journal of Solid State Chemistry*, vol. 180, no. 2, pp. 654–660, 2007.
- [67] J. Fang, Z. Cao, D. Zhang, X. Shen, W. Ding, and L. Shi, "Preparation and CO conversion activity of ceria nanotubes by carbon nanotubes templating method," *Journal of Rare Earths*, vol. 26, no. 2, pp. 153–157, 2008.
- [68] D. Zhang, C. Pan, J. Zhang, and L. Shi, "Solvothermal synthesis of necklace-like carbon nanotube/ceria composites," *Materials Letters*, vol. 62, no. 23, pp. 3821–3823, 2008.
- [69] Y. Li, J. Ding, J. Chen et al., "Preparation of ceria nanoparticles supported on carbon nanotubes," *Materials Research Bulletin*, vol. 37, no. 2, pp. 313–318, 2002.
- [70] J. Wei, J. Ding, X. Zhang et al., "Coated double-walled carbon nanotubes with ceria nanoparticles," *Materials Letters*, vol. 59, no. 2-3, pp. 322–325, 2005.
- [71] D. Zhang, L. Shi, H. Fu, and J. Fang, "Ultrasonic-assisted preparation of carbon nanotube/cerium oxide composites," *Carbon*, vol. 44, no. 13, pp. 2853–2855, 2006.
- [72] H. X. Fu, D. S. Zhang, L. Y. Shi, and J. H. Fang, "Synthesis and characterization of cerium oxide nanotubes based on carbon nanotubes," *Gaodeng Xuexiao Huaxue Xuebao*, vol. 28, no. 4, pp. 617–620, 2007.
- [73] D. Zhang, C. Pan, L. Shi, L. Huang, J. Fang, and H. Fu, "A highly reactive catalyst for CO oxidation: CeO₂ nanotubes synthesized using carbon nanotubes as removable templates," *Microporous and Mesoporous Materials*, vol. 117, no. 1-2, pp. 193–200, 2009.
- [74] D. Zhang, T. Yan, L. Shi, C. Pan, and J. Zhang, "Ethylene glycol reflux synthesis of carbon nanotube/ceria core-shell nanowires," *Applied Surface Science*, vol. 255, no. 11, pp. 5789–5794, 2009.
- [75] S. C. Laha and R. Ryoo, "Synthesis of thermally stable mesoporous cerium oxide with nanocrystalline frameworks using mesoporous silica templates," *Chemical Communications*, vol. 9, no. 17, pp. 2138–2139, 2003.
- [76] W. Shen, X. Dong, Y. Zhu, H. Chen, and J. Shi, "Mesoporous CeO₂ and CuO-loaded mesoporous CeO₂: synthesis, characterization, and CO catalytic oxidation property," *Microporous and Mesoporous Materials*, vol. 85, no. 1-2, pp. 157–162, 2005.
- [77] I. A. Kartsonakis, P. Liatsi, I. Daniilidis, and G. Kordas, "Synthesis, characterization, and antibacterial action of hollow ceria nanospheres with/without a conductive polymer coating," *Journal of the American Ceramic Society*, vol. 91, no. 2, pp. 372–378, 2008.
- [78] I. Kartsonakis, I. Daniilidis, and G. Kordas, "Encapsulation of the corrosion inhibitor 8-hydroxyquinoline into ceria nanocontainers," *Journal of Sol-Gel Science and Technology*, vol. 48, no. 1, pp. 24–31, 2008.

- [79] G. S. Wu, T. Xie, X. Y. Yuan, B. C. Cheng, and L. D. Zhang, "An improved sol-gel template synthetic route to large-scale CeO₂ nanowires," *Materials Research Bulletin*, vol. 39, no. 7-8, pp. 1023–1028, 2004.
- [80] D. E. Zhang, X. J. Zhang, X. M. Ni, J. M. Song, and H. G. Zheng, "Optical and electrochemical properties of CeO₂ spindles," *ChemPhysChem*, vol. 7, no. 12, pp. 2468–2470, 2006.
- [81] M. Hirano and E. Kato, "Hydrothermal synthesis of two types of cerium carbonate particles," *Journal of Materials Science Letters*, vol. 18, no. 5, pp. 403–405, 1999.
- [82] H. C. Wang and C. H. Lu, "Synthesis of cerium hydroxycarbonate powders via a hydrothermal technique," *Materials Research Bulletin*, vol. 37, no. 4, pp. 783–792, 2002.
- [83] M. Ge, C. Guo, L. Li, B. Zhang, Y. Feng, and Y. Wang, "Preparation of CeO₂ novel sponge-like rods by emulsion liquid membrane system and its catalytic oxidation property," *Materials Letters*, vol. 63, no. 15, pp. 1269–1271, 2009.
- [84] A. G. Macedo, S. E. M. Fernandes, A. A. Valente, R. A. S. Ferreira, L. D. Carlos, and J. Rocha, "Catalytic performance of ceria nanorods in liquid-phase oxidations of hydrocarbons with tert-butyl hydroperoxide," *Molecules*, vol. 15, no. 2, pp. 747–765, 2010.
- [85] X. He, D. Zhang, H. Li, J. Fang, and L. Shi, "Shape and size effects of ceria nanoparticles on the impact strength of ceria/epoxy resin composites," *Particuology*, 2010.
- [86] J. J. Miao, H. Wang, Y. R. Li, J. M. Zhu, and J. J. Zhu, "Ultrasonic-induced synthesis of CeO₂ nanotubes," *Journal of Crystal Growth*, vol. 281, no. 2–4, pp. 525–529, 2005.
- [87] M. L. Dos Santos, R. C. Lima, C. S. Riccardi et al., "Preparation and characterization of ceria nanospheres by microwave-hydrothermal method," *Materials Letters*, vol. 62, no. 30, pp. 4509–4511, 2008.
- [88] W. Q. Han, L. Wu, and Y. Zhu, "Formation and oxidation state of CeO_{2-x} nanotubes," *Journal of the American Chemical Society*, vol. 127, no. 37, pp. 12814–12815, 2005.
- [89] C. Tang, Y. Bando, B. Liu, and D. Golberg, "Cerium oxide nanotubes prepared from cerium hydroxide nanotubes," *Advanced Materials*, vol. 17, no. 24, pp. 3005–3009, 2005.
- [90] G. Chen, C. Xu, X. Song, W. Zhao, Y. Ding, and S. Sun, "Interface reaction route to two different kinds of CeO₂ nanotubes," *Inorganic Chemistry*, vol. 47, no. 2, pp. 723–728, 2008.
- [91] W. Wang, J. Y. Howe, Y. Li et al., "A surfactant and template-free route for synthesizing ceria nanocrystals with tunable morphologies," *Journal of Materials Chemistry*, vol. 20, no. 36, pp. 7776–7781, 2010.
- [92] K. Zhou, Z. Yang, and S. Yang, "Highly reducible CeO₂ nanotubes," *Chemistry of Materials*, vol. 19, no. 6, pp. 1215–1217, 2007.
- [93] Z. L. Wang and X. Feng, "Polyhedral shapes of CeO₂ nanoparticles," *Journal of Physical Chemistry B*, vol. 107, no. 49, pp. 13563–13566, 2003.
- [94] Y. C. Chen, K. B. Chen, C. S. Lee, and M. C. Lin, "Direct synthesis of Zr-doped ceria nanotubes," *Journal of Physical Chemistry C*, vol. 113, no. 13, pp. 5031–5034, 2009.
- [95] P. Martin, S. C. Parker, D. C. Sayle, and G. W. Watson, "Atomistic modeling of multilayered ceria nanotubes," *Nano Letters*, vol. 7, no. 3, pp. 543–546, 2007.
- [96] Y. Fu, Z. D. Wei, M. B. Ji, L. Li, P. K. Shen, and J. Zhang, "Morphology-controllable synthesis of CeO₂ on a Pt electrode," *Nanoscale Research Letters*, vol. 3, no. 11, pp. 431–434, 2008.
- [97] N. Bugayeva and J. Robinson, "Synthesis of hydrated CeO₂ nanowires and nanoneedles," *Materials Science and Technology*, vol. 23, no. 2, pp. 237–241, 2007.
- [98] K. S. Lin, S. Chowdhury, H. P. Yeh, W. T. Hong, and C. T. Yeh, "Preparation and characterization of CuO/ZnO-Al₂O₃ catalyst washcoats with CeO₂ sols for autothermal reforming of methanol in a microreactor," *Catalysis Today*, vol. 164, no. 1, pp. 251–256, 2011.
- [99] D. Zhang, T. Yan, C. Pan, L. Shi, and J. Zhang, "Carbon nanotube-assisted synthesis and high catalytic activity of CeO₂ hollow nanobeads," *Materials Chemistry and Physics*, vol. 113, no. 2-3, pp. 527–530, 2009.
- [100] T. Masui, K. Fujiwara, K. I. Machida, G. Y. Adachi, T. Sakata, and H. Mori, "Characterization of cerium(IV) oxide ultrafine particles prepared using reversed micelles," *Chemistry of Materials*, vol. 9, no. 10, pp. 2197–2204, 1997.
- [101] D. Zhang, F. Niu, H. Li, L. Shi, and J. Fang, "Uniform ceria nanospheres: solvothermal synthesis, formation mechanism, size-control and catalytic activity," *Powder Technology*, vol. 207, no. 1–3, pp. 35–41, 2011.
- [102] D. Zhang, F. Niu, T. Yan, L. Shi, X. Du, and J. Fang, "Ceria nanospindles: template-free solvothermal synthesis and shape-dependent catalytic activity," *Applied Surface Science*, vol. 257, no. 23, pp. 10161–10167, 2011.
- [103] J. Guzman, S. Carretin, and A. Corma, "Spectroscopic evidence for the supply of reactive oxygen during CO oxidation catalyzed by gold supported on nanocrystalline CeO₂," *Journal of the American Chemical Society*, vol. 127, no. 10, pp. 3286–3287, 2005.
- [104] M. B. Boucher, S. Goergen, N. Yi, and M. Flytzani-Stephanopoulos, "'Shape effects' in metal oxide supported nanoscale gold catalysts," *Physical Chemistry Chemical Physics*, vol. 13, no. 7, pp. 2517–2527, 2011.
- [105] K. S. Lin, C. Y. Pan, S. Chowdhury, M. T. Tu, W. T. Hong, and C. T. Yeh, "Hydrogen generation using a CuO/ZnO-ZrO₂ nanocatalyst for autothermal reforming of methanol in a microchannel reactor," *Molecules*, vol. 16, no. 1, pp. 348–366, 2011.
- [106] Y. Liu, T. Hayakawa, K. Suzuki, and S. Hamakawa, "Production of hydrogen by steam reforming of methanol over Cu/CeO₂ catalysts derived from Ce_{1-x}Cu_xO_{2-x} precursors," *Catalysis Communications*, vol. 2, no. 6-7, pp. 195–200, 2001.
- [107] D. J. Seo, W. L. Yoon, Y. G. Yoon, S. H. Park, G. G. Park, and C. S. Kim, "Development of a micro fuel processor for PEMFCs," *Electrochimica Acta*, vol. 50, no. 2-3, pp. 719–723, 2004.
- [108] M. B. Boucher, N. Yi, F. Gittleson, B. Zugic, H. Saltsburg, and M. Flytzani-Stephanopoulos, "Hydrogen production from methanol over gold supported on ZnO and CeO₂ nanoshapes," *Journal of Physical Chemistry C*, vol. 115, no. 4, pp. 1261–1268, 2011.
- [109] N. Yi, R. Si, H. Saltsburg, and M. Flytzani-Stephanopoulos, "Steam reforming of methanol over ceria and gold-ceria nanoshapes," *Applied Catalysis B*, vol. 95, no. 1-2, pp. 87–92, 2010.
- [110] G. Avgouropoulos, J. Papavasiliou, and T. Ioannides, "Hydrogen production from methanol over combustion-synthesized noble metal/ceria catalysts," *Chemical Engineering Journal*, vol. 154, no. 1–3, pp. 274–280, 2010.
- [111] N. Yi, R. Si, H. Saltsburg, and M. Flytzani-Stephanopoulos, "Active gold species on cerium oxide nanoshapes for methanol steam reforming and the water gas shift reactions," *Energy and Environmental Science*, vol. 3, no. 6, pp. 831–837, 2010.

- [112] X. Yu, S. T. Tu, Z. Wang, and Y. Qi, "Development of a microchannel reactor concerning steam reforming of methanol," *Chemical Engineering Journal*, vol. 116, no. 2, pp. 123–132, 2006.
- [113] P. J. De Wild and M. J. F. M. Verhaak, "Catalytic production of hydrogen from methanol," *Catalysis Today*, vol. 60, no. 1, pp. 3–10, 2000.
- [114] X. Yu, S. T. Tu, Z. Wang, and Y. Qi, "On-board production of hydrogen for fuel cells over Cu/ZnO/Al₂O₃ catalyst coating in a micro-channel reactor," *Journal of Power Sources*, vol. 150, no. 1-2, pp. 57–66, 2005.
- [115] T. Kim, D. H. Lee, D. E. Park, and S. Kwon, "Micromachined methanol reformer for portable PEM fuel cells," *Journal of Fuel Cell Science and Technology*, vol. 5, no. 1, Article ID 011008, 6 pages, 2008.
- [116] C. Horny, A. Renken, and L. Kiwi-Minsker, "Compact string reactor for autothermal hydrogen production," *Catalysis Today*, vol. 120, no. 1, pp. 45–53, 2007.
- [117] G. Germani, A. Stefanescu, Y. Schuurman, and A. C. van Veen, "Preparation and characterization of porous alumina-based catalyst coatings in microchannels," *Chemical Engineering Science*, vol. 62, no. 18–20, pp. 5084–5091, 2007.
- [118] C. G. Maclel, L. P. R. Profeti, E. M. Assaf, and J. M. Assaf, "Hydrogen purification for fuel cell using CuO/CeO₂-Al₂O₃ catalyst," *Journal of Power Sources*, vol. 196, no. 2, pp. 747–753, 2011.
- [119] G. Avgouropoulos and T. Ioannides, "Selective CO oxidation over CuO-CeO₂ catalysts prepared via the urea-nitrate combustion method," *Applied Catalysis A*, vol. 244, no. 1, pp. 155–167, 2003.
- [120] G. G. Park, S. D. Yim, Y. G. Yoon, C. S. Kim, D. J. Seo, and K. Eguchi, "Hydrogen production with integrated microchannel fuel processor using methanol for portable fuel cell systems," *Catalysis Today*, vol. 110, no. 1-2, pp. 108–113, 2005.
- [121] D. E. Park, T. Kim, S. Kwon, C. K. Kim, and E. Yoon, "Micromachined methanol steam reforming system as a hydrogen supplier for portable proton exchange membrane fuel cells," *Sensors and Actuators A*, vol. 135, no. 1, pp. 58–66, 2007.
- [122] A. Qi, B. Peppley, and K. Karan, "Integrated fuel processors for fuel cell application: a review," *Fuel Processing Technology*, vol. 88, no. 1, pp. 3–22, 2007.
- [123] M. S. Lim, M. R. Kim, J. Noh, and S. I. Woo, "A plate-type reactor coated with zirconia-sol and catalyst mixture for methanol steam-reforming," *Journal of Power Sources*, vol. 140, no. 1, pp. 66–71, 2005.
- [124] G. Huang, B. J. Liaw, C. J. Jhang, and Y. Z. Chen, "Steam reforming of methanol over CuO/ZnO/CeO₂/ZrO₂/Al₂O₃ catalysts," *Applied Catalysis A*, vol. 358, no. 1, pp. 7–12, 2009.

Research Article

Use of the Thermal Chemical Vapor Deposition to Fabricate Light-Emitting Diodes Based on ZnO Nanowire/p-GaN Heterojunction

Sheng-Po Chang and Ting-Hao Chang

Institute of Microelectronics and Department of Electrical Engineering, Center for Micro/Nano Science and Technology, Advanced Optoelectronic Technology Center, National Cheng Kung University, Tainan 70101, Taiwan

Correspondence should be addressed to Sheng-Po Chang, changsp@mail.ncku.edu.tw

Received 15 June 2011; Revised 4 August 2011; Accepted 11 August 2011

Academic Editor: Renzhi Ma

Copyright © 2011 S.-P. Chang and T.-H. Chang. This is an open access article distributed under the Creative Commons Attribution License, which permits unrestricted use, distribution, and reproduction in any medium, provided the original work is properly cited.

The fabrication and characteristics of grown ZnO nanowire/p-GaN heterojunction light-emitting diodes are reported. Vertically aligned ZnO nanowire arrays were grown on a p-GaN substrate by thermal chemical vapor deposition in quartz tube. The rectifying current-voltage characteristics indicate that a p-n junction was formed with a heterostructure of n-ZnO nanowire/p-GaN. The room temperature electroluminescent emission peak at 425 nm was attributed to the band offset at the interface between the n-ZnO nanowire and p-GaN and to defect-related emission from GaN; it was also found that there exist the yellow band in the heterojunction. It would be attributed to the deep defect level in the heterojunction.

1. Introduction

Recently, nanowire- (NW-) based light-emitting diodes (LEDs) have become the focus of many researches and have also drawn considerable attention owing to their many advantages over conventional thin-film-based devices. NWs can improve light extraction without the use of a reflector because they can act as direct waveguides, and their nanostructure can overcome lower carrier injection efficiency because of a large band offset at the heterojunction interface. The nanojunction can also increase the contact area and aspect ratio and, hence, enhance carrier injection efficiency and recombination. Zinc oxide (ZnO) has a wide bandgap ($E_g = 3.37$ eV) and a stronger excitation binding energy (60 meV) than gallium nitride (GaN) (~29 meV) [1]. In addition, ZnO is a natural n-type semiconductor and has a wurtzite structure [2, 3]. These properties make ZnO a potential material to be used for ultraviolet (UV) photodetectors and other optoelectronic applications [4]. Moreover, ZnO-based one-dimensional (1D) materials are widely used because of their high surface-area-to-volume ratio. Therefore, a large contact area of the p-n junction

structure could be fabricated to produce many kinds of optoelectronic devices such as LEDs and detectors. However, ZnO homojunction devices are difficult to fabricate because p-type doping in ZnO is not stable or reliable enough. Therefore, a heterojunction of ZnO and another material is needed to realize a p-n junction, which is an important part of many devices. Heterojunction devices fabricated in previous studies utilized semiconductors such as Cu_2O , Si, SiC, and GaN [5–8].

Although several studies have investigated the use of p-type ZnO to realize homojunction devices, the fabrication of such devices is difficult because p-type ZnO is not stable or reliable enough. GaN is a wide-bandgap semiconductor ($E_g = 3.39$ eV) and has similar physical properties to ZnO, including a small in-plane lattice mismatch (~1.8%) and the same wurtzite structure [9, 10]. Therefore, n-ZnO NW-based LEDs can be realized through a GaN heterojunction structure. Recently, many researchers have grown ZnO NWs using various techniques, including metal organic chemical vapor deposition (MOCVD), and electrodeposition. LED performance is not satisfactory with MOCVD [11–13]. Lupan et al. fabricated low-voltage UV LEDs with

an electroluminescence (EL) emission wavelength at 397 nm at an applied voltage of 4.2 V [11]. However, these methods of growing NWs are complex and expensive. In this study, ZnO NW heterojunction was grown with a simple method by thermal chemical vapor deposition in quartz tube, because this method has many advantages such as process simply and short growth time, lower cost than MOCVD, and mass manufactures. The physical and electrooptical properties of the fabricated LEDs are discussed.

2. Experiment

A p-GaN epitaxial film was deposited on a c-plane (0001) sapphire substrate by MOCVD; the sapphire substrate was purchased commercially. The ZnO NWs used in this study were grown on the p-GaN substrate by thermal chemical vapor deposition. Zinc powder (99%, Strem Chemicals) was used as a zinc vapor source. The zinc powder and substrates were inserted into a quartz tube using an alumina boat. Constant streams of argon gas at a rate of 54.4 SCCM (standard cubic centimeters per minute at STP) and oxygen gas at a rate of 0.8 SCCM were then introduced into the reaction system. The evaporation process was carried out for 30 min after the reaction system had reached a reaction temperature of 550°C. A mechanical pump was utilized to maintain a reactive pressure of 10 Torr. Finally, a novel light-emitting diode was fabricated and packaged by the following method. A 3% HCl aqueous solution was used to etch out the n-ZnO NW to expose the p-GaN layer for a p-electrode. Ni/Au (15/120 nm) ohmic contacts were deposited on the p-GaN layer by thermal evaporation. Figure 1 shows the device processing steps used in this study. The fabricated sample was reversed and placed on the prepared ITO/glass substrate. The tips of the ZnO NWs contacted the ITO/glass substrate and formed a ZnO NW/p-GaN structure to be used for the LED. In order to achieve good ohmic contact between the ZnO nanowires and ITO, the LED was placed into a thermal furnace and annealed at 200°C for 10 min. The size distribution of the NWs and surface morphologies of the samples were elucidated using a JEOL JSM-7000F field emission scanning electron microscope (FE-SEM) operated at 10 KeV. The photoluminescence (PL) spectrum of the sample was measured at room temperature using a 325-nm HeCd laser, which acted as the excitation source.

3. Results and Discussion

Figure 2(a) shows a top-view FE-SEM image of as-grown ZnO NWs on GaN film. The SEM measurement shows that the ZnO NWs grow vertically and are connected to the GaN film. The ZnO NWs are 1 μm and 50–100 nm in diameter. Figure 2(b) presents an X-ray diffraction (XRD) pattern of ZnO NWs on a p-GaN substrate. In this figure, we can observe three clear peaks. The ZnO (0002) diffraction peak is to the left of the GaN (0002) peak, and the sapphire substrate (0006) exhibits a peak at 41.9°. This measurement shows that the ZnO NWs are oriented with the *c*-axis, perpendicular to the GaN film. The ZnO and GaN peaks of the XRD pattern

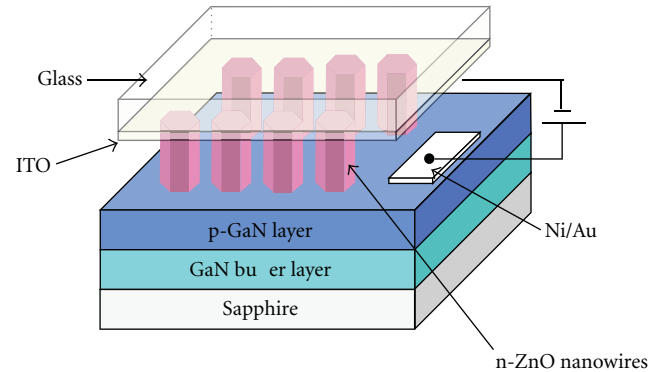


FIGURE 1: Structure of fabricated n-ZnO nanowire/p-GaN heterojunction LED.

are located close to each other at 34.2° and 34.8°, respectively, indicating that the strain existing between GaN and ZnO is very weak. The full width at half maximum (FWHM) values of GaN and ZnO are similar and sharp, indicating that the GaN film and ZnO NWs are of high quality. No other peak is observed, indicating that the preferred orientation of the NWs from the p-GaN film is achieved. Figure 2(c) shows an XRD rocking curve obtained for our sample. The extremely narrow FWHM observed from the rocking curve peak indicates that the ZnO nanowires prepared on the p-GaN substrate in this study are indeed single crystalline with high crystal quality.

Figure 3 presents the PL spectrum of the ZnO NWs and p-GaN film at room temperature. The PL spectrum of the p-GaN film consists of two broad bands, centered at maximum wavelengths (λ_m) of 432 and 583 nm. The broadband emission corresponds to a typical transition from the conduction band or shallow donors to the Mg acceptors. The PL spectrum of the ZnO NWs reveals a strong UV emission with a λ_m of 379 nm and a FWHM of 16 nm, because of near-band edge emission by ZnO with a wide bandgap.

In Figure 4, the current-voltage characteristics of the fabricated diode are plotted for bias voltages ranging from –5 to 10 V. This figure illustrates that the large turn-on voltage was approximately 5.5 V, which indicates that the thermal chemical vapor deposition procedure may produce a higher density of defects at the interface. From Figure 5, it is found that the EL emission rapidly increased with the applied forward bias, and the peak wavelengths were 425 nm, 425 nm, and 426 nm at 10 V, 15 V, and 20 V, respectively. The EL peak wavelength that is red shifted relative to the PL emission of ZnO is approximately 46 nm, which could be attributed to the recombination of electrons and holes in ZnO, causing an unexpected defect to occur in ZnO or at the interface between ZnO and GaN. Moreover, it is also found that there exists the yellow band in the heterojunction; it is attributed to the deep defect level in the heterojunction. The insert of Figure 5 shows the blue emission imaged with a CCD camera. The blue light radiating from

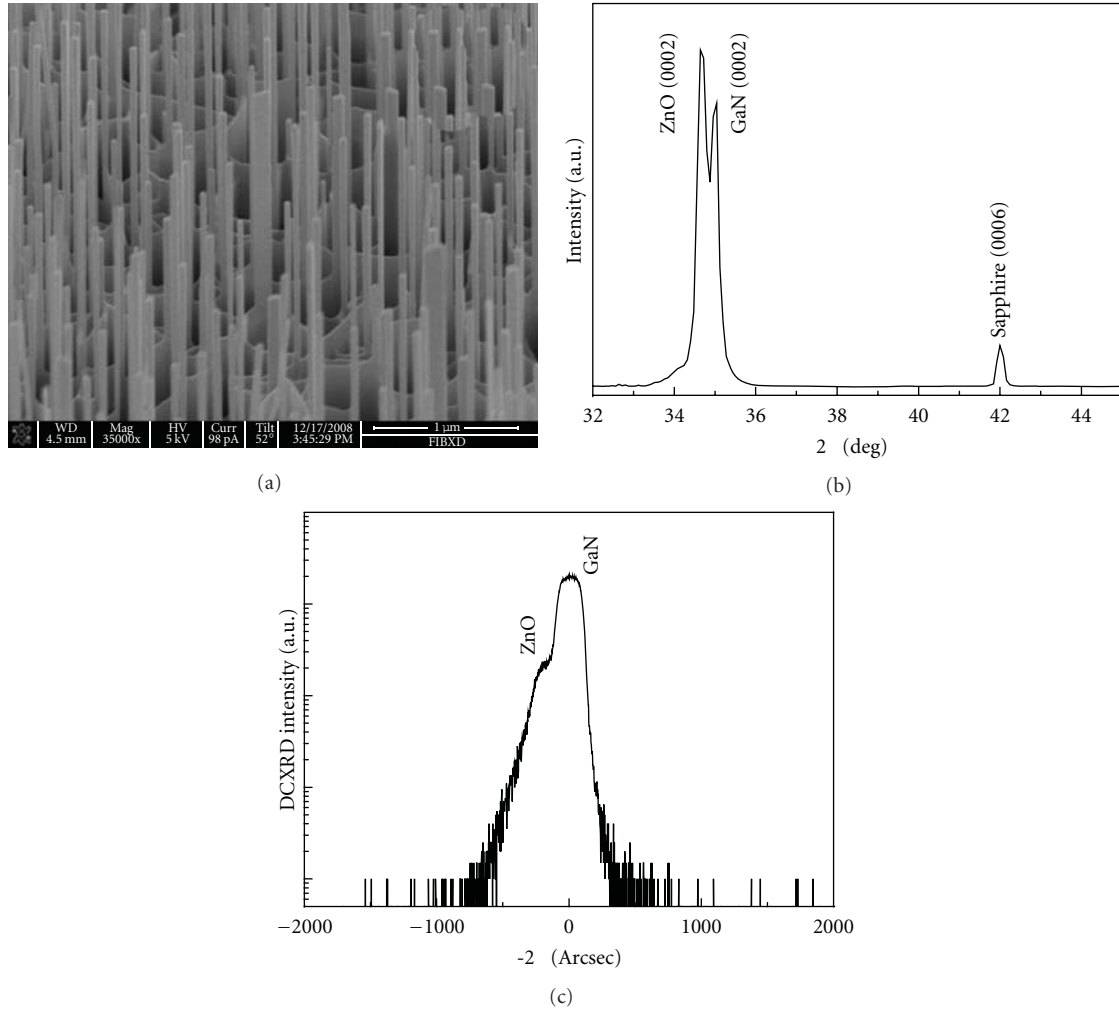


FIGURE 2: (a) FE-SEM image of as-grown ZnO nanowires on p-GaN film. (b) XRD pattern of as-grown ZnO nanowires. (c) XRD rocking curve of fabricated n-ZnO nanowire/p-GaN heterojunction structure.

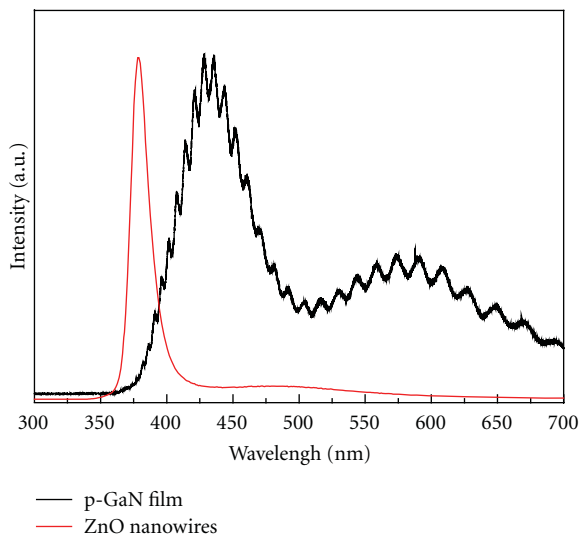


FIGURE 3: Room temperature PL spectra of as-grown p-GaN film and ZnO nanowires.

the heterostructure LED under DC current injection is strong enough to be seen by the naked eye.

4. Conclusion

In conclusion, we fabricated the ZnO NW/p-GaN heterostructure by thermal chemical vapor deposition using a quartz tube furnace and packaged an LED with ITO/glass by a simple process. The photoluminescence spectrum of the p-GaN film exhibited broad bands at 432 and 583 nm; these bands are attributed to near-band edge emission by ZnO with a wide bandgap. The current-voltage characteristics of the fabricated diode indicated that the turn-on voltage was large (approximately 5.5 V), which may indicate that the thermal chemical vapor deposition procedure produces a high density of defects at the interface. The room temperature EL emission peak at 425 nm was attributed to the recombination of electrons and holes in ZnO, causing an unexpected defect to occur in ZnO or at the interface between ZnO and GaN. Furthermore, there has been the

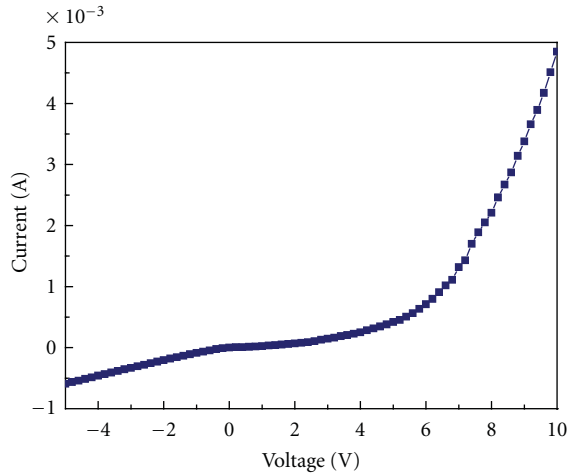


FIGURE 4: Current-voltage characteristics of fabricated n-ZnO nanowire/p-GaN heterojunction LED.

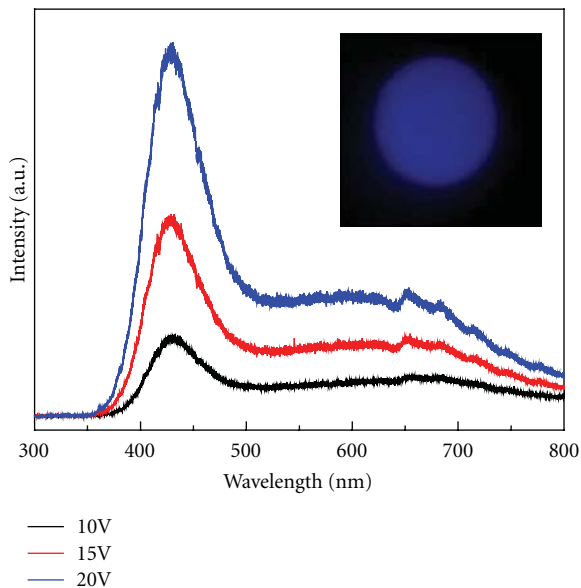


FIGURE 5: EL spectrum of fabricated n-ZnO nanowire/p-GaN heterojunction LED.

yellow band in the EL spectrum; it is attributed to the deep defect level in the heterojunction.

Acknowledgments

This work was supported by the National Science Council under contract numbers NSC 95-2221-E-006-314 and NSC 95-2221-E-006-357-MY3. This work was also supported in part by the Center for Frontier Materials and Micro/Nano Science and Technology, the National Cheng Kung University, Taiwan (D97-2700). This work was also supported in part by the Advanced Optoelectronic Technology Center, the National Cheng Kung University, under projects from the Ministry of Education.

References

- [1] J. Chen, Y. Zhang, B. J. Skromme, K. Akimoto, and S. J. Pachuta, "Properties of the shallow O-related acceptor level in ZnSe," *Journal of Applied Physics*, vol. 78, no. 8, pp. 5109–5119, 1995.
- [2] J. T. Yan, C. H. Chen, S. F. Yen, and C. T. Lee, "Ultraviolet ZnO nanorod/p-GaN-heterostructured light-emitting diodes," *IEEE Photonics Technology Letters*, vol. 22, no. 3, Article ID 5342485, pp. 146–148, 2010.
- [3] Y. He, J. A. Wang, X. B. Chen, W. F. Zhang, X. Y. Zeng, and Q. W. Gu, "Blue electroluminescence nanodevice prototype based on vertical ZnO nanowire/polymer film on silicon substrate," *Journal of Nanoparticle Research*, vol. 12, no. 1, pp. 169–176, 2010.
- [4] J. B. K. Law and J. T. L. Thong, "Simple fabrication of a ZnO nanowire photodetector with a fast photoresponse time," *Applied Physics Letters*, vol. 88, no. 13, Article ID 133114, 3 pages, 2006.
- [5] M. C. Jeong, B. Y. Oh, M. H. Ham, S. W. Lee, and J. M. Myoung, "ZnO-nanowire-inserted GaN/ZnO heterojunction light-emitting diodes," *Small*, vol. 3, no. 4, pp. 568–572, 2007.
- [6] J. D. Ye, S. L. Gu, S. M. Zhu et al., "Electroluminescent and transport mechanisms of n-ZnO/p-Si heterojunctions," *Applied Physics Letters*, vol. 88, no. 18, Article ID 182112, 3 pages, 2006.
- [7] A. C. Mofor, A. Bakin, U. Chejarla et al., "Fabrication of ZnO nanorod-based p-n heterojunction on SiC substrate," *Superlattices and Microstructures*, vol. 42, no. 1–6, pp. 415–420, 2007.
- [8] W. I. Park and G. C. Yi, "Electroluminescence in n-ZnO Nanorod Arrays Vertically Grown on p-GaN," *Advanced Materials*, vol. 16, no. 1, pp. 87–90, 2004.
- [9] S. J. An, J. H. Chae, G. C. Yi, and G. H. Park, "Enhanced light output of GaN-based light-emitting diodes with ZnO nanorod arrays," *Applied Physics Letters*, vol. 92, no. 12, Article ID 121108, 3 pages, 2008.
- [10] C. G. Van de Walle and J. Neugebauer, "Universal alignment of hydrogen levels in semiconductors, insulators and solutions," *Nature*, vol. 423, no. 6940, pp. 626–628, 2003.
- [11] O. Lupan, T. Pauporté, and B. Viana, "Low-voltage UV-electroluminescence from ZnO-Nanowire array/p-CaN light-emitting diodes," *Advanced Materials*, vol. 22, no. 30, pp. 3298–3302, 2010.
- [12] X. M. Zhang, M. Y. Lu, Y. Zhang, L. J. Chen, and Z. L. Wang, "Fabrication of a high-brightness blue-light-emitting diode using a ZnO-Nanowire array grown on p-GaN thin film," *Advanced Materials*, vol. 21, no. 27, pp. 2767–2770, 2009.
- [13] M. C. Jeong, B. Y. Oh, M. H. Ham, and J. M. Myoung, "Electroluminescence from ZnO nanowires in n-ZnO film/ZnO nanowire array/ p-GaN film heterojunction light-emitting diodes," *Applied Physics Letters*, vol. 88, no. 20, Article ID 202105, 3 pages, 2006.

Research Article

Structural and Optical Characteristics of γ -In₂Se₃ Nanorods Grown on Si Substrates

M. D. Yang,^{1,2} C. H. Hu,¹ S. C. Tong,¹ J. L. Shen,¹ S. M. Lan,³ C. H. Wu,² and T. Y. Lin⁴

¹Department of Physics and Center for Nano-Technology, Chung Yuan Christian University, Chung-Li 32023, Taiwan

²Institute of Nuclear Energy Research, Longtan, Taoyuan 32546, Taiwan

³Department of Electronic Engineering, Chung Yuan Christian University, Chung-Li 32023, Taiwan

⁴Institute of Optoelectronic Sciences, National Taiwan Ocean University, Keelung 20224, Taiwan

Correspondence should be addressed to J. L. Shen, jlshen@cycu.edu.tw

Received 7 July 2011; Accepted 9 August 2011

Academic Editor: Renzhi Ma

Copyright © 2011 M. D. Yang et al. This is an open access article distributed under the Creative Commons Attribution License, which permits unrestricted use, distribution, and reproduction in any medium, provided the original work is properly cited.

This study attempted to grow single-phase γ -In₂Se₃ nanorods on Si (111) substrates by metal-organic chemical vapor deposition (MOCVD). High-resolution transmission electron microscopy (HRTEM) and selected area electron diffraction (SAED) confirmed that the In₂Se₃ nanorods are singularly crystallized in the γ phase. The photoluminescence of γ -In₂Se₃ nanorods at 15 K was referred to as free and bound exciton emissions. The bandgap energy of γ -In₂Se₃ nanorods at room temperature was determined to be ~ 1.99 eV, obtained from optical absorption.

The III-VI semiconductors have been the subject of many investigations due to their peculiar electrical and optical properties, and their potential applications in electronic and optoelectronic devices, such as phase-change random access memories (PRAMs), solid-state batteries, and solar cells [1–4]. Among these III-VI semiconductors, In₂Se₃ is a defective structure of tetrahedral bonding, where one-third of the sites is vacant and forms a screw array along the *c* axis. Due to many different crystalline phases existing in In₂Se₃, growth of high-quality In₂Se₃ with a single phase is a challenging task. Several different methods have been demonstrated to grow In₂Se₃ epilayers, such as evaporation [5, 6], the Bridgman-Stockbarger Method [7, 8], and metal-organic chemical vapor deposition (MOCVD) [9–11]. Recently, one-dimensional III-VI semiconductor nanostructures, such as nanowires and nanotubes, exhibited novel and device applicable physical properties, which can be used in a wide variety of applications in nanoelectronic and nano-optoelectronic devices [12–17]. For example, α -phase layer-structured In₂Se₃ nanowires have been grown and have shown a large anisotropy in both structure and conductivity [12]. These III-VI semiconductor nanostructures can afford an efficient charge carrier transfer while maintaining

a small cross-section for the applications. However, so far, little attention has been given to γ -phase In₂Se₃ (γ -In₂Se₃) nanorods. Bulk γ -In₂Se₃ has been of particular interest for photovoltaic applications because it can be an absorbing layer in a solar cell. The one-dimensional γ -In₂Se₃ nanostructures may be more interesting materials since they exhibit excellent light absorption owing to their high surface-to-volume ratio. To be an absorbing layer in solar cells, γ -In₂Se₃ requires deposition on different substrates with a high crystalline quality. It is well known that Si can be a good substrate to grow nanostructures because it offers many attractive advantages, such as good doping properties and thermal conductivity. If Si substrate can be utilized in growing γ -In₂Se₃ nanostructures, various devices on Si-based integrated circuits could be developed in the future.

In our previous work, energy relaxation of hot electrons in γ -In₂Se₃ nanorods has been investigated [16]. It was found that the main path of energy relaxation for the hot electrons is LO-phonon emission. In this study, the detailed structures of the γ -In₂Se₃ nanorods on Si substrates were investigated by scanning electron microscopy (SEM), transmission electron microscopy (TEM), and selected area electron diffraction (SAED). Also, the optical properties

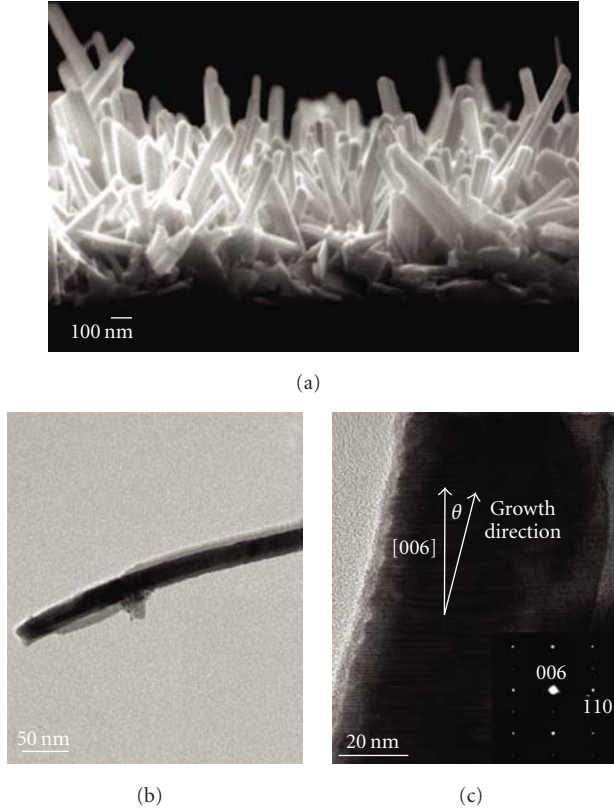


FIGURE 1: (a) Cross-section SEM image, (b) TEM image, and (c) HRTEM image of γ - In_2Se_3 nanorods grown on Si (111) substrates. The inset of (c) shows the SAED pattern along the [006] axis.

of γ - In_2Se_3 nanorods were explored by photoluminescence (PL), cathodoluminescence (CL), and the optical absorption spectra.

The γ - In_2Se_3 nanorods were directly grown on Si (111) substrates without any buffer layers using an MOCVD system with a vertical reactor [16]. The nanorods were grown using liquid MO and a trimethyl-indium (TMIn) compound at atmospheric pressure. Gaseous H_2Se was employed as the reactant source material. Gaseous N_2 was used as the carrier gas in this process. Before growth, Si substrates were baked at 1100°C for 10 min in gaseous HCl and H_2 in order to remove the native oxide. After the thermal etching process, the reactor cooled down to 425°C and then started to grow γ - In_2Se_3 nanorods. The total growth time was 50 min. The gaseous flow rate was kept at $3 \mu\text{mol}/\text{min}$ for TMIn and $40 \mu\text{mol}/\text{min}$ for H_2Se . Gaseous H_2Se was mixed with 85% hydrogen and 15% H_2Se . The gaseous flow rate and temperature play an essential role in growing nanorod structures in γ - In_2Se_3 . The TEM lattice image and the SAED pattern of an individual In_2Se_3 nanorod were taken by a JSM-2100F (JEOL Company) Transmission Electron Microscope. The room temperature CL measurement and morphology of the nanorods image were measured by using the JSM-7001F (JEOL Company). The PL measurements were performed using a 532 nm semiconductor laser as the excitation source. The temperature-dependent PL spectra were measured by a

close-cycle helium cryostat and were analyzed by means of a 0.75 m monochromator and silicon detector.

A cross-section image of the SEM for the grown In_2Se_3 nanorods is shown in Figure 1(a). The SEM image was taken with 10 keV of electron energy to present a magnification of 30,000. As shown in Figure 1(a), the In_2Se_3 nanorods are straight and not tapered. The average diameter and the average height of the In_2Se_3 nanorods are about 64 and 460 nm, respectively. To understand the structural and morphological characteristics of nanorods, TEM investigations were carried out. Figure 1(b) shows a low magnification TEM image of In_2Se_3 nanorods. The diameter and height of In_2Se_3 nanorods are in good agreement with the SEM image shown in Figure 1(a). Figure 1(c) is a high-resolution TEM (HRTEM) image recorded from a segment of an In_2Se_3 nanorod. The image exhibits the ordering feature across its entire width, with a uniform periodicity of ~ 1.7 nm. This superlattice structure within the nanorods is a structural characteristic due to the effect of the vacancy ordering [12]. A similar behavior was also reported for the vacancy ordering in α - In_2Se_3 nanowires and CuInSe_2 - CdS Core-Shell nanowires [12, 13]. The SAED pattern taken along the [006] zone axis of In_2Se_3 nanorods is displayed in the inset of Figure 1(c). The SAED pattern shows a rectangular array with characteristic distances of $d_1 = 28.9 \times 10^{-1}$ nm and $d_2 = 7.93 \times 10^{-1}$ nm, respectively. These regular spots in SAED suggest an epitaxial orientation relationship between the In_2Se_3 nanorods and substrates; that is, the In_2Se_3 nanorods are single crystalline. The SAED pattern is consistent with the previous established pattern for γ - In_2Se_3 with basis vectors of $(-1,1,0)$ and $(0,0,6)$ [17]. It is noted that the growth direction of the nanowire in Figure 1(c) is not along the [006] direction, but it makes an angle of 13.7° with respect to the [006] direction. Anyhow, the HRTEM image allows us to confirm that the grown In_2Se_3 nanorods are well crystallized in the γ phase.

The PL spectrum of the γ - In_2Se_3 nanorods on Si (111) substructure at 15 K is shown in Figure 2. Three Gaussian components, peaked at 2.126, 2.147, and 2.155 eV, are resolved in Figure 2. The full width at half maximum (FWHM) of the PL peak at 2.155 eV is 8 meV, indicating good crystal quality for the γ - In_2Se_3 nanorods. In previous reports, the PL peak of γ - In_2Se_3 epilayers at low temperatures was referred to as the exciton-related emission [9]. Therefore, the main PL peak positioned at 2.155 eV is suggested to be the free exciton emission and the peaks in the lower energy side are suggested to be the bond exciton emissions. Figure 3 shows the temperature-dependent PL spectra from 15 to 180 K. The peak energy of the PL in γ - In_2Se_3 nanorods is red-shifted with increased temperature. The open circles in the inset of Figure 3 show temperature-induced bandgap shrinkage extracted from the PL spectra in Figure 2. This relation was fitted by the Varshni Empirical Formula as

$$E(T) = E_0 - \frac{\alpha \cdot T^2}{(\beta + T)}, \quad (1)$$

where E_0 is the bandgap at 0 K, α is the average temperature coefficient and β is the Debye temperature of the material.

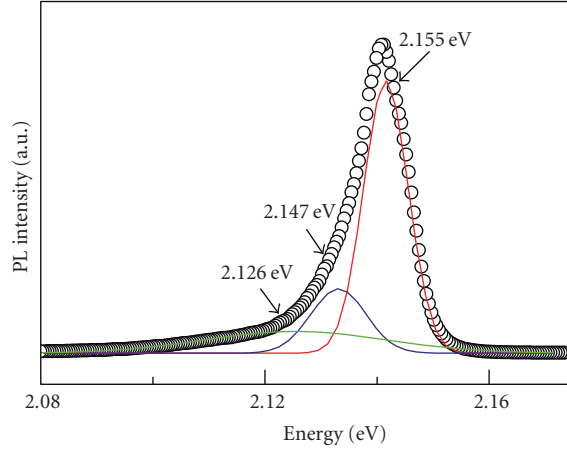


FIGURE 2: PL spectrum of γ - In_2Se_3 nanorods at 15 K. Three peaks are fitted with Gaussian line shape (solid line) to the experimental data (open circles).

Experimental data fitting is shown by the solid line in the inset in Figure 3. The experimental results show good agreement with data that fits using Varshini's Equation with $E_0 = 2.14$ eV, $\alpha = 1.1 \times 10^{-3}$ eV/K, and $\beta = 173$ K. By analyzing the variation of PL peak energy as a function of temperature and ability to fit with the Varshini Equation, the room temperature peak energy of the PL in the γ - In_2Se_3 nanorods was evaluated to be ~ 1.95 eV.

To explore the bandgap energy of γ - In_2Se_3 nanorods at room temperature, the CL and optical absorption spectra were investigated. The room temperature CL spectrum of γ - In_2Se_3 nanorods is shown in Figure 4(a). The peak energy of the CL is 1.95 eV, in good agreement with the predicated value by Varshini's relation, as displayed in the inset of Figure 3. The optical absorption spectrum taken at room temperature is displayed in Figure 4(b). It is known that γ - In_2Se_3 is a direct bandgap semiconductor. Thus, the absorption coefficient α near the band edge follows the relation of a direct bandgap transition [18] as

$$\alpha = \frac{A(h\nu - E_g)^{1/2}}{h\nu}, \quad (2)$$

where A is a constant, $h\nu$ is the photon energy and E_g is the energy, gap between the valence band and the conduction band. The bandgap can be derived from extrapolating the linear part of the curve to zero absorption. The straight line in Figure 4(b) shows the extrapolation, and the bandgap energy was estimated to be ~ 1.99 eV. Obtaining the bandgap energy and absorption coefficient is essential for developing γ - In_2Se_3 nanorods as absorber layers in photovoltaic applications.

Figure 5(a) shows the PL spectrum of γ - In_2Se_3 nanorods at 15 K in the infrared spectral range. A broad PL peak located at 1.24 eV was observed. The sharp peak with energy at 1.16 eV is the emission related to the excitation laser. To find out origin of the 1.24 eV PL, the dependence of PL intensity on the excitation intensity was studied. The PL

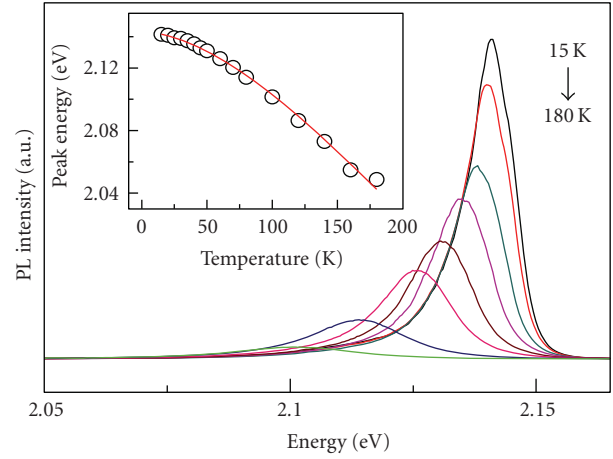


FIGURE 3: The temperature dependence of PL spectra in the γ - In_2Se_3 nanorods. The inset shows the temperature dependence of peak position in PL (open circles). The solid line in the inset shows the fit according to (1).

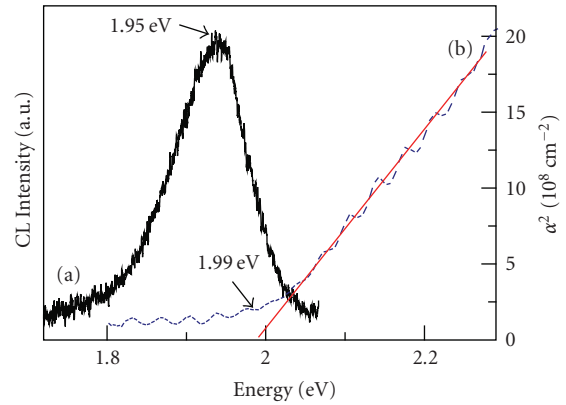


FIGURE 4: (a) CL and (b) optical absorption spectra of γ - In_2Se_3 nanorods at room temperature. The red solid line shows the fit according to (2).

spectra with the excitation power density varied from 17 to 270 W/cm^2 were shown in Figure 5. The open circles in Figure 6 show the PL intensity as a function of the laser excitation density, indicating a linear increase of the PL intensity with excitation density. The dependence of the PL intensity I on the excitation density P can be fitted by a relation [19]:

$$I = CP^m, \quad (3)$$

where C and m are constants. The exponent m depends on the mechanism of recombination: for an excitonic recombination $m = 1$, while for free carrier recombination $m = 2$. When $m < 1$, it may indicate a transition associated with the donor-acceptor pair transition or free-to-bound transition [20, 21]. The solid line in Figure 6 displays the fit from (3). A value of m was determined to be around 0.6, which corresponds to the emission from the donor-acceptor pair transition or free-to-bound transition.

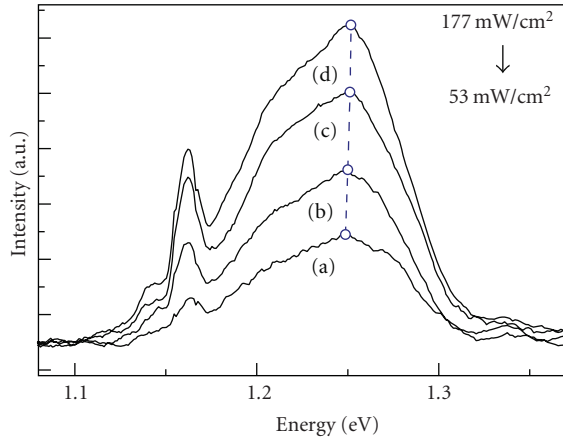


FIGURE 5: The infrared PL emission of γ - In_2Se_3 nanorods at 15 K on various excitation intensities: (a) 53 W/cm^2 , (b) 88 W/cm^2 , (c) 142 W/cm^2 , and (d) 177 W/cm^2 . The dashed line indicates that the PL peak shifts toward the high-energy side with increasing excitation density.

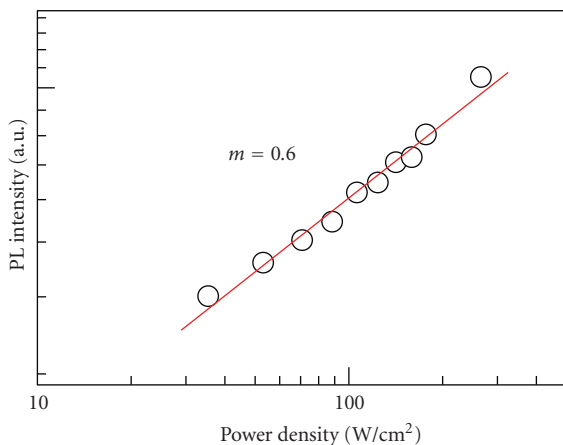


FIGURE 6: PL intensity of the 1.24 eV peak as a function of excitation density. The solid line shows the fit according to (3).

In Figure 6, the PL peak at 1.24 eV shifts to the high-energy spectral region with increasing the excitation density. This blue shift, originating from the increase of the interaction between more closed donor-acceptor pairs, is a characteristic of the donor-acceptor pair transition. Therefore, according to these observations, the observed PL peak at 1.24 eV can be ascribed to the donor-acceptor pair transition in γ - In_2Se_3 nanorods.

In summary, γ - In_2Se_3 nanorods deposited on Si (111) substrates were grown by MOCVD using dual-source precursors. The crystal structure and morphology of In_2Se_3 nanorods were characterized by SEM and HRTEM. The SAED analysis taken along [006] reveals a rectangle spot pattern, confirming the single crystalline in the γ phase. The optical absorption, CL, and temperature-dependent PL have been investigated. The PL at 15 K contains three peaks, which are identified with recombination of free excitons and bound excitons. The energy of the direct bandgap at

room temperature was found to be ~ 1.99 eV. An infrared PL, peaked at 1.24 eV, was observed in 15 K and assigned to be the donor-acceptor pair transition.

Acknowledgment

This project was supported in part by the National Science Council under Grant nos. NSC97-2112-M-033-004-MY3 and NSC 97-2627-B-033-002 and the Institute of Nuclear Energy Research under Grant no. 1002001INER042.

References

- [1] K. Lai, H. Peng, W. Kundhikanjana et al., "Nanoscale electronic inhomogeneity in In_2Se_3 nanoribbons revealed by microwave impedance microscopy," *Nano Letters*, vol. 9, no. 3, pp. 1265–1269, 2009.
- [2] Z. D. Kovalyuk, V. M. Katerynychuk, A. I. Savchuk, and O. M. Sydor, "Intrinsic conductive oxide-p-InSe solar cells," *Materials Science and Engineering B*, vol. 109, no. 1–3, pp. 252–255, 2004.
- [3] K. Yilmaz, M. Parlak, and Ç. Erçelebi, "Investigation of photovoltaic properties of amorphous InSe thin film based Schottky devices," *Semiconductor Science and Technology*, vol. 22, no. 12, pp. 1268–1271, 2007.
- [4] A. Zubiaga, J. A. Garcíá, F. Plazaola, V. Muñoz-Sanjosé, and C. Martínez-Tomás, "Near band edge recombination-mechanisms in GaTe," *Physical Review B*, vol. 68, no. 24, Article ID 245202, 6 pages, 2003.
- [5] C. H. De Groot and J. S. Moodera, "Growth and characterization of a novel In_2Se_3 structure," *Journal of Applied Physics*, vol. 89, no. 8, pp. 4336–4340, 2001.
- [6] M. Emziane and R. Le Ny, "Crystallization of In_2Se_3 semiconductor thin films by post-deposition heat treatment. Thickness and substrate effects," *Journal of Physics D*, vol. 32, no. 12, pp. 1319–1328, 1999.
- [7] A. A. Homs and B. Marí, "Photoluminescence of undoped and neutron-transmutation-doped InSe," *Journal of Applied Physics*, vol. 88, no. 8, pp. 4654–4659, 2000.
- [8] B. Gürbulak, "Urbach tail and optical investigations of Gd doped and undoped InSe single crystals," *Physica Scripta*, vol. 70, no. 2–3, pp. 197–201, 2004.
- [9] I. H. Choi and P. Y. Yu, "Properties of phase-pure InSe films prepared by metalorganic chemical vapor deposition with a single-source precursor," *Journal of Applied Physics*, vol. 93, no. 8, pp. 4673–4677, 2003.
- [10] K. J. Chang, S. M. Lahn, and J. Y. Chang, "Growth of single-phase In_2Se_3 by using metal organic chemical vapor deposition with dual-source precursors," *Applied Physics Letters*, vol. 89, no. 18, Article ID 182118, 3 pages, 2006.
- [11] D. Y. Lyu, T. Y. Lin, J. H. Lin et al., "Growth and properties of single-phase γ - In_2Se_3 thin films on (1 1 1) Si substrate by AP-MOCVD using H_2Se precursor," *Solar Energy Materials and Solar Cells*, vol. 91, no. 10, pp. 888–891, 2007.
- [12] H. Peng, C. Xie, D. T. Schoen, and Y. Cui, "Large anisotropy of electrical properties in layer-structured In_2Se_3 nanowires," *Nano Letters*, vol. 8, no. 5, pp. 1511–1516, 2008.
- [13] H. Peng, C. Xie, D. T. Schoen, K. McIlwrath, X. F. Zhang, and Y. Cui, "Ordered vacancy compounds and nanotube formation in CuInSe_2 -CdS core-shell nanowires," *Nano Letters*, vol. 7, no. 12, pp. 3734–3738, 2007.
- [14] T. Zhai, Y. Ma, L. Li et al., "Morphology-tunable In_2Se_3

- nanostructures with enhanced electrical and photoelectrical performances via sulfur doping,” *Journal of Materials Chemistry*, vol. 20, no. 32, pp. 6630–6637, 2010.
- [15] Y. Li, J. Gao, Q. Li et al., “Thermal phase transformation of In_2Se_3 nanowires studied by in situ synchrotron radiation X-ray diffraction,” *Journal of Materials Chemistry*, vol. 21, no. 19, pp. 6944–6947, 2011.
- [16] M. D. Yang, C. H. Hu, J. L. Shen et al., “Hot photoluminescence in $\gamma\text{-In}_2\text{Se}_3$ nanorods,” *Nanoscale Research Letters*, vol. 3, no. 11, pp. 427–430, 2008.
- [17] S. Marsillac, A. M. Combot-Marie, J. C. Bernède, and A. Conan, “Experimental evidence of the low-temperature formation of $\gamma\text{-In}_2\text{Se}_3$ thin films obtained by a solid-state reaction,” *Thin Solid Films*, vol. 288, no. 1-2, pp. 14–20, 1996.
- [18] C. M. Joseph and C. S. Menon, “Electrical, optical and structural properties of binary phase free CuInSe_2 thin films,” *Journal of Physics D*, vol. 34, no. 8, pp. 1143–1146, 2001.
- [19] X. Zhongying, X. Jizong, G. Weikun, Z. Baozhen, X. Junying, and L. Yuzhang, “The excitonic properties and temperature behaviour of the photoluminescence from GaAs-GaAlAs multiple quantum well structures,” *Solid State Communications*, vol. 61, no. 11, pp. 707–711, 1987.
- [20] S. Zott, K. Leo, M. Ruckh, and H. W. Schock, “Radiative recombination in CuInSe_2 thin films,” *Journal of Applied Physics*, vol. 82, no. 1, pp. 356–367, 1997.
- [21] R. Jayakrishnan, K. G. Deepa, C. Sudha Kartha, and K. P. Vijayakumar, “Tuning donor-acceptor and free-bound transitions in CuInSe_2 /indium tin oxide heterostructure,” *Journal of Applied Physics*, vol. 100, no. 4, Article ID 046104, 2006.

Research Article

Study on the Electrospun CNTs/Polyacrylonitrile-Based Nanofiber Composites

Bo Qiao, Xuejia Ding, Xiaoxiao Hou, and Sizhu Wu

Key Laboratory of Carbon Fiber and Functional Polymers, Ministry of Education, College of Materials Science & Engineering, Beijing University of Chemical Technology, Beijing 100029, China

Correspondence should be addressed to Sizhu Wu, wusz@mail.buct.edu.cn

Received 16 June 2011; Revised 21 July 2011; Accepted 3 August 2011

Academic Editor: Steve Acquah

Copyright © 2011 Bo Qiao et al. This is an open access article distributed under the Creative Commons Attribution License, which permits unrestricted use, distribution, and reproduction in any medium, provided the original work is properly cited.

CNTs/PAN nanofibers were electrospun from PAN-based solution for the preparation of carbon nanofiber composites. The as-spun polyacrylonitrile-based nanofibers were hot-stretched by weighing metal in a temperature controlled oven. Scanning electron microscopy (SEM) and transmission electron microscopy (TEM) were used to characterize the morphology of the nanofibers, which indicated that carbon nanotubes were dispersed well in the composites and were completely wrapped by PAN matrix. Because of the strong interfacial interaction between CNTs and PAN, the CNTs/PAN application performance will be enhanced correspondingly, such as the mechanical properties and the electrical conductivity. It was concluded that the hot-stretched CNTs/PAN nanofibers can be used as a potential precursor to produce high-performance carbon composites.

1. Introduction

Electrospinning provides a straightforward and cost-effective approach to produce fibers from polymer solutions or melts having the diameters ranging from submicrons to nanometers [1–4]. Various polymers have been successfully electrospun into ultrafine fibers in recent years mostly in solvent solution and some in melt form. Potential applications based on such fibers specifically used as reinforcement in nanocomposites have been realized [5]. PAN is the most widely used precursor for manufacturing high-performance fibers due to its combination of tensile and compressive properties as well as the high carbon yield [6]. Conventional PAN-based carbon fibers typically have diameters ranging from 5 to 10 μm [7]. However, the electrospun PAN nanofibers are uniform with the diameters of approximately 300 nm [8, 9], which is more than 30 times smaller than their conventional counterparts. The high specific surface area of electrospun polymer and carbon nanofibers leads to the enhanced properties in various applications such as electrodes in fuel cells and supercapacitors. In spite of significant improvements in specific surface area of the PAN nanofibers, several drawbacks of polymer nanofibers are still present. For instance, the electrical conductivity of PAN is

an order of $\mu\text{S}/\text{cm}$. The microstructures and the related mechanical and/or electrical properties of the electrospun carbon nanofibers are still not clear.

Carbon nanotubes (CNTs) possess several unique mechanical, electronic, and other kinds of characteristics. For instance, single carbon nanotube has a modulus as high as several thousands of GPa and a tensile strength of several tens of GPa [10]. It is found that reinforcement of polymers by CNTs may significantly improve their mechanical properties, thermal stability, electric conductivity, and other functional properties [11]. It has been shown that significant interactions exist between PAN chains and CNTs, which lead to higher orientation of PAN chains during the heating process [12]. These outstanding properties make the polymer nanofibers optimal candidates for many important applications. It is also noted that single-wall carbon nanotube (SWNT-) reinforced polyimide composite in the form of nanofibrous film was made by electrospinning to explore a potential application for spacecrafts [13]. Carbon nanofibers for composite applications can also be manufactured from precursor polymer nanofibers [14]. Such kind of continuous carbon nanofiber composite also has potential applications as filters for separation of small particles from gas or liquid, supports for high temperature catalysts, heat management

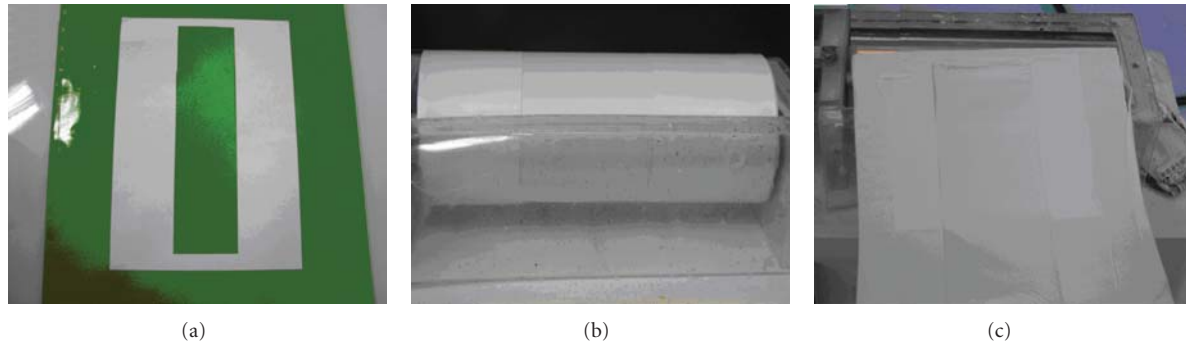


FIGURE 1: Schematic diagram of the frame to prepare the aligned nanofibers films. (a) The $16\text{ cm} \times 12\text{ cm}$ paper frame with the hollow of $16\text{ cm} \times 4\text{ cm}$ (b) on the rotating drum (c) after electrospinning.

materials in aircraft, and semiconductor devices, as well as promising candidates as small electronic devices, rechargeable batteries, and supercapacitors [15]. Fibrous materials used for filter media provide advantages of high filtration efficiency and low air resistance [16].

However, before full realization of their high performance, the following two crucial issues have to be solved: (i) dispersion and orientation of CNTs in the nanofiber [17, 18], good interfacial bonding is required to achieve load transfer across the CNT smatrix interface [19]; (ii) the macroscopic alignment in the nanofibers [20] and the orientation and crystallinity of polymer chains. Therefore, the manufacturing process and characterization methods for the microstructures and mechanical properties of PAN and PAN-based nanofibers have been studied in this paper.

2. Experimental

2.1. Materials. PAN used in this study included PAN/methyl acrylate/itaconic acid (93:5.3:1.7 w/w) (average molecular weight of 100 000 g/mol) which was purchased from UK Courtaulds Ltd. Since N,N-dimethylformamide (DMF) is the common solvent of PAN [3, 5, 8, 13, 14] which can easily evaporate during the electrospinning, so in this study the DMF was selected as solvent. It was purchased from Beijing Chemical Plant Co. To uniformly disperse the CNTs in the organic polymer matrix, the CNTs are modified to form an individually polymer-wrapped structure [17]. These effects caused the wrapped nanotubes to be much more readily suspended in concentrated SWNTs solutions and suspensions, which in turn substantially enabled manipulation of SWNTs into various bulk materials, including films, fibers, solids, and composites [21, 22].

2.2. Formation of Electrospun PAN/SWNTs Nanofiber Composites. The PAN and PAN-based nanofibers can be made by electrospinning with the nominal electric field on the order of 1 kV/cm. In the electrospun process, the PAN or CNTs/PAN solution is held by its surface tension at the end of a capillary, such as a stainless steel needle. The voltage between the electrode and the counter electrode could be controlled by the high voltage power supply such as setting at 14–16 kV. The collector rotated at 6.6 m/s surface speed,

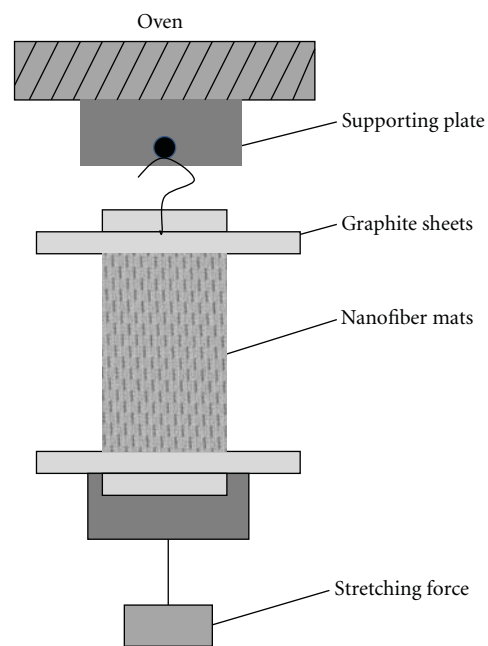


FIGURE 2: The schematic representation of the experimental setup for hot-stretching process.

by which the high speed rotating collector could align the nanofibers into the nanofiber sheets.

The relatively aligned PAN nanofibers and PAN/SWNTs composite nanofibers can be obtained by electrospinning with the set-up of a rotating instrument. Thus, for collection of the large area aligned nanofibers, a parallel rotating drum can be adopted. Such as in our study, the 0.16 m perimeter collector rotated at a surface speed about 6.6 m/s, that the high speed rotating collector could align the nanofibers into the nanofiber sheets. Figure 1 showed the schematic diagram of the frame to prepare the aligned nanofibers films with (a) the $16\text{ cm} \times 12\text{ cm}$ paper frame with the hollow of $16\text{ cm} \times 4\text{ cm}$ wrapping around (b) the rotating drum and (c) the sheet after electrospinning. And the SEM photographs of different speeds of rotation were shown in Figure 2, which that indicated the higher rotating speed leads to higher alignment of the nanofibers.

The SWNTs-based PAN composite solution was prepared as follows: (1) first, a given weight of SWNTs was first dispersed for 2 h in DMF through mild bath sonication, which was followed by the addition of PAN (128.91 mg per milliliter of SWNTs/DMF solution); (2) then, the mixture was mechanically stirred overnight at 40°C using a magnetic stirrer to yield a homogeneous solution.

During the electrospinning process, however, the whirlpool jet from the pinhead to the collector still made it difficult to get the unidirectional alignment in a large-area sheet [23] and the subsequent hot stretched procedure is particularly useful and is also the key process during the manufacturing of carbon fibers. Also, the electrospun nanofibers needed a subsequent hot-stretch to improve the fiber alignment. The PAN nanofibers and PAN/SWNTs composite nanofibers can be hot-stretched according to the method proposed by Johnson et al. [11, 12]. Both ends of the nanofiber sheet (size of 4 cm width \times 10 cm length with 17 μ m thickness) can be clamped with the pieces of graphite plates. Then, one end was fixed to the ceiling of the oven and the other end can be weighted by some of metal poise (75 g) to give a desired tension and elongation in the temperature-controlled oven at $135 \pm 2^\circ\text{C}$ for 5 min. The schematic diagram of hot stretching of nanofiber sheet is shown in Figure 2. The stretching ratio, λ , can be calculated from $\lambda = L/L_0$, where L and L_0 are the lengths of nanofiber sheet after and before the hot stretching, respectively.

2.3. Characterization. Morphological and structural examinations of the CNTs/PAN nanofibers were performed using scanning electron microscopy (SEM, HITACHI S-4700 FEG-SEM) and the transmission electron microscopy (transmission electron microscopy (TEM, HITACHI H-800)). The glass transition temperature T_g of the PAN nanofiber and PAN/SWNTs nanofiber were examined using differential scanning calorimetry (DSC, METTLER-TOLEDO STARE system). The samples were heated at a scanning rate of 20°C/min under nitrogen atmosphere in order to diminish oxidation. The value of T_g was found by differentiating the heat flow curve with the temperature. Mechanical test was performed by using an LR30K Electromechanical Universal Testing Machine (LLOYD Company). There were eight specimens used for each nanofiber sample where the samples were prepared in 5 mm width and 20 mm length. The tensile speed was 20 mm/min. Electrical conductivities of electrospun PAN/SWNTs nanofiber composites were measured using a ZC43 ultrahigh resistance measuring machine (Shanghai Meter Plant Co., Ltd.) at room temperature and ambient condition.

3. Results and Discussion

3.1. Morphology and Microstructures of the Electrospun Composites Nanofibers. It can be seen from Figure 3 that there is no obvious conglutination in the nanofibers after the introduction of SWNTs, which proved that SWNTs were relatively dispersed well in the composites. And Figure 3(c) showed the hot stretched PAN nanofibers, documenting the

better alignment along the sheet axis after the hot stretched process. It can further be found that the alignment of the fibers became closer to parallel after being hot stretched. Also, the average diameters of the original as-spun fibers were significantly reduced from 200 nm to 120 nm after hot stretching.

Figure 4 showed the SEM micrographs of PAN/SWNTs nanofibers with different SWNTs concentrations. The pure PAN nanofibers in Figure 4(a) were straight with a smooth surface and an average diameter of about 200 nm. The nanofibers became straighter, and the average diameter was increased with increasing SWNT concentrations. For instance, in Figure 4(b) the average diameter was about 300 nm. It was noted that SWNTs embedded in PAN nanofiber were mostly aligned along the nanofiber axis. When the concentration of the SWNTs increased to 1 wt%, the surface of the composite fibers became a little rough and the average diameter was a little bit smaller than the one of 0.5% wt SWNTs/PAN, which indicated that at high concentration some SWNTs might not be completely embedded into the nanofiber matrix [18].

In order to demonstrate that the prepared nanofibers do contain some oriented SWNTs, transmission electron microscopy (TEM) can be utilized to view the alignment and orientation of SWNTs within the nanofibers produced. Since the SWNTs possessed a high electron density compared with the PAN polymer matrix, SWNTs appeared as darker tubular structures embedded in the PAN/SWNTs composite nanofibers. It can be seen that the SWNTs are completely wrapped by the PAN matrix. TEM images revealed that in some regions nanotubes oriented well along the fiber axis but the nanotube distribution (number and orientation of the tubes) within a fiber may vary quite significantly (Figures 5(b), 5(c), and 5(d)).

The temperature at which the transition in the amorphous regions between the glassy and rubbery state occurs is called the glass transition temperature, which is related directly to the segment movement of polymer chain. The T_g of the PAN nanofiber and PAN/SWNTs nanofiber can be examined using differential scanning calorimetry (DSC). Figure 6(a) showed the DSC curves of PAN and PAN/SWNTs nanofibers. It can be seen that the T_g is increased by about 3°C by incorporating 0.75 wt% SWNTs into the PAN matrix. The improvement in the T_g stemmed from a stronger interfacial interaction and possible covalent bonding between PAN and the SWNTs. Figure 6(b) showed the DSC thermograms where the peak of PAN/SWNTs was higher than the one of pure PAN nanofibers. All these results suggested that the mobility of PAN chains is reduced due to the constraint effect of SWNTs [5].

3.2. Application Performance of the Electrospun Composites Nanofibers. One of the most important applications of engineering fibers such as carbon, glass, and Kevlar fibers was to be used as reinforcements in composites, which required that reinforced nanofibers should have a better mechanical properties [24]. Figure 7 showed the stress-strain curves of the PAN nanofibers and PAN/SWNTs nanofiber composites

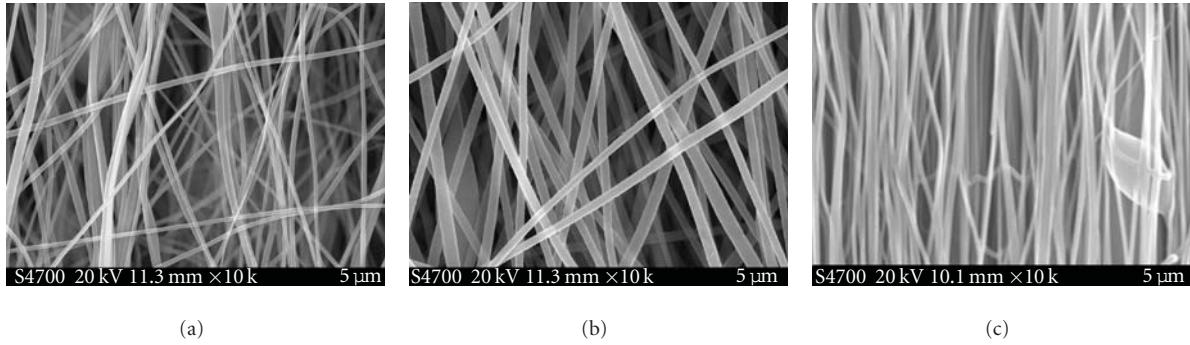


FIGURE 3: SEM micrographs: (a) as-spun pure partially aligned PAN nanofibers; (b) PAN/SWNTs composite nanofibers with SWNTs concentration 1 wt%; (c) hot-stretched pure PAN nanofibers.

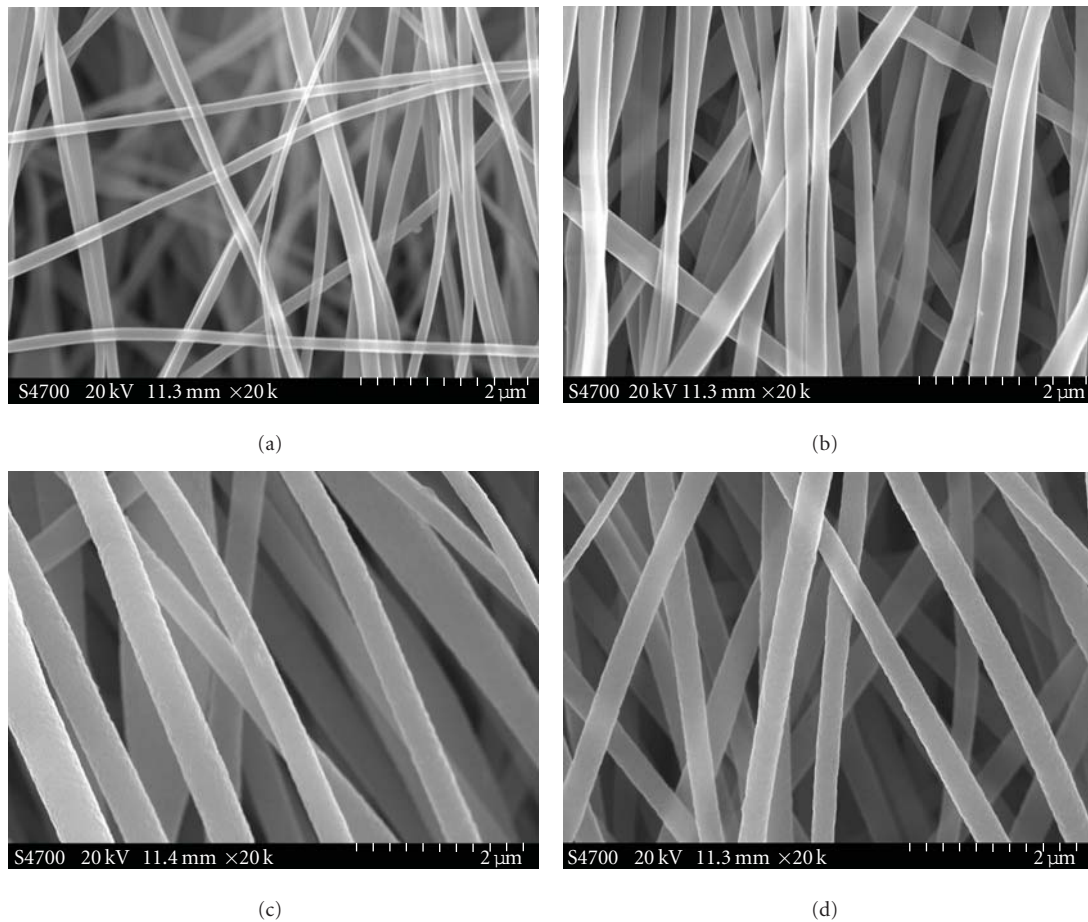


FIGURE 4: SEM micrographs of PAN/SWNTs nanofibers with different SWNTs concentration: (a) 0 wt%, (b) 0.25 wt%, (c) 0.5 wt%, (d) 1 wt%.

with different concentrations (hot stretching). It concluded that the introduction of SWNTs improves the modulus and tensile strength of the nanofiber. The tensile strength 128.76 MPa of the nanocomposites at about 0.75% SWNTs by weight was increased with 58.9%. Also the tensile modulus showed a peak value of 4.62 GPa with 66.8% improvement. The (e) curve in Figure 7 deviated from the trend, which

might be the reason of non uniform dispersion of SWNTs in high concentration. The significant improvement in strength and modulus was likely related to the good dispersion and orientation of SWNTs within the polymer matrix and the strong interfacial adhesion due to the SWNTs surface modification [5]. It can be concluded that both hot stretching and the introduction of SWNTs can improve the mechanical

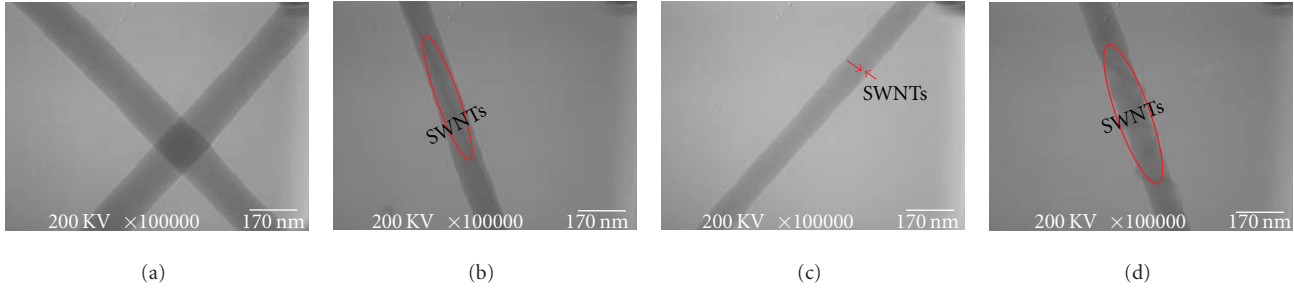


FIGURE 5: TEM images: (a) PAN nanofibers; (b)–(d) PAN/SWNTs nanofibers with SWNTs concentration 1 wt%.

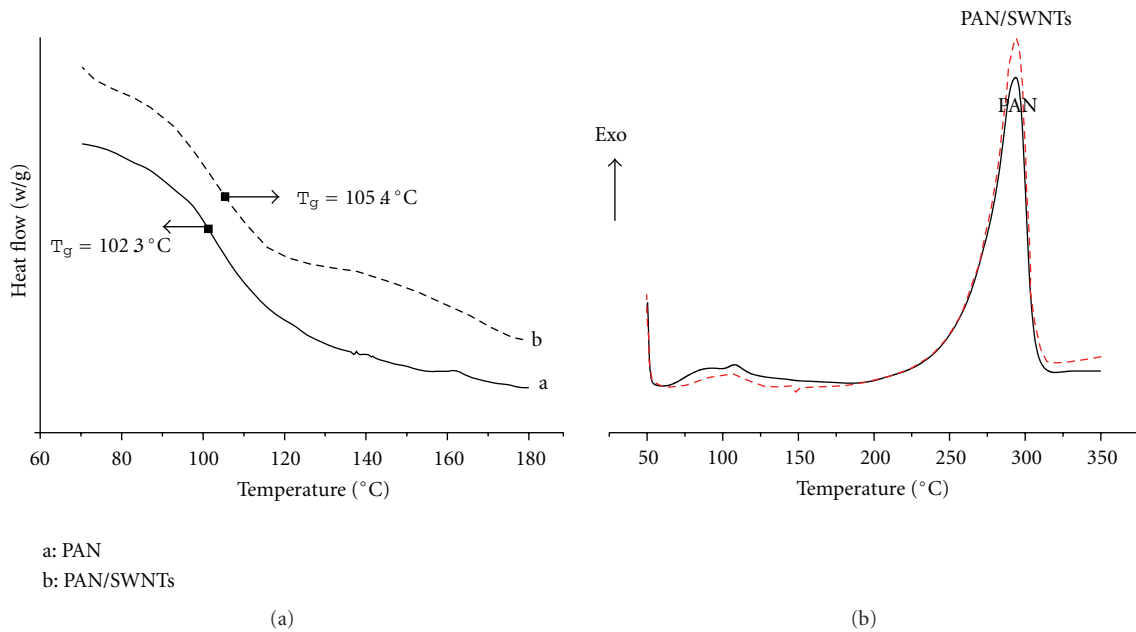


FIGURE 6: (a) T_g from DSC of electrospun nanofibers: a: PAN nanofibers; b: PAN/SWNTs composite nanofibers; (b) DSC thermograms of electrospun PAN and PAN/SWNTs nanofibers.

properties of PAN-based nanofibers significantly. With these reinforcements, the composite materials can provide superior structure properties such as high modulus and strength to weight ratios.

High electrical conductivity was always desired to have high capacitance and high power density in supercapacitors [25]. Conductive nanofibers were expected to be used in the fabrication of tiny electronic devices or machines such as sensors and actuators. The electrical conductivities of electrospun PAN/SWNTs nanofiber composites can also be measured using the ultrahigh resistance measuring machine at room temperature and ambient condition. The electrical conductivities of this nanofiber composites can be obtained according to the following [20]:

$$\rho_v = R_v \times \frac{21.23}{t}, \quad (1)$$

where ρ_v was volume resistivity, R_v was resistance, and t was the thickness of the nanofiber films, respectively.

The electrical conductivity of the pure PAN nanofiber usually was 0.2–0.5 S/cm [21]. Due to the superb electrical properties of SWNTs, a better electrical conductivity in PAN/SWNTs nanofiber composites was expected. There was no much change of the electrical conductivity in the SWNTs concentrations from 0 to 0.5%, but the electrical conductivity of 0.75% concentration was detected suddenly up to 2.5 S/cm. This was because a good electrical conductivity required the percolating network be formed by the SWNTs. Therefore, it can be concluded that the percolating network in composite nanofibers will be formed at the concentration of 0.75 wt.% SWNTs.

4. Conclusions

In summary, this study showed that polyacrylonitrile-based carbon nanofibers, embedded with wrapped carbon nanotubes, can be obtained by electrospinning process. The composites exhibited improvements in thermal, tensile properties, and so forth. The CNTs/PAN nanofiber sheets with

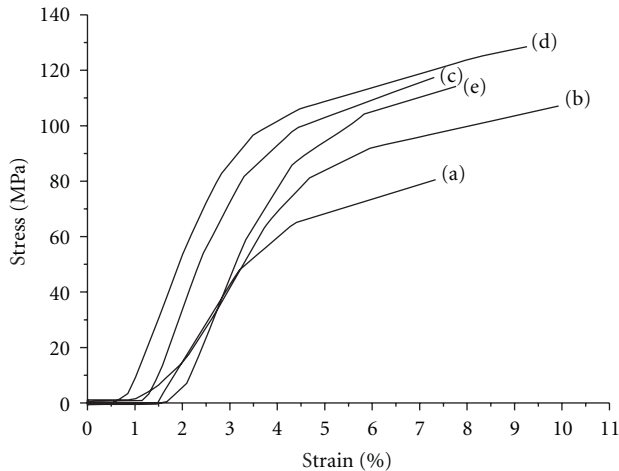


FIGURE 7: Stress-strain curves for PAN and PAN/SWNTs nanofiber: (a) pure PAN; (b) 0.25% SWNTs; (c) 0.5% SWNTs; (d) 0.75% SWNTs; (e) 1% SWNTs.

better alignments can be achieved by hot-stretched process. The morphology of the nanofibers characterized by SEM and TEM showed that carbon nanotubes were completely wrapped by the PAN matrix and oriented well along the fiber axis. Differential scanning calorimetry showed that the glass transition temperature of PAN increased by addition of SWNTs, indicating a strong interfacial interaction between PAN and SWNTs. Compared to pure PAN nanofibers, the mechanical property of the CNTs/PAN nanofibers exhibited quite improvement. For example, the tensile strength of the nanocomposites with 0.75% SWNTs by weight was increased with 58.9%. Incorporation of SWNTs into the nanofibers also increases the electrical conductivity to 2.5 S/cm for PAN/0.75% SWNTs nanofiber composites. Thus, the composite nanofibers with the component of SWNTs can be used as the potential precursor to produce high-performance carbon nanofibers.

Acknowledgment

The authors gratefully acknowledge the financial support sponsored by the NSF of China (50973007).

References

- [1] R. Andrews, D. Jacques, A. M. Rao et al., "Nanotube composite carbon fibers," *Applied Physics Letters*, vol. 75, no. 9, pp. 1329–1331, 1999.
- [2] R. H. Baughman, A. A. Zakhidov, and W. A. De Heer, "Carbon nanotubes—the route toward applications," *Science*, vol. 297, no. 5582, pp. 787–792, 2002.
- [3] Z. Bashir, S. P. Church, and D. Waldron, "Interaction of water and hydrated crystallization in water-plasticized polyacrylonitrile films," *Polymer*, vol. 35, no. 5, pp. 967–976, 1994.
- [4] Y. V. Basova, D. D. Edie, Y. S. Lee, L. K. Reid, and S. K. Ryu, "Effect of precursor composition on the activation of pitchbased carbon fibers," *Carbon*, vol. 42, no. 3, pp. 485–495, 2004.
- [5] W. J. Chou, C. C. Wang, and C. Y. Chen, "Characteristics of polyimide-based nanocomposites containing plasma-modified multi-walled carbon nanotubes," *Composites Science and Technology*, vol. 68, no. 10–11, pp. 2208–2213, 2008.
- [6] I. Chun, D. H. Reneker, H. Fong et al., "Carbon nanofibers from polyacrylonitrile and mesophase pitch," *Journal of Advanced Materials*, vol. 31, no. 1, pp. 36–41, 1999.
- [7] P. G. Collins, M. S. Arnold, and P. Avouris, "Engineering carbon nanotubes and nanotube circuits using electrical breakdown," *Science*, vol. 292, no. 5517, pp. 706–709, 2001.
- [8] J. B. Donnet, T. K. Wang, J. C. Peng, and S. Rebouillat, *Carbon Fibers*, Marcel Dekker, New York, NY, USA, 1998.
- [9] Y. Dzenis, "Spinning continuous fibers for nanotechnology," *Science*, vol. 304, no. 5679, pp. 1917–1919, 2004.
- [10] A. Javey, J. Guo, Q. Wang, M. Lundstrom, and H. Dai, "Ballistic carbon nanotube field-effect transistors," *Nature*, vol. 424, no. 6949, pp. 654–657, 2003.
- [11] J. Johnson, L. N. Phillips, and W. Watt, "The production of carbon fibers," British Patent, no. 1,110,790, 1965.
- [12] J. Johnson, W. Watt, L. N. Phillips, and R. Moreton, "Improvements in or relating to carbonisable fibre and carbon fibre and their production," British Patent, no. 1,166,251, 1966.
- [13] A. Koganemaru, Y. Z. Bin, and M. Matsuo, "Composites of polyacrylonitrile and multiwalled carbon nanotubes prepared by gelation/crystallization from solution," *Advanced Functional Materials*, vol. 14, pp. 842–850, 2004.
- [14] D. Li, Y. Wang, and Y. Xia, "Electrospinning of polymeric and ceramic nanofibers as uniaxially aligned arrays," *Nano Letters*, vol. 3, no. 8, pp. 1167–1171, 2003.
- [15] A. G. MacDiarmid, W. E. Jones, I. D. Norris et al., "Electrostatically-generated nanofibers of electronic polymers," *Synthetic Metals*, vol. 119, no. 1–3, pp. 27–30, 2001.
- [16] P. Miaudet, C. Bartholome, A. Derré et al., "Thermo-electrical properties of PVA-nanotube composite fibers," *Polymer*, vol. 48, no. 14, pp. 4068–4074, 2007.
- [17] E. R. Waclawik, J. M. Bell, R. G. S. Goh, A. Musumeci, and N. Motta, "Self-organization in composites of poly(3-hexylthiophene) and single-walled carbon nanotubes designed for use in photovoltaic applications," in *BioMEMS and Nanotechnology II*, vol. 6036 of *Proceedings of the SPIE*, Brisbane, Australia, December 2005.
- [18] R. E. Smalley, D. T. Colbert, K. A. Smith, and O. Michael, "Polymer-wrapped single wall carbon nanotubes," US Patent, no. 201,001,437,18A, 2007.
- [19] Z. M. Huang, Y. Z. Zhang, M. Kotaki, and S. Ramakrishna, "A review on polymer nanofibers by electrospinning and their applications in nanocomposites," *Composites Science and Technology*, vol. 63, no. 15, pp. 2223–2253, 2003.
- [20] N. W. H. Cheetham and L. Tao, "Variation in crystalline type with amylose content in maize starch granules: an X-ray powder diffraction study," *Carbohydrate Polymers*, vol. 36, no. 4, pp. 277–284, 1998.
- [21] D. H. Reneker and I. Chun, "Nanometre diameter fibres of polymer, produced by electrospinning," *Nanotechnology*, vol. 7, no. 3, pp. 216–223, 1996.
- [22] S. D. McCullen, D. R. Stevens, W. A. Roberts, S. S. Ojha, L. I. Clarke, and R. E. Gorga, "Morphological, electrical, and mechanical characterization of electrospun nanofiber mats containing multiwalled carbon nanotubes," *Macromolecules*, vol. 40, no. 4, pp. 997–1003, 2007.
- [23] E. P. S. Tan and C. T. Lim, "Mechanical characterization of nanofibers—a review," *Composites Science and Technology*, vol. 66, no. 9, pp. 1102–1111, 2006.

- [24] H. G. Chae, T. V. Sreekumar, T. Uchida, and S. Kumar, "A comparison of reinforcement efficiency of various types of carbon nanotubes in polyacrylonitrile fiber," *Polymer*, vol. 46, no. 24, pp. 10925–10935, 2005.
- [25] I. H. Chen, C. C. Wang, and C. Y. Chen, "Fabrication and structural characterization of polyacrylonitrile and carbon nanofibers containing plasma-modified carbon nanotubes by electrospinning," *Journal of Physical Chemistry C*, vol. 114, no. 32, pp. 13532–13539, 2010.

Research Article

Influence of pH, Precursor Concentration, Growth Time, and Temperature on the Morphology of ZnO Nanostructures Grown by the Hydrothermal Method

G. Amin, M. H. Asif, A. Zainelabdin, S. Zaman, O. Nur, and M. Willander

Department of Science and Technology, Linköping University, Norrköping Campus, 60174 Norrköping, Sweden

Correspondence should be addressed to G. Amin, gulam@itn.liu.se

Received 7 June 2011; Revised 27 July 2011; Accepted 29 July 2011

Academic Editor: Yanqiu Zhu

Copyright © 2011 G. Amin et al. This is an open access article distributed under the Creative Commons Attribution License, which permits unrestricted use, distribution, and reproduction in any medium, provided the original work is properly cited.

We investigated the influence of the pH value, precursor concentration (C), growth time and temperature on the morphology of zinc oxide (ZnO) nanostructures. The pH of the starting solution was varied from 1.8 to 12.5. It was found that the final pH reaches an inherent value of 6.6 independently of the initial pH solution. Various ZnO structures of nanotetrapod-like, flower-like, and urchin-like morphology were obtained at alkaline pH (8 to 12.5) whereas for pH solution lower than 8 rod-like nanostructures occurred. Moreover, we observed the erosion of the nanorods for a pH value less than 4.6. By changing the concentrations the density and size were also varied. On going from a high ($C > 400$ mM) to lower ($C < 25$ mM) C , the resulted ZnO nanostructures change from a film to nanorods (NRs) and finally nanowires (NWs). It was also found that the length and diameter of ZnO NRs follow a linear relation with time up to 10 hours, above which no further increase was observed. Finally the effect of growth temperature was seen as an influence on the aspect ratio.

1. Introduction

Zinc oxide (ZnO) is a promising material with wide bandgap of 3.4 eV and relatively large exciton binding energy of 60 meV [1]. Zinc oxide is also characterized by having excellent chemical stability, nontoxicity, and good electrical, optical, and piezoelectric properties [1, 2]. This material also possesses a rich family of nanostructures (NSs). It has been predicted that in general NSs will play an important role in the future in a variety of practical applications, including optoelectronic devices, for example, solar cells [3], UV sensors [4], biosensors [5], and light emitting diodes [6–8]. For these applications, it is essential to have a thorough understanding of the growth mechanism to achieve the desired morphology of the ZnO NSs needed. Since the properties of ZnO NSs strongly depend on its morphology and shape, it is also essential to precisely control their size, shape, and surface architecture to utilize its properties in different practical fields. However, many methods have been applied to the synthesis of ZnO NSs, such as metal organic chemical vapor deposition (MOCVD) [9], electrochemical

deposition techniques [10], sputter deposition techniques [11], and pulse laser deposition method [12]. But those methods require severe reaction conditions, such as high temperature, accurate gas concentration, and flow rate or complex processes. So it is important to find a simple, low-temperature method for the synthesis of ZnO NSs and find a way to control the growth parameters. Compared with the above synthesis processes, the ZnO NSs were grown by using the hydrothermal method. This growth method showed some advantages compared with others such as the use of simple setup, relatively low temperature, large area deposition, and low cost and is environment friendly. There are several parameters in the hydrothermal method that can affect the growth of the ZnO NSs such as seeding of the substrate which increases the density and alignment of the NSs [13], thickness of the seed layer which can be controlled simply by the speed of spin coating, and also presence of impurities in the seed layer which can strongly influence the growth and crystallinity of the ZnO NSs [14]. Other parameters like angle of the inclination, for example, whether the substrate is placed vertically or inclined with the walls of

heating bath, temperature, time, concentration, and pH have also an influence. Using different precursors from the one used here, the temperature was found to affect the synthesis of ZnO nanorods, for example, the length and diameter of the NRs increased with increasing the temperature [15]. It has been reported that the time is largely influencing the ZnO NRs diameter; longer synthesis time leads to larger diameter NRs [16]. The dimension of ZnO NRs was also found to be affected by the zinc ions concentration [16]. The role of the pH on the hydrothermal growth of the ZnO NRs was examined, and it was shown that the effect of the pH is crucial because hydroxide ions (OH^-) are strongly related to the reactions that produce the ZnO NSs [17–19]. Nevertheless, in the above-mentioned published results either only one parameter was considered or it was for a different precursor than the one used here. Furthermore, none of the published reports have been used to examine the growth of the ZnO NSs under a pH value $\ll 7$. Therefore, several fundamental reaction parameters need to be addressed to understand its influence on the growth.

In this paper, we present a study of the effect of different parameters on the morphology of ZnO NSs. These parameters are the solution pH (within a range of 1.8–12.5), temperature, time, and precursor concentration. We have conducted a systematic morphological and structural study of the grown samples. The results demonstrate that ZnO NSs morphological and structural characteristics can be controlled by adjusting the above-mentioned parameters.

2. Experimental Procedure

All the chemicals used in this study were of analytical reagent grade purchased from Sigma-Aldrich and used without further purification. The aqueous solutions containing the growth precursors were prepared using deionized water (DI) as a solvent. Silicon (100) substrates were chosen for the growth and were cleaned in ultrasonic bath using acetone, IPA (isopropyl alcohol), and DI water to remove dust and surface contamination. Then, they were etched by diluted hydrofluoric acid (HF) solution to get rid of the native oxide layer. For the ZnO NSs growth, a seed layer has been prepared using zinc acetate solution in ethanol as described in [20], and it was spin-coated on the substrates two times at a spin speed of 1000 rpm for 30 seconds, followed by soft baking at 120°C for 5 min. Figure 2(a) shows the atomic force microscope (AFM) image of seed layer coated substrate and its height profile which shows an average height of the particle 10–15 nm. Seeding of the substrate with ZnO nanoparticles was found to lower the thermodynamic barrier by providing nucleation sites and thus it is an important parameter to achieve uniform growth of ZnO NSs through hydrothermal process [20]. The same procedure and conditions of depositing the seed layer are applied to all samples used in the experiments. The aqueous solution for the growth of ZnO NSs was prepared using equimolar zinc nitrate hexahydrate ($\text{Zn}(\text{NO}_3)_2 \cdot 6\text{H}_2\text{O}$, 99%) and hexamethylenetetramine (HMT) ($\text{C}_6\text{H}_{12}\text{N}_4$, 99.5%). The solution was then transferred into different sealable glass beakers.

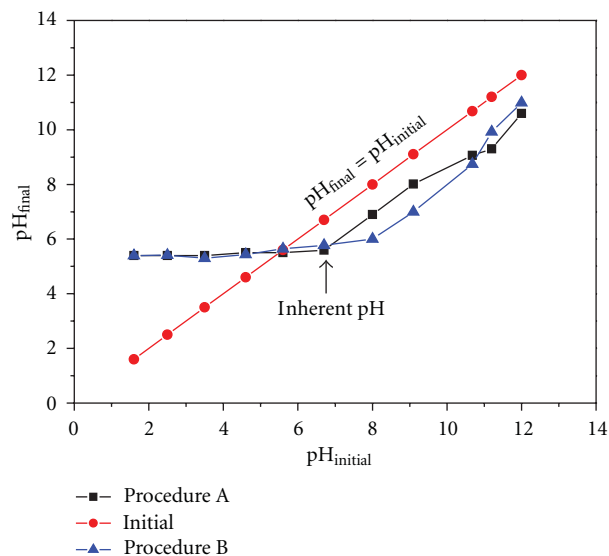


FIGURE 1: Plot of initial versus final pH of the precursor aqueous solution for the ZnO NSs in 5 hrs of growth time.

To investigate the role of the pH on the growth of the ZnO NSs, the solution was adjusted to different pH ranging from 1.8 to 12.5, and in each beaker a preseeded substrate was suspended vertically for 5 hours (hrs) at 90°C in an ordinary oven. The pH values were varied by adding precise amounts of nitric acid (HNO_3) or ammonia ($\text{NH}_3 \cdot \text{H}_2\text{O}$) (procedure A) and hydrochloric acid (HCl) or sodium hydroxide (NaOH) (procedure B) to the aqueous solutions as pH controlling agents. The inherent pH of the solution was 6.6. At the end of the growth, the substrates were taken out of the solution and rinsed several times with deionized water then they were dried using high purity N_2 gas at room temperature, and the pH of each solution was monitored after the growth ended. All the pH measurements were carried out with a pH meter from Metrohm Instruments.

To observe the effect of time and temperature, we used the same aqueous solution (100 mM concentration) for the growth of ZnO NRs at different reaction times (1 to 20 hrs) at 90°C and different temperatures (50°C to 110°C) for 5 hrs, respectively. To examine the influence of the concentration, an equimolar different precursor concentration solution (5 mM to 400 mM) was prepared for a growth time of 5 hrs at a temperature 90°C . The characterization of the NSs was performed using field emission scanning electron microscopy (SEM) and X-ray diffraction (XRD).

3. Results and Discussion

3.1. Influence of pH on the Growth of ZnO NSs. For the growth of materials with chemical route, the pH value has always an important influence on the final products. In order to better understand the effect of the pH on the growth of ZnO NSs, the initial and the final pH values were carefully measured before and after the growth. Two sets of chemicals were used to vary the pH of the reactants, that is, procedures A and B. The different initial pH ($\text{pH}_{\text{initial}}$) values of the

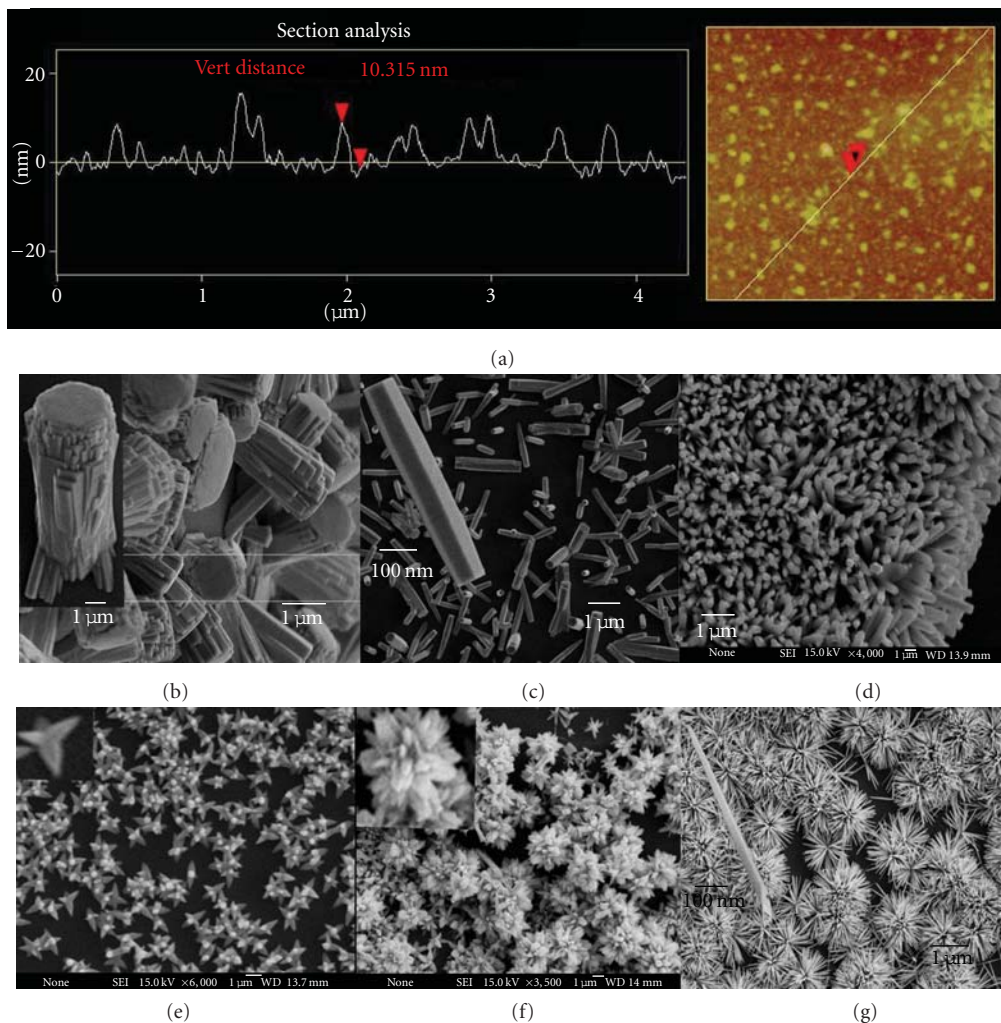


FIGURE 2: (a) shows the AFM image of the seed layer and the corresponding height profile. (b) SEM image of ZnO NSs on Si substrate grown with different aqueous solutions of pH value 1.8; (c) at pH value of 4.6; (d) at pH value of 6.6; (e) at pH value of 9.1; (f) at pH value of 10.8; (g) at pH value of 11.2. The insets show enlarged SEM images of ZnO NSs (scale bar = 100 nm).

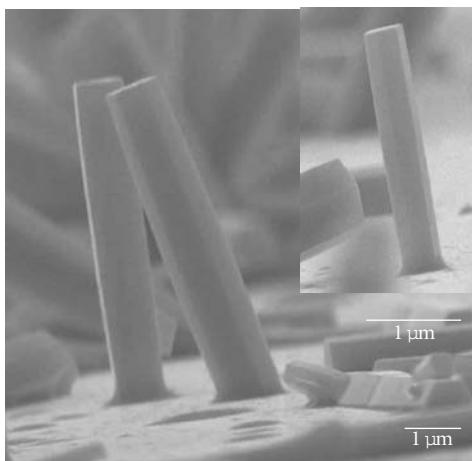


FIGURE 3: Cross-sectional SEM image of the ZnO NRs grown under conditions $T = 90^{\circ}\text{C}$, $t = 6$ hrs, $\text{pH} = 6.6$, and $C = 100$ mM.

growth solution were adjusted to 1.8, 2.5, 3.5, 4.6, 6.6, 8, 9.2, 10.7, 11.2, and 12.5, respectively. Figure 1 represents the plot of the $\text{pH}_{\text{initial}}$ versus the final pH (pH_{final}) recorded over a period of 5 hrs using 100 mM precursors concentration. The experiments carried out in this range of pH (1.8–12.5) either with procedure A or procedure B showed that the alkaline pH was relatively decreased with the same rate, while the acidic pH was converged to 5.4 apparently approaching the inherent value 6.6. It is to mention that the same experiments have been repeated four times giving the same results, indicating the reproducibility of this process. To correlate the growth rate of the ZnO NSs with the pH, a set of samples were grown on the preseeded Si substrates with $T = 90^{\circ}\text{C}$ and $t = 5$ hrs in adjusted $\text{pH}_{\text{initial}}$ growth solutions. The inherent pH solution was transparent, and there were some visible white precipitates in the solution. The obtained NRs from the inherent pH solution have an average length of $2.2\ \mu\text{m}$ and diameter of 400 nm. The length was measured

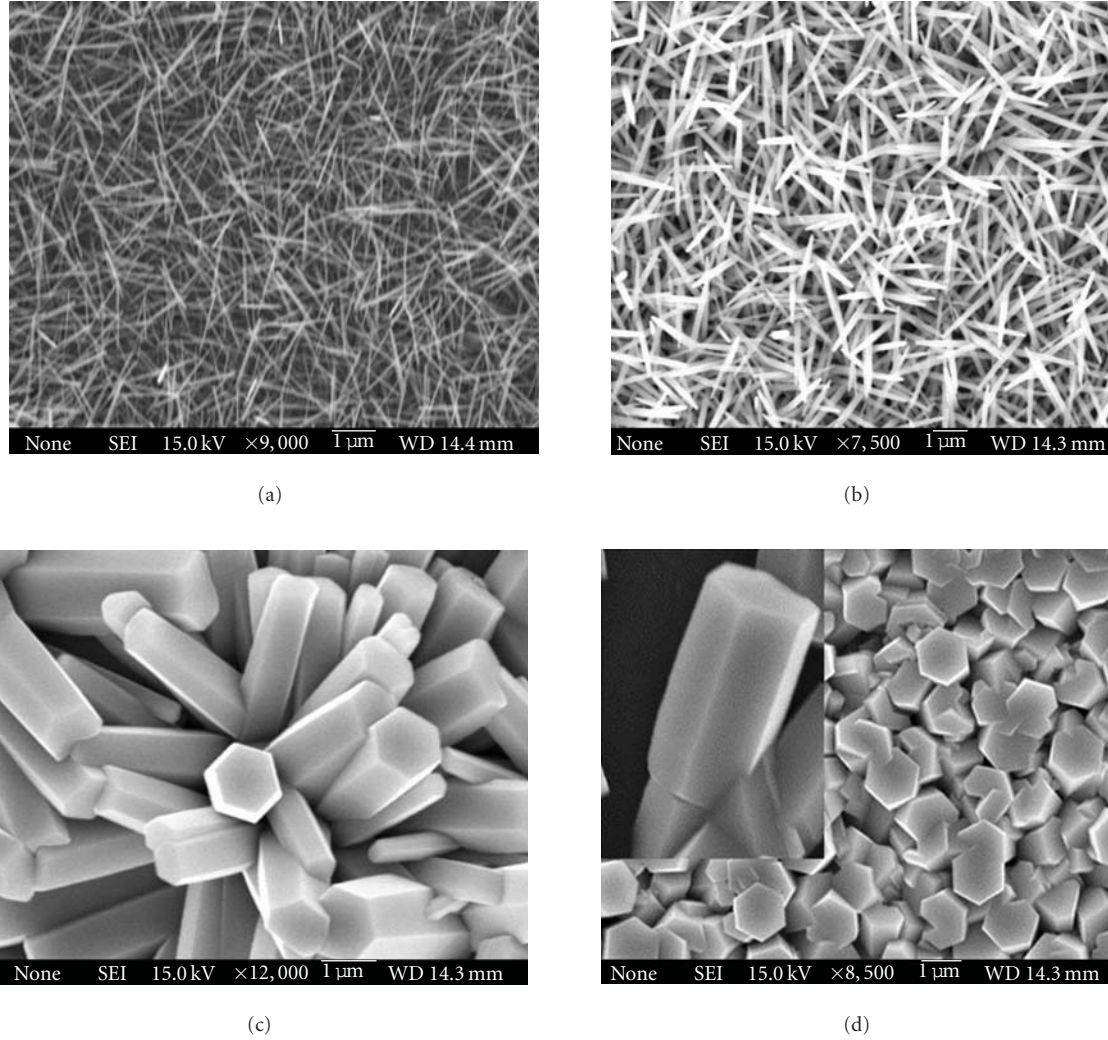


FIGURE 4: SEM images of ZnO NSs on Si substrate with different precursor concentrations of the growth aqueous solution (a) at 25 mM; (b) 50 mM; (c) 100 mM; (d) 300 mM. Inset shows the magnified view of the ZnO NSs (scale bar = 100 nm).

from the cross-sectional SEM image (Figure 3) while the diameter was measured from the top view SEM as shown in Figure 2(d). Since in the inherent solution HMT was used as a precursor for the growth of ZnO NSs, first it hydrolyzes to produce the OH^- and ammonia. Then, the OH^- forms a complex with Zn^{2+} , followed by thermal decomposition into ZnO. The chemistry of the reaction during growth in the solution is discussed by Zainelabdin et al. [21]. When the pH was increased by adding $\text{NH}_3 \cdot \text{H}_2\text{O}$, the ammonia hydrolyzed into NH_4^+ and hydroxide giving rise at the same way to the increases of OH^- concentration in the solution. The following chemical reactions are governing the growth process:

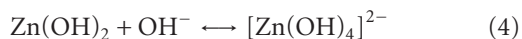
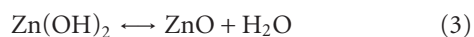
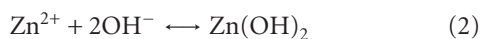
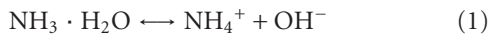


Figure 2 shows the SEM images of various NSs grown under different initial pH values. Figure 2(d) shows high density NRs structure prepared from solution at $\text{pH}_{\text{initial}} = 6.6$ without $\text{NH}_3 \cdot \text{H}_2\text{O}$, indicating that at this OH^- concentration only rod-like structures can be grown. When the pH was increased to 8 nanotetrapod ZnO NSs were obtained as shown in Figure 2(e); this can be attributed to the hydroxide concentration increase in the initial solution, giving rise to the anisotropic growth directions. When we increased the pH to 9.1 the growth rate increased due to the increases of OH^- concentration which gives rise to ZnO particles in the solution. The resulting structure (Figure 2(f)) was a flower-like structure with thick arms. Figure 2(g) shows ZnO urchin-like structures with needles length of $2 \mu\text{m}$ and a diameter of $\sim 50 \text{ nm}$ for samples prepared from a solution with $\text{pH} = 11.2$. The inset shows high magnification image of ZnO nanoneedle. Similar surface morphology structures were obtained at pH of 12.5. We believe that by increasing the OH^- ions as compared to Zn^{2+} concentrations reaction (4) immediately starts to take place.

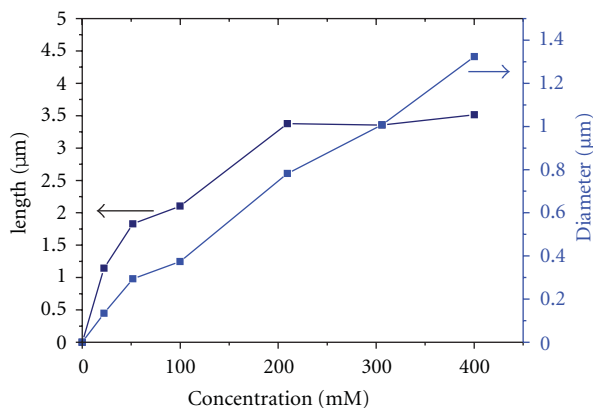


FIGURE 5: Plot of concentration versus average length and diameter of the ZnO NSs.

The $[\text{Zn}(\text{OH})_4]^{2-}$ acts as the new growth precursor while the nuclei obtained in reaction (3) serve as the seed. Therefore anisotropic growth of ZnO occurs at the active site of ZnO seed. Finally, we observed that for the high pH starting solution, the obtained structures were self-assembled.

By inspecting the cases for $\text{pH} < 7$ by adding either HNO_3 or HCl very different results were obtained. Figures 2(b) and 2(c) demonstrate the SEM images for the case with initial pH values of 1.8 and 4.6, respectively. The obtained structures were nanorods with hexagonal shape, the diameter and length were increased, and the density was largely decreased by the addition of HNO_3 or HCl or by lowering the pH values. The dissolution of precipitates occurs according to reaction (2). As the HNO_3 or HCl is added, more and more Zn^{2+} is formed and therefore the resulted ZnO nanorods grow to a larger length and diameter as shown in Figures 2(b) and 2(c). However, very large dimension rods were obtained at $\text{pH} < 4.6$ and down to 1.8 in the HNO_3 adjusted environment but they were eroded as clearly seen in the SEM image of Figure 2(a), and the etching was severe at the lowest pH values which also support the results that the ZnO starts to be etched in an acidic nature solution [22]. However, for $\text{pH} < 4.6$ no growth was obtained when the pH value was lowered by HCl . This can be due to the fact that the etching was dominating over the growth. It is also worthwhile to mention that after inspecting the SEM images of these samples there were no signs of a seed layer (ZnO nanoparticles) and the substrate was clean which shows that the etching was dominant.

3.2. Effect of the Precursor Concentration. In this section the concentration variation of the reactants using inherent pH value of 6.6 is discussed. It is well known that increasing or decreasing the concentration of the chemical reactants will eventually influence the resultant products. In the original paper which describes the growth of ZnO NRs via aqueous solutions, they have obtained microrods since a high concentration of the initial reactants was used [23]; when a relatively low concentration was used by the same authors the ZnO NRs were achieved [24]. This implies that a good control over the chemical reactants can be utilized

to gain direct control over the dimensions of the final ZnO NRs. According to this fact we have studied the effect of the reactants concentration on the dimensions of NRs as mentioned above starting by the inherent pH value. Scanning electron microscope images of ZnO NRs grown at different concentrations of the aqueous solution containing equimolar concentrations of $\text{Zn}(\text{NO}_3)_2 \cdot 6\text{H}_2\text{O}$ and HMT are shown in Figure 4; inset shows the magnified SEM image. The density, length, and diameter of the ZnO nano-/microrods are varied with the concentration applied during the synthesis; a higher concentration yields a micro-sized diameter with densely packed c-axis aligned ZnO rods as shown in Figure 4(d). Furthermore, for concentrations > 400 mM the microrod sized ZnO is converted into a polycrystalline thin film. On the other hand a low concentration (10 to 25 mM) of aqueous solution results in wire-like NRs with a diameter < 100 nm, and the length was found to be $1.2 \mu\text{m}$, evenly covering the substrate as revealed in Figures 4(a) and 4(b). Moreover, for concentrations less than 5 mM no growth was achieved on the substrate at the specified duration of 5 hrs, instead only residual ZnO was deposited on the bottom of the glass beaker suggesting that the longer time is required to grow ZnO NSs. When the growth was established for longer time (20 hrs) ultrathin NWs were achieved covering the substrate evenly. Nevertheless, Zhu et al. have synthesized ZnO-based core/shell structure at 5 mM at shorter time by modifying the aqueous solution [25]. The results of the precursor concentration variation with the ZnO NRs dimension are summarized in Figure 5. The graph clearly demonstrates that a linear relation can be drawn between the increase of the concentration and the NRs dimensions; interestingly the diameter of the NRs increases gradually, while the length becomes constant above 200 mM. This implies that there is a critical length for the ZnO NRs at which further increase of the concentration will not have any role in the axial growth direction whereas the radial direction grows continuously and at high enough concentration the rods merge to form continuous thin film.

3.3. Influence of the Growth Time. To investigate influence of the growth time on the ZnO NRs, we have grown the ZnO NRs in equimolar concentration (100 mM) of HMT and $\text{Zn}(\text{NO}_3)_2 \cdot 6\text{H}_2\text{O}$ at constant temperature of 90°C and inherent pH value of 6.6 for 1, 3, 6, 10, and 20 hrs. Figure 6 shows the cross-sectional SEM images of the ZnO NRs grown at different durations. It can be noticed from the figure that the growth duration is an important factor to control the size of the final ZnO structure. Figure 6(a) shows SEM image of ZnO NRs grown for a time of 1 hr, with an average length of 500 nm, indicating that rods are emerging on the nucleation sites. These embryonic NRs continue to grow with increasing the growth duration. When growth was conducted for 3 hrs average sized NRs with length of $1.0 \mu\text{m}$ were obtained (Figure 6(b)). By further increasing the growth time to 6 hrs the NRs length was boosted to $1.8 \mu\text{m}$ as revealed in Figure 6(c). The length has increased up to $2.2 \mu\text{m}$ when the growth time was increased to 10 hrs as seen in Figure 6(d), while no further increase of the ZnO NRs size was observed above 10 hrs. The inset in Figure 6 shows a top

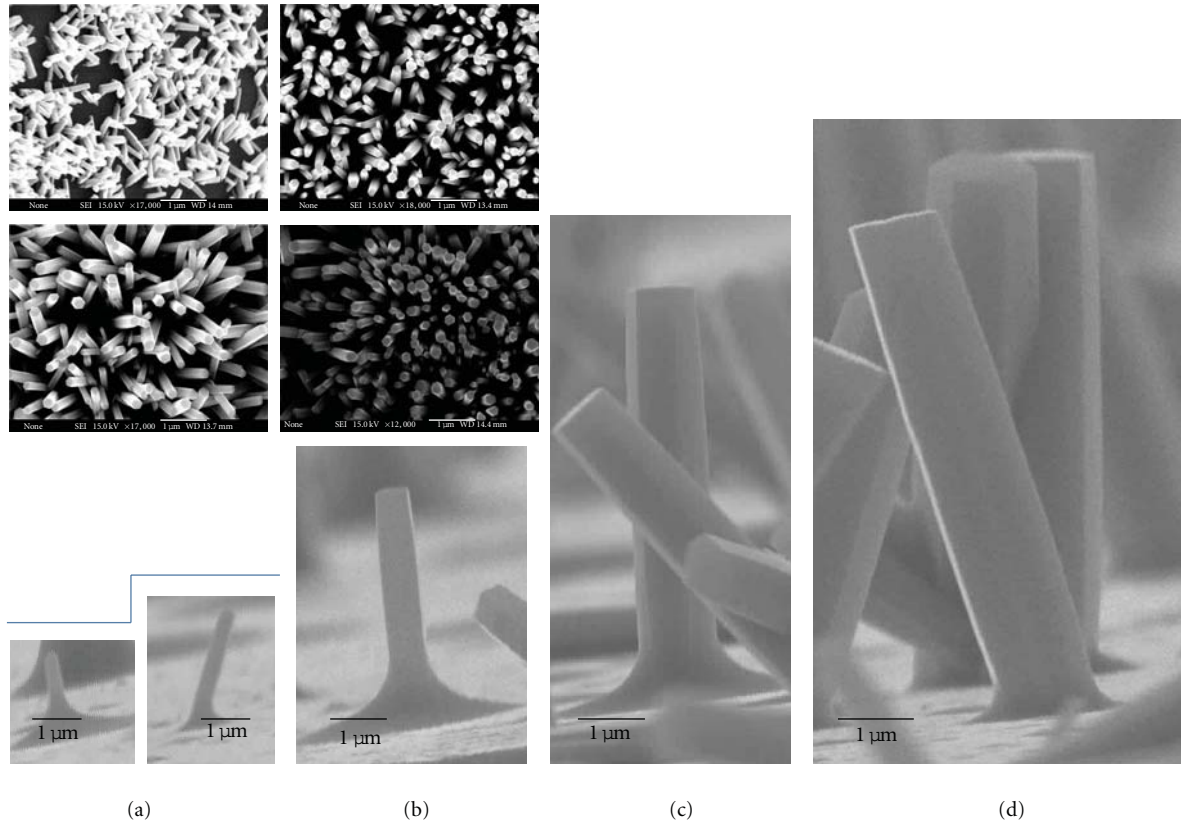


FIGURE 6: Cross-sectional SEM images of ZnO NRs on Si substrate at different growth times: (a) 1 hr; (b) 3 hrs; (c) 6 hrs; (d) 10 hrs at $T = 90^{\circ}\text{C}$. The inset shows the corresponding top view of the SEM images.

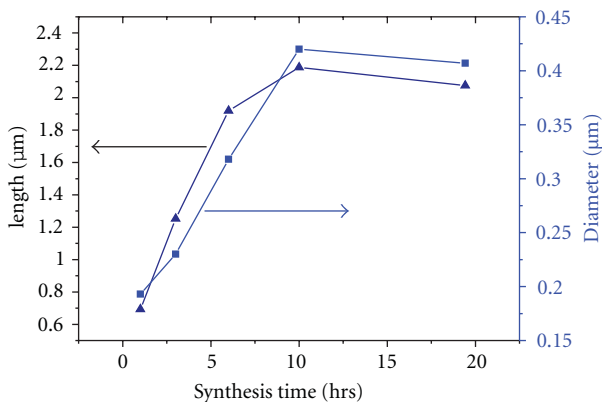


FIGURE 7: Plot of ZnO NRs synthesis time versus change in average length and diameter.

view of the corresponding SEM images to the ones shown in the figure; here the diameter of the obtained ZnO NRs was changed from 150 nm to 500 nm with the change of time as stated above. Utilizing the cross-sectional and top view SEM images we calculated the lengths and diameters of ZnO NRs with growth time, and the result is summarized in Figure 7. The results indicated that continuous and steady growth of ZnO nanostructures precedes until the first 10 hrs and then the system would be in closure-precipitation equilibrium

stage as indicated in Figure 7. It is believed that with the passage of time the OH^- would continuously hydrolyze in the water solution from HMT up to 10 hrs then the OH^- would be consumed. The results show that the density of the ZnO nanostructures depends on the reaction time. The threshold time for growing ZnO NRs was observed to be one hour; therefore no growth was obtained below one hour.

3.4. Influence of the Growth Temperature. The effect of T on the ZnO NSs was also investigated. In our experiments, a set of samples were grown in the aqueous solution using a pH = 6.6, $t = 5$ hrs, and 100 mM precursors concentration in a controlled digital laboratory oven. Our growth temperature was changed from 50°C up to 110°C . The SEM images of this set of samples are shown in Figure 8. Figure 9 shows the plot of the aspect ratio of ZnO NRs versus T when the growth was performed in aqueous solution with an initial pH of 6.6. From these figures it can be seen that by changing T the aspect ratio is gradually increased up to 95°C . However, no further increase in the aspect ratio was observed at 110°C . The structure remained rodlike and the density was almost the same. Therefore, we believe that the size of the ZnO NSs can be controlled by changing T , and we suggest that the feasible T for the growth is $<100^{\circ}\text{C}$ since it is an aqueous based (water-based) solution. The crystallinity of the ZnO NRs grown at 90°C for 5 hrs and with a pH 6.6

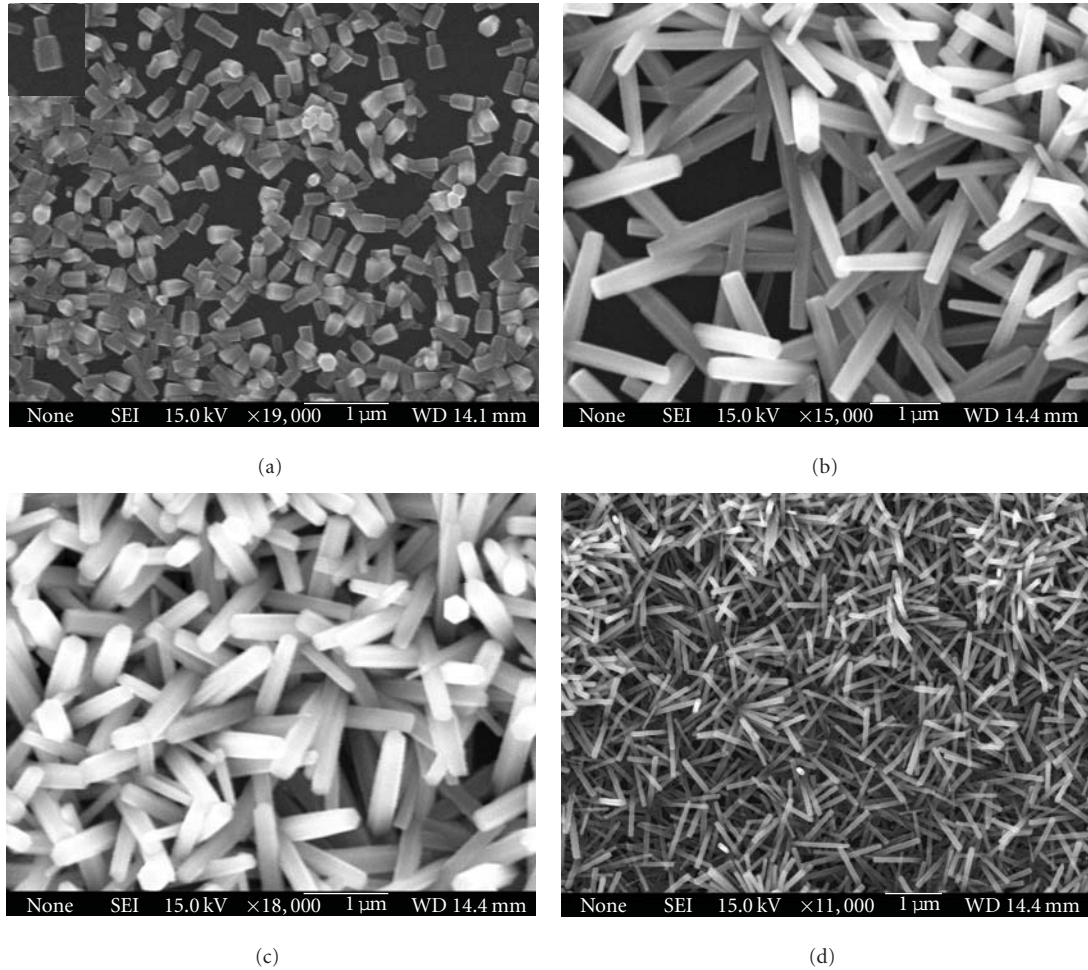


FIGURE 8: SEM images of ZnO NRs on Si substrates for the growth temperatures (a) 50°C; (b) 70°C; (c) 90°C; (d) 110°C for 5 hrs and at 100 mM concentration. The inset is the magnified image (scale 100 nm) of single rod.

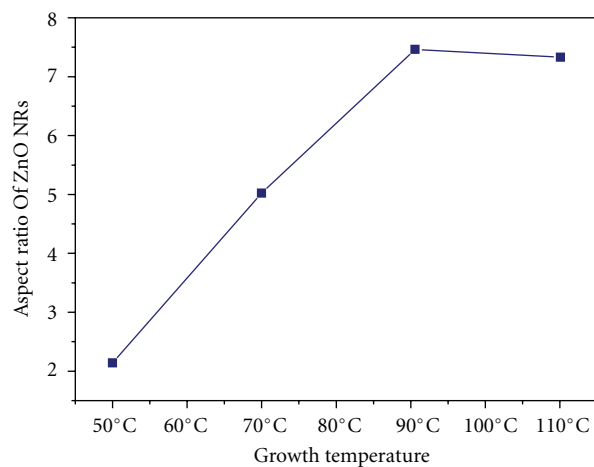


FIGURE 9: Plot of aspect ratio of ZnO NRs versus growth temperature (T) under the conditions of $C = 100$ mM, $t = 5$ hrs, and inherent pH.

was investigated by XRD as shown in Figure 10. The XRD pattern exhibited sharp diffraction peaks which correspond to ZnO wurtzite structure and agree well with the values available in the JCPDS 36-1451. From the above discussion

we can say that the pH controls the morphology and the precursor concentration controls the nucleation density, while the growth time controls the aspect ratio and finally the temperature control the aspect ratio and morphology. By

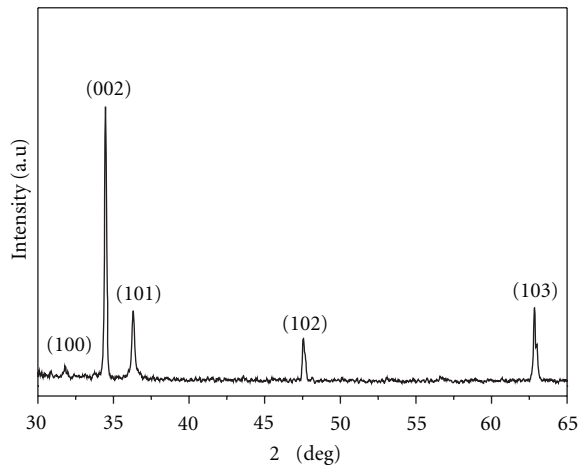


FIGURE 10: XRD pattern of ZnO NSs grown under the conditions of $T = 90^\circ\text{C}$, $t = 5$ hrs, and inherent pH.

adjusting these parameters, we can control the growth and obtain the desired ZnO NSs.

4. Conclusion

In conclusion, we studied the morphological control of ZnO nanostructures by adjusting possible parameters such as the pH, the concentration, the time, and the growth temperature. We have observed that the initial pH employed always changes during the growth, tending toward a neutral pH. Nanotetrapod-like, flower-like, and urchin-like ZnO nanostructures were obtained at higher pH values (≥ 8), while rod-like structures were obtained at lower pH. It was also noticed that the ZnO NRs were etched at a $\text{pH} \leq 4.6$. Furthermore, the precursor concentration, time, and temperature of growth were found to affect the morphology and dimensions of the ZnO nanostructures, changing from nanowires to nanorods and even to a film-like structure. We believe that the morphological and structural characteristics of the grown samples can be controlled by simply tuning the above-mentioned growth parameters to obtain the desired nanostructures as these experiments were reproducible.

Acknowledgment

The authors acknowledge the partial financial support from the advanced Functional Material project Sweden.

References

- [1] Ü. Özgür, Y. I. Alivov, C. Liu et al., "A comprehensive review of ZnO materials and devices," *Journal of Applied Physics*, vol. 98, no. 4, Article ID 041301, pp. 1–103, 2005.
- [2] C. F. Klingshirn, "ZnO: material, physics and applications," *ChemPhysChem*, vol. 8, no. 6, pp. 782–803, 2007.
- [3] W. J. E. Beek, M. M. Wienk, and R. A. J. Janssen, "Hybrid solar cells from regioregular polythiophene and ZnO nanoparticles," *Advanced Functional Materials*, vol. 16, no. 8, pp. 1112–1116, 2006.
- [4] A. J. Gimenez, J. M. Yáñez-Limón, and J. M. Seminario, "ZnO-paper based photoconductive UV sensor," *Journal of Physical Chemistry C*, vol. 115, no. 1, pp. 282–287, 2011.
- [5] Y. Wei, Y. Li, X. Liu, Y. Xian, G. Shi, and L. Jin, "ZnO nanorods/Au hybrid nanocomposites for glucose biosensor," *Biosensors and Bioelectronics*, vol. 26, no. 1, pp. 275–278, 2010.
- [6] X. M. Zhang, M. Y. Lu, Y. Zhang, L. J. Chen, and Z. L. Wang, "Fabrication of a high-brightness blue-light-emitting diode using a ZnO-Nanowire array grown on p-GaN thin film," *Advanced Materials*, vol. 21, no. 27, pp. 2767–2770, 2009.
- [7] M. Willander, O. Nur, Q. X. Zhao et al., "Zinc oxide nanorod based photonic devices: recent progress in growth, lightemitting diodes and lasers," *Nanotechnology*, vol. 20, no. 33, Article ID 332001, 2009.
- [8] H. J. Bolink, E. Coronado, D. Repetto, and M. Sessolo, "Air stable hybrid organic-inorganic light emitting diodes using ZnO as the cathode," *Applied Physics Letters*, vol. 91, no. 22, Article ID 223501, 2007.
- [9] S. Nicolay, S. Fay, and C. Ballif, "Growth Model of MOCVD Polycrystalline ZnO," *Crystal Growth and Design*, vol. 9, no. 11, pp. 4957–4962, 2009.
- [10] H. Zeng, J. Cui, B. Cao, U. Gibson, Y. Bando, and D. Golberg, "Electrochemical deposition of ZnO nanowire arrays: organization, doping, and properties," *Science of Advanced Materials*, vol. 2, no. 3, pp. 336–358, 2010.
- [11] Y. Sato, K. Yanagisawa, N. Oka, S. I. Nakamura, and Y. Shigesato, "Sputter deposition of Al-doped ZnO films with various incident angles," *Journal of Vacuum Science and Technology A*, vol. 27, no. 5, pp. 1166–1171, 2009.
- [12] J. P. Mosnier, R. J. O'Haire, E. McGlynn et al., "ZnO films grown by pulsed-laser deposition on soda lime glass substrates for the ultraviolet inactivation of *Staphylococcus epidermidis* biofilms," *Science and Technology of Advanced Materials*, vol. 10, no. 4, Article ID 045003, 2009.
- [13] X. Y. Chen, A. M. C. Ng, F. Fang et al., "The influence of the ZnO seed layer on the ZnO Nanorod/GaN LEDs," *Journal of the Electrochemical Society*, vol. 157, no. 3, pp. H308–H311, 2010.
- [14] J. Song and S. Lim, "Effect of seed layer on the growth of ZnO nanorods," *Journal of Physical Chemistry C*, vol. 111, no. 2, pp. 596–600, 2007.
- [15] D. Vernardou, G. Kenanakis, S. Couris, E. Koudoumas, E. Kymakis, and N. Katsarakis, "pH effect on the morphology of ZnO nanostructures grown with aqueous chemical growth," *Thin Solid Films*, vol. 515, no. 24, pp. 8764–8767, 2007.
- [16] S. D. G. Ram, M. A. Kulandainathan, and G. Ravi, "On the study of pH effects in the microwave enhanced rapid synthesis of nano-ZnO," *Applied Physics A*, vol. 99, no. 1, pp. 197–203, 2010.
- [17] H. Zhang, J. Feng, J. Wang, and M. Zhang, "Preparation of ZnO nanorods through wet chemical method," *Materials Letters*, vol. 61, no. 30, pp. 5202–5205, 2007.
- [18] Z. Zhang, M. Lu, H. Xu, and W. S. Chin, "Shape-controlled synthesis of zinc oxide: a simple method for the preparation of metal oxide nanocrystals in non-aqueous medium," *Chemistry—A*, vol. 13, no. 2, pp. 632–638, 2007.
- [19] J. Yahiro and H. Imai, "Morphological design of zinc oxide films grown in aqueous solutions," *Key Engineering Materials*, vol. 320, pp. 155–158, 2006.
- [20] L. E. Greene, M. Law, D. H. Tan et al., "General route to vertical ZnO nanowire arrays using textured ZnO seeds," *Nano Letters*, vol. 5, no. 7, pp. 1231–1236, 2005.
- [21] A. Zainelabdin, S. Zaman, G. Amin, O. Nur, and M. Willander, "Deposition of well-aligned ZnO nanorods at 50°C on metal,

- semiconducting polymer, and copper oxides substrates and their structural and optical properties,” *Crystal Growth and Design*, vol. 10, no. 7, pp. 3250–3256, 2010.
- [22] J. Zhou, N. Xu, and Z. L. Wang, “Dissolving behavior and stability of ZnO wires in biofluids: a study on biodegradability and biocompatibility of ZnO nanostructures,” *Advanced Materials*, vol. 18, no. 18, pp. 2432–2435, 2006.
- [23] L. Vayssieres, K. Keis, S. E. Lindquist, and A. Hagfeldt, “Purpose-built anisotropic metal oxide material: 3D highly oriented microrod array of ZnO,” *Journal of Physical Chemistry B*, vol. 105, no. 17, pp. 3350–3352, 2001.
- [24] L. Vayssieres, “Growth of arrayed nanorods and nanowires of ZnO from aqueous solutions,” *Advanced Materials*, vol. 15, no. 5, pp. 464–466, 2003.
- [25] Y. F. Zhu, D. H. Fan, and W. Z. Shen, “A general chemical conversion route to synthesize various ZnO-based core/shell structures,” *Journal of Physical Chemistry C*, vol. 112, no. 28, pp. 10402–10406, 2008.

Research Article

Characteristics of Progressive Damage of ZnO Nanowires during Contact Sliding under Relatively Low Loads

Kyeong Hee Kang, Hae Jin Kim, and Dae-Eun Kim

Department of Mechanical Engineering, Yonsei University 50 Yonsei-ro, Seodaemun-gu, Seoul 120-749, Republic of Korea

Correspondence should be addressed to Dae-Eun Kim, kimde@yonsei.ac.kr

Received 16 July 2011; Accepted 2 August 2011

Academic Editor: Renzhi Ma

Copyright © 2011 Kyeong Hee Kang et al. This is an open access article distributed under the Creative Commons Attribution License, which permits unrestricted use, distribution, and reproduction in any medium, provided the original work is properly cited.

ZnO nanowires have received much interest owing to their particular structural and piezoelectric properties. For widespread application of ZnO nanowires in various nanotechnologies, the mechanical reliability of the nanowires should be assessed. In this paper, the damage characteristics of vertically grown ZnO nanowires due to contact sliding against a 2 mm diameter steel ball under relatively low loads were investigated. Frictional behavior and wear characteristics of the specimens were assessed. Furthermore, contact sliding tests were performed inside an SEM to monitor the progression of damage of the nanowires. It was found that the friction coefficient was about 0.35 under all loads while the damage characteristics of the nanowires were quite different for each load. The large diameter nanowires tended to fracture earlier than the small diameter nanowires. Wear tests performed inside the SEM confirmed the surface damage characteristics observed during the friction tests.

1. Introduction

ZnO nanowires have been receiving much interest as a novel material due to its semiconducting and piezoelectric properties [1–3]. ZnO nanowires are frequently used as a structural material for the development of nanogenerators and nanosensors. Recently, ZnO nanowires have been commercially developed as a nanoenergy harvesting material from surrounding energy sources such as noise and vibration [4–7]. ZnO nanowires often experience contact against a counter surface which can be a packaging material for example. Also, in certain cases, the nanowires may be completely exposed to the atmosphere which can lead to direct contact against other objects. In such cases, the nanowires are susceptible to damage due to mechanical stress caused by intended or unintended contact events. In order to assess the durability or reliability of ZnO nanowires against mechanical stresses imparted by contact, it is necessary to understand the damage characteristics of the nanowires as they experience contact against a counter surface. Furthermore, since shear stresses are commonly generated at contact points accompanied by a lateral motion, the frictional behavior of the nanowires needs to be investigated as well [8, 9].

In this paper, the contact damage characteristics of ZnO nanowires grown vertically on a silicon substrate were investigated. The progression of nanowire damage was monitored by performing contact sliding experiments using a pin-on-reciprocator type tribotester as well as using a wear tester mounted inside a scanning electron microscope (SEM). The frictional behavior of the ZnO nanowires was also investigated by sliding the nanowires against a steel ball under loads ranging from 2 to 6 mN. The motivation was to identify the contact conditions under which ZnO nanowires get damaged and to understand the damage mechanism. The details of the experiments are described in the following sections.

2. Experimental Details

2.1. ZnO Nanowires Synthesis. ZnO nanowires were synthesized on (100) Si wafer with using the hydrothermal method. Prior to the coating processes, Si wafer through an intensive cleaning process to effectively remove all the organic residues. Si wafer was rinsed with warm (>55°C) acetone and methanol and cleaned by RCA number 1 method using 27% ammonium hydroxide (NH₄OH) and 30% hydrogen peroxide (H₂O₂). Si wafers were then dipped

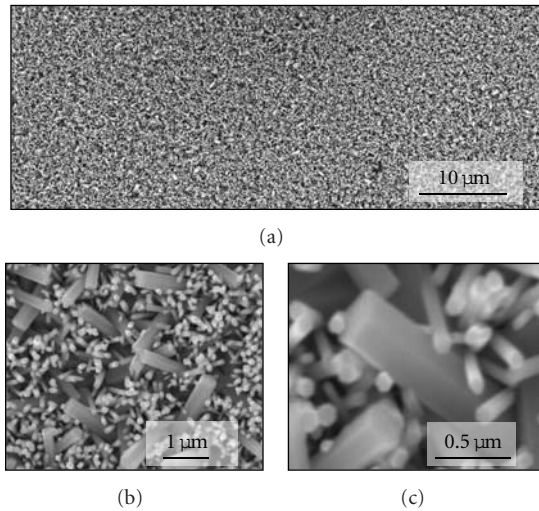
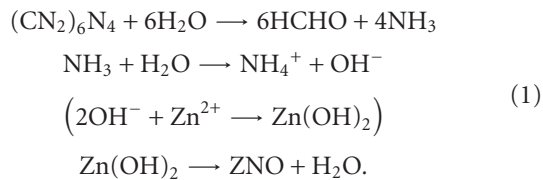


FIGURE 1: SEM images of ZnO nanowires (a) evenly coated on Si wafer and (b, c) at higher magnification that shows a mixture of nanowires with two distinct diameters.

into hydrogen fluoride (HF) to remove the native silicon dioxide (SiO_2) layer [10, 11]. Additionally, they were exposed under ultraviolet-ozone (UVO) light for 20 min to increase the adhesion property of the substrate surface.

The specimen fabrication process consisted of two steps: (1) ZnO seed-layer coating and (2) growth of ZnO nanowire arrays. For ZnO seed layer coating, a solution of 20 mM EtOH and Zinc acetate dihydrate ($(\text{C}_2\text{H}_3\text{O}_2)_2\text{Zn}\cdot 2\text{H}_2\text{O}$) were aged for more than 6 hours. The process of spin coating was repeated several times to attain adequate thickness. Si wafer with the seed layer was immersed in the solution of HPLC (high-performance liquid chromatography) grade deionized water, zinc nitrate hexahydrate ($\text{Zn}(\text{NO}_3)_2$), and hexamethylene-tetramine (HMT, $\text{C}_6\text{H}_{12}\text{N}_4$) at 80°C condition for 6 hours [12–14]. Finally, ZnO nanowires on Si wafers were carefully rinsed with deionized water and dried at room temperature. The main chemical process can be described as (1) [15].



The morphology of the ZnO nanowires coated by the above described method is shown in SEM images of Figure 1. Figure 1(a) shows that the nanowires are well distributed evenly over the entire area. High magnification images of Figures 1(b) and 1(c) show that the nanowires are vertically aligned on the average but not perfectly. Also, it can be seen that there are two distinct sizes in the nanowires grown on the silicon substrate. The majority of the nanowires have a diameter of less than 120 nm. However, mixed with these nanowires, those with a diameter of about 350 nm can be found. It was also found that the height of the smaller diameter nanowires was about $1.2\ \mu\text{m}$ while some of the

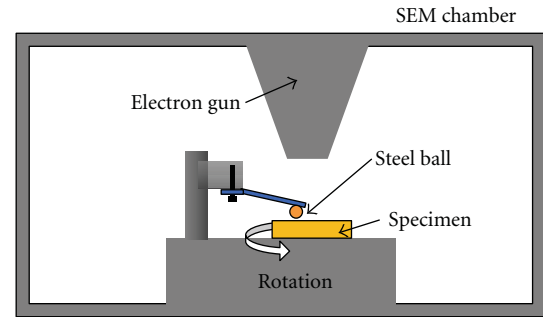


FIGURE 2: Schematic of the pin-on-disk type wear tester mounted inside the SEM.

larger diameter nanowires were about 0.1 to $0.3\ \mu\text{m}$ longer. The aspect ratio of the large and small diameter nanowires was about 4 and 10, respectively.

2.2. Friction Test. Contact sliding tests were performed using a pin-on-reciprocator type tribotester to investigate the frictional behavior of the ZnO nanowires. Frictional force was monitored in real time while reciprocating a 2 mm diameter steel ball in contact with the ZnO nanowire specimen surface. The tests were performed for 20 seconds with a linear speed of 4 mm/sec under the normal loads of 2, 4, and 6 mN. The friction tests were performed five times under the same condition. After each test, the steel ball was carefully cleaned with acetone, EtOH, and de-ionized water to minimize the effect of ball contamination. The wear of the steel ball was found to be insignificant after each test. Thus, the same ball could be used for all the friction tests after cleaning. The wear tracks formed on the ZnO nanowire specimen during the friction tests were observed using the SEM.

2.3. Wear Test Inside an SEM. In order to assess the progression of ZnO nanowire damage due to contact sliding without interruption of the sliding motion wear tests were performed inside an SEM. A pin-on-disk type wear tester was mounted inside the SEM to observe the wear behavior of ZnO nanowires in real time. Figure 2 shows the schematic of the wear tester system used in this paper. The normal load was applied using a z -axis microstage based on premeasured load-displacement calibration data. The tests were performed at the rotational speed of 2 RPM for 10 cycles under the normal loads of 2, 4, and 6 mN in vacuum condition ($10^{-3}\ \text{Pa}$). A 2 mm steel ball was used for the counter surface and cleaned after each experiment with acetone, EtOH, and de-ionized water to minimize contamination effects. The wear track was observed at the 5th and the 10th cycles to characterize the contact damage of ZnO nanowires for each load.

3. Tribological Characteristics of ZnO Nanowires

3.1. Results of the Friction Tests. The contact sliding tests were conducted using the ZnO nanowire specimens under various loads while obtaining the frictional force in real time.

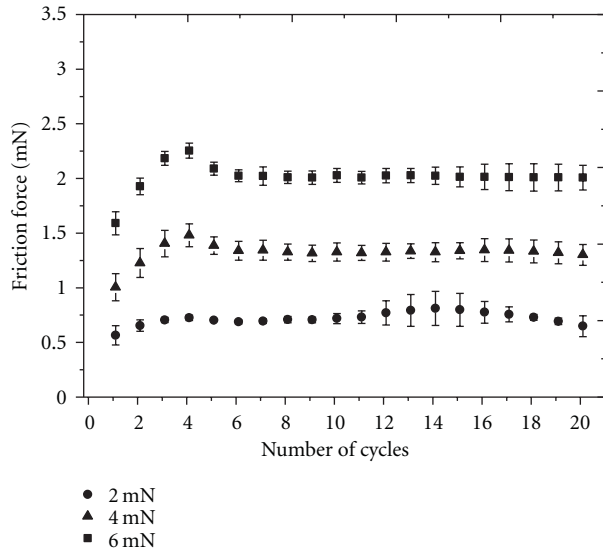


FIGURE 3: Frictional force of ZnO nanowires sliding against a 2 mm diameter steel ball with respect to number of sliding cycles for different applied loads.

Figure 3 shows the frictional behavior of ZnO nanowires with respect to the number of cycles for the normal loads of 2, 4, and 6 mN. The frictional forces were averaged over five repeated tests and the standard deviations were also calculated. It can be seen that for all cases the frictional force gradually increased to a steady state value after a few reciprocating cycles. Also, the frictional force increased with the increase in the applied load as expected.

Figure 4 shows the friction coefficients and their standard deviations calculated from the friction data. The friction coefficient during the first cycle for 2, 4, and 6 mN applied load was 0.28, 0.25, and 0.27, respectively. The values gradually increased with the number of sliding cycles. It was found that the steady state friction coefficient was about 0.35 for all three loads. The frictional behaviors of 4 and 6 mN applied load cases were almost identical. For the 2 mN case, there was an interval in the number of sliding cycles where the friction coefficient increased to about 0.4 and then decreased to about 0.35. The explanation for this behavior is not straightforward. A reasonable thought is that for the lowest applied load of 2 mN, the contact was less stable than for higher applied loads, and therefore, the frictional force was affected more by the disturbances introduced at the sliding interface such as wear particles. This view is supported by the high standard deviation in the friction data in that particular range of sliding cycles for the 2 mN applied load. Nevertheless, for the range of applied load used in this work, it would be acceptable to state that the friction coefficient was similar for all applied loads.

The damage of ZnO nanowires due to the frictional interaction was assessed by observing the wear tracks using the SEM. Figure 5 shows the SEM images of the wear track of ZnO nanowires after the friction tests conducted under 2, 4, and 6 mN for 1–20 cycles. The symbols shown in the SEM images indicate different damage characteristics

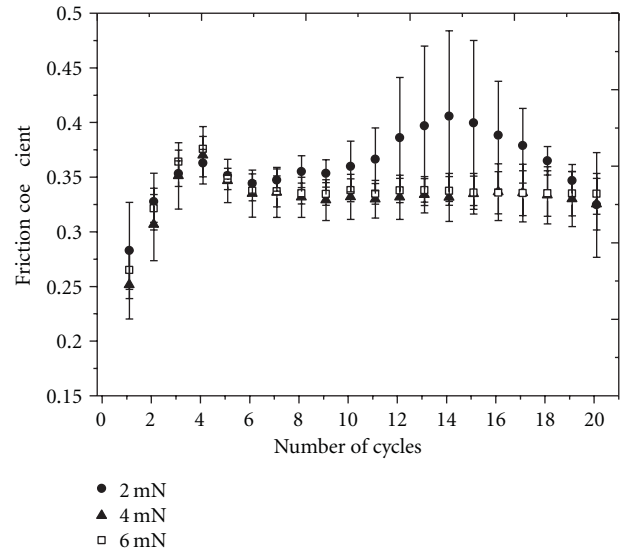


FIGURE 4: Friction coefficient of ZnO nanowires sliding against a 2 mm diameter steel ball with respect to number of sliding cycles for different applied loads.

of nanowires. The damage of ZnO nanowires with large diameter is indicated by a triangle symbol (\triangleright). The damage of ZnO nanowires with small diameter is specified with an arrow (\rightarrow). Finally, the dotted region shown in the SEM region indicates severe damage and compacted region of ZnO nanowires. Figure 5(a) shows the SEM images of the wear track of ZnO nanowires after the friction tests conducted under 2 mN for 10 and 20 cycles of sliding. For number of cycles below 7, the damage of the ZnO nanowires was too small to be identified with the SEM. It could be found that after 10 reciprocating cycles of sliding under 2 mN, the overall morphology of the ZnO nanowire specimen seemed to be intact. It was interesting to note that there were some fractured fragments of large diameter nanowire as indicated by the arrows in the figure. Less number of fractured small diameter nanowires could be found. This suggested that the large diameter nanowire tended to fail more readily than the small diameter nanowire when a mechanical stress was applied through contact sliding. After 20 cycles of sliding the number of fractured large diameter nanowires increased, but the damage of the small diameter nanowires was still not severe.

Under the 4 mN applied load, the damage of ZnO nanowires with large diameter occurred within the first cycle. The number of fractured ZnO nanowires with large diameter was slightly increased after 3 cycles. After 5 cycles, large diameter ZnO nanowires were damaged more severely. Small diameter ZnO nanowires also started to fracture into smaller pieces as the number of cycles increased. After 10 cycles under 4 mN applied load, the fractured ZnO nanowires were compressed to form a compacted surface morphology due to repetitive and relatively high contact stresses. After 20 cycles, it could be found that the extent of compressed fractured ZnO nanowires increased significantly (Figure 5(b)). As evident from Figure 5(c), the damage characteristics under

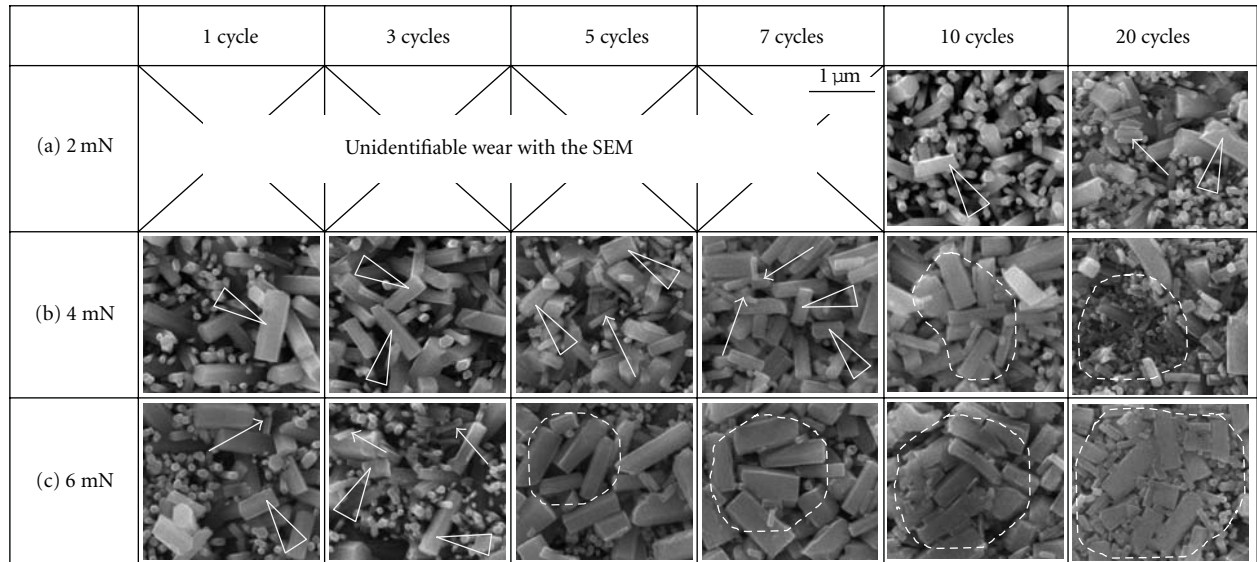


FIGURE 5: SEM image of the wear track on the ZnO nanowire specimen after the friction test under (a) 2 mN, (b) 4 mN, and (c) 6 mN applied load after 1–20 cycles of contact sliding. (\triangleright : fracture of ZnO nanowire with large diameter, \rightarrow : fracture of ZnO nanowire with small diameter, dotted regions: the severe damage and compacted region of ZnO nanowires).

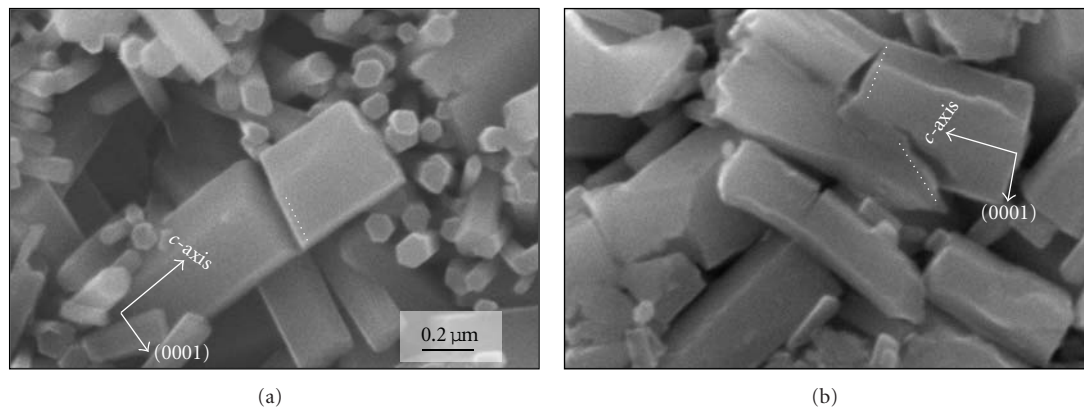


FIGURE 6: SEM image of ZnO nanowire fractured in (a) parallel to the (0001) plane after 3 cycles under 6 mN applied load and (b) both parallel and nonparallel to the (0001) plane after 10 cycles under 6 mN applied load. Dotted lines show the fractured plane of the ZnO nanowires. (0001) is the perpendicular plane to the c -axis of ZnO crystal that represents the growing direction of ZnO nanowires.

6 mN applied load was similar to the cases of 2 and 4 mN applied loads. However, the damage progressed at a faster rate at the higher load. The fracture of ZnO nanowires with both small and large diameter initiated within the first cycle. Patches of compressed region of fractured ZnO nanowires were found along the wear track after 5 cycles. The coverage area of the compressed region on the wear track continuously expanded with the increasing number of cycles. Overall, it would be reasonable to assert that the progression characteristics of damage of ZnO nanowires were similar for all applied loads tested in this work.

It was also interesting to observe the damage behavior of ZnO nanowires with the number of sliding cycles. Figure 6 shows the magnified image of the fractured nanowires. The fracture direction of a selected ZnO nanowire was indicated

by dotted lines in the figure. The ZnO nanowire was mostly fractured parallel to the (0001) plane after 3 cycles under 6 mN applied load as shown in Figure 6(a). Fractured ZnO nanowires with (0001) plane appeared commonly for most of the sliding cycles under all applied loads. ZnO nanowires that fractured along a different plane was also found after 10 cycles under 6 mN load as shown in Figure 6(b). The fracture of ZnO nanowire that occurred in a nonparallel plane to the (0001) plane was observed only among the fractured and compressed ZnO nanowires. However, they were found mostly in wear tests performed at high loads or after a sufficient number of cycles such as 10–20 cycles under 4 mN applied load or 5–20 cycles under 6 mN applied load. Therefore, it was noted that high and repetitive stresses can lead to ZnO nanowire fracture in a plane that is nonparallel

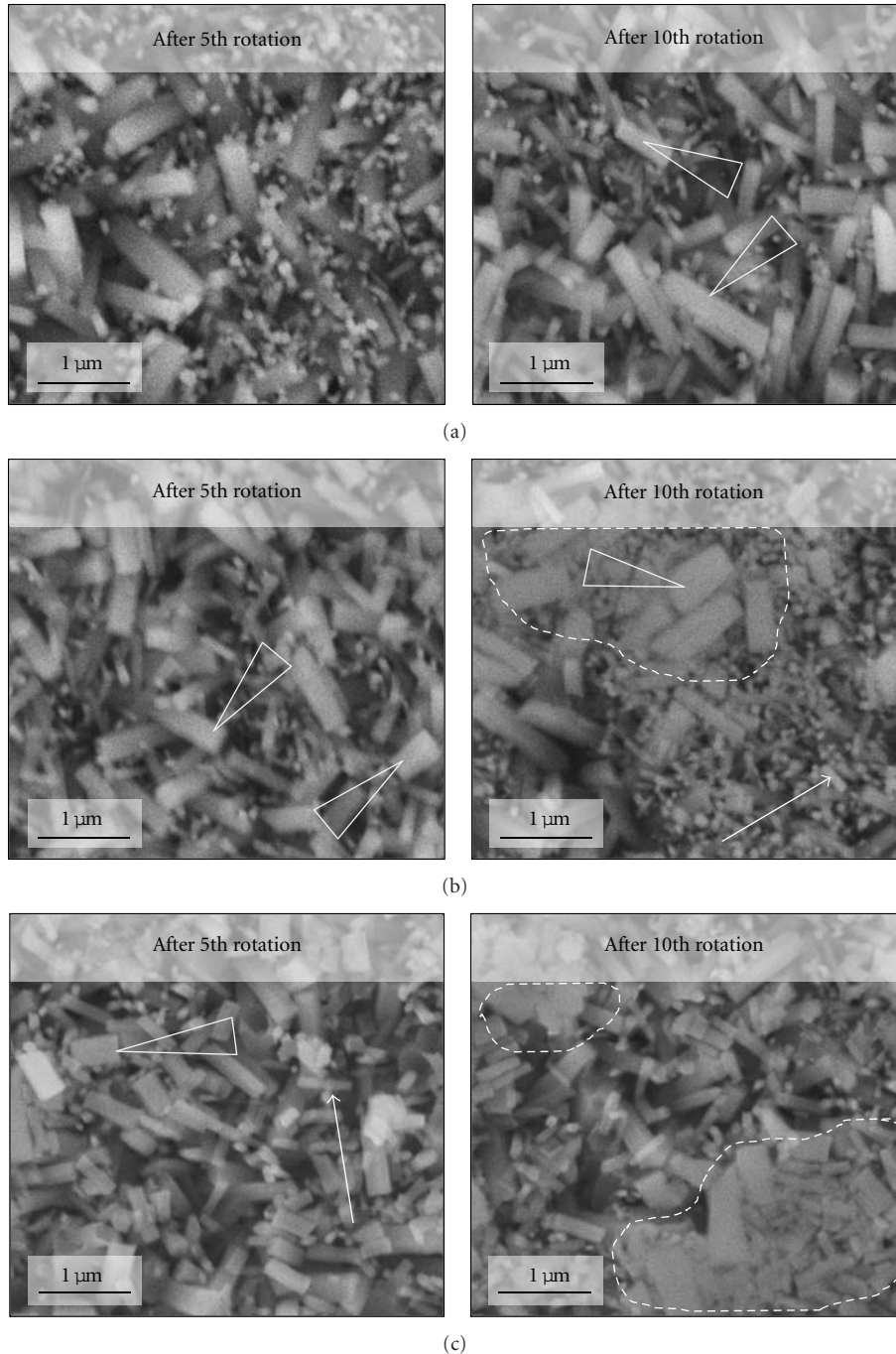


FIGURE 7: SEM image of the wear test under the load of (a) 2 mN, (b) 4 mN, and (c) 6 mN performed inside the SEM. Inset of triangle, arrow, and dotted regions show the large diameter, small diameter and compressed region of fractured ZnO nanowires, respectively.

to the (0001) plane. The different fracture behavior of ZnO nanowires with respect to the fracture plane was also reported in previous researches [16, 17].

3.2. Results of the Wear Test Inside an SEM. In order to investigate the progression of damage of ZnO nanowires during repeated contact sliding, wear tests were performed inside the SEM. Figure 7 shows the SEM images within the wear tracks of the ZnO nanowire specimens after sliding against the

steel ball under three different loads. The surface state of the ZnO nanowire specimens after 5 and 10 cycles of rotation is presented on the right and on the left sides, respectively. The damage characteristics of the ZnO nanowires were visually similar to the wear test results obtained from the friction test.

For the 2 mN wear test, the amount of fractured nanowires was minimal after the 5th rotation while some fracture of the large diameter nanowires could be found after the 10th rotation as shown in Figure 7(a). Under the load of 4 mN,

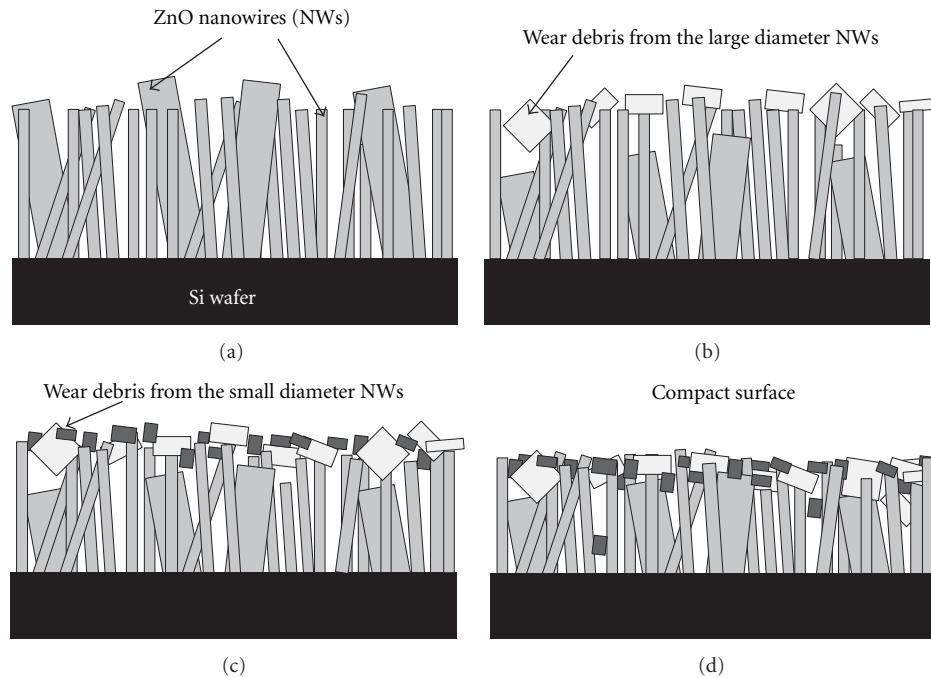


FIGURE 8: Illustration of ZnO nanowire damage process: (a) undamaged ZnO nanowires, (b) wear debris of fractured fragments of large diameter ZnO nanowires, (c) wear debris from fractured fragments of small diameter ZnO nanowires, and (d) compact surface formation due to compression of wear debris through repetitive and high contact stresses.

fracture of the large diameter ZnO nanowires could be found after the 5th rotation and severe damage was apparent after the 10th rotation as shown in Figure 7(b). Also, regions of fractured nanowires in a compacted form could be found along the wear track just as that observed after the friction tests. Figure 7(c) represents the result of the wear test under 6 mN applied load. ZnO nanowires were significantly damaged just after the 5th rotation and a large number of fractured nanowires covered the surface of vertically grown ZnO nanowires. After the 10th rotation, fractured ZnO nanowires on the surface were pressed down (dotted region) and penetrated into the ZnO nanowires due to high contact stresses.

3.3. Mechanism of the Contact Damage of ZnO Nanowire.

From the results of the contact sliding tests the mechanism of contact damage of ZnO nanowires was postulated as illustrated in Figure 8. The fractured fragments of the nanowires were distributed on the surface of the nanowires rather than penetrate into the nanowire structure. Fragments of the large diameter nanowires were initially created (Figure 8(a)) followed by those of the small diameter nanowires (Figure 8(b)). With repeated cycles of sliding the number of fractured fragments of the nanowires increased and got compressed due to the normal load. After a sufficient number of sliding cycles a continuous compact layer of fractured fragments of nanowires was formed on the surface (Figure 8(d)).

Unlike most sliding systems where the surface wears gradually, the damage of ZnO nanowires due to repeated contact sliding occurred mostly by fracture. Thus, the wear debris created were in the shape of fragmented portions of the nanowires. As mechanical stress was imparted on the

nanowires due to contact sliding some of the nanowires experienced fracture along the (0001) plane of the ZnO crystal. Fracture planes other than (0001) were also found. The extent of damage increased with increasing applied load and number of sliding cycles. At the lowest load of 2 mN used in this work nanowire damage was not evident during the first several cycles of sliding. On the other hand, damage of the nanowires by fracture occurred within the first sliding cycle at loads higher than 4 mN.

An interesting point to note in the behavior of nanowire damage was that the large diameter nanowires tended to fail more readily than the small diameter ones. This outcome was attributed to two factors. The first factor is regarding the length of the nanowires. Since the large diameter nanowires were slightly longer than the small diameter nanowires, they could have been fractured first while protecting the small diameter nanowires from being damaged. However, considering the small percentage of nanowires with longer length, this effect was not considered to be significant. The second factor is regarding the stiffness of the nanowires. As mentioned before, the aspect ratio of large diameter nanowires was much smaller than the small diameter nanowires. Thus, high stiffness due to low aspect ratio of the large diameter nanowires could have resulted in early failure. Due to the high stiffness, the large diameter nanowires were not prone to elastic deflection that was needed to dissipate the frictional energy without being plastically deformed. In the case of the small diameter nanowires dissipation of the frictional energy was possible through accumulation of the elastic energy within the nanowire which was then released once the contact event was over. Nevertheless, even the small diameter

nanowires got damaged by fracture when the load was sufficiently high or the number of contact cycles increased.

4. Conclusion

In this paper, the contact damage characteristics and frictional behavior of ZnO nanowires were investigated. The progression of damage of ZnO nanowires was investigated through analysis of the wear tracks after each cycle as well as by wear tests performed inside an SEM. Based on the experimental results, the following conclusions may be drawn.

- (1) The friction coefficient was about 0.35 for the applied loads of 2, 4, and 6 mN throughout the entire sliding cycles.
- (2) Large diameter nanowires tended to fracture more readily than small diameter nanowires during frictional interaction due to higher stiffness.
- (3) Gradually, compressed fragments of fractured nanowires covered the surface of vertically grown ZnO nanowires which resulted in the formation of a continuous compact surface.
- (4) The damage characteristics of ZnO nanowires could be classified into three steps: fracture of ZnO nanowires with large diameter, fracture of ZnO nanowires with large and small diameter, and compression of the fractured nanowires to form a compact surface.

Acknowledgment

This work was supported by the National Research Foundation of Korea (NRF) grant funded by the Korea government (MEST) no. 2011-0000409.

References

- [1] J. H. Ko, K. Jung, S. Kim, W. Kim, and M. Cho, "A proper orthogonal decomposition for parametric study of the mechanical behavior of nanowires," *Journal of Mechanical Science and Technology*, vol. 25, no. 1, pp. 157–162, 2011.
- [2] N. K. Park, G. B. Han, S. H. Yoon, S. O. Ryu, and T. J. Lee, "Preparation and absorption properties of ZnO nanostructures for cleanup of H₂S contained gas," *International Journal of Precision Engineering and Manufacturing*, vol. 11, no. 2, pp. 321–325, 2010.
- [3] Z. L. Wang, "Splendid one-dimensional nanostructures of zinc oxide: a new nanomaterial family for nanotechnology," *American Chemical Society Nano*, vol. 2, no. 10, pp. 1987–1992, 2008.
- [4] W. K. Hong, J. I. Sohn, D. K. Hwang et al., "Tunable electronic transport characteristics of surface architecture-controlled ZnO nanowire field effect transistors," *Nano Letters*, vol. 8, no. 3, pp. 950–956, 2008.
- [5] S. Xu, Y. Qin, C. Xu, Y. Wei, R. Yang, and Z. L. Wang, "Self-powered nanowire devices," *Nature Nanotechnology*, vol. 5, pp. 366–373, 2010.
- [6] Z. L. Wang and J. Song, "Piezoelectric nanogenerators based on zinc oxide nanowire arrays," *Science*, vol. 312, no. 5771, pp. 243–246, 2006.
- [7] J. I. Hahn and C. M. Lieber, "Direct ultrasensitive electrical detection of DNA and DNA sequence variations using nanowire nanosensors," *Nano Letters*, vol. 4, no. 1, pp. 51–54, 2004.
- [8] L. Y. Lin, J. M. Seo, M. C. Jeong, K. J. Koo, D. E. Kim, and J. M. Myoung, "Wear rate of vertically grown ZnO nanowires sliding against steel micro-sphere," *Materials Science and Engineering A*, vol. 460–461, no. 5, pp. 370–376, 2007.
- [9] K. H. Chung, H. J. Kim, L. Y. Lin, and D. E. Kim, "Tribological characteristics of ZnO nanowires investigated by atomic force microscope," *Applied Physics A*, vol. 92, no. 2, pp. 267–274, 2008.
- [10] E. M. Arnett, *Prudent Practices in the Laboratory*, National Academy Press, 1995.
- [11] W. Kern, *Handbook of Semiconductor Cleaning Technology*, William Andrew Publishing/Noyes, 1993.
- [12] L. Vayssieres, "Growth of arrayed nanorods and nanowires of ZnO from aqueous solutions," *Advanced Materials*, vol. 15, no. 5, pp. 464–466, 2003.
- [13] M. Wang, C. H. Ye, Y. Zhang et al., "Synthesis of well-aligned ZnO nanorod arrays with high optical property via a low-temperature solution method," *Journal of Crystal Growth*, vol. 291, no. 2, pp. 334–339, 2006.
- [14] L. W. Ji, S. M. Peng, J. S. Wu, W. S. Shih, C. Z. Wu, and I. T. Tang, "Effect of seed layer on the growth of well-aligned ZnO nanowires," *Journal of Physics and Chemistry of Solids*, vol. 70, no. 10, pp. 1359–1362, 2009.
- [15] Q. Ahsanulhaq, A. Umar, and Y. B. Hahn, "Growth of aligned ZnO nanorods and nanopencils on ZnO/Si in aqueous solution: growth mechanism and structural and optical properties," *Nanotechnology*, vol. 18, no. 11, Article ID 115603, 2007.
- [16] S. Hoffmann, F. Östlund, J. Michler et al., "Fracture strength and Young's modulus of ZnO nanowires," *Nanotechnology*, vol. 18, no. 20, Article ID 205503, 2007.
- [17] F. Xu, Q. Qin, A. Mishra, Y. Gu, and Y. Zhu, "Mechanical properties of ZnO nanowires under different loading modes," *Nano Research*, vol. 3, no. 4, pp. 271–280, 2010.

Research Article

Fabrication of VO₂ (B) Nanobelts and Their Application in Lithium Ion Batteries

Shibing Ni,¹ Haibo Zeng,² and Xuelin Yang¹

¹ College of Mechanical and Material Engineering, China Three Gorges University, Yichang 443002, China

² Key Laboratory for Intelligent Nanomaterials and Devices (MOE), Institute of Nanoscience and Department of Material Science, Nanjing University of Aeronautics and Astronautics, Yudao Road 29, Nanjing 210016, China

Correspondence should be addressed to Shibing Ni, shibingni07@gmail.com and Haibo Zeng, zeng.haibo.nano@gmail.com

Received 5 June 2011; Accepted 11 July 2011

Academic Editor: Renzhi Ma

Copyright © 2011 Shibing Ni et al. This is an open access article distributed under the Creative Commons Attribution License, which permits unrestricted use, distribution, and reproduction in any medium, provided the original work is properly cited.

VO₂ (B) nanobelts have been successfully synthesized via a simple hydrothermal route. The products were characterized by X-ray diffraction (XRD), field emission scanning electron microscopy (FE-SEM), and Raman spectrum. These nanobelts are of rectangular cross-section with mean length about 1 μm, mean width about 80 nm, and mean thickness about 50 nm. The as-synthesized VO₂ nanobelts were assembled as the cathode electrodes of lithium ion batteries. Their electrochemical properties were studied by conventional charge/discharge tests, which show an initial discharge capacity of 321 mAh g⁻¹ with voltage plateau near 2.5 V. These results indicated that such hydrothermally synthesized VO₂ (B) nanobelts could be an ideal candidate of cathode material for lithium ion battery.

1. Introductions

During the past few years, vanadium-oxides-based materials have attracted much attention due to their fascinating structures and electronic, optical, and magnetic properties, which are relevant to such diverse areas as lubrication, chemical sensor, catalysis, cathode materials in batteries, and minerals [1–7].

Metastable phase oxide VO₂ (B) is built up of distorted VO₆ octahedra sharing edges and corners [8] and has been found to be of interesting cathode properties in lithium ion batteries [9]. However, VO₂ (B) is very difficult to synthesize by conventional high temperature procedures because the phase change from metastable VO₂ (B) to thermodynamically more stable rutile VO₂ will occur at $T > 300^{\circ}\text{C}$ and the latter shows no attractive electrochemical properties [10]. The synthesis of VO₂ (B) hierarchical structures is generally achieved via low-temperature chemical methods [8, 11–13], which can hardly be separated from toxic reducing agent and usually need long reaction time. So we are interested in developing simple methods to synthesize VO₂ (B) nanostructures using nontoxic reducing agent and exploring its morphology-related electrochemical properties. Among

different nanostructures, one-dimensional (1D) nanostructured VO₂ (B) has attracted special attention due to its high surface-to-volume ratio, which is strongly relevant to its electrochemical performances. VO₂ (B) nanowires, nanobelts, nanoribbons, nanoneedles, and nanorods were respectively synthesized [14–18]. To the best of our knowledge, the synthesis of 1D nanostructured VO₂ (B) with rectangular cross-section is rarely achieved due to the intrinsic growth habit of VO₂ (B) crystal [13]. Here, we report a simple hydrothermal approach to synthesize VO₂ (B) nanobelts with rectangular cross-section using nontoxic glucose as reducing agent, and its electrochemical properties are studied by conventional charge/discharge tests.

2. Experimental

All the chemicals were of analytical grade and purchased from Shanghai Chemical Reagents. In a typical procedure, 1 mmol V₂O₅ and 0.5 mmol glucose were dissolved in 30 mL distilled water, and then 0.5 g sodium sulfate was put into the solution. After stirring for 20 minutes, the obtained homogeneous yellowy suspension was transferred into a 50 mL teflon-lined autoclave, and distilled water was

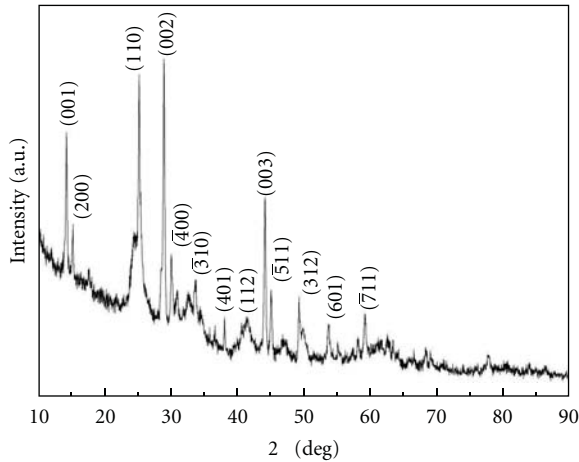


FIGURE 1: XRD pattern of the as-synthesized products.

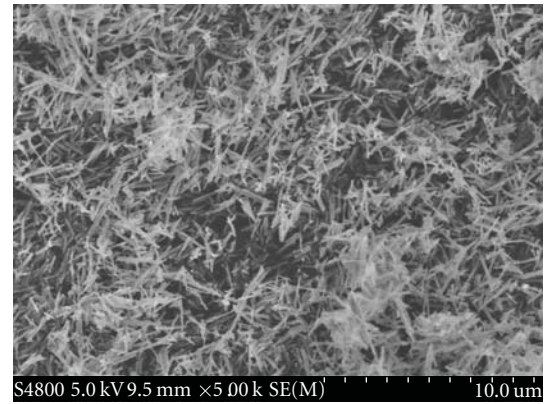
subsequently added up to 80% of its capacity. The autoclave was at last sealed and placed in an oven, heated at 160°C for 24 h. The precipitate was centrifuged with distilled water and ethanol both for 4 times and dried in an oven at 60°C for 24 h.

The morphology and structure of the resulting products were characterized by field-emission scanning electron microscopy (FE-SEM S-4800, Hitachi), X-ray powder diffraction (Rigaku RINT2400 with Cu K α radiation), and micro-Raman spectrometer (Jobin Yvon LabRAM HR800 UV, YGA 532 nm). For fabricating of lithium ion batteries, a mixture of 80 wt% of active material, 10 wt% of acetylene black, and 10 wt% of polyvinylidene fluoride (PVDF) dissolved in N-methylpyrrolidone (NMP) solution (0.02 g mL⁻¹) was coated on aluminum foil and cut into disc electrodes with a diameter of 14 mm using a punch. Coin-type cells (2025) of Li/1 M LiPF₆ in ethylene carbonate, dimethyl carbonate and diethyl carbonate (EC/DMC/DEC, 1 : 1 : 1 v/v/v + VC)/VO₂ were assembled in an argon-filled glove box. A Celgard 2400 microporous polypropylene was used as the separator membrane. The cells were tested in the voltage region between 1.5 V and 3.75 V with a multichannel batteries test system (LAND CT2001A).

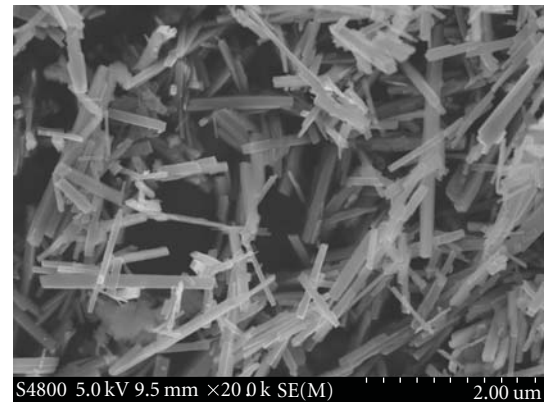
3. Results and Discussion

Typical XRD pattern of the as-synthesized products is shown in Figure 1. All diffraction peaks can be indexed as monoclinic cell of VO₂ (B) with cell parameters $a = 12.03$ Å, $b = 3.693$ Å, and $c = 6.42$ Å, which is in good agreement with the JCPDS, no. 31-1438, indicating the formation of pure phase VO₂ (B). The strong and sharp diffraction peaks suggest that the as-synthesized products are well crystallized.

Figure 2(a) is a low magnification SEM image of the as-synthesized VO₂ (B), showing a large quantity of nanobelts. For further clarification of the morphology and size of those nanobelts, an SEM image with high magnification is shown in Figure 2(b). It can be found that those nanobelts are of rectangular cross-section with mean length about 1 μ m,



(a)



(b)

FIGURE 2: SEM images of the products with low (a) and high (b) magnification.

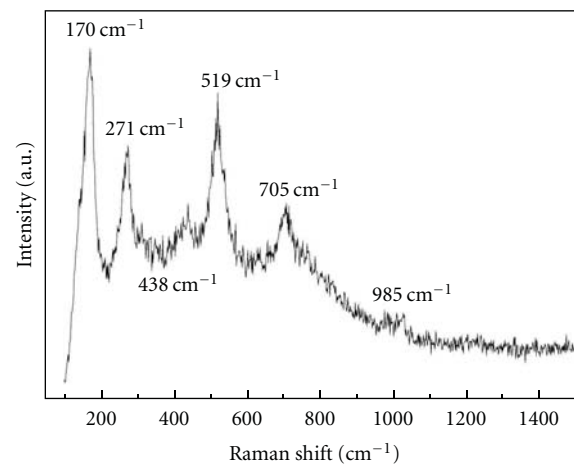


FIGURE 3: Raman spectrum of the products.

mean width about 80 nm, and mean thickness about 50 nm, respectively.

As shown in Figure 3, Raman spectrum in the wavelength range of 150 cm⁻¹ ~ 1500 cm⁻¹ is dominated by the peaks at 170 cm⁻¹, 271 cm⁻¹, 438 cm⁻¹, 519 cm⁻¹, 705 cm⁻¹, and 985 cm⁻¹, and these peaks are the vibration bands of VO₂

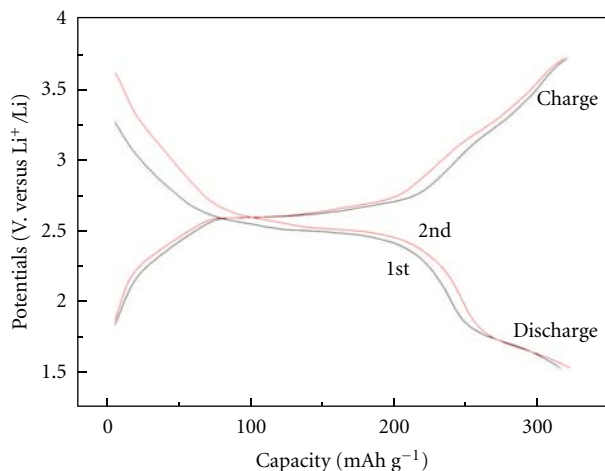


FIGURE 4: Initial two discharge and charge curves of the electrode made of VO_2 (B) nanobelts.

(B) [12]. The peaks at 170 cm^{-1} and 271 cm^{-1} can be assigned to V–O–V bending modes and external mode (bending/wagging), respectively. The peaks at 438 cm^{-1} and 519 cm^{-1} are attributed to V–O–V stretching mode. The peak at 705 cm^{-1} is due to coordination of vanadium atoms with three oxygen atoms, while the peak at 985 cm^{-1} is attributed to V=O stretching of distorted octahedral and distorted square-pyramids [19–22]. These Raman results are highly accordant with above XRD pattern and further confirm the formation of monoclinic VO_2 (B).

Figure 4 is the 1st and 2nd discharge and charge curves of VO_2 (B) nanobelts electrode at a current density of 214 mA g^{-1} . It shows a high initial discharge capacity of 316 mAh g^{-1} with clear voltage plateau near 2.5 V , while the first charge capacity is 321 mAh g^{-1} with distinct voltage plateau near 2.62 V . The charge and discharge capacities show little attenuation, which indicates a highly reversible intercalation and extraction of Lithium ions. In the 2nd discharge and charge curve, the discharge and charge capacities are 323 mAh g^{-1} and 319 mAh g^{-1} and the voltage plateaus locate at near 2.52 V and 2.64 V , respectively. The charge and discharge behavior of our VO_2 (B) nanobelts is similar to that reported in the literature [13, 17, 18], but with smaller capacity attenuation. We propose that the unique synthesis environment in hydrothermal method and the special morphology of the as-synthesized VO_2 (B) nanobelts are the causations of its good electrochemical performance.

4. Conclusion

In conclusion, VO_2 (B) nanobelts with rectangular cross-section are synthesized via a simple hydrothermal route. Electrochemical properties of the as-synthesized VO_2 nanobelts as cathode electrode of lithium ion batteries are studied by conventional charge/discharge tests, which show high discharge/charge capacity and steady voltage plateaus, indicating that it is suitable for the application in lithium ion batteries as cathode electrode material.

Acknowledgments

The authors gratefully acknowledge the financial support from Natural Science Foundation of China (NSFC, 50972075), key projects of Chinese Ministry of Education (D209083) and Education Office of Hubei Province (Q20111209, D20081304, and CXY2009A004). Moreover, the authors are grateful to Dr. Jianlin Li at China Three Gorges University for his kind support to their research.

References

- [1] E. Lugscheider, O. Knotek, S. Bärwulf, and K. Bobzin, "Characteristic curves of voltage and current, phase generation and properties of tungsten- and vanadium-oxides deposited by reactive d.c.-MSIP-PVD-process for self-lubricating applications," *Surface and Coatings Technology*, vol. 142–144, pp. 137–142, 2001.
- [2] A. Lavacchi, B. Cortigiani, G. Roviola et al., "Composition and structure of tin/vanadium oxide surfaces for chemical sensing applications," *Sensors and Actuators B*, vol. 71, no. 1-2, pp. 123–126, 2000.
- [3] W. P. Griffith, "Polyoxometallates as homogeneous catalysts for organic oxidations," *Transition Metal Chemistry*, vol. 16, no. 5, pp. 548–552, 1991.
- [4] I. V. Kozhevnikov, "Advances in catalysis by heteropolyacids," *Russian Chemical Reviews*, vol. 56, no. 9, pp. 811–825, 1987.
- [5] A. R. Armstrong, C. Lyness, P. M. Panchmatia, M. S. Islam, and P. G. Bruce, "The lithium intercalation process in the low-voltage lithium battery anode $\text{Li}_{1+x}\text{V}_{1-x}\text{O}_2$," *Nature Materials*, vol. 10, no. 3, pp. 223–229, 2011.
- [6] L. Mai, L. Xu, C. Han et al., "Electrospun ultralong hierarchical vanadium oxide nanowires with high performance for lithium ion batteries," *Nano Letters*, vol. 10, no. 11, pp. 4750–4755, 2010.
- [7] H. T. Evans and J. A. Kinnert, "The crystal chemistry of sherwoodite, a calcium 14-vanadoaluminate heteropoly complex," *American Mineralogist*, vol. 63, no. 9-10, pp. 863–868, 1978.
- [8] G. Grynoprez, L. Fiermans, and J. Vennik, "Structural properties of vanadium oxides," *Acta Crystallographica*, vol. A33, no. 5, pp. 834–837, 1977.
- [9] A. M. Kannan and A. Manthiram, "Synthesis and electrochemical evaluation of high capacity nanostructured VO_2 cathodes," *Solid State Ionics*, vol. 159, no. 3-4, pp. 265–271, 2003.
- [10] C. Tsang and A. Manthiram, "Synthesis of nanocrystalline VO_2 and its electrochemical behavior in lithium batteries," *Journal of the Electrochemical Society*, vol. 144, no. 2, pp. 520–524, 1997.
- [11] K. F. Zhang, S. J. Bao, X. Liu, J. Shi, Z. X. Su, and H. L. Li, "Hydrothermal synthesis of single-crystal VO_2 (B) nanobelts," *Materials Research Bulletin*, vol. 41, no. 11, pp. 1985–1989, 2006.
- [12] X. Wu, Y. Tao, L. Dong, Z. Wang, and Z. Hu, "Preparation of VO_2 nanowires and their electric characterization," *Materials Research Bulletin*, vol. 40, no. 2, pp. 315–321, 2005.
- [13] Z. Chen, S. Gao, L. Jiang, M. Wei, and K. Wei, "Crystalline VO_2 (B) nanorods with a rectangular cross-section," *Materials Chemistry and Physics*, vol. 121, no. 1-2, pp. 254–258, 2010.
- [14] G. Armstrong, J. Canales, A. R. Armstrong, and P. G. Bruce, "The synthesis and lithium intercalation electrochemistry of

- VO₂(B) ultra-thin nanowires,” *Journal of Power Sources*, vol. 178, no. 2, pp. 723–728, 2008.
- [15] X. Liu, G. Xie, C. Huang, Q. Xu, Y. Zhang, and Y. Luo, “A facile method for preparing VO₂ nanobelts,” *Materials Letters*, vol. 62, no. 12-13, pp. 1878–1880, 2008.
- [16] L. Mao and C. Liu, “A new route for synthesizing VO₂(B) nanoribbons and 1D vanadium-based nanostructures,” *Materials Research Bulletin*, vol. 43, no. 6, pp. 1384–1392, 2008.
- [17] F. Sediri, F. Touati, and N. Gharbi, “From V₂O₅ foam to VO₂(B) nanoneedles,” *Materials Science and Engineering B*, vol. 129, no. 1–3, pp. 251–255, 2006.
- [18] C. V. S. Reddy, E. H. Walker Jr., S. A. Wicker Sr., Q. L. Williams, and R. R. Kalluru, “Synthesis of VO₂ (B) nanorods for Li battery application,” *Current Applied Physics*, vol. 9, no. 6, pp. 1195–1198, 2009.
- [19] J. Twu, C. F. Shih, T. H. Guo, and K. H. Chen, “Raman spectroscopic studies of the thermal decomposition mechanism of ammonium metavanadate,” *Journal of Materials Chemistry*, vol. 7, no. 11, pp. 2273–2277, 1997.
- [20] F. D. Hardcastle and I. E. Wachs, “Determination of vanadium-oxygen bond distances and bond orders by Raman spectroscopy,” *Journal of Physical Chemistry*, vol. 95, no. 13, pp. 5031–5041, 1991.
- [21] J. Twu and P. K. Dutta, “Structure and reactivity of oxovanadate anions in layered lithium aluminate materials,” *Journal of Physical Chemistry*, vol. 93, no. 23, pp. 7863–7868, 1989.
- [22] S. Onodera and Y. Ikegami, “Synthesis and properties of chlorine(I) and bromine(I) trifluoromethanesulfonates and Raman spectra of CF₃SO₂X (X=fluorine, hydroxyl, hypochlorite),” *Inorganic Chemistry*, vol. 19, no. 3, pp. 615–618, 1980.

Research Article

Growth Behaviors of ZnO Nanorods Grown with the Sn-Based Bilayer Catalyst-Covered Substrates

Dong-Hau Kuo and Bo-Jie Chang

Department of Materials Science and Engineering, National Taiwan University of Science and Technology, Taipei 10607, Taiwan

Correspondence should be addressed to Dong-Hau Kuo, dhkuo@mail.ntust.edu.tw

Received 12 May 2011; Accepted 8 July 2011

Academic Editor: Renzhi Ma

Copyright © 2011 D.-H. Kuo and B.-J. Chang. This is an open access article distributed under the Creative Commons Attribution License, which permits unrestricted use, distribution, and reproduction in any medium, provided the original work is properly cited.

The growth of ZnO nanorods performed at 700°C with the mixture of Zn and ZnO as the Zn source was investigated by having the catalysts in bilayer configurations of Sn (top)/Au (bottom), Sn/Al, Sn/Ni, and Sn/In. These catalyst layers were preannealed at 700°C or 850°C in a gas mixture of argon and hydrogen. The variations in the process parameters are to give the modulations in growing ZnO rods for the purpose of investigating the growth behaviors. The results show that the different compositions and configurations of bilayer catalysts can lead to different reactions and interdiffusions or in different kinetic performance, which will produce different sizes and states of catalyst templates for growing different sizes of the ZnO rods. The small-diameter ZnO nanorods with a hexagonal cross-section at the size of 70–150 nm were obtained from the Sn/Ni catalyst systems preannealed at 850°C.

1. Introduction

Zinc oxide (ZnO) with a wide band gap of 3.37 eV and large exciton-binding energy (60 meV) has been an attractive semiconductor for optoelectronic applications in light emitting diodes and laser diodes at room temperature. Nanometer scale, one-dimensional (1D) materials, such as nanowires (NWs), nanorods, nanobelts, and nanotubes, have become of great interest due to their importance in basic scientific research, and potential technological applications in nanolaser, field emission devices, photovoltaic, piezoelectric transducer, photocatalysts, chemical and biosensors, and so forth [1, 2].

Vapor phase-grown one-dimensional (1D) ZnO nanomaterials were mainly obtained by using the Zn and Zn+ZnO sources with the growth temperatures at 650°C~900°C [3–6], the ZnO+C source at 850°C–1100°C [7, 8], and the diethyl zinc source at 350–500°C [9, 10]. 1D ZnO can grow at the uncoated substrates with the self-catalytic vapor-liquid-solid (VLS) growth mechanism. The major catalysts used on the coated substrates to grow 1D ZnO are gold, nickel, and tin. VLS mechanism has been related to the growth of 1D ZnO with catalysts on its tips, and it is the vapor-solid

(VS) growth mechanism for those without catalysts on tips. Although Au catalysts played an important role in forming the 1D ZnO, some grown 1D ZnO had the Au droplets [5, 7], and some had no catalysts on the tips [11, 12]. Ni was also used as a catalyst on the coated substrates. Umar et al. grew hexagonal-shaped ZnO nanorods at 500°C–550°C in an oxygen atmosphere on preannealed Ni-coated substrates with the Zn powder as a source material [3]. The Sn-based catalysts are the focus of this study for growing ZnO rods. 1D ZnO grown above 1000°C on the uncoated substrates with the mixture of ZnO and SnO₂ or Sn as source materials has pure Sn droplets observed on tips of nanowires [13–15]. These Sn droplets on the tips of ZnO NWs had the sizes 2-fold larger than those of ZnO rods. If 1D nanomaterials were grown on the Au-coated substrates with the mixture of ZnO and SnO powders as a source material at 1000°C, Zn₂SnO₄ nanowires with an inverse spinel structure were obtained [16, 17].

In the previous report, we had grown 1D ZnO nanorods on the untreated or preannealed bilayer catalyst-covered substrates to explore their growth behaviors and micromechanisms [18]. Three kinds of the bilayer catalysts were Au (the top layer)/Al (the bottom layer), Au/Ni, and Au/In or

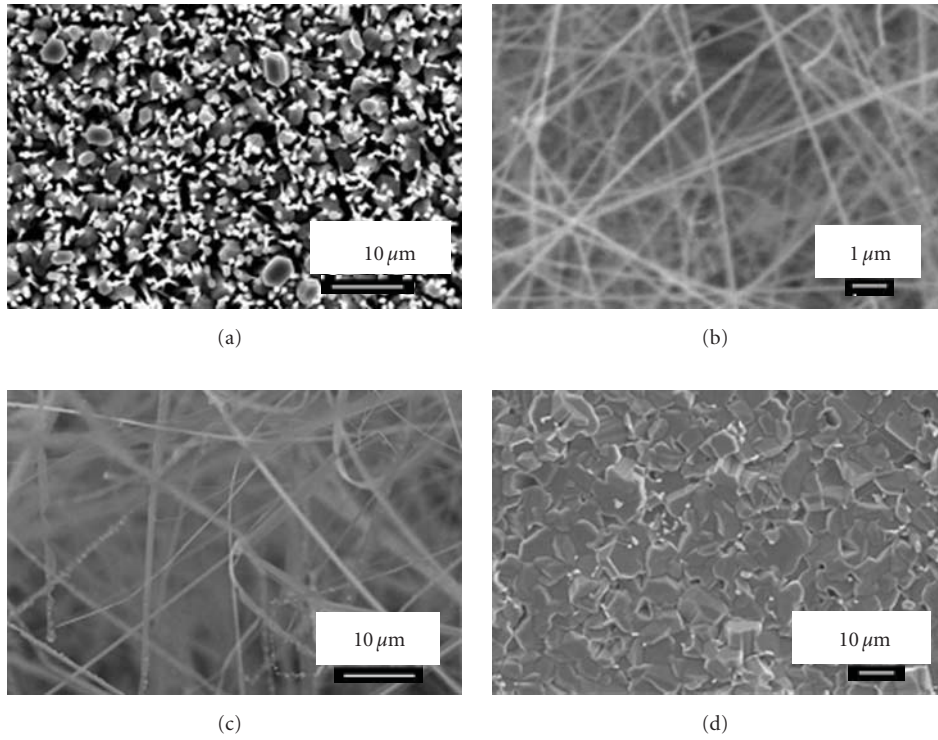


FIGURE 1: Surface morphologies of ZnO grown at (a) 600°C, (b) 700°C, (c) 800°C, and (d) 900°C for 2 h on Au-coated substrates by thermal evaporation with a Zn mixture of Zn and ZnO in a weight ratio of 1 : 1.

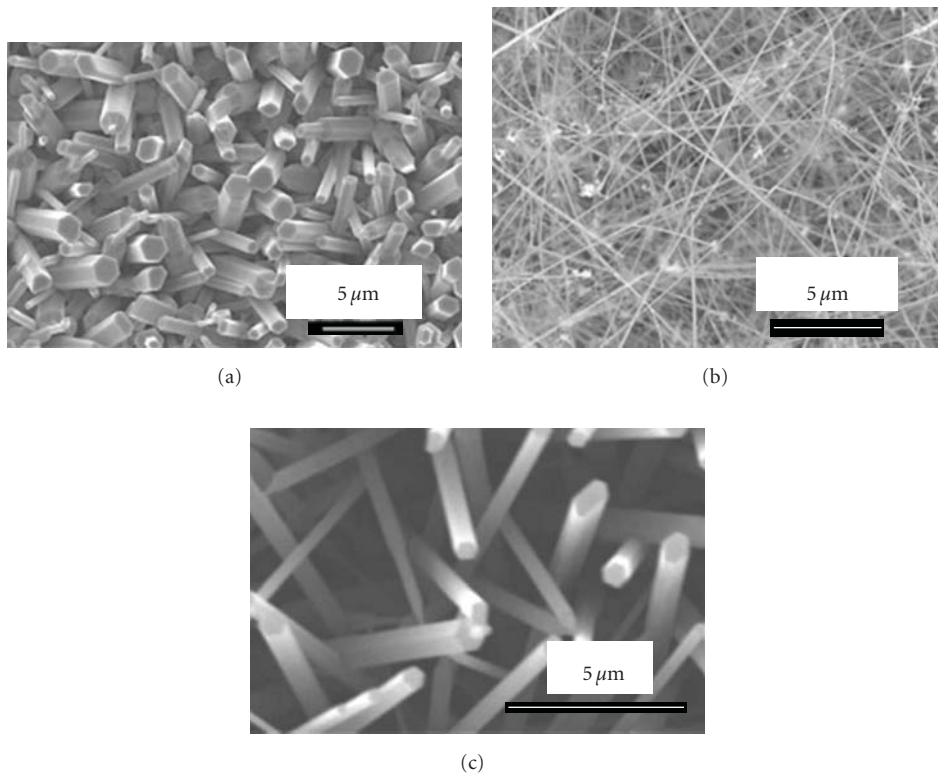


FIGURE 2: Surface morphologies of ZnO grown at 700°C for 2 h on Au-coated substrates by thermal evaporation with a Zn mixture of Zn and ZnO in weight ratios of (a) 2 : 1, (b) 1 : 1, and (c) 1 : 2.

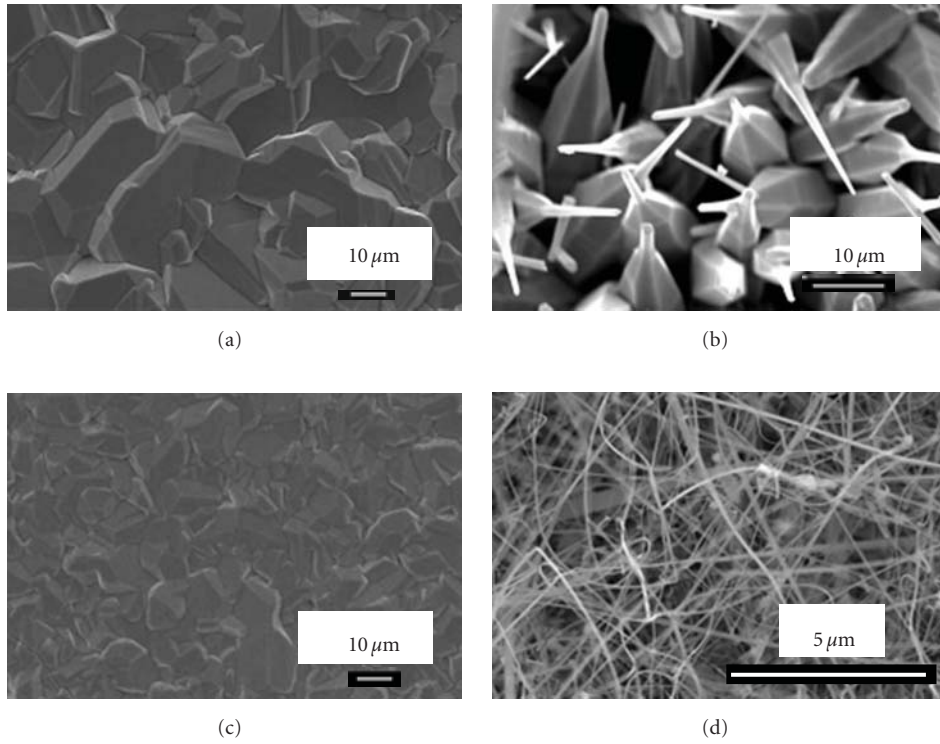


FIGURE 3: Surface morphologies of ZnO grown at 700°C for 2 h on (a) Al-, (b) Ni-, (c) In-, and (d) Sn-sputtering coated substrates by thermal evaporation with a Zn mixture of Zn and ZnO in a weight ratio of 1 : 1.

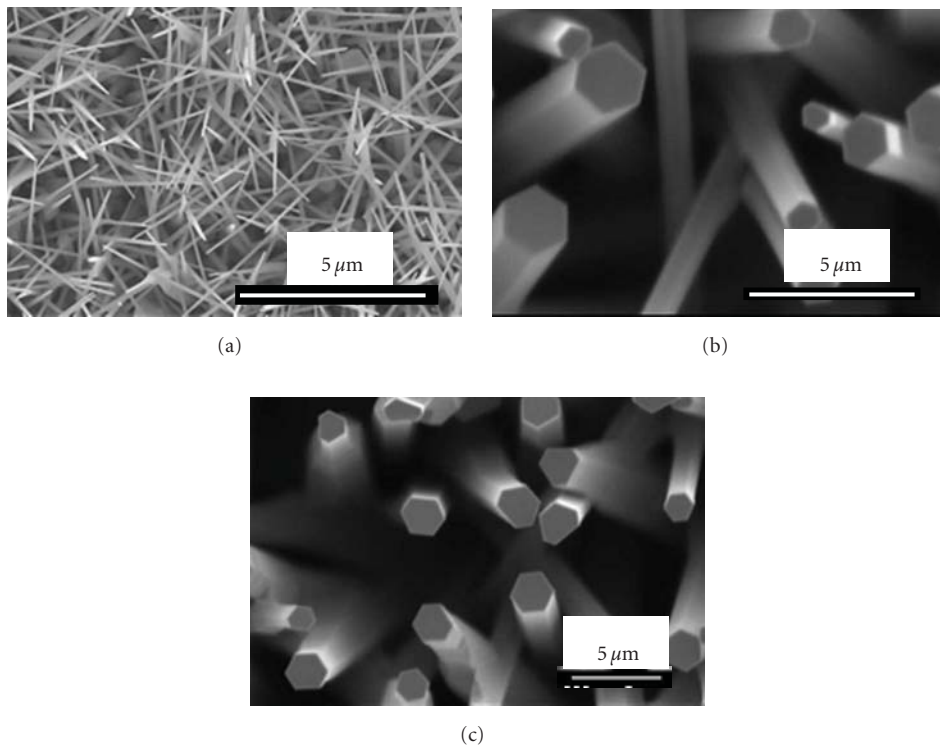


FIGURE 4: Surface morphologies of ZnO grown at 700°C for 2 h on (a) untreated, (b) 700°C preannealed, and (c) 850°C preannealed Sn/Au substrates by thermal evaporation with a Zn mixture of Zn and ZnO in a weight ratio of 1 : 1.

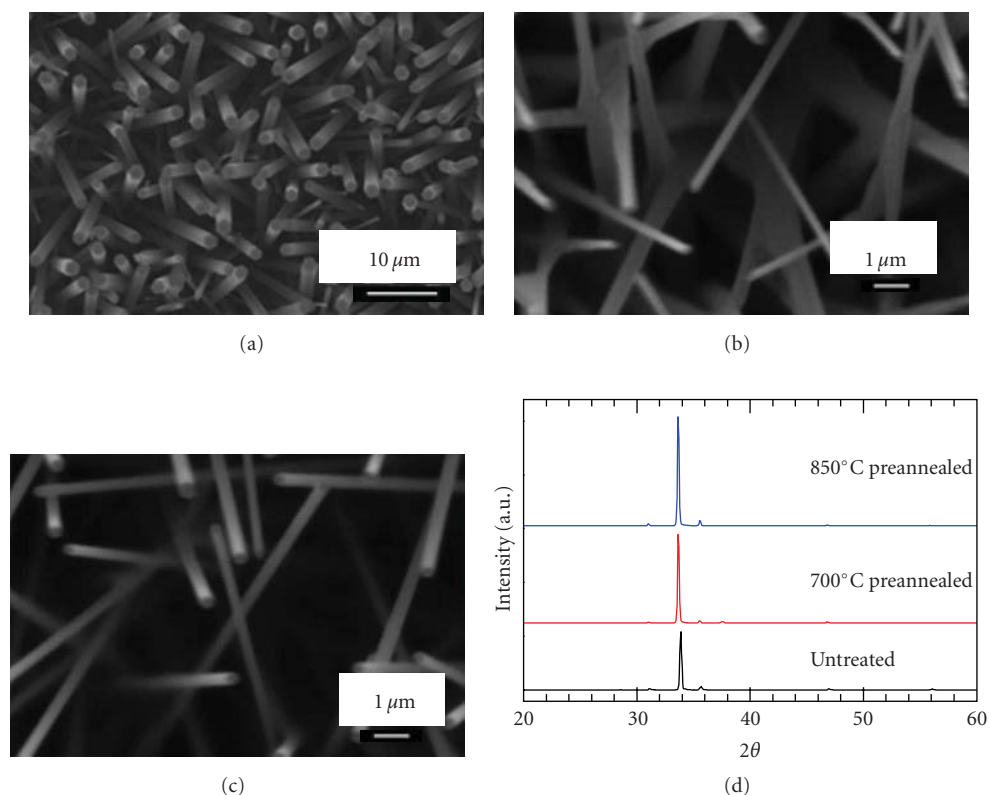


FIGURE 5: Surface morphologies of ZnO grown at 700°C for 2 h on (a) untreated, (b) 700°C preannealed, and (c) 850°C preannealed Sn/Al substrates by thermal evaporation with a Zn mixture of Zn and ZnO in a weight ratio of 1 : 1. (d) X-ray diffraction patterns of ZnO nanorods grown on three types of Sn/Al substrates.

the Au-based bilayer catalysts. The results indicated that the catalyst-confined nanowire growth *via* the VS growth mechanism was controlled by the size of catalysts, which was adjusted by alloying or catalyst reactions to change the surface tension and surface energy of the catalysts. There are few studies about the growth of hexagonal 1D ZnO on the bilayer catalyst substrates with Sn as the top layer or on the Sn-based substrates. Sn has a low melting temperature of 232°C and exists as a liquid at our growth condition of 700°C. It has very different behaviors to those grown on the bilayer substrates with the Au catalyst on the top layer. After we have some knowledge about the growth on the Au-based systems, the investigations of the growth of hexagonal ZnO rods on the Sn-based substrates become interesting.

The purpose of this study is to study the states of bilayer catalysts on the growth micromechanism of 1D ZnO by deliberately having different bilayer catalyst configurations with an Sn top layer and having different preannealing treatments. By differentiating and understanding the different 1D ZnO growth behaviors, the growth of 1D ZnO is expected to have a better control.

2. Experimental

ZnO nanowires were grown at 600–900°C for 2 h on the catalyst-coated Si wafer substrates under a mixture flow of

10-sccm (standard cubic centimeter per minute) O₂ and 200-sccm argon by thermal evaporation with a Zn mixture of Zn and ZnO at different weight ratios of 1.0 g:0.5 g or 2 : 1, 1.0 g:1.0 g or 1 : 1, and 0.5 g:1.0 g or 1 : 2. Other Zn sources, for example, Zn, ZnO, ZnCl₂, Zn+ZnCl₂, ZnO+ZnCl₂, and Zn+ZnCl₂+ZnO, were also used. The Zinc source was put nearby the substrate. Single-layer catalysts of Au, Al, Ni, In, and Sn were deposited on Si wafer substrates by d.c. (direct current) magnetron sputtering. For the bilayer catalysts, there were one top layer A and one bottom layer B, which was symbolized as A/B. In this study, the A layer was fixed with Sn and the four constituted systems were Sn/Au, Sn/Al, Sn/Ni, and Sn/In. These metallic catalyst layers had a thickness of 30–60 nm for each. The sputtered bilayer substrates were referred to as the untreated substrates. The effects of preannealing on the bilayer catalyst-covered substrates before the growth of 1D ZnO were studied by executing annealing at 700°C and 850°C for 30 min in a tube furnace under the atmosphere of argon and hydrogen, which were referred as 700°C and 850°C preannealing, respectively. The phase formation of 1D ZnO was analyzed by X-ray diffraction (XRD, Rigaku D/Max-RC, Japan). Scanning electron microscopes (SEM, JEOL JSM 6500F, Japan; Cambridge S360, UK) were used to observe the growth morphology. Microstructural characterization of nanowires was conducted by a transmission electron microscope (TEM, FEI Tecnai F20G², The Netherlands).

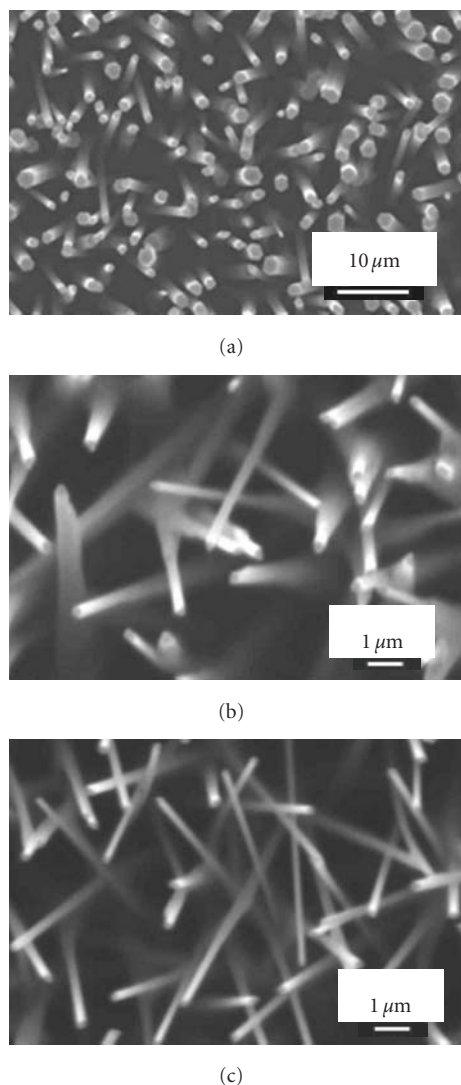


FIGURE 6: Surface morphologies of ZnO grown at 700°C for 2 h on (a) untreated, (b) 700°C preannealed, and (c) 850°C preannealed Sn/Ni substrates by thermal evaporation with a Zn mixture of Zn and ZnO in a weight ratio of 1 : 1.

The energy dispersive spectroscopies equipped on SEM and TEM were used to semiquantitatively analyze the phase composition. Room-temperature photoluminescence (PL) measurements were performed using a 325 nm He-Cd laser as the excitation source.

3. Results and Discussion

3.1. Growth of ZnO on Unilayer Catalyst-Covered Substrates. To choose the Zn source for thermal evaporation, seven sources were tested at 800°C. The pure zinc produced the ZnO polycrystalline films with a large grain size of 3–10 μm. Au nanoparticles instead of 1D ZnO were observed on substrates when ZnO, ZnCl₂, and ZnO+ZnCl₂ were used. Loose ZnO grains were obtained with the Zn sources of Zn+ZnCl₂ and Zn+ZnCl₂+ZnO. The only successful source

for this study of growing 1D ZnO was Zn+ZnO. The next step is to find the appropriate growth temperature. Figure 1 shows surface morphologies of ZnO grown at (a) 600°C, (b) 700°C, (c) 800°C, and (d) 900°C for 2 h on Au-coated substrates by thermal evaporation with a Zn mixture of Zn and ZnO in a weight ratio of 1 : 1. The growth temperature of 700°C was enough to form ZnO nanowires with a diameter of 100–120 nm and the length of hundreds of microns. The mixture of submicron-sized ZnO rods and ZnO nanorods was observed at growth temperature of 600°C. Microsized ZnO polycrystalline layers were obtained at 900°C. The growth temperature of 700°C was chosen for the following experiments.

Figure 2 shows surface morphologies of ZnO grown at 700°C for 2 h on Au-coated substrates by thermal evaporation with a Zn mixture of Zn and ZnO in weight ratios of (a) 2 : 1, (b) 1 : 1, and (c) 1 : 2. Hexagonal-shaped ZnO microrods with a diameter of 1.5–3.5 μm were obtained at the Zn/ZnO ratio of 2 : 1. Similar ZnO rods with a diameter of 300–600 nm were grown at the Zn/ZnO ratio of 1 : 2. The best condition was at the Zn/ZnO ratio of 1 : 1 to obtain ZnO nanowires with a diameter of ~100 nm. Different sizes of 1D ZnO were obtained at the different Zn/ZnO ratios. Because these three experiments were conducted on the same type of Au-covered substrates, the sizes of the Au catalysts were expected to be the same. The obtained 1D ZnO in different sizes indicates the Zn/ZnO_x vapor pressure is important in determining their morphologies. That is the reason why reports with the Zn metal as a source material had different results in nanowires [5] or in nanorods [3, 4]. The other evidence is that the larger sizes of the 1D ZnO will form the hexagonal shape, which will be explained at the next section about the bilayer catalysts.

Before bilayer catalysts with Sn at the top layer were investigated, the effects of unilayer Al-, Ni-, In-, and Sn-sputtered catalysts on the growth of 1D ZnO were tested. Figure 3 displays surface morphologies of ZnO grown at 700°C for 2 h on (a) Al-, (b) Ni-, (c) In-, and (d) Sn-coated substrates by thermal evaporation with a Zn mixture of Zn and ZnO in a weight ratio of 1 : 1. Large-grained ZnO layers were produced at the Al- and In-covered substrates. Nanopencils were obtained on the Ni-coated substrates. ZnO nanowires with a diameter of 20~100 nm were obtained on the Sn-coated substrates. Among catalysts of Au, Al, Ni, In, and Sn, the sputtering coated Au and Sn films were the two available catalysts for our system to generate 1D ZnO. Sn droplets were observed at the tips of the grown 1D ZnO when Sn or SnO₂ was used in a mixture with ZnO powders for an evaporation source [13, 15]. In this work, Sn was directly deposited on substrates, and the grown 1D ZnO had no liquid droplets on its tips.

3.2. Growth of ZnO on Bilayer Catalyst-Covered Substrates. The bilayer catalysts sputtered on substrates for the growth of 1D ZnO included Sn/Au, Sn/Al, Sn/Ni, and Sn/In. Figure 4 shows surface morphologies of ZnO grown at 700°C for 2 h on (a) untreated, (b) 700°C preannealed, and (c) 850°C preannealed Sn/Au substrates by thermal evaporation with

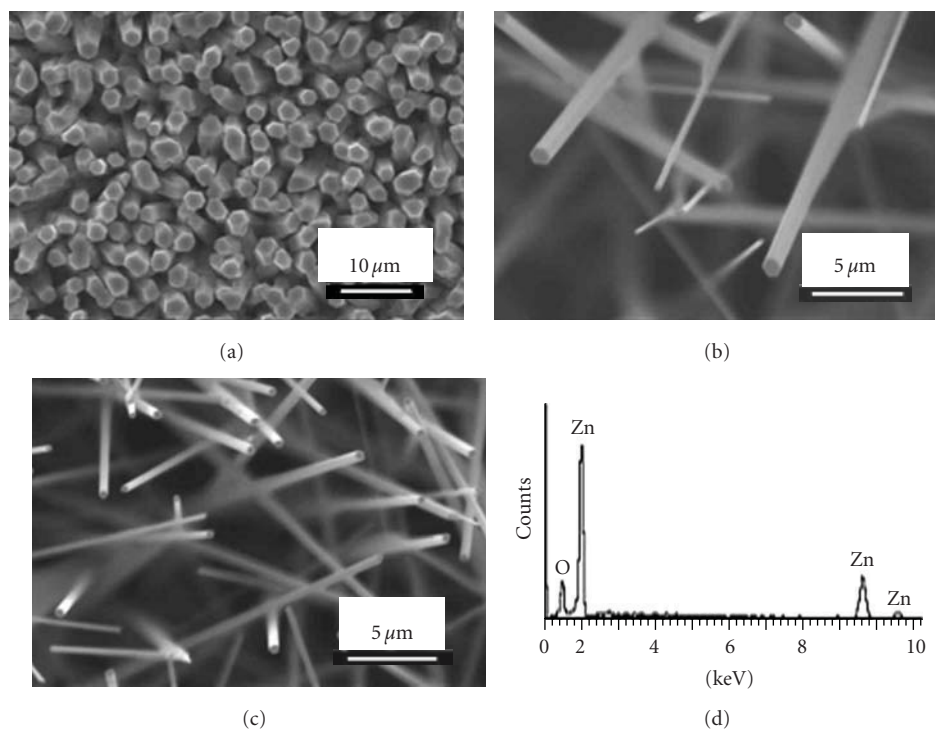


FIGURE 7: Surface morphologies of ZnO grown at 700°C for 2 h on (a) untreated, (b) 700°C preannealed, and (c) 850°C preannealed Sn/In substrates by thermal evaporation with a Zn mixture of Zn and ZnO in a weight ratio of 1 : 1. (d) EDS spectrum of the SEM image in (c).

a Zn mixture of Zn and ZnO in a weight ratio of 1 : 1. ZnO nanowires with sharp tips of ~ 50 nm were obtained on untreated substrates. After preannealing, the grown ZnO rods had a hexagonal tip. 1D ZnO had sizes of 0.8–2.0 μm and 1.0–2.0 μm in diameter after they were grown on the 700°C and 850°C preannealed substrates, respectively. The diameters of 1D ZnO became larger, and the shape changed to microrods after preannealing at higher temperatures. For the Sn/Au system as an example (Figure 4), different preannealing treatments have led to different ZnO sizes. The untreated Sn/Au system can produce the ZnO rods with a uniform diameter, while the system preannealed at 850°C obtained hexagonal rods with different sizes. Different preannealing treatments on the bilayer catalyst-covered substrates are to change the size, shape, or surface energy of catalysts by alloying, interdiffusion, or reactions of the bilayer components.

Figure 5 shows surface morphologies of ZnO grown at 700°C for 2 h on (a) untreated, (b) 700°C preannealed, and (c) 850°C preannealed Sn/Al substrates by thermal evaporation with a Zn mixture of Zn and ZnO in a weight ratio of 1 : 1. ZnO microrods with a diameter of 1.0–2.0 μm had a hexagonal shape at its cross-section. The 700°C and 850°C preannealed substrates grew nanorods of 150–500 nm and 150–300 nm in diameter, respectively. Figure 5(d) displays the X-ray diffraction patterns of ZnO nanorods grown on three types of Sn/Al substrates. All the three typed 1D ZnO with a wurtzite structure had the preferred growth direction of [0002].

Figure 6 shows surface morphologies of ZnO grown at 700°C for 2 h on (a) untreated, (b) 700°C preannealed, and (c) 850°C preannealed Sn/Ni substrates by thermal evaporation with a Zn mixture of Zn and ZnO in a weight ratio of 1 : 1. 1D ZnO had dimensions of 1.0–2.5 μm , 100–200 nm, and 70–150 nm for those grown on the untreated, 700°C preannealed, and 850°C preannealed substrates covered with Sn/Ni catalysts, respectively. The dimension of 1D ZnO reduced with a preannealing treatment at higher temperatures. The smaller diameters after preannealing at higher temperatures for the Sn/Ni system are different for the Sn/Au system in Figure 4. The major differences of these two systems are the capabilities of (1) forming spheroids for Au and Ni and (2) forming liquid catalyst templates or making templates as spheroids after preannealing. In the bilayer Sn/Ni system, the formation of intermediate compounds retards the formation of liquid templates and leads to the Sn-Ni liquid constricted on the Ni-based catalyst layers, which might contribute to the smaller-diameter rods. Basically, the comparative experiments indicate that the surface energy and the shape of bilayer templates will be changed for the different alloy systems. By adjusting the surface energy of templates *via* the manipulation of solubility of the second element in the ZnO-grown catalysts can modify the size of ZnO nanorods.

Figure 7 shows surface morphologies of ZnO grown at 700°C for 2 h on (a) untreated, (b) 700°C preannealed, and (c) 850°C preannealed Sn/In substrates by thermal evaporation with a Zn mixture of Zn and ZnO in a weight

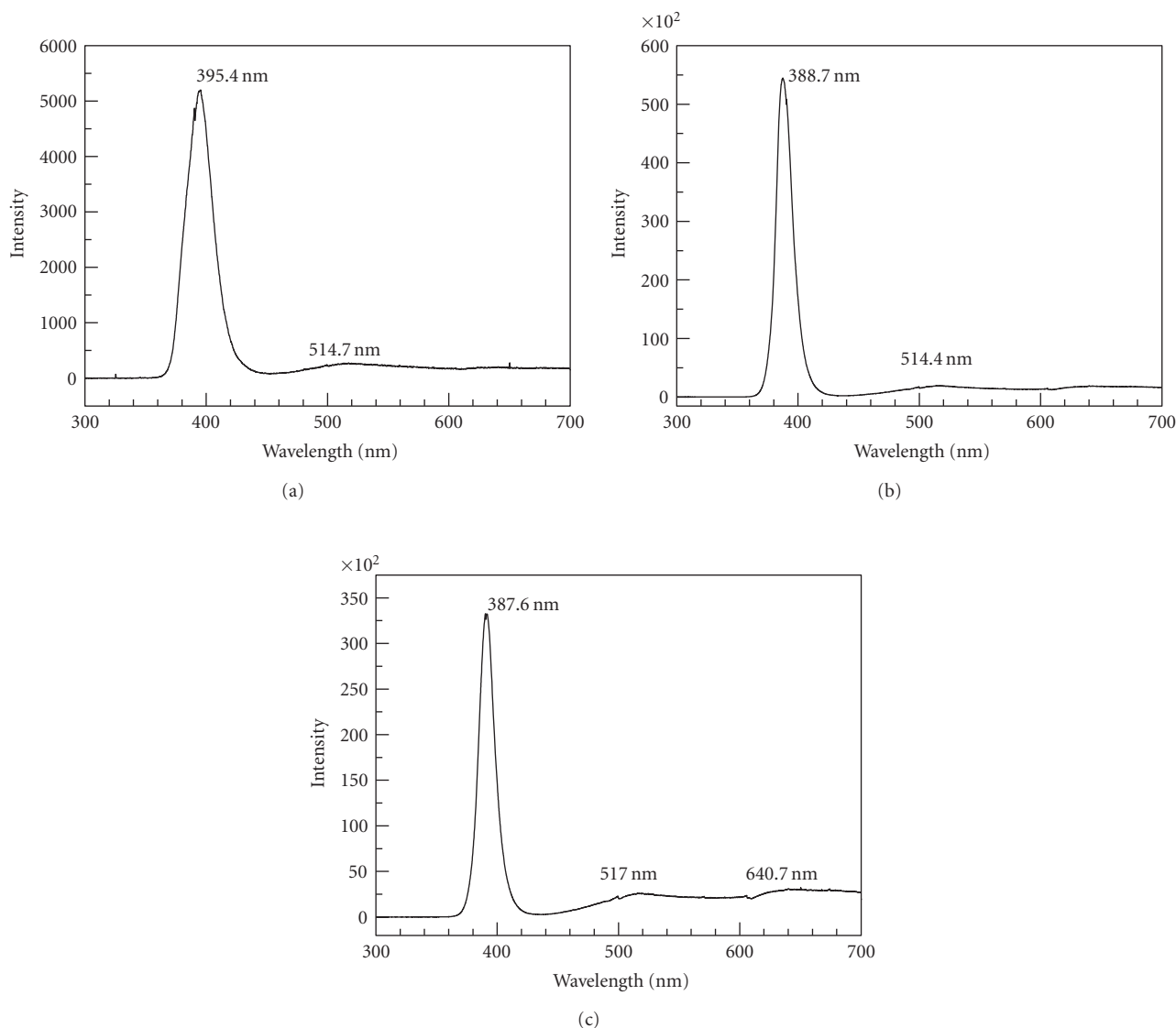


FIGURE 8: Photoluminescence spectra of ZnO grown at 700°C for 2 h on (a) untreated, (b) 700°C preannealed, and (c) 850°C preannealed Sn/Al substrates by thermal evaporation with a Zn mixture of Zn and ZnO in a weight ratio of 1 : 1.

ratio of 1:1. 1D ZnO had dimensions of 1.5–2.0 μm , bimodal 0.7 μm /70 nm, and 80–400 nm for those grown on the untreated, 700°C preannealed, and 850°C preannealed substrates covered with Sn/In catalysts, respectively. The dimensions of 1D ZnO after preannealing had a larger variation. The 700°C preannealed substrates led to two types of dimensions of 0.7 μm and 70 nm. The dimension of 1D ZnO grown on the 850°C preannealed substrates ranged between 80 nm and 400 nm. Therefore, the substrates covered with the bilayer Sn/In catalysts were not suitable for growing 1D ZnO rods with a uniform size. Figure 7(d) shows the EDS spectrum of the 1D ZnO in Figure 7(c). Only Zn and O were detected without other impurities.

Figure 8 displays the room-temperature photoluminescence spectra of ZnO grown at 700°C for 2 h on (a) untreated, (b) 700°C preannealed, and (c) 850°C preannealed Sn/Al substrates by thermal evaporation with a Zn

mixture of Zn and ZnO in a weight ratio of 1 : 1. There are two stronger peaks. One sharp and strong photoemission peak locates at 387–395 nm (3.20–3.14 eV), which corresponds to the near-band-edge peak. Full width at half maxima (FWHM) values of 210, 126, and 123 meV for the excitonic emissions were obtained from ZnO on the untreated, 700°C preannealed, and 850°C preannealed Sn/Al substrates, respectively. Small FWHM values indicate the good crystallinity for those rods after preannealing. Furthermore, a broad and weak green emission centered at 514–517 nm (2.41–2.40 eV) was observed, which was defect related.

Preannealing on the Sn/Au-covered substrates led to the micrometer-sized ZnO rods with a hexagonal shape, while the rods obtained from the Sn/Al-, Sn/Ni-, and Sn/In-coated ones had smaller diameters. Furthermore, most of the ZnO rods grown on the bilayer catalyst-covered substrates

displayed a hexagonal cross-section without the evidence of catalyst droplets at their ends, which indicates that a vapor-solid growth mechanism is preferred. The changes in the sizes of ZnO rods with the different preannealing treatments on different catalyst systems indicate the formation of different sizes of catalyst templates due to the considerations of the surface/interfacial energy. These different-sized templates provide the sites for the catalyst-confined growth *via* the VS growth mechanism. A similar approach to control diameter has been observed in the unilayer Au catalyst-coated system by varying the Au layer thickness [19]. About the considerations of surface/interfacial energy, Cai et al. observed that $\langle 111 \rangle$ is the most preferable growth direction for ZnSe nanowires with larger diameters of 17 nm; that is, the growth direction is mainly determined by the size of the catalyst [20]. His considerations have been based upon the principle that the growth of ZnSe nanowires is driven by the minimum state of the total system energy.

Our ZnO rods have a vapor-solid growth mechanism, different from those with the Sn droplets on the tips [13, 15]. In our experiments, the supplied oxygen and the vaporizing zinc vapor are participating in the growth of 1D ZnO at the growth temperature of 700°C. Because there is no solubility between Zn and Sn from the binary Zn-Sn phase diagram, the Zn vapor after adsorbed on the bilayer Sn/Au catalysts does not dissolve into Sn-Au melt. The adsorbed Zn adatoms will combine with oxygen to form the Zn-O molecules on catalysts. For the reason of considering surface/interfacial energy, the accumulation and stacking of Zn-O molecules on the liquid templates will form the hexagonal plates to obtain the 1D ZnO with a $[0001]$ growth orientation. This orientation is favored when the liquid templates have larger sizes [20]. To support in lowering the surface/interfacial energies, the liquid Sn-Au templates should adjust to provide a surface for the hexagonal nuclei by forming a ZnO/Sn-Au interface to lower the total free energy. The growth of $[0001]$ -oriented ZnO rods on the Sn droplets has shown the interfacial orientation relationship of $(020)_{\text{Sn}} \parallel (0001)_{\text{ZnO}}$ and $[\bar{1}01]_{\text{Sn}} // [2\bar{1}\bar{1}0]_{\text{ZnO}}$ between ZnO rod and Sn particle [14]. The hexagon in cross-section is preferred due to the lattice match between $(020)_{\text{Sn}}$ and $(0001)_{\text{ZnO}}$. Our liquid Sn-Au catalyst templates might provide a similar role to obtain hexagonal ZnO rods.

The approach of using the bilayer catalysts to obtain one-dimensional ZnO with the method of thermal evaporation and oxidation has demonstrated the advantages of adjusting the dimension and growth micromechanism of ZnO rods. Further investigations and understanding for catalysts in the alloy state are needed in order to have a better control in growing the ZnO nanorods.

4. Conclusions

Hexagonal ZnO rods have been successfully grown at 700°C on the untreated or the preannealed bilayer catalyst-covered substrates. The bilayer catalysts fabricated by the d.c. sputtering includes the Sn (top)/Au(bottom), Sn/Al, Sn/Ni, and Sn/In systems. The preannealing treatment refers

to the annealing of catalysts at 700°C or 800°C in the gas mixture of hydrogen and nitrogen before the substrates are put into the other furnace to grow 1D ZnO. The bilayer catalyst method has helped us to face growth micromechanism in order to distinguish the different sizes of rods at different catalyst systems and different process conditions. The growth behaviors of Sn-based catalyst systems are strongly affected by the second component located as the bottom layer. The size of the 1D ZnO from the Sn/Au system becomes larger after preannealing, but it becomes smaller for other catalyst systems. The different behaviors are caused by interdiffusion, reactions, surface tension, and the ability of making catalyst spheroids. The smaller-diameter ZnO nanorods with a hexagonal cross-section at the size of 70–150 nm were obtained from the Sn/Ni catalyst systems preannealed at 850°C.

Acknowledgment

The authors acknowledge the financial support by National Science Council under Grant no. 99-2221-E-011-045.

References

- [1] Z. L. Wang, X. Y. Kong, Y. Ding et al., "Semiconducting and piezoelectric oxide nanostructures induced by polar surfaces," *Advanced Functional Materials*, vol. 14, no. 10, pp. 943–956, 2004.
- [2] Z. L. Wang, "ZnO nanowire and nanobelt platform for nanotechnology," *Materials Science & Engineering R*, vol. 64, no. 3–4, pp. 33–71, 2009.
- [3] A. Umar, B. Karunakaran, E. K. Suh, and Y. B. Hahn, "Structural and optical properties of single-crystalline ZnO nanorods grown on silicon by thermal evaporation," *Nanotechnology*, vol. 17, no. 16, pp. 4072–4077, 2006.
- [4] G. Shen, Y. Bando, B. Liu, D. Golberg, and C. J. Lee, "Characterization and field-emission properties of vertically aligned ZnO nanonails and nanopencils fabricated by a modified thermal-evaporation process," *Advanced Functional Materials*, vol. 16, no. 3, pp. 410–416, 2006.
- [5] J. Park, H. H. Choi, K. Siebein, and R. K. Singh, "Two-step evaporation process for formation of aligned zinc oxide nanowires," *Journal of Crystal Growth*, vol. 258, no. 3–4, pp. 342–348, 2003.
- [6] B. Xiang, P. Wang, X. Zhang et al., "Rational synthesis of p-type zinc oxide nanowire arrays using simple chemical vapor deposition," *Nano Letters*, vol. 7, no. 2, pp. 323–328, 2007.
- [7] X. Wang, C. J. Summers, and Z. L. Wang, "Large-scale hexagonal-patterned growth of aligned ZnO nanorods for nano-optoelectronics and nanosensor arrays," *Nano Letters*, vol. 4, no. 3, pp. 423–426, 2004.
- [8] Y. X. Chen, M. Lewis, and W. L. Zhou, "Zno nanostructures fabricated through a double-tube vapor-phase transport synthesis," *Journal of Crystal Growth*, vol. 282, no. 1–2, pp. 85–93, 2005.
- [9] W. I. Park, G. C. Yi, M. Kim, and S. J. Pennycook, "ZnO nanoneedles grown vertically on Si substrates by non-catalytic vapor-phase epitaxy," *Advanced Materials*, vol. 14, no. 24, pp. 1841–1843, 2002.
- [10] M. C. Jeong, B. Y. Oh, W. Lee, and J. M. Myoung, "Comparative study on the growth characteristics of ZnO nanowires

- and thin films by metalorganic chemical vapor deposition (MOCVD)," *Journal of Crystal Growth*, vol. 268, no. 1-2, pp. 149–154, 2004.
- [11] H. J. Fan, F. Fleischer, W. Lee et al., "Patterned growth of aligned ZnO nanowire arrays on sapphire and GaN layers," *Superlattices and Microstructures*, vol. 36, no. 1–3, pp. 95–105, 2004.
- [12] G. D. Yuan, W. J. Zhang, J. S. Jie et al., "p-type ZnO nanowire arrays," *Nano Letters*, vol. 8, no. 8, pp. 2591–2597, 2008.
- [13] P. X. Gao, Y. Ding, and Z. L. Wang, "Crystallographic orientation-aligned ZnO nanorods grown by a tin catalyst," *Nano Letters*, vol. 3, no. 3, pp. 1315–1320, 2003.
- [14] Y. Ding, P. X. Gao, and Z. L. Wang, "Catalyst-nanostructure interfacial lattice mismatch in determining the shape of VLS grown nanowires and nanobelts: a case of Sn/ZnO," *Journal of the American Chemical Society*, vol. 126, no. 7, pp. 2066–2072, 2004.
- [15] J. Zhang, Y. Yang, F. Jiang, B. Xu, and J. Li, "Controlled growth of semiconducting oxides hierarchical nanostructures," *Journal of Solid State Chemistry*, vol. 178, no. 9, pp. 2804–2810, 2005.
- [16] J. X. Wang, S. S. Xie, H. J. Yuan et al., "Synthesis, structure, and photoluminescence of Zn₂SnO₄ single-crystal nanobelts and nanorings," *Solid State Communications*, vol. 131, no. 7, pp. 435–440, 2004.
- [17] J. X. Wang, S. S. Xie, Y. Gao et al., "Growth and characterization of axially periodic Zn₂SnO₄ (ZTO) nanostructures," *Journal of Crystal Growth*, vol. 267, no. 1-2, pp. 177–183, 2004.
- [18] D. H. Kuo and B. J. Chang, "From preannealing of bilayer catalysts to explore the growth micromechanisms of ZnO nanorods," *Crystal Growth & Design*, vol. 10, no. 2, pp. 977–982, 2010.
- [19] M. H. Huang, Y. Wu, H. Feick, N. Tran, E. Weber, and P. Yang, "Catalytic growth of zinc oxide nanowires by vapor transport," *Advanced Materials*, vol. 13, no. 2, pp. 113–116, 2001.
- [20] Y. Cai, S. K. Chan, I. K. Sou, Y. F. Chan, D. S. Su, and N. Wang, "The size-dependent growth direction of ZnSe nanowires," *Advanced Materials*, vol. 18, no. 1, pp. 109–114, 2006.

Research Article

A Facile Method for Preparing Transparent, Conductive, and Paper-Like Silver Nanowire Films

Yajie Wang, Tao Feng, Kai Wang, Min Qian, Yiwei Chen, and Zhuo Sun

Department of Physics, Engineering Research Center for Nanophotonics and Advanced Instrument, Ministry of Education, East China Normal University, Shanghai 200062, China

Correspondence should be addressed to Tao Feng, tfeng@phy.ecnu.edu.cn

Received 18 April 2011; Accepted 1 July 2011

Academic Editor: Yanqiu Zhu

Copyright © 2011 Yajie Wang et al. This is an open access article distributed under the Creative Commons Attribution License, which permits unrestricted use, distribution, and reproduction in any medium, provided the original work is properly cited.

Transparent, conductive, and flexible silver nanowire (AgNW) films have been fabricated by a facile two-step method. Firstly, the well-dispersed AgNW suspension is vacuum filtered using mixed esters of cellulose (MCE) membranes as filters. Then, the AgNW-MCE films are treated with acetone vapor. After the infiltration of acetone vapor, the white and porous MCE membranes change into transparent and pore-free, and AgNW-MCE films are obtained with extraordinary optical, conductive, and mechanical properties. An optimal result is obtained with transmittance of 85% at 550 nm and sheet resistance about 50 Ohm/sq. The flexibility of AgNW-MCE films is remarkable, which is comparable to that of the AgNW film on flexible polyethylene terephthalate (PET). More important, AgNW-MCE films show an excellent adhesion to the substrate, which causes a stable electrical conductivity even after scotch tape test and finger friction test. As a result of improved adhesion to the substrate, the sheet resistance of AgNW-MCE films is about 20% smaller than that of AgNW-PET films.

1. Introduction

Nowadays, as optoelectronic technology will move toward flexible and paper-like devices, great efforts have been made to search for suitable electrode materials which can be formed into films at low temperature and used in such applications. As we all know, indium tin oxide (ITO) as the most important transparent and conductive film (TCF) has been widely used in optoelectronics for 50 years, but it is completely unsuitable to flexible devices because of its brittle nature [1]. To our excitement, many promising materials have been emerging such as graphenes, carbon nanotubes, and metal nanowires [2–6]. For these materials, one of the most important advantages is that the flexibility does not come at the cost of performance in terms of sheet resistance and transparency [7]. Among these materials, random networks of AgNW, owing to its highest electrical conductivity and optical transparency, are the most promising replacement for ITO [4–6]. More recently, flexible AgNW electrodes have been fabricated and successfully used in organic solar cells [8] and organic light emitting devices [9],

and the performance of the electrode in terms of sheet resistance and transparency can match ITO. However, to be used in optoelectronic devices, the AgNW film should have a strong adhesion to the substrate, which is hard to achieve while AgNW films deposited on plastic substrate without further treatments [4]. Although some methods including encapsulation [5] and burying AgNW networks [9] have been taken to resolve the adhesion issue, both methods need more complicated steps after AgNW films prepared. So, a simple method to prepare flexible AgNW films with good adhesion is still urgently required.

Vacuum filtration is a low-temperature process in film production, which affords films with some advantages such as surface uniformity, high electric conductivity, and controllable thickness. Therefore, it has been widely used for fabricating AgNW films [4, 5]. To get transparent electrodes, AgNW films need to be transferred to a transparent substrate after deposited on the filter, but this process is usually complicated. In this paper, we use the hot block technique [10] to prepare transparent, conductive, and paper-like AgNW-MCE films with outstanding adhesion. As the mixed

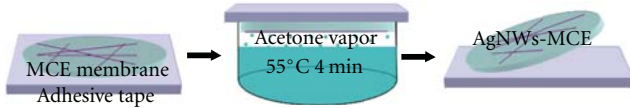


FIGURE 1: Schematic illustration of the preparing AgNW-MCE films process.

esters of cellulose (MCE) membrane, used as the filter, can become transparent and pore-free [11], the transfer process would be eliminated.

2. Experimental

Silver nanowires (average diameter of 90 nm, average length of 10 μm) were purchased from Blue Nano as suspensions with a concentration of 10 mg/mL in ethanol. The dispersion was further diluted down to 0.027 mg/mL with deionized water and then sonicated for 20 min. AgNW films were prepared by vacuum filtration with various volumes of nanowire solution using porous MCE membranes (0.45 μm , 47 mm) and then dried at room temperature.

2.1. Preparation of AgNW-MCE Films. The deposited film with AgNWs face up was placed on adhesive tapes and treated with acetone vapor for 4 min. Then, the MCE membrane became transparent and pore-free. MCE membrane was peeled off from the tape after it was dried at room temperature. The entire process is very simple and just takes only a few minutes. Adhesive tape was used necessarily to prevent potential curling and minimize the shrinkage of MCE membrane [10]. Schematic representation of preparing AgNW-MCE films is illustrated in Figure 1.

2.2. Preparation of AgNW-PET Films. The deposited film was placed on the PET with the AgNWs in contact with the PET and then placed on a flat plate while heated at 100°C on the bottom and pressed with a pressure of 0.6 MPa on the top for 20 min. MCE membrane was removed by treatment with acetone vapor for 4 min and subsequent acetone liquid baths for 20 min, and then, AgNW films were transferred to PET [12].

2.3. Characterization of Samples. The morphology of AgNW-MCE films and AgNW-PET films was characterized by SEM using S-4700. Sheet resistance (R_s) of these films was tested by an RS-8 4-point probes resistivity measurement system. The optical transmittance of these films was measured by a U-3900 UV-VIS spectrophotometer, with a transparent MCE membrane as reference.

For adhesion and flexibility comparison, the AgNW-MCE film and the AgNW-PET film prepared with the same volume (6 mL) were pressed under a pressure of 0.6 MPa for 20 min. Then, the adhesion test of those films was performed using a Scotch tape [6]. Tapes were put gently on the sample surface and pressed under a pressure of 0.6 MPa for 10 sec then were peeled off.

3. Results and Discussion

As seen in the photographs shown in Figure 2, the color of the MCE membrane is changed from white (Figure 2(a)) to transparent (Figure 2(b)). After treated with acetone vapor, the transmittance of the MCE membrane is over 90%, which is high enough as a matrix of TCF. When infiltrated with acetone vapor, the MCE membrane became viscous, so its pores were melted [11]. As is shown in Figures 3(a) and 3(b), there is no pore in the SEM image of AgNW-MCE films, and the morphology is similar to that of AgNW-PET films (Figure 3(c)). It is clear from Figure 3(d) that the MCE membrane is porous before treated with acetone vapor. The SEM image in Figure 3(a) shows networks of nanowires with big holes that are above percolation. The percolation problem, which could be detrimental to some electrode applications, can be overcome effectively by incorporating other materials into AgNW networks, such as CNTs, PEDOT, and graphenes.

We prepared samples with various densities of silver nanowires, using 1.5 mL, 2 mL, 2.5 mL, 3 mL, 3.5 mL, 4 mL, 5 mL, and 6 mL volume of previous nanowire solution separately. It is evident from Figure 4(a) that optical transmittance decreases with increasing of AgNWs density. The sample using 1.5 mL of starting solution has the highest transmittance about 88%. On the other hand, the R_s increases as the density increases, as shown in Figure 4(b). AgNW-MCE films with R_s around 50 Ohm/sq and $\sim 85\%$ optical transmittance (at 550 nm) were produced, which is very close to the performance of the ITO on PET for flexible optoelectronic devices. The properties of AgNW-MCE films show that they are suitable for the use of touch screen panels, electrowetting display, and liquid crystal display [13, 14]. We have to note that all the R_s values of AgNW-MCE films, shown in Figure 4(b), were obtained after the film pressed under the pressure of 10 MPa, resulting in the R_s of the film significantly decreasing by about 50%. We attributed the decrease to cutting down the contact resistance between AgNWs. The mechanical pressing method, reported by Hu et al. [6], is an available approach to reduce the junction resistance of AgNWs. They have reduced the R_s of the AgNW film from several hundreds ohms/sq to several tens ohms/sq after pressed up to 81 GPa pressure. According to that result, we believe that the conductivity of AgNW-MCE films can be considerably improved by pressing films under a higher pressure.

For AgNW-MCE films, the mechanical robustness against adhesion, friction, and bending is excellent. The equivalence thickness of the AgNW film used for the adhesion and flexibility test is 300 nm (for the deposition density is 130 mg/m²) [4]. It is notable in Figure 4(c) that there is no obvious increase in R_s of AgNW-MCE films after tape test and finger friction. In contrast, the conductivity of AgNW-PET films was nearly lost while it was peeled off from the tape and rubbed against by finger. From the inset figure of Figure 4(c), it was noticeable that the AgNWs on PET were mostly peeled off (left 2) or rubbed away (left 3), while AgNW-MCE films were without any visible change. The reason for the outstanding adhesion is as follows. (1) While treated with acetone vapor, the MCE membrane became sticky. As a result,

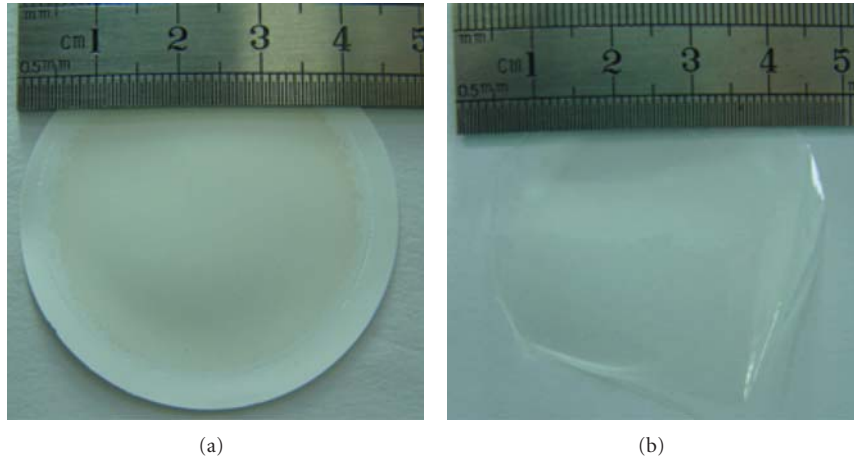


FIGURE 2: Photographs of a AgNW-MCE film (a) before and (b) after treated with acetone vapor.

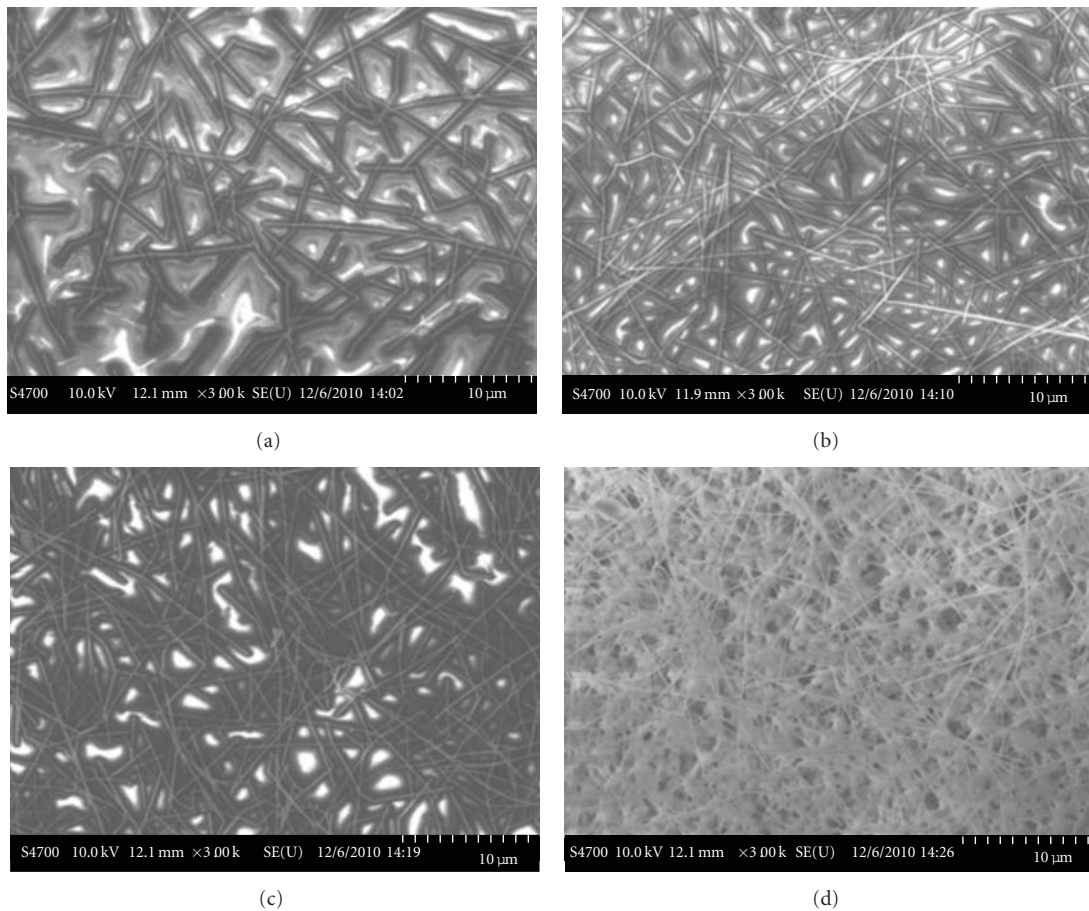


FIGURE 3: SEM images of AgNW-MCE films after treated with acetone vapor prepared using (a) 2 mL and (b) 6 mL volume of nanowire solution. (c) AgNW-PET films using 6 mL volume of nanowire solution. (d) AgNW-MCE films (6 mL) before treated with acetone vapor.

AgNWs were stuck to the MCE membrane. (2) The pore were melted after treated with acetone vapor; meanwhile, some ends of AgNWs were buried in the MCE membrane [10]. During the flexibility testing, as shown in Figure 4(d), the conductivity is nearly invariant while bending with

the AgNW-MCE film in compress and tension. The films were bent to a curvature of 1-2 mm (the inset figure of Figure 4(d)). If noting the difference of R_s between AgNW-MCE films and AgNW-PET films, as shown in Figure 4(d), we can see the R_s of AgNW-MCE films is about 20% lower

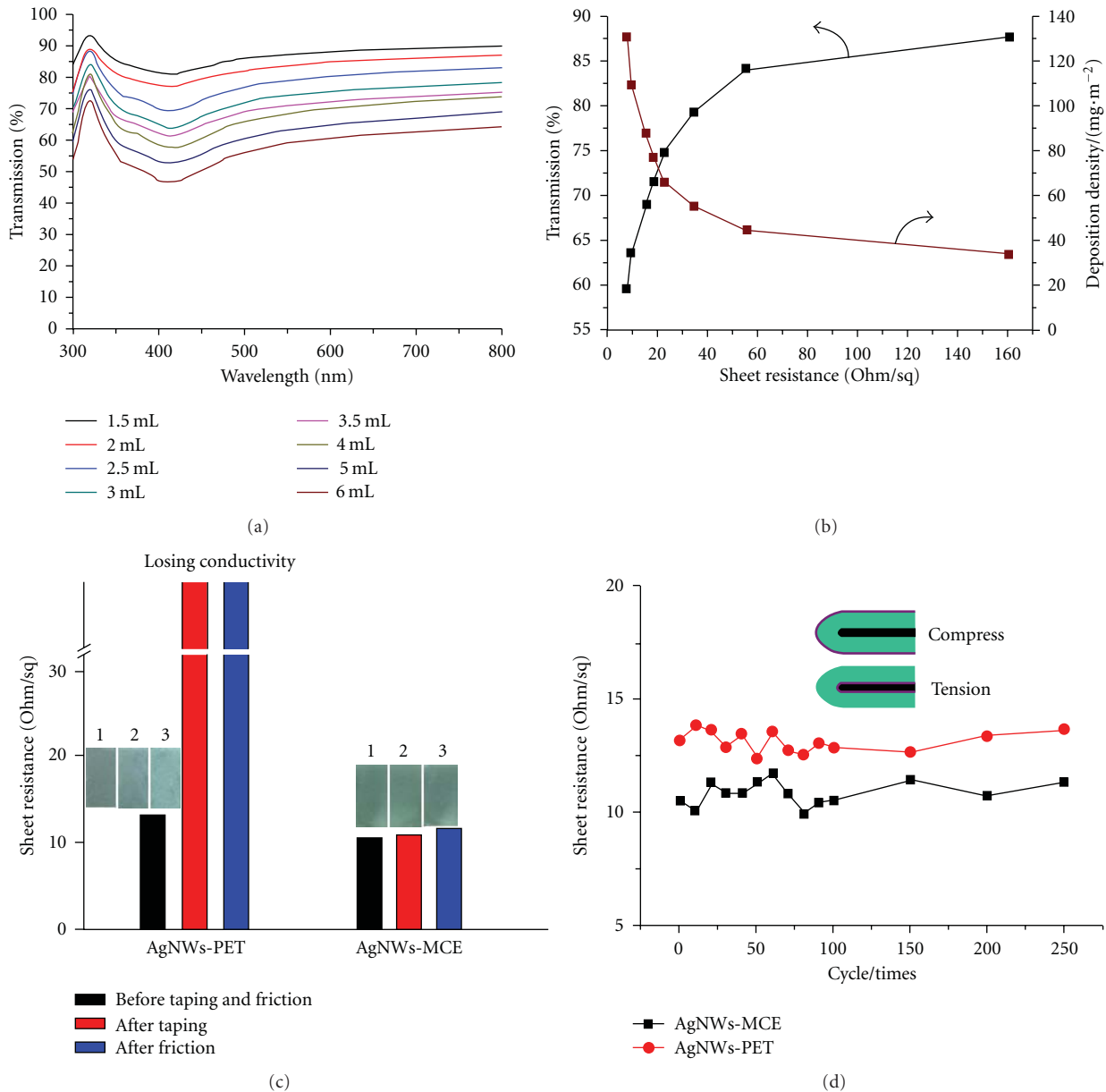


FIGURE 4: (a) Optical transmittance of AgNW-MCE films. (b) R_s versus transmission (at 550 nm) and deposition density of AgNWs-MCE films. (c) The R_s of AgNW-MCE and AgNW-PET films before and after taping and friction test, respectively. The inset photos are AgNW-PET films (left) and AgNW-MCE films (right) before (1) and after destroyed by tape adhesion (2) and finger friction (3). (d) The change in resistance of AgNW-MCE and AgNW-PET films after cycles of folding up.

than that of AgNW-PET films. That is possible because the contact between AgNWs to the substrate improved, which improves the morphology and the electrical contacts between wires [6].

4. Conclusions

In summary, we have demonstrated a simple, rapid, and low-cost method to fabricate transparent AgNW films. Unlike the AgNW film on PET with poor adhesion, the AgNW film prepared by this method adheres strongly on the MCE substrate, which causes a stable conductivity even if the film

is subjected to bending. We have obtained AgNW-MCE films with R_s around 50 Ohm/sq and ~85% visible transmittance, which is comparable to ITO on PET. As mentioned above, we believe that AgNW-MCE films can be widely used in flexible electronic and optoelectronic devices.

Acknowledgments

This work was supported by the Rising Star Program of Shanghai under Grant no. 07QA14019, Shanghai Talent Development Fund, and the Fundamental Research Funds for the Central Universities.

References

- [1] Z. Chen, B. Cotterell, and W. Wang, "The fracture of brittle thin films on compliant substrates in flexible displays," *Engineering Fracture Mechanics*, vol. 69, no. 5, pp. 597–603, 2002.
- [2] X. Wang, L. Zhi, and K. Müllen, "Transparent, conductive graphene electrodes for dye-sensitized solar cells," *Nano Letters*, vol. 8, no. 1, pp. 323–327, 2008.
- [3] L. B. Hu, W. Yuan, P. Brochu, G. Gruner, and Q. Pei, "Highly stretchable, conductive, and transparent nanotube thin films," *Applied Physics Letters*, vol. 94, no. 16, Article ID 161108, 3 pages, 2009.
- [4] S. De, T. M. Higgins, P. E. Lyons et al., "Silver nanowire networks as flexible, transparent, conducting films: extremely high DC to optical conductivity ratios," *ACS Nano*, vol. 3, no. 7, pp. 1767–1774, 2009.
- [5] A. R. Madaria, A. Kumar, F. N. Ishikawa, and C. Zhou, "Uniform, highly conductive, and patterned transparent films of a percolating silver nanowire network on rigid and flexible substrates using a dry transfer technique," *Nano Research*, vol. 3, no. 8, pp. 564–573, 2010.
- [6] L. B. Hu, H. S. Kim, J. Y. Lee, P. Peumans, and Y. Cui, "Scalable coating and properties of transparent, flexible, silver nanowire electrodes," *ACS Nano*, vol. 4, no. 5, pp. 2955–2963, 2010.
- [7] P. J. King, U. Khan, M. Lotya, S. De, and J. N. Coleman, "Improvement of transparent conducting nanotube films by addition of small quantities of graphene," *ACS Nano*, vol. 4, no. 7, pp. 4238–4246, 2010.
- [8] J. Y. Lee, S. T. Connor, Y. Cui, and P. Peumans, "Semitransparent organic photovoltaic cells with laminated top electrode," *Nano Letters*, vol. 10, no. 4, pp. 1276–1279, 2010.
- [9] X. Y. Zeng, Q. K. Zhang, R. M. Yu, and C. Z. Lu, "A new transparent conductor: silver nanowire film buried at the surface of a transparent polymer," *Advanced Materials*, vol. 22, no. 40, pp. 4484–4488, 2010.
- [10] J. S. Webber, A. G. Czuharnich, and L. J. Carhart, "Performance of membrane filters used for TEM analysis of asbestos," *Journal of Occupational and Environmental Hygiene*, vol. 4, no. 10, pp. 780–789, 2007.
- [11] G. J. Burdett and A. P. Rood, "Membrane-filter, direct-transfer technique for the analysis of asbestos fibers or other inorganic particles by transmission electron microscopy," *Environmental Science and Technology*, vol. 17, no. 11, pp. 643–648, 1983.
- [12] Z. C. Wu, Z. H. Chen, X. Du et al., "Transparent, conductive carbon nanotube films," *Science*, vol. 305, no. 5688, pp. 1273–1276, 2004.
- [13] L. B. Hu, G. Gruner, J. Gong, C. J. Kim, and B. Hornbostel, "Electrowetting devices with transparent single-walled carbon nanotube electrodes," *Applied Physics Letters*, vol. 90, no. 9, Article ID 093124, 3 pages, 2007.
- [14] D. Hecht, L. B. Hu, and G. Grüner, "Conductivity scaling with bundle length and diameter in single walled carbon nanotube networks," *Applied Physics Letters*, vol. 89, no. 13, 3 pages, 2006.